

Institute of Environmental Sciences

**SEMINAR ON
TESTING SOLAR ENERGY MATERIALS
AND SYSTEMS**

DISTRIBUTION STATEMENT A

Approved for public release;
Distribution Unlimited



PROCEEDINGS

DEPARTMENT OF DEFENSE
PLASTICS TECHNICAL EVALUATION CENTER
ARRADCOM, DOVER, N. J. 07801

**Gaithersburg, Maryland
May 22-24, 1978**

19960220 132

PLASTIC 33801
33815

Date: 9/9/95 Time: 3:58:42PM

Page: 1 Document Name: untitled

DTIC DOES NOT HAVE THIS ITEM

-- 1 - AD NUMBER: D428653
-- 6 - UNCLASSIFIED TITLE: SEMINAR ON TESTING SOLAR ENERGY MATERIALS
AND SYSTEMS.
--11 - REPORT DATE: MAY 22, 1978
--12 - PAGINATION: 278P
--20 - REPORT CLASSIFICATION: UNCLASSIFIED
--21 - SUPPLEMENTARY NOTE: PROCEEDINGS: 'SEMINAR ON TESTING SOLAR
ENERGY MATERIALS AND SYSTEMS', 22-24 MAY 78, GAITHERSBURG, MD.
-- SPONSORED BY INSTITUTE OF ENVIRONMENTAL STUDIES. (SEE PL-33808 - PL-
33814).
--22 - LIMITATIONS (ALPHA): APPROVED FOR PUBLIC RELEASE; DISTRIBUTION
-- UNLIMITED. AVAILABILITY: THE INSTITUTE OF ENVIRONMENTAL SCIENCES,
940 EAST NORTHWEST HIGHWAY, MT. PROSPECT, IL. 60056.
--33 - LIMITATION CODES: 1 24

Institute of Environmental Sciences

**SEMINAR ON
TESTING SOLAR ENERGY MATERIALS
AND SYSTEMS**



PROCEEDINGS

Co-Sponsors:

National Bureau of Standards

Department of Energy

American Society for Testing Materials

Gaithersburg, Maryland

May 22-24, 1978

Copyright 1978 by the Institute of Environmental Sciences.

All rights reserved. No part of this work may be reproduced or transmitted in any form or by any means, electronic or mechanical, including photocopying and recording, or by any information storage or retrieval system, without permission in writing from the publisher.

Copyright is not claimed in any portion of this work written by a United States Government employee as a part of his official duties.

Printed in the United States of America.

Library of Congress Catalog Card Number: 62-38584

ISBN: 0-915414-56-2

Additional copies of this publication are available from:

THE INSTITUTE OF ENVIRONMENTAL SCIENCES
940 EAST NORTHWEST HIGHWAY
MT. PROSPECT, IL 60056

\$ 22.00

Table of Contents

Page

PROBLEMS IN SOLAR TESTING - PHOTOVOLTAICS

ENVIRONMENTAL TESTING OF FLAT PLATE SOLAR CELL MODULES	1
- L. Dumas, A. Hoffman and J. Griffith, Jet Propulsion Laboratory	
SANDIA'S PHOTOVOLTAIC TEST EXPERIENCE.	12
- Jerry L. Watkins, Sandia Laboratories	
A LIFE PREDICTION METHODOLOGY FOR ENCAPSULATED SOLAR CELLS	18
- Clifford D. Coulbert, Jet Propulsion Laboratory	
MEASUREMENT REQUIREMENTS AND TECHNIQUES FOR DEGRADATION STUDIES AND LIFETIME PREDICTION TESTING OF PHOTOVOLTAIC MODULES.	24
- G. T. Noel, F. A. Sliemers, G. C. Derringer, V. E. Wood, K. E. Wilkes, G. B. Gaines, and D. C. Carmichael, Battelle Columbus Laboratories	
AN APPROACH FOR DEVELOPMENT OF PERFORMANCE CRITERIA AND TEST STANDARDS IN PHOTOVOLTAICS.	30
- Gary Nuss, Solar Energy Research Institute	

PROBLEMS IN SOLAR TESTING - THERMAL POWER

CONCENTRATING SOLAR COLLECTOR TEST RESULTS FROM DOE/SANDIA COLLECTOR MODULE TEST FACILITY.	34
- Vernon E. Dudley, EG&G, Inc. Robert M. Workhoven, Sandia Laboratories	
TESTING OF CENTRAL RECEIVER FOR CENTRAL THERMAL POWER SYSTEMS.	39
- R. P. Pauckert, R. D. Tobin, and J. M. Friefeld Rocketdyne Division, Rockwell International	
THE DOE 5 MW SOLAR THERMAL TEST FACILITY	45
- Larryl Matthews, Sandia Laboratories	
THE DEVELOPMENT OF THE ADVANCED COMPONENTS TEST FACILITY	50
- Ralph F. Altman and C. T. Brown, Georgia Institute of Technology	
WHITE SANDS SOLAR TEST FACILITY.	54
- Richard A. Hays, White Sands Missile Range	
SANDIA LABORATORIES' MIDTEMPERATURE SOLAR SYSTEMS TEST FACILITY.	58
- Robert M. Workhoven, Sandia Laboratories	
THE REAL TIME APERTURE FLUX SYSTEM AS PART OF THE SOLAR THERMAL TEST FACILITY.	63
- Dave B. Davis and Larryl K. Matthews, Sandia Laboratories	
DEVELOPMENT OF A DUAL-MEDIUM THERMAL STORAGE SYSTEM FOR SOLAR TURBO-ELECTRIC POWER GENERATION.	69
- G. R. Morgan, G. R. Schneider and W. Unterberg Rocketdyne Division, Rockwell International	

RADIATION MEASUREMENTS AND SPECTRUM DEFINITION

STATUS OF KNOWLEDGE OF THE EXTRATERRESTRIAL SOLAR "CONSTANT" AND SPECTRAL DISTRIBUTION	75
- R. C. Willson, Jet Propulsion Laboratory, California Institute of Technology	
SOLAR SPECTRAL IRRADIANCE AT GROUND LEVEL.	83
- Ann Thomas Mecherikunnel, NASA Goddard Space Flight Center Joseph C. Richmond, National Bureau of Standards	
INDOOR/OUTDOOR SOLAR ENERGY RADIOMETRIC INTERCOMPARISONS	108
- E. T. Neighbors, The Boeing Company	
THE NOAA/DOE SOLAR RADIATION FACILITY AND MEASUREMENT NETWORK.	112
- Edwin Flowers, NOAA/ERL-ARL	
SOLAR RADIATION DATA MODELING AND ITS ROLE IN SOLAR SYSTEM STUDIES	117
- Eldon C. Boes, Sandia Laboratories	

PROBLEMS IN SOLAR TESTING - OCEAN THERMAL

OTEC BIOFOULING AND CORROSION TESTING PROGRAM	125
- Eugene H. Kinelski, Division of Solar Technology, U. S. Department of Energy	
TESTING THE OTEC COLD WATER PIPE USING THE "DEEP OIL X-1" PLATFORM.	129
- Edward E. Horton and Leonardo Perez y Perez, Deep Oil Technology, Inc.	
J. Randolph Paulling, Jr., Dept. of Naval Architecture, University of California at Berkeley	
OCEAN THERMAL ENERGY CONVERSION (OTEC) POWER PLANT INSTRUMENTATION AND MEASUREMENT.	134
- Lloyd G. Lewis, Argonne National Laboratory	
OTEC-1 TEST CONDUCTOR PROGRAM	139
- P. Archbold, Technical Management	
J. O. Bates, ETEC	

PROBLEMS IN SOLAR TESTING - SOLAR HEATING AND COOLING

THE EFFICIENCY OF SOLAR ASSISTED HOT WATER SYSTEMS.	144
- John Herlihy, Dayton T. Brown, Inc.	
AIR COLLECTOR TESTING UTILIZING ASHRAE 93-77.	146
- Richard D. Whitaker and William T. Dokos, Desert Sunshine Exposure Tests, Inc.	
COST EFFECTIVE SOLAR COLLECTOR PERFORMANCE TESTING UNDER COMBINED INDOOR AND OUTDOOR CONDITIONS	152
- L. Harold Usher, Wyle Laboratories	
PROBLEMS IN COLLECTOR TESTING	156
- G. R. Mather and D. C. Beekley, Owens-Illinois, Inc.	
CORRELATION OF INSTANTANEOUS AND ALL-DAY THERMAL PERFORMANCE OF FLAT-PLAT SOLAR COLLECTORS. . .	159
- D. M. Deffenbaugh, Southwest Research Institute	

MATERIALS EVALUATION

SPECULAR REFLECTANCE LOSS OF SOLAR MIRRORS DUE TO DUST ACCUMULATION	164
- R. B. Pettit, J. M. Freese, D. E. Arvizu, Sandia Laboratories	
HELIOSTAT REFLECTIVITY VARIATIONS DUE TO DUST BUILDUP UNDER DESERT CONDITIONS	169
- J. B. Blackmon and M. Curcija, McDonnell Douglas Astronautics Company	
EXPOSURE TEST RESULTS FOR REFLECTIVE MATERIALS.	33812 184
- R. A. Rausch, Honeywell Inc.	
B. P. Gupta, Solar Energy Research Institute	
SPECULARITY MEASUREMENTS BY FOURIER TRANSFORM EXAMINATION	188
- H. L. Hampton, J. S. Hartman, M. A. Lind, Battelle Pacific Northwest Laboratories	
HIGH TEMPERATURE MATERIALS STUDY.	195
- Larryl Matthews and George P. Mulholland, Sandia Laboratories	
OPTICAL PROPERTIES OF MATERIALS UNDER SIMULATED OPERATING ENVIRONMENTS.	201
- Michael Ray Jacobson, Optical Sciences Center, University of Arizona	
PARAMETERS, MEASUREMENT AND CRITERIA OF SOLAR MATERIALS TESTING	206
- J. E. Gilligan, J. E. Brzuskiwicz and J. M. Madigan, IIT Research Institute	
SOLAR ENERGY SYSTEMS - SURVEY OF MATERIALS PERFORMANCE.	213
- L. F. Skoda and L. W. Masters, National Bureau of Standards	
DEGRADATION OF POLYMETHYLMETHACRYLATE BY RADIATION.	33813 218
- Mohamed Abouelezz and Larry Masters, National Bureau of Standards	
Paul Waters, American University	

COMPONENT TEST AND INSTRUMENTATION

SERI SOLAR ENERGY STANDARDS ACTIVITIES.	224
- Helen Barker, Jim Castle, Gordon Gross, Solar Energy Research Institute	
CAST ACRYLIC FRESNEL LENSES FOR SOLAR ENERGY CONCENTRATION.	33814 229
- Charles P. Lingle, Swedlow, Inc.	

SIMULATION OF TERRESTRIAL SOLAR RADIATION	234
- David Askin and Milton Resnick, ARRADCOM	
DATA ACQUISITION AND SIGNAL PROCESSING FOR A VERTICAL AXIS WIND ENERGY CONVERSION SYSTEM.	241
- B. Stiefeld and R. N. Tomlinson, Sandia Laboratories	
PHOTOTHERMAL CONVERSION SURFACE MEASUREMENTS USING PHOTOTHERMAL AND PHOTOTHERMAL SPECTROSCOPIES	245
- J. F. McClelland and R. N. Kniseley, Ames Laboratory	
ACTINOMETRIC MEASUREMENT OF SOLAR ULTRAVIOLET AND DEVELOPMENT OF A WEIGHTED SOLAR UV INTEGRAL	253
- Amitava Gupta and Clifford Coulbert, Jet Propulsion Laboratory	
THE NBS SELF-STUDY MANUAL ON OPTICAL RADIATION MEASUREMENTS	256
- Fred E. Nicodemus, National Bureau of Standards	
NBS CAPABILITIES FOR REFLECTANCE AND TRANSMITTANCE MEASUREMENTS	258
- Jack J. Hsia and William H. Venable, Jr., National Bureau of Standards	
AN AIR INTEGRALLY POWERED SOLAR ENERGY RECORDER	261
- D. D. Gibson, N. P. Bosted and W. R. Stephens, Sun Systems, Inc.	
SOLAR ENERGY SYSTEM TESTING: SOME EXPERIENCES WITH MINICOMPUTERS	265
- W. W. Shurtleff, Sandia Laboratories	

NOTE: Responsibility for the contents of papers published in this Proceedings rests upon the authors. Statements made in papers are not binding on the publisher or its members.

Author Index

	Page		Page
Altman, R. F.	50	Gross, G.	224
Archbold, P.	139	Gupta, B. P.	184, 253
Arvizu, D. E.	164		
Askin, D.	234	Hampton, H. L.	188
		Hartman, J. S.	188
Barker, H.	224	Hays, R. A.	54
Bates, J. O.	139	Herlihy, J.	144
Beekley, D. C.	156	Hoffman, A.	1
Blackmon, J. B.	169	Horton, E. E.	129
Boes, E. C.	117	Hsia, J. J.	258
Bosted, N. P.	261		
Brown, C. T.	50	Jacobson, M. R.	201
Brzuskiwicz, J. E.	206		
		Kinelski, E. H.	125
Carmichael, D. C.	24	Kniseley, R. N.	245
Castle, J.	224		
Coulbert, C. D.	18, 253	Lewis, L. G.	134
Curcija, M.	169	Lind, M. A.	188
		Lingle, C. P.	229
Davis, D. B.	63		
Deffenbaugh, D. M.	159	Madigan, J. M.	206
Derringer, G. C.	24	Masters, L. W.	218
Dokos, W. T.	146	Mather, G. R.	156
Dudley, V. E.	34	Matthews, L. K.	45, 63, 195
Dumas, L.	1	McClelland, J. F.	245
		Mecherikunnel, A. T.	83
Flowers, E.	112	Morgan, G. R.	69
Freese, J. M.	164	Mulholland, G. P.	195
Friefeld, J. M.	39	Neighbors, E. T.	108
		Nicodemus, F. E.	256
Gaines, G. B.	24	Noel, G. T.	24
Gibson, D. D.	261	Nuss, G.	30
Gilligan, J. E.	206	Pauckert, R. P.	39
Griffith, J.	1	Paulling, J. R.	129

	Page
Perez, L.	129
Pettit, R. B.	164
Rausch, R. A.	184
Resnick, M.	234
Richmond, J. C.	83
Schneider, G. R.	69
Shurtleff, W. W.	265
Skoda, L. F.	213
Sliemers, F. A.	24
Stephens, W. R.	261
Stiefeld, B.	241
Tobin, R. D.	39
Tomlinson, R. N.	241
Unterberg, W.	69
Usher, L. H.	152
Venable, W. H.	258
Waters, P.	218
Watkins, J. L.	12
Whitaker, R. D.	146
Wilkes, K. E.	24
Willson, R. C.	75
Wood, V. E.	24
Workhoven, R. M.	34, 58

Blank Pages

Introduction

The purpose of this seminar was to bring out to the entire technical community concerned with the utilization of solar energy, the problems of components and materials performance evaluation, new testing techniques being developed, and the need to standardize measurement and test procedures. Terrestrial solar irradiance measurement and the standardization of test procedures are a key to characterizing thermal performance of solar energy systems such as photovoltaic, thermal power, and solar collectors for heating and cooling. Presentations by the technical community of the existing methods of measurement and test facilities expanded the understanding of terrestrial solar energy utilization and application.

*Albert R. Lunde
Program Chairman
The Boeing Company*

ENVIRONMENTAL TESTING OF FLAT PLATE SOLAR CELL MODULES

By: J. Griffith, L. Dumas, and A. Hoffman
Jet Propulsion Laboratory

Mr. Griffith is the Test Director for the Operations Area of the JPL Low-Cost Solar Array Project, in charge of qualification and exploratory testing on production and developmental modules procured by this Project. After graduation with a degree in chemical engineering, he has had thirty-five years experience in test laboratories including work in space simulation and rocket and jet propulsion.

Mr. Dumas is an Engineering Group Supervisor at JPL where he also serves as the Operations Manager for the Low-Cost Solar Array Project, responsible for the large-scale procurement, test and evaluation of terrestrial solar cell modules. Prior experience includes development, test and flight operations for a number of planetary spacecraft. His B.S. and M.S. degrees are in mechanical engineering from the University of California at Berkeley.

Mr. Hoffman is a member of the technical staff at JPL supporting the Low-Cost Solar Array Project in environmental requirements research and development. Previously, he was active in the development of environmental requirements and planetary protection analyses for unmanned planetary missions. He received his bachelor's degree in physics at the University of Colorado and his master's degree in mathematics at the University of Southern California.

ABSTRACT

The Low-Cost Solar Array (LSA) Project at the Jet Propulsion Laboratory has as one objective the development and implementation of environmental tests for solar cell modules as part of the Department of Energy's terrestrial photovoltaic program. Modules procured under this program have been subjected to a variety of laboratory tests intended to simulate service environments, and the results of these tests have been compared to available data from actual field service. This comparison indicates that certain tests (notably temperature cycling, humidity and cyclic pressure loading) are effective indicators of some forms of field failures. Other tests have yielded results useful in formulating module design guidelines. Not all effects noted in field service have been successfully reproduced in the laboratory, however, and work is continuing to improve the value of the test program as a tool for evaluating module design and workmanship. This paper contains a review of these ongoing efforts, an outline of plans for upgrading the test program, and an assessment of significant test results to date.

INTRODUCTION

The Low-Cost Solar Array (LSA) Project is a part of the Department of Energy's national photovoltaic program. By means of technology development and

stimulation of the terrestrial photovoltaic industry, the Project objectives are, by 1986, to:

- (1) Reduce the selling price of photovoltaic arrays to \$500/kW (peak).
- (2) Achieve array efficiencies of greater than 10%.
- (3) Achieve array lifetimes of 20 years.
- (4) Reach a national manufacturing capability for terrestrial photovoltaics of 500 MW/year.

These objectives were formulated at Project inception in 1975, at which time the Jet Propulsion Laboratory (JPL) was given the management responsibility for their implementation. Over 100 contracts have been issued to the industrial organizations and educational institutions where the technological and manufacturing developments have been centered.

To evaluate the design and workmanship for both current and candidate solar cell module types, the LSA Project has instituted an ongoing module test and evaluation effort. Elements of this task include the generation of test requirements, the development of test facilities and procedures, the performance of tests under both real and simulated environments, the measurement of electrical performance before and after such tests, and the evaluation of results.

Most of the test results given herein are for modules procured by the Project for the test and applications projects of the Department of Defense (DOD), the Massachusetts Institute of Technology's Lincoln Laboratory (MIT/LL) and the Lewis Research Center (LeRC). Three separate procurements of solar cell modules have been made for this purpose: Block I was a 58-kW purchase of off-the-shelf module types, with deliveries mainly in 1976; Block II was a 110-kW purchase of modules to uniform design and test requirements, with deliveries mainly in 1977; Block III is the current purchase of 205-kW of modules to Block II design and test requirements but more uniform quality standards, with deliveries mainly in 1978. The next major DOE procurement of solar cell modules will be accomplished via the Albuquerque Operations Office's Program Research and Development Announcement (PRDA) for Flat Panel Applications Experiments (Ref 1). Proposals for these experiments, which are in the 20-500 kW range, are currently under evaluation.

Further information on the Block I and II procurements is given in Table 1 and these modules are shown in Figs. 1 and 2.

ENVIRONMENTAL TEST REQUIREMENTS GENERATION

The environmental test requirement development for flat plate solar cell modules is proceeding along

This paper presents the results of one phase of research conducted at the Jet Propulsion Laboratory, California Institute of Technology, for the Department of Energy, by agreement with the National Aeronautics and Space Administration.

Table 1. Large-scale module procurements

Manufacturer	Quantity procured	Dimensions, mm	Physical features
Block I			
Sensor Technology, Inc. Chatsworth, CA.	8 kW	571 x 165 x 11	Finned Al extrusion substrate 2.3-mm silicone encapsulant 25 cells, 50-mm diameter
Solar Power Corp. N. Billerica, MA.	30 kW	610 x 375 x 6	Epoxy fiberglass substrate 3.2-mm silicone encapsulant 22 cells, 87-mm diameter
Solarex Corp. Rockville, MD	10 kW	508 x 260 x 5	Epoxy fiberglass substrate 2.3-mm silicone encapsulant 18 cells, 75-mm diameter
Spectrolab, Inc. Sylmar, CA.	10 kW	663 x 124 x 69	Al "I-beam" extrusion substrate 2.3-mm glass over silicone encapsulant 20 cells, 50-mm diameter
Block II			
Sensor Technology, Inc. Chatsworth, CA.	40 kW	589 x 290 x 25	Stamped Al substrate 3.2-mm silicone encapsulant 44 cells, 56-mm diameter
Solar Power Corp. N. Billerica, MA	15 kW	1168 x 389 x 48	Molded polyester fiberglass substrate 2.8-mm silicone encapsulant 40 cells, 100-mm diameter
Solarex Corp. Rockville, MD	30 kW	582 x 582 x 33	Polyester fiberglass substrate, Al frame 2.3-mm silicone encapsulant 42 cells, 75-mm diameter
Spectrolab, Inc. Sylmar, CA	25 kW	1168 x 384 x 36	Formed Al frame 4.3-mm glass over PVB encapsulant 120 cells, 50-mm diameter

two parallel and complementary paths. The first is to subject early production versions of the modules to sets of environmental tests for verifying adequacy of design, fabrication processes, and workmanship. The second is to develop approaches and procedures for accelerated life testing of encapsulant materials. This paper addresses only the former test activity.

The required environmental tests for the Block I, II, and III buys and for the flat panel PRDA are indicated in Table 2. The first requirements established were for temperature cycling and humidity testing. Based on the Block I results and concurrent research and development efforts, additional tests were subsequently included and modifications were made to test levels.

The basic steps for generating environmental requirements for solar cell modules comprise:

- (1) Identification of an environmentally related problem, potential or observed.
- (2) Environmental assessment, e.g., data gathering and modeling.
- (3) Exploratory testing and generation of interim qualification requirements.

- (4) Application of interim requirements to production modules (in-house).
- (5) Revision of qualification specification.

The newest test to be specified for modules, the hail test, is a well-documented example of the application of these steps (Refs. 2, 3). Large hailstones, prevalent in certain parts of the United States, could result in significant damage to photovoltaic devices. On the basis of this concern, hail data were gathered, analyzed, and modeled (Ref. 2), and exploratory testing on sample Block I and II modules was performed (Ref. 3). An interim qualification test requirement was developed and incorporated into the specification for the Flat Panel Program Research and Development Announcement (Ref. 1, Appendix E).

ENVIRONMENTAL TEST DEVELOPMENT

The flow plan for the qualification testing of Block II and III modules is shown in Fig. 3. The diagram indicates the sequence of tests after initial inspection and the performance of baseline electrical measurements. The test conditions for this qualification testing are summarized in Table 2.

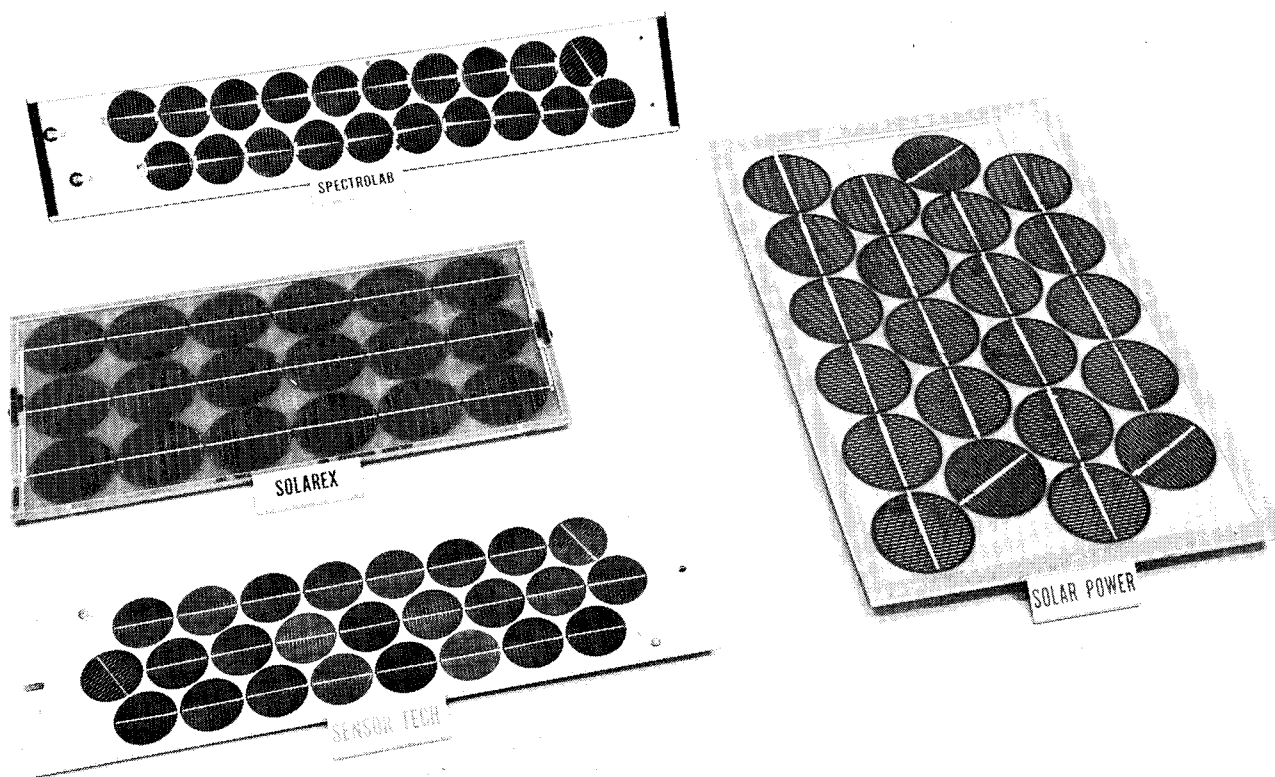


Fig. 1. Block I solar cell modules

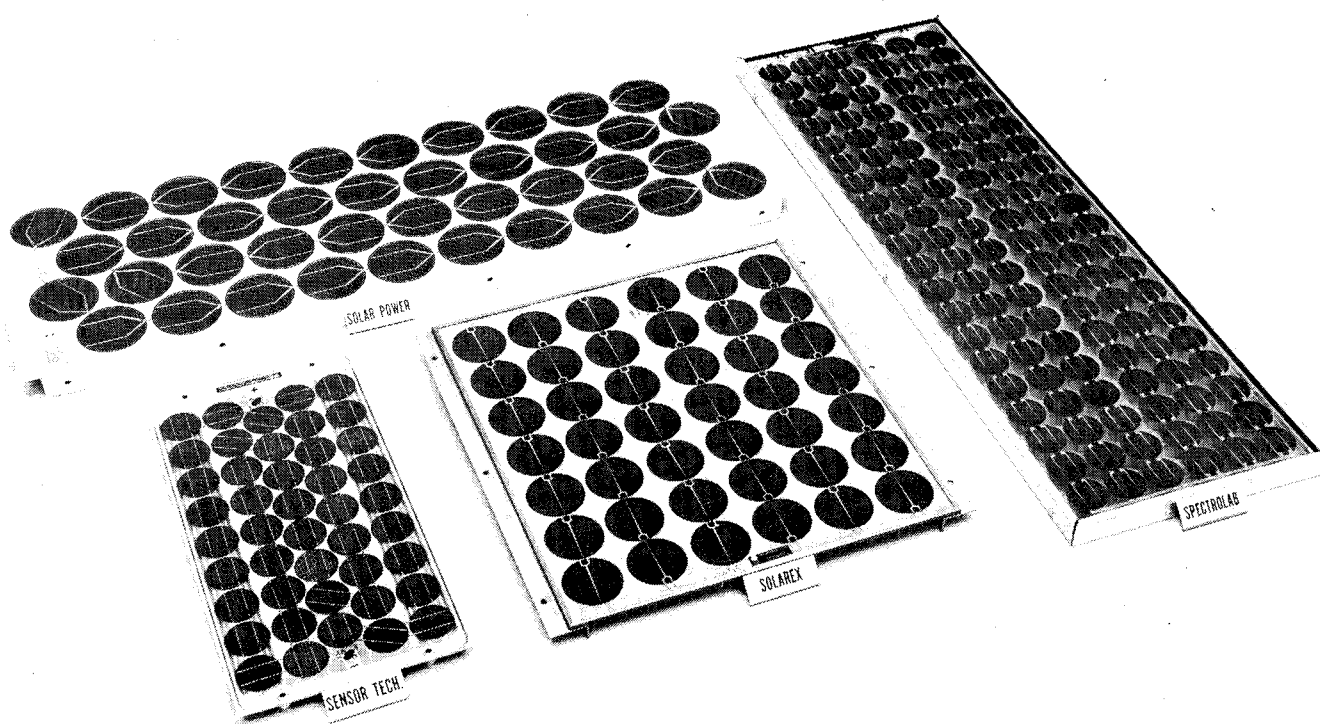


Fig. 2. Block II solar cell modules

Table 2. Required environmental qualification tests for flat plate solar cell modules

Tests	Modules				Present environmental test levels (Ref. 1)
	Block I	Block II	Block III	PRDA (Ref. 1)	
Temperature cycling ^a	X	X	X	X	+90°C, -40°C, 100°C/hr, 50 cycles
Humidity cycling ^a	X	X	X	X	+40°C, +23°C, 90% RH, 24 hr/cycle 5 Cycles (Blk I, 70°C at 90% RH, 68 hr)
Cyclic pressure loading ^a		X	X	X	±2400 Pa (±50 lb/ft ²), 10,000 cycles (Blk II, III: 100 cycles)
Warped mounting surface		X	X	X	±2 cm/m (±1/4" per ft)
Hail impact				X	3 hits at each of 3 points on module, application-dependent
Electrical isolation		X	X	X	Leakage current ≤50 µA @ application dependent voltage, e.g., 1500 Vdc (Blk II, III: ≤15 µA @ 1000 Vdc)

^a Modules mounted in a steel frame (except Block I).

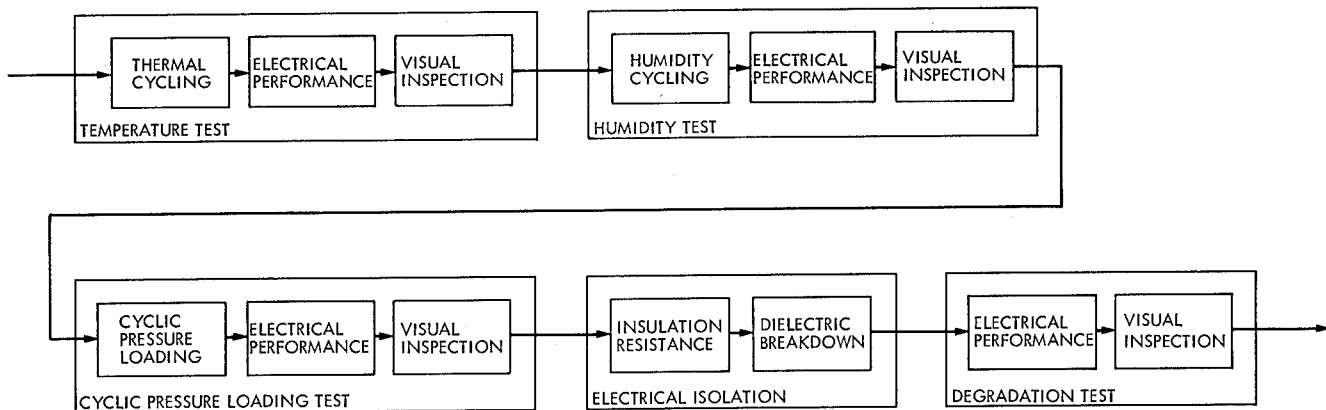


Fig. 3. Solar cell modules qualification test sequence

Several of these tests required equipment that was not readily available in-house or at commercial test labs at the outset of the Project. The necessary testing equipment was obtained by either modifying an existing testing facility or fabricating new testing equipment, as described below.

Temperature cycling and humidity tests were developed to simulate the diurnal and climatic variations of temperature and humidity which any solar energy conversion device must withstand. Standard temperature/humidity chambers are used for these tests. In order to simulate the effect of differential thermal expansion between the modules and their mounting structure, a special 1.2 x 1.2 m (4- x 4-ft) steel subarray frame was designed and fabricated such that equal mounting stresses were seen by each module in the test subarray. This frame was first used for the Block II procurement.

A new test apparatus was required at this time for the cyclic pressure loading test, which induces uniform peak pressure loads across the surface of the modules of 2400 pascals. A schematic of this device is shown in Fig. 4. The subarray is held, sandwich-fashion, between two stiffened aluminum sheets covered with a 0.4-mm (1/64-in.) neoprene sheet. The rubber sheets are slack to insure that the air pressure is transmitted uniformly to the subarray. A flush bearing surface for the diaphragm is provided by filling all of the spaces and non-uniformities in the modules with foam rubber until the foam is flush (less 5 mm) with the subarray frame. The apparatus provides automatic alternating front and back side pressure loading.

The warped mounting surface test is intended to simulate an installation or service condition in which the module substrate is twisted. The test

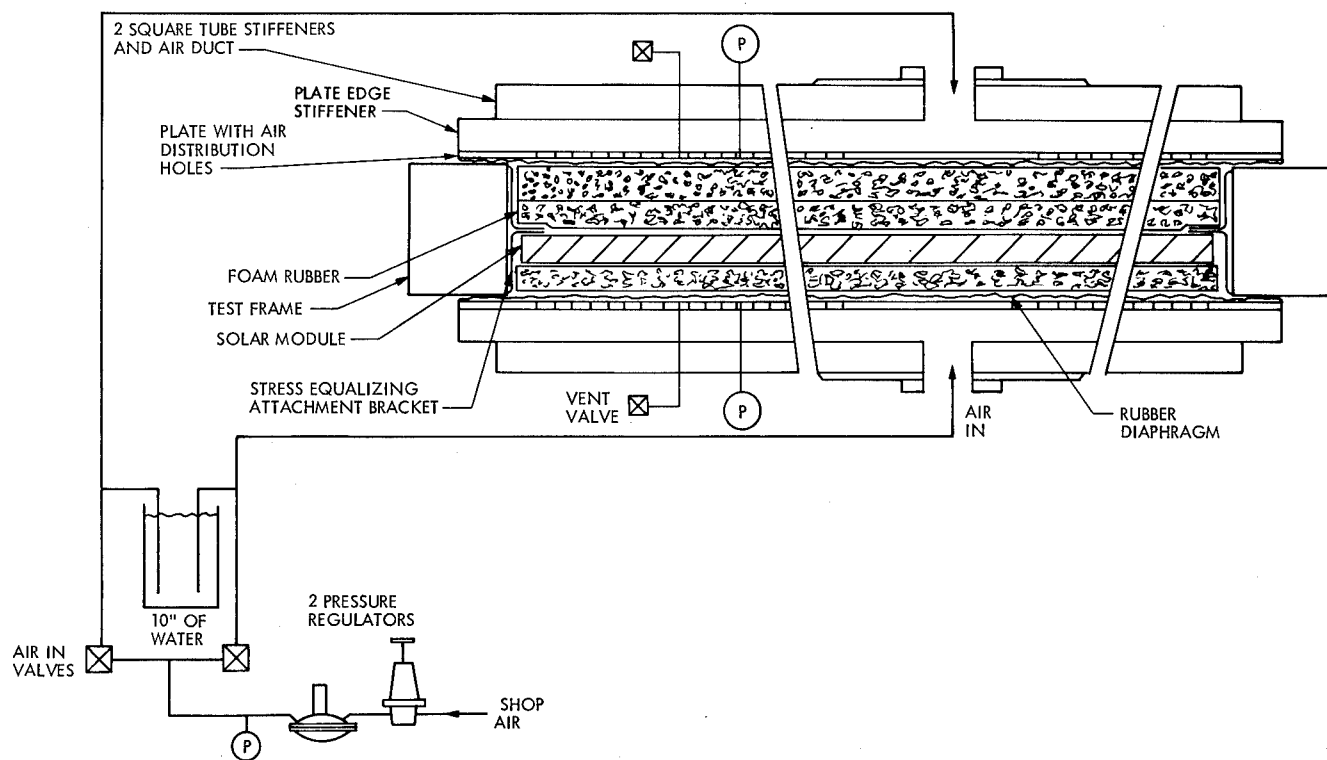


Fig. 4. Schematic of apparatus for cyclic pressure load test

can detect design deficiencies in interconnects, cells, and substrates. The test consists of raising and lowering one corner of the module ± 2 cm/m, measured along either mounting surface.

Insulation resistance and high-voltage-withstanding tests are intended to verify adequacy of module design for working voltages. These tests, performed with commercially available power supplies and instrumentation, apply voltage between the cell string and metal module frame (if any). Current leakage at 1000 Vdc must be within a specified range, and no evidence of insulation breakdown is permitted at 1500 Vdc.

In addition to the above tests, which have been required for Block II and III modules, a hail test and specification have been developed for future procurements. Figure 5 shows the hail test apparatus used at JPL, in which hailstones were simulated by spherical ice balls. The test consists of propelling ice balls of the required diameter at terminal velocity at three different points on the test specimen. Each point is struck at least three times (a minimum of 9 impacts). One of the three points is the specimen's most sensitive exposed point, which is experimentally determined through destructive testing of a sample panel.

A variety of additional performance characterization and exploratory environmental tests have been performed at JPL in addition to those tests described above. These tests are summarized in Table 3. In some cases, these tests are precursors of future qualification tests, while in other cases they are intended for evaluation of performance in unusual environments or simply for determination of normal

performance behavior under specified operating conditions.

The combined environments development is of special interest. Some of the more serious delamination of module encapsulant from cells, substrate and terminals during field test has not been observed in any of the laboratory tests. Although some work done with small coupons of material indicates that a combination of high temperature, high humidity, and far ultraviolet energy will produce delamination, the effect has not been replicated on full-scale modules. A test has been performed in which radiant (xenon lamp) heating and humidity were cyclically applied to test modules in an attempt to produce delamination. Although delamination results to date have been negative, further work is planned with different UV sources.

TEST RESULTS

Full environmental test programs have now been completed for Block I and II modules. For Block I, a minimum of two qualification test series was performed - first on the earliest units built, then on late production modules. Exploratory tests were performed on late production modules only. For Block II, preproduction prototype modules were used for qualification testing. Production was approved only after implementation of any design changes shown necessary by this test series. Production samples taken at random throughout the production run were also subjected to qualification testing, and late production modules were used for exploratory testing. Qualification test results are summarized in Tables 4 through 6, and exploratory



Fig. 5. Hail test apparatus

test results are given in Tables 7 and 8. The severity of problems resulting from qualification test exposure has been roughly indicated by the size of the "bullets."

The Block II module test results indicate that these modules are much superior to those of Block I. Delamination was greatly reduced throughout, and the humidity exposure resulted in very few discrepancies for Block II modules. Electric degradation occurred less frequently and individual power loss percentages were also lower. Problems with interconnects were virtually eliminated. However, cell cracking was at least as prevalent for Block II as it was for Block I, although the severe cracking problem with early Type V modules (Table 6) was corrected by a design change. It should be noted that cracked cells have been observed to some degree in all types of modules. This is regarded as a potentially serious problem in field reliability, since system output can be directly affected.

DISCUSSION

The essential indicator of the ability of an environmental test program to pinpoint potential problems is the degree of correlation between test and in-service degradation. Obtaining needed data from field tests and applications to make such a correlation is a significant task in itself, entailing identification of the parameters to be monitored, acquisition of in-situ measurements, reduction and interpretation of results. The uncon-

trolled, application-peculiar nature of the environmental and system-related stresses imposed on the module introduce uncertainties in attempting to establish the cause of the observed problems, which complicates the field vs test correlation.

The LSA Project, in cooperation with the test and applications projects, has established a problem/failure reporting and analysis system to provide a mechanism for identifying and correcting design and workmanship defects which lead to module problem/failures during test or service. The elements of this system are shown in Figure 6. An analysis of the data archived in this system, together with other available reports on module performance, shows the main causes of in-service degradation to be those summarized in Table 9. Where the results of the various tests described above show similar effects, this correspondence is also noted in the Table.

Examination of Table 9 shows that suitable qualification tests for two real-world effects - optical surface soiling and encapsulant delamination - remain to be developed, although work is progressing in these areas.

It will also be noted that the two remaining problem areas relate to macroscopic physical degradation, which may in turn induce electrical degradation. In both cases, the temperature cycling test appears to be the best indicator of such problems, with the humidity cycling test also showing fair correlation. These results suggest that the electrical failures so far observed in the field are mainly induced by differential thermal stress acting on the more fragile circuit elements within the module. A closer look at these two problem/failure modes will help clarify the reasons for the correlation (or lack thereof) between field and test results.

The problem of encapsulant delamination has been observed to some degree at all surfaces to which silicone rubber encapsulants (RTV 615 and Sylgard 184) have been bonded, but the most severe examples have occurred at epoxy-fiberglass module substrates. Figure 7 shows an extreme example from the field in which the accumulation of liquid water in the resultant void is evident. Poor initial adhesion due to inadequate surface preparation is probably a contributing factor in such cases, but environmental stresses appear to be more important. While some encapsulant delamination has been observed to result from laboratory tests performed to date, the nature and extent of field delamination has not been duplicated. Ongoing investigations into this phenomenon have centered on the combined effects of exposure to ultraviolet light and high humidity levels as possible causative agents.

The thin metallic interconnects between solar cells have proven susceptible to fatigue failures unless the interconnect design provides stress relief. When cells are series-connected to provide high voltage levels with no provision for current bypass around such faults, a sustained arc can be drawn across the fracture with destructive effect to the surrounding material. Figure 8 shows an example of a Block I module which failed in this fashion, charring the encapsulant and substrate near the

Table 3. Exploratory environmental tests for flat plate solar cell modules

Tests	Modules			Test levels and test equipment
	Block I	Block II	Planned Block III	
1. Heat-rain	X	X	X	Modules allowed to reach maximum temperature on a clear warm day; hard rain simulated with deionized water spray until modules reach equilibrium (about 8 min.), 5 cycles. Specially designed water spray equipment.
2. Wind-driven rain	X	X	X	Spray of deionized water at 40 mph and 2 mm average droplet size; modules slowly rotated in heavy spray for 15 minutes. Specially designed equipment.
3. Humidity-freezing	X	X	X	MIL-STD-202E, Meth. 106D (no vibration). 2 cycles 23 to 65°C at 95% RH in 16 hr; then, -13°C for 3 hours. 10 cycles. Standard temperature-humidity test chamber.
4. Humidity-heat	X	X	X	Modules are water-saturated in a chamber for 6 hr at 70°C, 95% relative humidity; then removed and irradiated at full simulated sun to stable temperature. 10 cycles. Standard temperature-humidity chamber and 3400°K lamp bank.
5. Humidity with voltage bias	X	X	X	Levels being developed. Standard temperature-humidity test chamber.
6. Salt fog	X	X	X	MIL-STD-810C, Meth. 509.1. Salt spray, 35°C, 95% R.H. for 48 hr. Salt fog chamber.
7. Hail impact	X	X	X	Iceballs of 1 to 5 cm diameter impact the modules at terminal velocities. Specially designed gas gun.
8. Fungus	X			MIL-STD-810B, Test Method 508.1. Modules sprayed with salt and fungal culture and placed in humidity chamber at 30°C and 95% RH for 28 days.
9. Combined environment: temperature, humidity, UV			X	Levels and equipment being developed
10. Optical surface soiling			X	Levels and equipment being developed.

point of failure. Figure 9 is a macroscopic view of an interconnect which failed in a similar way in a low-voltage application without resultant arcing. Temperature cycling and cyclic pressure loading tests are an effective screen for design problems of this sort. Early Block I modules exhibited these failures both in test and in service; Block II modules have not experienced failures in either case.

Since high-purity crystalline silicon is a brittle material, solar cells fracture rather easily under mechanical stress, particularly when the cells have edge chips or other flaws. Extreme cases lead to open-circuit conditions, while hairline

cracks may have little or no effect. Figure 10 shows a typical crack which originated at an edge chip, together with evidence of encapsulant delamination near the crack. Temperature cycling tests have proven to be the most effective of the current environmental simulations in inducing this failure mode, although any test which subjects the module to mechanical stress may cause occasional random cell cracks.

In reviewing these results, it is clear that the temperature cycling test is the most valuable of the current series of environmental tests when evaluated on the basis of the ability to reproduce

Table 4. Block I qualification test results

Suppliers	Cell cracks	Delamination	Damaged interconnects	Electrical degradation
V	● ○	● ○		○
W	●	●	●	● ○
Y (early)	●	●		● ○
Y (later)*				
Z	● ○	● ○	●	●

● temperature cycling
 ○ humidity
 *modified contact design

Table 5. Block II prototype qualification test results

Suppliers	Cell cracks	Delamination	Electrical degradation
V standard		● ○	
V glass cover		● ○ ⊕	●
W	●		●
Y			
Z	● ● ●	● ○	●

● temperature cycling
 ○ humidity
 ⊕ cyclic pressure loading

common field problems. The humidity test and the cyclic pressure loading tests have served well enough to merit retention, perhaps in modified form. The most serious shortcoming of the current qualification test series is the inability of these tests to reproduce the most common form of physical degradation - encapsulant delamination. Further efforts to isolate the nature and cause of this phenomenon are in order.

A forecast of near-term testing activity is given in Table 10. It should be stressed that the limited field experience available does not warrant the

Table 6. Block II production samples qualification test results

Suppliers	Cell cracks	Delamination	Electrical degradation
V (early)	● ○ ⊕	●	● ⊕
V (later)	●		
W	● ○		○ ⊕
Y	● ○		●
Z	● ○	●	●

● temperature cycling
 ○ humidity
 ⊕ cyclic pressure loading

assumption that all important failure modes have been identified. Indeed, it is likely that more complex and subtle degradation mechanisms such as cell metallization corrosion will only become evident after several years of field exposure; continuing comparison of test and service experience will be needed to account for such phenomena.

CONCLUSIONS

The principal conclusions to be drawn from these environmental testing efforts are:

- New qualification tests developed for flat panel modules are proving useful for detecting design and fabrication deficiencies. Temperature cycling, cyclic pressure load, and humidity have been especially useful. There is positive correlation between some of the observed field effects (e.g., power loss) and qualification-test-induced degradation.
- The data bank for environmentally induced field problems from DOE-purchased modules is very small because of the relatively short time (less than 18 months) of field experience. Continuing analysis of problem/failure reports and other field data is needed to improve the understanding of such problems.
- Test procedures for two field-related problems are needed and are being developed. The two problems are optical surface soiling (i.e., dirt) and encapsulant delamination.

Table 7. Results of exploratory testing of Block I modules

Supplier	Humidity-freezing	Salt fog	Hard rain	Heat-rain	Humidity-heat	Fungus
V	Discoloration, delamination	Slight corrosion	Pass	Pass	Delamination	Pass
W	Delamination, cracked terminals	Slight corrosion	Pass	Pass	Pass	Pass
Y	Pass	Pass	Pass	Pass	Pass	Pass
Z	Delamination, electrical degradation	Minor delamination	Pass	Pass	Pass	Pass

Table 8. Results of exploratory testing of Block II modules

Supplier	Humidity-Freezing	Salt fog	Heat-rain	Wind-driven rain	Humidity-heat
V	Electrical degradation, discoloration, delamination	Oxidation	Electrical degradation	Pass	Cracked cell
W	Pass	Electrical isolation	Cell cracked	Pass	Pass
Y	Delamination	Corrosion	Pass	Pass	Pass
Z	Minor delamination	Pass	Electrical degradation, split encapsulant	Pass	Electrical degradation

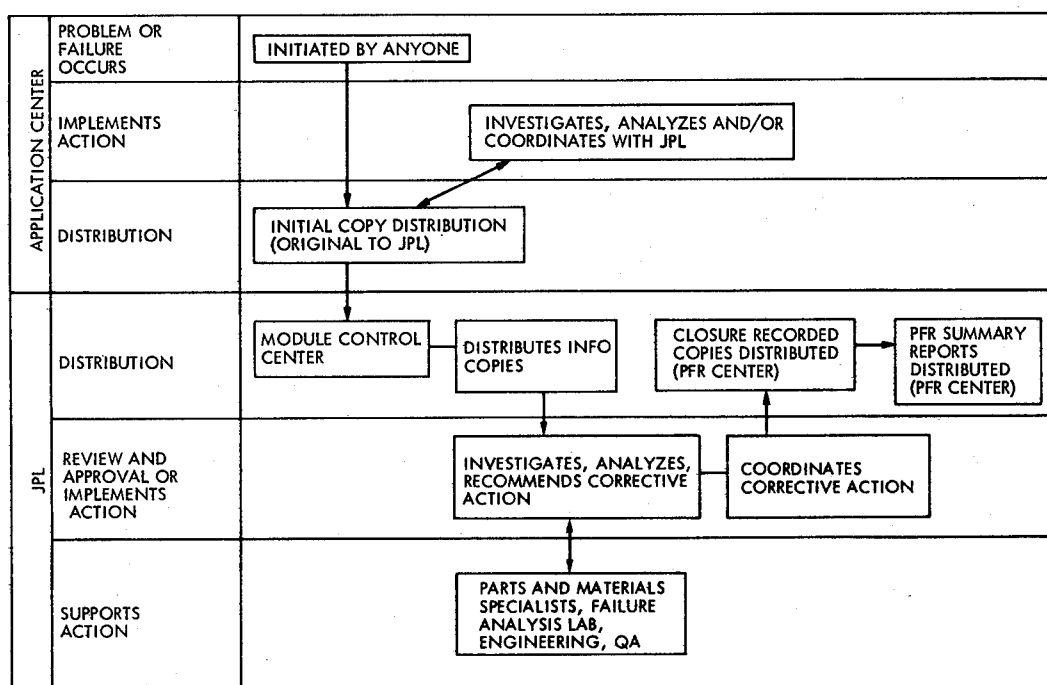


Fig. 6. Problem failure report flow diagram

Table 9. In-service degradation modes

Phenomenon	Field effect	Similar phenomenon/effect observed in present qualification tests
Optical surface soiling	5-30% power output reduction	No
Encapsulant delamination	No short-term power degradation observed. Long-term effects unknown.	Yes, some delamination but not to the degree observed in the field (humidity, temperature cycling)
Interconnect or interconnect/contact failure	Arcing and/or open circuit	Yes (temperature cycling, cyclic pressure loading)
Severely cracked or mismatched cell	Cell back-biasing and overheating; reduced module power output	Yes, (humidity, temperature cycling, cyclic pressure loading)

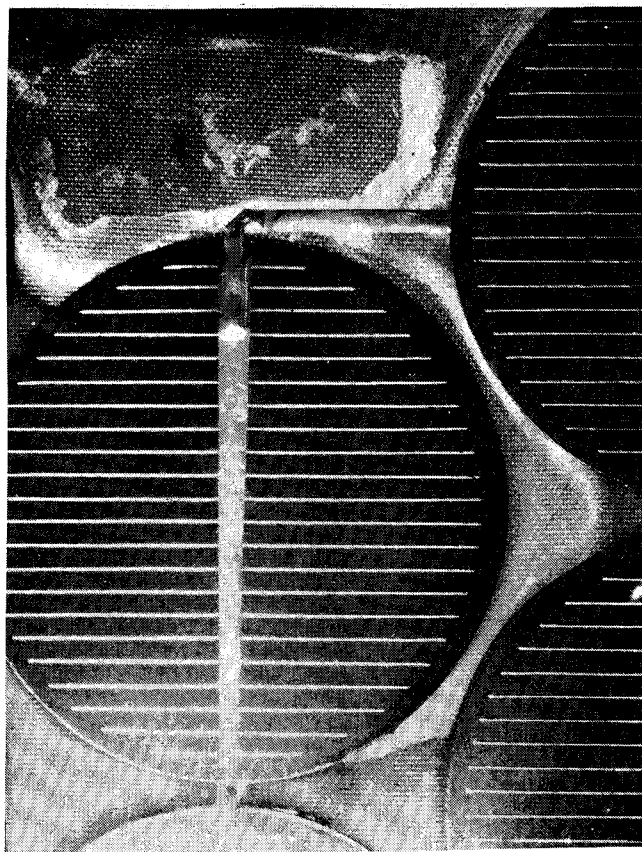


Fig. 7. Example of solar cell module encapsulant delamination

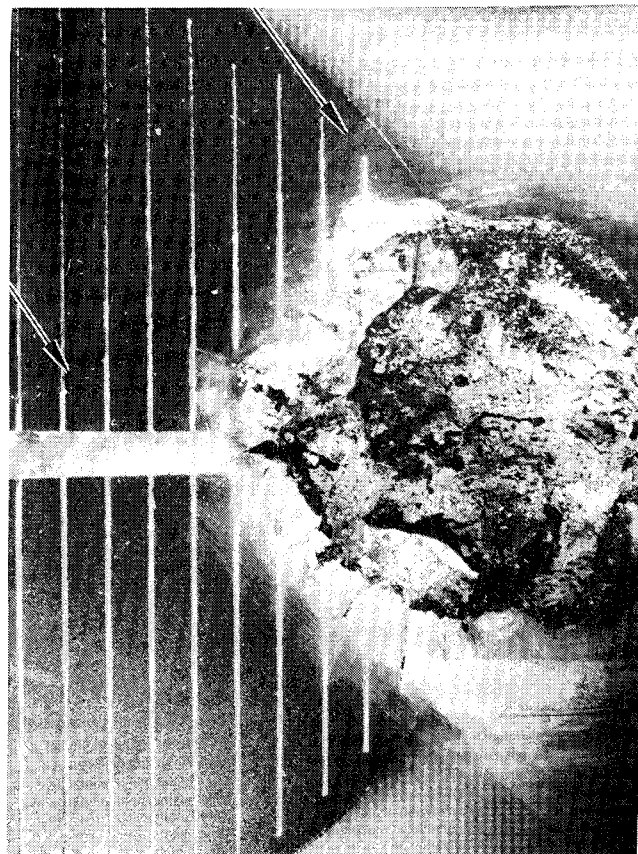


Fig. 8. Example of arc damage at an interconnect

REFERENCES

1. Program Research and Development Announcement (PRDA), Solar Photovoltaic Flat Panel Applications Experiments, Department of Energy, Albuquerque Operations Office, PRDA EM-78-D-04-0038.
2. Gonzales, C. C., "Hail Risk Model for Solar Collectors," in 1978 Proceedings of 24th Annual Technical Meeting, Institute of Environmental Sciences, April 18-20, 1978, pp. 278-286.
3. Moore, D., Wilson, A., and Ross, R., "Simulated Hail Impact Testing of Photovoltaic Solar Panels," in 1978 Proceedings of 24th Annual Technical Meeting, Institute of Environmental Sciences, April 18-20, 1978, pp. 419-430.

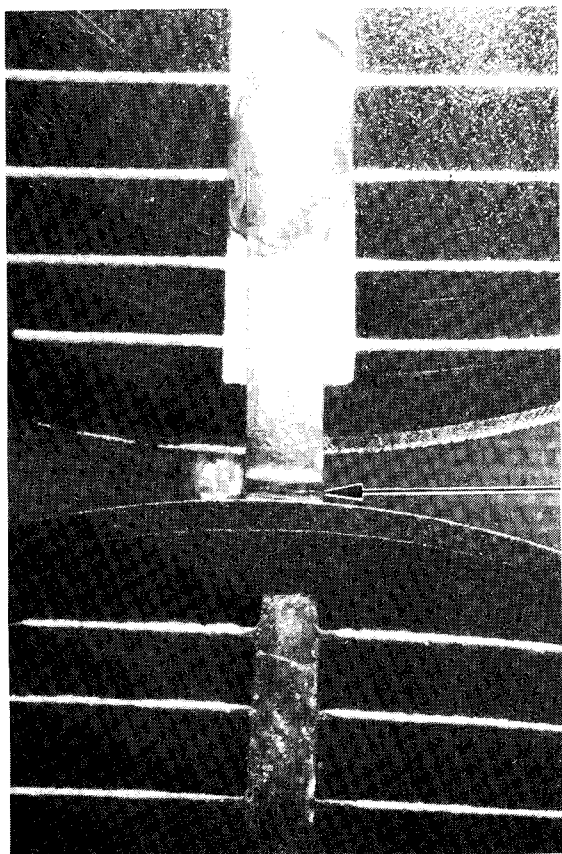


Fig. 9. View of interconnect fatigue failure

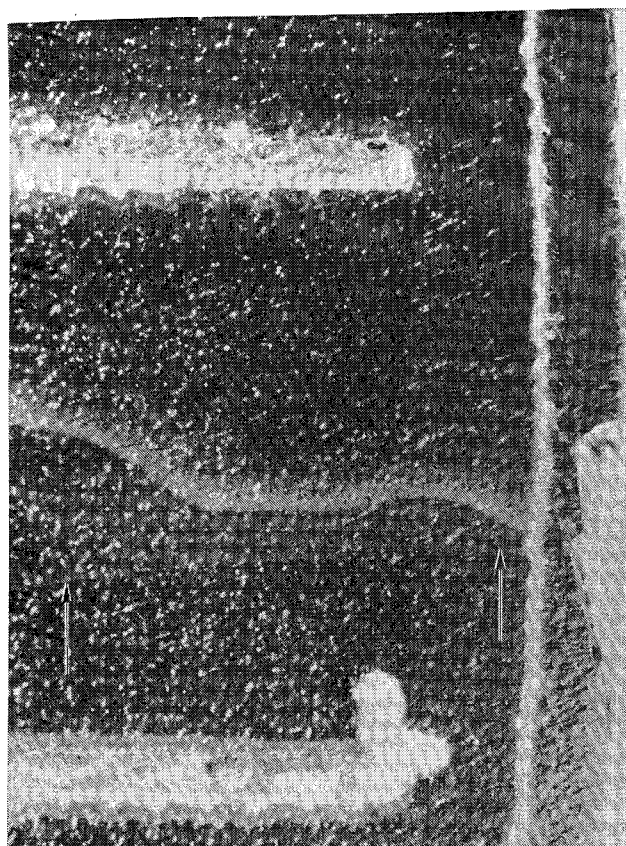


Fig. 10. Typical solar cell crack originating at an edge chip

Table 10. Environmental testing forecast for solar cell modules

Environment	Forecast	Remarks	Environment	Forecast	Remarks
Present qualification tests (Ref. 1)			Humidity with voltage bias	○	May be combined with humidity cycling when better understood
Temperature cycling	○		Salt fog	○△	Applicability as a qualification test site dependent May be made more severe
Humidity cycling	○		Hail impact	○	
Cyclic pressure load	○		Other tests		
Warped mounting surface	○		Fungus	△	Applicability site-dependent
Hail impact	△	Applicability site-dependent	Combined environment (temperature, humidity, UV)	●	Qualification test if proper test conditions are found to simulate field-type degradations.
Present exploratory tests			Optical surface soiling	●	Qualification test if representative test conditions can be developed.
Heat-rain	○				
Wind-driven rain	⊗				
Humidity-freezing	○	May be combined			
Humidity-heat	○				

Legend: ○ continue
⊗ discontinue

△ special qualification test
● qualification test needed and being developed

SANDIA'S PHOTOVOLTAIC TEST EXPERIENCE*

By: Jerry L. Watkins, Staff Member, Sandia Laboratories

The Author

Mr. Watkins has been working on the Photovoltaic System Definition Project at Sandia since October 1976. His responsibilities include contract management for photovoltaic power system studies and component development, and the operation of the Photovoltaic Advanced Systems Test Facility. Before his present assignment, Mr. Watkins worked in weapon systems study and development at Sandia. His B.S. in Mathematics is from New Mexico State University (1973) and his M.S. in Electrical Engineering and Computer Science is from the University of California at Berkeley (1974).

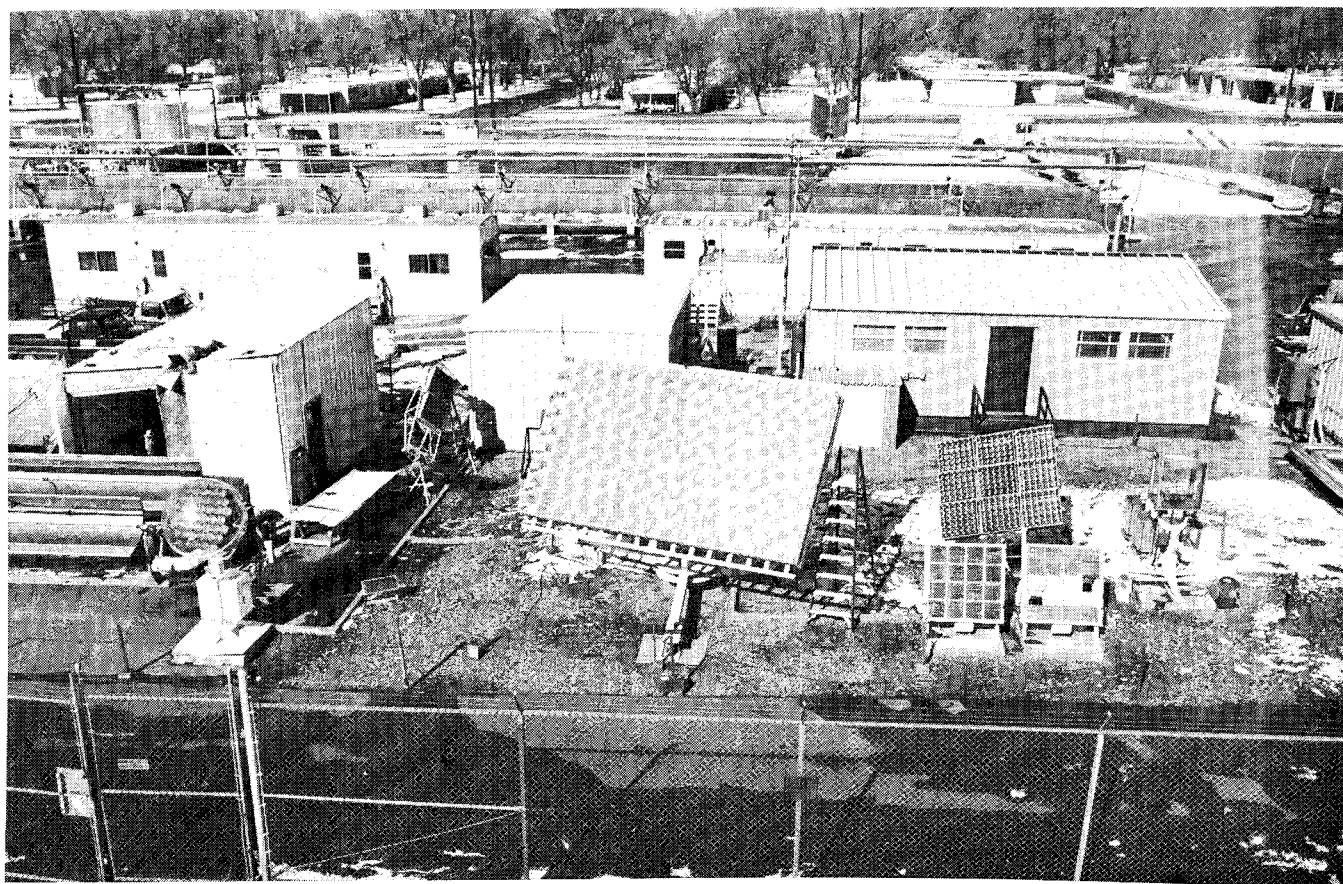
Test Facility Background

Testing began at the Photovoltaic Test Facility at Sandia Laboratories in January 1977, even before completion of the facility in June 1977. The initial purpose of the test facility was to evaluate prototype concentrating photovoltaic arrays obtained through development contracts. Also, the facility will be used to gather performance data and environmental effects information on photovoltaic arrays for feedback to designers and manufacturers.

Finally, the facility will evolve into a systems test facility for evaluation of other photovoltaic systems components (power conditioning, battery storage, and controls). The existing facility is shown in Figure 1.

The facility's data acquisition system is built around a Hewlett-Packard 9640A Minicomputer System. The system has both teletype terminal and graphics display terminal control devices along with a 9-track tape drive and a line printer for data storage and output. Two 16-bit relay registers control various activities at the test site as well as eight channels of digital-to-analog conversion capability. As many as 256 channels are available for data input to the system through peripherals that include high speed analog-to-digital converters, scanners, and voltmeters. The system, designed and constructed for ease of reconfiguration, is easily adapted to many test situations.

Environmental sensors, including two normal-incidence pyrheliometers, two pyranometers, an integrating insolometer, wind speed and direction instruments, and an ambient temperature sensing device, are integrated into the system. Presently, two electronic loads controlled by the computer are



* This work was supported by the U.S. Department of Energy, Division of Solar Technology.

installed and used to trace voltage-current curves on arrays with outputs from 50 W to 2.5 kW. These loads are also used in maximum power tracking modes to calculate array energy output throughout the day. The computer also controls a fluid loop used in testing combined thermal-photovoltaic collectors. The loop is controlled to vary fluid inlet temperature and flow rate, the independent parameters needed to calculate thermal efficiency.

The Photovoltaic Test Facility, located near the Personnel Building at Sandia, cannot accommodate some of the larger arrays and test items planned. A planned expansion will be explained more fully later in this paper.

Early Test Experience

Low-Concentration Arrays

Compound Parabolic Concentrators -- Two prototype concentrating photovoltaic arrays constructed by Argonne National Laboratories, each having external dimensions of $\sim 4 \times 4$ ft, were received for test and evaluation early in 1977. Both arrays used linear compound parabolic concentrators (CPC), with each array rated at a nominal 100-W output. Suitable structures were designed to accommodate testing and allow for seasonal adjustment.

The first array received and tested, the dielectric compound parabolic concentrator (DCPC), is based on analysis indicating that a broadened acceptance angle can be achieved by filling the CPC shape with a clear material having an index of refraction > 1 . If the concentrator wall shape is appropriately designed for the chosen value of the index of refraction and desired acceptance characteristic, total internal reflection occurs at the medium-air interface. This should lead to an efficient concentrator and a more relaxed seasonal tilt schedule for the array.

The 4×4 -ft array consists of 20 subunits or modules, each 27.4×23.3 cm and containing 108 separate silicon cells connected in a series-parallel matrix for maximum redundancy. Each module can produce ~ 7 W at 5 V. The rear surface of each module is a standard extruded-aluminum extended surface heat sink that provides adequate passive cooling for maintaining cell temperature below 60°C . Redundant outputs from each module are routed to a common junction box, allowing the modules to be wired in several series/parallel combinations.

Acrylic plastic with an index of refraction of 1.491 was the dielectric material used in the concentrator. The concentrator itself was injection-molded

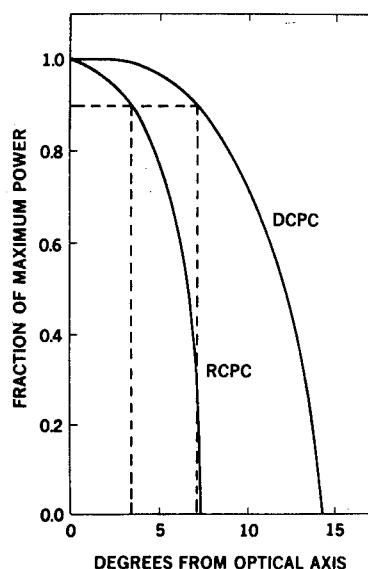
in a strip composed of nine single concentrators, each with a 1.91×3.05 -cm front surface and a 0.25×2.54 -cm exit aperture. The photovoltaic cells used then were specially designed by Spectrolab and Sensor Technology to have 0.25×2.54 -cm active area.

The geometric concentration ratio of the DCPC module as defined by incident aperture area divided by the illuminated solar cell area is 7.5:1. The efficiency, based on electrical measurements taken with a new modular subunit and scaled to 1 kW/m^2 input, was 10.9%. The measured efficiency of the entire array was 10%.

The construction of the second Argonne prototype CPC array, delivered to Sandia in February 1977, was similar to that of the DCPC except that an evaporated aluminum reflective surface was used in a hollow plastic trough of the appropriate shape, and no dielectric material was used. The cells, heat sink, and array frame were the same as those used in the DCPC. The geometric concentration ratio is 6.9:1. A protective plastic cover shields the cells and reflectors from dust and dirt. The reflective CPC (RCPC) was designed in a modular fashion like the DCPC, with sixteen 28×28 -cm modules comprising the 4×4 -ft array. These modular subunits, being of different dimensions than the DCPC modules, gave rise to an array with a smaller packing factor.

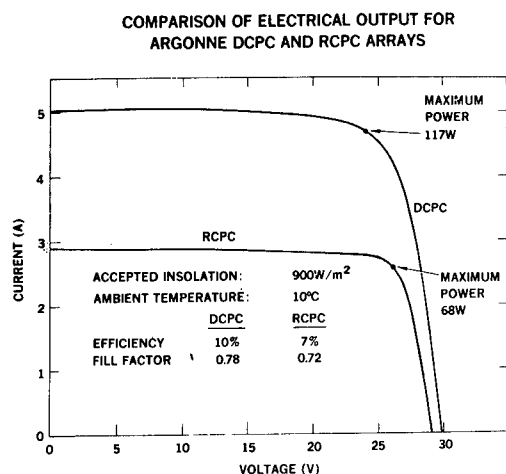
Comparing performance between the DCPC and the RCPC arrays leads to some interesting observations. Figure 2 shows the acceptance angle of both

COMPARISON OF ACCEPTANCE ANGLE
FOR ARGONNE DCPC AND RCPC ARRAYS



arrays. Note that the RCPC maintains $\sim 90\%$ maximum output out to $\pm 4^\circ$ off-axis, whereas the DCPC maintains 90% maximum output to $\sim \pm 6.5^\circ$. This implies a more rigid seasonal adjustment schedule for the RCPC than for the DCPC. Indeed, the RCPC required tilt adjustment 38 times/yr compared to 12 tilt adjustments/yr for the DCPC.

The current-voltage characteristics of the two arrays were different also. Figure 3 shows current-voltage curves from both the DCPC and RCPC arrays under similar operating conditions. The superior performance of the DCPC array can be accounted for because of an increased aperture area (1.28 m^2 for the DCPC versus 1.10 m^2 for the RCPC) and the more efficient nature of the total internal reflection vis-à-vis the reflection off the aluminized surface of the RCPC.



Both the DCPC and RCPC arrays are still being monitored at the Photovoltaic Test Facility. The DCPC array allowed moisture into the sealed area between the modular subunits, causing severe deterioration of the cells on several modules. Two modules were returned to Argonne for analysis. The RCPC continues to perform without visible deterioration and only minor degradation of electrical output.

Opto-Technology "Sun-Trac" Array -- Opto-Technology, Inc., produces the Sun-Trac unit primarily for cathodic protection of underground pipelines. This unit is a full two-axis tracking concentrator array enclosed in an acrylic sphere for protection from wind loading. The concentrators are conical silvered plastic units, each having an

entrance aperture ~ 6 in. in diameter and an exit aperture of 2-in. diameter, implying a geometric concentration ratio of 9:1. Forty-two of these concentrator units are mounted together on the tracking frame for a peak output of 50 W. Since the application calls for low-voltage, high-current dc power, the system runs at ~ 7 V open circuit, and a regulator circuit charges two large lead acid cells at 4 V for the cathodic protection and for powering the tracking electronics and drive motors. The array has been operating continuously for over a year at the test facility, and no significant degradation in performance has been noted.

High-Concentration Arrays

RCA Concentrator Arrays -- Several prototype high-concentration arrays that RCA has designed and constructed are based on a 6-cell x 6-cell module housed in a 24-in.-sq sheet-metal box. The lens system for all 36 cells in a module consists of thirty-six 4-in.-sq plano-convex lenses molded as a single unit. This lens matrix then forms the cover for the module.

The cells themselves are 1/8-in.-diam. silicon with gold metallization mounted on TO-3 transistor headers and bolted through the back plane of the module to commercial transistor heat sinks. Each module has a maximum output of 33 W. The geometric concentration ratio is 326:1. Passively cooling the cells at this high concentration ratio is possible because of the small cell size since heat dissipates proportionately easier for smaller diameter cells.

The 36 cell modules are then mounted on a two-axis tracking platform. Two versions of the array exist: one using three modules on a polar-mounted tracking structure for a 100-W nominal array, and nine modules on a similar structure for a 300-W unit. With the polar-mounting scheme, a clock drive can be used to track in azimuth, and the elevation needs adjustment only daily. RCA has designed a combination clock and closed-loop feedback tracking system for the azimuth drive. In the absence of sufficient sunlight to activate the sun sensor, the unit clocks at a 1-Hz rate, sufficient for one revolution in 24 hours. If the sun sensor can respond, however, the clock is overridden such that the unit clocks at a 2-Hz rate if it senses the sun ahead of the array, stopping when it senses the sun behind the array. Cams are periodically activated so that the elevation tracking mechanism adjusts for the seasonal variation in solar position.

Sandia received two 100-W arrays in February 1977 and one 300-W array in July 1977. During testing several problems appeared, and appropriate changes were incorporated in the RCA design.

First, the lens system degraded quickly after exposure to sunlight. The lens is constructed in two steps wherein a piece of acrylic is vacuum-formed to the appropriate shape, and a transparent potting material is then poured into the concave cavity and cured. It was this potting material that degraded (yellowed) after exposure to sunlight. Also, the lens did not present a sharp focus on each cell in the matrix. This was attributed to the inability to hold tolerances during potting. RCA has since designed a one-piece Fresnel lens incorporating a matrix of 36 lenses to replace the current lens. A second 300-W unit will soon be delivered incorporating these new lenses.

Next, it soon became apparent that the array was very sensitive to tracking error. Very little tracking error can be tolerated if peak output at the high-concentration level is to be maintained. Backlash in the drive mechanism caused problems for these arrays--as the center of gravity of the array moved from one side of the support pivot to the other, the output often decreased radically. RCA is examining this problem.

The first of the 100-W arrays has been returned to RCA after 1 year of testing, and the second 100-W array is being disassembled and examined at Sandia. The 300-W array will undergo performance testing for another 4 to 6 months.

Sandia Fresnel Concentrating Array -- Photovoltaic researchers at Sandia have constructed a nominal 1-kW concentrating array using 1-sq-ft Fresnel lenses. One-hundred thirty-five compression-molded acrylic lenses are mounted on a two-axis tracking structure. Approximately 12 in. behind the lens plane is a 135-sq-ft aluminum plate with the appropriate machining for mounting 2-in.-diam silicon concentrator cells such as those produced at Sandia. Also, coolant tubes are thermally bonded to the aluminum plate to extract thermal energy from the array while cooling the cells.

The array was designed as a testbed to study both passive and active cell cooling. In the passive mode, the aluminum-cell mounting plate is open on all sides to allow convection cooling of the cells. Testing in this mode has yielded an electrical output of > 900 W with 1 kW/m^2 direct normal solar insolation and a cell temperature of 30 to 35°C above ambient. Testing is continuing in this mode, and various different cells and cell mounting schemes are being investigated.

In the actively cooled mode, the cell mounting plane is covered on the sides and insulated from the rear to minimize heat loss. Then the coolant inlet temperature and flow rate are varied, and data taken on both the thermal and electrical output. The array is presently being tested in this mode.

Present Testing

Activities at the test facility include continued monitoring of the arrays described above as well as more detailed testing of array components. To more conveniently monitor the long-term output of photovoltaic arrays, we have recently designed and fabricated an array loading device. This unit, a small electronics package that mounts on or near the array, consists of a logic and control module and a power dissipation module. The logic and control module

1. computes array operating point corresponding to maximum array output;
2. integrates power output to yield energy;
3. senses and records array temperature;
4. senses and records array output voltage, current, and power; and
5. interfaces with the test facility computer to store information permanently on tape.

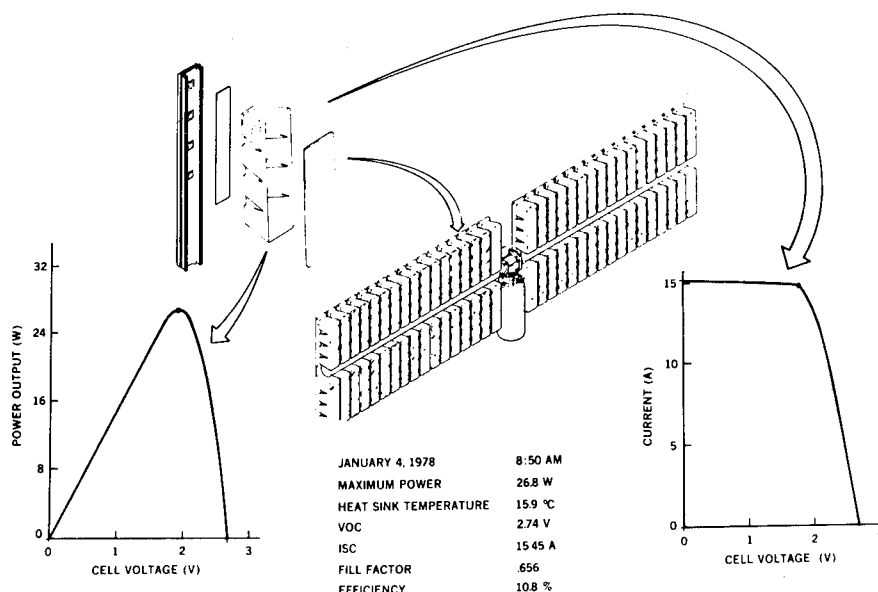
The power dissipation module consists of five power transistors operated up to saturation to provide a controllable variable load. Up to 16 of these units can be located throughout the test facility, and the system computer periodically interrogates each unit and records the data for later assembly and reduction.

In addition to real-time performance monitoring of the arrays, we continue to inspect the test units for visible signs of deterioration. Extensive photographic records are kept and can be used to modify manufacturing procedures leading toward increased life times. Also, a screening test procedure that includes hail impact tests, temperature humidity cycling, UV exposure, and other tests as needed has been established for array components.

To illustrate these screening procedures, we will describe the results of tests to support the 10-kW concentrating array development program underway at Martin-Marietta in Denver. The entire 2.5-kW array, which is composed of 68 four-cell modules, pivots around the central pedestal for azimuth tracking and rotates around the horizontal axis for elevation tracking (Figure 4). Several prototype four-cell modules have been constructed by Martin-Marietta and tested at Sandia.

Each module consists of four 2.25-in.-diam cells mounted on an extruded aluminum heat sink that also serves as a structural member. The housing is molded of ABS plastic, and the four 1-sq-ft lenses are epoxied to the housing. Not shown in the figure is a thin pressed aluminum shield inserted inside the plastic housing to avoid melting the housing when the unit is misaligned.

RESULTS FOR MARTIN-MARIETTA 10-kW ARRAY MODULE TEST



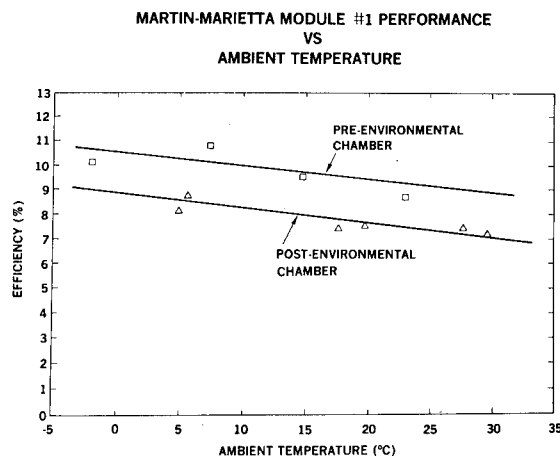
The first of the Martin-Marietta modules was received at Sandia in January of this year. Figure 4 also shows the performance data associated with that prototype module. The module produced 26.8 W with an efficiency of 10.8%; the direct normal solar insolation was 635 W/m²; and the cell temperature was ~20°C. The module was tested for ~1 mo, with data taken on its acceptance angle, its integrated energy output throughout a day, and other operating characteristics.

Test results after the environmental chamber exposure showed a significant decrease in performance (Figure 5). It is not known whether the moisture migration and subsequent corrosion caused the degradation, or if so, what mechanism was at work. Further testing is planned to help identify the exact cause of the degradation. Results will then be reported to Martin-Marietta to assist in design changes.

Following its initial characterization, the module was placed in an environmental test chamber where the module underwent 224 cycles of the following conditions:

Time (hr)	Temperature (°C)	Humidity Cycle
2	54	82%
2	Transition to low temperature	Same
2	-29	Same
2	Transition to high temperature	Same

Subsequently, the module was examined and re-tested. The module had allowed moisture migration into the environmentally sealed space. Corrosion was visible on the cell contacts and interconnects. Disassembly of the module disclosed that the thin-pressed aluminum reflector used to prevent module misalignment from damaging the ABS housing had not stopped an adjacent lens from focusing onto the back of the housing and melting a small hole. These holes allowed the moisture migration. Martin-Marietta has since redesigned the aluminum reflector.



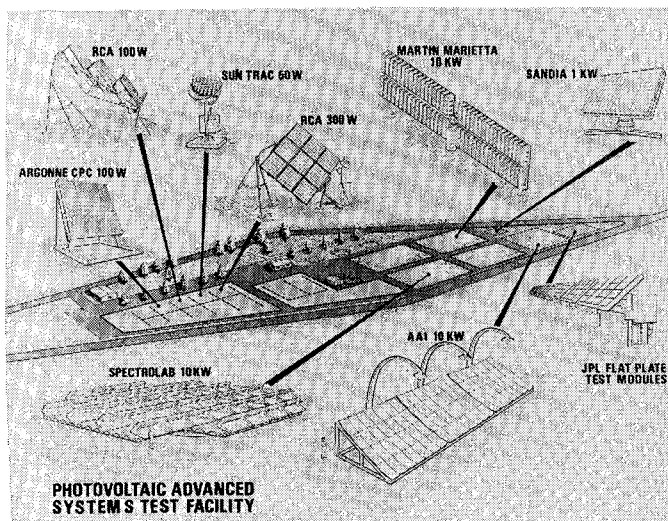
Plans

A variety of photovoltaic arrays are planned for installation at Sandia. In addition to the 10-kW array program at Martin-Marietta just mentioned, Spectrolab, Inc. of Sylmar, CA, is developing a 10-kW concentrating photovoltaic array based on a 250-W off-axis parabolic concentrator. Also, AAI Corporation in Baltimore, MD, is designing a high-concentration photovoltaic array in the 10-kW range. Recently an RFP was released from Sandia for the design of a combined thermal-photovoltaic 10-kW array that may also result in a prototype.

In addition to concentrating arrays, 4.5 kW of flat-plate arrays are to be installed to allow the comparative testing of both types of photovoltaic converters. Also, several small prototype flatplate combined thermal photovoltaic collectors have been obtained, and testing has begun on these units. Finally, it is expected that several prototype developmental and commercial units will be received and tested on a continuing basis. In addition to this, the facility has been designed with significant flexibility and can be reconfigured to accommodate most eventualities.

The testing facility will soon be expanded to include the remaining parts of a photovoltaic power system. Several power conditioning contracts are currently under way, and these will result in prototype photovoltaic power conditioning units. One contract, with Westinghouse in Lima, OH, is to design and construct a 50-kVA 3-phase ac power conditioning unit that will have application in intermediate-sized photovoltaic power systems. Also, a contract is under way at Abacus Controls, Inc., to modify their current 10-kW unit for use at the test facility. This unit will be very well-suited to residential photovoltaic power systems. In-house, various unique and original power conditioning schemes are being committed to hardware and will be tested. Finally, a modest amount of lead-acid battery storage will be added to the facility to evaluate power systems in which storage is required.

This planned activity has dictated the expansion of the test facility, and work has begun for the detailed design. An artist's conception of the new facility is shown in Figure 6.



The Photovoltaic Advanced Systems Test Facility will have an expanded data acquisition and control capability based on the existing computer system but augmented to include remote testing and data processing. The facility will have space for ~100 kW of photovoltaic arrays and will be equipped for both actively and passively cooled arrays up to 10 kW. Interactive utility ties will be available as will a variety of electronic loads. The facility should be fully operational by October 1978.

A LIFE PREDICTION METHODOLOGY FOR ENCAPSULATED SOLAR CELLS*

By: Clifford D. Coulbert, Jet Propulsion Laboratory

Clifford Coulbert is manager of the Encapsulation Task of the Low-Cost Solar Array Project at the Jet Propulsion Laboratory. He holds an M.S. degree in mechanical engineering from UCLA. A major focus of his 30-year career has been in the evaluation and prediction of the response of materials to hostile environments. These environments have included nuclear explosions, exotic fueled ramjet and rocket engines, fuel storage systems, human body implants, aircraft accident fires, and terrestrial solar arrays. He has published numerous papers and reports in the areas of heat transfer, refractory materials, rocket engine design, and combustion.

This paper presents an approach to the development of a life prediction methodology for encapsulated solar cells which are intended to operate for twenty years or more in a terrestrial environment. Such a methodology, or solar cell life prediction model, requires the development of quantitative intermediate relationships between local environmental stress parameters and the basic chemical mechanisms of encapsulant aging leading to solar cell failures. The use of accelerated/abbreviated testing to develop these intermediate relationships and in revealing failure modes is discussed. Current field and demonstration tests of solar cell arrays and the present laboratory tests to qualify solar module designs provide very little data applicable to predicting the long-term performance of encapsulated solar cells. An approach to enhancing the value of such field tests to provide data for life prediction is described.

AN IDEAL LIFE PREDICTION MODEL

A simplified ideal life prediction model (LPM) may be described as one in which the solar cell module design parameters and material properties are input along with a quantitative description of the predicted environmental stress-time history for a specific geographic location. The LPM output would be the predicted module life time in terms of a specified electrical performance decrement. Ideally, this would be a probabilistic model giving a failure rate distribution attributable to specific failure mechanisms. Thus, for 10,000 new modules described quantitatively and installed in a well documented environment, the life expectancy of that set of units would be described with considerable confidence by a probability distribution curve. The life expectancy of automobile tires due to tread wear is an example of a type of hardware to which such a model could apply.

It is useful to visualize such an ideal life prediction model because it helps define the difficulties in formulating it. These difficulties relate to describing both the environment and the life-limiting characteristics of a typical solar cell module.

SOME PROBLEMS IN DEVELOPING A LIFE PREDICTION MODEL

The failure modes which will predominate in the field after long exposure times are presently

unknown, and furthermore, it is likely that the life-limiting failure modes will vary with location (e.g., high desert versus humid sea coast).

Experience with the failure of solar modules and with most other types of hardware leads one to anticipate the existence of a "bathtub" curve of failure rate versus time. The bathtub curve may be described as the superposition of three curves or failure rates (as shown in Fig. 1) consisting first of those early failures due to various flaws acquired in the manufacturing process but not inherent in the hardware design. These failures should decrease with time as the faulty units are weeded out. The level portion of the failure rate curve describes the random failure rate during the useful life of the component and is characterized by the reliability rating or the mean time between failures (MTBF).

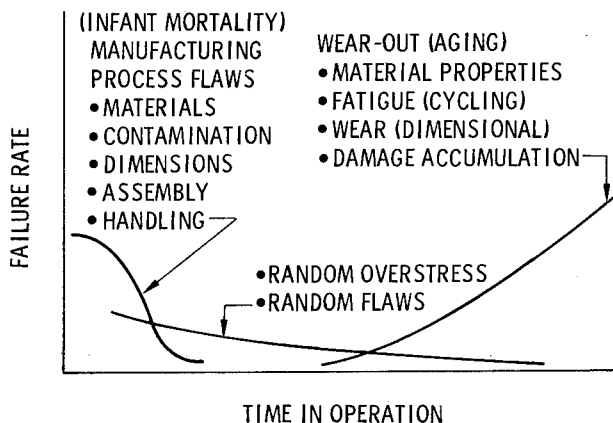


Fig. 1. Failure rate causes during field service

As time goes on, failure rates would be expected to increase due to wear out and material aging effects. Failure modes for solar cells in this long-term regime could include corrosion, fatigue, delaminations, loss in transmittance, and abrasion of the module cover. Fatigue failures would be due to combinations of thermal cycling, moisture cycling, and mechanical (wind) flexing and could result in cell cracking, electrical interconnect failures, propagation of delaminations, or cracks through the encapsulant itself.

It is the wear-out portion of the curve in Fig. 1 on which the life prediction model is focused. In attempting to develop an experimental basis for the wear-out curve, it is obvious that failure rate data as currently derived from field testing and qualification testing would have limited application. Its greatest value would be in defining potential failure modes and in improving the basic solar module design.

Another challenge in the development of a life prediction model for solar modules designed to last 20 years is that the methodology must be developed and validated in a period of much less than 20 years. The hope or expectation that solar modules may last for 20 years is currently based on general

experience with the basic materials. This experience indicates that glass and some polymers (e.g., acrylics, silicones, and fluorocarbons) could retain their useful physical, optical, and electrical properties for extended periods of years during outdoor exposure. Specific test experience with some other candidate solar cell encapsulants reveals that important degradation phenomena occur in periods of less than 1 year due to solar irradiation, temperature, moisture, and various atmospheric constituents.

The rates of degradation of these materials as a function of time and stress are unknown, and the potential for upgrading the weatherability of low-cost material candidates is yet to be evaluated in detail.

The development of a life prediction model basically requires that quantitative relationships be developed and validated among the individual and combined environmental stress elements and the individual module material and system degradation rates. Two examples of encapsulant degradation are the reduction in optical transmittance of a solar cell cover material as a function of ultraviolet exposure in specific wavelength bands, and the reduction in adhesive bond strength as a function of humidity. Both of these degradation modes could also be affected by temperatures, material thickness, adjacent materials, and processing contamination. Therefore, specific degradation rates will be some combined function of materials, module design, fabrication methods, and local environments.

The module environment parameters may result in two kinds of stress effects, reversible and irreversible. As the sun shines on the array, solar cell and encapsulant temperatures rise, producing both temperature and strain gradients. Interfacial stresses are produced between dissimilar materials as the materials expand. Cyclic temperature variations may produce reversible complex time-dependent viscoelastic strain responses which may result in some irreversible damage such as delamination. Moisture absorption and desorption are also reversible and may add to the complex strain effects in addition to producing local moisture concentrations at bonded interfaces and at corrosion-sensitive solar cell elements.

The irreversible or permanent stress effects of outdoor exposure on materials are generally referred to as aging. Chemical changes in encapsulant materials are induced at some rate by UV radiation, temperature, moisture, and air exposure as well as by contamination levels and the nature of adjacent materials. The effect of these chemical changes on solar cell performance may be manifested directly as loss in solar transmittance and a consequent loss in power. Physical property changes (such as embrittlement) resulting from chemical changes may increase interfacial stresses and consequent delamination. However, it must be appreciated that all changes in material properties such as modulus, elongation, hardness, permeability, and tensile strength do not necessarily contribute to actual encapsulation system failures.

The foregoing discussion has been intended to highlight the need to establish quantitative relationships between the environmental stress parameters and material property changes and between

material properties and the physical phenomena causing solar module performance losses. This must be accomplished in a systematic program of both laboratory material studies and outdoor validation tests employing both normal and overstressing exposure conditions.

MODELING TRANSMITTANCE DEGRADATION

It is helpful in formulating a life testing program and specifying useful data systems to consider the development of a simple performance degradation model such as the prediction of encapsulant transmittance loss. One can readily imagine a solar module cover material for which transmittance degrades with UV exposure to a specific wavelength band (e.g., wavelengths less than 320 nm). If module power output were proportional to transmittance, then a predicted performance loss curve, as shown in Fig. 2, in terms of the ratio of module power after a number of years of exposure to the initial peak power would constitute a life prediction model.

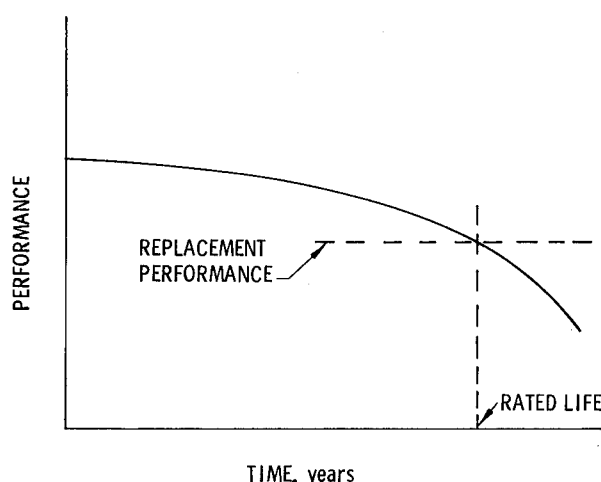


Fig. 2. Solar module life performance due to UV degradation of cover material

For this transmittance loss model, failure would be defined as a specified performance decrement determined from the economics of module replacement costs. In this example, it is assumed that all solar cells in the module degrade uniformly because they all receive the same radiation dosage. The predicted curve of Fig. 2 can be visualized as being derived from several data sources. One set of data would be solar UV spectral intensity curves showing the daily and annual variation for each array site of interest. The other useful relationships needed would be the time rate of change of cover material transmittance as a function of spectral intensity of UV in specific bandwidths or as a function of total UV incident or total UV absorbed. Some data are available on UV absorption of candidate encapsulants, as shown in Fig. 3 for a silicone (RTV 615), acrylics, and polyvinyl butyral (PVB). An additional experimental relationship is needed to relate UV absorbed to change in optical transmittance. Limited data on some materials is available. The effects of material temperature, humidity, and availability of oxygen must also be evaluated. These data are systematically being acquired at JPL for the Low-cost Solar Array (LSA) Project, along with a determination of allowable UV acceleration factors.

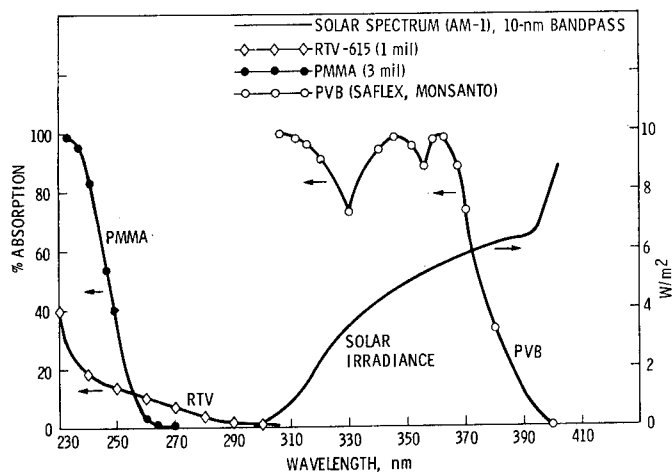


Fig. 3. Absorbance spectra for transparent polymers and solar irradiance at air mass one (AM-1)

It will be helpful if UV degradation effects are proportional only to total UV absorbed so that 20 years worth of UV in the correct wavelengths can be supplied in a period of days or weeks. Initial studies at JPL indicate that UV acceleration factors greater than 100 can be applied to specific materials.

Validation of this transmittance loss model during field testing is complicated by the daily, annual, and incident angle variation in both intensity and spectral distribution of solar UV. This complication may be eased by the successful application of a chemical actinometer being developed at JPL as a passive UV recorder capable of integrating incident UV in the field over long exposure times for the angles and spectral regions of interest.

Other failure modes such as fatigue, delamination, and corrosion may also be approached in a stepwise manner based on the development of appropriate intermediate relationships between environmental parameters and material characteristics and module performance. The use of accelerated environmental testing to gain insight into these failure mechanisms and to assess the sensitivity of the failure processes to various levels and combinations of stress is discussed in the following section.

ACCELERATED ENVIRONMENTAL TESTING AND LIFE PREDICTION

Accelerated environmental testing is a general term used to include both abbreviated over-stress testing and testing in which acceleration is achieved by increasing the frequency of the stress cycles (e.g., UV, temperature, moisture, etc.). Details of past and current accelerated test programs, methods, and measurements are given in numerous JPL and LSA contractor reports (e.g., Refs. 1 and 2). Performance and qualification tests of solar cell modules at JPL and elsewhere include some accelerated stressing conditions to evaluate module

initial performance, workmanship quality, and potential failure modes.

Four differing objectives may be defined for test programs employing accelerated testing conditions. These four test objectives are as follows:

- (1) Document system performance.
- (2) Define probable failure modes.
- (3) Define wear-out mechanisms and rates.
- (4) Verify predicted life and performance.

The chart of Fig. 4 summarizes the application of these testing objectives and the types of data expected from each test program. Because of the general use of the term "life testing," it may clarify the approach to "life prediction" to discuss the testing approaches used to achieve each of the above four objectives.

Introductory to consideration of each test category, the following definitions of the nomenclature in Fig. 4 are presented:

- (1) Design - The test specimen description including the material and material properties, the configuration geometry and dimensions, and the fabrication and processing history which could affect the initial state of the test item.
- (2) Stress - All elements of the testing environment which can be characterized and which would have some bearing on the response of the test item. These would be referred to as the test conditions or parameters. They would include the physical surroundings, the irradiation intensities versus wavelength, angle of incidence and time, plus humidity, wind, air temperature, air pollutants, precipitation, and imposed mechanical loads.
- (3) Performance - The measure of merit in fulfillment of the intended design function. Performance may be expressed as useful output as a function the values of each stress parameter.
- (4) Failure - A permanent (irreversible) degradation in the test specimen properties resulting in a performance decrement. Failure is usually construed as a performance decrement great enough to require repair or replacement of the item in service.
- (5) Degradation Rate - Progressive rate of property or performance degradation during the testing period prior to reaching the performance degradation limit requiring item replacement or repair.
- (6) Failure Rate - The time distribution of the number of test items exceeding a specified performance decrement.
- (7) Validation Testing - Testing conducted at values of design and stress parameters which have been previously used as inputs to a

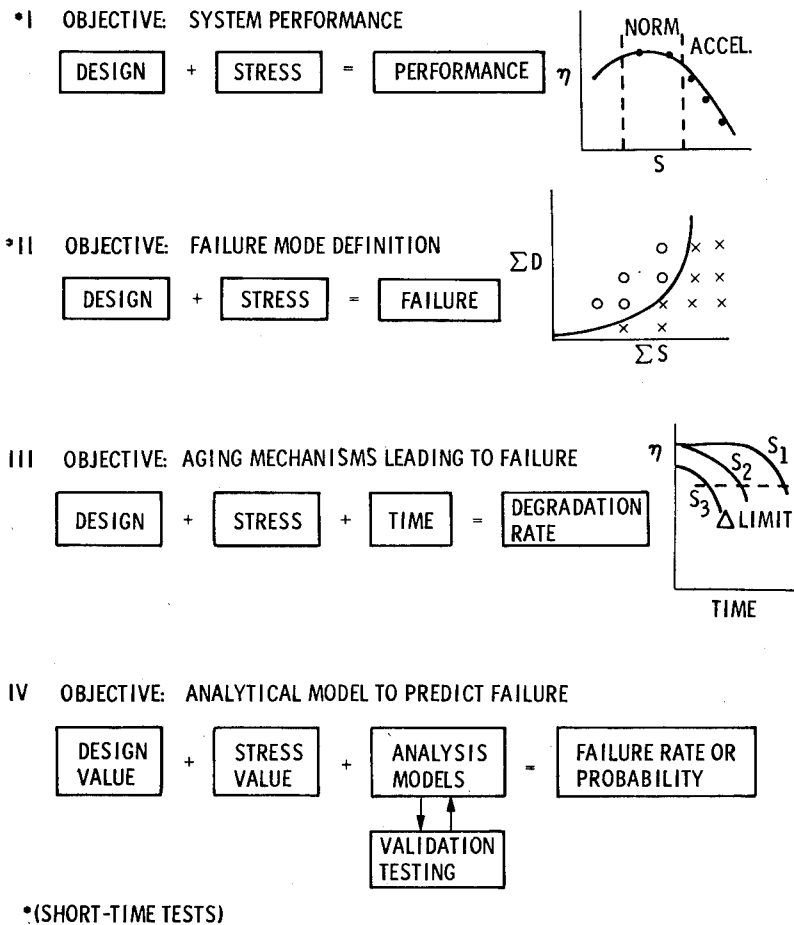


Fig. 4. Differing objectives for tests with accelerated testing conditions

performance prediction model to forecast the test results. The prediction model used may be a simple extrapolation based on a previous series of tests at similar conditions, or it may be a complex analytical computer model capable of forecasting test item performance over a wide range of untested design and stress combinations.

The chart of test objectives in Fig. 4 presents a general sequence of design development testing tasks. Of course, there is some overlap in objectives in all these testing tasks, but they are separated here for purposes of discussion.

Objective I: System Performance

Performance test parameters are normally varied over the expected range of operating conditions. Some stress acceleration may be introduced by the time compression of the varying operating environment. Where performance curves are generated as a function of stress level, stresses above normal are applied in order to generate a complete map of performance versus stress characteristics. The two primary characteristics of performance testing to meet Objective I are that the tests are nondestructive and repeatable and that time is not a basic parameter in the performance evaluation. (Time may enter the evaluation where rates-of-change of

parameters influence performance.) Some tests run to meet Objective I are called Qualification or Acceptance Tests, and production items so tested would be expected to be undamaged and put into service and operated over a normal lifetime. Tested production items which did not pass an acceptance test, due either to low performance or a manufacturing flaw, could be rejected in the process of weeding out weak units from a statistically variable product. These test results would not necessarily contribute to meeting the objectives of the second type of accelerated testing described below.

Objective II: Failure Mode Definition

In conducting a test program to meet Objective II, a wide range of combinations of both design and stress parameters would be encompassed. Weatherometer tests as well as field testing would fall in this test category. Since neither the modes of failure nor the combinations of stresses producing failure may be known initially, the systematic variation of all parameters may be impractical in terms of time and cost considerations. Judgement, intuition, and related experience may guide in the judicious selection of the initial test parameter combinations. Test severity may be set at values that are high, normal, and low. The initial output of such a testing program could be the formulation of a failure envelope, as shown conceptually in Fig. 4, with axis

coordinates of a combined design parameter function and a combined environmental stress function. The failure cases could represent one or more than one failure mode. The graphical presentation of test results might result from a series of test items containing design variations such as material thickness, modulus, expansion coefficient, adhesive type, permeability, and initial transmittance. The combination environmental stress function, which could include temperatures, humidity, and solar intensity, could also include a time function in terms of a total UV irradiation dose or number of stress cycles or rates of change of stress. Time, in terms of a 20-year lifetime, would not be included as a basic parameter in this phase of failure mode identification. In the process of failure mode identification from short-term testing, it would be beneficial to classify failure modes in terms of those associated with the initial design parameters and fabrication processes as distinguished from those failure modes related to time itself such as wear, fatigue, crack growth, corrosion, or loss in transmittance. Degradation modes may also have threshold stress limits which need to be identified because such threshold stresses may not be exceeded at normal operating conditions. With material aging over a period of years, changes in physical properties may occur and the stressing situation may change, exceeding the threshold for initiating degradation, thus resulting in gradual or rapid performance losses.

The concept of a maximum damage limit can be investigated during this testing phase. There are several types of failure or material degradations that would be limited in extent regardless of the severity and time of testing. Solar transmittance is one example. The total transmittance through a polymer cover sheet would probably remain at some value above zero no matter how long the material were exposed. Also, delamination between the solar cell and its cover material would result in some limited transmittance decrement even with total delamination. The determination of these damage limits should be a goal of Objective II testing.

A distinguishing characteristic of Objective II testing is that the test produces some measure of permanent damage or performance loss in the test item. Also the tests are usually run over a relatively short time compared to the total design lifetime. Normal aging and wear would not be primary causes of the failure or damage identified.

In the special cases for which failure or wear can be quantitatively related to the number of stress cycles, and the number of stress cycles over a normal lifetime can be closely estimated, the life of the test item could be predicted. Mechanical devices with moving parts may fall into this category. A potential solar array failure mode in this category may be the rate of growth of a delamination spreading from some initial flaw or edge condition. The goal of Objective II testing would be to determine the existence of such failure modes and their sensitivity to the various imposed environmental stresses. Thus testing with a large range of stress intensities may give insight into selecting future stress parameters and stress level intervals for evaluation of degradation rates and aging mechanisms.

Objective III - Evaluating Aging Mechanisms Leading to Failure

In evaluating system and material aging mechanisms leading to failure, the primary objective would be to quantitatively determine rates of degradation or rates of change of measurable system characteristics as a function of each separate or combined environmental stress over long operating times. For systems with 20-year lifetimes, the rates of degradation over short test periods may be very small and require great precision in measurement. It would be important to define the physical nature or mechanisms of short- and long-term degradation. This may come from direct observation, past experience, or an experimental study of similar physical or chemical systems.

The validity of accelerating stresses without changing the degradation mechanism must be established. Also the validity of accelerating one stress factor such as UV intensity, while leaving oxygen or moisture concentrations at normal levels, must be evaluated.

Three characteristic performance degradation curves which may occur are of the form shown in Fig. 5. Analytical expressions and physical phenomena producing these characteristic degradation curve shapes can readily be postulated. Their experimental verification may be much more difficult. However, the importance of determining the shape of these curves is obvious in being able to extrapolate performance from 2 years to 20 years.

Very complex curves may result from the combination of multiple or competing failure modes. Objective III testing requires a systematic, parameter-by-parameter evaluation of each degradation mode. These tests must be performed under completely controlled and characterized experimental conditions. Fluctuating conditions encountered in normal or

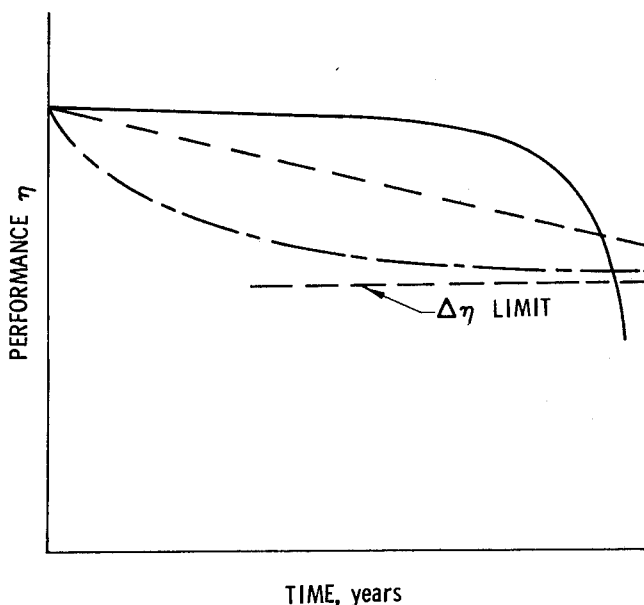


Fig. 5. Performance degradation curves determined by differing aging and failure mechanisms

accelerated outdoor exposures may aid in identifying failure modes and in indicating relative sensitivities, but controlled exposure conditions are required to establish the precise degradation rate relationships required for predicting lifetime performance up to 20 years or more.

After having identified various failure modes during testing of complete modules under normal or accelerated exposure conditions to achieve Objective II, it may be necessary to test subcomponents or materials alone to quantify rates of degradation and chemical structure changes as a function of each stress element alone and in combination. At the point of departure from complete module testing at normal environmental exposure conditions, it will be important to understand and define the connecting quantitative relationships between the laboratory aging studies and the outdoor exposure tests. The laboratory testing must be conducted at stress conditions which will encompass the range of outdoor stresses and which can be measured during outdoor testing. Thus, determining the rate of aging of polymers due to solar UV requires laboratory control of the spectral distribution and intensity of the laboratory radiation lamp covering the potential outdoor conditions. Then in predicting or validating the rate of outdoor aging, it would similarly be necessary to specify or measure the spectral distribution and intensity of normal solar irradiation falling on a test module at the outdoor test site.

The identification and precise measurement of a secondary chemical or physical material characteristic (such as IR absorption spectra or molecular weight) would aid in life prediction if the change in the measured characteristic could be related both to the rate of performance degradation and to the stress intensity/time function.

The statistical design of tests to produce the key quantitative relationships has been discussed by both Rockwell International (Ref. 1) and Battelle (Ref. 2) in their investigations of accelerated testing methods. It is the accurate formulation of these key intermediate aging rate relationships which will be the basis for a satisfactory life prediction methodology. The development of reduced variables in which several stress parameters are combined in a single variable would reduce the complexity of the life prediction model. This is facilitated by initial separation and control of the test stresses. This effort also may require a very extensive test matrix and precise control of test parameters. Preliminary experimental studies may be

conducted to determine the required range of test variables, the test precision required, and the basic shape of the resulting performance loss curves. Thus, Objective III testing may occur in two or more phases in developing the necessary quantitative aging relationships.

Objective IV - Validation of the Life Prediction Model

The foregoing discussion of the development of degradation rate quantitative relationships indicates that they are best developed under laboratory conditions with closely controlled exposure parameters. The validity of such relationships must then be established under full-scale field exposure conditions for which the environmental stresses may be imposed in a highly variable and random manner. Exercising the analytical models over selected ranges and combinations of environmental stresses will provide an evaluation of the accuracy and precision required in specifying and measuring the variations in environmental parameters such as insolation, temperature, humidity, wind velocity, etc. In some cases, integrated values or daily averages may suffice to predict total degradation during a given period.

In validation testing, anticipated results should be predicted prior to testing based on predicted stresses and predicted again, after testing, based on measured environmental stresses. The prediction model should be probabilistic to yield a range of probable test results based on the experimental variability of design properties and material aging rates. The number of validation tests and the selection of test parameters should be based on the requirements for statistical validity at confidence levels consistent with other elements of the overall solar power program.

REFERENCES

1. Kolyer, J. M., and Mann, N. R., Interim Report on Accelerated/Abbreviated Test Methods, Study 4 Task 3 (Encapsulation) of the Low-Cost Silicon Solar Array Project, Rockwell International Report ERDA-JPL-954458-77/7, October 24, 1977.
2. Gaines, G. B., Thomas, R. E., et al., Methodology for Designing Accelerated Aging Tests for Predicting Life of Photovoltaic Arrays, Battelle Columbus Laboratories Report ERDA/JPL-954328-77/1, February 1, 1977.

ACKNOWLEDGMENT

This paper presents the results of one phase of research conducted at the Jet Propulsion Laboratory, California Institute of Technology for the Department of Energy, by agreement with the National Aeronautics and Space Administration.

MEASUREMENT REQUIREMENTS AND TECHNIQUES FOR DEGRADATION
STUDIES AND LIFETIME PREDICTION TESTING OF PHOTOVOLTAIC
MODULES

G. T. Noel, F. A. Sliemers, G. C. Derringer, V. E. Wood,
K. E. Wilkes, G. B. Gaines, and D. C. Carmichael
Battelle Columbus Laboratories
Columbus, Ohio 43201

AUTHORS' BIOGRAPHY

The authors are members of a multidisciplinary team formed at Battelle to research measurement techniques for life prediction in photovoltaic modules. They represent expertise in photovoltaic devices and systems (G. T. Noel), life prediction and encapsulation of terrestrial photovoltaics (G. B. Gaines and D. C. Carmichael), polymer chemistry (F. A. Sliemers), statistical analysis (G. C. Derringer), optical measurements (V. E. Wood), and thermal and mechanical measurements (K. E. Wilkes).

INTRODUCTION

The validation of a 20-year service life for low-cost photovoltaic arrays is a critical requirement in meeting the economic goals for photovoltaic systems which have been established for photovoltaic projects sponsored by the Department of Energy, Division of Solar Technology, and specifically for the Low-Cost Solar Array Project conducted by the Jet Propulsion Laboratories. The long-term integrity and stability of the encapsulation system will ultimately determine the operational lifetime of the array. The materials that provide this protection must be low in cost and must not significantly decrease the output of the solar cells. There is then an urgent need for establishing reliable tests for characterizing the weathering and aging behavior of present and future encapsulation materials and systems and for identifying measurement techniques and instruments suitable for implementing these tests. These tests must, necessarily, include both accelerated life tests and real-time weathering tests. Methodologies for designing accelerated aging tests for predicting the service-life of photovoltaic arrays have been developed by Battelle and others. Instruments suitable for implementing these tests must provide sufficient sensitivity and precision to allow projections of the ultimate system lifetime, and of performance over that lifetime, from short-duration natural and/or simulated weathering tests. The measurements must provide sufficient confidence to permit selection among alternative designs and materials and to stimulate widespread deployment of such arrays. Further, the diversity of candidate materials and designs, and the variety of potential environmental stress combinations, degradation mechanisms, and failure modes require that combinations of measurement techniques be identified which are suitable for characterizing various en-

capsulation system-cell structure environment combinations.

DEGRADATION AND FAILURE TYPES

Life prediction studies are concerned with the time dependence (rate) of degradation of array performance. The loss of power output up to any point in time is usually due to, and provides a measure of, significant materials-related degradation that has taken place in the array. However, degradation of the protective properties of encapsulants may not immediately result in detectable changes in power output. In general, array-degradation is dependent on the individual and combined effects of array design, materials of construction, processing/fabrication methods, and the specific environment to which the array is exposed.

Figure 1 is a schematic of a hypothetical photovoltaic module illustrating possible encapsulation-system components. The major components include the cells (with metallization and antireflection coatings), interconnects (metal ribbons, wires, metallized plastics, etc.), pottants/adhesives (polymeric), substrates (glass, anodized aluminum, P C board, etc.), and sheet/film coverings (glass or polymers). Other possible constituents include various types of coatings for surface-property enhancement. There are many possible module configurations, or encapsulation-system designs, which use various combinations of these components and materials.

In the context of array performance and degradation, a "failure" is generally considered to be a change in the properties of the cell/module/array which results directly in a reduction in its power output below a specified minimum level. (The particular application, system design, and operating conditions, e.g., insulation level/range, ambient temperature, determine the minimum level.) Such a change can occur either catastrophically or gradually. A given failure mode can have many different causes. Some may be the direct result of degradative changes in the optical or electrical properties of materials or encapsulation systems; others may reflect indirect contributions from degradative changes in the ability of the encapsulation system to isolate the cells from environmental and mechanical stress factors. The lumped-constant model of the photovoltaic cell, shown in Figure 2, is useful in organizing failures due to degradation into four

types based on the components of this model. The failure of a cell or module corresponds, in effect, to a significant change in the value of one or more of these four components; correspondingly changes in the effective values of these lumped-constant components can be traced to major degradative changes in specific elements or combinations of elements of the module/array and ultimately to the microscopic (and in some cases, macroscopic) chemical and physical changes in materials--the earliest precursors to degradation and failure.

Figure 3 is a first-level breakdown showing the four failure types, based on the lumped-constant model, and potential causative degradation factors. It is generally considered that environmental conditions severe enough to affect the bulk properties, diffusion profiles, etc., of the silicon cells are not likely to be experienced during normal array operation, and hence, that junction and bulk-semiconductor changes will not be significant factors in determining the lifetime of terrestrial photovoltaic modules. Figures 4-6 shown second-level breakdowns of the degradation factors shown in Figure 3 (excluding bulk semiconductors and junction effects).

ENVIRONMENTAL FACTORS AND PROPERTY CHANGES ASSOCIATED WITH PRIMARY DEGRADATION MODES

The environmental factors generally considered to be of primary importance in the initiation and evolution of degradative changes are:

- Ultraviolet radiation (290nm-400nm), which results in broken chemical bonds in some polymers, and excited states and ionized molecules which contribute to other degradative chemical reactions.
- Thermal energy, which is generally a contributing rather than an initiating factor, and which is a major controlling factor in determining rates of reactions and degradative changes.
- Water, which (alone or in the presence of pollutants and/or impurities) can degrade encapsulants through hydrolysis, leaching, swelling, dissolution, etc.
- Oxygen, which is generally involved in synergistic effects with UV, elevated temperatures, etc.
- Physical stress, which contributes to fracture and bonding failures.
- Pollutants (NO_x , SO_2 , O_3 , particulates, etc.), which are generally involved in synergistic effects.
- Abrasives and dirt, which can directly alter surface optical properties and initiate flaws that

are nuclei for other degradation and failure modes.

These are the primary factors that give rise to the property changes whose detection and quantification are key to the early prediction of array lifetime. The quantitative link between these environmental factors and the degradation rate(s) is the ultimate objective of the life-prediction process.

Property changes associated with exposure to the above environmental factors can be identified in general terms for the various classes of materials used in module/array construction. For polymeric materials degradation can be defined in terms of the occurrence of one or more of a number of primary events within the material that produce changes at the molecular level. Principal among these primary events are chain scissions, cross-linking reactions, development of unsaturation, depolymerization, molecular rearrangement, volatile-product formation, and attendant reactions with foreign moieties (oxygen, H_2O , etc.). Glasses are susceptible, under certain conditions, to weathering by chemical attack and abrasive particles. Leaching or etching of glasses can result from attack by acidic or alkaline solutions and can induce flaws which can weaken the glass and lead to fracture. Metallic contacts and interconnects are subject to corrosive attack of various types resulting in removal/altering of material and reductions in conductivity. These elements are also subject to stress fracture. Other structural elements, such as substrates, frames, edge seals, etc., are subject to various types of corrosive or stress induced changes depending on the types of materials employed. The property changes are generally in the areas of increased permeability to corrosive agents (H_2O , etc.) or reduced mechanical strength.

MEASUREMENT TECHNIQUE/INSTRUMENT REQUIREMENTS AND SELECTION CRITERIA

A key requirement of an accelerated/abbreviated test for photovoltaic modules is the early detection of changes of the types described above. This establishes sensitivity (the ability to distinguish small changes) as an essential requirement for instruments used in life-prediction testing. Other essential or useful instrument characteristics, for this application, have been established for use in assessing candidate instruments. These are listed in Table 1. The two key characteristics for life-prediction are sensitivity and precision.

Applicable Measurement Techniques and Instruments

Using the above selection criterion and based on an understanding of the degradation modes and failure types, an in-depth survey of potentially applicable measurement techniques and instruments was conducted. This survey included computerized literature searches, discussions with experts/authorities on numerous techniques, and contacts

with equipment designers and manufacturers. As a result some specific techniques were selected and recommended as being immediately or potentially applicable to life-prediction studies of photovoltaic modules. The techniques selected are listed in six categories (chemical, electrical, mechanical, optical, thermal, and "other") in Tables 2-6. These tables also describe the specific areas of applicability of the technique and values for limits of sensitivity, precision, and accuracy where available. Generally agreed upon limits for these quantities were not found for many of the techniques and instruments which were felt to be potentially useful. The techniques which were selected include immediately useful as well as potentially desirable high-sensitivity techniques and cover the full spectrum of failure types.

CONCLUSIONS

Several important conclusions resulted from this study of measurement techniques for life-prediction testing of terrestrial photovoltaic arrays. Some of these can be summarized in brief as follows:

- There is a need for determination of the precision for measured properties for ESCA, FTIR, and the gas chromatography/mass spectroscopy combination.
- A major research effort is necessary to establish quantitative correlations between key measurable properties (e.g., carbonyl formation, glass transition temperature, molecular weight changes) and degradation/failure modes.
- A set of experiments to determine relative precision of the thermal-analytical techniques and the dynamic mechanical techniques for measuring the glass transition temperature is needed.
- There is a need to refine (i.e., maximize sensitivity, precision, etc.) cell characteristic measurements (I-V, spectral response) for life-prediction and degradation studies.
- Several promising techniques, including electrical noise measurements, chemiluminescence, dielectrometry, infrared thermovision, light scattering, and holographic interferometry, require experimental evaluation/development for applicability.
- There is a need to develop suitable instrumentation for in-situ measurements of optical and mechanical properties on photovoltaic modules.

ACKNOWLEDGEMENTS

This work was performed for the Jet Propulsion Laboratory, California Institute of Technology, under NASA Contract NAS7-100 for the U. S. Department of Energy, Division of Solar Technology. The JPL Low-Cost Solar Array Project is funded by DOE and forms part of the DOE Photovoltaic Conversion Program to initiate a major effort toward the development of low-cost solar arrays.

The authors wish to acknowledge the assistance in this study of R. Igou and E. Briich of Battelle; the contributions of H. Maxwell, C. Coulbert, and others of JPL; and the help of the numerous other researchers who provided information for the investigation in areas of their expertise.

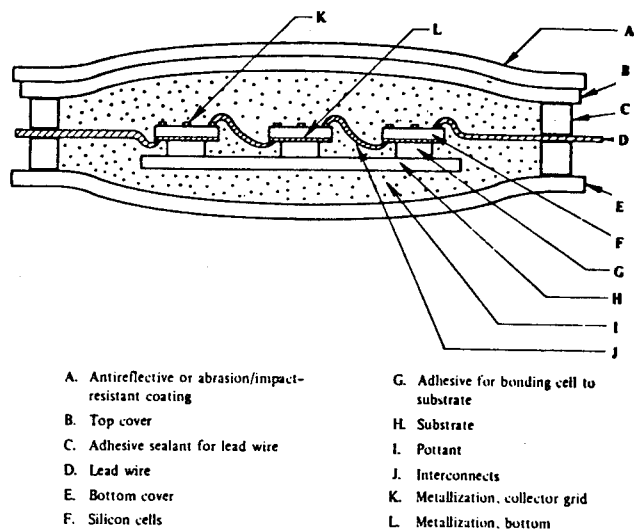
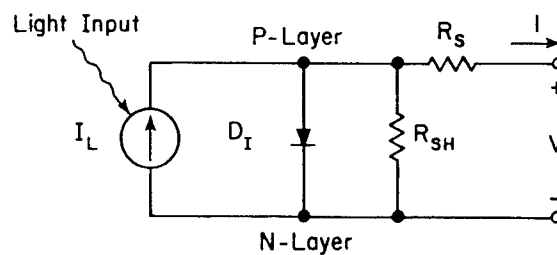


FIGURE 1. SCHEMATIC OF HYPOTHETICAL ARRAY MODULE IDENTIFYING ENCAPSULATION-SYSTEM COMPONENTS



Components of the model:
 I_L = Light-generated current source
 D_I = Ideal diode
 R_S = Series resistance
 R_{SH} = Shunt resistance

FIGURE 2. LUMPED-CONSTANT SOLAR CELL MODEL

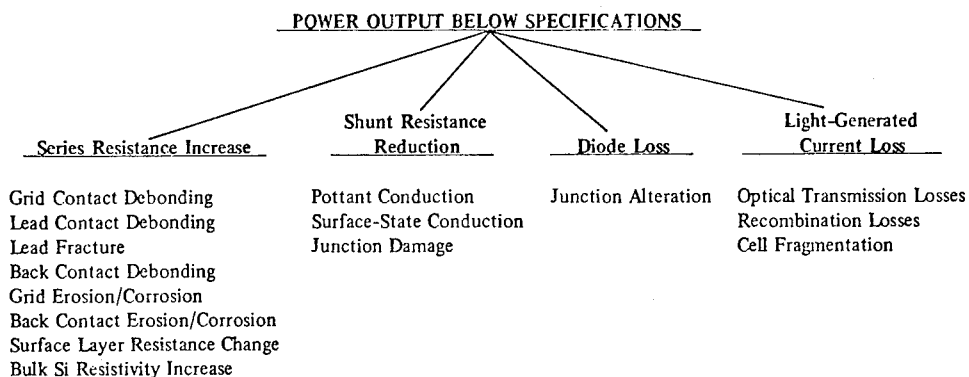


FIGURE 3. FOUR FAILURE TYPES BASED ON THE FOUR COMPONENTS OF THE LUMPED-CONSTANT CELL MODEL (FIGURE 2) AND A FIRST-LEVEL BREAKDOWN INTO CAUSATIVE DEGRADATION FACTORS

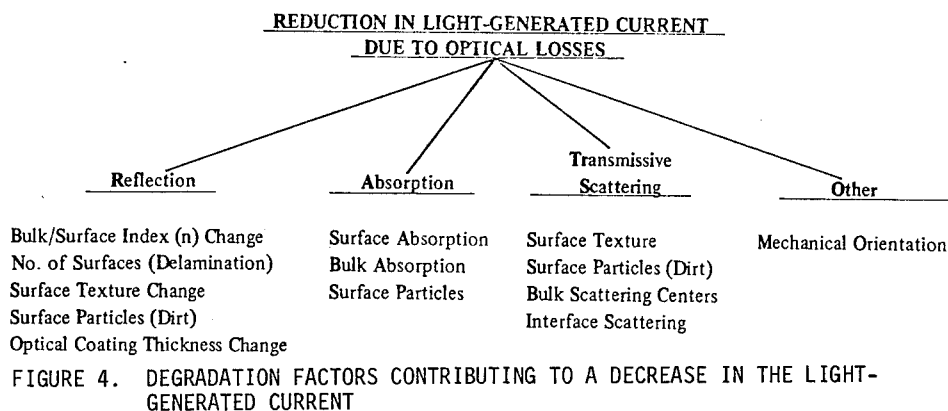


FIGURE 4. DEGRADATION FACTORS CONTRIBUTING TO A DECREASE IN THE LIGHT-GENERATED CURRENT

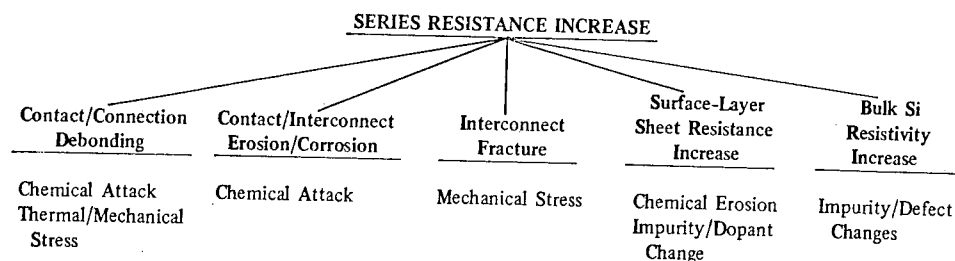


FIGURE 5. DEGRADATIVE CHANGES MANIFESTED AS SERIES RESISTANCE INCREASES

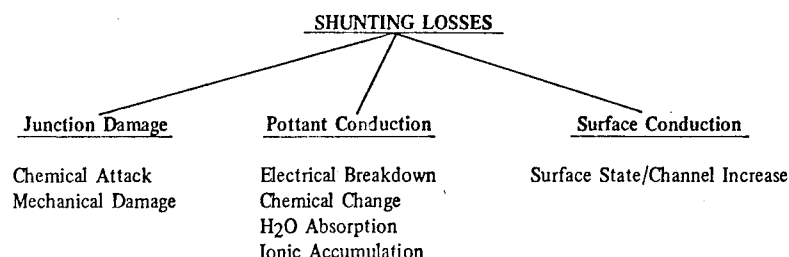


FIGURE 6. DEGRADATION FACTORS CONTRIBUTING TO LOSSES BY SHUNT RESISTANCE DECREASES

TABLE 1. INSTRUMENT AND TECHNIQUE EVALUATION CRITERIA

Properties Measured
Areas of Applicability
Measured Property Value Ranges and Sensitivity in Ranges
Accuracy in Ranges
Precision in Ranges
Required Form of Test Specimen
Effect of Measurement on Test Specimen
Suitability for In-Situ Measurements
Instrument Cost
Ease of Measurement
Cost of Test
Instrument Portability
Calibration Requirements and Reproducibility Among Instruments
Availability of Instruments

TABLE 2. RECOMMENDED CHEMICAL TECHNIQUES

Instrument/Technique	Properties Measured-Applicable	Sensitivity	Accuracy	Precision
	Degradation Modes			
Fourier Transform Infrared Spectroscopy including ATR	Surface and bulk carbonylization of polymers	100 ppm range?	<0.1 cm ⁻¹	<0.1 cm ^{-1**}
ESCA	Surface carbonylization of polymers. Depletion of surface species on glass plate, i.e., Na ⁺ . Interface evaluation after teardown analysis.	.01 - .02 atomic fraction	*	*
Gel Permeation Chromatography	Changes in polymer molecular wt. due to chain scission and crosslinking. Detection of low MW species such as residual monomers, plasticizers, etc.	*	20% at worst	5-12 for Mw or Mn. 1-2% for Mw/Mn
Chemiluminescence	Photon emission from degradative reactions	10 ⁻¹⁵ moles/yr degradation rate	*	*
Gas Chromatography/Mass Spectrometry	Volatile polymeric fragments - Photolytic breakdown of polymers	10 ng/ml	10% at worst	*
Surface Energy	Surface properties	*	*	*

* Could not be found.

** Repeatability.

TABLE 3. RECOMMENDED ELECTRICAL TECHNIQUES

Instrument/ Technique	Properties Measured- Applicable Degradation Modes	Sensitivity	Accuracy	Precision
Illuminated I-V Characteristics	I_{sc} , P_{max} , V_{oc} , R_{sh} , R_{oh} , any output degradation	Potentially high	I_{sc} - $\pm 2\%$	I_{sc} - $\pm 1\%$
Dark I-V Characteristics	I_{sc} , R_{sh} , Diode Parameters-cell/ module power dissipation	Potentially high	$\pm 0.03\%$ to $\pm 0.1\%$	Potentially high
Spectral response	I_L vs λ - optical trans- mission degradation	Potentially high	$\pm 5\%$ to $\pm 20\%$	$\pm 1\%$ at best
Electrical noise	Current noise - contact corrosion interconnect cor- rosion	--	± 0.5 dB (-40 to + 60 dB)	± 1 dB
Conductivity	Electrical con- ductivity- ionic impurities moisture content breakdown	Potentially high	$\pm 0.03\%$ to $\pm 4.0\%$	Potentially high
Dielectrometry	Permittivity, Loss factor- polar groups moisture ions	--	Temp. $\pm 1\%$ $C \pm 0.022$ loss $\pm 1\%$	Temp. $\pm 0.25^\circ C$
Special detectors	Detector Electrical Properties- presence of alien species	Potentially high	Potentially high	Potentially high

TABLE 5. RECOMMENDED THERMAL AND MECHANICAL TECHNIQUES

Instrument/ Technique	Property Measured	Sensitivity	Accuracy	Precision
Differential thermal analysis	Temperature differential/ due to "heat effects"	0.002 $^\circ C$ Temp. difference	$\pm 4.0^\circ C$ for T_g ; $\pm 2.0^\circ C$ for T_{melt}	$\pm 2.5^\circ C$ for T_g ; $\pm 1.5^\circ C$ for T_{melt}
Differential scanning calorimetry	Differential heat input	1 $\mu cal/sec.$	± 0.22 on Q $\pm 1^\circ C$ on T	$\pm 1\%$ on Q
Torsion Pendulum	Dynamic modulus and damping (G' and G'')	*	G' for T_g : 1% G' for T_g : 30% G'' for T_g : 10% G'' for T_g : 10% $\pm 3.0^\circ C$ for T_g	G' for T_g : 3.5% G' for T_g : 15% G'' for T_g : 10% G'' for T_g : 5%
Forced vibration Viscoelastic- ometer	Dynamic modulus and damping	*	5-10%	3%
Ultrasonic Pulse-echo	Flow detection	*	*	*
Infrared Thermo- vision	Temperature differences at flaws	0.2 $^\circ C$	*	*

TABLE 4. RECOMMENDED OPTICAL TECHNIQUES

Instrument/Technique	Properties Measured- Applicable Degradation Modes	Sensitivity (OPTO detectable)	Accuracy (a)	Precision (a)
Reflectometry	Reflectance-lac surface degradation, interface changes	200-500 \AA	0.1%	1% (long term)
Ellipsometry	Ellipticity of reflected light- delamination, other changes in optical path	5-10 \AA (frequently)	0.01%	0.01%
Holographic Interferometry	Phase change at points in light path-incipient delamination	50-3000 \AA	Variable	low long-term with available instruments
Light Scattering	Small angle forward scattering of light-delamination, bubble formation, surface damage	high	high	high
Microscopy	Surface structure- first surface damage	50-100 \AA resolution for SEM	--	--
Spectral Trans- mission	Transmitted light- optical transmission degradation, UV damage	high	high	$\pm 1\%$ - $\pm 2\%$ over 6 months

(a) Precision and accuracy are for the quantity measured and not for any derived quantities.

TABLE 6. OTHER RECOMMENDED TECHNIQUES

Instrument/Technique	Properties Measured- Applicable Degradation Modes	Sensitivity	Accuracy
Profilometry	Surface roughness - surface etch/leach abrasion	CLA $\pm 2\%$ (2-400 μ in.) MC 1 to 200 μ in. (20-4000 μ in.)	--
Water Vapor & Gas Permeability	Flow rate of Gas/ UV through material- molecular wt., crystallinity cross linking, density	WTR-0.01 g/100 in. ² /24 hr	Temp. $\pm 0.5^\circ F$ WTR: $\pm 2\%$
Photoacoustic Spectroscopy	Optical Absorption, Thermal Diffusion- optical properties	11 mW/m ²	*

AN APPROACH FOR DEVELOPMENT OF PERFORMANCE CRITERIA AND TEST STANDARDS IN PHOTOVOLTAICS

By: Gary Nuss, SERI

Background Standards The need to begin activities to develop photovoltaic "standards" is--I believe--well recognized because of the important roles that standards play at all levels of product development from basic research to field installation and operation. "Standards" can allow:

- The performance of photovoltaic devices (materials, components, subsystems, and systems) to be measured, understood, utilized, and communicated.
- For interchangeability between devices or compatibility between interfacing devices.
- The life expectancy/reliability of photovoltaic devices to be measured, understood, and/or compared against minimum acceptable levels.
- The safety characteristics of photovoltaic devices to be measured and/or compared against minimum acceptable levels.
- For the safe and proper application of photovoltaic devices.

Various types of standards activities have historically been implemented to provide for the above actions. For instance, the activities include:

- A. Developing and maintaining working definitions and terminology for important product (material, component, subsystem, or system) characteristics related to performance, reliability, and safety. Where possible, definitions should provide for quantitative physical meaning and should reference a specific procedure for measurement. Examples include definition of module efficiency, peak power, concentration ratio, etc.
- B. Developing and maintaining Test Method Standards which describe and proscribe test procedures to be used in determining properties, composition, or performance characteristics. Test method standards do not include numerical limits for the properties, composition, or performance. Examples include the thermal cycling test procedure, electrical output measurement technique using standard cells, etc.
- C. Developing and maintaining Recommended Practice Procedures. Examples of such include selection, preparation, application, inspection, necessary

precautions for use, disposal, installation, maintenance, and operation of test apparatus. Specific examples include series/paralleling guidelines for photovoltaic systems, operation and maintenance safety considerations, and so forth.

- D. Providing for the certification of testing laboratories and/or test apparatus.

Before presenting our approach for a photovoltaic standards development plan, it is important to delineate the objective and goals of the effort. The objective is to aid the advancement of photovoltaics in the laboratory, manufacturing plant, market place, and field by accelerating the development of photovoltaic standards within the photovoltaic community. It is recognized that to be useful the standards must be accepted--"consensus standards"--of this community and need to be maintained over the long term by the traditional standards organizations such as ANSI, ASTM, ASME, IEEE, UL, etc., and in the form of model building codes.

One element of the DOE Photovoltaic Program Plan is the establishment of standards and performance criteria. Such criteria are important to the timely commercialization of an emerging technology where risks of use and uncertainty of performance and life can be perceived to be relatively high. Criteria for performance and standardized test procedures are needed to enable the comparisons of technological elements and to ensure the safety and protection of users. (Indeed, one of the primary benefits of standards is improved communications between researchers and developers.) Standards and performance criteria need to be developed for components, subsystems, systems, installations, and for health and safety.

The goals of this standards development program for FY78 are:

- To identify, rank priorities, and to begin development of preliminary performance criteria and test standards needed for the continued growth of photovoltaic applications within the private sector.
- To encourage the early involvement of industry and professional societies in the photovoltaic standards development and adoption process.

Although these are the immediate near-term objectives, subsequent objectives for FY79-FY81 include developing:

- Procedures for identification and criteria for accreditation of testing labs;
- Establishment of certification procedures and programs;
- Interim performance and lifetime criteria for appropriate applications;
- To assist in industry adoption of photovoltaic performance criteria and standards; and
- To assist the state and local regulatory agencies in the review, approval, and adoption of uniform photovoltaic health, safety, and performance codes.

These goals are dependent on a crucial activity for the first year's effort--namely, the establishment of a viable working group dedicated to standards development in photovoltaics and of an effective rapport with consensus standards organizations. Establishment of this network is necessary to effect the standards and performance criteria elements of the Photovoltaic Program Plan. However, this activity is but one of several which can accelerate the generation of photovoltaic standards. Besides enlisting the early cooperation and interest of the traditional standards associations and of the community at large, the program can:

- Assist the identification of needed standards;
- Facilitate the development of draft standards; and
- Provide an organizational focus to coordinate the overall photovoltaic standards activity.

However, the generation of photovoltaic standards must rest heavily on the participation of representatives of the traditional standards organizations and on the future photovoltaic user/manufacturing industry.

This reliance on members of an emerging industry will require some modification of the traditional approach to standards generation. For example, the generation of relevant standards for some applications will certainly require not only the insight of representatives from the manufacturer/user community, but will also require data from study contracts and application experiments since little or no past experience with reasonable analogies may exist.

As Bruce Steiner of NBS has observed, this consideration recognizes a new role for standards. The standards development system in the United States has been structured to respond to needs in existing technology driven by commercial incentives, needs perceived and ranked initially by managers who likely are, themselves, outside of the standards system.

Standards for anticipated technology are now being called for. Such standards are meant also to stimulate new technology, to guide its development, and to optimize transfer within the private sector.

Many specific research needs have to be anticipated. Execution of this research will have to be closely coordinated and widely communicated.

An important objective of the DOE photovoltaic standards activity, therefore, is to bring representatives of future users and traditional standards organizations together with knowledgeable representatives of the photovoltaics R&D and manufacturing community.

Proposed Approach to Photovoltaic Standards The development of standards over the broad range of system components and application types is a monumental task. The diversity of scope can be noted by listing some of the key elements in photovoltaic standards development:

- Hardware elements (solar cells, flat-plate modules, concentrators, combined collectors, systems, novel materials, power conditioners, storage, etc.).
- Application types (small remote, marine, residential, central power, agriculture, etc.).
- Types of standards/criteria: performance, reliability, etc. Also implicit in these is the necessity for uniform, consistent measurement techniques.
- And overlaid on these three elements are the perspectives of all interested parties (utilities, A&E firms, PV manufacturers, industry associations, military, research institutions, commercial business, regulatory bodies, etc.).

Considering the above, it is clear that the standards development activity is a matrix problem spanning at least three dimensions. The scope of our approach attempts to address all aspects of photovoltaic criteria for each of the photovoltaic system technologies and applications. The Photovoltaic Standards Development Program will focus on standards relating to photovoltaic devices and systems, and it will maintain an interface/coordination role with standards organizations with cognizance over interfacing hardware such as storage and power conditioning.

Most national standards in the United States are developed within a voluntary system of producers, users, suppliers, government, institutions, and individuals. Participation in the give-and-take of standards development is voluntary, and the standards resulting from such efforts are used within other existing regulations and codes. The approach proposed

here is designed to preserve the voluntary nature of standards activity and--at the same time--to accelerate and to augment the process as much as possible.

There are several key aspects of the photovoltaic standards development program which need to be considered in an implementation structure. These include:

1. Close interaction with photovoltaic R&D groups. The R&D community provides the principle near-term need for standards and also represents the best source of technical expertise in the field of photovoltaics. The principal involvement of near-term future users and manufacturers is also within the DOE Photovoltaics R&D Program;
2. Close interaction with groups that provide commercial-practice experience in the field of standards. Examples include the traditional standards organizations such as ANSI, ASTM, ASME, IEEE, UL, building code representatives, regulatory bodies, and representatives of manufacturing and user industries;
3. Responsiveness to the needs of the DOE Photovoltaics Program including large-scale procurements, applications experiments, PON's, PRDA's, etc. Here a critical element is the time required to achieve consensus standards involving the entire community; and
4. The vast size of the task at hand and the finite resources available.

Major Tasks Several preliminary tasks need to be accomplished in 1978 in order to meet the project's objectives in subsequent years. The first of these tasks was the selection of an Advisory Committee. The management activity will be exercised through--and counsel and planning offered by--the Advisory Committee which represents as many of the affected and involved constituencies as possible.

The Advisory Committee needs to be large enough to encompass all concerned organizations, yet small enough to be an effective planning and steering body. Membership needs to include representatives of DOE's prime contractors as well as industry, utilities, standards groups, professional organizations, and test facilities. All members will have equal status on the committee. DOE's prime contractors, however, are expected to have major roles and contributions to make in conducting standards development projects and in drafting preliminary standards. But the other organizations are equally important as they offer capabilities and perspectives different from DOE's prime contractors.

The second task was the preliminary review of PV standards development. The following activities

are underway:

- Review of past and current standards activities in PV--for example, early work by EIA, NASA-Lewis, JPL, and others;
- Review of ANSI SHAC Steering Committee work to identify applicable standards and to replicate their process where appropriate; and
- Preliminary definition of requirements for PV standards by generic areas of technology, applications, attributes, functions, etc. The need here is to define performance criteria and test standards categories on the "first cut" basis.

The Advisory Committee has established terminology and definitions for PV subsystems and components, has identified important performance characteristics for which measurements need to be made, has made a preliminary assessment of the status of test methods to make those measurements, and has established priorities for standards development projects.

The third task is the establishment of subcommittee groups to address specific elements of PV systems and particular types of standards requirements. These subcommittees are now formed and include representation from outside the Advisory Committee. The subcommittees will address:

- PV subsystems' performance criteria;
- Reliability and durability;
- Safety;
- Storage subsystems; and
- Power conditioning and controls subsystems.

The subcommittees will address the same problems and issues as did the Advisory Committee--terminology and definitions, performance characteristics, measurement and test methods, and priorities for development.

From the work of the subcommittees will come an identification of standards needs and priorities for these needs. These decisions lead to the fourth task--initiation of standards development projects to devise and to document preliminary test methods for measurement of important performance characteristics. Some of these requirements have already been identified. For example:

- loading characteristics of arrays;
- soiling problems;
- acceptance angle for concentrators;

- efficiency measurements; and
- others.

5. Provide near-term "standards" as needed on a quick response basis to support the immediate needs of the photovoltaic R&D Program.

With the photovoltaic standards activity closely aligned with the current photovoltaic R&D program structure, we can make maximum use of the R&D technical base and can provide responsiveness to the R&D community's program needs. Sharing of various technical personnel and laboratory facilities also can lead to improved communication and to expanded output for the limited resources available. Because of the large research and standards development effort required, the national laboratories most likely will be used as focal points for the generation of draft standards.

During the remainder of this year and in 1979, work will proceed in devising preliminary test methods and providing drafts of preliminary "standards" for referral to consensus standards groups.

The fifth task is the synthesis of the subcommittee judgments into a cohesive plan for development of the priority items and subsequently other criteria development requirements including accreditation and certification programs, model code provisions, and assistance in adoption of these criteria and codes.

The sixth task is the discussion of the plan and its elements in an open meeting/workshop to communicate the direction of the project to obtain the judgments, review, and suggestions of a broader community of interests, and to incorporate these judgments, as appropriate, into the plan. This meeting will be held in early September, probably in Washington, DC, and will be open to all interested persons in the solar energy community.

In summary, we expect the photovoltaic standards development program to:

1. Provide an organizational focus to coordinate the overall photovoltaic standards activity;
2. Create a mechanism for the identification and development of consensus standards which meet the needs of all interested parties and are maintained in the long term within the traditional standards organizations;
3. Fund near-term development activities needed to provide draft standards;
4. Foster interaction between all members of the standards community through a program of direct involvement of representatives of present and future users and manufacturers, traditional standards organizations, the photovoltaic R&D community, etc.; and

CONCENTRATING SOLAR COLLECTOR TEST RESULTS FROM
DOE/SANDIA COLLECTOR MODULE TEST FACILITY

By: Vernon E. Dudley, EG&G, Inc.
Robert M. Workhoven, Sandia Laboratories

Mr. Dudley is an electronics engineer with many years experience in nuclear effects research at the Air Force Weapons Laboratory. He was Technical Director for several nuclear weapons effects test shots in Nevada. Since early 1977 he has been operating the Collector Module Test Facility for Sandia Laboratories. He is a member of Eta Kappa Nu and Tau Beta Pi.

Mr. Workhoven received his B.S. in Mechanical Engineering from the University of Iowa in 1959 and his M.S. in Mechanical Engineering from the University of New Mexico in 1967. He joined Sandia Laboratories in 1959 and worked in various phases of environmental testing until he joined Sandia's Solar Energy Projects Department in March 1977. His current assignment is Project Engineer of the Collector Module Test Facility in the Midtemperature Solar Systems Test Facility. He is a member of Pi Tau Sigma and Tau Beta Pi.

Introduction

A series of concentrating solar collectors are being tested in the Collector Module Test Facility (CMTF) at Sandia Laboratories. This facility is a part of the Midtemperature Solar Systems Test Facility and is operated for the Department of Energy's continuing program to characterize selected collector modules for possible future systems use (see Reference 1).

The solar collectors tested may have important commercial applications in replacing fossil-fuel energy sources with solar thermal power systems for irrigation pumping, electric-utility power generation, combined electric power and heat energy (total energy systems), and as a source for high-temperature process heat.

Test Objective

The objective of the test series is to characterize the performance of concentrating solar collectors. Of primary concern is the peak thermal efficiency at solar noon and receiver thermal losses of these collectors over the temperature range from about 100°C to 300°C.

Five collectors were tested from August 1977 to January 1978, and results of these tests are reported here. Others are now being tested, with more scheduled for test at about 2 month intervals.

Collector Descriptions

Table 1 summarizes some of the collector characteristics; more complete descriptions are given below.

TABLE I
COLLECTOR MODULE CHARACTERISTICS

Collector	Aperture Area m ²	Collector Type	Focal Length cm	Concentration Ratio	Reflector Surface
Suntec (SLATS)	35.97	Rotating Mirror Fresnel Reflector	305.0	35:1	glass
General Atomic	16.26	Fixed Mirror Fresnel Reflector	302.0	43:1	glass
Hexcel	15.91	Parabolic Trough	91.4	67:1	FEK-163 acrylic
McDonnell Douglas	15.54	Fresnel Lens Rotating Array	92.7	24:1	cast acrylic Fresnel lens ⁵
Solar Kinetics	12.7	Parabolic Trough	26.7	41:1	FEK-244 acrylic

Notes:

1. McDonnell Douglas is two-axis, fully tracking design.
2. All others are single-axis tracking, oriented E-W.
3. All reflectors are second surface.
4. All receivers are black chrome plated.
5. Transmission lens, not a reflector.

Suntec Systems, Inc.

Suntec's Solar Linear Array Thermal System (SLATS) is a linear Fresnel reflector system consisting of two bays of 10 silvered-glass reflectors each, supporting structure, and a fixed receiver assembly. The module tested was 12.5 m long and 3.5 m wide. The individual reflectors were 6.1 m long, 30.5 cm wide and slightly curved, achieving a concentration ratio of 3.5:1. Each reflector is set at a slightly different angle so that reflected sunlight from all the reflectors converges on the fixed 8.64 cm wide receiver aperture. Sunlight concentration ratio for the complete array is 35:1. The individual reflectors are mechanically linked together and are rotated on command of the sun tracking system to focus on the receiver. When not in operation, the reflectors are rotated to a face-down position. The receiver assembly was a double pass system, with the heat-transfer fluid entering one end of the receiver, passing the length of the receiver through one absorber tube, then traveling through a turnaround at the end and back across the receiver through the second absorber tube. The steel absorber tubes were plated with a selective black chrome to enhance solar absorption and minimize thermal radiation losses.

The SLATS solar collector could be designed to use a low pressure, synthetic-oil heat-transfer fluid; however, as tested at the CMTF it was configured for use with 330 °C water pressurized to 18.3 MPa. Reference 2 contains complete descriptions, photographs and results of tests on the SLATS collector.

Hexcel Corporation

The Hexcel solar concentrator used four aluminum honeycomb mirror panels arranged to form a linear focus parabolic reflector. The reflecting surface was FEK 163, an aluminumized second-surface acrylic film manufactured by the 3M Corp. Overall dimensions of the collector module were 7.7 m x 2.6 m.

The black-chrome-plated absorber was a steel tube with internal fins and an internal plug tube to confine the fluid flow to the tube wall area and improve heat-transfer characteristics. To reduce conduction and convection losses, a half-cylinder of Pyrex glass was fitted over the absorber tube on the radiation absorbing side. The back half of the tube was covered with a double-layer metal shield. The inner surface of the metal cover was polished aluminum to serve as a secondary concentrator; insulation was placed between the two layers to reduce losses. See Reference 3 for complete descriptions, photographs, and test results.

General Atomic Company

The General Atomic Fixed Mirror Solar Concentrator (FMSC) is a concave array of long, narrow, flat mirror facets fixed on a segment of a cylindrical surface. One mirror

facet near the center of the module is tangent to the basic cylindrical curvature of the module. The remaining mirror facets are set at different angles such that all reflect incident light to the focal point. The array of flat reflecting facets produces a narrow focal line that follows a circular path as the sun moves. Because the focal line path is on the same basic cylindrical surface as the mirror facets, the focal line can be tracked by a movable heat receiver assembly that rotates about the center of curvature of the reflector module. In all positions, the receiver is aimed at the tangent mirror facet. See Reference 4 for a more complete description of the optical principles of the FMSC.

The FMSC modules tested at the CMTF were constructed from reinforced cast concrete. The concrete modules were cast over a precision metal mold. A transferable film adhesive was used to fasten the 43 second-surface, silvered-glass mirror facets to the concrete surface. The complete module as tested was 7.2 m long and 2.6 m wide.

The internal construction of the FMSC receiver assembly was quite different from that of the Suntec SLATS receiver. The black-chrome-plated absorber tube was a flattened oval, supported by an aluminum channel enclosure and surrounded by a highly effective silica-foam insulation. The secondary concentrators had polished-aluminum mirrors on their inner surfaces to assist in concentrating sunlight onto the absorber surface. Reference 5 should be obtained for complete descriptions, photographs and test results.

McDonnell Douglas

The McDonnell Douglas Fresnel Lens Rotating Array Solar Collector was an aluminum box 5.94 m x 3.63 m x 1.07 m deep. It was mounted on a pedestal to allow full sun tracking in both azimuth and elevation. The front (illuminated) face of the collector was a series of eight sections of cast acrylic linear Fresnel lenses focusing sunlight on four receiver assemblies within the box.

Each receiver assembly contained a black-chrome-plated, steel absorber tube; secondary reflectors to aid in capturing stray sunlight; and a low-iron glass cover to minimize thermal convection losses. The whole receiver assembly was insulated with glass fiber batts and glass cloth. For fluid flow, the four individual absorber tubes were interconnected in series. Each absorber tube contained an inner plug tube to confine the fluid flow to the wall area of the absorber. Reference 6 contains more complete descriptions and test results.

Solar Kinetics, Inc.

The Solar Kinetics Model T-500 solar collector is a linear parabolic trough concentrator. The parabolic mirrors were 1.3 m wide

and 6.1 m long; two of these mirrors were placed end-to-end to form a row 12.2 m long for testing at Sandia.

The linear parabolic mirror was an aluminum monocoque construction. Precision aluminum castings were used for internal bulkheads, and the skin was 18-gage, T6 aluminum sheet.

The reflective surface was FEK-244, a second-surface, aluminized-acrylic film by the 3-M Co. The Solar Kinetics receiver assembly was made up of a black-chrome-plated steel tube inside a Pyrex glass tube.

All the other collectors tested used electric motors for obtaining mechanical motion for sun tracking; Solar Kinetics used a hydraulic system. The hydraulic system had a unique advantage: sufficient hydraulic fluid was stored under pressure in an accumulator to drive the system out of focus in case of a power failure that would cause a loss of fluid flow through the receiver. Reference 7 contains more complete details of the Solar Kinetics collector and results of tests at the CMTF.

Test Facility Description

All the collectors were tested over a temperature range from about 100°C to about 310°C, at flow-rates from about 4 to 40 liters/min. All except the Suntec SLATS were tested on the CMTF's Fluid Loop 1, using Therminol 66 as the heat transfer fluid. The SLATS collector was tested on the CMTF's Fluid Loop 3, using water pressurized to 18.3 MPa as the heat transfer fluid.

Temperature data for performance measurements was obtained from thermocouples in the fluid stream at the input and output of the collector's receiver assemblies. Fluid flow rates were measured with turbine flowmeters.

Data from the various measurements were converted to digital format and processed with a minicomputer to obtain a real time printout of the collector performance parameters. Speed of the data system was such that a line of data could be printed about every 15 seconds. An average value for each data point was calculated and printed each time 10 readings were accumulated. Reported data are based on these 10-point averages.

Performance Test Definitions

During a test run temperatures and flow rates were measured, and specific heat and density of the heat transfer fluid were calculated for each data set using the average temperature of the fluid in the absorber tube. Heat gain (or loss) was then calculated from

$$Q = \dot{m} C_p \Delta T$$

where

Q = heat gain, kJ/hr

\dot{m} = mass flowrate of fluid, kg/hr

C_p = specific heat of fluid, kJ/kg°C

ΔT = in-out temperature differential, °C

For an efficiency test, efficiency was calculated from

$$\eta = \frac{Q/A}{I}$$

where

η = solar collector efficiency

Q = heat gain, W

A = collector aperture area, m²

I = insolation, W/m²

Our test experience has shown that stability of the operating conditions is the most important factor in achieving good performance data. For example, an input or output temperature drift of only 1°C over a 3-5 minute time span will cause an error of several percent in measured efficiency. Highly stable temperatures are even more critical for loss measurements because the temperature differential across the receiver is usually much smaller than during efficiency tests. For these reasons, a "good" performance data point must be at least one of the 10-point data averages during which input and output temperatures change by 0.1°C or less, flow rate varies by 0.1 liter/min or less, and delta temperature remains constant within 0.1°C or less. For an efficiency data point, solar radiation input must also be constant to about 1% and greater than about 950 W/m². The magnitude and stability of solar radiation are not quite so critical for loss measurements, but the difference is not great. Loss measurements made under variable clouds or low insolation conditions are not representative of losses under full sunlight operating conditions.

In addition to all the above, temperatures, flow rate, insolation, etc, must be nearly as stable as described for at least 5-10 minutes prior to the "good" data point to be believable. In most cases, every effort is made to maintain stable conditions for about 30 minutes before each reported measurement. To insure stability and a good definition of the peak efficiency at solar noon, most of the collectors tested for this report were operated at a single temperature and flow rate from about 1 hour before noon to about 1 hour after noon.

Another factor that has been found important in efficiency measurements is consistent cleanliness of the reflector and receiver surfaces. Variations of more than 5% in measured efficiency have been observed between clean and dusty mirror surfaces.

Test Results

Figures 1 and 2 summarize the results of efficiency testing of the five collector

modules. Figure 1 shows measured efficiency at solar noon vs. receiver output temperature. Figure 2 is the same data plotted as efficiency vs. T/I , where T/I is defined as average receiver temperature above ambient temperature divided by solar radiation. Hexcel's parabolic trough collector has the highest efficiency we have tested so far. The efficiency performance of Solar Kinetics, McDonnell Douglas and Suntec collectors was several percentage points less than Hexcel; these three were essentially identical over the temperature range. The measured efficiency of the General Atomic FMSC was significantly lower at low temperatures but only a few percent less at an operating temperature near 300 °C.

Reasons for the differences in efficiency were identified in each case. The Hexcel design would probably be difficult to improve, except for reducing losses as mentioned later. Solar Kinetics was penalized by a manufacturing defect in the mirror support castings, which caused much of the reflected light from the outer 15 cm of the mirror to miss the receiver. McDonnell Douglas experienced lower than expected transmissivity through their acrylic Fresnel lenses.

The Suntec SLATS mirrors were not of optimum shape, causing considerable light spillage outside the receiver. Planned replacement of both Suntec and Solar Kinetics mirrors and repeating the efficiency measurements may significantly improve their performance.

The General Atomic FMSC modules tested were early models which experienced mirror positioning difficulties and large amounts of light spillage. Preliminary tests on a later module recently installed in the Mid-Temperature Solar Systems Test Facility at Sandia Laboratories indicate that an improvement of as much as 10 percentage points in efficiency may be possible.

Extensive measurements of thermal loss were made on each of these collectors. Because they differ widely in size and in design concept, not much is learned by direct comparison of total thermal loss between the various collectors. No universally accepted design independent method of comparison is available for loss normalization in the same sense as an efficiency comparison. But some comparisons are possible that produce useful information if the results are not taken out of context.

Figure 3 shows loss for each collector as loss per unit length of receiver. This comparison is most valid for receivers of similar design and size, such as Hexcel and Solar Kinetics. Such a comparison indicates that Hexcel's efficiency could be improved by several percentage points at high temperatures by adopting a lower loss receiver design. A comparison of loss per unit length is probably unfair to a system such as the

Suntec SLATS, which must use a relatively large, wide receiver because of its design concept.

Figure 4 illustrates another loss comparison which many designers have found useful, that of loss per unit area of collector aperture. This comparison tends to penalize low concentration ratio collectors such as McDonnell Douglas, which shows the highest loss per unit aperture, but has the lowest loss per unit receiver length.

Note that in both loss comparisons, the General Atomic FMSC shows very low losses, probably because of the highly effective silica foam insulation used in the receiver.

Summary of Results

In every case, the measured performance of the various collectors was not as good as their designers expected. The reasons for the lowered performance were usually readily identified and should be correctable when building new models of these designs. The prime reason for lowered efficiency was insufficient mechanical accuracy in building the components that determine the optical path. No compromises are advisable here; efficiency falls off rapidly when sunlight misses the receiver. General Atomics FMSC, Suntec and Solar Kinetics all suffered significant reductions in efficiency from scattered light. The Hexcel collector was the best because of a highly accurate focal line.

A second important factor was poor performance of optical materials. Poor transmissivity of the acrylic Fresnel lens on the McDonnell Douglas collector was the most severe example, but most were affected by deteriorating absorptance of black chrome absorber tubes. Early models of the Suntec SLATS were penalized by rapidly deteriorating Teflon reflective film. Similarly, the first set of second surface, silvered-glass mirrors used by General Atomic peeled and pinholed in a short time.

Finally, thermal losses must be minimized. The Solar Kinetics and General Atomic FMSC receiver designs might be difficult to improve further, but Hexcel could probably gain several percentage points in efficiency by adopting a lower loss receiver design similar to Solar Kinetics.

Testing of other collectors continues at the CMTF. We hope solar collector designers will find the test results useful in improving future collectors.

References

1. Sandia Laboratories, "Solar Total Energy Program Plan," SAND76-0167, (revised), August 1976.

2. Sandia Laboratories, "Performance Testing of the Suntec SLATS Solar Collector," SAND78-9623, (to be published).
3. V. E. Dudley and R. M. Workhoven, "Performance Testing of the Hexcel Parabolic Trough Solar Collector," Sandia Laboratories Report SAND78-0381, March 1978.
4. J. L. Russell Jr., E. P. DePlomb and R. K. Bansal, "Principles of the Fixed Mirror Solar Concentrator," General Atomic Company Report GA-A12902, May 31, 1974.
5. V. E. Dudley and R. M. Workhoven, "Performance Testing of the General Atomic Fixed Mirror Solar Concentrator," Sandia Laboratories Report SAND78-0624, May 1978.
6. V. E. Dudley and R. M. Workhoven, "Performance Testing of the McDonnell Douglas Fresnel Lens Rotating Array Solar Collector," Sandia Laboratories Report SAND780625 (to be published).
7. V. E. Dudley and R. M. Workhoven, "Performance Testing of the Solar Kinetics Parabolic Trough Solar Collector," Sandia Laboratories Report SAND78-0626 (to be published).
8. V. E. Dudley and R. M. Workhoven, "Summary Report: Concentrating Solar Collector Test Results, Collector Module Test Facility," Sandia Laboratories Report SAND78-0815, May 1978.

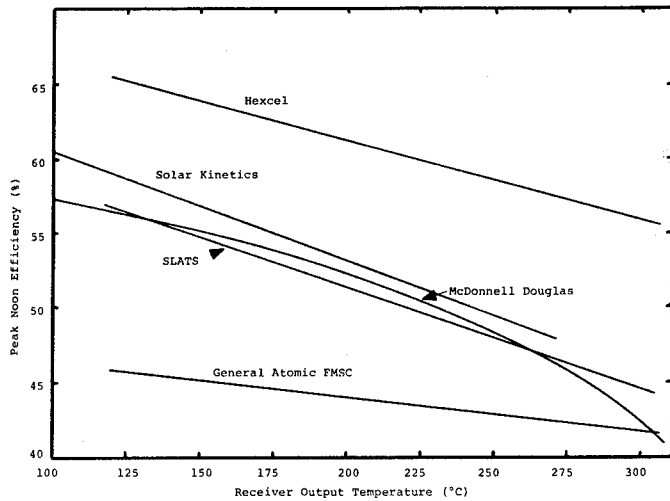


Figure 1. Comparison of Efficiency at Solar Noon

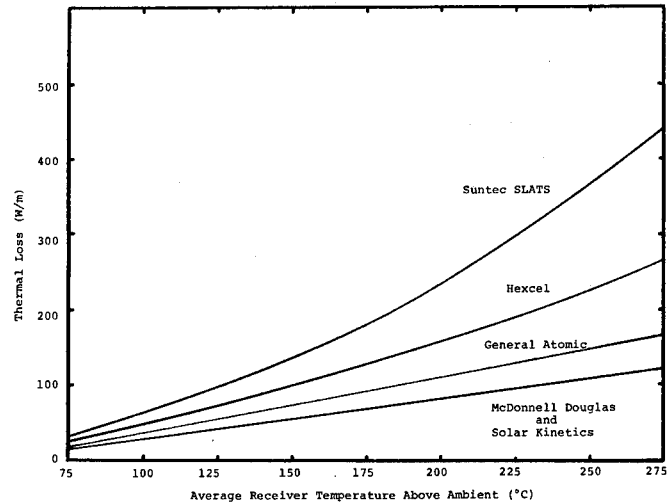


Figure 3. Comparison of Thermal Loss Per Meter of Receiver Length

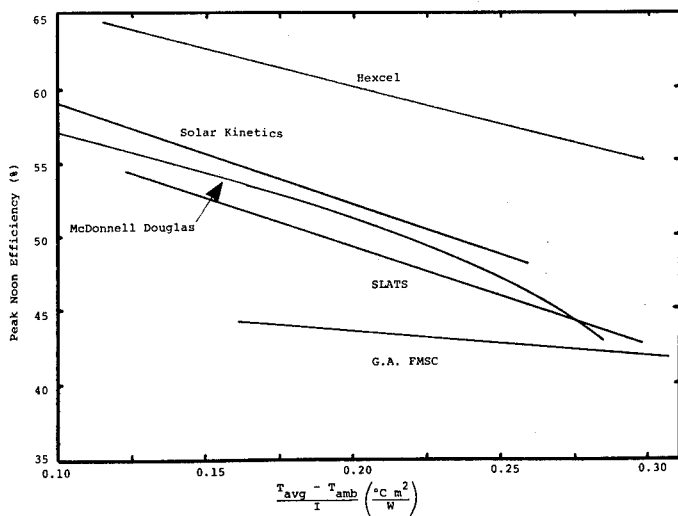


Figure 2. Comparison of Efficiency at Solar Noon

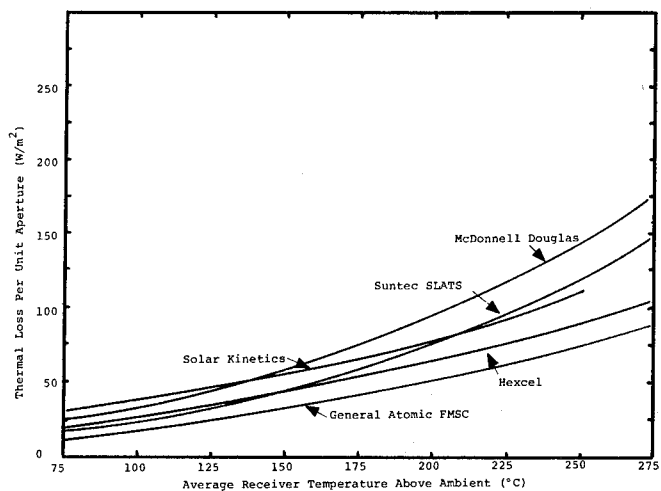


Figure 4. Comparison of Thermal Loss Per Unit Area Collector Aperture

TESTING OF CENTRAL RECEIVER FOR CENTRAL THERMAL POWER SYSTEMS

By: R. P. Pauckert, R. D. Tobin, J. M. Friefeld
Rocketdyne Division, Rockwell International

R. P. Pauckert is the Solar Receiver Project Engineer at Rocketdyne. He received his B.S.Ch.E. from the Cooper Union in 1955 and his M.S.M.E. from the University of Southern California in 1962.

R. D. Tobin is a member of the Technical Staff in the Aerothermodynamics Unit at Rocketdyne. He received B.S. and M.S. Engineering degrees at U.C.L.A. in 1961 and 1965. He has been involved in the areas of thermal analysis and fluid flow since joining Rocketdyne in 1961. He was Project Engineer on the initial high flux solar panel tests (Ref. 2) at Rocketdyne on which a portion of this paper is based.

J. M. Friefeld is the Program Manager for Solar Power Programs at Rocketdyne which he joined in 1961. He received his M.S.M.E. at University of Southern California in 1965. He is a member of Phi Kappa Phi.

ABSTRACT

Methods of testing the materials and components related to the receiver subsystem of a Central Thermal Power System are described in this paper. In many cases, this testing has required the adaptation of existing methods to the new design or the use of innovative new testing methods. The experiments are structured to verify critical aspects of the system or provide basic data used to calculate system characteristics. These characteristics include flow uniformity and stability, controllability, structural integrity and life, and performance. The unique potential of the external once-thru receiver with respect to scaling for testing and the application of the test results to the full scale receiver is noted.

Electrical simulation of solar energy using resistance and radiant heating is discussed in terms of methods, applications, advantages and limitations. Typical configurations which have been tested in electrical facilities as part of the solar receiver program are described. Methods of testing the absorptivity of the heated surface coating and evaluating its durability are described. Instrumentation requirements specific to solar testing in the various types of facilities are noted. The degree of success of several approaches to satisfying instrumentation requirements is discussed.

INTRODUCTION

Current interest in alternate energy sources has led to increased effort in the utilization of solar energy. In particular, central thermal power systems which utilize a large heliostat field focused on a tower-mounted solar receiver steam generator, have been extensively investigated. These investigations have included subscale testing of key components such as the central receiver. The purpose of this paper is to summarize the test approach and results for one such central receiver concept which was subsequently selected by DOE as the baseline for the 10 MW_e pilot plant near Barstow, California.

TECHNICAL DISCUSSION

CONCEPT DESCRIPTION

The basic function of the receiver subsystem in a central receiver solar power plant is to absorb the solar radiation reflected from the collector subsystem (heliostat field) and convert that energy into superheated steam for delivery to either the turbine of the electrical power generation subsystem or to the thermal storage subsystem. The receiver subsystem consists of the absorber, the supporting control and instrumentation equipment, and the appurtenant structure and plumbing.

The receiver unit concept selected by Rocketdyne is an external cylindrical receiver utilizing a once-through (to steam) flow circuit as depicted in Figure 1. The primary advantages of the concept are its simplicity and light weight (which impacts the tower structural requirements). The pilot plant receiver unit consists of 24 identical multi-tube panels with individual flow control to maintain desired outlet steam temperature (and pressure) as a function of solar heat input variations with time and circumferential position. The use of identical interchangeable panels requires testing of only a single panel over the range of plant heat loads and operating conditions to verify the concept feasibility.

In the once-through steam generation concept the sub-cooled water enters the inlet manifold at the bottom of each panel and flows upward with the heat absorbed from the incident solar energy converting the water into superheated steam by the time it reaches the upper exit manifold. No steam drum separators or water recirculation is required thereby resulting in a simple lightweight system.

DESIGN REQUIREMENTS

The receiver subsystem is subjected to numerous design requirements some of which are summarized in Table 1.

Table 1. Central Solar Tower Receiver Design Requirements

Electrical Power Output, MW		10 - 100
Incident Heat Flux,	MW/m ²	
Inlet Pressure,	MN/m ² (PSIA)	
Outlet Pressure,	MN/m ² (PSIA)	
Inlet Temperature,	C (F)	
Outlet Temperature,	C (F)	
Life,	Years	30
	Cycles	10,000

One of the most demanding requirements, in terms of system control, is the wide range of incident heat flux resulting from diurnal, and seasonal variations as well as cloud cover transients. In addition there is substantial variation in heat load around the receiver circumference with the north panel (i.e., south facing heliostats) receiving approximately 3 times greater heat input as the south panel.

The receiver must also meet various environmental requirements pertaining to wind loads, dust, and local seismic conditions. In addition the receiver absorber panels are designed to the ASME Boiler Code.

EXPERIMENTAL OBJECTIVES

During the course of the studies on the central receiver concept, several technical issues arose for which it was desirable to generate empirical data to assure adequate design margin in the receiver unit. These key issues ranged from basic cooling considerations for a single tube to operating characteristics of the entire system. The technical issues determined to be best verified experimentally or by analysis using factors determined experimentally were:

- A. The ability to deliver dry steam under rated (turbine) or derated (thermal storage) temperature conditions over the required range of power level.
- B. The ability to withstand peak heat flux at corresponding Pilot or Commercial Plant flowrates.
- C. Operation with tube wall temperatures compatible with the design requirements to operate for a 30-year life (10,000 cycles).
- D. That the absorber surface maintains its high absorptivity for a reasonable period of time under conditions of thermal cycling and high intensity solar radiation.
- E. Adequate provision for expansion and contraction of the panel under thermal influences so as to prevent undue stresses.
- F. Operation over the entire power/flow range, particularly at the lower end of the range, without undue cycling of the discharge temperature or significant variations of temperature from tube-to-tube.
- G. Reaction to a passing cloud cover over the collector field with no degradation of the receiver or other plant subsystems.

EXPERIMENTAL APPROACH

The experimental approach to fulfill the foregoing technical objectives utilized a variety of test hardware and facilities. The overall criteria guiding the experimental effort was to simulate central solar receiver conditions to the maximum extent possible. This required development of facilities capable of supplying radiant heat flux levels as high as 0.3 MW/m^2 for pilot plant simulation and 1.0 MW/m^2 for commercial plant conditions for test panel lengths to 65 feet.

Test Hardware

The test hardware for radiant heating experiments included single tube and 5-tube panels in both pilot plant and commercial plant geometries. In addition a full scale Pilot Plant segment, including a 70 tube absorber panel (as shown in Fig. 2) and controls was fabricated to ASME Boiler Code specifications.

The absorptance coating evaluation hardware utilized in the WSTF solar furnace consisted of a water cooled Incoloy block coated with stripes of the candidate S-31 and Pyromark high solar absorptance paints which were exposed to concentrated solar radiation.

In addition the coating thermal cycling tests were conducted with uncooled electrically resistance heated lengths of tubing of the same cross-section and material used in the Pilot Plant panel. These tubes were about one meter (3 Ft.) long and were grit-blasted and painted with Pyromark or S-31 paints.

Test Facilities

The system testing (single tube, five-tube panel, and receiver segment) was conducted at the Rockwell LAD Thermodynamics Laboratory. The absorptive surface tests also utilized the White Sands Solar Furnace Test Facility and the TRW Thermophysics Laboratory. The special equipment required to support the system tests at the Thermodynamics Laboratory consisted of the heater arrays to simulate solar energy and the flash tank assembly to simulate the bypass valve and flash tank of the Pilot Plant receiver. The heliostats at the White Sands Facility concentrate the solar energy to simulate the function of the Pilot Plant heliostats. The Rockwell and White Sands facilities had been previously used in connection with aerodynamic and nuclear heating tests.

Thermodynamics Laboratory - The Rockwell LAD Thermodynamics Laboratory was used as the facility to test the single tube, narrow panel, and receiver segment. All the above mentioned test hardware was oriented horizontally for initial tests, then vertically so that the direction of the gravity vector was similar to that experienced in Plant operation.

Two different heater arrays were used. One array consisted of heaters oriented along the axis of the tubes. This array was used to provide simulated solar inputs to both the single tube and the five-tube panel. Graphite heaters were used for the single tube tests. Both graphite and metallic heaters were used for the tests on the five-tube panel. Metallic heaters provided long duration tests at the lower heat flux levels. Water-cooled polished aluminum reflectors enclosed the heater-panel assemblies. An argon purge was utilized for the graphite heaters. The width of the 70 tube panel required that the heaters be oriented normal to the axis of the tubes. The Pilot Plant panel is shown being installed in the test tower in Fig. 3.

A simplified flow schematic of the radiant heating test facility is shown in Fig. 4. Water enters the segment through a shedding vortex flowmeter which features no moving parts in the flow stream to enhance reliability. The next component in line is a

control valve which regulates water flow through the absorber panel. The inlet piping is firmly fixed to the Pilot Plant tower or to the facility downstream of the throttle valve. An expansion joint is provided in the plumbing which provides for the thermal expansion of the panel during operation. A filter is included in the plumbing to protect the panels in the event of a failure of the upstream filter. A stop check valve defines the limits of ASME Section I jurisdiction in the boiler region. All components from this stop check valve to a stop valve on the steam discharge side of the boiler are fabricated of Incoloy 800.

The flash tank separator used for the segment tests consisted of 31-cm (14 in) nominal diameter pipe approximately 4m (13-ft) long. A water level control valve drains water from the lower portion of the tank and a backpressure regulator regulates the flow of steam out of the top of the tank. Boiler quality water was utilized throughout the tests.

A low-pressure GN_2 pressurizing system was used to provide an inert blanket for the system during periods of non-use. The 2.1-MN/m² (300 psig) GN_2 system was used to provide a pressure in excess of the vapor pressure during the startup operation to prevent boiling. The GN_2 supply system indicated in the figure provides the high pressure GN_2 to force the water through the system from the heated supply tank (WT-1).

Analog (strip chart) and digital data acquisition systems were utilized. The digital system includes multiplexors and analog/digital convertors, a double tape unit for recording the incoming data together with a programmer for organizing and formatting data and converting it to engineering units. Digital and analog display and printout equipment was used.

TRW Thermal Physics Lab - This facility, located in Redondo Beach, California, was used to determine the absorptivity and emissivity of several samples of Incoloy coated with various high absorptivity paints. The facility includes a Beckman DK2A spectrophotometer with an integrating sphere which was used to determine reflectance data over the wavelength region of 0.282-2.5 microns. A Gier Dunkle mobile solar reflectometer (MS 250) was used to measure reflectivity of the specimen sent to White Sands. This method was used because the sample would not fit into the integrating sphere and the Gier Dunkle instrument provided sufficient assurance to determine whether any shift in the absorptivity resulted from the solar exposure.

White Sands Solar Furnace - The White Sands solar furnace, located in southern New Mexico, was used to provide concentrated solar energy for long periods of time to determine the effect of this energy on absorptivity. This facility includes a large plane tracking mirror and a fixed concentrator which directs solar energy into a test section where powers far in excess of the required 0.3 MW/m² can be generated.

Subscale Calibration Tests

Prior to build-up of the primary radiant heating facility subscale tests were conducted for purposes of heater characterization and thermocouple

instrumentation evaluation.

Thermocouple Evaluation - One of the most important aspects of the current experimental program was the measurement of the single tube and panel surface temperatures when exposed to a high radiant heat flux environment. Knowledge of the tube heated surface temperature over a range of operating conditions is vital for verifying the basic feasibility of the once-through boiler concept for advanced commercial solar tower receiver application. The measured heated surface temperatures in conjunction with the corresponding measured back surface temperatures is also utilized to predict the fatigue life capability of the receiver tubes.

The primary difficulty in the measurement of the heated surface is that the thermocouple must be interposed between the tube surface and the radiant heater. A significant amount of heat is, therefore, absorbed by the thermocouple device itself causing its temperature to increase above that of the surface to which it is attached. The actual temperature differential between the surface and the thermocouple is dependent on various factors such as thermocouple type and geometry, attachment technique, and thermocouple reflectance.

The most common thermocouple type, particularly for high temperature application, utilizes a metallic sheath to contain the thermocouple wires. The thermocouple wires are isolated from the sheath and each other (except at the junction) by means of a suitable insulator such as MgO . If the sheath is enclosed at the measurement end, it is commonly referred to as a closed tip thermocouple. In this case, the thermocouple junction can either be attached to the sheath tip (grounded) or not (ungrounded). If the thermocouple wires are exposed at the tip of the sheath, the device is usually referred to as an open tip thermocouple. If the exposed thermocouple wires are then attached directly to the surface to be measured, a grounded junction is formed. Based on previous experience, and verified in the calibration tests, the grounded type thermocouple junction (either open or closed tip) is unsatisfactory in a high energy electrical field due to high noise levels. The use of ungrounded thermocouples appear to be the only feasible approach for use in the radiant heating facility.

The attachment technique can also have a significant effect on the measured temperature, particularly for a sheathed ungrounded thermocouple. For example, one approach is to simply weld the thermocouple tip to the surface to be measured. In the proposed application, this would mean welding the thermocouple tip to the tube crown only. The remainder of the thermocouple sheath exposed to the radiant heat input is essentially uncooled and the absorbed energy must be transmitted through the thermocouple tip and weld joint. The result is an increased measurement error (i.e., higher tip temperature) as well as possible excessive sheath temperature at some point around the circumference of the tube or panel. If the attachment surface area is increased, (e.g. by brazing) both the measurement error and maximum sheath temperature are diminished.

The heater calibration tests were also utilized to evaluate thermocouple installation techniques in conjunction with the computer data acquisition system. Two five-foot long O.D. CRES tubes instrumented using various thermocouple installation techniques were

utilized in these tests. The calibration tests were conducted using low pressure subcooled water which permits accurate analytical prediction of wall temperature as a function of imposed heat flux. The water flowrate was reduced gradually at a fixed heat flux level until the wall temperature no longer increased thereby insuring operation in the nucleate boiling regime.

An analytical wall temperature prediction was made using the Rocketdyne Differential Equation Analyzer Program in conjunction with test operating conditions. The maximum surface temperature was predicted to be 500 F. This compares with a measured value of 590 F for the silver brazed thermocouple indicating a discrepancy of 90 F. The estimated error in the calculated wall temperature is about ± 25 F at these nucleate boiling conditions. The thermocouple bias due to radiant heat input would, therefore, be estimated at $90 \text{ F} \pm 25 \text{ F}$ at a nominal heat flux of $1.0 \text{ Btu/in.}^2\text{-sec}$. Reduced heat flux levels result in reduced temperature error. At nominal Pilot Plant heat flux conditions the thermocouple bias is estimated at less than 25 F for this installation method.

The tip-welded thermocouples recorded temperatures several hundred degrees higher than the silver brazed thermocouple indicating that the former attachment technique is unsatisfactory in a high radiant heat flux environment. The grounded thermocouples were unsatisfactory in terms of system noise at the high power levels utilized in the calibration tests.

The thermocouple installed through the tube such that its tip was flush with the tube crown also proved unsatisfactory due to excessive cooling by the water flowing through the tube and around the exposed thermocouple sheath. This thermocouple tended to measure temperatures only slightly above the coolant bulk temperature.

Based on the foregoing results, the silver brazed thermocouple attachment technique was selected for use in the single tube and panel tests.

Panel Instrumentation

The single and five tube panels and pilot plant 70 tube segment were instrumented to measure wall temperature (both heated surface and back outer wall), inlet and exit coolant temperatures and pressures and water flowrate. The coolant pressure drop was also monitored on a gauge.

The wall temperature measurements were obtained with thermocouples silver brazed to the hardware. The coolant bulk temperatures on the 5 tube panel were measured by inserting thermocouple through bosses into the center of the tubes. The outlet fluid temperature was measured in each tube of all panel assemblies including the 70 tube segment by attaching thermocouples to the wall and insulating so that the wall and fluid temperatures were approximately equal. Inlet temperature and inlet and outlet pressure measurements were made in the respective inlet and outlet manifolds.

A liquid slug detector was also placed in the downcomer line near the boiler. The detector

was a thermocouple downstream of a bend in the fluid stream that indicates the superheated steam temperature. A slug of water entering the turn is thrown against the thermocouple which then indicates saturation temperature. The detector indicated slug-free flow at all times during superheat operation with smooth transitions through the two-phase region.

TEST RESULTS

The test results obtained during the experimental effort are too extensive to include in detail in this paper. The reader is referred to Ref. 1 and 2 for the detailed results. Included herein are typical data and result summaries in key areas.

A typical steady state tube temperature profile is presented in Fig. 5 for a single tube test. The primary characteristic of these results is that the measured maximum temperature in the two-phase region were less than predicted from various correlations. As a result the pilot plant panel was capable of feasible operation at heat flux levels far in excess of that required for pilot plant operation.

Closed loop control experiments indicated satisfactory operation of the system as shown in Fig. 6. These results were similarly duplicated during testing for stability and startup.

Cloud passage and loss of coolant experiments were also conducted with satisfactory results. In essence the thermal capacity of the panel is sufficient to damp out the effect of rapid changes in heat load or coolant flow on panel temperatures. Outlet temperature uniformity across the 70 tube panel was deemed quite satisfactory.

The coating durability and cycling tests at WSTF solar furnace indicated satisfactory coating durability. After irradiation of more than 160 hours and 100 full thermal cycles the coating absorptance was essentially unchanged.

CONCLUSIONS

The results of the experimental effort relating to the central receiver concept lead to the general conclusion that the once-through steam generator external receiver concept is feasible in terms of thermal, structural, flow stability and control characteristics.

In addition, the use of graphite and/or inconel radiant heaters to simulate heat flux levels associated with concentrated solar energy is a feasible and viable alternative to testing with an actual heliostat array.

Detailed conclusions as related to the pilot plant receiver test articles are:

1. The devices which provide for thermal expansion of the panel function very satisfactorily.
2. The receiver surface coating maintains its high absorptivity and structural integrity under extended exposure to cyclic and highly concentrated solar isolation.
3. The panel can operate at maximum Pilot Plant heat fluxes with tube temperatures well below

the predicted values. Differential tube temperatures were such as to ensure a 30-year panel life.

4. During steady-state operation, flow is uniform from tube to tube and is stable, even under extreme variations in pressure, flow or solar insolation.
5. The panel can survive flow cessations for significant periods without excessive temperatures or damage.
6. The panel control loop will automatically maintain steam outlet conditions within specified limits under anticipated transient conditions of pressure, flow or insolation.
7. The panel can reach steady-state temperature conditions in 7 to 12 minutes (depending on the heat flux) after a constant heat load is applied.

In general, the tests have resulted in a high confidence in satisfactory operation of the Pilot Plant receiver segment and thus, in the commercial receiver design concept.

REFERENCES

1. PDR, Central Receiver Solar Thermal Power System Phase I Pilot Plant Preliminary Design Report, Vol. IV Receiver Subsystem, McDonnell Douglas Astronautics Corp. Oct. 1977.
2. Tobin, R. D., Solar Receiver Heat Flux Capability and Structural Integrity - Final Report, R-9958 Rocketdyne, Canoga Park, CA May 1976.

ACKNOWLEDGEMENTS

The work reported herein was funded primarily by the McDonnell-Douglas Astronautics Company-West under sub-contract number 075008. The technical monitor was G. C. Coleman. This effort was in support of the Central Receiver Solar Thermal Power System, Phase I study for the Department of Energy (Contract No. EY-76-E-03-1108). In addition, some of the effort reported was funded under Department of Energy Contract No. E(04-3)-1103.

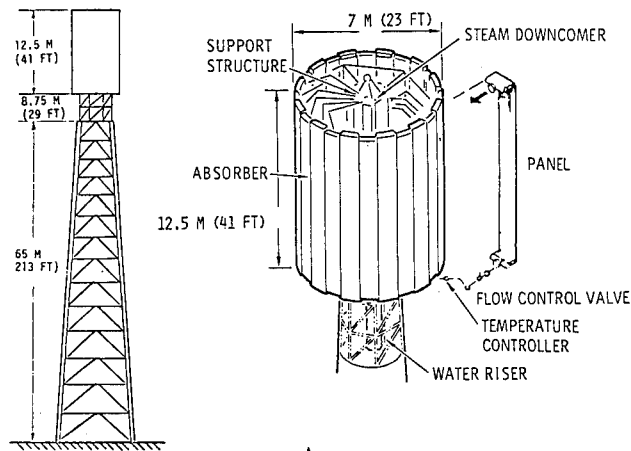


Figure 1. Pilot Plant Receiver

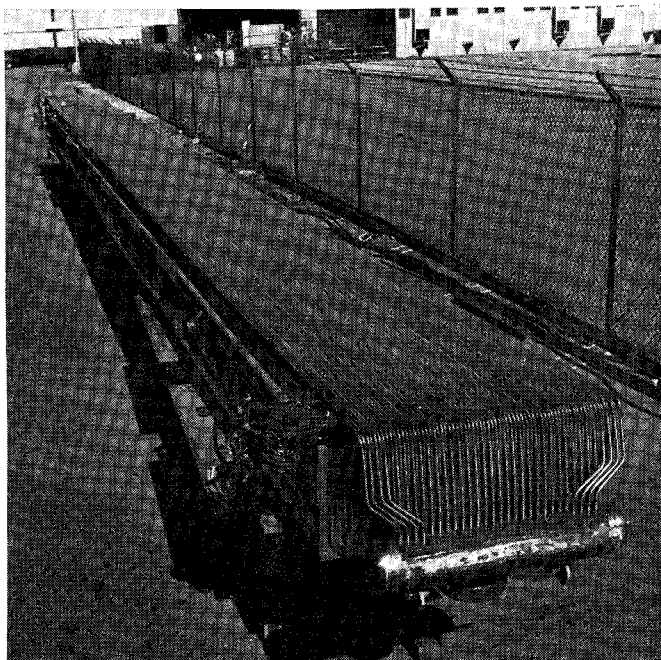


Figure 2. Pilot Plant Segment With a 70-Tube Absorber Panel

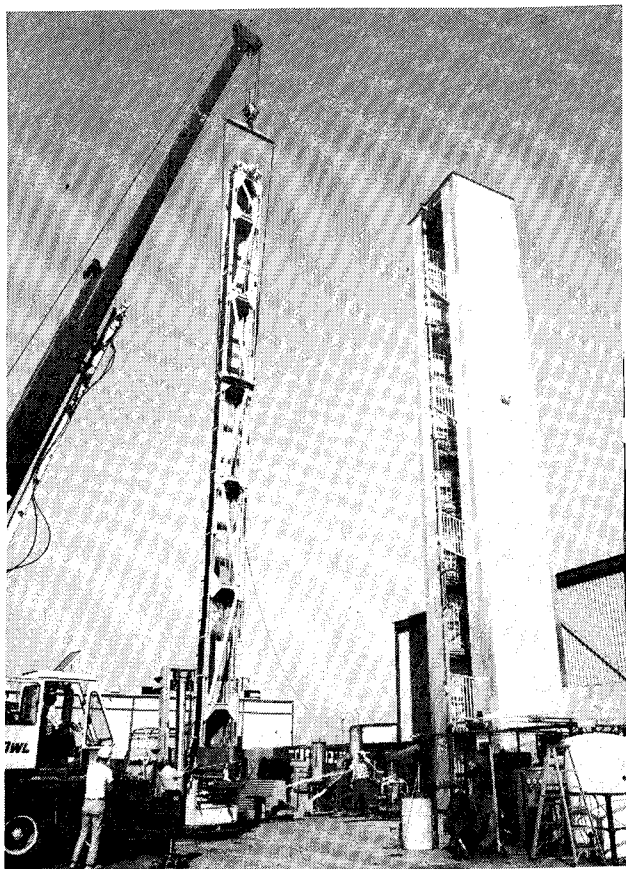


Figure 3. Pilot Plant Panel Being Installed in Test Tower

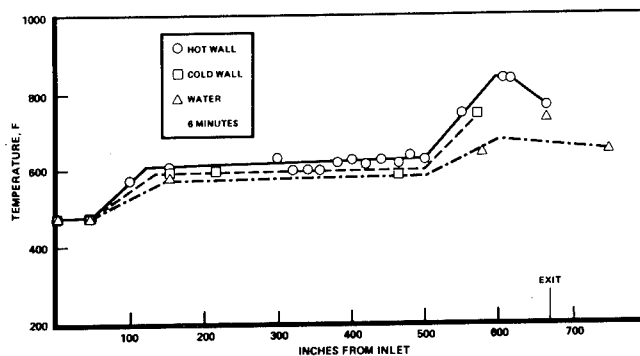


Figure 5. Temperature Profiles (Single-Tube Test 9)

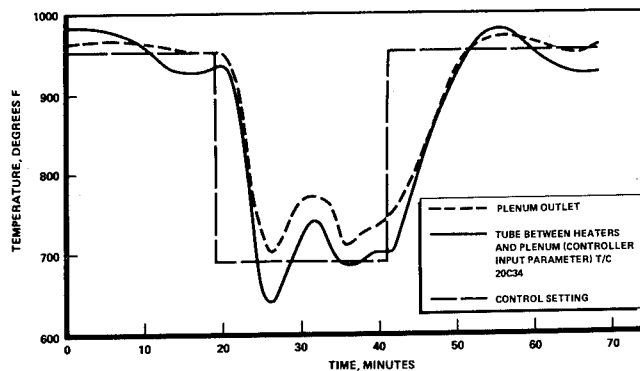


Figure 6. Receiver Operation With Outlet Temperature Change

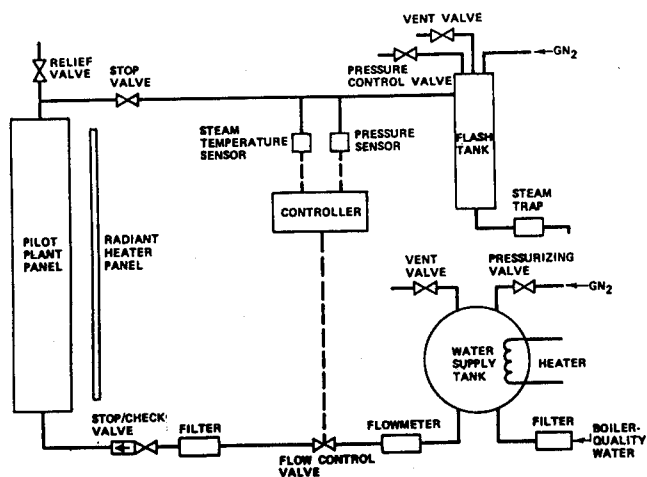


Figure 4. Simplified Schematic for Receiver SRE Pilot Plant Panel Tests

THE DOE 5 MW SOLAR THERMAL TEST FACILITY

Larryl Matthews received his masters in Mechanical Engineering from New Mexico State University in 1975. Since then he has worked with Sandia Laboratories in Albuquerque at the Solar Thermal Test Facility.

ABSTRACT

The Solar Thermal Test Facility in Albuquerque, New Mexico is operated for the Department of Energy by Sandia Laboratories.

This facility is the largest and most capable of its kind in the world.

With as much as 5 MW of thermal power available to the experimenter the Solar Thermal Test Facility is capable of testing almost any type of experiment requiring the clean heat of the sun.

Initial testing at the Solar Thermal Test Facility will involve components scheduled to be used for solar central receiver power plants.

INTRODUCTION

The 5 MW Solar Thermal Test Facility (STTF) (1) was constructed to test prototype components for solar central receiver power plants. Refer to Figure 1.

Initial testing of such components is scheduled for summer, 1978. The McDonnell Douglas solar receiver and the Boeing Engineering Corporation solar receiver will be the first tested at the STTF. Testing of various other receivers will follow.

The STTF is capable of testing a wide variety of experiments. The capabilities exist for high flux density, high temperature testing as well as high power testing.

The STTF consists of a 60.96m concrete tower with numerous test bays, 222 mirror assemblies (called heliostats), computer control and data acquisition systems, and much more.

The STTF and its capabilities is to be covered in the following sections.

TOWER

One major component of the STTF is the 60.96m above ground concrete tower. The purpose of this tower is to locate experiments and necessary auxilliary equipment in a central location for testing.

The tower has four areas available for testing, the tower top and three test

levels on the north side. The tower top is used for large experiments. The three lower level test bays are for smaller experiments. The three lower level test bays are for smaller experiments. These test bays are located 36.6m, 42.7m, and 48.8m above ground level. Refer to Figure 1. The test bays located at 36.6m and 42.7m are configured as rooms with a door opening 6.71m wide and 4.57m high. The test bay at 48.8m is 6.71m wide with no ceiling.

Equipment for lifting experiments to the tower test areas varies from 4535.9 Kg (10000lbm) jib cranes to an elevating module capable of lifting 90700 Kg (200,000 lbm).

The jib cranes are positioned for easy access both inside and outside of the tower. In addition, 4535.9 Kg bridge cranes are positioned in the 36.6m and 42.7m test bays for maneuvering experiments.

The elevating module is in the center of the tower and its 9.1m (30 ft.) by 7.6m (25 ft.) size is used only for large experiments.

In addition to providing test areas for experiments the tower houses several important components of the STTF. These components are used to support experiments and operating equipment at the STTF. Some of these components are:

- Heat Rejection Equipment
- Data Acquisition Equipment
- Heliostat Alignment Equipment

Each of these will be described in further detail.

HEAT REJECTION SYSTEM (HRS)

Most of the heat rejection system is housed in the tower. The heat rejection system is capable of handling water or air as the primary fluid.

Figure 2 shows the water heat rejection system. This system is composed of dry cooling towers, pumps, heat exchangers, and other necessary equipment.

The HRS can supply demineralized water at a maximum rate of 3.16 l/s (50gpm) and a maximum temperature and pressure of 288°C (550°F) and 15.5MPa (2240 psi), respectively. 9000 Kg/hr (20000 lbm/hr) of 518°C (965°F) steam at 13.8MPa (2000 psi) can be accommodated by the HRS.

To assure the experimenter of high quality demineralized water, a water sampling system is used. This system measures the following:

Temperatures
Specific Conductance
pH
Various Alarms
Cation Conductance

Hydrazine and a deaerator are used to control the water pH and oxygen content.

The air supply system can supply 2.72 Kg/s (6 lbm/s) air at a maximum temperature and pressure of 121.11°C (250°F) and 1.04 MPa (150 psia), respectively. Refer to Figure 3.

Four rotary type diesel driven compressors are presently being used by the air supply system. Two hydrocarbon analyzers are used to monitor the hydrocarbon content of the air being supplied. One is used to monitor and display hydrocarbon content for the experiment and the other is used to operate a valve if the content exceeds a certain limit.

The hydrocarbon analyzers are designed to measure one ppm.

As is true for the water system the air system can be used at any test location.

HELIOSTAT ARRAY SUBSYSTEM

222 heliostats are used at the STTF to redirect the sun's energy to an experiment. These heliostats were designed and built by Martin-Marietta Corporation. Refer to Figures 1 and 4.

Each heliostat consists of a 5 by 5 array of 1.22m by 1.22m mirrors. This adds to 37.16m² of area per heliostat. Each individual mirror is focusable and each heliostat is aligned such that every mirror image overlaps on the target at alignment time rather than having 25 individual images from each heliostat.

The alignment of a heliostat is accomplished using a collimated laser light beam the size of a facet which is directed to the facet of interest and the reflection is returned to a target. The laser collimator and target system is located in the tower and is computer controlled from the STTF central computer system.

This procedure requires that an operator adjusts the mirror on the heliostat until the reflected laser image is centered on the target thus bringing the mirror into alignment.

These heliostats track the sun in an altitude-azimuth configuration using the computer system for control.

With this heliostat system a reflected beam of approximately 2 meters can impinge on the experiment with a maximum flux density in the range of 2.5 MW/m². The beam size can be made smaller and more intense with flux redirectors.

More detailed information can be obtained from sources (1 and 2).

As an on going project for the STTF, heliostats will be evaluated versus time. This includes checking for changing reflectivity and structural integrity of the heliostats. In addition, the characteristics of the reflected beam will be monitored using various measuring devices.

There are several devices that will be used to evaluate heliostats.

A ground based moving bar is capable of measuring flux density from a single heliostat using circular foil heat flux gages. This bar will move through the reflected beam from the heliostat and transmit data to a data acquisition and control system. This system then displays the data in a format requested by the experimenter.

Another system is the Real Time Aperture Flux (RTAF) System (3 and 4). The RTAF is capable of measuring from one heliostat to the entire field. Special photon sensors are used along with circular foil heat flux gages on a water cooled moving bar. The RTAF can be positioned at virtually any location on the ground or the tower. The RTAF is usually placed in front of the experiment to measure arriving flux density during actual operation. The RTAF is shown in Figure 5.

Other systems are being developed for heliostat evaluation at this time, however none is completed. These systems include a transportable rotating arm system and a photovisual system.

The STTF expects to evaluate several different types of heliostats. Any manufacturer can bring a heliostat to the STTF for evaluation.

COMPUTER CONTROL AND DATA ACQUISITION SYSTEM

The STTF is controlled by a Master Control System (MCS). The MCS is an overall command, control, and data system performing control management and supervision as well as data collection, analysis, and presentation.

The MCS is designed using digital mini-computers in a modular, function-oriented network. MCS consists of three main mini-computers as illustrated in Figure 6.

1. MCS-Control is the interface for the facility operator's and experimenter's consoles through which the entire STTF can be controlled.
2. MCS-Data is used to control and acquire data from the heat rejection system, four meteorological stations, and from the

MCS-Tower satellite mini-computer.

3. The MCS-Tower minicomputer is operated remotely as a satellite to MCS-Data.

Up to 500 channels of analog data can be connected to the MCS measurement equipment multiplexers at any tower elevation.

Three RAMTEK color graphics displays are used to display data. These displays are used for facility control and experiment data display. Refer to Figure 7.

Further information on the MCS can be obtained from sources 1 and 2.

OTHER CAPABILITIES

The STTF has the equipment and personnel to accommodate most any experiment.

Additional capabilities not mentioned include the taking of Meteorological data on site with information on wind velocity and direction, temperature, particulate matter, visibility, circumsolar data, solar insolation and more.

For experiments requiring flux densities in the range of 10000 Kw/m² a concentrator is available.

Thermocouples, pyrometers, net radiometers, flux density measuring devices and much more are available for the experimenter to use.

In short, the STTF has been developed to meet the needs of a wide range of experimenters.

STTF USERS ASSOCIATION

An active Users Association including government contractors, research institutions, universities, private companies, and foreign interests has been founded to assist experimenters and to encourage utilization of the STTF. Prospective experimenters are invited to contact the STTF Users Association, Suite 1507, first National Bank Building, East, Albuquerque, NM 87108.

CONCLUSIONS

The DOE STTF is a capable solar test facility designed for a wide range of experiments. The initial effort will be in testing solar components for the DOE Central Receiver Power Plant. Afterwards experiments can be tested on most any subject.

All inquiries are welcome and should be addressed to the STTF Experiment Coordination Office, Division 5713, Sandia Laboratories, Albuquerque, NM 87185. (505) 264-2280.

References

1. Darsey, D. M., Holmes, J. T., Seamons, L. O., Kuehl, D. J., Davis, D. B., Stomp, J. M., Matthews, L. K., Otts, J. V.; Solar Thermal Test Facility Experiment Manual, Sandia Laboratories, SAND77-1173, October, 1977.
2. Otts, J. V., Holmes, J. T., Seamons, L. O., Kuehl, D. J., Davis, D. B., Matthews, L. K., Arvizu, D. E., Darsey, D. M., Brandvold, G. E.; The USA 5 MW Solar Thermal Test Facility, ISES International Congress, January, 1978.
3. Matthews, L. K., Davis, D. B.; Real Time Aperture Flux System As Part Of The Solar Thermal Test Facility, IES, NBS, DOE, ASTM, Solar Seminar, May, 1978.
4. Matthews, L. K., Davis, D. B.; Real Time Aperture Flux (RTAF) System, 24th ISA Symposium, May, 1978.

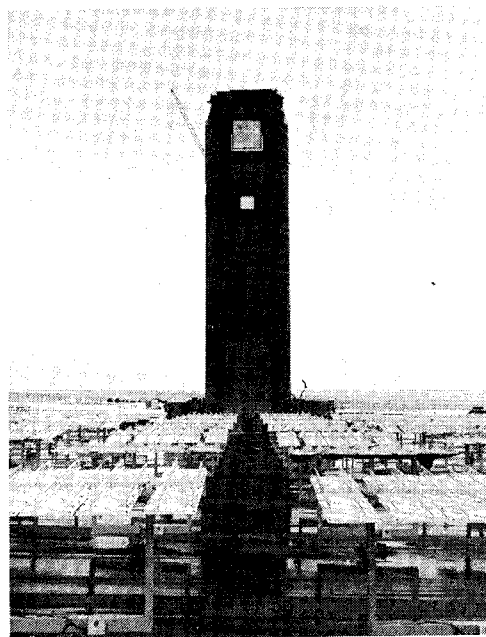


Figure 1.

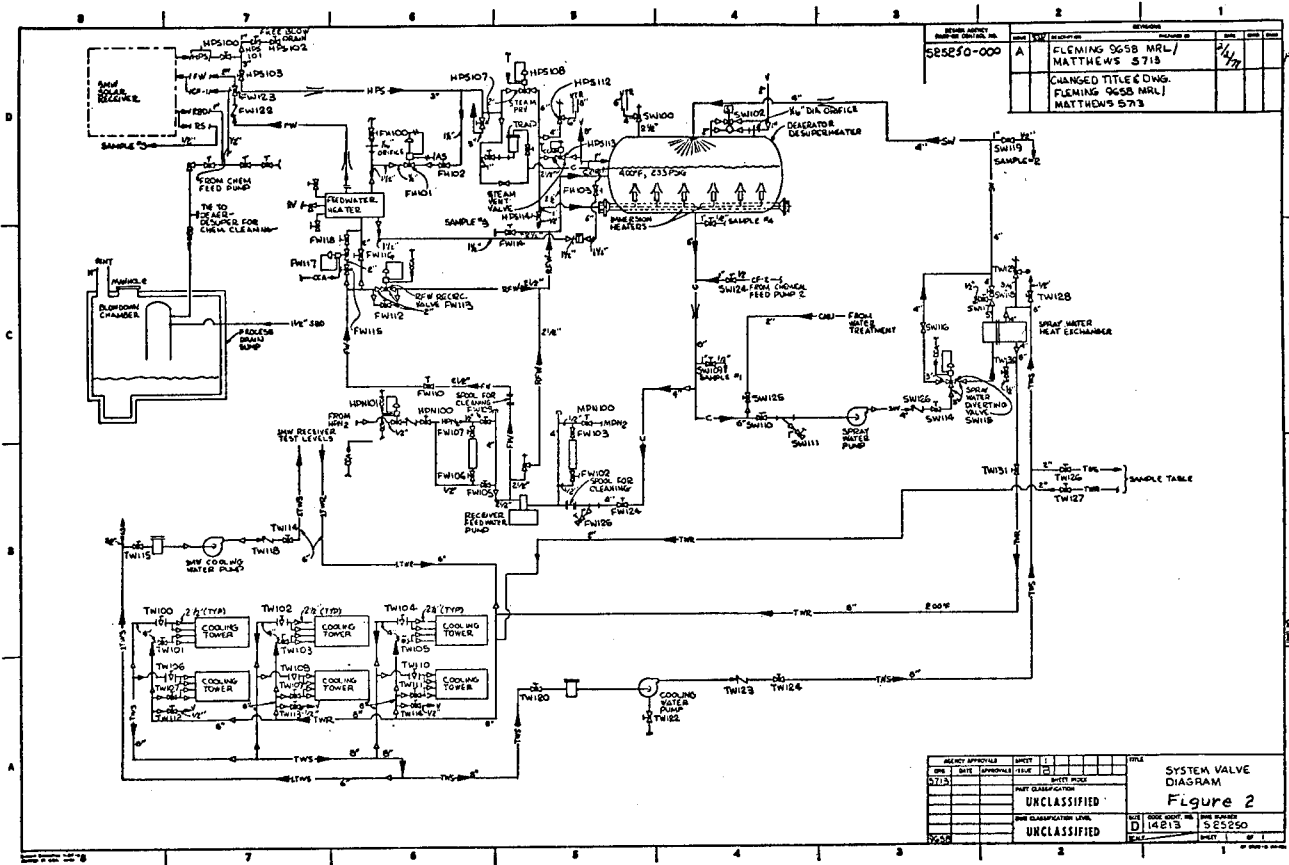


Figure 2.

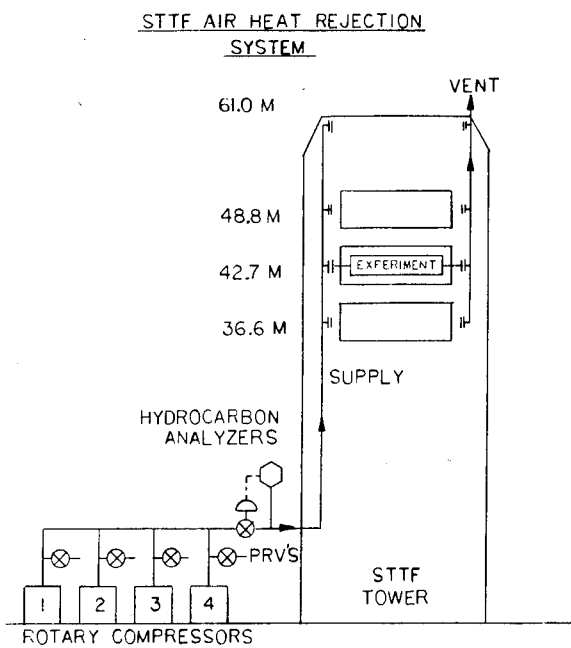


Figure 3.

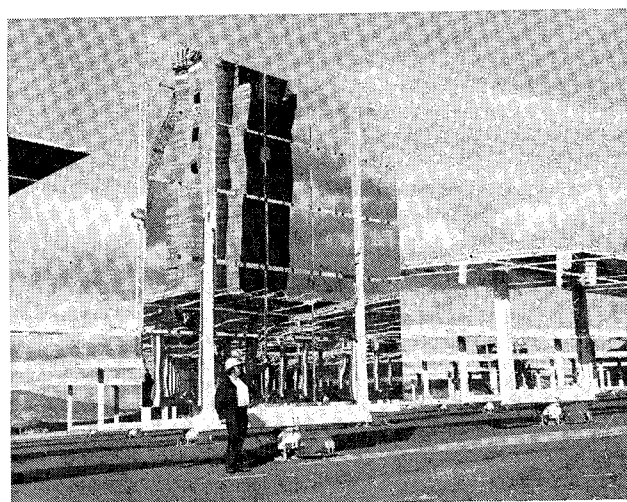


Figure 4.

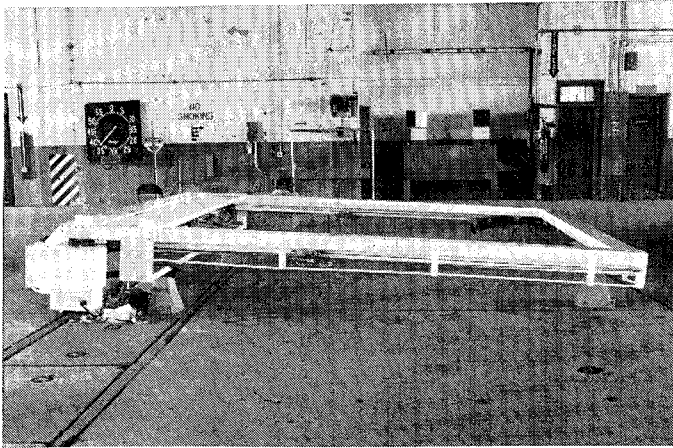


Figure 5.



Figure 7.

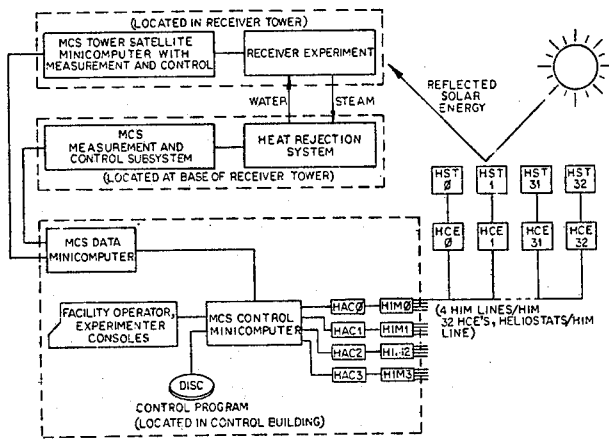


Figure 6.

THE DEVELOPMENT OF THE ADVANCED COMPONENTS TEST FACILITY

By: Ralph F. Altman and C. T. Brown, Georgia Institute of Technology

INTRODUCTION

In 1965, Professor Giovanni Francia built and operated the first of several solar powered steam generators. The solar collector was a tracking mirror field that focused sunlight into a cone shaped receiver located above the center of the mirror field. A unique feature of the field was the mirror tracking mechanism. This mechanical coupling, which Professor Francia called a kinematic motion, moved the mirror it supported in such a way that sunlight reflected from the mirror passed through a stationary focal zone throughout the day. The tracking system required no feedback, either mechanical or electrical, in order to operate. A second unique feature of the system was the antiradiating structure located in the receiver. This structure was constructed of pyrex tubes, closed at the top and open at the bottom, mounted vertically in the lower portion of the receiver.

Since the operation of this first system, Professor Francia has refined and enlarged the design through three generations of systems. The largest and latest test system was first operated at St. Ilario, Italy, in 1972. The mirror field contained 271 tracking mirrors with a total surface area of 135 m² (1450 ft²). The mirrors were round, second surface reflectors with a diameter of 78 cm (30.7 in.). The receiver for the system has generated 150 atm. (2200 psi), 600° C (1110° F) steam with an overall collection efficiency of 73 percent.

In 1975, the Energy Research and Development Administration, decided to purchase a solar powered steam generator of the Francia design through the Italian firm of Ansaldo, SpA. Figure 1 contains a photograph of the recently installed Department of Energy facility.

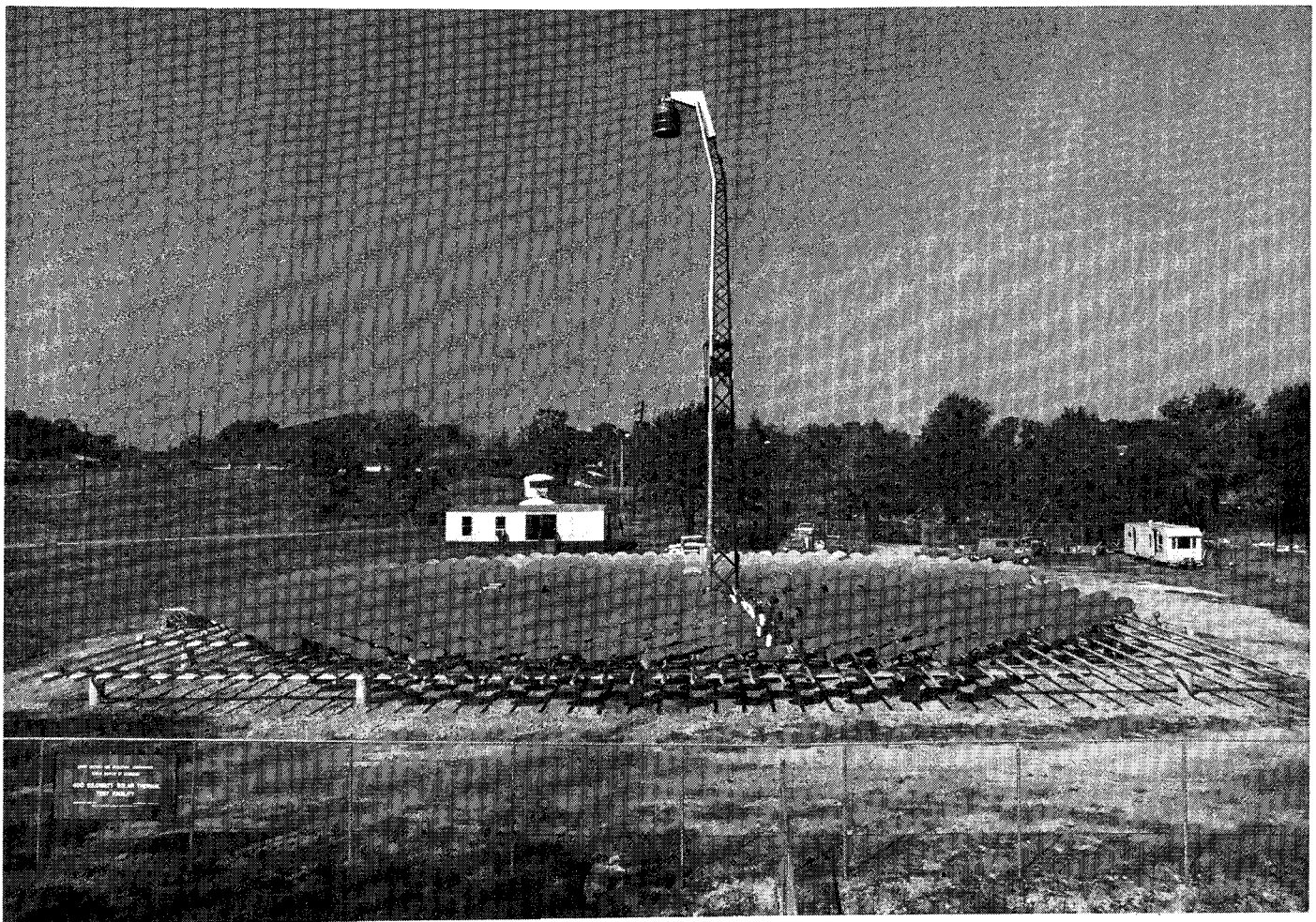


Figure 1. Advanced Components Test Facility.

This system, which is now known as the Advanced Components Test Facility, would be located on the campus of Georgia Tech. The operation of the facility would accomplish two objectives. First, it would effect a technology transfer and second; it would make it possible to test innovative solar receivers and systems on a moderate scale. The system would be operated by Georgia Tech's Engineering Experiment Station and the performance of the mirror field and central receiver determined and documented in order to accomplish the first objective. Following the completion of the characterization phase, the system would be converted to a general purpose test facility, thereby accomplishing the second objective.

CHARACTERIZATION PROGRAM

The solar steam plant was installed at Georgia Tech in 1977 and became operation in November 1977. Figure 1 shows the facility in the "steam plant" configuration. The mirror field contains 550 Francia type heliostats or kinematic motions. These devices are mechanically interconnected by torque tubes, and the entire field is driven by one $1\frac{1}{2}$ horsepower electric motor. Each kinematic motion supports and manipulates a 111 cm diameter circular, second surface, low iron glass mirror, which can be operated either flat or focused.

The receiver shown in Figure 1 is a once through steam generator. It is located at the geometrical center of the field at an elevation of 21.46 meters above the mirror plane. This height, combined with the extent of the field, gives a nominal rim angle for the field of 45 degrees.

The principle of operation of a kinematic motion is diagrammed in Figure 2. Point A is the center of a sphere of fixed radius. Point B is the point at which the extension of a line drawn from the sun through point A intersects the sphere. Point C is the intersection of a line drawn from A to the receiver with the sphere. Lines CA and AB are of equal length and form the equal sides of the equilateral triangle ACB. A mirror is placed at point M perpendicular to line MCB. Since line MCB is parallel to the bisector of angle SAR, the mirror surface will reflect the light from the sun (point S) onto the receiver (point R). Point B rotates about axis TA, (parallel to the earth's axis) at $15^\circ/\text{hr}$ and MCB rotates around point C. This rotation forces point B to follow the sun throughout the day, and keeps the sunlight reflected by the mirror centered in the receiver.

A drawing of an Advanced Components Test Facility kinematic motion is also shown in Figure 2. The relevant points are indicated on the drawing

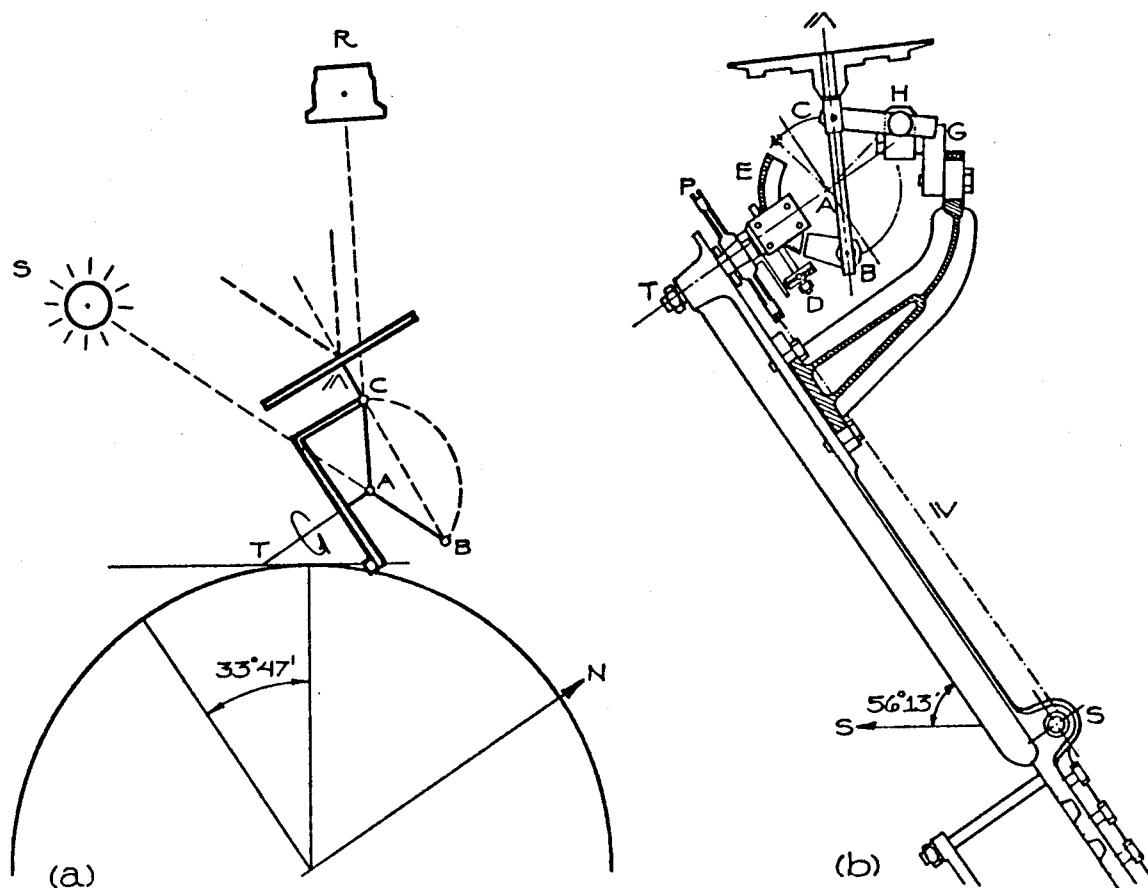


Figure 2. Principle of Kinematic Motion Operation.

of the kinematic motion. The axis of rotation is shown by line AT which is located parallel to the earth's axis. Rotation is provided by a cable W around the pulley at P and driven through the shaft S. Alignment with the sun (line AB) is provided by a worm gear at D acting on the circumferential gear arm E. Declination adjustments also are provided through D. Alignment with the receiver (line AC) is provided through point H attached to a movable collar on the fixed rod G.

The receiver supplied with the system is depicted in Figure 3. It is a once through steam generator and is constructed entirely of stainless steel. Chemically treated water is first circulated through the tubes that curl around the shell of receiver. The preheated water then flows into the inner ring of boiling tubes and then into the outer ring of boiling tubes. The boiling sections are in the middle of the receiver. Steam leaving the last boiling section flows through the serpentine superheater tube in the top section of the receiver. The receiver is designed to generate 600° C (1110° F) steam at the 120 atm. (1700 psi). The large cylinders shown in Figure 3 are the pyrex tubes that make up the antiradiating structure.

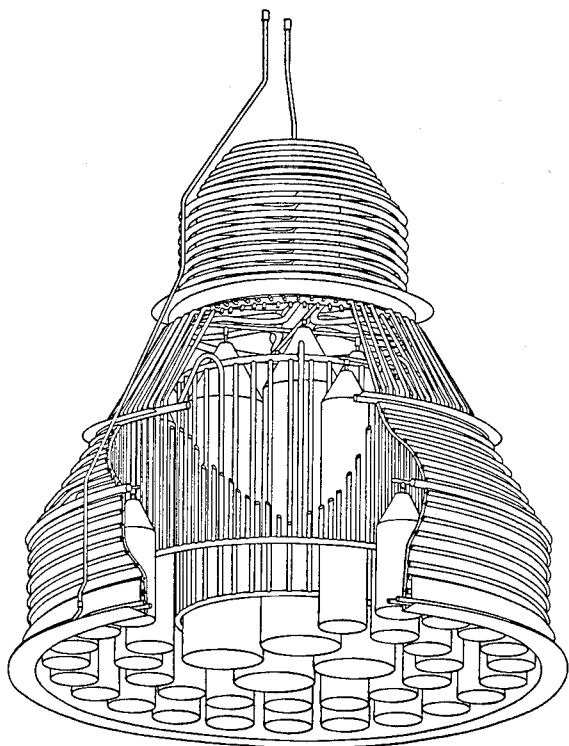


Figure 3. Francia Once Through Steam Generator.

The characterization of the basic Francia type facility has been partially completed. The focusing capability of individual mirrors has been determined and the tracking errors of the kinematic motions have been measured. The steam generator has been operated at its design temperature and pressure. The tests to date have been of a preliminary or shake-down nature. Flux measurements in the focal zone are scheduled to take place in June 1978, and the performance of the receiver will be determined in late 1978.

FACILITY CONVERSION

The conversion of the Francia steam plant to a general purpose test facility is proceeding while the characterization tasks are being completed. The conversion process started in December 1977 with the design of a new central tower to replace the articulating tower supplied as part of the Francia solar steam plant. An artist's concept of the new tower appears in Figure 4. The new tower will provide an increased load capability and better access to the experimental area. The old tower had a capacity of approximately 1500 lbs. The new tower has a capacity of 20,000 lbs. The focal point for the facility will be centered on the tower legs and at the floor level of the experiment platform. Access to the top of the platform is by ladder and man/material work hoist; access to the area below the platform is by scissors lift. The scissors lift can be withdrawn to the 50 ft level during a test so as to minimize the blocking of radiation incident on the focal plane. The cantilevered part of the platform will house an instrument building.

Support equipment at the DOE Advanced Components Test Facility includes a computerized data acquisition system, a scanning flux calorimeter, pyrhemometers, a pyrometer, and a solar blind infrared TV camera system. The computerized data acquisition system consists of two mini-computers. One will be located atop the tower and will control a 120 channel multiplexed A-to-D system. The second computer will be located in a control room adjacent to the mirror field. This processor manages the tower top computer and also manipulates, stores and displays data according to the needs of the experimenter. Data output from the system includes strip chart recorder type displays on a video terminal, line printer listings of selected channels, mag tape copies of both raw and processed data, and diskette copies of data. Data input to the computerized data acquisition system can be from virtually any type of analog output transducer.

A scanning flux calorimeter will be used in the characterization experiment and will be available for use in following advanced receiver tests. This device is a water cooled bar housing 37 Gardon gage type calorimeters on 2 inch centers. The bar is mounted on a water cooled support structure that can in turn be mounted to the tower or to an experiment. The device operates under computer control in such a manner that a 2 x 2 inch grid of the incident flux distribution can be produced by scanning the bar through the distribution. The output of the calorimeters is stored by the data acquisition system.

Presently, two major Department of Energy contractors have tests scheduled at the Advanced Components Test Facility. In the first series of experiments, a prototype of a high temperature ceramic air cooled receiver will be tested. This receiver is designed to be used in an open Brayton cycle to produce electricity. Testing will begin in July 1977. A sodium heat pipe receiver is scheduled for testing in 1979. It is anticipated that the Advanced Components Test Facility will continue to play an important role in advancing new concepts to practical, functioning high temperature solar powered systems for the next several years.

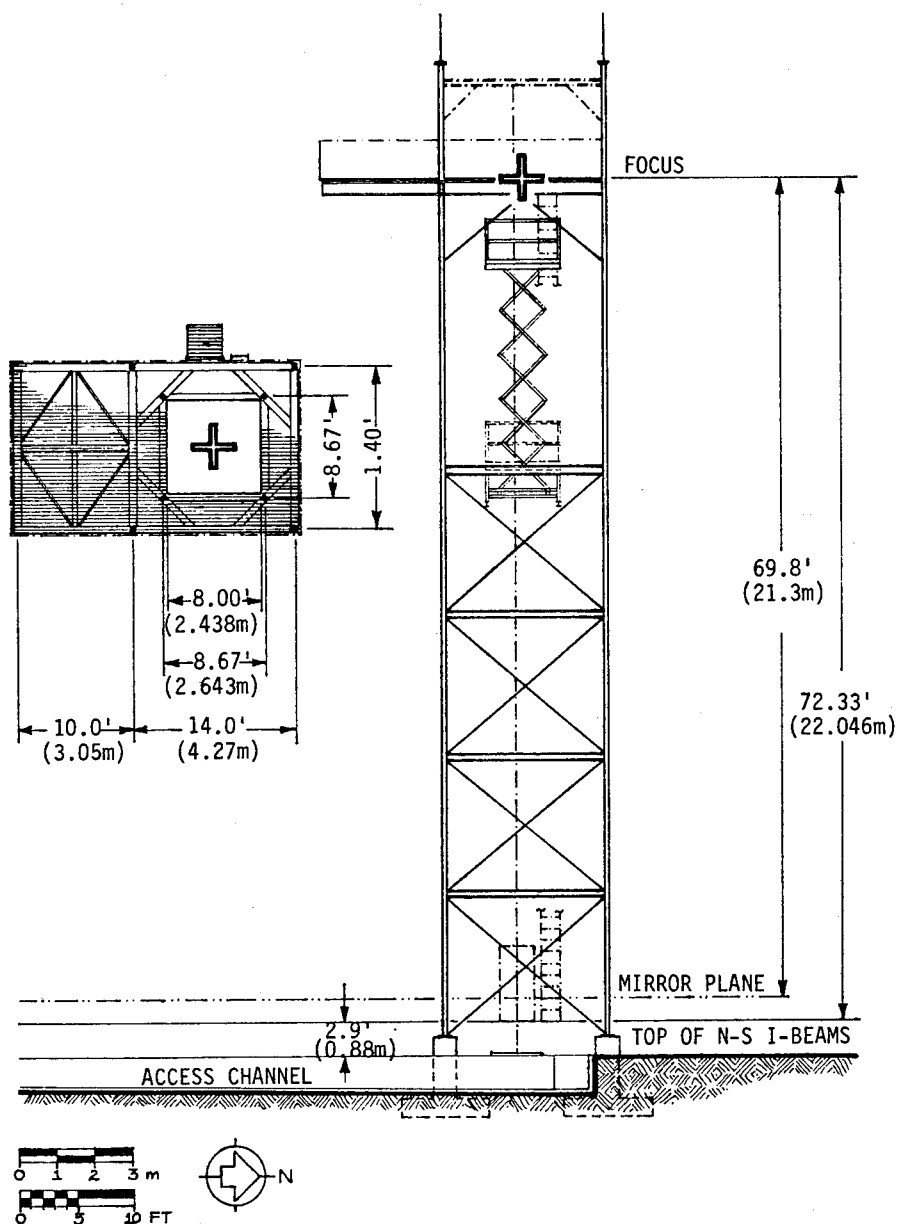


Figure 4. Drawing of New Central Tower.

WHITE SANDS SOLAR TEST FACILITY

By: Richard A. Hays, White Sands Missile Range, New Mexico

Graduate of New Mexico State University with a MSE.E. registered professional engineer in the state of New Mexico. Employed by the Nuclear Weapon Effects Laboratory, White Sands Missile Range since 1969 and presently Chief Engineer of the White Sands Solar Furnace.

INTRODUCTION

The WSSF was originally constructed in 1958 and operated by the Quartermaster Research and Engineer Center at Natick, Massachusetts. In 1973 the WSSF was relocated at the White Sands Missile Range, New Mexico. The WSSF is available for use by the Department of Defense and its contractors, other Government agencies and private industry.

The facility is operated by the Army's Nuclear Weapon Effects Laboratory primarily for nuclear weapon thermal effects testing but is also used for solar energy research by numerous Government agencies and universities.

DESCRIPTION OF THE WSSF

The WSSF is comprised of four main parts; the Heliostat, Attenuator, Concentrator and Test and Control Chamber.

The Heliostat consists of 356 flat plate mirrors, each 0.635cm in thickness and 62 by 62cm square, mounted on a steel framework 1.2 meters wide and 11 meters high. The heliostat moves in azimuth +60 degrees about 180 degree north-south orientation and 0 to 90 degrees in elevation. The heliostat is an elevation over azimuth mounting with the drive systems located in the vertical and horizontal turret sections. The heliostat mirrors are front surfaced standard flat plate glass. The reflective surface consists of vacuum deposited aluminum with an overcoating of silicon monoxide. Each mirror is mounted on three compression springs with stainless steel bolts through the mirror and spring and attached to the heliostat framework. There are three modes of movement of the heliostat; slew, manual track and auto track. In the slew mode, two 1/2 HP AC motors (one AZ., one EL.) operating at 1725 rpm used to move the heliostat at rates of 7.2 degrees per minute in azimuth and 6.5 degrees per minute in elevation. The slew mode is used to bring the heliostat from the stow position to sun acquisition. In the manual mode the same mechanical drive systems are used as in the slew mode. The difference between the slew and manual track modes being a further gear reduction and a variable speed 1/15 HP 0-1725 rpm DC motor, coupled to the drive system through an electro-mechanical clutch. In the manual track mode the heliostat is moved in azimuth at a maximum rate of 11.6 degrees per hour and in elevation at a maximum rate of 7.8 degrees per hour. The third mode of movement is auto track, which is the same as manual track mode with the exception that the motor speed is controlled by position feedback from a photo detector. In

this mode the heliostat automatically tracks the sun keeping the heliostat positioned within 30 seconds of Arc. The auto track system keeps the solar image at the focal plane positioned within 0.25cm. Gusty winds above 15 knots and clouds passing between the sun and the heliostat can cause tracking instabilities with up to 1.25cm of the solar image or loss of track. If required, moon tracking can be accomplished with the same auto track system. By using the moon as a source, precise alignment of optical experiments can be performed without the intense concentrated solar heat and light associated with the sun.

The Concentrator consists of 180 spherical mirrors mounted on aluminum rings 59.7cm in diameter, which are attached to the 9.1 meter square concentrator framework so that a solar image is positioned at the WSSF focal plane 10.7 meters away. All the concentrator mirrors are front surfaced with vacuum deposited aluminum and overcoated with silicon monoxide.

The Attenuator controls the useable thermal power of the WSSF varying the power from zero to maximum within two minutes. The attenuator consists of 17 rows of rotatable horizontal blades. The blade angle is controlled by the solar furnace operator and varies from 45 to 90 degrees from vertical for complete to minimum attenuation of the solar energy. If a hazardous condition occurs during testing, automatic safety circuits are coordinated with the attenuator drive circuits so that the attenuator may be closed within 0.5 seconds. The attenuator can operate in an auto control mode compensating for changing atmospheric conditions thus keeping a constant flux level at the focal plane during long steady state exposures. See Figure 2 for attenuator transmission characteristic. The test and control chamber is 2.4 by 2.4 meters in cross section presented to the solar energy reflected from the heliostat and 4.8 meters in the direction of the optical axis and houses the experimental area, the control console and the fast shutter system. Cooling water and high pressure air supplies are available in the test and control chamber.

The Fast Shutter System consists of a water cooled shutter, exposure shutter, and a limit shutter. The water cooled aluminum shutter is 45.7cm in diameter and protects the fast shutters and experiment from the 30,000 watts of thermal energy during non exposure. The exposure and limit shutters have rise and fall times of 25 milliseconds and are mounted 5.1cm in front of the focal plane. These two shutters produce a rectangular pulse

duration as short as 100 milliseconds. The thermal pulse shaper for nuclear weapon simulation is mounted behind the fast shutters and can be for steady state operation. Also a wind tunnel which will accommodate 7.6 by 10cm test specimens can be used inconjunction with the WSSF to provide air flow with velocities up to a maximum of 40,000 feet per minute.

EXPOSURE CHARACTERISTICS

The thermal exposure area is approximately 16cm in diameter at the focal plane located 81.25cm from the south wall of the test chamber and 1.06 meters above the test chamber floor. Larger exposure areas can be obtained by moving out of the focal plane but with reduced flux levels. The maximum available flux at the focal plane to date is 100 cal/cm² sec, (90 cal/cm² sec readily obtainable) with a total available power of 30,000 watts thermal. Maximum flux levels with a 10% uniformity are obtained over an exposure diameter of 5cm. The thermal flux profile at the focal plane has the 50% flux points occurring at a 5cm radius from the center of the solar image as shown in Figure 3. Table I gives some of the important exposure characteristics of the WSSF.

OPERATIONAL CHARACTERISTICS

Since the WSSF is dependent upon weather conditions for operations, the following weather data is used to help schedule experiments to be conducted at the ASSF. Wind and cloud cover data taken over a period of 22 years, by the Atmospheric Sciences Laboratory, indicates WSMR as a good location for the WSSF in regard to availability of usable operational hours. Information on wind and cloud cover by month and hour indicates an average of 1200 hours of operation time per year is available at the ASSF. This is based on a 2080 hour work year, 5 day work week, and an 0800 to 1600 hour work day. See Tables II and III. It must be remembered that the WSSF has two operational constraints cloud cover and wind when planning thermal tests.

TABLE I

DIAMETER (In)	1	2	3	4	5	6	6.5
% Total Power	6.5	24.6	49.5	74.5	91.5	99.1	100
Power Kilowatts	1.89	7.21	14.56	21.91	26.97	29.17	29.47
Min Flux cal/cm ² Sec	88.2	79.2	59.4	39.7	14.4	4.5	0
Mean Flux cal/cm ² Sec	89.1	83.7	69.3	49.1	26.6	9.4	2.2

TABLE II

CATEGORY	CLOUDCOVER	WINDS	AVAILABLE HOURS
I	Clear	< 5 Knots	395
II	Clear	< 14 Knots	666
III	< 50%	< 5 Knots	666
IV	< 50%	< 14 Knots	1200

TABLE II lists month of the year according to percent operational time available for that month in category IV of TABLE IV.

TABLE III

<u>MONTH</u>	<u>% OPERATIONAL TIME</u>
September	71
October	70
June	70
May	61
November	60
August	59
July	57
December	53
April	51
January	50
February	50
March	48

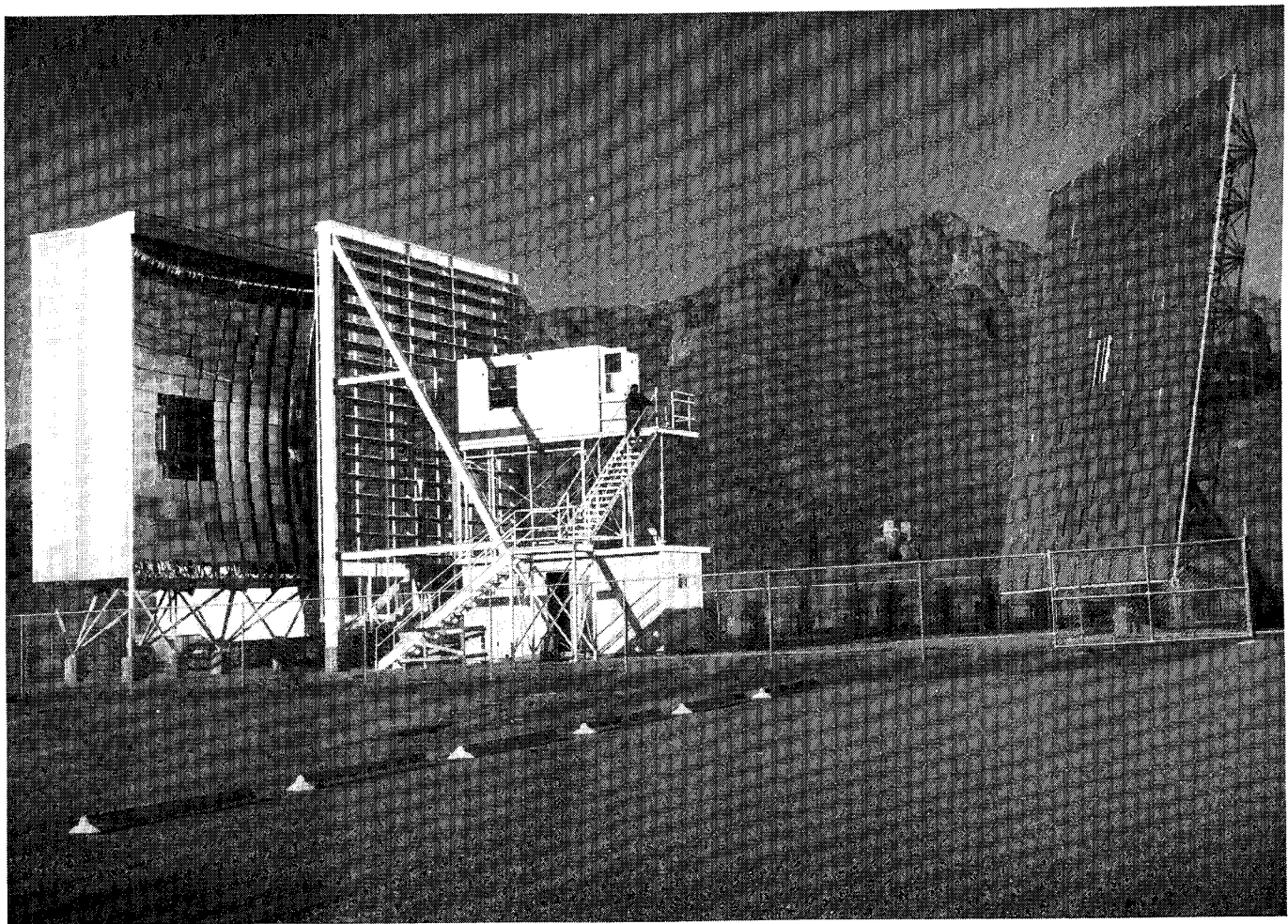


FIGURE 1

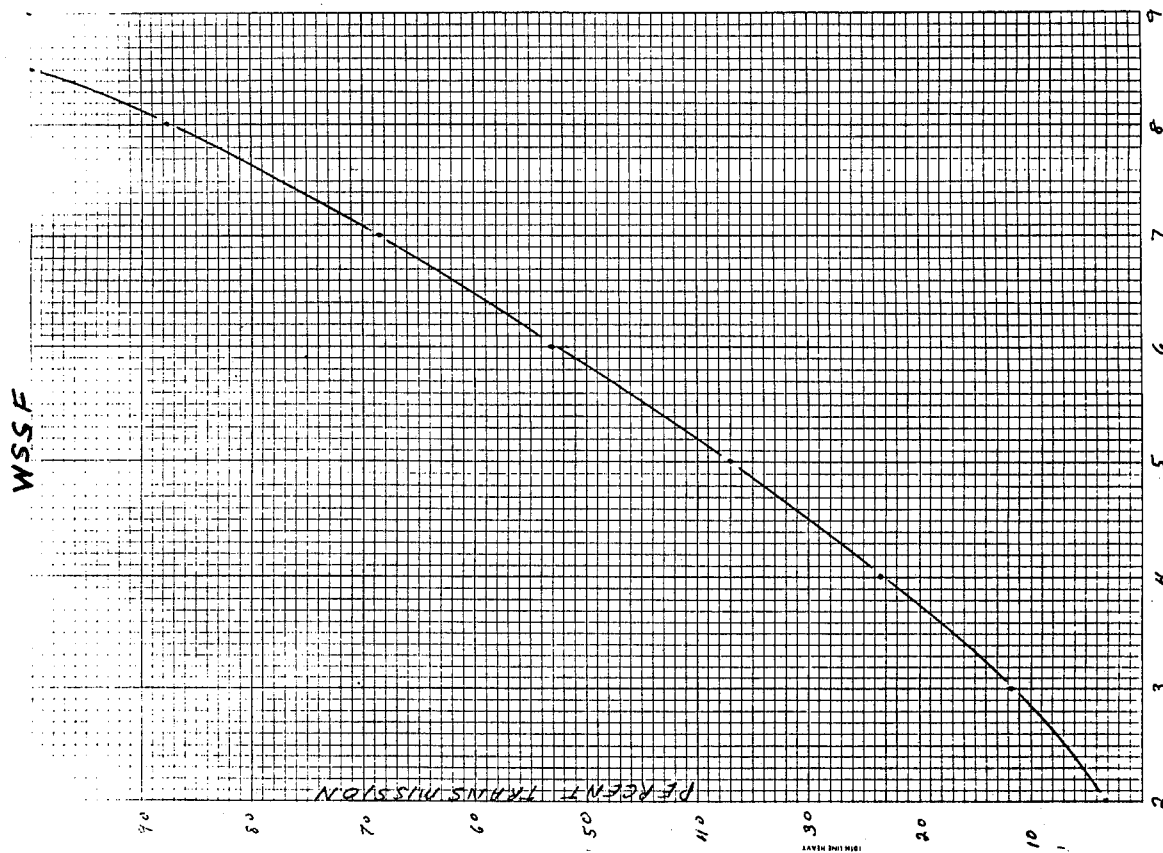


FIGURE 2

WSSF IRRADIANCE PROFILE
AT
FOCAL PLANE

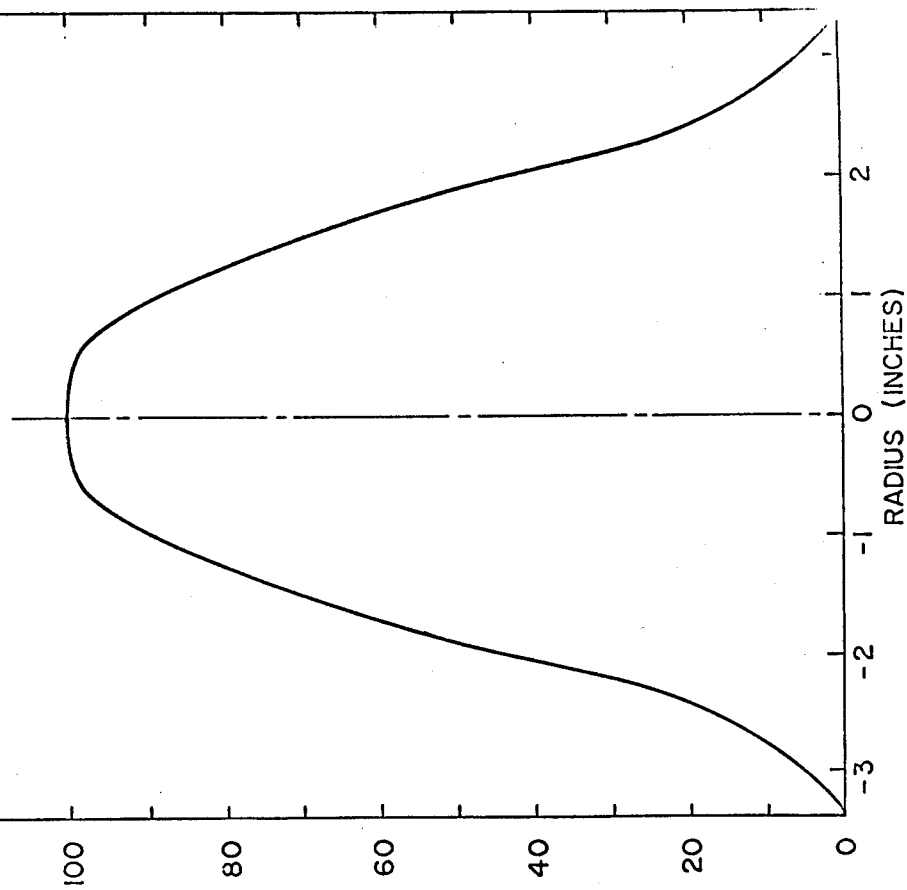


FIGURE 3

SANDIA LABORATORIES' MIDTEMPERATURE SOLAR SYSTEMS TEST FACILITY*†

By: Robert M. Workhoven, Staff Member, Sandia Laboratories

The Author

R. M. Workhoven received his B.S. in Mechanical Engineering from the University of Iowa in 1959 and his M.S. in Mechanical Engineering from the University of New Mexico in 1967. He joined Sandia Laboratories in 1959 and worked in various phases of environmental testing until he joined Sandia's Solar Energy Projects Department in March 1977. His current assignment is Project Engineer of the Collector Module Test Facility in the Midtemperature Solar Systems Test Facility. He is a member of Pi Tau Sigma and Tau Beta Pi.

Objectives and Scope

The Midtemperature Solar Systems Test Facility (MSSTF) at Sandia Laboratories, Albuquerque, NM, supports the Department of Energy's (DOE) national Dispersed Solar Thermal Power Systems Program. It was established as a national test laboratory to develop technology that applies solar energy principles and to demonstrate the feasibility of the solar total energy concept.

Research, development, and testing of materials and components at Sandia produce data and experience that are important to larger system design and commercial uses. Although Sandia manages the project and is responsible for system engineering, many companies from private industry have provided equipment and helped construct the test facility. By encouraging their participation, Sandia and DOE promote within the private sectors a technology that can be economically competitive with nonrenewable energy sources.

Other goals of the MSSTF are to analyze the results of these activities, to publish and disseminate reports and make presentations, and to accommodate facility visitors.

The MSSTF (Figure 1) is large enough to require realistic integration of all solar total energy (STE) subsystems and to identify areas requiring further research and development. It consists of two independent installations--the System Test Facility (STF) and the Collector Module Test Facility (CMTF).

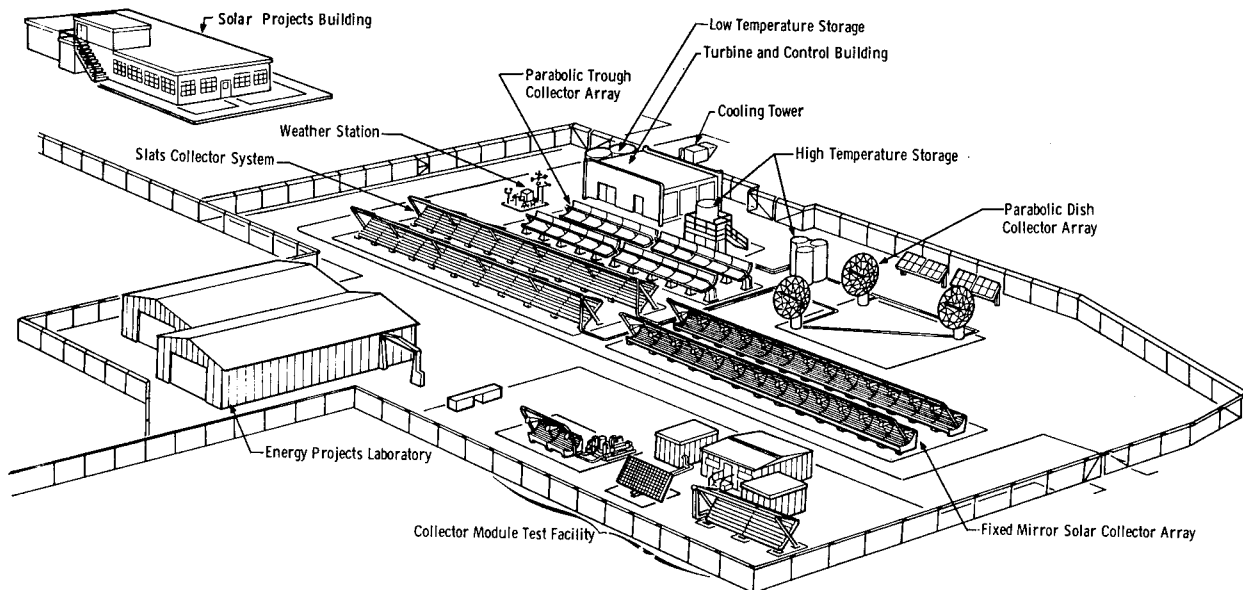


Figure 1.

* This work was supported by the U.S. Department of Energy, Division of Solar Technology.

† On March 6, 1978, the name of this facility was changed from the Solar Total Energy Test Facility to the Midtemperature Solar Systems Test Facility.

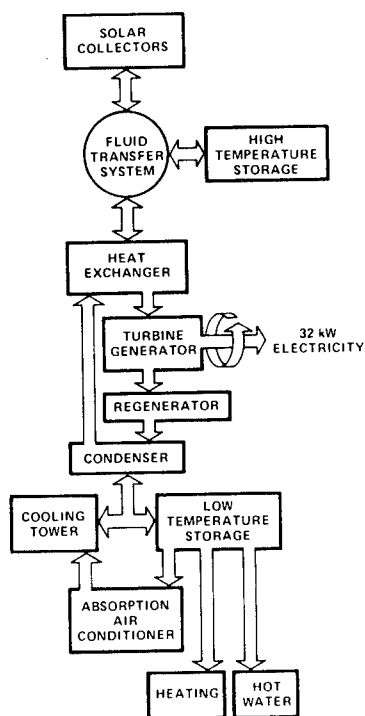
The System Test Facility (STF)

The System Test Facility was sized to meet the energy requirements of the Solar Projects Building (visible in the background of Figure 1). It is an 1130-m² (12,200-ft²) office building that houses, among other groups, the solar engineering project staff. The building's electrical load is 32 kW for an 11-hr day, or a daily total of 352 kWh. The cascaded energy from a turbine condenser (~200 kWh) meets about 70% of the building's peak heating and cooling demand and is supplemented by conventional means on peak-load days.

After electrical power had been furnished to this building in April 1977, the world's first application of solar total energy was made to the Solar Projects Building in June 1977.

The major parts of the STF are the collector fields, the fluid transfer system, high-temperature storage system, toluene heat exchanger, turbine/generator, control and equipment center, low-temperature storage, and cooling tower. Figure 2 is a simplified schematic depicting operation of the STE system.

Figure 2.



Collector Field

The collector fields are made up of four different collector types. Each subsystem can operate independently or with the other three. The collectors include these diverse types:

Parabolic Trough--This subsystem, designed by Sandia, has been operative since late 1975. It consists of four 18.3-m (60 ft)-long parabolic troughs in two rows along an east-west axis.

Reflective surfaces of the collectors are aluminized Teflon laminated to Mylar and bonded to aluminum sheet. The reflectors are attached to plywood troughs with spring-loaded edge clamps and screws. The steel receiver tubes, coated with highly absorptive black chrome, are sealed in evacuated glass tubing and extend the full length of each set of troughs. Tracking and control of the collector field are done by a minicomputer that compares collector elevation angle with a sun position program and sends appropriate correction signals to the drive motors.

Parabolic Dish--This is a single collector module designed by Raytheon, Inc. The 6.7-m (22-ft)-diam collector is a segmented dish with silvered-glass mirror surfaces that concentrate solar radiation on a receiver mounted at the focal point. The receiver cavity has black chrome plating on its absorbing surface. Nonabsorbing surfaces are heavily insulated to prevent heat loss. The collector has two-axis computer controlled tracking.

Fixed Mirror Solar Collector--This design by General Atomic Co. features fixed precision cast-concrete troughs with longitudinal silvered-glass facets. There are two rows of collectors, each 61 m (200 ft) long and 2 m (7 ft) wide. The collectors are oriented on an east-west axis and have a movable receiver assembly that tracks the sun's reflected and focused image. Sun sensors detect changes in the sun's position and send signals to activate the receiver-tracking motor.

Solar Linear-Array Thermal System (SLATS)--Designed by Suntec Inc., the SLATS consists of two rows of reflectors, each 43 m (140 ft) long and 3 m (10 ft) wide. This east-west axis system has mirrored slats that track the sun and concentrate the solar radiation onto a fixed receiver assembly. This system also uses a sun sensor to activate its tracking system. The SLATS subsystem is the only one that uses water as the collector thermal-transfer fluid; therefore, it is the only one that requires piping capable of operating at pressures up to 21 MPa (3000 psi) for temperatures of 338°C (640°F). A heat exchanger next to the collectors transfers the energy to Therminol 66 (T66), the fluid that is common to the rest of the test system.

Fluid-Transfer System

The fluid-transfer system interconnects all facility subsystems. The fluid loops consist of valves, pumps, insulated pipelines, and flow sensors. The T66 heat-transfer fluid for the collector field and high-temperature storage tanks is a high-boiling-point oil that remains liquid at system working temperatures, about 315°C (600°F).

High-Temperature Storage

Two high-temperature storage systems maintain the temperature of the T66 at acceptable working levels. The first, a single-tank stratified-storage system, has a capacity of $\sim 6 \text{ m}^3$ (1560 gal).

The second system consists of three 11.9-m^3 (3150-gal) tanks located inside a berm for fire protection and tank-rupture containment. The berm is sized to hold the volume of the tanks plus water from a deluge system that automatically floods the tanks and the berm in case of fire.

The three-tank system allows management of the heat-storage liquid without having to mix hot and cold liquids in the same tanks and with a lower total tank capacity than with two tanks. At least three tanks are required to evaluate all combinations of the multitank system.

In the morning and the evening not enough energy is collected to operate the generator system. During the day, however, there is an excess of collected energy that is stored. Daily startup at 7 a.m. begins with one tank of hot fluid at 310°C , one tank of cold fluid at 250°C , and one empty tank. In early morning the hot fluid powers the generator and is then dumped into the empty tank. Enough energy is collected during the day to operate the generator and heat both tanks of fluid to 310°C . Starting at midafternoon, the system exhausts one hot tank and, at evening shutdown, there is one tank of hot fluid, one of cold fluid, and one empty tank. Each tank has a capacity of at least half the total liquid (23.8 m^3 or 6300 gal) to be stored.

A complex instrumentation system monitors storage-tank fluid temperatures and levels and supplies information to the minicomputer, which controls valves to manage the system as described.

Toluene Heat Exchanger

The heat exchanger is the interface between the heat-transfer fluid (T66) and the turbine working fluid (toluene). Heat exchange is done in four phases: one for preheating, two for boiling, and one for superheating. The toluene is heated to 310°C (588°F) and 1.8 MPa (275 psi), and enters the turbine as superheated high-pressure gas.

Turbine/Generator

The single-stage organic Rankine-cycle (ORC) turbine is driven at 25,000 rpm by the toluene gas. Reduction gears drive the generator at 1800 rpm to produce up to 32 kW of electrical energy. Turbine condenser coolant is water that is stored in low-temperature storage tanks and becomes the energy source for heating and air-conditioning. The turbine condenser-coolant temperature is set

to 88°C (190°F) for air-conditioning needs, 74°C (165°F) for heating needs, and as low as possible at other times for maximum electrical generation.

Control and Equipment Center

The Control Center is located in the same building with the toluene heat exchanger and the turbine/generator; it also contains the control and data equipment.

A minicomputer gathers and analyzes input from the temperature-and-flow instrumentation systems and manipulates fluid-control valves as required. It also records data from the STF weather station and supplies sun-position data for the computer-controlled tracking systems.

Low-Temperature Storage

Two tanks, with a capacity of 19 m^3 (5000 gal) each, store the heated condenser-cooling water until needed for operation of heating or cooling components.

Cooling Tower

The induction-spray evaporative cooling tower performs several functions in the system. It dissipates excess heat from the turbine and absorption air conditioner and serves as part of the test load for systems under evaluation. The cooling tower can cool 1300 L/min (350 gpm) of water.

The Collector Module Test Facility (CMTF)

The CMTF (Figure 3) obtains thermal and optical performance data for prototype collectors of up to about 45 m^2 (500 ft^2) in aperture. This facility has three separately controlled fluid loops capable of testing three different collectors simultaneously. The three test stations use Therminol 66 heat-transfer oil to 315°C (600°F), high-pressure water to 330°C (630°F) and 18.3 MPa (2650 psi), and low-pressure water to 110°C (230°F) and 0.51 MPa (75 psi). The low-pressure water loop will soon be relocated in Sandia's Photovoltaics Advanced Systems Test Facility and replaced with a higher temperature [550°C (1020°F)] heat-transfer oil loop.

Time to complete testing of a collector ranges from 3 to 10 wk, depending on the weather, the nature of the collector, and the complexity of the test plan. After each test, a report that contains test-efficiency data, heat-loss data, and information about assembly, operation, and maintenance of the prototype collector is issued to wide distribution. These reports are assembled into a summary report semiannually. (The most recent semiannual report was SAND78-0815, May 1978.)

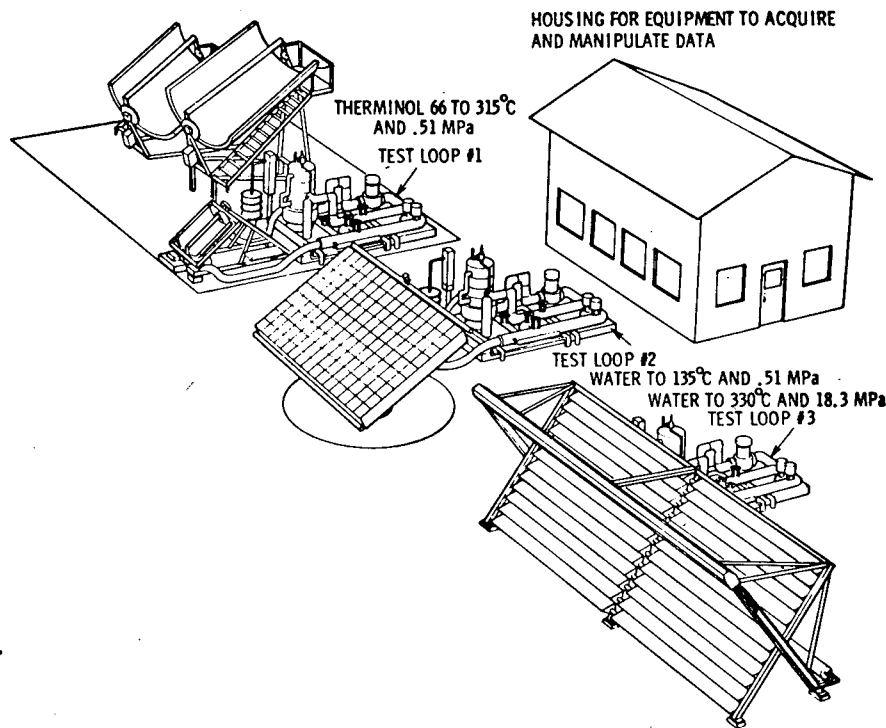


Figure 3.

Prototype collectors are either developed or purchased for testing to obtain performance data and to identify potential design improvements. Companies providing collectors include Hexcel, Soltrax, Scientific Atlanta, Solar Kinetics, FMC, Del-Jacobs, GE, Itek, McDonnell Douglas, General Atomic, and Suntec.

Large-Scale Experiments (LSEs)

A technical basis for STE demonstrations is needed. Not only must technological development be accelerated, but the associated programmatic risk must be minimized. Sandia is providing technical management support for DOE's large-scale experiments (LSEs) designed to develop experience with large hardware systems and to foster the engineering capability required for STE demonstrations.

Westinghouse Electric Corporation is designing an STE system for part of a 1500-man barracks complex at Ft. Hood, TX. The 40,700-m² (438,000-ft²) complex includes barracks, commander's office, administration building, gymnasium, storage, support buildings, and a central energy facility. The conceptual design is based on a parabolic trough collector, multitank storage, and steam Rankine power-conversion cycle.

A second LSE in Shenandoah, GA, will incorporate an STE system in a new knitwear factory (Figure 4). The 2300 m² (25,000 ft²) plant will employ 70 people to begin with, later expanding to 3900 m² (42,000 ft²) and 300 employees. The solar energy

system there is designed to generate 9.7×10^6 MJ (9.2×10^9 Btu) thermal and 1.36×10^6 MJ (378 MWh) electrical per year. With this capacity, the system will supply 169°C (337°F) process steam in addition to normal electrical, heating, air-conditioning, and hot-water requirements. General Electric Company, the contractor selected competitively to design the project, will use an array of 192 7-m (23-ft)-diam parabolic dish collectors, rock and oil storage, and a steam Rankine power-conversion cycle.

Component development for the Shenandoah LSE is being supported at the MSSTF. GE has an engineering prototype collector under test on the CMTF. It is a 5-m Scientific-Atlanta communications antenna dish covered with FEK244 reflective film and with a GE cavity receiver. Four 7-m dish collectors derived from the 5-m design will be installed in the extreme northeast corner of the STF. This subsystem will be configured as closely as possible to the final Shenandoah site configuration. It will be operated as another part of the STF collector field during the definitive design phase of the LSE project.

Other LSEs are being planned. These experiments will provide a data base for evaluating system and component performance in actual environments. DOE can then assess the economic practicality of large systems; users can determine the value of solar total energy in reducing energy costs.

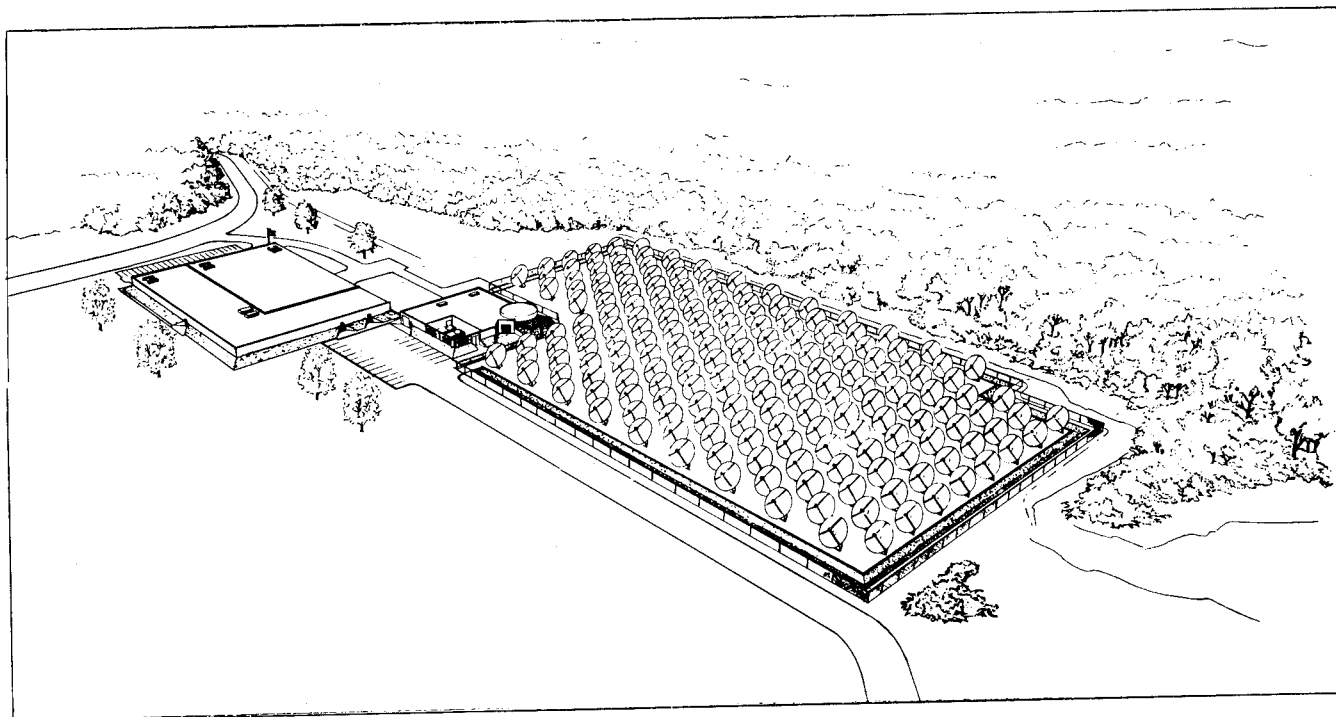


Figure 4.

References

J. A. Leonard, Solar Total Energy at Sandia Laboratories, SAND76-5176, Sandia Laboratories, Albuquerque, NM, Feb. 1976.

Solar Total Energy Program Plan, SAND76-0167 (revised), Sandia Laboratories, Albuquerque, NM, Aug. 1976.

Fy 78 Annual Operating/Management Plan: Solar Total Energy Division of Solar Technology, SAND78-0128, Sandia Laboratories, Albuquerque, NM, Jan. 1978.

THE REAL TIME APERTURE FLUX SYSTEM
As Part Of The
SOLAR THERMAL TEST FACILITY

By: Dave B. Davis and Larryl K. Matthews

Dave Davis received his masters in Electrical Engineering from the University of New Mexico in 1973. His major areas of activity are computer systems, instrumentation, and electronics.

Larryl Matthews received his masters in Mechanical Engineering from New Mexico State University in 1975. Since then he has worked with Sandia Laboratories in Albuquerque at the Solar Thermal Test Facility.

ABSTRACT

The Real Time Aperture Flux (RTAF) system will be used at the 5MW_t Solar Thermal Test Facility (STTF) operated for the Department of Energy by Sandia Laboratories in Albuquerque, New Mexico.

The RTAF system was developed for measuring flux density in the ranges of 40 KW/m² to 4000 KW/m².

The RTAF is attached to a solar receiver for measuring flux density in the aperture plane. The system consists of thermal sensors and photon sensors arranged on a moving bar that scans the plane of the aperture.

This system must operate in a severe and changing solar environment. Total power levels as high as 6.5 MW_t can be delivered to an experiment to which the RTAF is attached.

The design of this system requires fast response times and accurate measurements over the entire operating range of the STTF.

This paper will discuss the measuring and heat transfer problems associated with the RTAF and its components.

INTRODUCTION

The Real Time Aperture Flux (RTAF) system as used at the Solar Thermal Test Facility (STTF) is composed of several subsystems. These subsystems are required to fulfill the design requirements imposed on the RTAF system as a whole. The STTF is shown in Figure 1. The STTF is described in reference (1).

The RTAF design requirements are:

1. The sensing devices must measure flux density from 40 kw/m² to 4000 kw/m² with an accuracy of 2% to 5%.

2. The sensing elements must be capable of response times in the range of 10μ seconds.
3. The sensing devices must be capable of handling the effects of a changing solar spectrum.
4. The sensing devices should be linear over this entire range.
5. The system must be attached to the experiment with the capability of measuring flux density over an area of 3.66mx3.66m with minimal blocking of the experiment.
6. The sensing devices must be kept cool under the most severe conditions to maintain accuracy.
7. The system will present data in real time using a format applicable to the experimenter's needs.

The subsystems that will be used to achieve these requirements are:

- Photon Sensors
- Thermal Sensors
- Mechanical Drive Subsystem
- Cooling Subsystem
- Computer Control and Data Acquisition Subsystem

These subsystems will be covered in detail.

A general description of the RTAF system will be valuable not only to the experimenter but also to the STTF operators.

The data obtained is displayed in real time on color graphics. The experimenter can use the information for efficiency calculations. The STTF operator can use the RTAF data to monitor changes in flux density due to clouds, changing air mass, apparent heliostat pointing errors, or any other change that might arise. The operator can also see the effects of moving heliostats on or off target.

The RTAF system is therefore an important operational and data acquiring tool for the STTF.

PHOTON SENSORS AND THERMAL SENSORS

Two types of sensors are used in the RTAF system. Refer to Figure 2. This is necessary to meet requirements 1, 2, 3, and 4.

The thermal sensors are standard HY-Cal circular foil heat flux gages. These sensors are designed as:

- a. calorimeter type (versus radiometer type),
- b. measure flux density to 4000 kw/m^2 , with accuracy of 2% full scale,
- c. response times around 300m seconds,
- d. optical coating with flat absorption characteristics from $.2\mu$ to 30μ .

The thermal sensors meet RTAF design requirements 1, 3, and 4. However, these sensors are not capable of response times in the micro second range as is necessary from requirement 2. Therefore, a very fast response photon sensor was developed at Sandia Laboratories.

The photon sensor was designed to meet the following requirements:

Dynamic Range - 40 to 4000 kw/m^2
 Deviation of Short Circuit Current Response from Linearity
 vs 2% or less over full dynamic range
 vs Temperature 5% or less for 50°C change

Angular Acceptance $\pm 60^\circ$ with less than 10% deviation from cosine law.

The photon sensor response is not flat over the entire possible spectral range.

The spectrum arriving at the sensors at any given time of day is a function of many variables, such as water vapor, dust particles, air mass, etc. To accommodate these changes it is necessary to calibrate in place the photon sensors whenever the spectrum arriving at the sensors has changed significantly.

The operational procedure for the RTAF system is designed to do the necessary calibration of the photon sensors.

As will be described in more detail later, a copper bar is used to house the sensors, both photon and thermal, and traverse the plane of the aperture. The traverse speed is controlled by the computer subsystem. At first, a slow traverse is initiated and readings from the photon and thermal sensors are taken. The slow speed is necessary for the thermal sensors. The slow traverse allows a baseline to be drawn for the photon sensor. Therefore, a calibration has been done on the photon sensor using the thermal sensor.

Several fast traverses of the aperture plane are now done using only the fast response photon sensors. This is continued until the engineer in charge believes that the spectrum has changed enough to warrant another calibration on the photon sensors.

The photon sensors were tested at the White Sands Solar Furnace at White Sands Missile Range, New Mexico. (3) The linear re-

sponse versus changing flux density is shown in Figure 3. The x axis is a circular foil heat flux gage as described earlier and the y axis is the photon sensor. This is actual data taken from the White Sands Solar Furnace.

MECHANICAL DRIVE SUBSYSTEM

The mechanical drive subsystem consists of a moving copper bar, structural frame, drive gear box and motor, and accessories for transmission of motor power to move the copper bar. Refer to Figure 4.

The copper bar instrumented with sensors traverses across the aperture on a roller, chain, and rail system. The drive mechanism is a modified geneva drive which has a velocity curve similar to a sine wave. This means that the velocity of the bar has a maximum and then a zero at various positions of travel. These positions occur every 10.16cm (4 inches). Therefore, every 10.16cm the bar velocity is zero and a reading is taken by the sensors. The bar is controlled by the computer system. This will be explained later.

Besides housing the sensors and moving across the plane of the aperture the copper bar must allow cooling for the sensors and also house the electronics used with the sensors. Therefore, the copper bar is a multipurpose and vital part of the RTAF mechanical system.

The structural frame is used to hold the traversing copper bar and the geneva drive mechanism and motor.

The frame is attached to a support structure fabricated for the specific experiment being tested. The frame can be tilted at any angle from vertical to horizontal. The frame is water cooled and painted white for minimal heat problems.

The accessories that accompany the mechanical drive subsystem include water hoses, take-up pulleys, cables for electronics, drive chains and tapes, and various other parts. Figure 5 shows the hose take-up procedure.

COOLING SUBSYSTEM

In an environment such as will be present at the STTF a cooling subsystem must be part of the RTAF system.

This subsystem must be capable of protecting all components of the mechanical drive subsystem and the sensor bodies should be kept below 40°C . This is necessary to keep the photon sensor mounted on the sensor body below 95°C .

To achieve this a highly reflective white paint was put on the mechanical subsystem components. The sensor bodies have a gold plating. The plating is reflective and

durable. This also allows eutectic bonding of the photon sensor to the sensor body.

Cooling water is supplied to the structural frame from the STTF tower cooling water system at a rate of 300gpm. The frame is not in as severe environment as the copper bar. The frame should see only spillage power from the heliostats.

The copper bar, however, will be in a very hazardous environment with flux densities as high as 2.5 MW/m².

The following analysis was used to determine the cooling necessary for the traversing copper bar.

Bar

$$(1) \rho_c V_c c p_c \frac{\partial T_c}{\partial t} = A_c I - h_1 A_c (T_c - T_{am}) - h_2 A_c (T_f - T_f) - \sigma \epsilon A_c (T_c^4 - T_{sr}^4)$$

Fluid

$$(2) \rho_f V_f c p_f \frac{\partial T_f}{\partial t} + U \frac{\partial T_f}{\partial x} = -h_2 A_f (T_f - T_c)$$

Storage

$$(3) \rho_f V_s c p_f \frac{dT_s}{dt} = -q_r + \dot{m} c p_f (T_f(x) - T_s)$$

Where

- A_c - surface area of copper being irradiated on
- $c p_c$ - specific heat at constant pressure for copper
- $c p_f$ - specific heat at constant pressure for fluid
- h_1 - film coefficient for outside of copper bar
- h_2 - film coefficient for inside of copper bar
- q_r - heat removed by refrigeration unit
- T_{am} - ambient temperature
- T_c - temperature of copper
- T_f - temperature of fluid
- T_{sr} - temperature for radiation
- U - fluid velocity
- V_c - volume of copper bar
- V_f - volume of fluid in bar
- V_s - volume of storage fluid
- x - length along bar
- x_1 - outlet of bar
- α - surface absorptivity
- ϵ - surface emissivity
- ρ_c - density of copper
- ρ_f - density of fluid

σ - Stefan Boltzmann constant

These equations were solved simultaneously using numerical techniques.

The system used to cool the sensor bar is an air to fluid refrigeration system (water chiller) with 100 gallon reserve fluid capacity. The water chiller is a 15 ton size chiller.

The equations tell us that for continuous, steady state operation a 2.5 MW/m² over the entire bar 15 tons is not sufficient, however, the fluid reserve is used as a buffer to the bar while a scan is taking place. Between scans the bar must stay in a no flux density region until the reserve is cooled back down.

RTAF CONTROL SUBSYSTEM

Movement of the RTAF sensor bar is controlled by drive electronics located close to the RTAF structure. Commands for drive operation are obtained either locally through a push button interface at the drive electronics or remotely through a computer interface accessed by a multi-conductor cable. Remote interfaces are all light-isolated for groundloop free operation. A block diagram of the control system is given in Figure 6.

The operational modes of operation are Home, Scan, Slew and Stop. The Home mode is the "reset mode", ie, with the sensor bar housed in the flux-free enclosure with no bar movement. The Scan mode provides for controlled bar movement with a programmable variable delay at low velocity points as the bar traverses the plane of interest. Data is taken at these low velocity points. The Slew mode provides for maximum speed of sensor bar movement across the flux field. The Stop mode allows one to single-step the bar across the flux field with the bar stopping at each low velocity point.

In addition to satisfying the obvious drive control requirements, the control system automatically responds to various system safety monitoring parameters such as coolant flow, coolant temperature, etc. The control system also provides the data subsystem with a data strobe that indicates when the sensor bar velocity is low for data taking.

The control system makes available to the remote control minicomputer the status information necessary for bar movement definition. Among the status parameters passed are operating mode, present bar location with respect to the sensor bar coordinate system, and programmed delay time. Closed loop bar control is accomplished with these parameters.

DATA ACQUISITION SUBSYSTEM

The flux data presented by the photon sensors and the heat flux gages (Gardon gages) on the RTAF sensor bar are processed, digitized, and transmitted to the host computer by a bar-resident microcomputer-controlled data acquisition subsystem. The data transmitted are archived, analyzed, and presented by the host minicomputer. A block diagram of the data acquisition subsystem is given in Figure 7.

The host minicomputer provides for real-time data analysis and presentation for the experimenter. Data access is also orchestrated by the host and carried out by the microcomputer on the sensor bar. Data are presented on a color graphics system and archived on a 15m-byte disc. Some types of data presented are flux-time histories, flux contour maps, and total aperture power.

The sensor outputs are conditioned by integrated circuit instrumentation amplifiers and are presented to CMOS multiplexers which will select channels to be digitized. Differential multiplexers are used to select one of sixteen analog channels to be processed by the sample-and-hold amplifier preceeding the analog-to-digital converter. As can be seen, the digitizing process is modularized in groups of sixteen channels each. The sample-and-hold output is digitized by a 12-bit CMOS A/D converter and stored in a buffer memory. The digitizing process is continuous in a round-robin fashion through the sixteen channels assigned to a particular converter. Data stored in the buffer is available on demand by the microcomputer for transfer to the host computer. Varying numbers of channels are accommodated by using enough 16-channel A/D systems to cover the channel requirements.

The microcomputer system on the bar communicates with the host computer and controls data flow in and out of the bar. Upon command the microprocessor accesses the A/D buffer memories (which are memory-mapped) to gather the data to be transferred to the host. The data is processed and sent to the host over a 9600 baud serial communications line. The data in the buffers are accessed when the data strobe from the bar drive system is detected or when the host computer commands an immediate access.

All components in the on-bar data system were selected for extended temperature operation. Although the bar is cooled, temperatures in the instrumentation cavity will rise during the bar's traverse of the flux field.

The host computer, the RTAF drive control system, and the data acquisition system provides the electronic support for the mechanical subsystems.

CONCLUSION

The Real Time Aperture Flux system is a very versatile and vital part of the Solar Thermal Test Facility.

The RTAF system will supply important information to the user and the operator on a real time graphics system which gives the experimenter tremendous control of his experiment.

References:

- (1) Otts, J. V., Holmes, J. T., Seamons, L. O., Kuehl, D. J., Davis, D. B., Matthews, L. K., Arvizu, D. E., Darsey, D. M., Brandvold, G. E.; The USA 5MW Solar Thermal Test Facility, ISES International Congress, January, 1978.
- (2) Matthews, L. K., Davis, D. B.; Real Time Aperture Flux (RTAF) System, 24th ISA Symposium, May, 1978.
- (3) Hays, R., White Sands Solar Facility (WSSF): Experimenter's Guide, 1977, Nuclear Weapon Effects Branch Applied Sciences Division, Army Materiel Test and Evaluation, White Sands Missile Range, New Mexico.

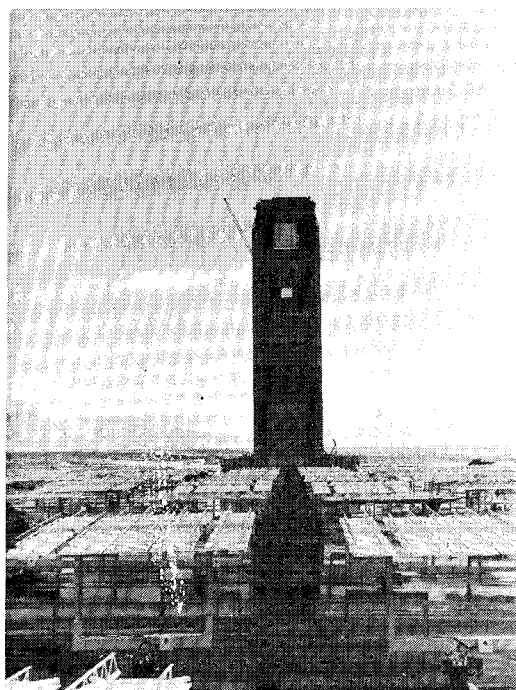
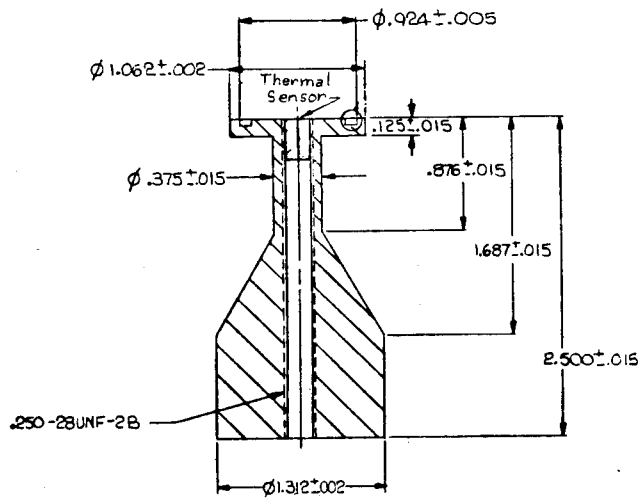


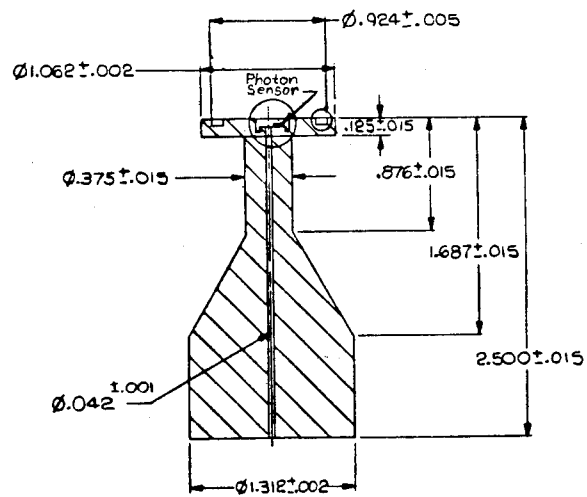
FIGURE 1.

Thermal Sensor Body



1. GENERAL REQUIREMENTS ARE DEFINED IN 99000Q0.
2. MATL: USE OXYGEN FREE HIGH CONDUCTIVITY COPPER.

Photon Sensor Body



1. GENERAL REQUIREMENTS ARE DEFINED IN 99000Q0.
2. MATL: USE OXYGEN FREE HIGH CONDUCTIVITY COPPER.

FIGURE 2.

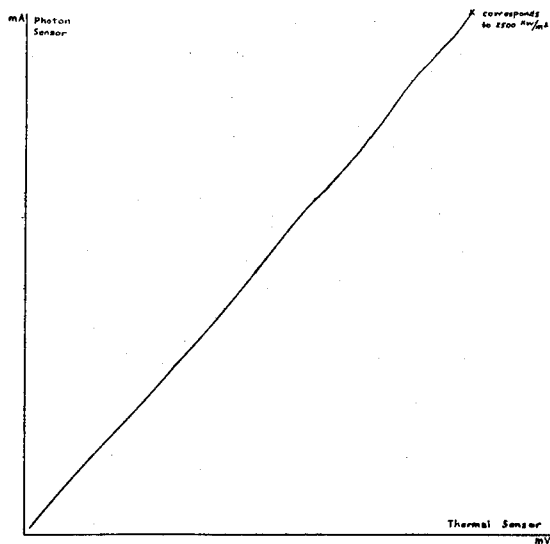


FIGURE 3. PHOTON SENSOR VS. THERMAL SENSOR.

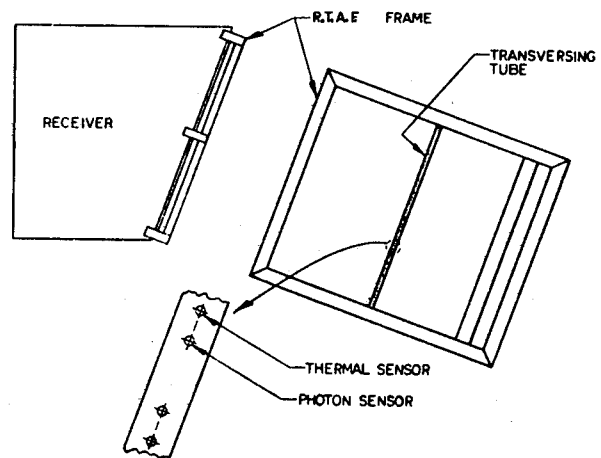


FIGURE 4.

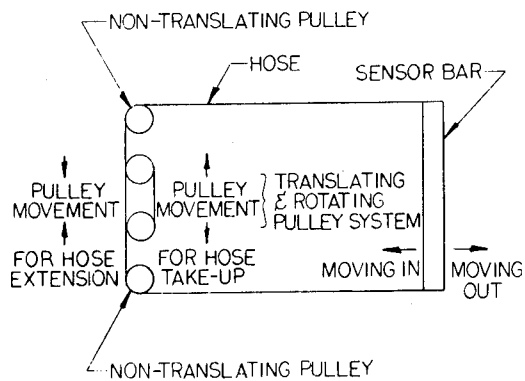


FIGURE 5.

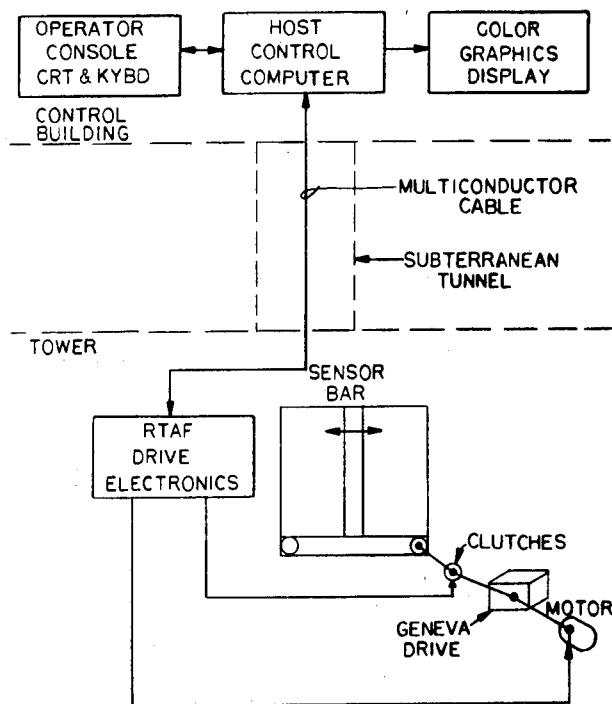


FIGURE 6. RTAF CONTROL SYSTEM BLOCK DIAGRAM.

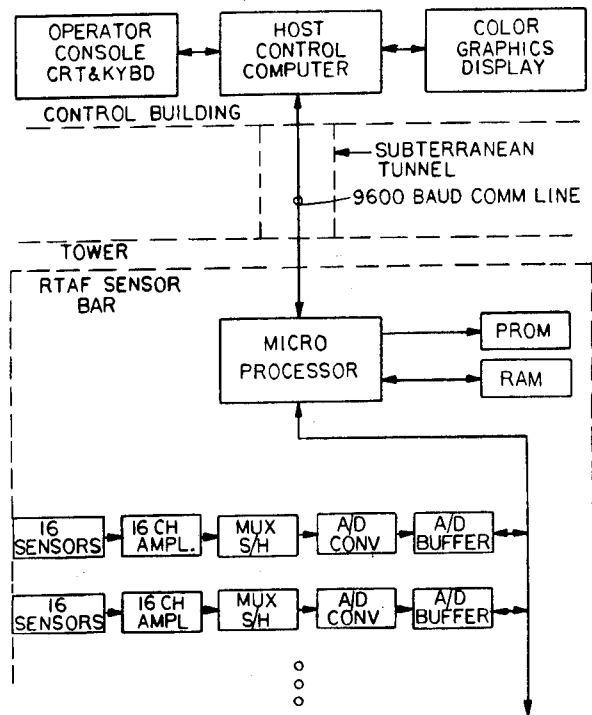


FIGURE 7. DATA ACQUISITION SUBSYSTEM BLOCK DIAGRAM.

DEVELOPMENT OF A DUAL-MEDIUM THERMAL STORAGE SYSTEM
FOR SOLAR TURBO-ELECTRIC POWER GENERATION
By: G. R. Morgan, G. R. Schneider and W. Unterberg
Rocketdyne Division, Rockwell International
Canoga Park, California

INTRODUCTION

Solar thermal electrical power generation plants have many attractive features as a future element of the world's energy supply system. A thermal storage subsystem (TSS) is an important part of a solar thermal plant. The TSS extends the plant's generating capacity into periods of little or no insolation and acts as a buffer to the turbine during periods of rapid variation in insolation.

The primary function of the TSS is to supply electrical power after sundown. Power demand studies indicate that 6 hours of storage is optimum for plants in the Southwestern United States.

Energy storage using thermal methods was selected as best suited for application to solar thermal electrical power generation. Concepts that first require electrical power generation, such as pumped water, compressed air, flywheel or battery storage, do not provide buffering of the turbine. They also require expensive conversion equipment (turbo-generators instead of heat exchangers) which suffer considerable performance loss over the wide range of input and output rates characteristic of solar thermal power plants.

THERMAL STORAGE CONCEPT SELECTION

After consideration of various factors (economic, state of technology, scalability, near-term application, and 30-year life with low maintenance), the thermal storage concept selected for solar thermal applications uses a low-cost, solid bed to store most of the energy with a suitable liquid to transfer energy into and out of the bed. This dual-medium type of system (patent pending to Rocketdyne and McDonnell Douglas Astronautics Corporation) combines advantages of a low-cost solid with the flexibility, low pumping power, and moderate heat exchanger requirements of a liquid energy storage system.

Thermal storage systems utilizing heat of fusion or chemical reaction were considered to have major development problems and not suited for near-term application. The conventional pebble bed using air or another gas to heat a rock bed was unattractive because of excessive blower power and large heat exchanger sizes.

Conceptually, in its simplest form, the system uses a bed (shown in the center of Fig. 1) of an inexpensive particulate solid in an appropriate containment vessel. A suitable high-temperature liquid fills the voids and circulates through the bed to deposit or withdraw energy. Heating of the bed (charging) is achieved by removing lower temperature fluid from the bottom of the bed and returning the heated fluid to the top of the tank. A sharp, temperature interface (a thermocline) is maintained naturally between hot and cold fluid because of the lower density of hot fluid. This thermocline moves downward through the bed during charging and upward during extraction.

When the storage unit is completely charged, all of the bed and the fluid is at the maximum temperature.

The extraction loop utilizes the fluid to remove energy from the storage unit and produces steam for power plant operation or other plant functions such as equipment heating.

The dual-medium system has three major advantages compared to conventional thermal storage systems. First, for large systems as envisioned for capturing significant amounts of solar energy, the fluid cost is a driving parameter. For an all-liquid thermal storage system, the storage medium may cost up to 75 percent of the total subsystem. The use of low-cost solids can reduce this by two-thirds.

Secondly, the solids bed allows both hot and cold fluid to be stored in a single tank. This not only eliminates the cost of a second tank (of equal volume), but significantly reduces the heat loss to the environment through a 50-percent reduction in surface area.

Thirdly, selection of a low vapor pressure heat transfer liquid allows the use of a conventional low-cost gravity head petroleum storage tank which is commercially available up to very large sizes. Similarly, a wide range of low vapor pressure commercial heat transfer fluids have been available for years with operating temperatures to 1000 F (a limit usually satisfactory for reasonably efficient steam turbine operation).

System configuration is dependent somewhat on the collector fluid. If the fluid used in the solar collector has a low vapor pressure and is compatible with solids, then it may be used as the transfer fluid and run directly into the storage tank. If the collector fluid has a high vapor pressure (such as steam), then a heat exchanger is needed on the charging side to heat the low vapor pressure transfer fluid. For all conventional turbine applications, a heat exchanger is needed on the heat extraction side of the TSS. For some duty cycles, a single heater may serve both functions.

DOE EXPERIMENTAL PROGRAM

The test program reported herein represents the results of 3 months of testing under a Department of Energy contract for Phase I of the Central Receiver Solar Thermal Electrical Power Generation effort. The experimental portion of the program was designed to prove the dual-medium approach was a workable concept and met the objectives listed earlier under Concept Selection. Of primary concern was that the test results and hardware design could be scaled to the 10 MW (electrical) Pilot Plant to be operational at Barstow in the early 1980s and much larger commercial-size plants that might soon follow. Commercial plant thermal storage systems would be on the order of 1500 to 2000 MWH thermal capacity.

Economic, reliability, and operational consideration led to the selection of 600 F as a maximum upper storage limit for near-term applications. Above this temperature, fluid costs increase five- to ten-fold. A variety of low-cost commercial heat transfer fluids is available with demonstrated capability to 600 F.

Screening tests conducted at Rocketdyne prior to the contract work indicated that commercial rock was compatible with commercially available heat transfer fluids up to 600 F.

The experimental program was then structured into (1) subsystem tests to demonstrate the thermocline performance of a scalable dual-medium thermal storage system, and (2) long-term fluid life and compatibility tests of commercial rock and heat transfer fluids.

SUBSYSTEMS RESEARCH EXPERIMENTS (SRE)

The complete thermal storage subsystem tested consisted of a thermal storage unit (TSU) containing the rock bed; two fluid circulation pumps; an ullage maintenance unit to provide a positive pressure inert blanket in the TSU; fluid heater; a steam generator; interconnecting fluid lines; and control valves and sensors. The TSU in place during testing is shown in Fig. 2. The SRE subsystem has the same major components as the pilot plant. The SRE subsystem has a 5 MWhr storage capacity, and matches the pilot plant flow and heat transfer conditions when operated at rates of about 1 MWt, although it is capable of rates up to 5 MWt. The subsystem was assembled at Rocketdyne by installing the TSU and associated components in an existing steam generation system at Rocketdyne's Santa Susana Field Laboratory.

The TSU tank is welded steel with overall interior dimensions of 3.2 m (10.5 ft) diameter by 13.3 m (43.7 ft) high (Fig. 2). The vessel is filled with approximately 190 megagrams (210 tons) of granite rock plus about 30,000 liters (8000 gallons) of Caloria HT43 fluid. The TSU design for these tests is modelled after the pilot plant by maintaining the same intensive (i.e., not related to size) variables that determine the fluid/solid heat transfer in the packed bed. The media (gravel, sand, and heat transfer fluid) and their use are identical, as are the fluid velocities during charging and extraction. The thermal storage unit was fabricated of the same structural steel planned for the pilot plant unit by a commercial tank fabricator. Details of tank construction and installation are given in Ref. 1.

SUBSYSTEM TEST RESULTS

The basic objectives of the thermal storage SRE system tests were to: (1) evaluate performance of a large, scalable TSU over all ranges of equivalent operating conditions in the pilot plant, (2) demonstrate mode change-over and emergency operation, and (3) obtain additional engineering design data. All test objectives were met or exceeded during a 3-month test program completed in December 1976. A large variety of tests were conducted with thermal charging and discharging ranges from 0.1 to 2 MWt and with hold periods up to 144 hours.

The use of a single tank for sensible heat storage depends directly on the ability to create and main-

tain a fairly sharp temperature interface (a thermocline) between the hotter and cooler regions in the storage tank. The extensive test program with the SRE subsystem demonstrated that the dual-medium type of storage produces sharp thermoclines which are stable, reliable, and predictable.

Figures 3 and 4 show typical performance for the SRE thermal storage unit, while operating at the temperature and flow conditions planned for the DOE 10 MW_e pilot plant. Figure 3 shows a series of thermoclines in the TSU, each curve representing the temperature profile at a particular time. At the start of the extraction test depicted, the entire TSU was charged to 302 C (575 F). Shortly after the start of extraction (Curve 1), a small portion of the bottom of the TSU (zero axial distance is the bottom) had dropped to 218 C (425 F), but the remainder of the tank, above a sharp thermocline, remains at the top operating temperature of 302 C (575 F). As energy extraction continues, the thermocline moves upward in the TSU (e.g., Curves 2 through 6), with the top of the TSU remaining at the upper operating temperature until almost all of the stored energy is extracted. Then, the thermocline begins to "break through" the top of the bed and the top temperature begins to fall (e.g., Curve 7).

The temperature of the hot fluid delivered from the top of the TSU is shown in the top half of Fig. 4. It can be seen that the temperature is very flat throughout the extraction until very near the end, when the temperature begins to fall, as predicted by Rocketdyne's computer model. A temperature of 293 C (560 F) has been selected as practical cutoff point to terminate extraction and begin recharging. 293 C (560 F) represents an excursion of only 10 percent of the operating temperature range of 218 to 302 C (425 to 575 F). In this test, 5.1 MWhr of energy was delivered with fluid temperatures above 293 C (560 F). This performance is even better than estimated during design for a unit of this size. Further, the volumetric efficiency increases as the TSU size and capacity increase.

The 70 thermocouples mounted throughout the bed also showed that the thermoclines are extremely flat and uniform across the cross-section of the TSU. The absence of channelling, "rat-holing," or other non-uniformities in fluid flow and heat transfer was striking and positive.

Among the other tests of the SRE subsystem was an all-day duty cycle, typical of solar thermal power plant operation, with a variety of charging, discharging, and hold periods and rates. Movement within the TSU during this duty cycle occurred without hysteresis and changes in shape, as the system went through many changes in operating mode, rates, and even hold periods. The hot fluid was delivered at the essentially top operating temperature of 302 C (575 F) during all of the discharging periods during the all-day cycle.

Demonstration of such uniform thermoclines and high performance in a large-scale dual-medium system is especially positive evidence of the practicality of the concept and the bed loading techniques used to install the rock bed in the TSU. There is almost no influence of the TSU walls beyond a short distance; therefore, the performance of the TSU should scale directly to larger units where the influence of the

walls is even less. This result greatly increases the confidence in applying the results to pilot plant and subsequent commercial plant thermal storage subsystems.

Measurements of strain in the storage tank walls were made to determine the level of stress imposed on the tank walls from repeated thermal cycling and possible settling of the rock bed in the tank. The SRE tank was designed for the maximum potential stress; however, the test data during approximately 30 thermal cycles showed that the actual stress was still near the minimum potential value.

Heat loss data were also obtained during the testing program, with separate measurements at various locations in the TSU walls, top, and bottom. It was found that the heat losses correlate well with design calculations for the configuration tested.

The effect of heat losses, and their magnitude relative to the stored energy, decreases substantially as the size of the storage unit increases. In the pilot plant size, total heat losses from the TSU are predicted to be below 3 percent of the stored energy per 24 hours. In commercial plants, the heat losses will be even lower, e.g., 1 to 2 percent per 24 hours.

Initial conditioning of the rock bed was accomplished easily, in place, following the original plan. Water was removed from the rock by initially heating the bed and fluid to about 100 C (212 F) and holding for a few days. A second aspect of initial bed conditioning was removal of dust from the rock and sand, again accomplished in place and according to the original plan with two in-line filters. The results show clearly that dust and silt migration in the system is primarily, if not entirely, an initial startup phenomenon, and that filter clean-out in the pilot and commercial plants will be minimal, e.g., in the range of once per month.

FLUID LIFE AND COMPATIBILITY TESTS

To meet the 30 year life requirement for the solar powerplant, heat transfer fluid life as affecting operating costs throughout this period must be considered. Potential fluid degradation occurs due to high temperature exposure and interaction with the bed solids. Any fluid degradation, typically thermal cracking and polymerization, can produce vapor pressure and viscosity changes in the fluid as well as coking. These effects may be reflected in fluid weight loss, heat transfer, surface fouling, clogging of manifold orifices, and the need for increased pumping power. The costs of fluid cleanup and replacement to overcome such problems need to be determined.

Accordingly, laboratory tests were conducted to evaluate the high temperature, 288 to 343°C (550 to 650°F), thermal stability, material compatibility, and surface fouling of selected commercial heat transfer fluids for extended periods of time. The fluids tested were Caloria HT43 (Exxon), Therminol 66, Therminol 55 (Monsanto), and Mobiltherm XMTL 123 (Mobil).

THERMAL STABILITY/COMPATIBILITY TESTS

The long-term thermal stability tests were conducted

at 288, 302, and 316°C (550, 575, and 600°F) in the presence and absence of weighed amounts of rock, silica sand, and materials of construction (stainless steel and carbon steel). All tests were carried out in round bottom Pyrex flasks, each fitted with an air-cooled condenser, operated at atmospheric pressure, and in a nitrogen atmosphere. At intervals of about 1000 hours, the flasks of fluid were removed from the baths for weighing and fluid kinematic viscosity measurement. Fluid samples were withdrawn for further tests, e.g., permeation chromatographic and infrared spectroscopic analyses, which are reported in Ref. 2.

WEIGHT LOSS RATE AND VISCOSITY RESULTS

The fluid replacement rates for Caloria HT43, Therminol 66, and Mobiltherm XMTL 123 (determined at each test temperature from the slope of the weight-loss vs time curves) used (assuming an Arrhenius correlation) to obtain the decomposition rate equations 1, 2 and 3 given below with R in wt %/hr and T in °K).

$$R = 5.38 \times 10^{10} \exp (-17650/T) \text{ (for Caloria HT43)} \quad (1)$$

$$R = 1.78 \times 10^{12} \exp (-19990/T) \text{ (for Mobiltherm XMTL 123)} \quad (2)$$

$$*R = 1.93 \times 10^{27} \exp (-39580/T) \text{ (for Therminol 66)} \quad (3)$$

These equations were used to predict the fluid losses for the TSU. For a typical TSU operating cycle with 7.5 equivalent hours at the upper temperature and 16.5 at the bottom temperature, Eqs. 1, 2, and 3 were used to determine the percent fluid replacement per 330-cycle year. The results computed for an upper temperature of 302°C and a lower temperature of 218°C, are 7 percent for Caloria HT43, 6.07% for Therminol 66, and 3.5% for Mobiltherm XMTL 123. Curves of percent weight loss vs time such as those given in Fig. 5 for Caloria HT43 at 302 and 316°C, were obtained for all fluids tested. Therminol 55 was eliminated from further consideration when early test results indicated that the fluid could not be used at temperatures exceeding 288°C because of excessive weight losses.

It was expected that any material added to the fluids would be more likely to enhance than hinder the fluid thermal degradation process. Data for Therminol 66 and Mobiltherm XMTL 123 indicate that the presence of solids (rock, sand and metals) may increase the thermal decomposition rate of the fluid. For Caloria HT43, however, the data appear to be unaffected by the solids.

The kinematic viscosity data obtained for Caloria HT43 as a function of temperature and time (Fig. 6), showed that in general, thermal degradation of the fluids reduced the kinematic viscosity and that the higher the test temperature, the greater the percent reduction. These results are typical for fluids tested. Those time intervals in which fluid weight losses were quite high coincided with intervals in which the kinematic viscosity was probably caused by the accumulation of smaller molecules (less viscous components) produced as the original fluid molecules underwent thermal cracking. When cracking

*The results for Therminol 66 may be high. More recent thermal stability tests yield lower rates for this fluid.

products were vaporized from the fluid sample, as indicated by a large weight loss in some time interval, the remaining fluid became more viscous.

Samples of Caloria HT43 removed from the flasks during the thermal stability experiments were reported to exhibit less than 1 percent polymerization after 2000 hours at 316°C (Ref. 2). It would appear then, that for the heating times covered, changes in kinematic viscosity are not attributable to fluid polymerization.

HEAT TRANSFER SURFACE FOULING

Tests were performed to determine the extent and rate of fouling of Caloria HT43, Therminol 66 and Mobiltherm XMTL 123 at surface temperatures of 316, 329 and 343°C (600, 625 and 650°F). A 304 stainless steel electrical heated cylinder was immersed in a pool of the fluids. Heat transfer from the hot surface to the fluid occurs by natural convection which should, because of the low fluid velocity over the heater, represent a worst possible fouling situation.

The results of these tests indicate no problems in practice due to fouling of heated surfaces. Tests with Therminol 66 produced no visible fouling deposits after 16,000 hours while tests with Caloria HT43 (over 10,000 hours) and Mobiltherm XMTL 123 (up to 5,000 hours) have produced only slight deposits near the bottom of the heaters where the convective velocity is lowest.

ECONOMICS OF FLUID SELECTION

The choice of a heat transfer fluid is based on the initial, capital, cost and also on the subsequent replacement cost. Currently typical costs per gallon are 0.066 dollars for rock, 1.05 dollars for Caloria HT43, 7.15 dollars for Therminol 66, and 1.90 dollars for Mobiltherm XMTL 123. First, it is to be noted that the heat storage capacity per unit volume is identical for all these substances, within 10%. Thus the cost, for a given amount of heat to be stored, for a 25% fluid/75% rock TSU is only 31.2% of that of a 100% fluid TSU, for the least expensive fluid, Exxon Caloria HT43. Using the figures quoted in the section on "Weight Loss" for the different fluids, the annual fluid replacement costs for Caloria HT43, Therminol 66 and Mobiltherm XMTL 123 are as 1.8: 12: 1.7. Thus, considering initial plus 30 years replacement costs Caloria HT 43 and Mobiltherm XMTL 123 are the most economical. Caloria HT43 was the fluid chosen for the SRE testing described above because of economics and availability.

CONCLUSIONS

The dual-medium type of thermal storage system offers the simplicity, flexibility, and other advantages of an all-liquid sensible heat storage system, but at much lower cost. The test results with this thermal storage system have demonstrated the practicality and high performance of the dual-medium thermal storage system on a large scale. Scaleup to the DOE 10 MW_e pilot plant and larger commercial plants can now be made with high confidence. There are also many other potential applications for this type of thermal storage system, including total energy systems, nuclear and conventional power plants,

and industrial and agricultural applications. In each case, the subsystem design (including storage media selection) and operating details would be tailored to the specific applications.

There are many variations and improvements on the basic concept outlined above. These include: (1) choice of solid material (e.g., various types of rock, ore, metal, scrap, block, brick, ceramic, etc.), (2) size distributions consequent void fractions of solid bed, (3) method of bed placement, (4) choice of liquid (e.g., water, various petroleum products, heat transfer fluids, molten salts, liquid metals), (5) single or multiple thermal storage unit tanks, (6) combinations of various liquids and solids in series tanks to achieve maximum high-temperature performance at minimum cost, and (7) use of immiscible liquids. Many of these variations were explored during this project, and are being considered for other applications.

ACKNOWLEDGEMENT

The authors are grateful for the support of the U.S. Department of Energy under Contract No. E(04-3)-1108 and for the interest of the many individuals at DOE, Sandia Laboratories/Livermore, and the Aerospace Corporation who fill various Project Office functions. They are also grateful for the support of McDonnell Douglas Astronautics Company, the prime contractor under this contract, for support under P.O. 075008, and the interested involvement of Mr. G. C. Coleman, the Technical Project Coordinator with Rocketdyne from MDAC.

REFERENCES

1. MDC G6776, Central Receiver Solar Thermal Power System Phase 1: Pilot Plant Preliminary Design Report, CDRL Item, Volume V, Thermal Storage Subsystem, McDonnell Douglas Astronautics Company, Huntington Beach, California, May 1977.
2. Burolla, V.P., Analysis of Thermally Degraded Sensible Heat Storage Hydrocarbons, Sandia Laboratories, Livermore, California, SAND77-8264, UC-62, December 1977.

AUTOBIOGRAPHIES

G. R. Morgan is from Long Beach, CA. He graduated from the California Institute of Technology with a B.S. in Mechanical Engineering in 1949 and since that time has been working on various energy conversion systems for ground and aerospace applications. He is currently Project Engineer on solar thermal energy storage systems at Rocketdyne.

George R. Schneider was born in Chicago, IL in 1932. He received a B.S. in Chemical Engineering from IIT in 1953 and the Sc.D. in Chemical Engineering from MIT in 1960. He has been employed in the Advanced Programs Dept. of Rocketdyne since 1961 and has worked on a number of programs concerned with combustion, chemical kinetics, and mass transfer, in connection with propulsion and environmentally related areas.

Walter Unterberg, a native of Vienna, Austria, graduated from the Univ. of Manchester, England, with first class honours in Mechanical Engineering and later obtained a Ph.D. in Chemical Engineering from UCLA. He has worked on solar powerplants and heat storage at Rocketdyne since 1969, and has been associated with the dual medium thermal storage project since its inception in 1974.

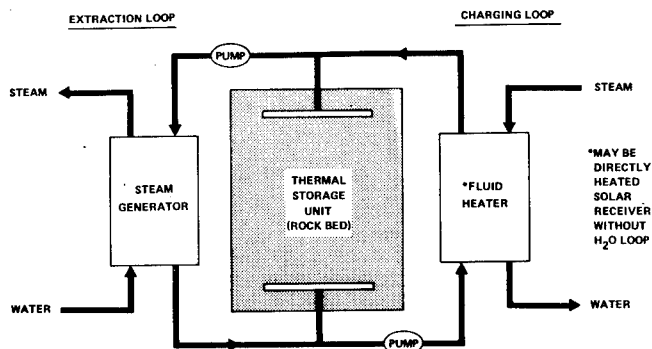


Figure 1. Dual-Medium Thermal Storage Unit Flow Schematic

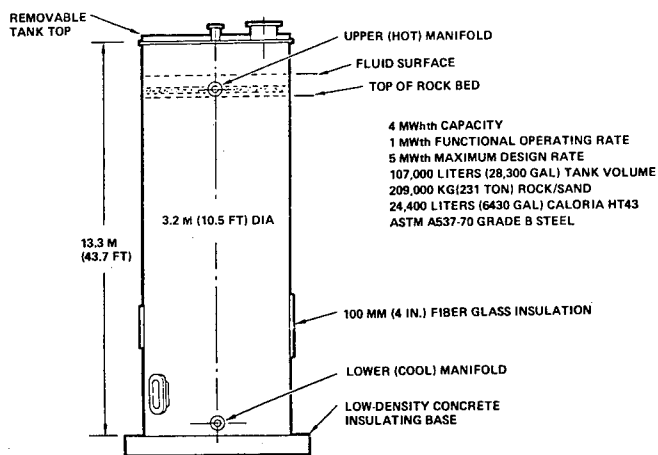


Figure 2. Dual-Medium TSU Built and Operated by Rocketdyne

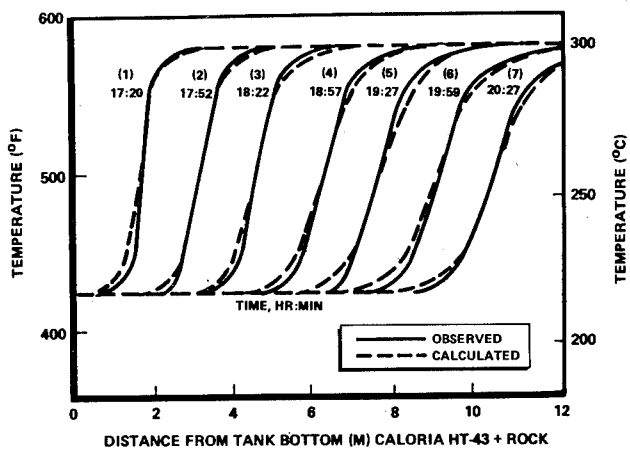


Figure 3. Typical Extraction Thermoclines: SRE Subsystem Tests and Design Predictions

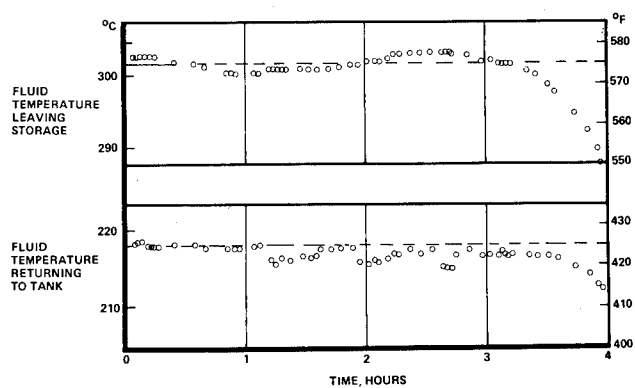


Figure 4. Typical Performance Data During Extraction

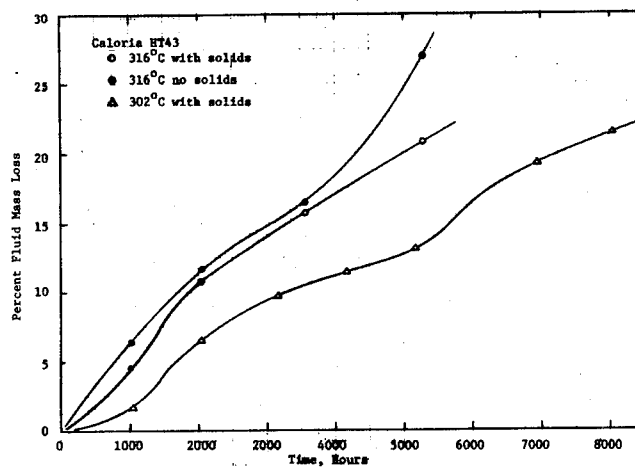


Figure 5. Effect of Temperature and Time on Caloria HT 43 Mass Loss

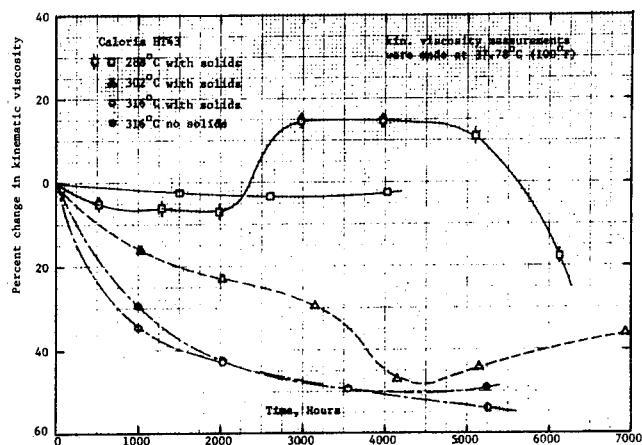


Figure 6. Effect of Temperature and Time on Kinematic Viscosity of Caloria HT 43

I. INTRODUCTION

The primary driving force for the formation of weather systems and the determination of climate is the interaction of the sun's optical radiation with the earth-atmosphere system. Small variations in the sun's total and spectral radiant output would have substantial effects on the weather and climate of the earth. There is a large body of evidence suggesting past climate changes of various magnitudes with periodicities ranging from less than a hundred years to several hundred million years (Refs. 1, 2). Climate fluctuations with periods in the 10^4 to 10^5 year range have recently been shown to be due to periodic variations in certain earth orbital parameters (Refs. 3, 4). Important climate cycles of both shorter and longer periodicities exist, however, for which the most likely explanation is variation in solar radiant output.

The solar "constant" has not been monitored consistently with state-of-the-art observations in the past. Recently observed changes in the earth's climate have stimulated strong interest in conducting a long-term program to detect solar total flux variability at the $\pm 0.1\%$ level, the sensitivity threshold of present climatological models.

Observations of the solar spectral irradiance in flight experiments outside the atmosphere have focused mainly on the wavelengths shorter than 0.25 μm and longer than 6.0 μm in recent years. While these are wavelengths significant to processes in both the solar and terrestrial atmospheres, the dominant solar-terrestrial interactions relevant to climate occur with the radiation between these limits (the solar flux from 0.25 to 6.0 μm includes about 99% of the total radiant energy.) Absorption by ozone in the Hartley, Huggins and Chappuis bands is the dominant source of thermal energy for the stratosphere. Absorption by water vapor is the dominant source in the troposphere. Significant heating (and cooling) occurs in both the troposphere and stratosphere due to the radiative interactions of solar flux in this wavelength range with atmospheric aerosol distributions and carbon dioxide.

The solar spectrum over a majority of the 0.25 to 6.0 μm range has never been determined with an uncertainty near the state-of-the-art for defining irradiance in the International System of Units (SI). Instrumentation, calibration and observational difficulties have frustrated achievements in this field by two aircraft experiments during the late 1960's (Refs. 5, 6). Over a more limited range (0.40 - 1.25 μm) the best determination to date has been made from a high altitude terrestrial observatory (Refs. 7, 8). Disagreements between the various solar spectrum models currently extant range up to 20% in the ultra-violet and infrared. The best understood region, the visible, is probably no less than $\pm 3\%$ uncertain in the International System of Units.

II. PYRHELIOMETRY AND RADIATION SCALES

The science of measuring total solar optical radiation is pyrheliometry, derived from the Greek words *pyr* (heat), *helios* (sun) and *meter* (to measure). The accuracy of solar "constant" observations depends on the state-of-the-art in pyrheliometry. The instrumentation used to "measure the heat of the sun" are pyrheliometers, a special purpose type of the class of instrumentation known as radiometers. Two basic types of pyrheliometers have been commonly used in solar observations. The first is an absolute or self-calibrating detector which can accurately relate radiation measurements to S.I. units. The second and most common is a relative detector that responds to solar heating and must be calibrated by comparison to a self-calibrating pyrheliometer to produce a quantitative result. Relative pyrheliometers most commonly use thermopile sensors and plane-surface detectors. Changes in their surface absorptance for solar flux with prolonged exposure to the sun, the dependence of their sensitivity on absolute temperature and pressure and the required external calibration, make the error bounds of relative pyrheliometers large compared to self-calibrating pyrheliometers.

Self-calibrating pyrheliometers have been constructed in various forms, but they all have certain features in common. They are flux meters in which the heating effect of solar radiation on a detector is compared with that of an electrical current passed through a heating element in intimate thermal contact with the detector. An accurate knowledge of the effective absorptance of the detector for the solar flux, the area over which the detector is irradiated and the electrical heating power facilitates the accurate measurement of solar radiation on an absolute basis in terms of the International System of Units (SI).

Figure 1 summarizes the development of pyrheliometry and solar "constant" determinations from 1900 to the present. The Angstrom 1905 and Smithsonian 1913 scales, based on the performance of pyrheliometers developed by Angstrom and Abbot, resp., defined the absolute radiation scale with an S.I. uncertainty of less than 3%. In 1932 Abbot designed a dual detector water flow instrument that used the differential measurement approach pioneered by Angstrom. Coupled with the advantages of the cavity detectors, the new Smithsonian instrument was able to define the absolute scale with less than $\pm 0.5\%$ uncertainty in S.I. units (Ref. 9).

The International Pyrheliometric Scale adopted in 1956 was based on a subset of the information available at the time (Ref. 10). While intended as a compromise between the Angstrom 1905 and Smithsonian 1913 scales, we now know it was close to the Angstrom 1905 scale. Observations of solar irradiance on a world wide basis, related to the IPS 56 for more than a decade, were shown to contain a systematic error of at least 2.2% in a series of

*This paper presents the results of one phase of research carried out at the Jet Propulsion Laboratory, California Institute of Technology, under Contract No. NAS7-100, sponsored by the National Aeronautics and Space Administration.

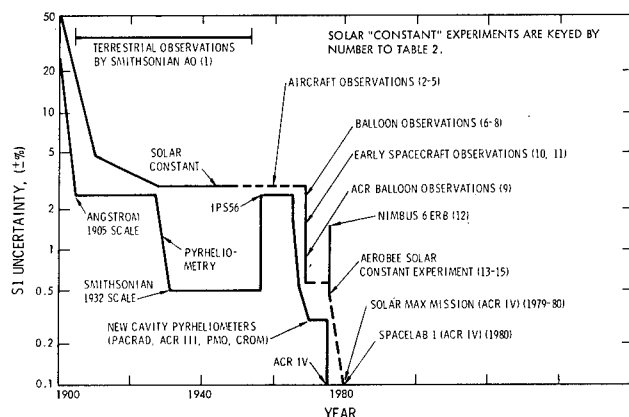


Figure 1. Uncertainty of Pyrheliometry and Solar "Constant" Determinations (1900-1980) relative to the International System of Units (SI).

experiments begun in 1968 (Refs. 11-16). The increased uncertainty in pyrheliometry shown occurring in 1956 (Fig. 1) reflects the international adoption of the IPS56.

Development of a new generation of cavity pyrheliometers began in the latter half of the 1960's at several laboratories in the US and Europe. The IPS56 error and the high accuracy of the new generation of cavity pyrheliometers were widely accepted by 1974 when the First International Comparison of Absolute Cavity Pyrheliometers was held at Davos, Switzerland. During this comparison and the subsequent International Pyrheliometric Comparisons (IPC IV) held at the same site in 1975, a group of the most advanced of the new cavity pyrheliometers were inter-compared. A new reference scale based on the results, the World Radiometric Reference (WRR), has now officially replaced the IPS56 (Refs. 17, 18). Definition of the new scale is to be accomplished by the performances of five pyrheliometers - ACRs 310 and 311 (Willson, JPL), PACRAD III (Kendall, JPL), PMO-2 (Frohlich, Davos) and the CROM (Crommelynck, Brussels). (See Table 1.)

Measurements on the WRR exceed measurements on the IPS56 by 2.2%. The WRR was considered to be uncertain by less than 0.3% relative to S.I. units

Table 1. Performances of the Defining Instrumentation for The World Radiometric Reference Scale (WRR) during the First International Comparison of Absolute Cavity Radiometers (1974-75)

Instrument	Developer	Mean Performance Relative to WRR (%)
ACR 310	Willson (USA)	+0.04
PMO 2	Frohlich (Switzerland)	+0.10
ACR 311	Willson (USA)	+0.11
PACRAD I	Kendall (USA)	-0.19
CROM	Crommelynck (Belgium)	-0.20

at the time of its adoption in 1976 by the Commission on Instruments and Methods of Observation.

The steep drop in S.I. uncertainty shown in fig. 1 for 1965-1970 reflects the rapid advances made in cavity pyrheliometry in this period. By 1968 the S.I. uncertainty of the PACRAD I and ACR II during their first comparisons with the IPS56 at Table Mtn. was less than 0.5%. By 1970 the PACRAD III and ACR III were uncertain by about 0.3% (Refs. 19, 20), as were the group of pyrheliometers defining the WRR in 1975.

A new Active Cavity Radiometer (Type IV) was developed at JPL during 1975-1976 for solar constant monitoring in space. The ACR IV is capable of measurements of solar flux at the solar "constant" level with an S.I. uncertainty of $\pm 0.1\%$ (Ref. 21.) Comparisons of the ACR IV technology with the WRR began in 1976 during preparation of ACR 402 for a solar "constant" rocket experiment. During the limited time available prior to integration of ACR 402 into the rocket payload, ACRs 401 and 402 were compared with ACRs 310 and 311, using the sun as a source. A systematic difference was observed with both ACRs 401 and 402 yielding 0.3% higher irradiances than the mean results of ACRs 310 and 311. This result was apparently confirmed by comparisons with PMO-2 during a brief experiment in May 1976, just preceding the June rocket flight.

The amount of comparison data is limited. Other than verifying by post-rocket flight comparisons of ACRs 310, 311, 401 and 402 that their relative performances had not changed, no other definitive experiments have since been completed. The apparent differences between the WRR and the ACR IV observations exceeds the S.I. uncertainty predicted for the ACR IVs. If confirmed by experimental work presently in progress, an upward adjustment of the WRR by about the amount of its currently projected S.I. uncertainty would be required.

III. SOLAR "CONSTANT"

Terrestrial Observations

Determination of the solar flux outside the atmosphere from ground-based observations is complicated by the absorption and scattering of solar radiation at nearly all wavelengths by the earth's atmosphere. From 1902 through 1952, the Smithsonian Astrophysical Observatory (SAO) made total and spectral radiation measurements at widely separate high mountain sites (which they hoped would minimize the effects of the atmosphere and of local meteorological conditions on the deduction of "extra-atmospheric" values) to derive a long term record of the solar "constant" (Ref. 9). Their observations over the 1902-1952 period were a model of careful attention to measurement detail. Since the variability of the solar "constant" was of prime concern, their chief effort was to maintain an internally consistent set of observations. To this end they established the Smithsonian 1913 scale based on the performance of Abbot's water flow and water stir pyrheliometers. While the need for a -2.5% correction to the 1913 scale to more accurately represent S.I. units was published in 1932, solar "constant" values continued to be reported on the 1913 scale to provide continuity.

The SAO deduced $\pm 5\%$ solar "constant" variations from their early observations (1902-1912). They

later concluded most of this range was accounted for by fluctuations in the optical properties of the earth's atmosphere not accurately accounted for. The principal variable phenomena are absorption by water vapor, scattering by aerosols and absorption by ozone. On at least one occasion, a temporary perturbation of about -20% in total solar flux was observed due to the eruption of the Mt. Katmai volcano in 1912. While this clearly exceeded the threshold of "noise" in their observations, the SAO eventually concluded that ground observations were not capable of deducing extra-atmospheric values of the solar "constant" with a precision of less than about $\pm 1\%$ due to fluctuations in atmospheric radiative properties, considerably in excess of that required for climatology. (The S.I. uncertainty of their ground-based solar constant determinations was probably no less than $\pm 3\%$.) This realization was a major factor in their decision to halt routine observations in 1952.

The large decreases in solar "constant" uncertainty shown in Fig. 1 between 1900 and 1932 were due to decreases in uncertainties of pyrheliometry and the techniques used to deduce extra-atmospheric irradiance from ground observations. Although steady progress in understanding the effects of atmospheric absorption and scattering occurred in the three succeeding decades, it was not used to improve solar constant determinations.

Aircraft Observations

In an attempt to surmount some of the limitations of ground-based observations, instruments have been flown on high altitude aircraft by more recent observers (Ref.'s 6, 22). Observations made from stratospheric aircraft have minimized the uncertainty due to absorption by water vapor (since most is in the troposphere). Also, a significant amount of the atmospheric aerosol burden is below the stratosphere. Aircraft fly below the majority of stratospheric ozone, however, which is a significant and variable absorber. The necessity for making stratospheric aircraft measurements through windows, whose effective transmittance for total solar flux is dependent on the spectral distribution of the incident sunlight, is an additional source of uncertainty. Due to the variability of ozone absorption, the solar spectrum at the aircraft and therefore the transmittance of the aircraft window are variable. While aircraft observations have played a historical role in the development of solar "constant" observations, they cannot provide accuracies substantially better than ground-based observations and have little to offer present day research in this field. (See Table 2.)

Balloon Observations

Most aircraft solar observations have been made on research aircraft whose service ceilings are just above the tropopause (~ 12 km). The majority of ozone and some aerosol remain above. The high altitude balloon has been successfully employed to raise instrumentation to higher altitudes, leaving most of the atmospheric aerosol and ozone below. Ozone has a distribution with height that is a maximum in the region of 22-25 km. at middle latitudes. Stratospheric aerosol quantities reach maxima in layers whose heights, numbers, thicknesses and densities vary.

The Smithsonian Astrophysical Observatory pioneered in the use of balloons for solar "constant" observations. They flew relative pyrheliometers of the "Silver Disk" type to altitudes of 25 km. in 1914 to observe the solar total flux. The results were uncertain by more than their ground-based solar "constant" determinations because of additional environmental sources of error at high altitude, but their achievement was a significant one in view of the instrumentation available at the time (Ref. 11).

Nearly fifty years later Kondratyev (Ref. 23) and Murcray (Ref. 24) each made a series of observations of solar irradiance using relative pyrheliometers in balloon flights ranging from 20 to 35 km. in altitude. The largest single source of uncertainty for both was the -2.2% systematic error in the International Pyrheliometric Scale of 1956 (IPS56), to which their relative pyrheliometers were calibrated before flight. The first high altitude observations by self-calibrating pyrheliometers were made in 1968 and 1969 by Willson using active cavity radiometers in balloon experiments at 25 and 36 km., respectively (Ref.'s 13, 25). The 36 km. experiment yielded a solar constant result of 1369 W/M^2 with an S.I. uncertainty of less than $\pm 0.6\%$.

High altitude balloons can attain an altitude of 40 km. today where the total solar flux is attenuated by less than 1%, of which 90% is due to ozone. Relatively simple ancillary spectral measurements can be made to determine the overlying ozone attenuation with an uncertainty of less than 20%, resulting in an overall atmospheric attenuation uncertainty of less than $\pm 0.2\%$. High altitude balloon experiments offer a research platform for solar "constant" monitoring with uncertainties in the less than $\pm 0.5\%$ range.

The sharp decline of solar "constant" uncertainty (fig. 1) corresponds to the first use of self-calibrating cavity pyrheliometers in flight experiments in 1968 and 1969. The failure of the Kondratyev and Murcray experiments to achieve higher accuracies, in spite of the relatively small atmospheric attenuation uncertainty, was their use of relative, thermopile-type detectors, calibrated to the IPS56.

Rocket Observations

It is desirable to eliminate the atmosphere's effects entirely if possible. Short, extra-atmospheric observational opportunities are provided by ballistic, suborbital sounding rocket experiments. The first use of such a platform was by Drummond and Laue in 1967. (Ref. 22) A relative pyrheliometer calibrated to the IPS56 was flown to an altitude greater than 80 km. on the X-15 rocket aircraft. Although above the significant absorbers in the atmosphere, a large S.I. uncertainty was introduced into their result by uncertainties in pre-flight calibrations and instrument window transmittances. (Ref. 35)

The first rocket experiment using self-calibrating pyrheliometers occurred in 1976. (Ref. 26) Three types of cavity pyrheliometers—the ESP of Hickey (Ref. 27), the PACRAD of Kendall (Ref. 28) and the ACR IV of Willson (Ref.'s 21, 29) were flown to a peak altitude of 250 km. by an aerobee sounding rocket. The mean solar "constant" result of all instruments of 1367 W/M^2 with an S.I. uncertainty of less than 0.5% is the most accurate

29) were flown to a peak altitude of 250 km. by an aerobee sounding rocket. The mean solar "constant" result of all instruments of 1367 W/m^2 with an S.I. uncertainty of less than 0.5% is the most accurate measurement to date. A second flight of this payload is scheduled for 1978.

While observation time is limited on sounding rockets (5 minutes above 120 km. in 1976) it is adequate to obtain "snapshots" of the total solar flux. The accuracy is limited only by the performance of the instrumentation. The rapid pressure and temperature changes associated with the sounding rocket ascent can add to the experimental uncertainty, but with careful instrumentation design, uncertainties of less than $\pm 0.2\%$ should be achievable with self-calibrating, active cavity radiometers.

Spacecraft Observations

The first spacecraft solar "constant" observations were made in 1969 by self-calibrating, cavity pyrheliometers flown on the Mariner 6 and 7 satellites by Plamondon (Ref. 30). Their solar "constant" results, after correction for drift, were uncertain by about $\pm 1\%$. The principal value of these observations was the 140 day record of continuous measurements (see fig. 2). The longest continuing observations outside the atmosphere have been by the solar channels of the Earth Radiation Budget (ERB) instrument on the Nimbus 6 satellite (Ref.'s 31, 32). Launched in mid 1975, Hickey reports continuing observations at present, although degradation of sensors, windows and filters is apparent (Ref. 33). The ERB solar instruments are relative pyrheliometers with plane-surface detectors and thermopile sensors. They were calibrated prior to launch by a complex chain of comparisons, ending with a self-calibrating cavity pyrheliometer (Ref. 34).

The initial solar "constant" results of the Nimbus 6 ERB exceeded the 1969 self-calibrating cavity pyrheliometer results of Willson and Plamondon by 1.5% and 2.1% resp. The 1976 rocket experiment described above was designed to check the ERB result. A set of solar sensors identical in design to those on the Nimbus 6 ERB were included in the 1976 rocket payload. Although the rocket ERB channel 3 detector agreed with the ESP and ACR IV in pre-flight tests, the Nimbus 6 and rocket ERB channel 3 detectors yielded the same solar "constant" result at the time of the rocket experiment,

which exceeded the average result of the self-calibrating pyrheliometers by 1.6% (Table 3). The cause of the difference between pre-flight and flight performance by the ERB detectors is unknown (Ref. 33).

The results of Nimbus 6 ERB represented a sudden increase in the uncertainty of knowledge of the solar "constant", as shown in fig. 1. The uncertainty was reduced to less than its pre-Nimbus 6 ERB value by the 1976 rocket experiment. Nimbus 6 is scheduled for launch in 1978 with a similar ERB instrument. The 1976 rocket experiment will be repeated to calibrate its solar sensors.

Table 3. Summary of results of the June, 1976 Aerobee sounding rocket experiment to determine the solar "constant" and calibrate the total irradiance channel (#3) of the Nimbus 6 ERB instrument

Experiment	Solar "Constant"
Active Cavity Radiometer, type IV (ACR IV) (S/N 402) channel A (Ref. 21)	1368 W/m^2
Active Cavity Radiometer, type IV (ACR IV) (S/N 402) channel B (Ref. 21)	1368 W/m^2
Eclectic Satellite Pyrheliometer (ESP) (Ref. 15)	1369 W/m^2
Primary Absolute Cavity Radiometer (PACRAD) (Ref. 16)	1364 W/m^2
Unweighted average solar "constant":	1367 W/m^2
Nimbus 6 ERB channel 3 (satellite) (Ref. 17)	1389 W/m^2
ERB Reference Sensor Model channel 3 (rocket) (Ref. 17)	1389 W/m^2
Difference between ERB channels 3 and unweighted average of rocket pyrheliometer results	1.6%

The Solar Constant Today

The solar constant experiments discussed above are summarized in Table 2. The type of instrument or name is in parentheses after the experimenter. The relative instruments are: TP = Thermopile, AP = Angstrom Pyrheliometer. All the other instruments are self-calibrating, cavity pyrheliometers of various types.

The calibration of the originally reported results were by self-calibration during the solar observations (S.C.), or by pre-flight calibration to the S.I. or IPS56. The ESP and PACRAD rocket sensors were capable of operation as self-calibrating instruments on the ground, but were not operated in this mode during the rocket experiment. Their flight results were related to S.I. units defined by pre-flight operation as self-calibrating pyrheliometers by making the necessary

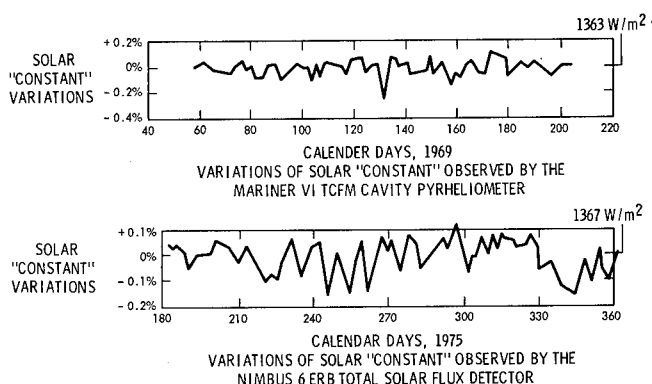


Figure 2. Temporal Variation of Solar "Constant" Observed During Flight Experiments.

Table 2. Solar "constant" experiments since 1900

	YEAR	EXPERIMENTOR (INSTRUMENT) ¹	OBSERVATION SITE	ALTITUDE (km)	CALIBRATION OF ORIGINALLY REPORTED RESULT ²	SOLAR CONSTANT (W/m ²)	S.I. UNCERTAINTY (%)
1	1902-1952	SMITHSONIAN (CAVITY)	TERRESTRIAL	0-1.7	SC/SI	1358	< 3
2	1966-1968	DRUMMOND (TP)	AIRCRAFT	12-13	R/IP556	1387	> 3
3	1967	DUNCAN (AP)	AIRCRAFT	12	R/IP556	1375	> 3
4	1967	KRUGER (CAVITY)	AIRCRAFT	12	SC/SI	1372	> 2.5
5	1968	KENDALL (PACRADI)	AIRCRAFT	12	SC/SI	1373	> 2.5
6	1962-1968	KONDRATYEV (TP)	BALLOON	28-34	R/IP556	1376	< 2
7	1967-1968	MURCRAE (TP)	BALLOON	31-35	R/IP556	1373	< 2
8	1968	WILLSON (ACR III)	BALLOON	25	SC/SI	1373	< 2
9	1969	WILLSON (ACR III)	BALLOON	36	SC/SI	1369	< 0.6
10	1967	DRUMMOND (TP)	SPACECRAFT		R/IP556	1385	> 1
11	1969	PLAMONDON (TCFM)	SPACECRAFT	>1000	SC/SI	1363	> 1
12	1975-1977	HICKEY (TP)	SPACECRAFT	1100	R/SI	1367	< 2
13	1976	HICKEY (ESP)	ROCKET	250	R/SI	1369	< 0.5
14	1976	KENDALL (PACRADI)	ROCKET	250	R/SI	1364	< 0.5
15	1976	WILLSON (ACR IV)	ROCKET	250	SC/SI	1368	< 0.5

1. TP and AP refer to Thermopile and Angstrom Pyrheliometers - relative instruments.
All others are self-calibrating, cavity pyrheliometers.

2. Abbreviations denote mode of detector operation during flight observations/scale of reference:
SC - Self-calibrating during flight; R - relative to preflight ground calibration; SI - System
Internationale - IP556 - International Pyreheliometric Scale of 1956.

corrections for changes in instrument performances under flight conditions.

The solar constant values and S.I. uncertainties listed for experiments 1-11 in Table 2 are derived from references 35 and 36. Adjustments were made to refer each result to the S.I. as nearly as possible, reflecting the results of recent discoveries in pyrheliometry.

The weighted mean solar "constant" result from all types of observation in 1369 W/M². The most accurate observations thus far were by the instruments on the 1976 rocket experiment, which yielded the unweighted mean value of 1367 W/M² (with an S.I. uncertainty of less than 0.5%). The close agreement between these values is not fortuitous, since the weight factor for each observation is the inverse square of its S.I. uncertainty. This heavily weights the most accurate measurements: the 1969 ACR balloon result and the results of the four 1967 rocket flight instruments, all of which were close to 1369 W/M².

The close ($\sim 0.1\%$) agreement between the 1969 balloon result of Willson (1369 W/M²) and the 1976 rocket mean result (1367 W/M²) does not prove that the solar "constant" did not vary by more than 0.1% over this solar "max" to solar "min" period. The error bounds for these experiments were ± 0.6 and $\pm 0.5\%$ resp. The most that can be said is that any change in the solar "constant" was probably less than 0.7% ($0.6 + 0.1$) and almost certainly less than 1.2% ($0.6 + 0.1 + 0.5$). If the solar "constant" is constant, its most probable value is 1368 W/M², with an S.I. uncertainty less than $\pm 0.5\%$.

Future Observations

The data base on solar total flux variability with the $\pm 0.1\%$ level of long term uncertainty required by climatological studies has yet to be provided. A program for 0.1% observations over at least one twenty-two year solar magnetic cycle is currently being developed. It will be comprised of an optimum combination of flight experiments using rocket, spacelab and free flying spacecraft observations. The first step in this program will be taken in 1979 when a three detector version of the ACR IV, similar to the ACR 402 rocket instrument, will be flown on the Solar Maximum Mission. The minimum mission lifetime is one year with a high probability of extension to several years.

An instrument similar to the Solar Max ACR IV is being developed for the Spacelab 1 mission in late 1980. Direct comparison of the Solar Max and Spacelab 1 experiments will increase the proba-

bility of maintaining the 0.1% measurement lifetime of the Solar Max ACR IV beyond its first year of operation.

Of the various experimental approaches, re-flights of the Spacelab instrumentation have the maximum potential for sustaining a long term data base on solar variability with 0.1% S.I. uncertainty. The spacelab mission lifetimes of about one week duration are adequately long to obtain sufficient data, yet not long enough to allow significant degradation of the cavity detectors by solar UV and energetic particles. Verification of flight performance is provided by pre and post flight comparisons with carefully maintained reference instrumentation.

IV. SOLAR SPECTRAL IRRADIANCE

Present models of the solar spectral irradiance in the .25-6.0 μm range, which contains more than 99% of the total solar flux, are constructed from the results of many different experiments. They include data from observations made from the surface, aircraft, balloons, rockets and spacecraft. Experiments made at the surface or in aircraft cannot detect a significant amount of the solar UV and IR. No single rocket or spacecraft experiment has covered a large fraction of the required wavelength range and most have been substantially below the available state-of-the-art in calibration traceability to the international system of units (S.I.). The most comprehensive experiments to date have been made from the ground, aircraft and balloons, but flaws in calibration, restricted wavelength coverage and uncertainties in atmospheric attenuation have limited the accuracy for their results. Relativity of calibrations for the various experiments to each other or to S.I. is difficult to ascertain.

There have been many experiments designed to measure the solar spectrum and numerous efforts to model it. Here discussion will be limited to the three recent efforts of Thekaekara (Ref. 6, 37), Arvesen (Ref. 5) and Labs and Neckel (Ref.'s 7, 8). They have each added to the experimental data base and have incorporated the results of earlier work in modeling the solar spectrum.

Thekaekara

The data used by Thekaekara to assemble his model of the solar spectrum was derived principally from the results of aircraft experiments by a group of investigators from NASA's Goddard Space Flight Center flown just above the troposphere in 1967. (Ref. 6). Additional filter radiometer data gathered by Drummond (Ref. 22, 38, 39) was incorporated into the model.

The GSFC-Thekaekara experiment used five instruments to cover the 0.3 to 15 μm wavelength range of the solar spectrum. Different types of instrumentation, modes of operation, aircraft windows, entrance optics and calibration procedures were used. Some large discrepancies between the spectra obtained by the various instruments in overlapping wavelength ranges occurred in the visible. Differences in spectral irradiances of up to 30% occurred between .4 and .6 μm , a range containing nearly 30% of the total solar flux (Ref. 6).

Calibration of the instrumentation over the .3 - 2.5 μm range was performed using a commercially-supplied standard of spectral irradiance traceable to the National Bureau of Standards (NBS). The S.I. uncertainties of these transfer standards were probably no less than $\pm 3\%$ in the visible and IR and $\pm 5\%$ in the UV under laboratory conditions. The aircraft calibration environment was characterized as less than optimum by the GSFC investigators (Ref. 6). Considerable difficulty was experienced with the calibration lamps used in the experiment (Ref. 40).

Thekaekara derived the extra-atmospheric solar spectrum from the aircraft data by extrapolation using "Langley plots". The log of spectral irradiance at the aircraft altitude (after correction for the window transmissivity) was plotted against the log of: the secant of the solar zenith angle times the ratio of pressure at aircraft altitude to that at sea level ("air mass"). The range of "air mass" during the GSFC aircraft experiments was between 1 and 8. An extrapolation to "zero air mass" was performed at 77 wavelengths to produce the extra-atmospheric irradiance.

The extrapolation procedure relies on the assumption of temporal and spatial homogeneity in the atmosphere above the observing site. The high speed of the aircraft amplifies the effects of inhomogeneities in overlying ozone, aerosol and water distributions. Uncertainty from this source was further increased by the large solar zenith angles at which data were taken during the experiment.

A solar spectrum model was produced by Thekaekara for the wavelength range 0.14 to 20.0 μm . The data for wavelengths shorter than 0.3 μm and longer than 15 μm were derived from several other experimental efforts (Ref. 37). Although an average uncertainty of $\pm 5\%$ is claimed by Thekaekara, the S.I. uncertainty of the solar spectral irradiance in this model must significantly exceed that value over most of its range. The spectra produced by three of the five instruments used in the experiment disagree by more than 5% over most of the 0.3 - 1.0 μm range, which includes about 60% of the total solar flux. (Ref. 6).

Arvesen

Air aircraft experiment to measure solar spectral irradiance over the 0.3 - 2.5 μm range was conducted by Arvesen, et. al., of NASA's Ames Research Center. His experiment was flown on the same set of NASA CV990 aircraft flights used by the GSFC-Thekaekara group, plus five additional flights in which GSFC did not participate. (Ref. 5).

The Cary 14 instrumentation used by Arvesen covered the 0.3 - 2.5 μm wavelength range. Traceability to S.I. units was provided by a commercially-supplied spectral irradiance standard traceable to NBS. Calibration through the input optics is automatically provided on a continuous basis by routinely chopping the standard lamp against both zero and solar irradiance. An independent procedure was used to calibrate the spectral properties of the two optics outside the internal calibration process. (The spectral transmissivity and reflectivity of the aircraft window and the experiment's turning mirror, resp.)

The data were extrapolated to "zero air mass" using the Langley procedure. A solar spectrum model was developed covering the 0.2 to 40 μm wavelength range. Data from other experiments and a 5800° K greybody model were used to construct the spectrum below 0.3 μm and above 2.5 μm , resp.

In the same environment, the Arvesen experiment was more successful than Thekaekara's. The principal reasons were: better instrumentation and calibration procedures, better understanding and control of various sources of experimental uncertainty, and a well conceived plan for data and error analysis. The parametric error analysis performed by Arvesen indicates an S.I. uncertainty ranging from 25% at 0.3 μm to 3.1% in the visible. Although a systematic error of about -2% in the standard lamp and some minor wavelength calibration uncertainty were reported following his initial publication of results, the Arvesen experiment provides a relatively accurate data base on a significant fraction of the extra atmospheric solar spectral irradiance. An S.I. uncertainty of about $\pm 5\%$ was probably achieved over the wavelength range 0.40 to 2.5 μm which contains more than 90% of the total solar flux.

Labs and Neckel

The experiment to determine the solar spectral irradiance of Labs and Neckel was ground based. Their data were gathered at a high altitude site in Switzerland, the Jungfraujoch Observatory at a 3.6 km. elevation. The disadvantages of observing below the tropopause were partially offset by the laboratory-quality experimental environment. The well controlled experiment was comprised of precision observations of the spectral distribution at the center of the solar disk in the .33 to 1.25 μm range. (Ref. 7, 8).

The instrumentation employed by Labs and Neckel was comprised of telescope input optics and a double monochromator. Calibration was by a standard radiance lamp calibrated to black body emitters located at the Happel-Laboratory and the Berlin Institute of the Physikalisch-Technisch Bundesanstalt (PTB). Observing procedures included regular calibration of the monochromator before and after each spectral scan. They measured the intensity of the central part of the solar disk and derived the irradiance from empirical relationships for limb darkening. Scans were made for numerous solar zenith angles and "Langley" extrapolation used to derive extra atmospheric spectra.

The instrumentation scheme employed a nearly differential observation of calibration source and sun, the exception being an additional collimating mirror used with the standard lamp. The reflectivity of the mirror was measured separately. The system was required to operate over a large dynamic range due to the difference in intensity of the standard lamp and the sun. A neutral density filter was used to reduce the solar intensity to near that of the standard lamp. The transmissivity of the filter was determined separately.

The days for which data were used to compute their results were selected for minimum variance of atmospheric transmission. This is a severe constraint since the gathering of data over the required range of solar zenith angles takes a significant fraction of a day. Their criteria for

selecting data were: (1) an RMS deviation from the mean extinction for an observing day of less than $\pm 1\%$; (2) an RMS deviation from all derivations of extra atmospheric values of less than $\pm 2\%$.

The S.I. traceability of their standard lamp was one of the most significant experimental error sources. Labs and Neckel claim a $\pm 2\%$ uncertainty for their calibration procedure.

The method of measuring central intensity and subsequent derivation of irradiance from the entire solar disk provides sources of error comparable to that of the radiance standard. The angular field of view (less than $.01^\circ$) represents about 1.5% of the solar diameter. Variations in photospheric intensities on that scale and the disagreements between various empirical relationships derived from limb darkening observations produce two types of model-dependent uncertainty for the derivation of irradiance from the entire solar disk.

Labs and Neckel have constructed a solar irradiance model, based primarily on their data, covering the 0.2 to 100 μm wavelength range. A $\pm 2\%$ S.I. uncertainty is claimed except for the UV region. (No parametric error analysis is given.) It is probable that an error bound of $\pm 3\text{--}5\%$ is required to accommodate the experimental and analytical uncertainties discussed above.

Solar Spectral Irradiance Summary

In the 0.4 - 1.25 μm range over which all three experimentors made direct observations, the results of Labs and Neckel appear to have the least S.I. uncertainty, probably within the $\pm 3\text{--}5\%$ range. The uncertainty increases rapidly toward shorter wavelengths. The disagreements between the Labs and Neckel spectrum and that of Arvesen and Thekaekara are about 5 and 10%, resp., in the 0.3 - 0.4 μm range and near 10 and 20, resp., by 0.25 μm .

The Arvesen and Thekaekara spectra both exceed the Labs and Neckel model below 0.4 μm . Since with decreasing wavelength successively more and variable atmospheric attenuation occurs, a corresponding increase in uncertainty for longer optical paths would be expected. This tends to offset the other advantages of the Labs and Neckel observations in this region and mitigates against the Thekaekara results which were obtained at relatively large values of "air mass." Most of Arvesen's data were taken at "air mass" values less than 0.4. After corrections for intensity and wavelength calibration errors in his originally published spectra, the results of Arvesen are probably the most accurate in the 0.3 to 0.4 μm region with S.I. uncertainty ranging from ± 10 to $\pm 5\%$, resp.

Intensities in the wavelength range from 1.25 to 2.5 μm are determined most accurately from Arvesen's data. The Labs and Neckel model agrees within a few percent, the Thekaekara model disagrees by 5-10%. The S.I. uncertainty of Arvesen's results in this range are probably within $\pm 5\%$.

The wavelength range between 0.3 and 2.5 μm contains about 95% of the total solar flux, with about 1% at shorter and 4% at longer wavelengths. The S.I. uncertainties of UV intensities shortward of .3 μm are large, probably in excess of $\pm 25\%$. (Ref. 7).

The best model of spectra at wavelengths longer than 2.5 μm is that of Labs and Neckel who have used a combination of modeling and an assessment of experimental results of others to construct the 2.5 and 12.0 μm range. The S.I. uncertainty here is probably $\pm 5\%$. Disagreement between this model and those of Thekaekara derived from his measurements and from the 5800° K solar model used by Arvesen are as large as 20% in this range.

REFERENCES

1. Opik, E. J., *Icarus*, 4, 289, 1965.
2. Hartmann, W. K., *Icarus*, 22, 301, 1974.
3. Milankovitch M., K. Serb. Akad. Beogr. Spec. Publ. 132, 1941.
4. Hays, J. D., J. Imbrie, M. J. Shackleton, *Science*, 194, 1121, 1976.
5. Arvesen, J. C., et al.; *Appl. Optics*, 8, 2215, 1969.
6. Thekaekara, M. P., R. Kruger, C. H. Duncan, *J. Appl. Optics*, 8, 1713, 1969.
7. Labs, D.; Neckel, H.; *Z. F. Astrophysik*, 69, 1, 1968.
8. Labs, D.; Neckel, H.; Proc. Solar Constant Workshop, Big Bear Solar Observatory, May, 1975.
9. Annals of the Astrophysical Observatory of the Smithsonian Inst., Vol.'s 1-7, 1902 - 1952.
10. Frohlich, C.; Proc. Symposium on Solar Radiation, Radiation Biology Lab of Smithsonian Inst., Rockville, Md., 1973.
11. Willson, R. C., *Nature*, 239, 208, 1972.
12. Fröhlich, C., Geist, S., Marchgraber, R. M., Kendall, J. M. "IPC III Comparisons of Pyrheliometers and a Comparison of Radiation Scales," *J. Solar Energy*, 14, 157, 1973.
13. Willson, R. C., *J. Geophys. Res.*, 76, 4325, 1971.
14. Willson, R. C., JPL Tech. Rept. 32-1365, Jet Propulsion Lab., Pasadena, CA, 1969.
15. Willson, R. C., "Radiometer Comparison Tests," JPL Report 900-446, Jet Propulsion Lab., Pasadena, CA, 1971.
16. Willson, R. C., "Results of the 1972 Table Mountain Radiometer and Radiation Scale Comparisons," Jet Propulsion Lab., Pasadena, CA, 1972.
17. Brusa, R. W., C. Frohlich, "Scientific Discussions IPC IV," World Radiation Center, Davos, Switzerland, 1975.
18. Frohlich, C.; Private Communication, 1977.

19. Willson, R. C., J. App. Optics, 12, 810, 1973.
20. Kendall, J. M. Sr.; Berdahl, C. M.; J. App. Optics, 9, 1082, 1970.
21. Willson, R. C.; Proc. Electro-Optics/Laser 77 Conference, Anaheim, CA., p. 430, 1978.
22. Laue, E. G.; Drummond, A. J.; Science, 161, 888, 1968.
23. Kondratyev, K., Ya, Nikolsky, G. A., Q. J. Roy. Met. Soc., 96, 509, 1970.
24. Murcray, D. G., et al, AFCL Report-69-0070, Air Force Cambridge Research Labs, Bedford, Mass., 1969.
25. Willson, R. C., Solar Energy, 14, 203, 1973.
26. Duncan, C. H., et al, Appl. Optics, 16, 2690, 1977.
27. Hickey, J. R., "Preliminary Design Review of the Eclectic Satellite Pyrheliometer," AFFE Report, March 2, 1976.
28. Kendall, J. M. Sr., C. M. Berdahl, J. Appl. Optics, 9, 1082, 1970.
29. Willson, R. C., Proc. Soc. Photo-Optical Instrumentation Engineers Annual Mtg., San Diego, CA, 68, 31, 1975.
30. Plamondon, J., JPL Space Program Summary, 37-69, 3, 162, 1969.
31. Hickey, J.R., F.J. Griffin, D.T. Hilleary, H.B. Howell, "Extra-terrestrial Solar Irradiance Measurements from the Nimbus 6 Satellite," Proc. of Joint Conference on Sharing the Sun, Winnipeg, Manitoba, Canada, August 1976.
32. Hickey, J.R., "ERB Solar Channel Values," memo to distribution, the Eppley Laboratory, Newport, R.I., October 10, 1976.
33. Hickey, J.R., Personal communication, 1978.
34. Hickey, J.R., A.R. Karoli, Appl. Optics, 13, 453, 1974.
35. Fröhlich, C., "Contemporary Measures of the Solar Constant," in The Solar Output and Its Variation, ed. O.R. White, U. of Colorado Press, Boulder, CO., 1977.
36. Willson, R.C. and Hickey, J., "1976 Rocket Observations of the Solar 'Constant' and their Implications for Variation to Solar Output in Cycle 20," The Solar Output and Its Variation, ed. O.R. White, U. of Colorado Press, Boulder CO., p. 11, 1977.
37. Thekaekara, M.P.; J. App. Optics, 13, 518, 1974.
38. Drummond, A.J.; et. al.; J. Spacecraft and Rockets, 4, 1200, 1967.
39. Drummond, A.J., Hickey, J.R.; J. Solar Energy, 10, 1, 1966.
40. Kennard, D.C.; et. al., NASA PUB. X-322-68-304, NASA GSFC, 1968.

SOLAR SPECTRAL IRRADIANCE AT GROUND LEVEL
By: Ann Thomas Mecherikunnel, NASA/Goddard Space Flight Center
Greenbelt, Md. 20771

and

Joseph C. Richmond, National Bureau of Standards
Washington, D.C. 20234

BIOGRAPHY

Dr. Ann T. Mecherikunnel (Anna Thomas) has been associated with NASA Goddard Space Flight Center since 1975 doing research in Solar Total and Spectral Irradiance and its Variability.

She received her Ph.D. in Chemistry from George Washington University in 1970. Her research experience includes UV-visible absorption and emission spectroscopy, Photochemistry, experimental and theoretical studies of atmospheric optical parameters that affect solar energy. She has taught at George Washington University. She has been a National Academy Post Doctoral Resident Associate (1975-1977) at Goddard Space Flight Center and worked with late Dr. M.P. Thekaekara in the U-2 SEMIS Project and Solar Total and Spectral Irradiance Measurements.

Joseph C. Richmond has B.S. degrees in both Ceramic Engineering and Liberal Arts from Alfred University, an M.S. degree with a major in Ceramic Engineering and the professional degree of Ceramic Engineer from N.C. State University. He has also taken numerous graduate courses from the NBS graduate school, the Oak Ridge Institute of Nuclear Studies and the University of Rhode Island.

He has been employed by the National Bureau of Standards since 1939, and has over 100 publications, many of them in the field of thermal radiation properties of materials. He is now a Senior Research Engineer in the Thermal Processes Division of the Center for Mechanical Engineering and Process Technology of NBS.

ABSTRACT

Available quantitative data on solar total and spectral irradiance is examined in the context of utilization of solar irradiance for terrestrial applications of solar energy. A brief review is given on the extraterrestrial solar total and spectral irradiance values. Computed values of solar spectral irradiance at ground level for different air mass values and various levels of atmospheric pollution or turbidity are also presented. Wavelengths are given for computation of solar absorptance, transmittance and reflectance by the 100-selected-ordinate method and by the 50-selected-ordinate method from air mass two solar spectral irradiance for the four degrees of atmospheric pollution. Total solar spectral irradiance measured with a prism monochromator is examined to evaluate the direct solar spectral irradiance for a surface normal to the sun's rays and to compare the computed spectrum with the experimentally observed one.

INTRODUCTION

Detailed knowledge of solar irradiance at ground locations is needed in the direct utilization of solar energy for practical applications. Design and stability of terrestrial solar energy collectors, precise prediction of the output of solar cells, performance and degradation of potential coatings, glazings, adhesives and sealants, all require the characterization of the total

amount of energy available from the sun, the spectral distribution of this energy and its temporal variations.

Solar total and spectral irradiance at a particular site at ground level depends on several parameters—the geometry of the site (altitude, latitude, and longitude), sun-earth distance, time of the day, season of the year, cloudiness of the atmosphere, orientation of the collector surface, shading, and atmospheric attenuation due to water vapor, ozone, carbon dioxide and aerosols. Measurement of solar spectral irradiance is a complex problem. Precise measurement of the total and spectral irradiance at each location is expensive and not always feasible. Solar irradiance data necessary for terrestrial applications of solar energy can be obtained from a combination of ground measurements and computation based on the extraterrestrial solar spectrum and the atmospheric optical parameters.

This paper will attempt a brief survey of the quantitative data on solar total and spectral irradiance which is currently available. Solar spectral irradiances are presented for air mass values 1, 2, 3, 4, 7, and 10 computed from NASA/ASTM standard extraterrestrial solar spectral irradiance and atmospheric optical parameters of 20 mm precipitable water vapor, 3.4 mm ozone and Angström turbidity coefficients corresponding to four different levels of atmospheric pollution. Wavelengths are given for computation of solar absorptance, transmittance and reflectance by the 50-selected-ordinate method and the 100-selected-ordinate method. Total solar spectral irradiance measured on a horizontal surface with a prism monochromator for different air mass values for two clear days are also presented. Air mass remained fairly stable at 1.2 for more than three hours around noon on both days. Direct solar spectral irradiance for this air mass value was evaluated from the measured spectral irradiance and a comparison is made of the experimentally observed spectrum with the theoretically computed spectral irradiance. Computed values for turbidity coefficients $\alpha = 0.9$; $\beta = 0.13$ were found to agree with the experimentally observed values for one of the days.

I. EXTRATERRESTRIAL SOLAR TOTAL AND SPECTRAL IRRADIANCE

A. Solar Constant

Solar radiation is usually described in terms of the solar constant and solar spectral irradiance. The solar constant is the amount of total radiant energy received from the sun per unit time, per unit area exposed normally to the sun's rays at the mean sun-earth distance in the absence of the earth's atmosphere. The air mass zero solar spectral irradiance is the distribution of this power (surface) density as a function of wavelength.

Earlier estimates of solar constant and extraterrestrial solar spectral irradiance were based on terrestrial measurements made at different solar zenith angles which were then extrapolated to zero air

mass. Ground measurements are limited in accuracy due to the strong and highly variable absorption and scattering properties of the atmosphere. Measurements made from aircraft, balloons and rockets in recent years have narrowed the wide margin of uncertainty in solar constant and solar spectral irradiance values. An examination of the available literature on the subject shows that there is disagreement among various authors as to the value of the solar constant, and uncertainties in the spectral distribution of solar energy as a function of wavelength are considerably greater than those in the solar constant itself.

The NASA/ASTM standard solar total irradiance value is 1353 W m^{-2} with an uncertainty of $\pm 1.5\%$. This value was obtained as an average of many series of measurements made from high altitude platforms, ranging in values from 1338 W m^{-2} to 1368 W m^{-2} (1). According to the authors, the two extreme values are those which claim the least estimated error (2). Solar total irradiance value of 1367 W m^{-2} with an uncertainty of less than $\pm 0.5\%$ is reported for the rocket measurement of June 1976 (3).

B. Air Mass Zero Solar Spectral Irradiance

A comparison of air mass zero solar spectral irradiance values that have received a great deal of attention in recent years is given in the wavelength range $0.2 - 1.7 \mu\text{m}$ in Figure 1 and in the range $1.0 \mu\text{m} - 4.0 \mu\text{m}$ in Figure 2. The x-axis gives the wavelength in micrometer (μm) and y-axis gives the solar spectral irradiance in $\text{W m}^{-2} \mu\text{m}^{-1}$. The spectral curves derived

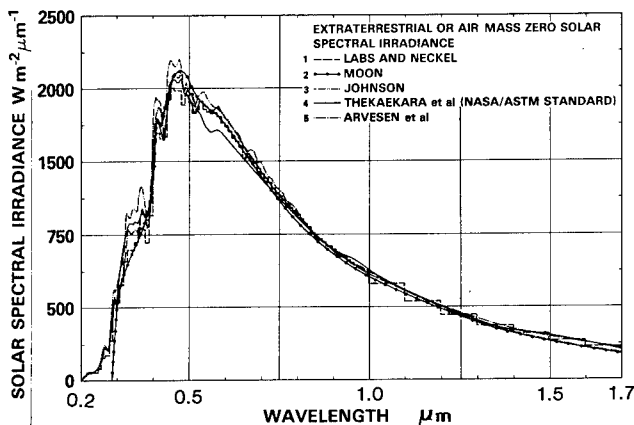


Figure 1. Solar Spectral Irradiance Outside the Atmosphere $0.2 \mu\text{m} - 1.7 \mu\text{m}$ reported by:

1. Labs and Neckel, 2. P. Moon, 3. F.S. Johnson,
4. Thekaekara et al (NASA/ASTM Standard),
5. Arvesen et al.

by Johnson (4), Moon (5) and Labs and Neckel (6) were based on measurements made from high altitude mountain stations. The spectral curves derived by Thekaekara et al. (7) and Arvesen et al. (8) were based on observations from aircraft at mean altitudes of $11.6 - 12.5 \text{ km}$. Definitive measurements have not yet been made from space, and the observations made from sea level, mountain tops and even from research aircraft do not have the required accuracy and precision because of the highly variable atmospheric attenuation and errors inherent in the extrapolation to zero air mass.

According to a recent consensus of solar and atmospheric physicists (White 1977) the best presently available data of solar spectral irradiance in the interval $0.3 \mu\text{m}$ to $3 \mu\text{m}$ are those given by Thekaekara et al., Labs and Neckel, and Arvesen et al. (9) (10). The overall accuracy claimed for each of these sets of ob-

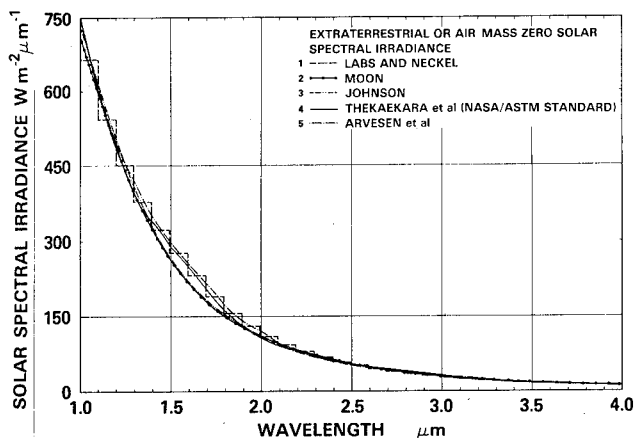


Figure 2. Solar Spectral Irradiance Outside the Atmosphere $1.0 \mu\text{m} - 4.0 \mu\text{m}$ reported by:

1. Labs and Neckel, 2. P. Moon, 3. F.S. Johnson,
4. Thekaekara et al (NASA/ASTM Standard),
5. Arvesen et al.

servations is about $\pm 5\%$ (Thekaekara), $\pm 3\%$ (Arvesen) and $\pm 2\%$ (Labs and Neckel) (9).

The total irradiance or solar constant values obtained from the integral of the spectral irradiance reported by these authors are very close—Thekaekara 1353 W m^{-2} or $1.940 \text{ cal cm}^{-2} \text{ min}^{-1}$, Labs and Neckel 1358 W m^{-2} ($1.947 \text{ cal cm}^{-2} \text{ min}^{-1}$), Arvesen et al. 1390 W m^{-2} or $1.99 \text{ cal cm}^{-2} \text{ min}^{-1}$. Despite the good agreement in the value of the integrated flux of solar radiation, the spectral irradiance values converge much more poorly. The most significant variations are in the spectral region $0.3 - 1.5 \mu\text{m}$ in which about 90% of the total flux is generated. The differences among these values can amount to more than 10% at some wavelengths with the largest difference occurring in the important spectral interval $0.5 - 0.7 \mu\text{m}$. It is important to note that the $0.3 \mu\text{m} - 0.7 \mu\text{m}$ range is a region rich in Fraunhofer (solar absorption) structure which each instrument displays in a different way according to the wavelength resolution (2). In the near infrared beyond $1.0 \mu\text{m}$ the average difference in the measurement is about 3% (9).

The wavelength range $0.27 \mu\text{m}$ to $2.6 \mu\text{m}$ contains over 96% of the sun's energy. Extending the spectral range to $4.0 \mu\text{m}$ increases the energy content to 99%. This region is responsible for all life processes and for making of weather and climate. Photosynthesis essential for all life support is due to wavelength bands centered around $0.44 \mu\text{m}$ and $0.75 \mu\text{m}$. The major input into the energy budget of the earth comes from this region. Absorption by water vapor occurs at about $0.7, 0.8, 0.9, 1.1, 1.4, 1.9, 2.7, 3.2,$ and $6.3 \mu\text{m}$ and by carbon dioxide at about $1.6, 2.0, 2.7,$ and $4.3 \mu\text{m}$.

Solar cells are spectrally sensitive and the spectral region 0.4 to $1.1 \mu\text{m}$ is important for the photovoltaic conversion; 0.3 to $4.0 \mu\text{m}$ is the important spectral region for the thermal conversion systems.

In many of the applications of the solar irradiance values, both total and spectral a question of major concern is the variability of these values. The solar constant is defined for the average sun-earth distance. As the earth moves in its elliptical orbit around the sun the total solar energy received varies by $\pm 3.5\%$. There are also small and undetermined variations due to cyclic or sporadic changes in the sun itself. These variations are more significant in certain portions of the spectrum than in others. The cyclic variations in solar energy output are about 2 or 3% and occasionally greater changes occur when a large sunspot crosses the solar disc.

A conclusion that can be drawn from this survey is that the uncertainty in the solar constant is about $\pm 1.5\%$. The extraterrestrial solar spectral irradiance on the other hand, is uncertain in as much as 10 to 15% at some wavelengths.

II. SOLAR TOTAL AND SPECTRAL IRRADIANCE AT GROUND LEVEL

A. Computation from extraterrestrial spectral irradiance

Direct solar radiation reaches the surface of the earth considerably weakened and with its energy distribution greatly changed due to the attenuation along its path through the atmosphere. The attenuation is small in pure air but increases with the amount of contamination or turbidity due to variable components such as dust, aerosol particles and water vapor. The attenuation increases both with the extinction coefficient and the optical absolute air mass. Therefore, the solar radiation is found to vary with time of day, season, geographical latitude and altitude even when the extinction remains constant.

The discussion given below is taken from references (11) (12). Throughout most of the solar spectrum the absorption of a monochromatic beam of light is governed by the logarithmic decrement law known as Bouguer's Law.

$$E_{\lambda} = E_{\lambda}^{\circ} e^{-(C_1 + C_2 + C_3)m} \quad (1)$$

where E_{λ}° and E_{λ} are spectral irradiance at a given wavelength λ outside the atmosphere and after transmittance through air-mass m respectively. The coefficient C_1 is due to Rayleigh Scattering, and C_3 is due to ozone optical depth. C_1 and C_3 at different wavelengths were obtained by linear interpolation of Elterman data (13). C_2 is the attenuation coefficient due to turbidity and the equation developed by A. Ångström (14) is used in the computation, where λ is the wavelength in micrometer,

$$C_2 = \beta \lambda^{-\alpha} \quad (2)$$

and the effect of pollution is expressed by two parameters α and β known as Ångström turbidity coefficients. In the infrared ($\lambda > 0.69 \mu\text{m}$) a fourth parameter is needed to account for the molecular absorption bands. In the infrared equation 1 has to be modified as:

$$E_{\lambda} = E_{\lambda}^{\circ} e^{-(C_1 + C_2 + C_3)m} \cdot T_{\lambda_i} \quad (3)$$

where T_{λ_i} is a transmission factor which can have one of the three forms

$$T_{\lambda_1} = e^{-C_4 (wm)^{\frac{1}{2}}} \quad (4)$$

$$T_{\lambda_2} = e^{-C_5 wm} \quad (5)$$

$$T_{\lambda_3} = 1 - C_6 m^{\frac{1}{2}} \quad (6)$$

where m is the air mass, and w is the amount of precipitable water vapor, C_4 , C_5 , and C_6 are empirical constants (15).

Solar irradiance received on a surface has two components: (1) that received directly from the sun and (2) that diffused by the sky. Computations of direct solar spectral irradiance at ground level have been made for different sets of parameters for ozone density, precipitable water vapor, turbidity coefficients and air mass 1, 4, 7, and 10 by Thekaekara and reported in references (11), (12), (16). An example of the results of such computation is given in Figure 3. It shows four curves related to solar spectral irradiance. The topmost curve is the NASA/ASTM Standard of Solar Spectral irradiance for air mass zero, that is,

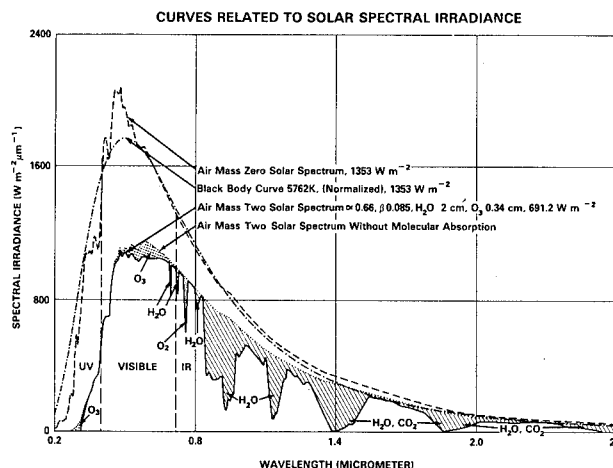


Figure 3. Solar Spectral Irradiance Outside The Atmosphere And On The Ground, And Related Spectral Curves.

irradiance outside the Earth's atmosphere at the average Sun-Earth distance on unit area exposed normal to the Sun's rays. It gives the E_{λ}° of Equation (3). The area under this curve is the solar constant, 1353 W m^{-2} . Below is the normalized black body curve. The lower curve with many sharp dips is the solar spectrum for air mass two, that is spectral irradiance on unit area on the ground exposed normal to the Sun's rays, assuming relatively clean air and no clouds and the Sun at 60° from the vertical. This is a curve computed by using Equation (3) from the air mass zero curve with atmospheric parameters; 20 mm of precipitable water vapor, 3.4 mm of ozone, and turbidity coefficients $\alpha = 0.66$ and $\beta = 0.085$. The total direct solar energy transmitted by the atmosphere in this case is obtained by integrating the area under the curve and it is found to be 691.2 W m^{-2} or 51.1% of that received above the atmosphere. The relatively smooth curve (curve 4) is the computed air mass two spectrum in the absence of molecular absorption.

Spectral irradiance values for air mass 1, 2, 3, 4, 7 and 10 computed from NASA/ASTM standard of solar spectral irradiance outside the atmosphere (E_{λ}°) and for U.S. Standard atmosphere 20 mm of precipitable water vapor, 3.4 mm of ozone from equation (3) are given in Tables 1-4 in the wavelength range 300 nm - 4045 nm. As the solar zenith angle increases the transmitted energy decreases.

α and β Ångström turbidity coefficients are related to the size distribution and density of aerosols. Solar spectral irradiance values given in Table 1 is for $\alpha = 1.3$, $\beta = 0.02$ and corresponds to a very clear atmosphere. A higher value of β corresponds to a more turbid atmosphere. Table 2 is for $\alpha = 1.3$ and $\beta = 0.04$ representing a rather clear atmosphere. As turbidity increases the transmitted energy decreases.

The wavelength exponent α generally is within the range from 0.5 to 2.5 and according to Ångström (1929) has a mean value of 1.3. An α value of 0.5 indicates a greater than average proportion

of large particles while an α value of 2.5 indicates a less than average proportion of large particles (17). Considerably higher levels of pollution typical of large cities and industrial centers are represented by $\alpha = 0.66$, $\beta = 0.17$ in Tables 3 and 4 respectively.

The total irradiance at ground level is obtained by integration of the area under the spectral irradiance curves. Table 5 gives total irradiance at ground level for air mass values 1, 2, 3, 4, 7 and 10 and for four sets of turbidity parameters. The partition of energy between the UV, visible and IR ranges of the spectrum is also shown.

It is significant that as the air mass increases or as turbidity increases the relative amount of energy in the infrared increases and that in the visible and UV decreases.

B. Computation of Solar Absorptance, Reflectance, and Transmittance by 50- & 100-Selected-Ordinate Method

Spectral irradiances are listed in Tables 1, 2, 3, and 4 in units of watts per square meter and micrometer of spectral wavelength interval. The wavelengths, in the first column, are in units of nanometers to give values in convenient whole numbers. (Note that different length units are deliberately used for area and for the spectral parameter in order to avoid the confusingly misleading appearance of a volume unit when the units of irradiance are given in the standard SI form of W m^{-3} , which is not watts per cubic meter but rather watts per square meter per meter of spectral wavelength interval.)

In order to sum up the total irradiance represented by these tabulated values of spectral irradiance, each must be multiplied by the width of a wavelength bandwidth interval to which that spectral irradiance is assigned. Because of the irregularity of the spectral curve, quite narrow wavelength intervals must be associated with some spectral irradiance values in regions where the change is more gradual and consistent. The choice of the boundaries between these wavelength intervals, as well as their widths, is also somewhat arbitrary.

Accordingly, in reducing the spectral irradiance values of Tables 1, 2, 3, and 4 to obtain the irradiances in Tables 6, 7, 8, and 9, the spectral irradiance $E_\lambda(\lambda_i)$ at wavelength λ_i was multiplied by the wavelength interval $\Delta\lambda(\lambda_i)$ associated with λ_i to obtain the irradiance increment $\Delta E(\lambda_i) = E_\lambda(\lambda_i) \cdot \Delta\lambda(\lambda_i)$. However, in Tables 6, 7, 8, and 9, this increment is shown, instead, as associated with the upper boundary of the wavelength interval, i.e., as $\Delta E(\lambda_m)$ where the boundary wavelength $\lambda_m = \frac{1}{2}(\lambda_i + \lambda_{i+1})$ is the average between λ_i and the next higher λ_{i+1} . Furthermore, the size of the interval $\Delta\lambda(\lambda_i)$ was then that between the two boundaries λ_m and λ_{m-1} : $\Delta\lambda(\lambda_i) = \lambda_m - \lambda_{m-1} = \frac{1}{2}(\lambda_{i+1} - \lambda_{i+1})$.

The tabulated values of cumulative irradiance $E(0-\lambda_m)$ are the sums of the ΔE 's, in each case up to and including the ΔE for the interval for which the wavelength λ_m is the upper boundary, as defined in the preceding paragraph. These values of cumulative irradiance $E(0-\lambda_m)$ were each divided by the sum of all the ΔE 's to obtain the ratio $E(0-\lambda_m)/E(0-\infty)$ which is tabulated as a percentage, the percentage of the total solar irradiance at wavelengths shorter than wavelength λ_m .

The wavelengths for the 100-selected-ordinate method of computing solar properties from measured spectral properties (reflectance, transmittance, and absorptance) in Table 11 were taken at values of $E(0-\lambda_m)/E(0-\infty)$ corresponding to the odd half-percentage points 0.5%, 1.5%, --- 98.5%, 99.5%, by linear interpolation between the next adjacent values on either side of the desired percentage. The wavelengths for the 50-selected-ordinate method in Table 10 were taken in the same way at the odd percentage points 1%, 3%, --- 97%, 99%.

C. Solar Spectral Irradiance Measurements with a Prism Monochromator

Spectral Irradiance values in the wavelength range 300 nm - 1100 nm were measured as the total sun and sky (global) irradiance using a spectroradiometer developed for U-2 Solar Energy Monitor in Space (SEMIS) flights by Thekaekara. The optical schematic of the instrument is shown in Figure 4. The instrument is a prism monochromator with a Littrow mirror. The radiant energy was measured by two sensors, an MOS photo-

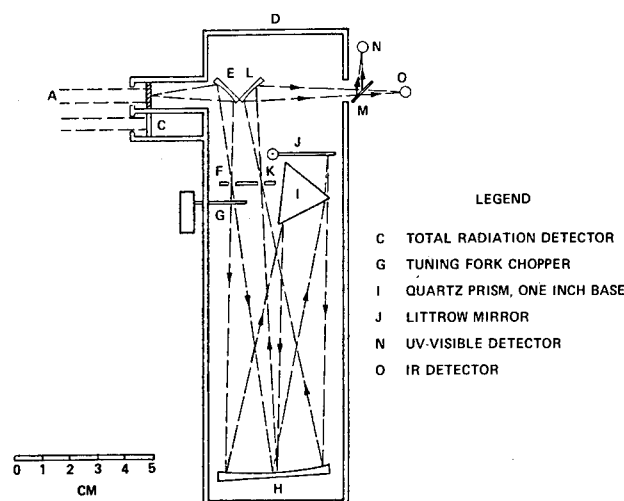


Figure 4. SEMIS, Optical Schematic of the Instrument.

diode for wavelength range 0.25 to 1.1 μm and a PbS infrared detector for $\lambda > 0.7 \mu\text{m}$. This combination enables measurements to be made over the entire 300 to 2500 nm wavelength region. The thermal detector consists of a wirewound thermopile and measures the total irradiance incident on the detector. All data were recorded on digital cassette recorders. The scanning rate is about 10 minutes for a complete scan of the spectrum. Calibration of the system is based on NBS standards of total and spectral irradiance.

Spectral irradiance measurements were made for two clear days, August 31, 1976 and September 10, 1976 on the roof top of Optronics Lab, Silver Spring, Maryland. Spectral irradiance on the horizontal surface was continuously recorded on a digital cassette recorder and later processed by a program developed at GSFC. Thirty-three (33) spectral scans were made on August 31, 1976 from 11:07 a.m. to 4:30 p.m. and 21 spectral scans on September 10, 1976 from 12:20 p.m. to 3:40 p.m. (local time). August 31 was a very clear day but September 10 turned out to be rather hazy with intermittent clouds in the afternoon.

Results and Discussion

Tables 12 & 13, give the total spectral irradiance for different air mass values corrected for average sun-earth distance of one Astronomical unit. The spectral irradiance given is the average irradiance for a 10 nm bandwidth centered at the wavelengths in the range 270-400 nm; 20 nm in the range 400-700 nm; 50 nm in the range 750-1000 nm and 100 nm in the range 1000-2600 nm.

Air-mass values were computed for 10-minute intervals from the coordinates of the site (longitude, latitude), solar declination for the day, and the time of observation.

Figures 5 & 6 give the spectral distribution for air mass values 1.1595-1.1583, 1.3180-1.2904, and 1.4583-1.5066 for August 31, 1976 and 1.2087-1.2066, 1.2884-1.3099, and 1.5186-1.5703, for September 10, 1976. The x-axis is the wavelength in micrometers and y-axis is the solar spectral irradiance in $\text{W m}^{-2} \mu\text{m}^{-1}$. The air mass value remained fairly constant at about 1.2 for more than 3 hours on both days and the spectral curves for consecutive scans fall on top of each other. As air mass increases the decrease in spectral intensity in the visible region is highly pronounced. The absorption bands of ozone Chappuis bands, 500-600 nm, are quite apparent in both figures. Water vapor reported for August 31 was 11 mm, and for September 10, 17.6 mm, by N.W.S.

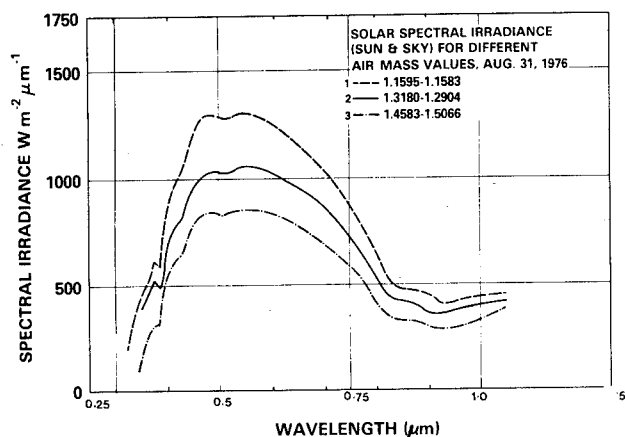


Figure 5. Spectral Irradiance Measured with SEMIS For Air Mass 1.1595-1.1583 (12:57-1:07 P.M.), 1.3180-1.2904 (11:07-11:17 A.M.), 1.4583-1.5066 (3:47-4:07 P.M.) on August 31, 1976

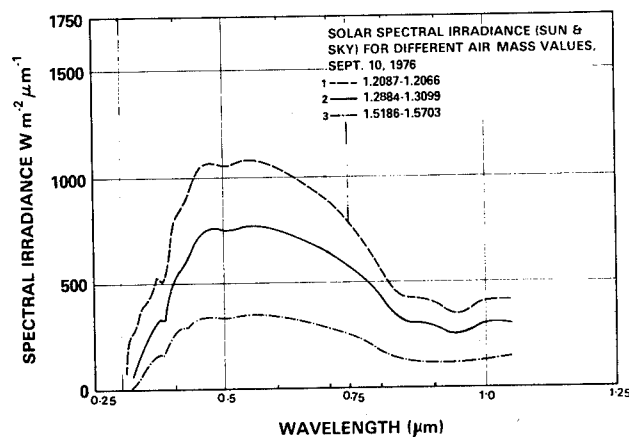


Figure 6. Spectral Irradiance Measured With SEMIS For Air Mass 1.2087-1.2066 (1:10-1:20 P.M.), 1.2884-1.3099 (12:20-12:30 P.M.) and 1.5186-1.5703 (3:40-3:50 P.M.) on September 10, 1976

Comparison of Computed and Measured Solar Spectral Irradiance

Irradiance (G_λ) measured with the instrument is the spectral distribution of the total irradiance consisting of the direct component spectrum I_λ and the diffuse component spectrum D_λ often referred to as sky radiation, while the spectral flux

$$G_\lambda = I_\lambda + D_\lambda \quad (7)$$

is designated Global radiation (18). The horizontal plane terrestrial direct component spectral flux (I_λ) is related to solar spectral irradiance by Robinson (19),

$$I_\lambda = E_\lambda \cos Z \quad (8)$$

where E_λ is the direct solar irradiance normal to the surface, and Z is the solar zenith angle. To get any meaningful comparison between the experimentally observed and theoretically computed spectral curves, the direct solar irradiance normal to the surface has to be computed by subtracting the diffuse radiation and then dividing by $\cos Z$ or reciprocal of air-mass value.

The diffuse sky radiation is a function of all the atmospheric parameters discussed earlier, but cannot be expressed in a simple mathematical expression. The ratio of the diffuse radiation to direct solar radiation (for air-mass one) is very high in the UV and drops rapidly in the visible and IR. Representative values of this ratio based on references (20) are: 72% at 300 nm, 42% at 350 nm, 23% at 400 nm, 8% at 500 nm, and 10% at 700 nm.

Figure 7 gives a comparison between the direct normal irradiance computed for air-mass 1.2 from the experimental data on September 10, 1976 and computed spectral curves based on NASA/ASTM standard and atmospheric parameters water vapor 17.6 mm observed for that day and ozone 0.34 cm. Spectral irradiance values computed for $\alpha = 1.3$ and $\beta = 0.04$ were found to give good agreement with the direct irradiance values obtained for the very clear day (Aug. 31, 1976) and for $\alpha = 0.9$ and $\beta = 0.13$ were found to give good agreement with the clear day (September 10, 1976) that turned hazy in the afternoon.

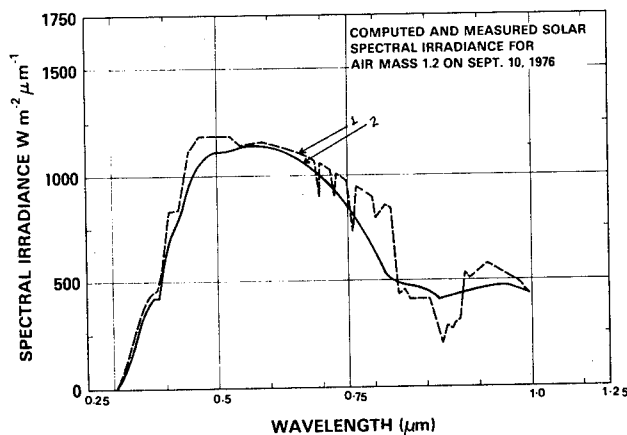


Figure 7. Direct Solar Spectral Irradiance 1. Computed for Air Mass 1.2, H_2O 17.6, $\alpha = 0.9$, $\beta = 0.13$ 2. Measured for Air Mass 1.2 on September 10, 1976.

REFERENCES

1. Anon: Standard Specification for Solar Constant and Air Mass Zero Solar Spectral Irradiance, ASTM Standard, E490-73a, 1974 Annual Book of ASTM Standards, Part 41, Philadelphia, PA, 1974.
2. Anon: Solar Electromagnetic Radiation, NASA SP8005, Washington, D. C., May 1971.
3. Duncan, C.H., Harrison, R.G., Hickey, J.R., Kendall, J.M. Sr., Thekaekara, M.P., and Willson, R.C., Rocket Calibration of the Nimbus-6 Solar Constant Measurements, *Applied Optics*, Vol. 16, No. 10, Oct. 1977, pp. 2690-2697.
4. Johnson, F.S., The Solar Constant, *J. of Meteorology*, Vol. II, No. 6 December 1954, pp. 431-439.
5. Moon, P., Proposed Standard Solar-Radiation Curves for Engineering Use. *J. Franklin Inst.* Vol. 230, Nov. 1940, pp. 583-617.
6. Labs, D., and Neckel, H; Transformation of the Absolute Solar Radiation Data into the International Practical Temperature Scale of 1968. *Solar Physics*, 15, 1970, pp. 79-87.
7. Thekaekara, M.P.; ed; The Solar Constant and Solar Spectrum Measured from a Research Aircraft, NASA TR R-351, Washington, D.C., Oct. 1970.
8. Arvesen, J.C., Griffin, N.R., Jr., and Pearson, B.D., Jr., Determination of Extraterrestrial Solar Spectral Irradiance from a Research Aircraft., *Applied Optics*, 8, 1969, pp. 2215.
9. Pierce, A.K. and Richard, G.A., 1977. The Solar Spectral Radiation Between 0.3 and 10 μm . The Solar Output and Its Variation ed. by O.R. White, Colorado Associated University Press.
10. London, J., Observations of the Solar Flux at the Top of the Atmosphere—A Brief Overview, Proceedings of the Symposium on Radiation in the Atmosphere 19-28, Aug. 1976, Garmisch-Partenkirchen, FRG., Radiation in the Atmosphere, Edited by H. J. Bolla, Science Press, Princeton, 1977.
11. Thekaekara, M.P., Survey of Quantitative data on the Solar Energy and its Spectral Distribution, Conference of Complex; Daharan, Saudi Arabia, 1975.
12. Thomas, Anna and Thekaekara, M.P., Experimental and Theoretical Studies on Solar Energy for Energy Conversion. International Solar Energy Society, American Section, SESCI, Conference, Winnipeg, Manitoba, Canada, August 1976, Proceedings, Vol. 1, pp. 338-355.
13. Elterman, L., UV, Visible and IR Attenuation for Altitudes to 50 km, 1968, AFCRL 68-0153, Office of Air Force Research, U.S. Air Force, 1968.
14. A. Ångström, on the Atmospheric Transmission of Sun Radiation and on Dust in the Air, *Geograph. Ann.* 11, 1929, pp. 156-166.
15. Gates, D.M. and Harrop, W.J., Infrared Transmission of the Atmosphere to Solar Radiation, *App. Optics*, 2, 1963, p. 887.
16. Thekaekara, M.P., Ed. The Energy Crisis and Energy from the Sun, Ch. 2, Data on Incident Solar Energy. Institute of Environmental Sciences, Mt. Prospect, IL, 1974.
17. Bilton, T., Flowers, E.C., McCormick, R.A. and Kurfis, K.R., Atmospheric Turbidity with the Dual-Wavelength Superphotometer, Report and Recommendations of the Solar Energy Data Workshop, Nov. 29-30, 1973. Charles Turner, Editor, NOAA, Environmental Research Laboratories, Air Resources Laboratories, Silver Spring, Md.
18. McCullough, E.C., and Porter, W.P., Computing Clear Day Solar radiation spectra for the Terrestrial Ecological Environment, *Ecology* Vol. 52, No. 6, 1971 pp. 1008-1015.
19. Robinson, N. 1966. Solar radiation. Elsevier, N.Y. p. 347.
20. Dave, J.V. and Furukawa, P.M., Scattered Radiation in the Ozone Absorption Bands, *Meteorological Monographs*, Vol. 7, No. 29, Am. Met. Soc., Boston, 1966.

Table 1. Solar Spectral Irradiance for Different Air Masses,
W m⁻² μm⁻¹

H ₂ O 20 mm, O ₃ 3.4 mm								
Wave Length nm	Air Mass	0	α = 1.3			β = 0.02		
			1	2	3	4	7	10
290		482.0	0.0	0.0	0.0	0.0	0.0	0.0
295		584.0	0.0	0.0	0.0	0.0	0.0	0.0
300		514.0	4.5	0.0	0.0	0.0	0.0	0.0
305		603.0	12.5	0.0	0.0	0.0	0.0	0.0
310		689.0	33.5	2.0	0.0	0.0	0.0	0.0
315		764.0	87.1	10.0	1.0	0.1	0.0	0.0
320		830.0	222.2	59.0	16.0	4.3	0.1	0.0
325		975.0	295.6	90.0	27.0	8.2	0.2	0.0
330		1059.0	363.6	125.0	43.0	14.7	0.6	0.0
335		1081.0	420.3	163.0	64.0	24.7	1.5	0.1
340		1074.0	472.9	208.0	92.0	40.4	3.4	0.3
345		1069.0	492.4	227.0	104.0	48.1	4.7	0.5
350		1093.0	526.6	254.0	122.0	58.9	6.6	0.7
355		1083.0	545.7	275.0	139.0	69.8	8.9	1.1
360		1068.0	562.9	297.0	156.0	82.4	12.1	1.8
365		1132.0	614.8	334.0	181.0	98.5	15.8	2.5
370		1181.0	661.0	370.0	207.0	115.9	20.3	3.6
375		1157.0	667.3	385.0	222.0	128.0	24.6	4.7
380		1120.0	665.6	396.0	235.0	139.7	29.3	6.2
385		1098.0	667.5	406.0	247.0	150.0	33.7	7.6
390		1098.0	682.8	425.0	264.0	164.2	39.5	9.5
395		1189.0	756.3	481.0	306.0	194.7	50.1	12.9
400		1429.0	929.7	605.0	394.0	256.1	70.5	19.4
405		1644.0	1085.9	717.0	474.0	312.9	90.2	26.0
410		1751.0	1174.0	787.0	528.0	353.9	106.7	32.2
415		1774.0	1207.4	822.0	559.0	380.7	120.0	37.8
420		1747.0	1207.0	834.0	576.0	398.0	131.3	43.3
425		1693.0	1187.3	833.0	584.0	409.5	141.2	48.7
430		1639.0	1166.7	830.0	591.0	420.8	151.8	54.7
435		1663.0	1201.5	868.0	627.0	453.2	170.9	64.5
440		1810.0	1327.3	973.0	714.0	523.5	206.4	81.4
445		1922.0	1430.6	1065.0	793.0	589.9	243.2	100.3
450		2006.0	1515.4	1145.0	865.0	653.3	281.6	121.4
455		2057.0	1565.6	1192.0	907.0	690.3	304.4	134.2
460		2066.0	1584.3	1215.0	932.0	714.4	322.1	145.3
465		2048.0	1582.2	1222.0	944.0	729.6	336.5	155.2
470		2033.0	1582.4	1232.0	959.0	746.2	351.9	165.9
475		2044.0	1602.8	1257.0	986.0	772.9	372.7	179.7
480		2074.0	1638.4	1294.0	1023.0	807.8	398.3	196.4
485		1976.0	1572.6	1252.0	996.0	792.7	399.6	201.4
490		1950.0	1563.4	1253.0	1005.0	805.7	415.3	214.0
495		1960.0	1583.0	1279.0	1033.0	834.1	439.5	231.5
500		1942.0	1580.1	1286.0	1046.0	851.1	458.4	246.9
505		1920.0	1567.5	1280.0	1045.0	853.1	464.2	252.6
510		1882.0	1541.8	1263.0	1035.0	847.7	466.1	256.2

Table 1. (Continued)

H ₂ O 20 mm, O ₃ 3.4 mm								
Wave Length nm	Air Mass	0	α = 1.3			β = 0.02		
			1	2	3	4	7	10
515		1833.0	1506.8	1239.0	1018.0	836.9	464.9	258.2
520		1833.0	1511.9	1247.0	1029.0	848.4	476.1	267.1
525		1852.0	1532.7	1268.0	1050.0	868.8	492.5	279.2
530		1842.0	1529.6	1270.0	1055.0	875.8	501.5	287.2
535		1818.0	1514.7	1262.0	1052.0	876.1	506.7	293.1
540		1783.0	1490.5	1246.0	1042.0	870.8	508.7	297.2
545		1754.0	1471.2	1234.0	1035.0	868.1	512.3	302.3
550		1725.0	1451.7	1222.0	1028.0	865.2	515.7	307.3
555		1720.0	1450.4	1223.0	1031.0	869.6	521.4	312.7
560		1695.0	1432.2	1210.0	1022.0	863.9	521.1	314.3
565		1705.0	1443.0	1222.0	1035.0	875.9	531.5	322.5
570		1712.0	1452.3	1232.0	1045.0	886.5	541.1	330.3
575		1719.0	1461.1	1242.0	1056.0	897.2	550.9	338.3
580		1715.0	1460.5	1244.0	1059.0	902.1	557.2	344.2
585		1712.0	1460.8	1247.0	1064.0	907.6	563.9	350.3
590		1700.0	1453.4	1243.0	1062.0	908.3	567.6	354.7
595		1682.0	1440.8	1234.0	1057.0	905.6	596.2	357.8
600		1666.0	1429.9	1227.0	1053.0	903.9	571.5	361.3
605		1647.0	1420.2	1225.0	1056.0	910.7	583.9	374.4
610		1635.0	1416.5	1227.0	1063.0	921.2	599.1	389.6
620		1602.0	1401.0	1225.0	1072.0	937.2	626.9	419.3
630		1570.0	1386.0	1224.0	1080.0	953.5	656.0	451.3
640		1544.0	1375.8	1226.0	1092.0	973.4	688.7	487.3
650		1511.0	1359.0	1222.0	1099.0	988.8	719.4	523.4
660		1486.0	1344.0	1216.0	1100.0	995.6	737.3	546.0
670		1456.0	1325.0	1206.0	1097.0	998.6	752.7	567.3
680		1427.0	1306.2	1196.0	1095.0	1001.9	768.5	589.4
690		1402.0	1290.9	1189.0	1094.0	1007.5	786.4	613.8
698		1374.6	1090.0	946.0	833.0	739.7	530.2	387.7
700		1369.0	1267.8	1174.0	1087.0	1006.9	799.7	635.1
710		1344.0	1248.0	1159.0	1076.0	999.2	800.0	640.5
720		1314.0	1223.4	1139.0	1060.0	987.3	796.8	643.1
728		1295.5	1081.0	963.0	867.0	784.8	592.9	454.4
730		1290.0	1204.2	1124.0	1049.0	979.6	796.9	648.3
740		1260.0	1179.3	1104.0	1033.0	966.9	792.8	650.0
750		1235.0	1158.9	1088.0	1021.0	957.7	791.4	654.0
762		1205.5	854.3	695.0	575.0	478.6	273.2	143.8
770		1185.0	1117.8	1054.0	995.0	938.2	787.4	660.9
780		1159.0	1096.1	1037.0	980.0	927.1	784.1	663.2
790		1134.0	1075.2	1019.0	967.0	916.4	781.0	665.7
800		1109.0	1054.1	1002.0	952.0	905.3	777.5	667.7
806		1095.1	939.2	856.0	788.0	729.1	587.2	479.3
825		1048.0	1000.0	954.0	910.0	868.6	754.5	655.4
830		1036.0	989.0	945.0	902.0	861.3	749.8	652.8
835		1024.5	979.0	936.0	894.0	854.3	745.4	650.4

Table 1. (Continued)

Air Mass Wave Length nm	0	$\alpha = 1.3$ $\beta = 0.02$					
		1	2	3	4	7	10
846	998.1	510.8	377.0	296.0	239.5	140.2	89.0
860	968.0	542.9	417.0	337.0	280.1	174.7	116.8
870	947.0	486.4	360.0	284.0	230.4	136.3	87.4
875	936.5	481.3	357.0	281.0	228.6	135.5	87.1
887	912.5	480.4	360.0	286.0	234.6	141.8	92.7
900	891.0	480.6	364.0	292.0	241.3	148.8	98.9
907	882.8	487.2	373.0	302.0	250.6	157.1	105.8
915	874.5	493.9	382.0	311.0	260.2	165.8	113.2
925	863.5	298.0	188.0	131.0	96.4	44.8	23.8
930	858.0	237.0	137.0	89.0	61.3	24.7	11.7
940	847.0	335.1	224.0	163.0	124.2	63.2	36.1
950	837.0	316.9	208.0	149.0	112.6	55.8	31.2
955	828.5	343.0	233.6	172.7	133.2	69.9	40.9
965	811.5	367.6	260.0	197.9	156.4	87.1	53.5
975	794.0	615.6	544.1	491.3	448.7	354.0	287.4
985	776.0	580.9	506.2	452.3	409.4	316.2	252.6
1018	719.2	657.9	601.8	550.5	503.6	385.5	295.0
1082	620.0	544.0	477.4	418.9	367.6	248.3	167.8
1094	602.0	492.3	446.6	412.1	383.6	318.3	270.2
1098	596.0	534.3	479.0	429.4	384.9	277.3	199.8
1101	591.8	535.4	505.6	480.9	459.0	403.6	358.0
1128	560.5	143.2	80.3	51.3	35.0	13.7	6.4
1131	557.0	161.3	95.3	63.3	44.7	19.0	9.5
1137	550.1	151.7	87.8	57.4	40.0	16.5	8.0
1144	542.0	202.7	133.1	95.9	72.5	36.5	20.8
1147	538.5	185.0	117.3	82.3	60.8	29.0	15.8
1178	507.0	423.2	353.3	294.9	246.2	143.2	83.3
1189	496.0	426.2	366.3	314.7	270.5	171.6	108.9
1193	492.0	449.3	427.0	408.4	392.0	350.2	315.4
1222	464.3	415.0	371.0	331.6	296.4	211.7	151.2
1236	451.2	414.1	380.0	348.7	320.4	247.3	191.1
1264	426.5	348.6	313.9	286.8	263.8	209.3	167.5
1276	416.7	362.8	337.5	317.3	299.9	257.5	223.7
1288	406.8	367.6	332.2	300.2	271.3	200.2	147.7
1314	386.1	315.6	258.0	210.9	172.4	94.2	51.5
1335	369.7	201.6	155.3	126.6	106.4	69.2	48.6
1384	343.7	6.0	1.1	0.3	0.1	0.0	0.0
1432	321.0	47.1	21.1	11.3	6.7	1.9	0.7
1457	308.6	90.1	53.7	36.0	25.6	11.2	5.7
1472	301.4	81.6	47.1	30.8	21.5	8.9	4.4
1542	270.4	252.2	235.2	219.3	204.5	165.9	134.5
1572	257.3	234.5	223.5	214.6	206.8	187.4	171.4
1599	245.4	227.5	219.0	211.0	204.8	188.5	174.8
1608	241.5	219.5	209.0	201.0	193.3	174.9	159.9
1626	233.6	217.5	210.0	203.0	197.1	182.2	169.7
1644	225.6	208.2	200.0	193.0	186.7	171.4	158.6
1650	223.0	205.9	198.0	191.0	184.8	169.7	157.2

Table 1. (Continued)

Air Mass Wave Length nm	0	$\alpha = 1.3$ $\beta = 0.02$					
		1	2	3	4	7	10
1676	212.1	191.3	173.0	156.0	140.3	103.0	75.6
1732	187.9	169.7	153.0	138.0	124.9	92.0	67.7
1782	166.6	143.5	124.0	107.0	91.8	58.8	37.6
1862	138.2	4.2	1.0	0.3	0.1	0.0	0.0
1955	112.9	44.7	30.0	22.0	17.4	9.4	5.7
2008	102.0	72.6	60.0	51.0	43.0	24.4	10.1
2014	101.2	78.2	68.0	61.0	54.6	39.6	28.0
2057	95.6	72.7	63.0	56.0	49.4	34.7	23.2
2124	87.4	73.1	61.0	51.0	42.9	25.1	14.7
2156	83.8	69.0	57.0	47.0	38.5	21.4	12.0
2201	78.9	69.0	65.0	61.0	58.4	51.4	45.8
2266	72.4	64.3	61.0	58.0	55.5	49.6	44.9
2320	67.6	59.6	56.0	53.0	51.1	45.4	40.8
2338	66.3	57.0	53.0	50.0	47.2	40.7	35.6
2356	65.1	54.2	50.0	46.0	42.9	35.5	29.7
2388	62.8	37.5	30.0	25.0	22.1	15.6	11.8
2415	61.0	33.9	26.0	22.0	18.6	12.5	9.1
2453	58.3	31.0	24.0	19.0	16.1	10.5	7.5
2494	55.4	21.2	14.0	10.0	8.0	4.2	2.5
2537	52.4	4.8	2.0	1.0	0.4	0.1	0.0
2900	35.0	3.0	1.0	0.3	0.1	0.0	0.0
2941	33.4	6.2	3.0	2.0	1.1	0.4	0.2
2954	32.8	5.9	3.0	2.0	1.1	0.3	0.1
2973	32.1	9.0	5.0	4.0	2.5	1.1	0.6
3005	30.8	8.1	5.0	3.0	2.1	0.9	0.4
3045	28.8	4.8	2.0	1.0	0.8	0.3	0.1
3056	28.2	5.1	3.0	1.0	0.9	0.3	0.1
3097	26.2	3.3	1.0	1.0	0.4	0.1	0.0
3132	24.9	7.1	4.0	3.0	2.0	0.9	0.4
3156	24.1	19.3	17.0	16.0	14.5	11.4	8.9
3204	22.5	2.2	1.0	0.2	0.0	0.0	0.0
3214	22.1	3.5	2.0	1.0	0.6	0.2	0.1
3245	21.1	4.1	2.0	1.0	0.8	0.3	0.1
3260	20.6	3.8	2.0	1.0	0.7	0.2	0.1
3285	19.7	14.7	13.0	11.0	9.7	6.5	4.0
3317	18.8	13.4	11.0	9.0	7.9	4.5	1.8
3344	18.1	4.4	2.0	2.0	1.0	0.4	0.2
3403	16.5	12.7	11.0	10.0	8.9	6.5	4.5
3450	15.6	13.0	12.0	11.0	10.2	8.4	7.0
3507	14.5	12.9	12.0	12.0	11.3	10.2	9.3
3538	14.2	12.1	11.0	11.0	10.1	8.7	7.6
3573	13.8	11.3	9.0	7.0	6.1	3.3	1.8
3633	13.1	11.1	10.0	10.0	9.4	8.4	7.7
3673	12.6	9.4	8.2	8.0	7.0	5.7	4.9
3696	12.3	10.8	10.0	10.0	9.3	8.4	7.8
3712	12.2	11.2	11.0	11.0	10.2	9.6	9.0

Table 1. (Continued)

		H ₂ O 20 mm, O ₃ 3.4 mm						
Wave Length nm	Air Mass	$\alpha = 1.3$			$\beta = 0.02$			
		0	1	2	3	4	7	10
3765	11.5		9.8	9.0	9.0	8.2	7.3	6.7
3812	11.0		9.2	8.0	8.0	7.6	6.7	6.0
3888	10.4		8.4	8.0	7.0	6.3	5.0	3.9
3923	10.1		8.3	7.0	7.0	6.4	5.2	4.2
3948	9.9		8.1	7.0	7.0	6.2	5.0	4.0
4045	9.1		6.9	6.0	5.0	4.7	3.2	2.1
Total Irradiance W m ⁻²	1353		956.2	798.2	683.6	594.2	412.4	301.6

Table 2. Solar Spectral Irradiance for Different Air Masses, W m⁻² μm^{-1}

		H ₂ O 20 mm, O ₃ 3.4 mm						
Wave Length nm	Air Mass	$\alpha = 1.3$			$\beta = 0.02$			
		0	1	2	3	4	7	10
290	482.0	0.0	0.0	0.0	0.0	0.0	0.0	0.0
295	584.0	0.0	0.0	0.0	0.0	0.0	0.0	0.0
300	514.0	4.1	0.0	0.0	0.0	0.0	0.0	0.0
305	603.0	11.4	0.0	0.0	0.0	0.0	0.0	0.0
310	689.0	30.6	1.0	0.0	0.0	0.0	0.0	0.0
315	764.0	79.7	8.0	1.0	0.1	0.0	0.0	0.0
320	830.0	203.5	50.0	12.0	3.0	0.0	0.0	0.0
325	975.0	271.2	75.0	21.0	5.8	0.1	0.0	0.0
330	1059.0	334.1	105.0	33.0	10.5	0.3	0.0	0.0
335	1081.0	386.9	138.0	50.0	17.7	0.8	0.0	0.0
340	1074.0	436.0	177.0	72.0	29.2	2.0	0.1	
345	1069.0	454.6	193.0	82.0	35.0	2.7	0.2	
350	1093.0	486.9	217.0	97.0	43.0	3.8	0.3	
355	1083.0	505.4	236.0	110.0	51.3	5.2	0.5	
360	1068.0	522.0	255.0	125.0	60.9	7.1	0.8	
365	1132.0	570.9	288.0	145.0	73.2	9.4	1.2	
370	1181.0	614.6	320.0	166.0	86.6	12.2	1.7	
375	1157.0	621.2	334.0	179.0	96.2	14.9	2.3	
380	1120.0	620.4	344.0	190.0	105.4	17.9	3.0	
385	1098.0	622.9	353.0	200.0	113.7	20.8	3.8	
390	1098.0	638.0	371.0	215.0	125.1	24.5	4.8	
395	1189.0	707.4	421.0	250.0	149.0	31.4	6.6	
400	1429.0	870.5	530.0	323.0	196.8	44.5	10.1	
405	1644.0	1017.8	630.0	390.0	241.5	57.3	13.6	
410	1751.0	1101.5	693.0	436.0	274.2	68.3	17.0	
415	1774.0	1134.0	725.0	463.0	296.2	77.4	20.2	
420	1747.0	1134.7	737.0	479.0	310.9	85.2	23.2	
425	1693.0	1117.2	737.0	487.0	321.1	92.3	26.5	
430	1639.0	1098.8	737.0	494.0	331.1	99.8	30.1	
435	1663.0	1132.7	771.0	525.0	357.9	113.1	35.7	
440	1810.0	1252.4	867.0	600.0	414.8	137.4	45.5	
445	1922.0	1350.9	949.0	667.0	469.1	162.9	56.5	
450	2006.0	1432.2	1022.0	730.0	521.2	189.7	69.0	

Table 2. (Continued)

		H ₂ O 20 mm, O ₃ 3.4 mm						
Wave Length nm	Air Mass	$\alpha = 1.3$			$\beta = 0.04$			
		0	1	2	3	4	7	10
455	2057.0	1480.8	1066.0	767.0	552.5	206.1	76.9	
460	2066.0	1499.7	1089.0	790.0	573.6	219.4	83.9	
465	2048.0	1498.9	1097.0	803.0	587.6	203.4	90.3	
470	2033.0	1500.2	1107.0	817.0	602.7	242.2	97.3	
475	2044.0	1520.6	1131.0	842.0	626.1	257.8	106.1	
480	2074.0	1555.5	1167.0	875.0	656.3	276.9	116.8	
485	1976.0	1494.1	1130.0	854.0	645.8	279.2	120.7	
490	1950.0	1486.3	1133.0	864.0	658.2	291.5	129.1	
495	1960.0	1506.0	1157.0	889.0	683.2	309.9	140.6	
500	1942.0	1504.1	1165.0	902.0	698.9	324.7	150.9	
505	1920.0	1493.2	1161.0	903.0	702.3	330.3	155.4	
510	1882.0	1469.5	1147.0	896.0	699.6	333.1	158.6	
515	1833.0	1437.0	1127.0	883.0	692.4	333.6	160.8	
520	1833.0	1442.8	1136.0	894.0	703.5	343.1	167.3	
525	1852.0	1463.5	1156.0	914.0	722.2	356.4	175.9	
530	1842.0	1461.3	1159.0	920.0	729.7	364.3	181.9	
535	1818.0	1447.9	1153.0	918.0	731.5	369.6	186.7	
540	1783.0	1425.6	1140.0	911.0	728.7	372.4	190.4	
545	1754.0	1408.0	1130.0	907.0	728.0	376.4	194.6	
550	1725.0	1389.9	1120.0	902.0	727.0	380.3	198.9	
555	1720.0	1389.3	1122.0	907.0	732.2	385.9	203.4	
560	1695.0	1372.6	1111.0	900.0	728.8	387.0	205.5	
565	1705.0	1384.1	1124.0	912.0	740.4	396.1	211.9	
570	1712.0	1393.2	1134.0	923.0	750.8	404.6	218.0	
575	1719.0	1402.3	1144.0	933.0	761.3	413.3	224.4	
580	1715.0	1402.4	1147.0	938.0	766.9	419.4	229.3	
585	1712.0	1403.3	1150.0	943.0	772.9	425.7	234.5	
590	1700.0	1396.8	1148.0	943.0	774.9	429.8	238.4	
595	1682.0	1385.3	1141.0	940.0	774.0	432.4	241.6	
600	1666.0	1375.4	1135.0	937.0	773.8	435.4	245.0	
605	1647.0	1366.7	1134.0	941.0	780.9	446.2	254.9	
610	1635.0	1363.7	1137.0	949.0	791.2	459.1	266.4	
620	1602.0	1349.8	1137.0	958.0	807.5	483.1	289.0	
630	1570.0	1336.4	1137.0	968.0	824.1	508.2	313.4	
640	1544.0	1327.5	1141.0	981.0	843.8	536.3	340.9	
650	1511.0	1312.3	1140.0	990.0	859.6	563.0	369.0	
660	1486.0	1299.1	1136.0	993.0	867.9	579.8	387.3	
670	1456.0	1281.2	1127.0	992.0	872.8	594.7	405.1	
680	1427.0	1263.8	1119.0	991.0	877.9	609.9	423.7	
690	1402.0	1249.7	1114.0	993.0	885.1	626.8	443.9	
698	1374.6	1055.7	887.0	757.0	651.1	424.1	281.8	
700	1369.0	1228.1	1102.0	988.0	886.6	640.1	462.1	
710	1344.0	1209.6	1089.0	980.0	881.9	642.9	468.7	
720	1314.0	1186.5	1071.0	967.0	873.4	642.9	473.3	
728	1295.5	1048.6	906.0	792.0	695.4	479.8	335.8	
730	1290.0	1168.5	1058.0	959.0	868.5	645.5	479.7	
740	1260.0	1145.0	1040.0	945.0	859.0	644.5	483.6	

Table 2. (Continued)

Wave Length nm	Air Mass	0	$\alpha = 1.3$				$\beta = 0.04$	
			1	2	3	4	7	10
750	1235.0	1125.7	1026.0	935.0	852.6	645.7	489.0	
762	1205.5	830.3	656.0	528.0	427.1	223.8	108.2	
770	1185.0	1086.8	997.0	914.0	838.5	646.8	499.0	
780	1159.0	1066.2	981.0	902.0	803.1	646.2	503.1	
790	1134.0	1046.4	965.0	891.0	822.0	645.7	507.3	
800	1109.0	1026.3	950.0	879.0	813.5	644.8	511.1	
806	1095.1	914.7	812.0	728.0	655.8	487.8	367.8	
825	1048.0	974.6	906.0	843.0	783.8	630.4	507.0	
830	1036.0	964.4	898.0	836.0	777.8	627.3	506.0	
835	1024.5	954.6	889.0	829.0	772.1	624.5	505.1	
846	998.1	498.3	359.0	275.0	216.9	117.8	69.4	
860	968.0	529.8	397.0	313.0	254.1	147.4	91.6	
870	947.0	474.8	344.0	264.0	209.4	115.3	68.8	
875	936.5	470.0	340.0	262.0	207.8	114.7	68.6	
887	912.5	469.4	344.0	267.0	213.7	120.4	73.4	
900	891.0	470.0	348.0	273.0	220.1	126.7	78.7	
907	882.8	476.3	357.0	282.0	228.8	134.0	84.4	
915	874.5	482.9	365.0	291.0	237.8	141.7	90.4	
925	863.5	291.9	180.0	123.0	88.2	38.4	19.1	
930	858.0	232.0	131.0	83.0	56.2	21.2	9.4	
940	847.0	327.9	214.0	153.0	113.9	54.3	29.0	
950	837.0	310.2	199.0	140.0	103.3	48.0	25.2	
955	828.5	335.8	223.9	162.0	122.3	60.2	33.1	
965	811.5	360.0	249.3	185.8	143.8	75.2	43.4	
975	794.0	603.0	522.1	461.9	413.2	306.4	233.9	
985	776.0	569.2	486.0	425.4	377.3	274.2	206.0	
1018	719.2	645.1	578.7	519.1	465.6	336.0	242.5	
1082	620.0	534.3	460.5	396.9	342.0	218.9	140.2	
1094	602.0	483.6	431.0	390.7	357.3	281.0	226.2	
1098	596.0	524.9	462.3	407.2	358.6	245.0	167.4	
1101	591.8	526.0	488.0	456.0	427.6	356.5	300.0	
1128	560.5	140.8	77.6	48.7	32.7	12.2	5.4	
1131	557.0	158.6	92.1	60.1	41.7	16.9	8.0	
1137	550.1	149.2	84.9	54.6	37.4	14.7	6.8	
1144	542.0	199.3	128.7	91.2	67.8	32.4	17.6	
1147	538.5	181.9	113.4	78.2	56.9	25.8	13.4	
1178	507.0	416.5	342.1	281.0	230.8	127.9	70.9	
1189	496.0	419.5	354.8	300.1	253.8	153.6	92.9	
1193	492.0	442.2	413.6	389.4	367.8	313.3	269.1	
1222	464.3	408.7	359.7	316.6	278.7	190.1	129.6	
1236	451.2	407.8	368.6	333.2	301.1	222.3	164.2	
1264	426.5	343.5	304.7	274.3	248.7	188.7	144.4	
1276	416.7	357.6	327.9	303.8	283.0	232.6	193.5	
1288	406.8	362.4	322.8	287.5	256.1	181.0	127.9	
1314	386.1	311.2	250.9	202.3	163.1	85.4	44.8	
1335	369.7	198.8	151.1	121.5	100.6	62.8	42.3	
1384	343.7	6.0	1.1	0.3	0.1	0.0	0.0	

Table 2. (Continued)

Wave Length nm	Air Mass	0	$\alpha = 1.3$				$\beta = 0.04$	
			1	2	3	4	7	10
1432	321.0	46.5	20.5	10.9	6.4	1.7	0.6	
1457	308.6	89.0	52.4	34.7	24.4	10.3	5.1	
1472	301.4	80.6	46.0	29.7	20.5	8.2	3.9	
1542	270.4	249.3	229.9	211.9	195.4	153.2	120.0	
1572	257.3	231.9	218.6	207.6	197.8	173.4	153.4	
1599	245.4	225.0	214.0	204.0	196.1	174.7	156.8	
1608	241.5	217.0	205.0	194.0	185.1	162.2	143.5	
1626	233.6	215.2	205.0	197.0	188.9	169.2	152.6	
1644	225.6	206.0	196.0	187.0	179.0	159.2	142.8	
1650	223.0	204.0	193.0	185.0	177.2	157.8	141.6	
1676	212.1	189.3	169.0	151.0	134.7	95.9	68.2	
1732	187.9	168.0	150.0	134.0	120.1	85.9	61.4	
1782	166.6	142.2	121.0	104.0	88.4	55.0	34.2	
1862	138.2	4.1	1.0	0.3	0.1	0.0	0.0	
1955	112.9	44.4	30.0	22.0	16.8	8.9	5.2	
2008	102.0	72.0	59.0	50.0	41.6	23.1	9.4	
2014	101.2	78.0	67.0	59.0	52.9	37.5	25.9	
2057	95.6	72.0	62.0	54.0	47.9	32.8	21.5	
2124	87.4	72.6	60.0	50.0	41.6	23.8	13.7	
2156	83.8	68.5	56.0	46.0	37.3	20.4	11.1	
2201	78.9	68.5	64.0	60.0	56.8	48.9	42.6	
2266	72.4	63.8	60.0	57.0	54.0	47.3	41.9	
2320	67.6	59.2	55.0	52.0	49.7	43.3	38.2	
2338	66.3	56.6	52.0	49.0	45.9	38.9	33.3	
2356	65.1	53.8	49.0	45.0	41.7	33.9	27.8	
2388	62.8	37.3	30.0	25.0	21.5	14.9	11.0	
2415	61.0	33.6	26.0	21.0	18.1	12.0	8.5	
2453	58.3	30.6	23.0	19.0	15.7	10.1	7.0	
2494	55.4	21.0	14.0	10.0	7.8	4.0	2.4	
2537	52.4	4.8	2.0	1.0	0.4	0.1	0.0	
2900	35.0	3.0	1.0	0.3	0.1	0.0	0.0	
2941	33.4	6.2	3.0	2.0	1.1	0.4	0.2	
2954	32.8	5.9	3.0	2.0	1.0	0.3	0.1	
2973	32.1	9.0	5.0	4.0	2.5	1.1	0.5	
3005	30.8	8.1	5.0	3.0	2.1	0.9	0.4	
3045	28.8	4.8	2.0	1.0	0.8	0.2	0.1	
3056	28.2	5.1	2.0	1.0	0.9	0.3	0.1	
3097	26.2	3.3	1.0	1.0	0.4	0.1	0.0	
3132	24.9	7.0	4.0	3.0	1.9	0.8	0.4	
3156	24.1	19.2	17.0	16.0	14.2	11.0	8.5	
3204	22.5	2.2	1.0	0.3	0.1	0.0	0.0	
3214	22.1	3.5	2.0	1.0	0.5	0.2	0.1	
3245	21.1	4.1	2.0	1.0	0.8	0.3	0.1	
3260	20.6	3.8	2.0	1.0	0.7	0.2	0.1	
3285	19.7	14.7	13.0	11.0	9.6	6.3	3.8	
3317	18.8	13.3	11.0	9.0	7.8	4.3	1.7	

Table 2. (Continued)

		H ₂ O 20 mm, O ₃ 3.4 mm						
Wave Length nm	Air Mass	$\alpha = 1.3$			$\beta = 0.04$			
		0	1	2	3	4	7	10
3344	18.1	4.3	2.0	2.0	1.0	0.4	0.2	
2403	16.5	12.7	11.0	10.0	8.8	6.3	4.4	
3450	15.6	12.9	12.0	11.0	10.0	8.2	6.8	
3507	14.5	12.9	12.0	12.0	11.1	9.9	8.9	
3538	14.2	12.1	11.0	10.0	9.9	8.5	7.3	
3573	13.8	11.2	9.0	7.0	6.0	3.0	1.7	
3633	13.1	11.1	10.0	10.0	9.3	8.2	7.4	
3673	12.6	9.4	8.0	7.0	6.9	5.6	4.7	
3696	12.3	10.7	10.0	10.0	9.2	8.2	7.5	
3712	12.2	11.2	11.0	10.0	10.0	9.3	8.7	
3765	11.5	9.7	9.0	9.0	8.1	7.1	6.4	
3812	11.0	9.1	8.0	8.0	7.5	6.5	5.8	
3888	10.4	8.3	7.0	7.0	6.2	4.8	3.8	
3923	10.1	8.2	7.0	7.0	6.3	5.1	4.1	
3948	9.9	8.0	7.0	7.0	6.1	4.9	3.9	
4045	9.1	6.9	6.0	5.0	4.6	3.1	2.0	
Total Irradiance W m ⁻²	1353	924.5	748.5	623.7	527.7	340.8	233.49	

Table 3. Solar Spectral Irradiance for Different Air Masses
W m⁻² μm^{-1}

		H ₂ O 20 mm, O ₃ 3.4 mm						
Wave Length nm	Air Mass	$\alpha = 0.66$			$\beta = 0.085$			
		0	1	2	3	4	7	10
290	482.0	0.0	0.0	0.0	0.0	0.0	0.0	0.0
295	584.0	0.0	0.0	0.0	0.0	0.0	0.0	0.0
300	514.0	4.1	0.0	0.0	0.0	0.0	0.0	0.0
305	603.0	11.4	0.0	0.0	0.0	0.0	0.0	0.0
310	689.0	30.5	1.0	0.0	0.0	0.0	0.0	0.0
315	764.0	79.4	8.0	1.0	0.1	0.0	0.0	0.0
320	830.0	202.6	49.0	12.0	2.9	0.0	0.0	0.0
325	975.0	269.5	75.0	21.0	5.7	0.1	0.0	0.0
330	1059.0	331.6	104.0	33.0	10.2	0.3	0.0	0.0
335	1081.0	383.4	136.0	48.0	17.1	0.8	0.0	0.0
340	1074.0	431.3	173.0	70.0	27.9	1.8	0.1	0.1
345	1069.0	449.2	189.0	79.0	33.3	2.5	0.2	0.2
350	1093.0	480.5	211.0	93.0	40.8	3.5	0.3	0.3
355	1083.0	498.0	229.0	105.0	48.4	4.7	0.5	0.5
360	1068.0	513.7	247.0	119.0	57.2	6.4	0.7	0.7
365	1132.0	561.3	278.0	138.0	68.4	8.3	1.0	1.0
370	1181.0	603.5	308.0	158.0	80.5	10.7	1.4	1.4
375	1157.0	609.4	321.0	169.0	89.0	13.0	1.9	1.9
380	1120.0	608.0	330.0	179.0	97.2	15.6	2.5	2.5
385	1098.0	609.8	339.0	188.0	104.5	17.9	3.1	3.1
390	1098.0	623.9	355.0	201.0	114.5	21.0	3.9	3.9
395	1189.0	691.2	402.0	234.0	135.8	26.7	5.2	5.2

Table 3. (Continued)

		H ₂ O 20 mm, O ₃ 3.4 mm						
Wave Length nm	Air Mass	$\alpha = 0.66$			$\beta = 0.085$			
		0	1	2	3	4	7	10
400	1429.0	849.9	505.0	301.0	178.8	37.6	7.9	7.9
405	1644.0	992.8	600.0	362.0	218.7	48.2	10.6	10.6
410	1751.0	1073.7	658.0	404.0	247.5	57.1	13.2	13.2
415	1774.0	1104.5	688.0	428.0	266.5	64.3	15.5	15.5
420	1747.0	1104.3	698.0	441.0	278.9	70.4	17.8	17.8
425	1693.0	1086.5	697.0	448.0	287.2	75.9	20.1	20.1
430	1639.0	1067.9	696.0	453.0	295.4	81.7	22.6	22.6
435	1663.0	1100.1	728.0	481.0	318.4	92.2	26.7	26.7
440	1810.0	1215.5	816.0	548.0	368.2	111.5	33.8	33.8
445	1922.0	1310.0	893.0	609.0	415.3	131.6	41.7	41.7
450	2006.0	1388.4	961.0	665.0	460.3	152.6	50.6	50.6
455	2057.0	1434.8	1001.0	698.0	486.9	165.2	56.1	56.1
460	2066.0	1452.2	1021.0	718.0	504.4	175.2	60.8	60.8
465	2048.0	1450.7	1028.0	728.0	515.7	183.3	65.1	65.1
470	2033.0	1451.2	1036.0	739.0	527.9	192.0	69.8	69.8
475	2044.0	1470.3	1058.0	761.0	547.3	203.7	75.8	75.8
480	2074.0	1503.4	1090.1	790.0	572.6	218.1	83.1	83.1
485	1976.0	1443.3	1054.0	770.0	562.4	219.2	85.4	85.4
490	1950.0	1435.2	1056.0	777.0	572.2	228.2	91.0	91.0
495	1960.0	1453.6	1078.0	800.0	592.9	241.9	98.7	98.7
500	1942.0	1451.2	1084.0	810.0	605.6	252.7	105.5	105.5
505	1920.0	1440.0	1080.0	810.0	607.6	256.4	108.2	108.2
510	1882.0	1416.8	1067.0	803.0	604.4	257.8	110.0	110.0
515	1833.0	1384.9	1046.0	791.0	597.3	257.6	111.1	111.1
520	1833.0	1390.0	1054.0	799.0	606.1	264.3	115.2	115.2
525	1852.0	1409.5	1073.0	816.0	621.3	273.9	120.7	120.7
530	1842.0	1406.9	1075.0	821.0	626.9	279.4	124.5	124.5
535	1818.0	1393.6	1068.0	819.0	627.7	282.8	127.4	127.4
540	1783.0	1371.7	1055.0	812.0	624.5	284.4	129.5	129.5
545	1754.0	1354.2	1046.0	807.0	623.2	286.8	132.0	132.0
550	1725.0	1336.6	1036.0	802.0	621.7	289.2	134.5	134.5
555	1720.0	1335.7	1037.0	806.0	625.5	293.0	137.2	137.2
560	1695.0	1319.2	1027.0	799.0	622.0	293.3	138.3	138.3
565	1705.0	1330.0	1037.0	809.0	631.3	299.6	142.2	142.2
570	1712.0	1338.4	1046.0	818.0	639.5	305.6	146.0	146.0
575	1719.0	1346.9	1055.0	827.0	647.8	311.6	149.9	149.9
580	1715.0	1346.7	1057.0	830.0	652.0	315.7	152.8	152.8
585	1712.0	1347.3	1060.0	834.0	656.6	320.0	156.0	156.0
590	1700.0	1340.7	1057.0	834.0	657.7	322.6	158.3	158.3
595	1682.0	1329.4	1051.0	830.0	656.4	324.1	160.0	160.0
600	1666.0	1319.6	1045.0	828.0	655.8	325.9	162.0	162.0
605	1647.0	1311.0	1044.0	831.0	661.3	333.6	168.2	168.2
610	1635.0	1307.9	1046.0	837.0	669.6	342.8	175.5	175.5
620	1602.0	1294.2	1046.0	845.0	682.4	359.9	189.7	189.7
630	1570.0	1280.9	1045.0	853.0	695.6	377.8	205.2	205.2
640	1544.0	1272.1	1048.0	863.0	711.4	397.9	222.5	222.5
650	1511.0	1257.1	1046.0	870.0	723.9	416.9	240.1	240.1

Table 3. (Continued)

Air Mass Wave Length nm	0	$\alpha = 0.66$ $\beta = 0.085$					
		1	2	3	4	7	10
660	1486.0	1244.2	1042.0	872.0	730.2	428.6	251.6
670	1456.0	1226.8	1034.0	871.0	733.8	438.9	262.5
680	1427.0	1209.9	1026.0	870.0	737.4	449.5	273.9
690	1402.0	1196.2	1021.0	871.0	742.9	461.3	286.5
698	1374.6	1010.3	813.0	664.0	546.1	311.8	181.6
700	1369.0	1175.3	1009.0	866.0	743.7	470.6	297.7
710	1344.0	1157.4	997.0	858.0	739.2	472.1	301.5
720	1314.0	1135.1	981.0	847.0	731.7	471.6	304.0
728	1295.5	1003.1	829.0	693.0	582.3	351.7	215.5
730	1290.0	1117.8	969.0	839.0	727.1	473.0	307.7
740	1260.0	1095.1	952.0	827.0	718.9	471.9	309.8
750	1235.0	1076.6	938.0	818.0	713.2	472.4	313.0
762	1205.5	794.0	600.0	462.0	357.1	163.6	69.1
770	1185.0	1039.2	911.0	799.0	700.8	472.7	318.8
780	1159.0	1019.4	897.0	789.0	693.6	472.0	321.1
790	1134.0	1000.3	882.0	778.0	686.7	471.4	323.6
800	1109.0	981.2	868.0	768.0	679.4	470.5	325.8
806	1095.1	874.4	742.0	636.0	547.7	355.9	234.4
825	1048.0	931.6	828.0	736.0	654.3	459.6	322.8
830	1036.0	921.8	820.0	730.0	649.3	457.3	322.1
835	1024.5	912.4	813.0	724.0	644.4	455.2	321.5
846	998.1	476.2	328.0	240.0	181.0	85.9	44.2
860	968.0	506.4	363.0	274.0	212.0	107.4	58.3
870	947.0	453.8	314.0	231.0	174.7	84.0	43.8
875	936.5	449.2	311.0	229.0	173.4	83.6	43.7
887	912.5	448.6	314.0	233.0	178.3	87.7	46.7
900	891.0	448.9	318.0	238.0	183.7	92.3	50.0
907	882.8	455.2	326.0	246.0	190.9	97.6	53.7
915	874.5	461.5	334.0	254.0	198.5	103.2	57.5
925	863.5	279.0	165.0	107.0	73.6	28.0	12.1
930	858.0	221.8	119.0	72.0	46.9	15.4	6.0
940	847.0	313.4	196.0	133.0	95.0	39.6	18.5
950	837.0	296.5	182.0	122.0	86.3	35.0	16.0
955	828.5	321.1	205.0	142.0	102.3	44.1	21.2
965	811.5	344.4	228.0	162.3	120.4	55.1	27.8
975	794.0	576.4	477.1	403.4	345.0	223.5	149.0
985	776.0	544.1	444.0	371.6	315.0	199.9	131.2
1018	719.2	616.8	529.0	453.7	389.1	245.4	154.8
1082	620.0	511.0	421.2	347.2	286.2	160.2	89.7
1094	602.0	462.6	394.3	341.8	299.0	205.8	144.9
1098	596.0	502.1	422.9	356.3	300.1	179.4	107.3
1101	591.8	503.1	446.5	399.0	357.9	261.1	192.2
1128	560.5	134.7	71.0	42.6	27.4	8.9	3.5
1131	557.0	151.7	84.3	52.6	34.9	12.4	5.1
1137	550.1	142.7	77.7	47.8	31.3	10.8	4.4

Table 3. (Continued)

Air Mass Wave Length nm	0	$\alpha = 0.66$ $\beta = 0.085$					
		1	2	3	4	7	10
1144	542.0	190.7	117.8	79.9	56.8	23.8	11.3
1147	538.5	174.1	103.9	68.5	47.7	18.9	8.6
1178	507.0	398.5	313.3	246.3	193.6	94.0	45.7
1189	496.0	401.5	325.0	263.1	212.9	112.9	59.9
1193	492.0	423.2	378.9	341.4	308.6	230.4	173.5
1222	464.3	391.2	329.6	277.7	234.0	140.0	83.7
1236	451.2	390.5	337.9	292.4	253.0	164.0	106.3
1264	426.5	328.9	279.4	240.9	209.1	139.4	93.7
1276	416.7	342.4	300.7	266.8	238.0	171.8	125.5
1288	406.8	347.1	296.1	252.6	215.5	133.9	83.1
1314	386.1	298.1	230.2	177.8	137.3	63.2	29.1
1335	369.7	190.5	138.7	106.9	84.8	46.6	27.6
1384	343.7	5.7	1.0	0.3	0.1	0.0	0.0
1432	321.0	44.6	18.9	9.6	5.4	1.3	0.4
1457	308.6	85.4	48.2	30.6	20.6	7.7	3.3
1472	301.4	77.3	42.3	26.2	17.3	6.1	2.6
1542	270.4	239.3	211.7	187.4	165.8	114.9	79.6
1572	257.3	222.6	201.4	183.0	168.0	130.2	101.9
1599	245.4	216.0	197.0	181.0	166.7	131.5	104.5
1608	241.5	208.5	189.0	172.0	157.4	122.1	95.7
1626	233.6	206.7	189.0	174.0	160.7	127.5	101.9
1644	225.6	197.9	180.0	166.0	152.4	120.1	95.5
1650	223.0	195.7	178.0	164.0	150.9	119.1	94.7
1676	212.1	181.9	156.0	134.0	114.8	72.4	45.7
1732	187.9	161.5	139.0	119.0	102.5	65.1	41.3
1782	166.6	136.7	112.0	92.0	75.6	41.8	23.1
1862	138.2	4.0	1.0	0.3	0.1	0.0	0.0
1955	112.9	42.7	28.0	20.0	14.5	6.8	3.6
2008	102.0	69.4	55.0	44.0	35.8	17.7	6.4
2014	101.2	74.7	62.0	53.0	45.5	28.8	17.8
2057	95.6	69.5	58.0	49.0	41.3	25.3	14.8
2124	87.4	70.0	56.0	45.0	35.9	18.4	9.5
2156	83.8	66.0	52.0	41.0	32.3	15.8	7.7
2201	78.9	66.1	59.0	54.0	49.1	38.0	29.7
2266	72.4	61.6	56.0	51.0	46.8	36.8	29.3
2320	67.6	57.2	52.0	47.0	43.2	33.8	26.8
2338	66.3	54.7	49.0	44.0	39.9	30.4	23.4
2356	65.1	52.0	46.0	41.0	36.3	26.5	19.6
2388	62.8	36.0	28.0	23.0	18.7	11.7	7.8
2415	61.0	32.5	24.0	19.0	15.8	9.4	6.0
2453	58.3	29.6	22.0	17.0	13.7	7.9	5.0
2494	55.4	20.3	13.0	9.0	6.8	3.2	1.7
2537	52.4	4.6	2.0	1.0	0.4	0.1	0.0
2900	35.0	2.9	1.0	0.3	0.2	0.0	0.0
2941	33.4	6.0	3.0	2.0	1.0	0.3	0.1
2954	32.8	6.0	3.0	2.0	0.9	0.3	0.1

Table 3. (Continued)

		H ₂ O 20 mm, O ₃ 3.4 mm						
Wave Length nm	Air Mass	$\alpha = 0.66$			$\beta = 0.085$			
		0	1	2	3	4	7	10
2973		32.1	8.7	5.0	3.0	2.2	0.9	0.4
3005		30.8	8.0	4.0	3.0	1.8	0.7	0.3
3045		28.8	4.7	2.0	1.0	0.7	0.2	0.1
3056		28.2	4.9	2.0	1.0	0.8	0.2	0.1
3097		26.2	3.2	1.0	1.0	0.4	0.1	0.0
3132		24.9	6.8	4.0	3.0	1.7	0.7	0.3
3156		24.1	18.7	16.0	14.0	12.6	8.9	0.3
3204		22.5	2.1	1.0	0.3	0.2	0.0	0.0
3214		22.1	3.4	2.0	1.0	0.5	0.1	0.0
3245		21.1	3.9	2.0	1.0	0.7	0.2	0.1
3260		20.6	3.7	2.0	1.0	0.6	0.2	0.1
3285		19.7	14.2	12.0	10.0	8.5	5.1	2.8
3317		18.8	12.9	10.0	8.0	6.9	3.5	1.3
3344		18.1	4.2	2.0	1.0	0.9	0.3	0.1
3403		16.5	12.3	10.0	9.0	7.8	5.1	3.2
3450		15.6	12.5	11.0	10.0	8.9	6.7	5.0
3507		14.5	12.5	11.0	11.0	9.9	8.1	6.7
3538		14.2	11.8	11.0	10.0	8.8	6.9	5.5
3573		13.8	10.9	9.0	7.0	5.4	2.6	1.3
3633		13.1	10.8	10.0	9.0	8.3	6.7	5.5
3673		12.6	9.1	8.0	7.0	6.1	4.6	3.5
3696		12.3	10.4	10.0	9.0	8.2	6.7	5.6
3712		12.2	10.9	10.0	10.0	9.0	7.6	6.5
3765		11.5	9.5	9.0	8.0	7.2	5.9	4.8
3812		11.0	8.9	8.0	7.0	6.7	5.4	4.4
3888		10.4	8.1	7.0	6.0	5.6	4.0	2.9
3923		10.1	8.0	7.0	6.0	5.6	4.2	3.1
3948		9.9	7.8	7.0	6.0	5.5	4.0	3.0
4045		9.1	6.7	6.0	5.0	4.1	2.6	1.5
Total Irradiance W m ⁻²		1353	889.3	691.2	552.1	448.0	254.5	152.95

Table 4. (Continued)

		H ₂ O 20 mm, O ₃ 3.4 mm						
Wave Length nm	Air Mass	$\alpha = 0.66$			$\beta = 0.170$			
		0	1	2	3	4	7	10
340		1074.0	362.7	123.0	41.0	14.0	0.5	0.0
345		1069.0	378.4	134.0	47.0	16.8	0.7	0.0
350		1093.0	405.4	150.0	56.0	20.7	1.1	0.1
355		1083.0	420.8	164.0	64.0	24.7	1.4	0.1
360		1068.0	434.8	177.0	72.0	29.3	2.0	0.1
365		1132.0	475.7	200.0	84.0	35.3	2.6	0.2
370		1181.0	512.3	222.0	96.0	41.8	3.4	0.3
375		1157.0	518.0	232.0	104.0	46.5	4.2	0.4
380		1120.0	517.6	239.0	111.0	51.1	5.0	0.5
385		1098.0	519.9	246.0	117.0	55.2	5.9	0.6
390		1098.0	532.6	258.0	125.0	60.8	6.9	0.8
395		1189.0	590.8	294.0	146.0	72.5	8.9	1.1
400		1429.0	727.4	370.0	188.0	95.9	12.7	1.7
405		1644.0	850.8	440.0	228.0	117.9	16.3	2.3
410		1751.0	921.3	485.0	255.0	134.2	19.5	2.8
415		1774.0	948.8	507.0	271.0	145.2	22.2	3.4
420		1747.0	949.8	516.0	281.0	152.7	24.5	3.9
425		1693.0	935.6	517.0	286.0	157.9	26.7	4.5
430		1639.0	920.7	517.0	291.0	163.2	28.9	5.1
435		1663.0	949.5	542.0	310.0	176.7	32.9	6.1
440		1810.0	1050.3	609.0	354.0	205.2	40.1	7.8
445		1922.0	1133.5	668.0	394.0	232.5	47.7	9.8
450		2006.0	1202.2	721.0	432.0	258.8	55.7	12.0
455		2057.0	1243.7	752.0	455.0	274.9	60.8	13.4
460		2066.0	1260.1	769.0	469.0	285.9	64.9	14.7
465		2048.0	1260.1	775.0	477.0	293.5	68.4	15.9
470		2033.0	1261.8	783.0	486.0	301.6	72.1	17.2
475		2044.0	1279.6	801.0	501.0	313.9	77.0	18.9
480		2074.0	1309.6	827.0	522.0	329.7	83.0	20.9
485		1976.0	1258.5	802.0	510.0	325.1	84.0	21.7
490		1950.0	1252.6	805.0	517.0	332.0	88.0	23.3
495		1960.0	1269.8	823.0	533.0	345.3	93.9	25.5
500		1942.0	1268.8	829.0	542.0	353.9	98.7	27.5
505		1920.0	1260.2	827.0	543.0	356.3	100.8	28.5
510		1882.0	1240.9	818.0	539.0	355.7	101.9	29.2
515		1833.0	1214.0	804.0	533.0	352.7	102.5	29.8
520		1833.0	1219.5	811.0	540.0	359.1	105.7	31.1
525		1852.0	1237.6	827.0	553.0	369.3	110.2	32.9
530		1842.0	1236.4	830.0	557.0	373.9	113.1	34.2
535		1818.0	1225.6	826.0	557.0	375.5	115.1	35.3
540		1783.0	1207.3	817.0	554.0	374.8	116.4	36.1
545		1754.0	1192.8	811.0	552.0	375.2	118.0	37.1
550		1725.0	1178.2	805.0	550.0	375.4	119.6	38.1
555		1720.0	1178.3	807.0	553.0	378.8	121.8	39.2
560		1695.0	1164.7	800.0	550.0	377.8	122.6	39.8
565		1705.0	1175.0	810.0	558.0	384.6	125.9	41.2

Table 4. Solar Spectral Irradiance for Different Air Masses, W m⁻² μm⁻¹

		H ₂ O 20 mm, O ₃ 3.4 mm						
Wave Length nm	Air Mass	$\alpha = 0.66$			$\beta = 0.170$			
		0	1	2	3	4	7	10
290		482.0	0.0	0.0	0.0	0.0	0.0	0.0
295		584.0	0.0	0.0	0.0	0.0	0.0	0.0
300		514.0	3.4	0.0	0.0	0.0	0.0	0.0
305		603.0	9.4	0.0	0.0	0.0	0.0	0.0
310		689.0	25.4	1.0	0.0	0.0	0.0	0.0
315		764.0	66.2	6.0	0.0	0.0	0.0	0.0
320		830.0	169.2	34.0	7.0	1.4	0.0	0.0
325		975.0	225.5	52.0	12.0	2.8	0.0	0.0
330		1059.0	277.9	73.0	19.0	5.0	0.1	0.0
335		1081.0	321.8	96.0	29.0	8.5	0.2	0.0

Table 4. (Continued)

Wave Length nm	Air Mass	0	$\alpha = 0.66$ $\beta = 0.170$					
			1	2	3	4	7	10
570	1712.0	1183.3	818.0	565.0	390.7	129.0	42.6	
575	1719.0	1191.6	826.0	573.0	396.9	132.2	44.0	
580	1715.0	1192.3	829.0	576.0	400.6	134.6	45.2	
585	1712.0	1193.6	832.0	580.0	404.5	137.1	46.5	
590	1700.0	1188.6	831.0	581.0	406.3	138.9	47.5	
595	1682.0	1179.4	827.0	580.0	406.6	140.2	48.3	
600	1666.0	1171.5	824.0	579.0	407.3	141.6	49.2	
605	1647.0	1164.5	824.0	582.0	411.8	145.6	51.5	
610	1635.0	1162.6	827.0	588.0	418.0	150.3	54.0	
620	1602.0	1151.9	828.0	596.0	428.2	159.2	59.2	
630	1570.0	1141.4	830.0	603.0	438.6	168.5	64.8	
640	1544.0	1134.9	834.0	613.0	450.7	179.0	71.1	
650	1511.0	1122.8	834.0	620.0	460.8	189.1	77.6	
660	1486.0	1112.5	833.0	624.0	466.9	195.9	82.2	
670	1456.0	1098.2	828.0	625.0	471.2	202.2	86.8	
680	1427.0	1084.3	824.0	626.0	475.6	208.6	91.5	
690	1402.0	1073.1	821.0	629.0	481.1	215.7	96.7	
698	1374.0	907.1	655.0	480.0	354.9	146.7	61.8	
700	1369.0	1055.4	814.0	627.0	483.6	221.6	101.6	
710	1344.0	1040.4	805.0	624.0	482.7	223.9	103.9	
720	1314.0	1021.3	794.0	617.0	479.6	225.2	105.8	
728	1295.5	903.3	672.0	506.0	382.8	168.8	75.5	
730	1290.0	1006.7	786.0	613.0	478.5	227.4	108.1	
740	1260.0	987.2	773.0	606.0	474.8	228.4	109.9	
750	1235.0	971.4	764.0	601.0	472.8	230.1	112.0	
762	1205.5	717.2	490.0	340.0	237.8	80.3	25.0	
770	1185.0	939.4	745.0	590.0	467.9	233.1	116.1	
780	1159.0	922.3	734.0	584.0	464.7	234.1	118.0	
790	1134.0	905.8	723.0	578.0	461.6	235.2	119.9	
800	1109.0	889.1	713.0	572.0	458.2	236.1	121.7	
806	1095.1	792.7	610.0	474.0	370.0	179.2	88.0	
825	1048.0	845.9	683.0	551.0	444.8	233.9	123.0	
830	1036.0	837.3	677.0	547.0	442.0	233.3	123.2	
835	1024.5	829.1	671.0	543.0	439.4	232.9	123.4	
846	998.1	433.1	271.0	180.0	123.8	44.2	17.1	
860	968.0	461.0	301.0	206.0	145.6	55.6	22.8	
870	947.0	413.4	260.0	174.0	120.4	43.7	17.2	
875	936.5	409.4	258.0	173.0	119.6	43.6	17.3	
887	912.5	409.2	261.0	177.0	123.4	46.1	18.6	
900	891.0	409.8	265.0	181.0	127.6	48.8	20.1	
907	882.8	415.8	272.0	187.0	132.9	51.8	21.7	
915	874.5	421.8	279.0	194.0	138.4	54.9	23.4	
925	863.5	255.1	138.0	82.0	51.5	14.9	5.0	
930	858.0	202.9	100.0	55.0	32.8	8.3	2.4	
940	847.0	286.9	164.0	102.0	66.7	21.3	7.6	
950	837.0	271.6	153.0	94.0	60.7	18.9	6.7	

Table 4. (Continued)

Wave Length nm	Air Mass	0	$\alpha = 0.66$ $\beta = 0.170$					
			1	2	3	4	7	10
955	828.5	294.1	171.7	108.8	71.9	23.8	8.8	
965	811.5	315.5	191.4	125.0	84.8	29.8	11.6	
975	794.0	528.7	401.3	311.2	244.1	122.0	62.7	
985	776.0	499.3	374.0	287.3	223.5	109.7	55.6	
1018	719.2	567.1	447.2	352.6	278.0	136.3	66.8	
1082	620.0	471.4	358.4	272.5	207.2	91.1	40.0	
1094	602.0	426.9	335.9	268.9	217.0	117.5	65.1	
1098	596.0	463.5	360.5	280.4	218.0	102.6	48.2	
1101	591.8	464.6	380.7	314.2	260.2	149.5	86.6	
1128	560.5	124.5	60.7	33.7	20.0	5.2	1.6	
1131	557.0	140.3	72.1	41.6	25.5	7.2	2.3	
1137	550.1	132.0	66.5	37.8	22.9	6.2	2.0	
1144	542.0	176.4	100.9	63.3	41.6	13.8	5.2	
1147	538.5	161.0	88.9	54.3	34.9	11.0	3.9	
1178	507.0	369.3	268.9	195.9	142.7	55.1	21.3	
1189	496.0	372.2	279.3	209.6	157.2	66.4	28.1	
1193	492.0	392.4	325.7	272.1	228.1	135.7	81.4	
1222	464.3	363.2	284.0	222.2	173.8	83.1	39.8	
1236	451.2	362.6	291.5	234.3	188.3	97.7	50.7	
1264	426.5	305.8	241.6	193.6	156.3	83.7	45.2	
1276	416.7	318.5	260.2	214.8	178.3	103.6	60.9	
1288	406.8	323.0	256.4	203.6	161.7	80.9	40.5	
1314	386.1	277.7	199.8	143.7	103.3	38.5	14.3	
1335	369.7	177.6	120.5	86.6	64.0	28.5	13.7	
1384	343.7	5.3	0.9	0.2	0.1	0.0	0.0	
1432	321.0	41.7	16.5	7.9	4.1	0.8	0.2	
1457	308.6	79.9	42.2	25.1	15.8	4.8	1.7	
1472	301.4	72.4	37.1	21.5	13.3	3.9	1.3	
1542	270.4	224.5	186.4	154.7	128.4	73.5	42.1	
1572	257.3	209.0	177.6	152.0	130.6	83.8	54.3	
1599	245.4	203.0	174.0	150.0	129.9	85.0	56.0	
1608	241.5	195.9	167.0	143.0	122.7	79.1	51.4	
1626	233.6	194.3	167.0	145.0	125.6	82.8	55.0	
1644	225.6	186.1	160.0	138.0	119.3	78.3	51.8	
1650	223.0	184.1	158.0	136.0	118.2	77.6	51.4	
1676	212.1	171.2	138.0	112.0	90.1	47.5	25.0	
1732	187.9	152.2	123.0	100.0	80.9	43.0	22.9	
1782	166.6	129.0	100.0	77.0	59.9	27.9	12.9	
1862	138.2	3.8	2.0	1.0	0.1	0.0	0.0	
1955	112.9	40.5	25.0	17.0	11.6	4.6	2.1	
2008	102.0	65.7	49.0	38.0	28.9	12.2	3.8	
2014	101.2	70.8	56.0	45.0	36.7	19.8	10.4	
2057	95.6	66.0	52.0	42.0	33.4	17.5	8.7	
2124	87.4	66.4	51.0	38.0	29.2	12.8	5.6	
2156	83.8	62.7	47.0	35.0	26.3	11.0	4.6	
2201	78.9	62.8	54.0	46.0	40.1	26.7	17.9	
2266	72.4	58.6	50.0	44.0	38.4	26.0	17.9	

Table 4. (Continued)

		H ₂ O 20mm, O ₃ 3.4mm						
Wave Length nm	Air Mass	$\alpha = 0.66$			$\beta = 0.170$			
		0	1	2	3	4	7	10
2320	67.6	54.4	47.0	41.0	35.5	24.0	16.5	
2338	66.3	52.1	44.0	38.0	32.8	21.6	14.4	
2356	65.1	49.5	41.0	35.0	29.9	18.9	12.1	
2388	62.8	34.3	25.0	20.0	15.5	8.3	4.8	
2415	61.0	31.0	22.0	17.0	13.0	6.7	3.7	
2453	58.3	28.0	20.0	15.0	11.3	5.7	3.1	
2494	55.4	19.4	12.0	8.0	5.6	2.3	1.1	
2537	52.4	4.4	1.0	1.0	0.3	0.1	0.0	
2900	35.0	2.8	1.0	0.3	0.2	0.0	0.0	
2941	33.4	5.7	3.0	1.0	0.8	0.2	0.1	
2954	32.8	5.5	2.0	1.0	0.8	0.2	0.1	
2973	32.1	8.4	5.0	3.0	1.8	0.6	0.3	
3005	30.8	7.5	4.0	2.0	1.6	0.5	0.2	
3045	28.8	4.5	2.0	1.0	0.6	0.1	0.0	
3056	28.2	4.7	2.0	1.0	0.7	0.2	0.1	
3097	26.2	3.1	1.0	1.0	0.3	0.1	0.0	
3132	24.9	6.5	4.0	2.0	1.5	0.5	0.2	
3156	24.1	17.9	15.0	13.0	10.7	6.7	4.2	
3204	22.5	2.0	1.0	0.4	0.2	0.0	0.0	
3214	22.1	3.3	1.0	1.0	0.4	0.1	0.0	
3245	21.1	3.8	2.0	1.0	0.6	0.2	0.1	
3260	20.6	3.5	2.0	1.0	0.5	0.1	0.0	
3285	19.7	13.7	11.0	9.0	7.3	3.9	1.9	
3317	18.8	12.4	10.0	8.0	5.9	2.7	0.9	
3344	18.1	4.1	2.0	1.0	0.8	0.2	0.1	
3403	16.5	11.9	10.0	8.0	6.7	3.9	2.2	
3450	15.6	12.0	10.0	9.0	7.7	5.1	3.5	
3507	14.5	12.1	11.0	9.0	8.5	6.2	4.6	
3538	14.2	11.3	10.0	9.0	7.6	5.3	3.8	
3573	13.8	10.5	8.0	6.0	4.6	2.0	0.9	
3633	13.1	10.4	9.0	8.0	7.1	5.2	3.8	
3673	12.6	8.8	7.0	6.0	5.3	3.5	2.5	
3696	12.3	10.0	9.0	8.0	7.1	5.2	3.9	
3712	12.2	10.5	9.0	9.0	7.8	5.9	4.6	
3765	11.5	9.1	8.0	7.0	6.3	4.6	3.4	
3812	11.0	8.6	7.0	7.0	5.8	4.2	3.1	
3888	10.4	7.8	7.0	6.0	4.8	3.1	2.0	
3923	10.1	7.7	7.0	6.0	4.9	3.3	2.2	
3948	9.9	7.6	6.0	6.0	4.8	3.2	2.1	
4045	9.1	6.5	5.0	4.0	3.6	2.0	1.1	
Total Irradiance W m ⁻²	1353	799.86	562.87	408.84	302.6	132.9	63.2	

Table 5. Solar Total Irradiance for Different Air Mass Values, U.S. Standard Atmosphere, H₂O = 20mm, O₃ = 3.4mm

Air Mass	Solar Zenith Angle (Degrees)	Turbidity Factors		Total Irradiance W m ⁻²	Ratio of Total Irradiance to Solar Constant %	Fraction of Total Energy in the		
		α	β			UV $\lambda < 400\text{nm}$ %	Visible $400\text{nm} < \lambda < 720\text{nm}$ %	IR $\lambda > 720\text{nm}$ %
0	0			1353	100	8.7	40.1	51.1
1	0	1.3	0.02	956.2	70.7	4.8	46.9	48.3
2	60	1.3	0.02	798.2	59	3.0	46.7	50.3
3	70.5	1.3	0.02	683.6	50.5	1.9	45.7	52.4
4	75.5	1.3	0.02	594.2	44	1.2	44.3	54.5
7	81.8	1.3	0.02	412.4	30.5	0.35	39.45	60.2
10	84.3	1.3	0.02	301.6	22.3	0.102	34.7	65.2
1	0	1.3	0.04	924.5	68.4	4.6	46.4	49.0
2	60	1.3	0.04	748.5	55.3	2.8	45.6	51.6
3	70.5	1.3	0.04	623.7	46.1	1.7	44.0	54.3
4	75.5	1.3	0.04	527.7	39.0	1.05	42.15	56.8
7	81.8	1.3	0.04	340.8	25.2	0.26	35.9	63.8
10	84.3	1.3	0.04	233.49	17.3	0.065	30.3	69.5
1	0	0.66	0.085	889.3	65.7	4.7	46.4	48.9
2	60	0.66	0.085	691.2	51.1	2.9	45.8	51.3
3	70.5	0.66	0.085	552.1	40.8	1.8	44.3	53.9
4	75.5	0.66	0.085	448.0	33.1	1.14	42.4	56.4
7	81.8	0.66	0.085	254.5	18.8	0.3	36.4	63.3
10	84.3	0.66	0.085	152.95	11.3	0.1	30.9	69.0
1	0	0.66	0.17	799.86	59.1	4.5	45.4	50.1
2	60	0.66	0.17	562.87	41.4	2.6	43.5	53.9
3	70.5	0.66	0.17	408.84	30.2	1.5	41.2	57.3
4	75.5	0.66	0.17	302.6	22.4	0.88	38.4	60.7
7	81.5	0.66	0.17	132.9	9.83	0.19	30.0	69.8
10	84.3	0.66	0.17	63.2	4.67	0.04	22.95	77.0

Table 6. Terrestrial Irradiance for Air Mass 2 Computed from the Spectral Data in Table 1 for $\alpha = 1.3$, $\beta = 0.02$

λ nm	$E\lambda$ W m ⁻² μm^{-1}	λ_m nm	$\Delta\lambda$ nm	ΔE W m ⁻²	E (0 - λ_m) W m ⁻²	$\frac{E(0 - \lambda_m)}{E(0 - \infty)}$ %
300	0	302.5	5	0	0	0
305	0	307.5	5	0	0	0
310	2	312.5	5	.010	.010	.0012
315	10	317.5	5	.050	.060	.0075
320	59	322.5	5	.295	.355	.0445
325	90	327.5	5	.450	.805	.1009
330	125	332.5	5	.625	1.430	.1792
335	163	337.5	5	.815	2.245	.2813
340	208	342.5	5	1.040	3.285	.4116
345	227	347.5	5	1.135	4.420	.5538
350	254	352.5	5	1.270	5.690	.7129
355	275	357.5	5	1.375	7.065	.8852
360	297	362.5	5	1.485	8.550	1.0713
365	334	367.5	5	1.670	10.220	1.2805
370	370	372.5	5	1.850	12.070	1.5123

Table 6. (Continued)

λ nm	$E\lambda$ $W\ m^{-2}\ \mu m^{-1}$	λ_m nm	$\Delta\lambda$ nm	ΔE $W\ m^{-2}$	E ($0-\lambda_m$) $W\ m^{-2}$	$\frac{E(0-\lambda_m)}{E(0-\infty)}$ %
375	385	377.5	5	1.925	13.995	1.7535
380	396	382.5	5	1.980	15.975	2.0016
385	406	387.5	5	2.030	18.005	2.2559
390	425	392.5	5	2.125	20.130	2.5222
395	481	397.5	5	2.405	22.535	2.8235
400	605	402.5	5	3.025	25.560	3.2025
405	717	407.5	5	3.585	29.145	3.6517
410	787	412.5	5	3.935	33.080	4.1447
415	822	417.5	5	4.110	37.190	4.6597
420	834	422.5	5	4.170	41.360	5.1822
425	833	427.5	5	4.165	45.525	5.7040
430	830	432.5	5	4.150	49.675	6.2240
435	868	437.5	5	4.340	54.015	6.7678
440	973	442.5	5	4.865	58.880	7.3773
445	1065	447.5	5	5.325	64.205	8.0445
450	1145	452.5	5	5.725	69.930	8.7618
455	1192	457.5	5	5.960	75.890	9.5086
460	1215	462.5	5	6.075	81.965	10.2697
465	1222	467.5	5	6.110	88.075	11.0353
470	1232	472.5	5	6.160	94.235	11.8071
475	1257	477.5	5	6.285	100.520	12.5946
480	1294	482.5	5	6.470	106.990	13.4052
485	1252	487.5	5	6.260	113.250	14.1896
490	1253	492.5	5	6.265	119.515	14.9745
495	1279	497.5	5	6.395	125.910	15.7758
500	1286	502.5	5	6.430	132.340	16.5814
505	1280	507.5	5	6.400	138.740	17.3833
510	1263	512.5	5	6.315	145.055	18.1746
515	1239	517.5	5	6.195	151.250	18.9508
520	1247	522.5	5	6.235	157.485	19.7320
525	1268	527.5	5	6.340	163.825	20.5263
530	1270	532.5	5	6.350	170.175	21.3219
535	1262	537.5	5	6.310	176.485	22.1126
540	1246	542.5	5	6.230	182.715	22.8931
545	1234	547.5	5	6.170	188.885	23.6662
550	1222	552.5	5	6.110	194.995	24.4317
555	1223	557.5	5	6.115	201.110	25.1979
560	1210	562.5	5	6.050	207.160	25.9560
565	1222	567.5	5	6.110	213.270	26.7215
570	1232	572.5	5	6.160	219.430	27.4933
575	1242	577.5	5	6.210	225.640	28.2714
580	1244	582.5	5	6.220	231.860	29.0507
585	1247	587.5	5	6.235	238.095	29.8319
590	1243	592.5	5	6.215	244.310	30.6106
595	1234	597.5	5	6.170	250.480	31.3837
600	1227	602.5	5	6.135	256.615	32.1524
605	1225	607.5	5	6.125	262.740	32.9198
610	1227	615.0	7.5	9.2025	271.9425	34.0728
620	1225	625.0	10	12.250	284.1925	35.6077
630	1224	635.0	10	12.240	296.4325	37.1413

Table 6. (Continued)

λ nm	$E\lambda$ $W\ m^{-2}\ \mu m^{-1}$	λ_m nm	$\Delta\lambda$ nm	ΔE $W\ m^{-2}$	E ($0-\lambda_m$) $W\ m^{-2}$	$\frac{E(0-\lambda_m)}{E(0-\infty)}$ %
640	1226	645.0	10	12.260	308.6925	38.6774
650	1222	655.0	10	12.220	320.9125	40.2085
660	1216	665.0	10	12.160	333.0725	41.7321
670	1206	675.0	10	12.060	345.1325	43.2431
680	1196	685.0	10	11.960	357.0925	44.7416
690	1189	694.0	9	10.701	367.7935	46.0824
698	946	699.0	5	4.730	372.5235	46.6750
700	1174	705.0	6	7.044	379.5675	47.5576
710	1159	715.0	10	11.590	391.1575	49.0098
720	1139	724.0	9	10.251	401.4085	50.2942
728	963	729.0	5	4.815	406.2235	50.8975
730	1124	735.0	6	6.744	412.9675	51.7424
740	1104	745.0	10	11.040	424.0075	53.1257
750	1088	756.0	11	11.968	435.9755	54.6252
762	695	766.0	10	6.950	442.9255	55.4960
770	1054	775.0	9	9.486	452.4115	56.6845
780	1037	785.0	10	10.370	462.7815	57.9838
790	1019	795.0	10	10.190	472.9715	59.2606
800	1002	803.0	8	8.016	480.9875	60.2650
806	856	815.5	12.5	10.700	491.6875	61.6056
825	954	827.5	12	11.448	503.1355	63.0400
830	945	832.5	5	4.725	507.8605	63.6320
835	936	840.5	8	7.488	515.3485	64.5702
846	377	853.0	12.5	4.7125	520.061	65.1606
860	417	865.0	12	5.004	525.065	65.7876
870	360	872.5	7.5	2.700	527.765	66.1259
875	357	881.0	8.5	3.0345	530.7995	66.5061
887	360	893.5	12.5	4.500	535.2995	67.0699
900	364	903.5	10	3.640	538.9395	67.5260
907	373	911.0	7.5	2.7975	541.737	67.8765
915	382	920.0	9	3.438	545.175	68.3073
925	188	927.5	7.5	1.410	546.5850	68.4839
930	137	935.0	7.5	1.0275	547.6125	68.6127
940	224	945.0	10	2.240	549.8525	68.8933
950	208	952.5	7.5	1.560	551.4125	69.0888
955	233.6	960.0	7.5	1.752	553.1645	69.3083
965	260	970.0	10	2.600	555.7645	69.6341
975	544.1	980.0	10	5.441	561.2055	70.3158
985	506.2	1001.5	21.5	10.8833	572.0888	71.6794
1018	601.8	1050.0	48.5	29.1873	601.2761	75.3364
1082	477.4	1088.0	38	18.1412	619.4173	77.6094
1094	446.6	1096.0	8	3.5728	622.9901	78.0571
1098	479.0	1099.5	3.5	1.6765	624.6666	78.2671
1101	505.6	1114.5	15	7.584	632.2506	79.2173
1128	80.3	1129.5	15	1.2045	633.4551	79.3682
1131	95.3	1134.0	4.5	.42885	633.8840	79.4220
1137	87.8	1140.5	6.5	.5707	634.4546	79.4935
1144	133.1	1145.5	5	.6655	635.1202	79.5769
1147	117.3	1162.5	17	1.9941	637.1142	79.8267
1178	353.3	1183.5	21	7.4193	644.5336	80.7563

Table 6. (Continued)

λ nm	$E\lambda$ $W\ m^{-2}\ \mu m^{-1}$	λ_m nm	$\Delta\lambda$ nm	ΔE $W\ m^{-2}$	E ($0-\lambda_m$) $W\ m^{-2}$	$\frac{E(0-\lambda_m)}{E(0-\infty)}$ %
1189	366.3	1191.0	7.5	2.74725	647.2808	81.1005
1193	427.0	1207.5	16.5	7.0455	654.3263	81.9833
1222	371.0	1229.0	21.5	7.9765	662.3028	82.9827
1236	380	1250.0	21	7.980	670.2828	83.9825
1264	313.9	1270.0	20	6.278	676.5608	84.7692
1276	337.5	1282.0	12	4.050	680.6108	85.2766
1288	332.2	1301.0	19	6.3118	686.9226	86.0674
1314	258.0	1324.5	23.5	6.063	692.9856	86.8271
1335	155.3	1359.5	35	5.4355	698.4211	87.5081
1384	1.1	1408.0	48.5	.0534	698.4744	87.5148
1432	21.1	1444.5	36.5	.7702	699.2446	87.6113
1457	53.7	1464.5	20	1.074	700.3186	87.7459
1472	47.1	1507.0	42.5	2.0018	702.3204	87.9967
1542	235.2	1557.0	50	11.760	714.0804	89.4701
1572	223.5	1585.5	28.5	6.3698	720.4501	90.2682
1599	219.0	1603.5	18	3.942	724.3921	90.7621
1608	209.0	1617.0	13.5	2.8215	727.2136	91.1157
1626	210.0	1635.0	18	3.780	730.9936	91.5893
1644	200.0	1647.0	12	2.400	733.3936	91.8900
1650	198.0	1663.0	16	3.168	736.5616	92.2869
1676	173.0	1704.0	41	7.093	743.6546	93.1756
1732	153.0	1757.0	53	8.109	751.7636	94.1916
1782	124.0	1822.0	65	8.060	759.8236	95.2015
1862	1.0	1908.5	86.5	.0865	759.9101	95.2123
1955	30.0	1981.5	73	2.190	762.1001	95.4867
2008	60.0	2011.0	29.5	1.770	763.8701	95.7085
2014	68.0	2035.5	24.5	1.666	765.5361	95.9173
2057	63.0	2090.5	55	3.465	769.0011	96.3514
2124	61.0	2140.0	49.5	3.0195	772.0206	96.7297
2156	57.0	2178.5	38.5	2.1945	774.2151	97.0047
2201	65.0	2233.5	55	3.575	777.7901	97.4526
2266	61.0	2293.0	59.5	3.6295	781.4196	97.9074
2320	56.0	2329.0	36.0	2.016	783.4356	98.1600
2338	53.0	2347	18.0	.954	784.3896	98.2795
2356	50.0	2372	25	1.250	785.6396	98.4361
2388	30.0	2401.5	29.5	.885	786.5246	98.5470
2415	26.0	2434	32.5	.845	787.3696	98.6529
2453	24.0	2473.5	39.5	.948	788.3176	98.7716
2494	14.0	2515.5	42	.588	788.9056	98.8453
2537	2.0	2718.5	203	.406	789.3116	98.8962
2900	1.0	2920.5	202	.202	789.5136	98.9215
2941	3.0	2947.5	27	.081	789.5946	98.9316
2954	3.0	2963.5	16	.048	789.6426	98.9377
2973	5.0	2989	25.5	.1275	789.7701	98.9536
3005	5.0	3025	36	.180	789.9501	98.9762
3045	2.0	3050.5	25.5	.051	790.0011	98.9826
3056	3.0	3076.5	26	.078	790.0791	98.9923
3097	1.0	3114.5	38	.038	790.1171	98.9971
3132	4.0	3144	29.5	.118	790.2351	99.0119
3156	17.0	3180	36	.612	790.8471	99.0886
3204	1.0	3209	29	.029	790.8761	99.0922

Table 6. (Continued)

λ nm	$E\lambda$ $W\ m^{-2}\ \mu m^{-1}$	λ_m nm	$\Delta\lambda$ nm	ΔE $W\ m^{-1}$	E ($0-\lambda_m$) $W\ m^{-2}$	$\frac{E(0-\lambda_m)}{E(0-\infty)}$ %
3214	2.0	3229.5	20.5	.041	790.9171	99.0973
3245	2.0	3252.5	23	.046	790.9631	99.1031
3260	2.0	3272.5	20	.040	791.0031	99.1081
3285	13.0	3301	28.5	.3705	791.3736	99.1545
3317	11.0	3330.5	29.5	.3245	791.6981	99.1952
3344	2.0	3373.5	43	.086	791.7841	99.2060
3403	11.0	3426.5	53	.583	792.3671	99.2790
3450	12.0	3478.5	52	.624	792.9911	99.3572
3507	12.0	3522.5	44	.528	793.5191	99.4234
3538	11.0	3555.5	33	.363	793.8821	99.4688
3573	9.0	3603	47.5	.4275	794.3096	99.5224
3633	10.0	3653	50	.500	794.8096	99.5851
3673	8.2	3684.5	31.5	.2583	795.0679	99.6174
3696	10.0	3704	19.5	.195	795.2629	99.6418
3712	11.0	3738.5	34.5	.3795	795.6424	99.6894
3765	9.0	3788.5	50	.450	796.0924	99.7458
3812	8.0	3850	61.5	.492	796.5844	99.8074
3888	8.0	3905.5	55.5	.444	797.0284	99.8631
3923	7.0	3935.5	30	.210	797.2384	99.8894
3948	7.0	3996.5	61	.427	797.654	99.9429
4045	6.0	4072.5	76	.456	798.1214	100.0000

Table 7. Terrestrial Irradiance for Air Mass 2 Computed from the Spectral Data in Table 2 for $\alpha = 1.3$, $\beta = 0.04$

λ nm	$E\lambda$ $W\ m^{-2}\ \mu m^{-1}$	λ_m nm	$\Delta\lambda$ nm	ΔE $W\ m^{-2}$	E ($0-\lambda_m$) $W\ m^{-2}$	$\frac{E(0-\lambda_m)}{E(0-\infty)}$ %
300	0	302.5	5	0	0	
305	0	307.5	5	0	0	
310	1	312.5	5	.005	.005	.007
315	8	317.5	5	.040	.045	.0060
320	50	322.5	5	.250	.295	.0394
325	75	327.5	5	.375	.670	.0895
330	105	332.5	5	.525	1.195	.1596
335	138	337.5	5	.690	1.885	.2518
340	177	342.5	5	.885	2.770	.3700
345	193	347.5	5	.965	3.735	.4988
350	217	352.5	5	1.085	4.820	.6438
355	236	357.5	5	1.180	6.000	.8014
360	255	362.5	5	1.275	7.275	.9717
365	288	367.5	5	1.440	8.715	1.1640
370	320	372.5	5	1.600	10.315	1.3777
375	334	377.5	5	1.670	11.985	1.6007
380	344	382.5	5	1.720	13.705	1.8304
385	353	387.5	5	1.765	15.470	2.0662
390	371	392.5	5	1.855	17.325	2.3139
395	421	397.5	5	2.105	19.430	2.5951
400	530	402.5	5	2.650	22.080	2.9490
405	630	407.5	5	3.150	25.230	3.3697
410	693	412.5	5	3.465	28.695	3.8325

Table 7. (Continued)

λ nm	$E\lambda$ $W\ m^{-2}\ \mu m^{-1}$	λ_m nm	$\Delta\lambda$ nm	ΔE $W\ m^{-2}$	E ($0-\lambda_m$) $W\ m^{-2}$	$\frac{E(0-\lambda_m)}{E(0-\infty)}$ %
415	725	417.5	5	3.625	32.320	4.3167
420	737	422.5	5	3.685	36.005	4.8088
425	737	427.5	5	3.685	39.690	5.3010
430	737	432.5	5	3.685	43.375	5.7932
435	771	437.5	5	3.855	47.230	6.3081
440	867	442.5	5	4.335	51.565	6.8871
445	949	447.5	5	4.745	56.310	7.5208
450	1022	452.5	5	5.110	61.420	8.2033
455	1066	457.5	5	5.330	66.750	8.9152
460	1089	462.5	5	5.445	72.195	9.6424
465	1097	467.5	5	5.485	77.680	10.3750
470	1107	472.5	5	5.535	83.215	11.1142
475	1131	477.5	5	5.655	88.870	11.8695
480	1167	482.5	5	5.835	94.705	12.6489
485	1130	487.5	5	5.650	100.355	13.4035
490	1133	492.5	5	5.665	106.020	14.1601
495	1157	497.5	5	5.785	111.805	14.9327
500	1165	502.5	5	5.825	117.630	15.7107
505	1161	507.5	5	5.805	123.435	16.4861
510	1147	512.5	5	5.735	129.170	17.2520
515	1127	517.5	5	5.635	134.805	18.0046
520	1136	522.5	5	5.680	140.485	18.7633
525	1156	527.5	5	5.780	146.265	19.5352
530	1159	532.5	5	5.795	152.060	20.3092
535	1153	537.5	5	5.765	157.825	21.0792
540	1140	542.5	5	5.700	163.525	21.8405
545	1130	547.5	5	5.650	169.175	22.5951
550	1120	552.5	5	5.600	174.775	23.3431
555	1122	557.5	5	5.610	180.385	24.0923
560	1111	562.5	5	5.555	185.940	24.8343
565	1124	567.5	5	5.620	191.560	25.5849
570	1134	572.5	5	5.670	197.230	26.3422
575	1144	577.5	5	5.720	202.950	27.1061
580	1147	582.5	5	5.735	208.685	27.8721
585	1150	587.5	5	5.750	214.435	28.6401
590	1148	592.5	5	5.740	220.175	29.4067
595	1141	597.5	5	5.705	225.880	30.1687
600	1135	602.5	5	5.675	231.555	30.9266
605	1134	607.5	5	5.670	237.225	31.6839
610	1137	615.0	7.5	8.5275	245.7525	32.8228
620	1137	625	10	11.370	257.1225	34.3414
630	1137	635	10	11.37	268.4925	35.8600
640	1141	645	10	11.41	279.9025	37.3839
650	1140	655	10	11.40	291.3025	38.9065
660	1136	665	10	11.36	302.6625	40.4238
670	1127	675	10	11.27	313.9325	41.9290
680	1119	685	10	11.19	325.1225	43.4236
690	1114	694	9	10.026	335.1485	44.7626
698	887	699	5	4.435	339.5835	45.3549
700	1102	705	6	6.612	346.1955	46.2381
710	1089	715	10	10.890	357.0855	47.6926

Table 7. (Continued)

λ nm	$E\lambda$ $W\ m^{-2}\ \mu m^{-1}$	λ_m nm	$\Delta\lambda$ nm	ΔE $W\ m^{-2}$	E ($0-\lambda_m$) $W\ m^{-2}$	$\frac{E(0-\lambda_m)}{E(0-\infty)}$ %
720	1071	724	9	9.639	366.7245	48.9799
728	906	729	5	4.530	371.2545	49.5850
730	1058	735	6	6.348	377.6025	50.4328
740	1040	745	10	10.400	388.0025	51.8218
750	1026	756	11	11.286	399.2885	53.3292
762	656	766	10	6.560	405.8485	54.2054
770	997	775	9	8.973	414.8215	55.4038
780	981	785	10	9.810	424.6315	56.7140
790	965	795	10	9.650	434.2815	58.0029
800	950	803	8	7.600	441.8815	59.0180
806	812	815.5	12.5	10.150	452.0315	60.3736
825	906	827.5	12	10.872	462.9035	61.8257
830	898	832.5	5	4.490	467.3935	62.4254
835	889	840.5	8	7.112	474.5055	63.3752
846	359	853	12.5	4.4875	478.9930	63.9746
860	397	865	12	4.764	483.7570	64.6109
870	344	872.5	7.5	2.580	486.3370	64.9555
875	340	881	8.5	2.890	489.2270	65.3414
887	344	893.5	12.5	4.300	493.5270	65.9158
900	348	903.5	10	3.480	497.0070	66.3805
907	357	911	7.5	2.6775	499.6845	66.7382
915	365	920	9	3.285	502.9695	67.1769
925	180	927.5	7.5	1.350	504.3195	67.3572
930	131	935	7.5	.9825	505.3020	67.4884
940	214	945	10	2.140	507.4420	67.7743
950	199	952.5	7.5	1.4925	508.9345	67.9736
955	223.9	960	7.5	1.67925	510.6138	68.1979
965	249.3	970	10	2.493	513.1068	68.5308
975	522.1	980	10	5.221	518.3278	69.2282
985	486	1001.5	21.5	10.449	528.7768	70.6237
1018	578.7	1050	48.5	28.06695	556.8437	74.3724
1082	460.5	1088	38	17.499	574.3427	76.7096
1094	431	1096	8	3.448	577.7907	77.1701
1098	462.3	1099.5	3.5	1.61805	579.4088	77.3862
1101	488	1114.5	15	7.320	586.7288	78.3638
1128	77.6	1129.5	15	1.164	587.8928	78.5193
1131	92.1	1134	4.5	.41445	588.3072	78.5747
1137	84.9	1140.5	6.5	.55185	588.8590	78.6484
1144	128.7	1145.5	5	.6435	589.5026	78.7343
1147	113.4	1162.5	17	1.9278	591.4304	78.9918
1178	342.1	1183.5	21	7.1841	598.6144	79.9513
1189	354.8	1191	7.5	2.661	601.2754	80.3067
1193	413.6	1207.5	16.5	6.8244	608.0998	81.2182
1222	359.7	1229	21.5	7.73355	615.8334	82.2511
1236	368.6	1250	21	7.7406	623.5740	83.2849
1264	304.7	1270	20	6.094	629.6680	84.0988
1276	327.9	1282	12	3.9348	633.6028	84.6243
1288	322.8	1301	19	6.1332	639.7360	85.4435
1314	250.9	1324.5	23.5	5.89615	645.6322	86.2310
1335	151.1	1359.5	35	5.2885	650.9206	86.9373
1384	1.1	1408	48.5	.05335	650.9740	86.9445

Table 7. (Continued)

λ nm	$E\lambda$ $W\ m^{-2}\ \mu m^{-1}$	λ_m nm	$\Delta\lambda$ nm	ΔE $W\ m^{-2}$	E ($0-\lambda_m$) $W\ m^{-2}$	$\frac{E(0-\lambda_m)}{E(0-\infty)}$ %
1432	20.5	1444.5	36.5	.74825	651.7222	87.0444
1457	52.4	1464.5	20	1.048	652.7702	87.1844
1472	46	1507	42.5	1.955	654.7252	87.4455
1542	229.9	1557	50	11.495	666.2202	88.9808
1572	218.6	1585.5	28.5	6.2301	672.4504	89.8129
1599	214	1603.5	18	3.852	675.3024	90.3298
1608	205	1617	13.5	2.7675	679.0698	90.6970
1626	205	1635	18	3.690	682.7598	91.1898
1644	196	1647	12	2.352	685.1118	91.5039
1650	193	1663	16	3.088	688.1998	91.9164
1676	169	1704	41	6.929	695.1288	92.8418
1732	150	1757	53	7.950	703.0788	93.9036
1782	121	1822	65	7.865	710.9438	94.9541
1862	1	1908.5	86.5	.0865	711.0304	94.9656
1955	30	1981.5	73	2.190	713.2204	95.2581
2008	59	2011	29.5	1.7405	714.9608	95.4906
2014	67	2035.5	24.5	1.6415	716.6024	95.7098
2057	62	2090.5	55	3.410	720.0124	96.1653
2124	60	2140	49.5	2.970	722.9824	96.5620
2156	56	2178.5	38.5	2.156	725.1384	96.8499
2201	64	2233.5	55	3.520	728.6584	97.3200
2266	60	2293	59.5	3.570	732.2284	97.7969
2320	55	2329	36	1.980	734.2084	98.0613
2338	52	2347	18	.936	735.1444	98.1863
2356	49	2372	25	1.225	736.3694	98.3499
2388	30	2401.5	29.5	.885	737.2544	98.4681
2415	26	2434	32.5	.845	738.0994	98.5810
2453	23	2473.5	39.5	.9085	739.0078	98.7023
2494	14	2515.5	42	.588	739.5958	98.7809
2537	2	2718.5	203	.406	740.0018	98.8351
2900	1	2920.5	202	.202	740.2038	98.8621
2941	3	2947.5	27	.081	740.2848	98.8729
2954	3	2963.5	16	.048	740.3328	98.8793
2973	5	2989	25.5	.1275	740.4604	98.8963
3005	5	3025	36	.180	740.6404	98.9204
3045	2	3050.5	25.5	.051	740.6914	98.9272
3056	2	3076.5	26	.052	740.7434	98.9341
3097	1	3114.5	38	.038	740.7814	98.9392
3132	4	3144	29.5	.118	740.8994	98.9550
3156	17	3180	36	.612	741.5114	99.0367
3204	1	3209	29	.029	741.5404	99.0405
3214	2	3229.5	20.5	.041	741.5814	99.0460
3245	2	3252.5	23	.046	741.6274	99.0522
3260	2	3272.5	20	.040	741.6674	99.0575
3285	13	3301	28.5	.3705	742.0378	99.1070
3317	11	3330.5	29.5	.3245	742.3624	99.1504
3344	2	3373.5	43	.086	742.4484	99.1618
3403	11	3426.5	53	.583	743.0314	99.2397
3450	12	3478.5	52	.624	743.6554	99.3231
3507	12	3522.5	44	.528	744.1834	99.3936

Table 7. (Continued)

λ nm	$E\lambda$ $W\ m^{-2}\ \mu m^{-1}$	λ_m nm	$\Delta\lambda$ nm	ΔE $W\ m^{-2}$	E ($0-\lambda_m$) $W\ m^{-2}$	$\frac{E(0-\lambda_m)}{E(0-\infty)}$ %
3538	11	3555.5	33	.363	744.5464	99.4421
3573	9	3603	47.5	.4275	744.9738	99.4991
3633	10	3653	50	.500	745.4738	99.5659
3673	8	3684.5	31.5	.252	745.7258	99.5996
3696	10	3704	19.5	.195	745.9208	99.6256
3712	11	3738.5	34.5	.3795	746.3004	99.6763
3765	9	3788.5	50	.450	746.7504	99.7364
3812	8	3850	61.5	.492	747.2424	99.8021
3888	7	3905.5	55.5	.3885	747.6308	99.8540
3923	7	3935.5	30	.210	747.8408	99.8820
3948	7	3996.5	61	.427	748.2678	99.9391
4045	6	4072.5	76	.456	748.72385	100.0000

Table 8. Terrestrial Irradiance for Air Mass 2 Computed from the Spectral Data in Table 3 for $\alpha = 0.66$, $\beta = 0.085$

λ nm	$E\lambda$ $W\ m^{-2}\ \mu m^{-1}$	λ_m nm	$\Delta\lambda$ nm	ΔE $W\ m^{-2}$	E ($0-\lambda_m$) $W\ m^{-2}$	$\frac{E(0-\lambda_m)}{E(0-\infty)}$ %
300	0	302.5	5	0	0	
305	0	307.5	5	0	0	
310	1	312.5	5	.005	.005	.0007
315	8	317.5	5	.040	.045	.0065
320	49	322.5	5	.245	.290	.0419
325	75	327.5	5	.375	.665	.0962
330	104	332.5	5	.520	1.185	.1714
335	136	337.5	5	.680	1.865	.2698
340	173	342.5	5	.865	2.730	.3949
345	189	347.5	5	.945	3.675	.5316
350	211	352.5	5	1.055	4.730	.6842
355	229	357.5	5	1.145	5.875	.8498
360	247	362.5	5	1.235	7.110	1.0285
365	278	367.5	5	1.390	8.500	1.2296
370	308	372.5	5	1.540	10.040	1.4523
375	321	377.5	5	1.605	11.645	1.6845
380	330	382.5	5	1.650	13.295	1.9232
385	337	387.5	5	1.685	14.980	2.1669
390	355	392.5	5	1.775	16.755	2.4237
395	402	397.5	5	2.010	18.765	2.7144
400	505	402.5	5	2.525	21.290	3.0797
405	600	407.5	5	3.000	24.290	3.5136
410	658	412.5	5	3.290	27.580	3.9895
415	688	417.5	5	3.440	31.020	4.4872
420	698	422.5	5	3.490	34.510	4.9920
425	697	427.5	5	3.485	37.995	5.4961
430	696	432.5	5	3.480	41.475	5.9995
435	728	437.5	5	3.640	45.115	6.5261
440	816	442.5	5	4.080	49.195	7.1162
445	893	447.5	5	4.465	53.660	7.7339
450	961	452.5	5	4.805	58.465	8.4572

Table 8. (Continued)

λ nm	$E\lambda$ $W\ m^{-2}\ \mu m^{-1}$	λ_m nm	$\Delta\lambda$ nm	ΔE $W\ m^{-2}$	E ($0-\lambda_m$) $W\ m^{-2}$	$\frac{E(0-\lambda_m)}{E(0-\infty)}$ %
455	1001	457.5	5	5.005	63.470	9.1812
460	1021	462.5	5	5.105	68.575	9.9196
465	1028	467.5	5	5.140	10.6631	73.715
470	1036	472.5	5	5.180	78.895	11.4125
475	1058	477.5	5	5.290	84.185	12.1777
480	1090	482.5	5	5.450	89.635	12.9660
485	1054	487.5	5	5.270	94.905	13.7284
490	1056	492.5	5	5.280	100.185	14.4921
495	1078	497.5	5	5.390	105.576	15.2718
500	1084	502.5	5	5.420	110.995	16.0558
505	1080	507.5	5	5.400	116.395	16.8370
510	1067	512.5	5	5.335	121.730	17.6087
515	1046	517.5	5	5.230	126.960	18.3652
520	1054	522.5	5	5.270	132.230	19.1276
525	1073	527.5	5	5.365	137.595	19.9036
530	1075	532.5	5	5.375	142.970	20.6811
535	1068	537.5	5	5.340	148.310	21.4536
540	1055	542.5	5	5.275	153.585	22.2166
545	1046	547.5	5	5.230	158.815	22.9732
550	1036	552.5	5	5.180	163.995	23.7225
555	1037	557.5	5	5.185	169.180	24.4725
560	1027	562.5	5	5.135	174.315	25.2153
565	1037	567.5	5	5.185	179.500	25.9653
570	1046	572.5	5	5.230	184.730	26.7219
575	1055	577.5	5	5.275	190.005	27.4849
580	1057	582.5	5	5.285	195.290	28.2494
585	1060	587.5	5	5.300	200.590	29.0161
590	1057	592.5	5	5.285	205.875	29.7806
595	1051	597.5	5	5.255	211.130	30.5407
600	1045	602.5	5	5.225	216.355	31.2965
605	1044	607.5	5	5.220	221.575	32.0516
610	1046	615	7.5	7.845	229.420	33.1864
620	1046	625	10	10.46	239.880	34.6995
630	1045	635	10	10.45	250.330	36.2112
640	1048	645	10	10.48	260.810	37.7271
650	1046	655	10	10.46	271.270	39.2402
660	1042	665	10	10.42	281.690	40.7475
670	1034	675	10	10.34	292.030	42.2432
680	1026	685	10	10.26	302.290	43.7274
690	1021	694	9	9.189	311.479	45.0566
698	813	699	5	4.065	315.544	45.6446
700	1009	705	6	6.054	321.598	46.5203
710	997	715	10	9.970	331.568	47.9625
720	981	724	9	8.829	340.397	49.2397
728	829	729	5	4.145	344.542	49.8393
730	969	735	6	5.814	350.356	50.6803
740	952	745	10	9.520	359.876	52.0574
750	938	756	11	10.318	370.194	53.5499
762	600	766	10	6.000	376.194	54.4178
770	911	775	9	8.199	384.393	55.6039

Table 8. (Continued)

λ nm	$E\lambda$ $W\ m^{-2}\ \mu m^{-1}$	λ_m nm	$\Delta\lambda$ nm	ΔE $W\ m^{-2}$	E ($0-\lambda_m$) $W\ m^{-2}$	$\frac{E(0-\lambda_m)}{E(0-\infty)}$ %
780	897	785	10	8.970	393.363	56.9014
790	882	795	10	8.820	402.183	58.1773
800	868	803	8	6.944	409.127	59.1817
806	742	815.5	12.5	9.275	418.402	60.5234
825	828	827.5	12	9.936	428.338	61.9607
830	820	832.5	5	4.100	432.438	62.5537
835	813	840.5	8	6.504	438.942	63.4946
846	328	853	12.5	4.100	443.042	64.0877
860	363	865	12	4.356	447.398	64.7178
870	314	872.5	7.5	2.355	449.753	65.0584
875	311	881	8.5	2.6435	452.3965	65.4408
887	314	893.5	12.5	3.925	456.3215	66.0086
900	318	903.5	10	3.180	459.5015	66.4686
907	326	911	7.5	2.445	461.9465	66.8223
915	334	920	9	3.006	464.9525	67.2571
925	165	927.5	7.5	1.2375	466.190	67.4361
930	119	935	7.5	.8925	467.0825	67.5652
940	196	945	10	1.960	469.0425	67.8487
950	182	952.5	7.5	1.365	470.4075	68.0462
955	205	960	7.5	1.5375	471.945	68.2686
965	228	970	10	2.280	474.225	68.5984
975	477.1	980	10	4.771	478.996	69.2885
985	444	1001.5	21.5	9.546	488.542	70.6694
1018	529	1050	48.5	25.6565	514.1985	74.3807
1082	421.2	1088	38	16.0056	530.2041	76.6960
1094	394.3	1096	8	3.1544	533.3585	77.1523
1098	422.9	1099.5	3.5	1.48015	534.8386	77.3664
1101	446.5	1114.5	15	6.6975	541.5362	78.3352
1128	71	1129.5	15	1.065	542.6012	78.4893
1131	84.3	1134	4.5	.37935	542.9805	78.5441
1137	77.7	1140.5	6.5	.50505	543.4856	78.6172
1144	117.8	1145.5	5	.589	544.0746	78.7024
1147	103.9	1162.5	17	1.7663	545.8408	78.9579
1178	313.3	1183.5	21	6.5793	552.4202	79.9096
1189	325	1191	7.5	2.4375	554.8576	80.2622
1193	378.9	1207.5	16.5	6.25185	561.1095	81.1666
1222	329.6	1229	21.5	7.0864	568.1959	82.1916
1236	337.9	1250	21	7.0959	575.2918	83.2181
1264	279.4	1270	20	5.588	580.8798	84.0264
1276	300.7	1282	12	3.6084	584.4882	84.5484
1288	296.1	1301	19	5.6259	590.1141	85.3622
1314	230.2	1324.5	23.5	5.4097	595.5238	86.1447
1335	138.7	1359.5	35	4.8545	600.3783	86.8469
1384	1	1408	48.5	.0485	600.4268	86.8539
1432	18.9	1444.5	36.5	.68985	601.1166	86.9537
1457	48.2	1464.5	20	.964	602.0806	87.0932
1472	42.3	1507	42.5	1.79775	603.8784	87.3532
1542	211.7	1557	50	10.585	614.4634	88.8844
1572	201.4	1585.5	28.5	5.7399	620.2033	89.7147
1599	197	1603.5	18	3.546	623.7493	90.2276

Table 8. (Continued)

λ nm	$E\lambda$ $W\ m^{-2}\ \mu m^{-1}$	λ_m nm	$\Delta\lambda$ nm	ΔE $W\ m^{-2}$	E ($0-\lambda_m$) $W\ m^{-2}$	$\frac{E(0-\lambda_m)}{E(0-\infty)}$ %
1608	189	1617	13.5	2.5515	626.3008	90.5967
1626	189	1635	18	3.402	629.7028	91.0888
1644	180	1647	12	2.160	631.8628	91.4013
1650	178	1663	16	2.848	634.7108	91.8133
1676	156	1704	41	6.396	641.1068	92.7385
1732	139	1757	53	7.367	648.4738	93.8041
1782	112	1822	65	7.280	655.7538	94.8572
1862	1	1908.5	86.5	.0865	655.8403	94.8697
1955	28	1981.5	73	2.044	657.8843	95.1654
2008	55	2011	29.5	1.6225	659.5068	95.4001
2014	62	2035.5	24.5	1.519	661.0258	95.6198
2057	58	2090.5	55	3.190	664.2158	96.0813
2124	56	2140	49.5	2.772	666.9878	96.4822
2156	52	2178.5	38.5	2.002	668.9898	96.7718
2201	59	2233.5	55	3.245	672.2348	97.2412
2266	56	2293	59.5	3.322	675.5668	97.7232
2320	52	2329	36	1.872	677.4388	97.9940
2338	49	2347	18	.882	678.3208	98.1216
2356	46	2372	25	1.150	679.4708	98.2880
2388	28	2401.5	29.5	.826	680.2968	98.4074
2415	24	2434	32.5	.780	681.0768	98.5203
2453	22	2473.5	39.5	.869	681.9458	98.6400
2494	13	2515.5	42	.546	682.4918	98.7250
2537	2	2718.5	203	.406	682.8978	98.7837
2900	1	2920.5	202	.202	683.0998	98.8129
2941	3	2947.5	27	.081	683.1808	98.8246
2954	3	2963.5	16	.048	683.2288	98.8316
2973	5	2989	25.5	.1275	683.3563	98.8500
3005	4	3025	36	.144	683.5003	98.8708
3045	2	3050.5	25.5	.051	683.5513	98.8782
3056	2	3076.5	26	.052	683.6033	98.8857
3097	1	3114.5	38	.038	683.6413	98.8912
3132	4	3144	29.5	.118	683.7593	98.9083
3156	16	3180	36	.576	684.3353	98.9916
3204	1	3209	29	.029	684.3643	98.9958
3214	2	3229.5	20.5	.041	684.4053	99.0017
3245	2	3253.5	23	.046	684.4513	99.0084
3260	2	3272.5	20	.04	684.4913	99.0142
3285	12	3301	28.5	.342	684.8333	99.0637
3317	10	3330.5	29.5	.295	685.1283	99.1063
3344	2	3373.5	43	.086	685.2143	99.1188
3403	10	3426.5	53	.530	685.7443	99.1954
3450	11	3478.5	52	.572	686.3163	99.2782
3507	11	3522.5	44	.484	686.8003	99.3482
3538	11	3555.5	33	.363	687.1633	99.4007
3573	9	3603	47.5	.4275	687.5908	99.4625
3633	10	3653	50	.500	688.0908	99.5349
3673	8	3684.5	31.5	.252	688.3428	99.5713
3696	10	3704	19.5	.195	688.5378	99.5995
3712	10	3738.5	34.5	.345	688.8828	99.6494

Table 8. (Continued)

λ nm	$E\lambda$ $W\ m^{-2}\ \mu m^{-1}$	λ_m nm	$\Delta\lambda$ nm	ΔE $W\ m^{-2}$	E ($0-\lambda_m$) $W\ m^{-2}$	$\frac{E(0-\lambda_m)}{E(0-\infty)}$ %
3765	9	3788.5	50	.450	689.3328	99.7145
3812	8	3850	61.5	.492	689.8248	99.7857
3888	7	3905.5	55.5	.3885	690.2133	99.8419
3923	7	3935.5	30	.210	690.4233	99.8723
3948	7	3996.5	61	.427	690.8503	99.9340
4045	6	4072.5	76	.456	691.3063	100.0000

Table 9. Terrestrial Irradiance for Air Mass 2 Computed from the Spectral Data in Table 4 for $\alpha = 0.66$, $\beta = 0.17$

λ nm	$E\lambda$ $W\ m^{-2}\ \mu m^{-1}$	λ_m nm	$\Delta\lambda$ nm	ΔE $W\ m^{-2}$	E ($0-\lambda_m$) $W\ m^{-2}$	$\frac{E(0-\lambda_m)}{E(0-\infty)}$ %
300	0	302.5	0	0	0	0
305	0	307.5	0	0	0	0
310	1	312.5	5	.005	.005	.0009
315	6	317.5	5	.03	.035	.0062
320	34	322.5	5	.17	.205	.0364
325	52	327.5	5	.26	.465	.0826
330	73	332.5	5	.365	.830	.1475
335	96	337.5	5	.48	1.310	.2327
340	123	342.5	5	.615	1.925	.3419
345	134	347.5	5	.67	2.595	.4610
350	150	352.5	5	.75	3.345	.5943
355	164	357.5	5	.82	4.165	.7400
360	177	362.5	5	.885	5.050	.8972
365	200	367.5	5	1.000	6.050	1.0748
370	222	372.5	5	1.11	7.160	1.2720
375	232	377.5	5	1.16	8.320	1.4781
380	239	382.5	5	1.195	9.515	1.6904
385	246	387.5	5	1.23	10.745	1.9090
390	258	392.5	5	1.29	12.035	2.1381
395	294	397.5	5	1.47	13.505	2.3993
400	370	402.5	5	1.85	15.355	2.7280
405	440	407.5	5	2.20	17.555	3.1188
410	485	412.5	5	2.425	19.980	3.5496
415	507	417.5	5	2.535	22.515	4.0000
420	516	422.5	5	2.580	25.095	4.4584
425	517	427.5	5	2.585	27.680	4.9176
430	517	432.5	5	2.585	30.265	5.3769
435	542	437.5	5	2.710	32.975	5.8583
440	609	442.5	5	3.045	36.020	6.3993
445	668	447.5	5	3.340	39.360	6.9927
450	721	452.5	5	3.605	42.965	7.6332
455	752	457.5	5	3.760	46.725	8.3012
460	769	462.5	5	3.845	50.570	8.9843
465	775	467.5	5	3.875	54.445	9.6727
470	783	472.5	5	3.915	58.360	10.3682
475	801	477.5	5	4.005	62.365	11.0798
480	827	482.5	5	4.135	66.500	11.8144

Table 9. (Continued)

λ nm	$E\lambda$ W m ⁻² μm^{-1}	λ_m nm	$\Delta\lambda$ nm	ΔE W m ⁻²	E (0- λ_m) W m ⁻²	$\frac{E(0-\lambda_m)}{E(0-\infty)}$ %
485	802	487.5	5	4.010	70.510	12.5268
490	805	492.5	5	4.025	74.535	13.2419
495	823	497.5	5	4.115	78.650	13.9730
500	829	502.5	5	4.145	82.795	14.7094
505	827	507.5	5	4.135	86.930	15.4440
510	818	512.5	5	4.090	91.020	16.1706
515	804	517.5	5	4.020	95.040	16.8848
520	811	522.5	5	4.055	99.095	17.6052
525	827	527.5	5	4.135	103.230	18.3398
530	830	532.5	5	4.150	107.380	19.0771
535	826	537.5	5	4.130	111.510	19.8109
540	817	542.5	5	4.085	115.595	20.5366
545	811	547.5	5	4.055	119.650	21.2570
550	805	552.5	5	4.025	123.675	21.9721
555	807	557.5	5	4.035	127.710	22.6890
560	800	562.5	5	4.000	131.710	23.3996
565	810	567.5	5	4.050	135.760	24.1191
570	818	572.5	5	4.090	139.850	24.8458
575	826	577.5	5	4.130	143.980	25.5795
580	829	582.5	5	4.145	148.125	26.3159
585	832	587.5	5	4.160	152.285	27.0550
590	831	592.5	5	4.155	156.440	27.7931
595	827	597.5	5	4.135	160.575	28.5278
600	824	602.5	5	4.120	164.695	29.2597
605	824	607.5	5	4.120	168.815	29.9917
610	827	615	7.5	6.2025	175.0175	31.0936
620	828	625	10	8.280	183.2975	32.5646
630	830	635	10	8.3	191.5975	34.0392
640	834	645	10	8.34	199.9375	35.5209
650	834	655	10	8.34	208.2775	37.0026
660	833	665	10	8.33	216.6075	38.4825
670	828	675	10	8.28	224.8875	39.9535
680	824	685	10	8.24	233.1275	41.4174
690	821	694	9	7.389	240.5165	42.7302
698	655	699	5	3.275	243.7915	43.3120
700	814	705	6	4.884	248.6755	44.1797
710	805	715	10	8.050	256.7255	45.6099
720	794	724	9	7.146	263.8715	46.8794
728	672	729	5	3.360	267.2315	47.4764
730	786	735	6	4.716	271.9475	48.3142
740	773	745	10	7.730	279.6775	49.6875
750	764	756	11	8.404	288.0815	51.1805
762	490	766	10	4.900	292.9815	52.0511
770	745	775	9	6.705	299.6865	53.2423
780	734	785	10	7.340	307.0265	54.5463
790	723	795	10	7.230	314.2565	55.8308
800	713	803	8	5.704	319.9605	56.8442
806	610	815.5	12.5	7.625	327.5855	58.1988
825	683	827.5	12	8.196	335.7815	59.6549
830	677	832.5	5	3.385	339.1665	60.2563

Table 9. (Continued)

λ nm	$E\lambda$ W m ⁻² μm^{-1}	λ_m nm	$\Delta\lambda$ nm	ΔE W m ⁻²	E (0- λ_m) W m ⁻²	$\frac{E(0-\lambda_m)}{E(0-\infty)}$ %
835	671	840.5	8	5.368	344.5345	61.2100
846	271	853	12.5	3.3875	347.9220	61.8118
860	301	865	12	3.612	351.5340	62.4535
870	260	872.5	7.5	1.950	353.484	62.8000
875	258	881	8.5	2.193	355.6770	63.1896
887	261	893.5	12.5	3.2625	358.9395	63.7692
900	265	903.5	10	2.650	361.5895	64.2400
907	272	911	7.5	2.040	363.6295	64.6024
915	279	920	9	2.511	366.1405	65.0485
925	138	927.5	7.5	1.035	367.1755	65.2324
930	100	935	7.5	.750	367.9255	65.3657
940	164	945	10	1.640	369.5655	65.6570
950	153	952.5	7.5	1.1475	370.7130	65.8609
955	171.7	960	7.5	1.28775	372.0008	66.0897
965	191.4	970	10	1.914	373.9148	66.4297
975	401.3	980	10	4.013	377.9278	67.1427
985	374	1001.5	21.5	8.041	385.9688	68.5712
1018	447.2	1050	48.5	21.6892	407.6580	72.4245
1082	358.4	1088	38	13.6192	421.2772	74.8441
1094	335.9	1096	8	2.6872	423.9644	75.3215
1098	360.5	1099.5	3.5	1.26175	425.2261	75.5457
1101	380.7	1114.5	15	5.7105	430.9365	76.5602
1128	60.7	1129.5	15	.9105	431.8471	76.7220
1131	72.1	1134	4.5	.32445	432.1716	76.7796
1137	66.5	1140.5	6.5	.43225	432.6038	76.8564
1144	100.9	1145.5	5	.5045	433.1083	76.9460
1147	88.9	1162.5	17	1.5113	434.6196	77.2145
1178	268.9	1183.5	21	5.6469	440.2665	78.2178
1189	279.3	1191	7.5	2.09475	442.3612	78.5899
1193	325.7	1207.5	16.5	5.37405	447.7353	79.5447
1222	284	1229	21.5	6.106	453.8413	80.6295
1236	291.5	1250	21	6.1215	459.9628	81.7170
1264	241.6	1270	20	4.832	464.7948	82.5755
1276	260.2	1282	12	3.1224	467.9172	83.1302
1288	256.4	1301	19	4.8716	472.7888	83.9957
1314	199.8	1324.5	23.5	4.6953	477.4841	84.8298
1335	120.5	1359.5	35	4.2175	481.7016	85.5791
1384	.9	1408	48.5	.04365	481.7452	85.5869
1432	16.5	1444.5	36.5	.60225	482.3475	85.6939
1457	42.2	1464.5	20	.844	483.1915	85.8438
1472	37.1	1507	42.5	1.57675	484.7682	86.1239
1542	186.4	1557	50	9.320	494.0882	87.7797
1572	177.6	1585.5	28.5	5.0616	499.1498	88.6790
1599	174	1603.5	18	3.132	502.2818	89.2354
1608	167	1617	13.5	2.2545	504.5364	89.6359
1626	167	1635	18	3.0050	507.5424	90.1700
1644	160	1647	12	1.920	509.4624	90.5111
1650	158	1663	16	2.528	511.9904	90.9602
1676	138	1704	41	5.658	517.6484	91.9654
1732	123	1757	53	6.519	524.1674	93.1236

Table 9. (Continued)

λ nm	$E\lambda$ $W\ m^{-2}\ \mu m^{-1}$	λ_m nm	$\Delta\lambda$ nm	ΔE $W\ m^{-2}$	E ($0-\lambda_m$) $W\ m^{-2}$	$\frac{E(0-\lambda_m)}{E(0-\infty)}$ %
1782	100	1822	65	6.500	530.6674	94.2784
1862	2	1908.5	86.5	.173	530.8404	94.3091
1955	25	1981.5	73	1.825	532.6654	94.6333
2008	49	2011	29.5	1.4455	534.1108	94.8901
2014	56	2035.5	24.5	1.372	535.4828	95.1339
2057	52	2090.5	55	2.860	538.3428	95.6420
2124	51	2140	49.5	2.5245	540.8674	96.0905
2156	47	2178	38.5	1.785	542.6534	96.4078
2200	54	2233	55	2.970	545.6234	96.9355
2266	50	2293	59.5	3.000	548.6234	97.4684
2320	47	2329	36	1.692	550.3154	97.7690
2338	44	2347	18	.792	551.1074	97.9097
2356	41	2372	25	1.025	552.1324	98.0919
2388	25	2401.5	29.5	.7375	552.8698	98.2229
2415	22	2434	32.5	.715	553.5848	98.3499
2453	20	2473.5	39.5	.790	554.3748	98.4902
2494	12	2515.5	42	.504	554.8788	98.5798
2537	1	2718.5	203	.203	555.0818	98.6158
2900	1	2920.5	202	.202	555.2838	98.6517
2941	3	2947.5	27	.081	555.3648	98.6661
2954	2	2963.5	16	.032	555.3968	98.6718
2973	5	2989	25.5	.1275	555.5244	98.6945
3005	4	3025	36	.144	555.6684	98.7201
3045	2	3050.5	25.5	.051	555.7194	98.7291
3056	2	3076.5	26	.052	555.7714	98.7384
3097	1	3114.5	38	.038	555.8094	98.7451
3132	4	3144	29.5	.118	555.9274	98.7661
3156	15	3180	36	.540	556.4674	98.8620
3204	1	3209	29	.029	556.4964	98.8672
3214	1	3229.5	20.5	.0205	556.5168	98.8708
3245	2	3252.5	23	.046	556.5628	98.8790
3260	2	3272.5	20	.040	556.6028	98.8861
3285	11	3301	28.5	.3135	556.9164	98.9418
3317	10	3330.5	29.5	.295	557.2114	98.9942
3344	2	3373.5	43	.086	557.2974	99.0095
3403	10	3426.5	53	.530	557.8274	99.1036
3450	10	3478.5	52	.520	558.3474	99.1960
3507	11	3522.5	44	.484	558.8314	99.2820
3538	10	3555.5	33	.330	559.1614	99.3406
3573	8	3603	47.5	.380	559.5414	99.4081
3633	9	3653	50	.450	559.9914	99.4881
3673	7	3684.5	31.5	.2205	560.2118	99.5272
3696	9	3704	19.5	.1755	560.3874	99.5584
3712	9	3738.5	34.5	.3105	560.6978	99.6136
3765	8	3788.5	50	.400	561.0978	99.6846
3812	7	3850	61.5	.4305	561.5284	99.7611
3888	7	3905.5	55.5	.3885	561.9168	99.8301
3923	7	3935.5	30	.210	562.1268	99.8675
3948	6	3996.5	61	.366	562.4928	99.9324
4045	5	4072.5	76	.380	562.87285	100.0000

Table 10. Wavelengths for Computation of Solar Absorptance by the Selected Ordinate Method, 50 Selected Ordinates

No.	%	$\alpha = 1.3$ $\beta = 0.02$	$\alpha = 1.3$ $\beta = 0.04$	$\alpha = 0.66$ $\beta = 0.085$	$\alpha = 0.66$ $\beta = 0.17$
1	1	360.6	363.2	361.7	365.4
2	3	399.8	403.1	401.4	406.0
3	5	420.8	424.4	422.4	428.4
4	7	439.4	443.4	441.5	447.6
5	9	454.1	461.3	456.2	462.6
6	11	467.3	471.7	469.7	476.9
7	13	480.0	484.8	482.7	490.8
8	15	492.7	497.9	495.8	504.5
9	17	505.1	510.9	508.6	518.3
10	19	517.8	526.6	521.7	532.0
11	21	530.5	537.0	534.6	545.7
12	23	543.2	550.2	547.7	559.7
13	25	556.2	563.6	561.1	573.6
14	27	569.3	576.8	574.3	587.1
15	29	582.2	589.8	587.4	600.7
16	31	595.0	603.0	600.5	614.4
17	33	609.5	616.2	613.8	628.0
18	35	621.0	629.3	627.0	641.5
19	37	634.1	642.5	640.2	655.0
20	39	647.1	655.6	653.4	668.5
21	41	660.2	668.8	666.7	682.1
22	43	671.8	682.2	680.1	696.3
23	45	686.7	697.8	693.6	710.7
24	47	701.2	710.2	708.3	725.0
25	49	714.9	724.2	722.3	732.7
26	51	729.7	739.1	737.3	754.7
27	53	744.1	753.6	751.9	773.2
28	55	760.3	772.0	770.4	788.5
29	57	777.4	787.2	785.8	804.4
30	59	793.0	802.9	801.6	822.1
31	61	809.9	820.6	819.5	838.1
32	63	827.2	837.3	836.3	876.9
33	65	849.6	873.5	871.2	919.0
34	67	892.0	916.3	914.7	978.0
35	69	949.1	976.7	957.8	1006.9
36	71	990.8	1006.4	1005.8	1032.1
37	73	1022.3	1032.2	1032.0	1059.0
38	75	1053.9	1060.2	1060.2	1090.6
39	77	1079.1	1093.0	1093.3	1148.9
40	79	1111.1	1162.7	1163.4	1198.1
41	81	1188.8	1203.6	1204.5	1236.2
42	83	1229.4	1244.2	1245.5	1279.2
43	85	1275.5	1290.7	1292.5	1332.5
44	87	1333.4	1428.3	1451.1	1533.5
45	89	1541.0	1557.7	1561.0	1595.6
46	91	1612.6	1628.1	1631.8	1664.6

Table 10. (Continued)

No.	%	$\beta = 0.02$	$\beta = 0.04$	$\beta = 0.085$	$\beta = 0.17$
47	93	1695.9	1711.9	1717.0	1751.3
48	95	1809.0	1917.1	1940.7	2022.0
49	97	2177.8	2196.1	2205.2	2240.3
50	99	3120.3	3163.8	3223.6	3346.8

Table 11. Wavelengths for Computation of Solar Absorptance by the Selected Ordinate Method, 100 Selected Ordinates

No.	%	$\alpha = 1.3$ $\beta = 0.02$ λ, nm	$\alpha = 1.3$ $\beta = 0.04$ λ, nm	$\alpha = 0.66$ $\beta = 0.085$ λ, nm	$\alpha = 0.66$ $\beta = 0.17$ λ, nm
1	.5	345.6	347.5	346.3	349.0
2	1.5	372.2	375.2	373.5	378.0
3	2.5	392.1	395.8	393.8	399.0
4	3.5	405.8	408.9	407.3	411.9
5	4.5	415.9	419.4	417.6	423.0
6	5.5	425.5	429.5	427.5	433.8
7	6.5	435.0	439.2	437.3	443.3
8	7.5	443.4	447.3	445.6	451.4
9	8.5	450.7	454.6	452.8	459.0
10	9.5	457.4	461.5	459.7	466.2
11	10.5	464.0	468.3	466.4	473.4
12	11.5	470.5	475.1	473.1	480.4
13	12.5	476.9	481.5	479.5	487.3
14	13.5	483.1	488.1	486.0	494.3
15	14.5	489.5	494.7	492.6	501.1
16	15.5	495.8	501.1	499.0	507.9
17	16.5	502.0	507.6	505.3	514.8
18	17.5	508.2	514.1	511.8	521.8
19	18.5	514.6	520.8	518.4	528.6
20	19.5	521.0	527.3	524.9	535.4
21	20.5	527.3	533.7	531.3	542.2
22	21.5	533.6	540.3	537.8	549.2
23	22.5	540.0	546.9	544.4	556.2
24	23.5	546.4	553.5	551.0	563.2
25	24.5	552.9	560.2	557.7	570.1
26	25.5	559.5	566.9	564.4	577.0
27	26.5	566.1	573.5	571.0	583.7
28	27.5	572.5	580.1	577.6	590.5
29	28.5	579.0	586.6	584.1	597.3
30	29.5	585.4	593.1	590.7	604.2
31	30.5	591.8	599.7	597.2	611.0
32	31.5	598.3	606.3	603.8	617.8
33	32.5	604.8	612.9	610.5	624.6
34	33.5	611.3	619.5	617.1	631.3
35	34.5	617.8	626.0	623.7	638.1
36	35.5	624.3	632.6	630.3	644.9
37	36.5	630.8	639.2	636.9	651.6

Table 11. (Continued)

No.	%	$\alpha = 1.3$ $\beta = 0.02$ λ, nm	$\alpha = 1.3$ $\beta = 0.04$ λ, nm	$\alpha = 0.66$ $\beta = 0.085$ λ, nm	$\alpha = 0.66$ $\beta = 0.17$ λ, nm
38	37.5	637.3	645.8	643.5	658.4
39	38.5	643.8	652.3	650.1	665.1
40	39.5	650.4	658.9	656.7	671.9
41	40.5	656.9	665.5	663.4	678.7
42	41.5	663.5	672.1	670.0	685.6
43	42.5	670.1	678.8	676.7	692.4
44	43.5	676.7	685.5	683.5	700.3
45	44.5	683.4	692.2	690.2	707.2
46	45.5	690.1	700.0	697.8	714.2
47	46.5	697.5	706.8	704.9	721.3
48	47.5	704.6	713.7	711.8	729.1
49	48.5	711.5	720.6	718.8	736.4
50	49.5	718.4	728.3	726.2	743.6
51	50.5	725.7	735.5	733.7	751.0
52	51.5	733.3	742.7	741.0	759.7
53	52.5	740.5	749.9	748.3	769.4
54	53.5	747.7	757.9	755.6	777.0
55	54.5	755.1	768.2	766.6	784.6
56	55.5	766.0	775.7	774.2	792.4
57	56.5	773.6	783.4	781.9	800.3
58	57.5	781.3	791.1	789.7	809.1
59	58.5	789.0	798.9	797.6	818.0
60	59.5	796.9	807.4	806.0	826.2
61	60.5	805.2	816.5	815.3	834.5
62	61.5	814.5	824.8	823.7	846.5
63	62.5	823.0	833.1	832.0	866.0
64	63.5	831.4	843.1	840.6	887.7
65	64.5	839.9	862.9	860.9	908.9
66	65.5	859.5	884.5	882.3	939.6
67	66.5	880.9	906.0	904.2	978.0
68	67.5	902.9	935.4	931.2	985.4
69	68.5	928.4	969.1	967.0	1000.4
70	69.5	965.9	984.2	983.3	1013.2
71	70.5	982.9	999.6	998.9	1025.8
72	71.5	998.7	1012.8	1012.4	1038.4
73	72.5	1012.4	1025.8	1025.4	1051.2
74	73.5	1025.6	1038.7	1038.5	1066.9
75	74.5	1038.9	1052.1	1052.0	1082.6
76	75.5	1052.7	1068.3	1068.4	1098.8
77	76.5	1069.5	1084.6	1084.8	1113.6
78	77.5	1086.2	1101.2	1101.6	1168.5
79	78.5	1103.2	1127.6	1130.4	1189.2
80	79.5	1140.9	1173.6	1174.5	1206.7
81	80.5	1177.7	1194.5	1195.3	1226.4
82	81.5	1198.5	1213.4	1214.5	1245.8
83	82.5	1218.6	1234.1	1235.3	1268.2

Table 11. (Continued)

No.	%	$\alpha = 1.3$ $\beta = 0.02$ λ nm	$\alpha = 1.3$ $\beta = 0.04$ λ nm	$\alpha = 0.66$ $\beta = 0.085$ λ nm	$\alpha = 0.66$ $\beta = 0.17$ λ nm
84	83.5	1239.9	1255.3	1257.0	1290.1
85	84.5	1263.2	1279.2	1280.9	1315.2
86	85.5	1287.4	1302.7	1305.1	1355.8
87	86.5	1314.4	1337.8	1342.2	1518.4
88	87.5	1359.1	1508.8	1511.8	1548.6
89	88.5	1524.1	1541.3	1544.4	1579.8
90	89.5	1558.1	1574.8	1578.1	1612.4
91	90.5	1593.9	1609.8	1613.5	1646.6
92	91.5	1631.6	1646.9	1650.8	1685.0
93	92.5	1672.8	1688.9	1693.4	1728.5
94	93.5	1720.9	1736.9	1741.9	1778.2
95	94.5	1776.8	1793.9	1800.0	1951.5
96	95.5	1983.3	2012.1	2022.1	2075.1
97	96.5	2109.9	2132.3	2142.4	2187.6
98	97.5	2239.7	2256.0	2265.4	2296.8
99	98.5	2389.0	2410.7	2428.2	2478.1
100	99.5	3583.1	3603.7	3628.9	3662.6

Table 13. Solar Spectral Irradiance (G_{λ}) Measured with SEMIS for Different AIR-MASSSES* (m) on September 10, 1976 at 1. A.U.

		G_{λ} in $W\ m^{-2}\ \mu m^{-1}$					
Wave Length nm	Air Mass m	1.2283 to 1.2196	1.2196 to 1.2130	1.2087 to 1.2066	1.2131 to 1.2196	1.2884 to 1.3099	1.5186 to 1.5703
		Time (P.M.) 12:20-12:30	12:30-12:40	12:50-1:00	1:30-1:40	2:30-2:40	3:40-3:50
305	37		5		—	—	—
315	361		232	68	—	—	—
325	394		334	243	109	53	2
335	376		347	282	183	128	25
345	466		439	376	295	203	65
355	463		445	406	329	235	97
365	465		460	446	362	268	123
375	533		531	523	448	323	154
385	495		499	501	434	318	151
395	597		598	612	544	401	198
410	758		765	798	720	536	266
430	805		833	874	797	597	282
450	939		969	1020	942	711	325
470	989		1012	1061	981	746	337
490	989		1009	1058	979	745	334
510	972		992	1050	965	740	331
530	984		1000	1065	977	751	337
550	998		1005	1079	997	761	343
570	990		989	1065	985	755	342
590	973		975	1051	972	747	336
610	949		954	1036	956	735	328
630	925		928	1003	926	717	320
650	894		897	971	900	695	311
670	863		866	942	873	675	299
690	834		834	909	849	653	288
725	752		747	821	766	589	260
775	616		616	680	638	491	217
825	417		417	460	432	331	145
875	380		376	417	385	294	126
925	333		324	360	329	252	107
975	368		343	382	347	269	118
1050	—		363	410	356	293	145

*Computed from coordinates of the Site

Latitude 38.98° N
Longitude 76° 50' 15" W
Solar declination 4° 58' 30.7"Table 12. Solar Spectral Irradiance (G_{λ}) Measured with SEMIS for Different AIR-MASSSES* (m) on August 31, 1976 at 1. A.U.

		G_{λ} in $W m^{-2} \mu m^{-1}$							
Wave Length nm	Air Mass m	1.3180 to 1.2904	1.2904 to 1.2659	1.2659 to 1.2444	1.2444 to 1.2257	1.1958 to 1.843	1.1595 to 1.1583	1.4583 to 1.5066	1.5066 to 1.5609
		Time 11:07-11:17 A.M.	Time 11:17-11:27 A.M.	Time 11:27-11:37 A.M.	Time 11:37-11:47 A.M.	Time 12:07-12:17 P.M.	Time 12:57-1:07 P.M.	Time 3:47-3:57 P.M.	Time 4:57-5:07 P.M.
305	68	42	30	10	—	—	—	—	—
315	413	358	320	268	157	4	—	—	—
325	411	405	394	387	335	195	—	—	—
335	396	387	389	380	369	290	—	—	—
345	466	481	481	460	469	412	87	66	—
355	466	479	488	490	497	456	156	132	—
365	461	483	496	498	517	500	219	192	—
375	521	554	569	580	601	606	291	261	—
385	485	509	527	560	566	575	303	279	—
395	581	601	635	692	694	709	413	370	—
410	756	781	821	897	903	933	576	530	—
430	808	859	875	976	974	1027	638	609	—
450	949	1015	1031	1147	1156	1210	771	738	—
470	1019	1080	1104	1208	1236	1278	829	785	—
490	1031	1094	1121	1210	1245	1289	836	794	—
510	1020	1089	1105	1196	1228	1278	824	790	—
530	1039	1100	1114	1201	1249	1287	838	801	—
550	1060	1110	1130	1209	1269	1297	852	802	—
570	1054	1101	1124	1193	1258	1280	843	791	—
590	1032	1085	1105	1170	1232	1257	828	780	—
610	1007	1061	1075	1138	1194	1224	809	768	—
630	980	1030	1040	1099	1154	1183	787	748	—
650	951	997	1008	1059	1114	1145	765	726	—
670	921	962	978	1020	1077	1105	742	702	—
690	892	926	947	982	1037	1064	715	678	—
725	801	825	850	876	925	946	640	604	—
775	646	665	687	708	749	766	520	494	—
825	434	446	462	476	506	516	349	332	—
875	396	404	422	432	462	469	315	298	—
925	348	346	372	372	409	405	277	253	—
975	382	361	411	390	449	424	305	267	—
1050	476	387	512	418	547	449	376	283	—

*Computed from coordinates of the Site

Latitude 38.98° N
Longitude 76° 50' 15" W
Solar declination 8° 49' 35.9"

INDOOR/OUTDOOR SOLAR ENERGY RADIOMETRIC INTERCOMPARISONS

By: E. T. Neighbors, The Boeing Company

Ed Neighbors joined The Boeing Company in 1958 and was assigned to the Environmental Test Laboratory. Early assignments were in the radiant heat field and general instrumentation. For the past twelve years he has specialized in solar energy, solar devices, space and terrestrial applications. His most recent accomplishments are in performance tests on the Boeing heliostat evaluation program.

INTRODUCTION

Solar radiation measurements are being taken around this country more now than ever before. Thermal performance determination of flat plate collectors, concentrators, heliostats and thermal power systems require accurate measurements of solar irradiance. Intercomparison calibrations of radiometers is extremely important in determining accuracy and in gaining confidence in any particular radiometer measurement. The purpose for radiometer comparison tests is to provide calibration and standardization or operational verification of various radiometers used in the measurement of solar and simulated solar irradiance. Calibrations of radiometers by intercomparison at high altitude sites have been performed annually by the Boeing Company for the past twelve years. Records maintained over these years reveal a high degree of reliability and confidence in most types of laboratory radiometers. During these calibrations, laboratory radiometers are compared with the company's primary standard radiometers.

Outdoor intercomparisons or operational checks, whether at high altitude test sites or at sea level on a building roof top, are costly and/or time consuming. If the need to verify an instruments response is now and the weather is inclement, an alternate method for intercomparing laboratory radiometers should be used. Our laboratory has been using a solar simulator for this alternate indoor method.

Recent indoor/outdoor intercomparisons made in preparation for thermal performance testing of flat plate collectors and in support of a HUD Solar Energy Demonstration Program has re-emphasized a high degree of confidence in the indoor method as well as the outdoor method of intercomparing.

The Eppley Pyranometer used at each of the Solar Energy Demonstration sites, is intercompared for an operational check. This operational verification can be performed indoors or outdoors, but for purposes of program scheduling commitments, weather conditions and cost savings, the indoor comparison was chosen.

The comparison format was to verify the calibration of two primary standard radiometers and a secondary standard radiometer outdoors, and then to repeat this verification indoors. An added test during these indoor operational checks was to tilt the pyranometers at various angles and to verify their response compared to the cosine function.

DESCRIPTION OF TEST FACILITIES

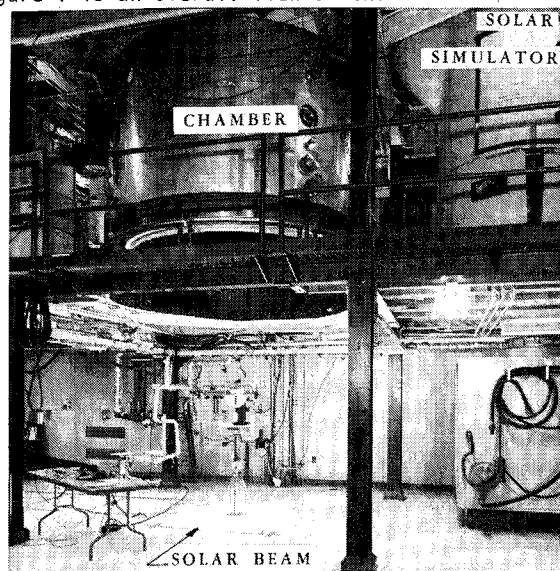
High Altitude Test Site

This test site is located in the Cascade mountain range at Lion Rock Mountain, Washington at a

latitude of 47° . It is approximately 193 kilometers (120 miles) from Seattle, and at an altitude of 2.13 kilometers (7000 ft). It has an "A" frame personnel building with provisions for four persons. The test platform is 7.9 meters x 10.4 meters (26 ft. x 34 ft). This test site is used for intercomparison of radiometers, for high voltage technology of solar panels and for terrestrial solar power research using direct solar radiation.

Indoor Test Facility

The 1.2 meter diameter (4 ft.) solar simulator is an off-axis collimated solar source. It is composed of 19 each 2.5 KW xenon short arc lamps. Around each lamp is an aconic collector which collects and directs the solar beam downward. A folding mirror directs the solar beam at approximately 45° up through a set of integrating optics, spectral filter and a quartz window located on the side of a chamber. Inside and at the top of this chamber is a 1.52 meter (60 inch) parabolic mirror which collimates and directs the solar beam into the black chamber. Incorporated with the integrating optics is a beam douser which will allow cycling the solar beam from on to off. Power controllers for each lamp are coupled to a master control where solar beam irradiance levels can be adjusted and closely controlled. This solar beam is uniform (+2% uniformity of irradiance), stable to $\pm 1/2\%$, collimated 2° half angle and is spectrally filtered to match the suns spectral energy distribution. Table 1 shows the solar simulator spectral energy distribution at AM2. Figure 1 is an overall view of the solar simulator.



DESCRIPTION OF RADIOMETERS

Primary Standard Radiometers

The two primary standard radiometers are an Eppley Angstrom pyrheliometer (International Pyrheliometric Scale), IPS, and a Radiometrics Corp., Active Cavity Radiometer ACR, (Absolute Radiation Scale, SI). Traceability to these scales, provided by the manufacturer, has been verified and/or updated by participating in intercomparisons at the Jet Propulsion Laboratory's Table Mountain Industrial Users

Site at Wrightwood, California. The reference standards used were the JPL ACR's No. 6 and No. 8 and the Eppler Angstrom pyrheliometer No. 2273, which is the property of the National Oceanic and Atmospheric Administration (NOAA) and is recognized by the World Meteorological Organization as the North American Standard instrument defining the International Pyrheliometric Scale.

Angstrom Pyrheliometer S/N 7257

This instrument is used as the primary working standard for the outdoor calibration of secondary pyrheliometers and radiometers. It uses the principle of simultaneously compensating by electrical means, the radiant energy converted to heat within the detector. It has a viewing angle of 7.4° mean ($4.2^\circ \times 10.6^\circ$ actual).

Active Cavity Radiometer, Type V-2, S/N 501-V2

This instrument is used as the primary working standard for the outdoor or indoor calibrations of secondary radiometers. It is an automatic pyrheliometer that has the capability of defining the absolute radiation scale. It has viewing angles of 5° , 10° or 15° .

TRW Differential Radiometer Model DR-2

This instrument is used both indoors and outdoors for solar radiation measurements. Outdoor measurements are made with a collimating tube that allows a viewing angle of 5.4° .

Eppler Precision Pyranometer - Model PSP

This instrument is used outdoors for the measurement of global radiation, which is comprised of the direct component of the sunlight and the diffused component of the skylight. This type instrument has been quite frequently used with solar collectors on the HUD Solar Energy Demonstration Program with sites located across the country.

TESTS

Outdoor

The comparison tests were conducted at the company's high altitude facility at Lion Rock Mountain, Washington on August 18, 1977. The primary purpose of these tests was to provide the continued traceability for radiometers to the International Pyrheliometric Scale and to the Absolute Radiation Scale.

The comparison format was the simultaneous measurement of solar irradiance by all instruments. The length of time required to produce a single measurement varies from several minutes for the Angstrom pyrheliometer to a few seconds for others. This was not a problem, however, since irradiance fluctuations were minimal and data points are recorded by taking average irradiance values over twenty minute time periods.

The test procedure was as follows:

1. Determine and record
 - a) Outdoor weather conditions; temperature, humidity, sky conditions, etc.
 - b) Position the instruments on the equatorial tracker, with 5° view angle attachment for the ACR and DR-2 radiometers.

- c) Optical zero - Record masked output of instrument at beginning and end of each observation set.
- d) Electrical zero - Record indicated reading of recording device (input shorted) at beginning and end of each observation set.
- e) Sky Radiation -
$$\frac{I \text{ uncollimated} - I \text{ collimated}}{I \text{ uncollimated}} \times 100\%$$

(To be taken periodically during the day, depending on sky conditions.) I=Irradiance
- f) TRW DR-2 Control Voltages - Measured at the head cable connector. Adjust to maintain at $5.00 \pm .01$ volts, if necessary.

2. Verify that equatorial tracker is operating.

3. Intercomparison data

Take time synchronized readings in sets of at least 10, as directed by the test conductor. Average each set of direct readings. Note any changing environmental conditions which may invalidate any particular reading. The new radiometer calibration factor is found as follows:

$$\frac{\text{Radiometer Calibration Factor}}{(\text{in } \text{mw cm}^{-2} \text{ mv}^{-1})} = \frac{\text{Avg. Primary Standard Reading (mw cm}^{-2})}{\text{Avg. Radiometer Reading (mv)}}$$

Example:

$$\begin{aligned} \text{Calibration Factor} &= \frac{95.2 \text{ mw cm}^{-2} \text{ (Angstrom)}}{7.20 \text{ mv (Instrument being checked)}} \\ &= 13.22 \text{ mw cm}^{-2} \text{ mv}^{-1} \text{ International Pyrheliometer Scale} \\ \text{or:} \\ \text{Calibration Factor} &= \frac{97.20 \text{ mw cm}^{-2} \text{ ACR}}{7.20 \text{ mv}} \\ &= 13.50 \text{ mw cm}^{-2} \text{ mv}^{-1} \text{ Absolute Radiation Scale} \end{aligned}$$

Indoor

Indoor verification tests to support the outdoor intercomparison held on August 18, 1977, were started in December, 1977. These tests were restricted to the ACR primary instrument, TRW DR-2 and the Eppler pyranometers. The Angstrom pyrheliometer was not included due to the collimation angle of the solar simulator and the view angle of the pyrheliometer.

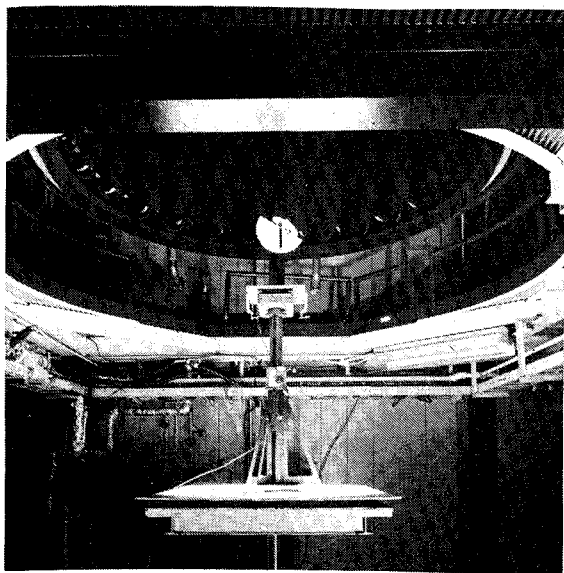
The comparison format was to position each instrument at the same location in the solar beam, control the solar beam at a constant irradiance and then measure this solar irradiance with each instrument. More than 65 Eppler Pyranometers have been verified using this comparison format.

The test procedure was as follows:

1. Position the ACR radiometer with the 15° view angle attachment in the center of the solar beam and adjust the irradiance level to equal 100 mw/cm^2 .
2. Record the output of the solar beam monitor radiometer that has been located in a fixed position elsewhere in the solar beam.
3. Determine the calibration factor for the beam monitor radiometer. The solar beam irradiance is controlled by the response of this beam monitor.

4. Remove the ACR instrument and install the instrument to be verified in this same geometrical position.
5. With the solar irradiance set to 100 mw/cm^2 as measured with the beam monitor, compare the output of the instrument being verified to this preset irradiance.
6. For the pyranometer cosine response test, the pyranometer is mounted in the same position as the previous test, only rotate the pyranometer about the center of the sensing element to the desired angle (15° , 30° , 45° , 60° and 75°). See Figure 2.

NOTE: The pyranometer views only the solar source and black painted chamber walls at these angular tilt positions.



RESULTS

Outdoor

An HP Model 9825 programmable calculator with print-out was used to record the synchronized readings, make zero corrections, calculate new calibration factors and to print out in the desired engineering units. The comparison of the two primary standard instruments revealed close agreement, Table 2. The ACR referenced to the absolute scale is typically 2.1 percent higher than the Angstrom referenced to the IPS. Table 3 shows the new calibration factor of the DR-2 radiometer referenced to the ACR. This established response was then used to compare the DR-2 radiometer, view angle tube removed, with the Eppley PSP pyranometers, 180° field of view. Table 4 illustrates that the operation and calibration of the PSP pyranometers provided by the manufacturer very closely compares to the DR-2 radiometer.

TABLE 1

SPECTRAL RANGE OF IRRADIATION	ENERGY OUTPUT, mw/cm^2	
	AM 2 SUNLIGHT*	SOLAR SIMULATOR
ULTRAVIOLET	2.0	3.7
VISIBLE	33.7	35.1
INFRARED	40.2	37.1
TOTAL	75.9	75.9

*Reference: Handbook of Geophysics, 2nd Edition, 1960

TABLE 2

PRIMARY STANDARD INSTRUMENT COMPARISON				
TIME SPAN (MINUTES)	NUMBER OF READINGS	EPPLEY ANGSTROM, IPS (mw/cm^2)	ACR, SI (mw/cm^2)	AVERAGE % DIFFERENCE*
10	9	85.18	87.02	-2.11
15	9	85.13	86.11	-1.14
15	9	87.08	87.61	-0.60
10	9	86.30	88.10	-2.04
10	8	86.78	88.72	-2.19
				AVG = -1.62

*ACR Reference

Location: Lion Rock Mountain, Washington, Latitude 47° , Altitude: 2.13 kilometers (7,000 ft)

Date: August 17, 1977

TABLE 3

CALIBRATION FACTOR - AVERAGE RESPONSE

TIME SPAN (MINUTES)	DR-2 S/N 152 ($\text{mw cm}^{-2} \text{mw}^{-1}$)*
10	13.78
15	13.82
15	13.79
10	13.80
10	13.80
AVG = 13.80	

*Reference ACR, DR-2 with 5.4° collimating tube.

Location: Lion Rock Mountain, Washington

Date: August 17, 1977

TABLE 4

EPPLEY PYRANOMETER - DR-2 RADIOMETER COMPARISON

S/N	PSP PYRANOMETER OUTPUT (mw/cm^2)*	DR-2 S/N 152 OUTPUT (mw/cm^2)**	% DIFFERENCE
15452	99.60	99.45	+0.15
15456	99.30	99.45	-0.15
15396	98.80	99.60	-1.00
			AVG = 0.33

*From manufacturer's calibration, absolute radiation scale

**From calibration factor, Table 3

NOTE: DR-2 without collimating tube.

RESULTS

Indoor

The outdoor calibration of the DR-2, S/N 152, referenced to the ACR was compared to the indoor calibration with a difference of less than one percent. Table 5 shows this verification and the linear response of the DR-2 at different irradiance levels. The cosine response test revealed that the pyranometer response falls below the theoretical cosine curve. Figure 3 shows this response for pyranometer S/N 16296. This is typical for the four instruments tested.

The 65 pyranometers, all were operationally verified indoors with the solar simulator. They show an average percent difference of -0.96 percent when compared to the secondary radiometer.

TABLE 5

INDOOR COMPARISON OF LINEARITY ACR & DR-2 RADIOMETER

ACR (mw/cm ²)	DR-2 S/N 152 mw/cm ² *	% DIFFERENCE
141.9	142.8	+0.6
123.8	124.2	+0.3
100.00	101.0	+1.0

*Using calibration factor established on August 17, 1978 (Table 3)

NOTES:

1. Irradiance held constant at 100 mw/cm² throughout experiment
2. Pyranometer was located in a black chamber with a view of the solar source and black chamber walls only

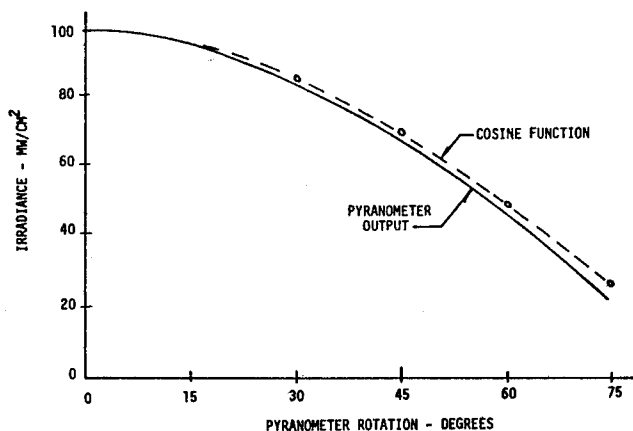


Figure 3

CONCLUSIONS

These indoor/outdoor comparisons confirm:

- Agreement outdoors of the two primary standard instruments.
- Agreement indoors of less than one percent of the ACR primary standard instrument and the secondary DR-2 radiometer.
- Agreement indoors of less than one percent of 65 pyranometers with the secondary radiometer.

- Agreement outdoors of less than one percent of 3 pyranometers with the secondary radiometer.

These agreements build confidence in the calibration method. However, these comparisons were made between Boeing controlled instruments. To continue to gain confidence in the calibration of the primary standard instruments, they in turn, must be compared with other instruments. The value of intercomparisons cannot be over emphasized. I recommend that intercomparison calibrations by government agencies and industry be conducted annually at suitable high altitude test site. This intercomparison technique would surely increase the accuracy and confidence in the data being recorded around the country.

THE NOAA/DOE SOLAR RADIATION FACILITY AND MEASUREMENT NETWORK
Edwin Flowers, NOAA/ERL-ARL, Boulder, CO

The Air Resources Laboratories of the Environmental Research Laboratories, NOAA, with support from the Division of Solar Energy, Department of Energy, has established the Solar Radiation Facility in Boulder, Colorado. Primary functions of the Facility are: (1) to maintain standard instruments; (2) to calibrate pyranometers and pyrhemometers; (3) to test specimen instruments from different manufacturers; and (4) to make radiation measurements and develop interrelationships.

Before the establishment of the Facility in Boulder, radiation instruments were calibrated and tested by the National Weather Service, NOAA, in Washington, DC. The changes that occurred with the move to Boulder were an increase in staff from one to three, improved laboratory facilities, and a fundamental change in the method of calibration of pyranometers. In Washington, the NWS used an integrating sphere with incandescent lamps to perform these calibrations. In Boulder, all pyranometer calibrations are performed outdoors in sunlight. Since November 1976 when the Facility began calibrations in Boulder, over 275 pyranometers and 100 pyrhemometers have been calibrated. Of this number about 90 pyranometers and 40 pyrhemometers have been or are in use at the NOAA/DOE solar network stations. The rest of the instruments we have calibrated were for a variety of sources so that our calibration level is in widespread use around the United States.

The radiation scale used at our Facility is the Absolute Radiation Scale. This scale is embodied in an absolute radiometer, PACRAD IIL, maintained at the World Radiation Center, Davos, Switzerland. With the exception of the Eppley Laboratory which converted to the Absolute scale in April, 1977, most manufacturers calibrate radiation instruments on the International Pyrhemometric Scale 1956. The difference between the scales is from 2 to 3 percent with the Absolute scale yielding larger values of irradiance.

Our Facility has a Kendall cavity radiometer as the primary reference. This instrument is self-calibrating and makes measurements of absolute irradiance. Secondary reference instruments which we maintain are an Ångström compensation pyrhemometer and a Smithsonian silver disk pyrhemometer. All of these instruments took part in the International Pyrhemometric Comparison in Davos, Switzerland in 1975 (1). At these comparisons, the ratio between the Davos PACRAD III and our Kendall radiometer was 1.0004.

All pyrhemometer calibrations at Boulder are done by direct comparison with the Kendall radiometer. Two or three Eppley pyrhemometers (NIPs) are always included in the calibration array as controls. Usually two or three days are used for a calibration with each day typically consisting of about 100 one-minute comparisons. Each day gives a mean calibration value and a measure of the variation of the one-minute values. The final calibration value is the average of the several days of comparison. Table 1 is a summary of the control pyrhemometer comparisons with the Kendall along with a Kahl pyrhemometer and a Matrix solar cell pyrhemometer. The Kahl was operated only during the period from April to October 1977. The response

values give the relationship between the manufacturers radiation calibration scale and the Absolute scale, with the exception that instrument Eppley 1330 embodies the NOAA version of the IPS. Eppley instruments 14856 and 14857 were purchased from them before they changed to the Absolute scale. The measures of variability given in the two right columns are the standard deviation of the daily value divided by the overall average to indicate the long term variation and the average of the standard deviation of a single observation within a day divided by the average to indicate the variation within a day. The Eppley instruments give a larger long term variation probably because of a small temperature response. Since the Kahl was used only during the warm half-year any temperature effects are minimized. The larger variation of the Matrix instrument is due to the spectral sensitivity of the photocell detector (silicon) and the fact that the spectral quality of direct sunlight changes with the sun's zenith angle and consequent changing path length of the radiation through the atmosphere. Since instrument 1330 carries the NOAA version of IPS, the significance of the response value is that all instruments calibrated by NWS/NOAA before November 1976 will yield irradiance values about 2.7 percent lower than instruments calibrated by our Facility after that date.

Calibration is transferred from a pyrhemometer to a pyranometer by the shade method. In this procedure, separate measurements are made of the global (direct plus diffuse) and the diffuse irradiance with the pyranometer. The difference of these two measurements is the vertical component of the direct radiation. This difference is compared with a simultaneous measurement of the direct irradiance made with a pyrhemometer to derive the pyranometer calibration factor. In practice these calibrations are made over a large range of solar zenith angles to obtain an empirical measure of the instruments cosine response. Figure 1 is a plot of shade calibrations made on a Spectrolab pyranometer and shows a marked variation with sun angle.

Shade calibrations are performed only for the reference pyranometers. Other pyranometers are calibrated by direct comparison in sunlight with the reference pyranometer. The method of calibration involves the calculation of a linear regression equation from ten-minute average values of the outputs of the test and reference instruments. The calibration value for the test instrument is obtained by substituting the calibration value for the reference instrument into this equation:

$$C(\text{test}) = a + b C(\text{ref})$$

where C is the calibration value and a and b are the intercept and slope from the regression calculation. The final calibration value for the pyranometer is the average of from 10 to 15 daily values. The daily calibration period is the entire sunlight period and all days excepting for those with snow, rain or low overcast cloudiness are used.

Table 2 is a summary for the month of September 1977 of pyranometer calibrations of instruments from a variety of manufacturers. As previously, the response value relates the manufacturers calibration level to the Absolute scale. The two Eppley instruments were manufactured before that company converted

to the Absolute scale. The Hy-Cal and Lintronic are seriously off scale. The Spectran instrument was received uncalibrated but with a nominal output of 10 millivolts per solar constant. The Lambda, Matrix and Rho Sigma instruments are silicon photocell detectors; all of the others are thermopile detectors. The measures of variation are the standard deviation of the daily value divided by the monthly average and the average daily standard error of a single ten-minute value divided by the monthly average and expressed in flux units of watts/square meter. The S.D./AVG shows the day to day variability in the calibration value and the S.E. gives the variability within the day. The reference instrument for these calibration was an Eppley PSP so that the values in the Table for instrument Eppley 14886F3 show the degree of comparability between like instruments. The Matrix and Lambda photocell pyranometers show good comparability with the Eppley reference in contrast to several thermopile instruments poor comparability. The Eppley 10018 (M 8-48) and Kahl 1292 (manufactured by Schenk) are black and white pyranometers.

Table 3 gives a comparison of the specimen instruments for a cloudless day and shows the degree of comparability on an hourly basis. For this table the calibration values used to derive the irradiance numbers were those determined for September 1977 and all are on the Absolute scale. The differences in the daily sums are all small with the exception of those for the Lintronic, Kahl 56114 and Hy-Cal. The average hourly departure which is the average difference between the test and reference irradiance values regardless of sign, is probably the best measure of hourly variability. The Lambda and Matrix photocell instruments give good hourly comparability. The last two instruments listed in the table are old-style Eppley pyranometers frequently referred to a light bulb types. For these instruments, the PB indicates Parsons black and LB lamp black to identify the nature of the black surface of the instrument. The bulb Eppleys were used extensively in the NOAA solar network before January 1977.

Temperature response tests are carried out on all of the pyranometers used in the NOAA/DOE network and on the group of specimen instruments from the various manufacturers. These tests are performed in the laboratory with the instrument in a temperature chamber and the light source (a 500w GE "Quartz-line" flood lamp) irradiating the instrument from outside the chamber. Figure 2 shows typical response curves for a variety of instruments. The Eppley and Spectrolab instruments have compensation circuitry to minimize the effects of temperature. The sense of the curves is that for temperatures colder than +30°Celsius, a response value greater than 1.0 indicates the sensor will give irradiance values too large by that fraction.

Ten different pyranometers from eight manufacturers were tested in the laboratory to determine changes in sensitivity caused by operating the instruments at angles tilted from the horizontal. A box 8 foot long by 15 inches square was used for the tests. The light source (a 650w quartz halogen lamp) was mounted in the center of the box on the axis of rotation. The test pyranometer and a control pyranometer were located at opposite ends of the box and were separated from the lamp chamber by apertures covered with flat opal glass windows. All of the chambers were ventilated with fans. Lamp voltage was carefully controlled and tests showed that variations in lamp output accounted for less than 0.05 percent change in the pyranometer output and were

insignificant. Figure 3 shows idealized results of the tests. In each case the curves represent either several tests of the same pyranometer or of the same kind of pyranometer. The Eppley model 8-48 pyranometer, whose sensing surface consists of alternate white and black pie-shaped segments, was tested in two modes, one with the white segment facing up and the second with the black segment up. The white up orientation showed less of a tilt effect but the difference was about the same magnitude as was found between two different model 8-48s.

The tilt effects shown in the figure are less than those found by other investigators. Since this experiment tested only the effects due to tilt, use of the instrument outdoors at tilt will introduce other problems caused by other instrument characteristics such as deviations from a true cosine response, temperature variations and spectral response errors.

NOAA/DOE inaugurated a revamped solar measurement network in January 1977. Many of the stations involved were part of the earlier NOAA network but all stations were supplied with new sensors and recorders. Figure 4 shows the network on January 1, 1978. All of the stations make global radiation measurements and within a few months all of them will be making direct radiation measurements. Ten of the stations have pyranometers mounted within a shade ring to separately measure the scattered radiation. Data is recorded on both a digital recorder equipped with both a cassette tape and a paper printer and an analog strip chart. The cassette records are one-minute integrals while the printed paper tape gives only hourly totals. The strip chart is used as a back-up and in the quality control checking of the digital tape data.

The data from the network stations is processed and checked by the Center for Experiment Design and Analysis (CEDDA) of NOAA in Washington, DC. The processing involves transfer of the data from cassette to standard magnetic tape and checking of the data against irradiance values calculated by a model devised by L. Machta of ARL/NOAA. After the checks are completed the data are sent to the Environmental Data Service/NOAA archiving facility in Asheville, NC for publication and archiving. Although problems were encountered initially in processing the network data, these have been mostly resolved and the data are now flowing smoothly through the system. Data for 1977 should be available shortly in both a publication of hourly values and on computer tape, and gradually the lag between data collection and publication should be reduced to a few months by the end of 1978.

TABLE 1
PYRHELIOMETER CALIBRATIONS

COMPARISONS WITH PACRAD (TMI 67502) - BOULDER, 1976-1978

INSTRUMENT	NUMBER		RESPONSE	S.D./AVG ¹ . (%)	S.D./AVG ² . (%)
	DAYS	OBS			
EPPLEY 1330	53	4791	0.973	±0.43	±0.37
EPPLEY 14856E6	55	6364	0.966	±0.41	±0.21
EPPLEY 14857E6	47	5210	0.961	±0.45	±0.20
KAHL 56115	(a) 16	1180	0.949	±0.16	±0.15
	(b) 10	1267	0.937	±0.19	±0.19
MATRIX 2457	36	4474	0.955	±1.30	±0.81

NOTES: 1. Standard deviation of the daily value divided by the overall average
2. Standard deviation of a single observation within a day divided by the overall average

(a) April-June, 1977
(b) July-October, 1977

TABLE 2
PYRANOMETER CALIBRATIONS

INSTRUMENT	NUMBER OF DAYS	SEPTEMBER 1977		
		RESPONSE	S.D./AVG ⁽¹⁾ (%)	S.E. ⁽²⁾ (W/M ²)
HY-CAL 56237	30	1.15	±1.65	20.1
KAHL 56114	30	1.00	2.17	20.3
LAMBDA 658-7607	15	1.02	0.95	8.1
LINTRONIC S1103A	30	0.79	3.43	34.3
MATRIX 2484	30	0.97	0.96	9.5
EPPLEY 10018 (M 8-48)	30	1.01	0.70	7.4
KAHL 1292 (SCHEVO)	30	0.97	0.65	9.8
SPECTRAN 2069	30	(0.89)	0.58	15.1
RHO SIGMA 129	30	0.95	2.07	16.7
KIPP 752492	30	0.94	0.40	5.7
EPPLEY 14886F3 (PSP)	30	0.98	0.34	5.8
SPECTROLAB 73-35 (SR75)	30	0.96	0.27	5.8

(1) STANDARD DEVIATION OF THE DAILY VALUE DIVIDED BY THE MONTHLY AVERAGE

(2) AVERAGE STANDARD ERROR OF A 10-MINUTE VALUE

TABLE 3

BOULDER - SEPT. 25, 1977					
CLOUDLESS DAY IRRADIANCE MEASUREMENTS					
INSTRUMENT	(IRRADIANCE VALUES IN W-HR/M ²)				
	SUM	DAY DIFF	%	HOUR AVG	DIFF
EPPLEY 9012 REFERENCE	5767			444	
HY-CAL 56237	5558	-209	-3.6	428	-16
KAHL 56114	5378	-389	-6.7	414	-30
LAMBDA 658	5752	-15	-0.2	443	-1
LINTRONIC 1103A	6245	+478	+8.3	480	+36
MATRIX 2484	5696	-71	-1.2	438	-6
EPPLEY 10018 (8-48)	5790	+23	+0.4	445	+1
KAHL 1292 (SCHEVO)	5758	-9	-0.2	443	-1
SPECTRAN 2069	5745	-22	-0.4	442	-2
RHO SIGMA 129	5808	+41	+0.7	447	+3
KIPP 752492	5742	-25	-0.4	442	-2
EPPLEY 14886 (PSP)	5716	-51	-0.9	440	-4
EPPLEY 12687 (PSP-072)	5704	-63	-1.1	439	-5
EPPLEY 1881 (PB BULB)	5674	-93	-1.6	436	-8
EPPLEY 2663 (LB BULB)	5778	+11	+0.2	444	0

FIGURE 1

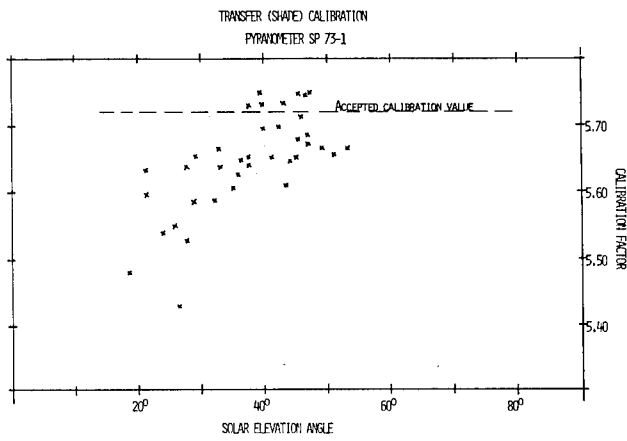


FIGURE 2

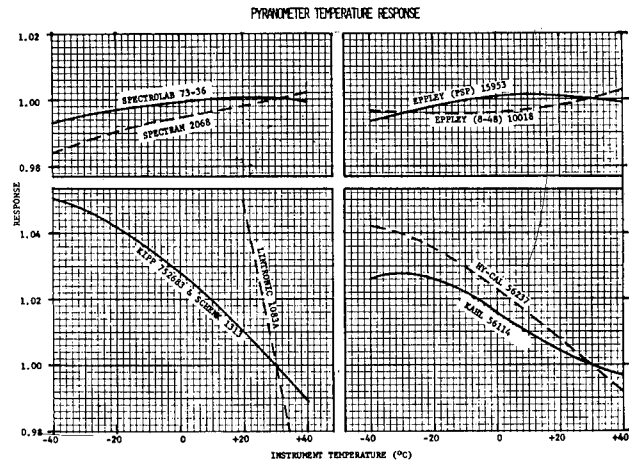
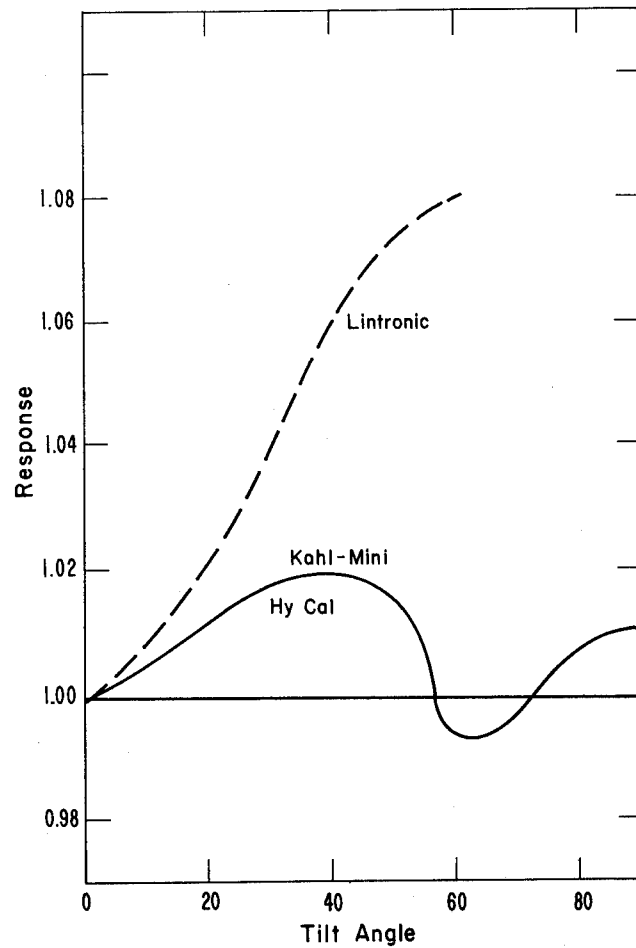
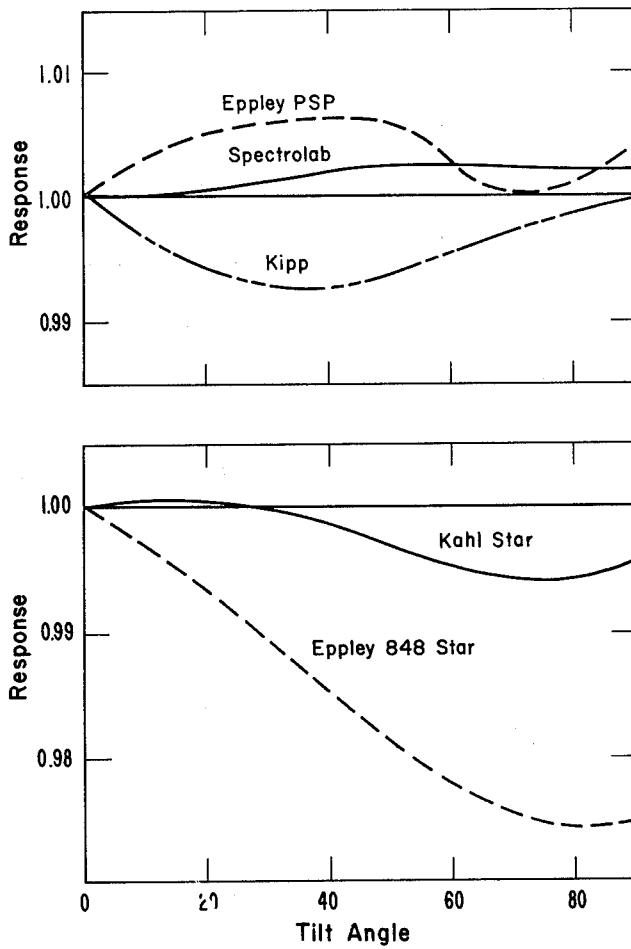
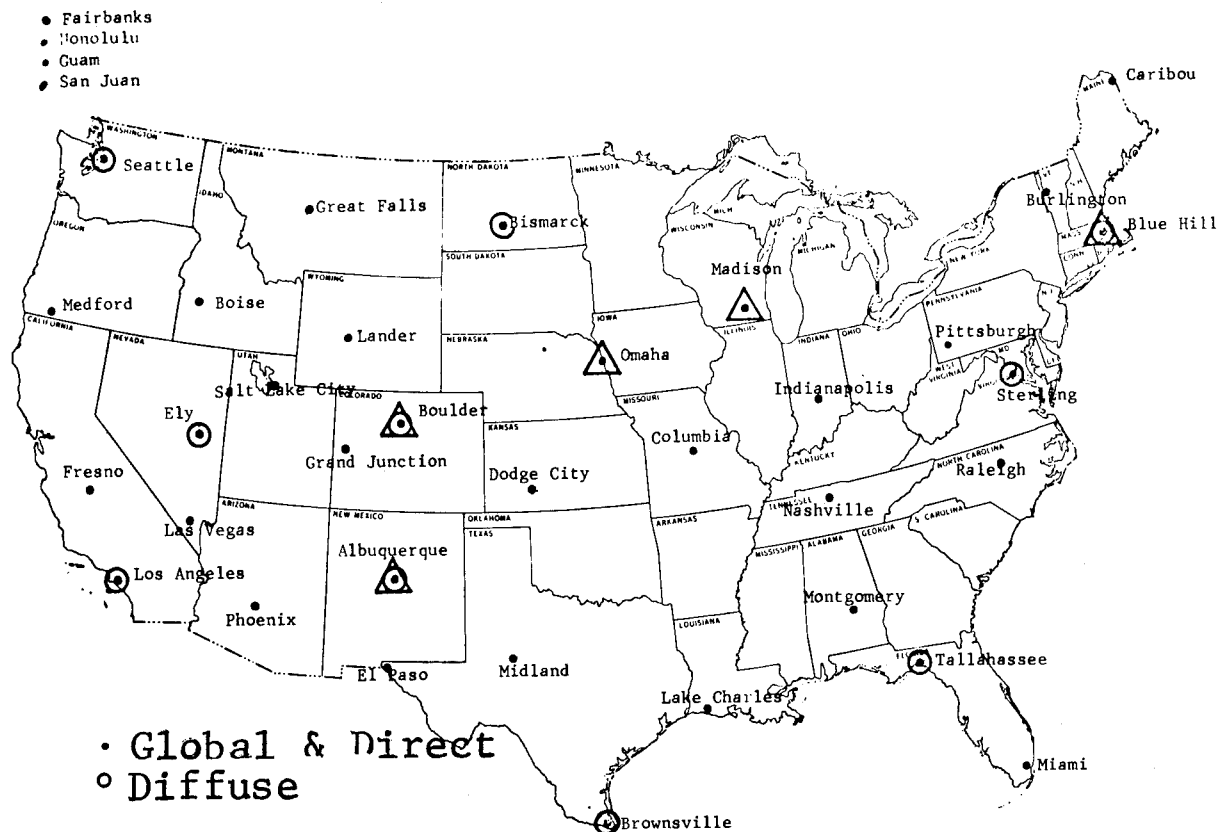


FIGURE 3





NOAA SOLAR NETWORK - 1978

FIGURE 4

Solar Radiation Data Modeling and Its Role in Solar System Studies*
Eldon C. Boes, Sandia Laboratories

Eldon Boes received his Ph.D. in mathematics from Purdue University in 1968. After spending eight years as a mathematics professor, he joined the Solar Energy Department of Sandia Laboratories in 1974. His primary areas of interest in solar energy are solar radiation resource assessment, solar data modeling, photovoltaic concentrator development, and photovoltaic system design. He has authored numerous articles and reports on solar data analysis. His hobbies include tinkering, gardening, tennis, fishing, and beekeeping. Eldon is married and has four children.

1. INTRODUCTION

Any attempt to estimate the performance of a solar energy system involves, first of all, an estimate of the amount of solar radiation available to the system. Most of these estimates are based at least partially upon solar radiation data conversion models because actual measurements of solar radiation usually refer to total energy on a horizontal surface or direct-normal energy, whereas solar energy collectors are designed in a wide variety of different configurations and orientation schemes. For example, the solar energy available to a flat-plate collector tilted upward toward the south is usually estimated from measurements (or estimates) of the amount of energy available to a horizontal surface at that location, plus measurements of direct-normal solar radiation if they are available for that location, and an estimate of the ground reflectivity in front of the collector.

This paper presents an overview of solar radiation data estimation and conversion models, and the changing role these models have played in solar system analysis over the past two decades.

Prior to the recent surge in interest in the direct utilization of solar energy, most solar system performance estimates were based upon calculations of the monthly average performances of collector arrays, thermal transport subsystems, and storage subsystems under average conditions for that month and location. For such calculations, only an estimate of the monthly average solar energy available to the particular collector scheme was required. Section 2 of this paper discusses

some of the approaches used in solar data modeling for such monthly average calculations.

In the past few years, perhaps because of the vastly increased computer capabilities as well as the increased support for solar energy research, many solar system performance analyses have utilized hour-by-hour calculations. These require hourly estimates of the solar radiation available to the particular collector design under consideration. The development of tools and solar data bases for hourly system simulations is presented in Section 3.

Section 4 presents a very brief summary of some of the current solar data modeling projects, whose results will be available in the near future.

At the present time solar system designers and modelers are faced with the problem of deciding which solar radiation data base or data model to use in their calculations. Section 5 presents recommendations regarding which solar radiation data source is considered by the author to be most appropriate for various types of system simulations.

2. SOLAR DATA MODELING BEFORE 1970

By far the most important contributions to solar data modeling for solar system performance calculations prior to 1970 were those of Liu and Jordan. Some of their principal results are summarized here; complete treatments can be found in the references [1,2].

The performance of a solar collector is strongly dependent on the amount of incident radiation, which, in turn, depends on the continuously changing solar position. Consequently, even in estimates of the monthly average performance of a solar system, the performance of the collector is usually calculated for each hour of an average solar day. The procedure for estimating the solar input for each hour of this average day, as developed by Liu and Jordan, is outlined in Figure 1. The procedure begins, in Step 1, with a value of the average daily total-horizontal solar radiation \bar{H} for the given month and location. Monthly means of total-horizontal radiation, based upon pyrometer measurements for reasonably long periods, are available for quite a few locations; the appendix in [2] lists these averages for 80 U. S. and Canadian sites. In addition, there are models for estimating these mean daily values of total-horizontal radiation based upon records of sunshine duration; see, for example, [3].

*This work was supported by the Department of Energy, Division of Solar Technology.

- Step 1: Start with an estimate of \bar{H} , the monthly average daily total radiation on a horizontal surface.
- Step 2: Calculate \bar{H}_o , the monthly average daily total extraterrestrial radiation on a horizontal surface.
- Step 3: Estimate \bar{D} , the monthly average daily diffuse radiation on a horizontal surface.
- Step 4: Decompose these average daily values, \bar{H} and \bar{D} , into average hourly values, \bar{I}_{th} and \bar{I}_{dh} .
- Step 5: Convert the hourly direct component ($\bar{I}_{th} - \bar{I}_{dh}$) and diffuse component \bar{I}_{dh} to the appropriate collector orientation.

Figure 1. A solar radiation modeling procedure for average solar system performance estimates.

Step 2 of the procedure in Figure 1 involves a straightforward calculation of H_o , the daily total radiation on a horizontal surface outside the earth's atmosphere; the formula is given in [1]. The problem of selecting the most appropriate day of the month in order to best represent the monthly mean value, \bar{H}_o , is addressed in [4].

Step 3 of the procedure represents one of the significant contributions of Liu and Jordan. In [1] they present an empirical relationship between \bar{D}/\bar{H}_o and the monthly clearness index, $\bar{K}_t = \bar{H}/\bar{H}_o$. This relationship is tabulated in Figure 2; it permits the separation of \bar{H} into direct and diffuse components.

The decomposition of these average daily values \bar{H} and \bar{D} into average hourly values of total-horizontal and diffuse-horizontal radiation, \bar{I}_{th} and \bar{I}_{dh} in Step 4 of Figure 1 are also based upon empirical relationships presented by Jordan and Liu in [1]. These daily-to-hourly decomposition relationships for \bar{H} are presented as curves in Figures 3; the decomposition curves for \bar{D} are similar in nature; see [1].

The transposition of the hourly direct-horizontal component, $(\bar{I}_{th} - \bar{I}_{dh})$, to direct radiation available to the collector's orientation in Step 5 is a straightforward geometric calculation. Converting the hourly diffuse component \bar{I}_{dh} to the orientation of the collector is more complicated; the usual procedure utilizes an assumption of uniform sky intensity and an

estimate of surface reflectivity in the foreground of the collector.

$\bar{K}_t = \bar{H}/\bar{H}_o$	\bar{D}/\bar{H}_o
0.3	0.179
0.4	0.183
0.5	0.188
0.6	0.174
0.7	0.149
0.75	0.125

Figure 2. A relationship between \bar{H}/\bar{H}_o and \bar{D}/\bar{H}_o , from [1].

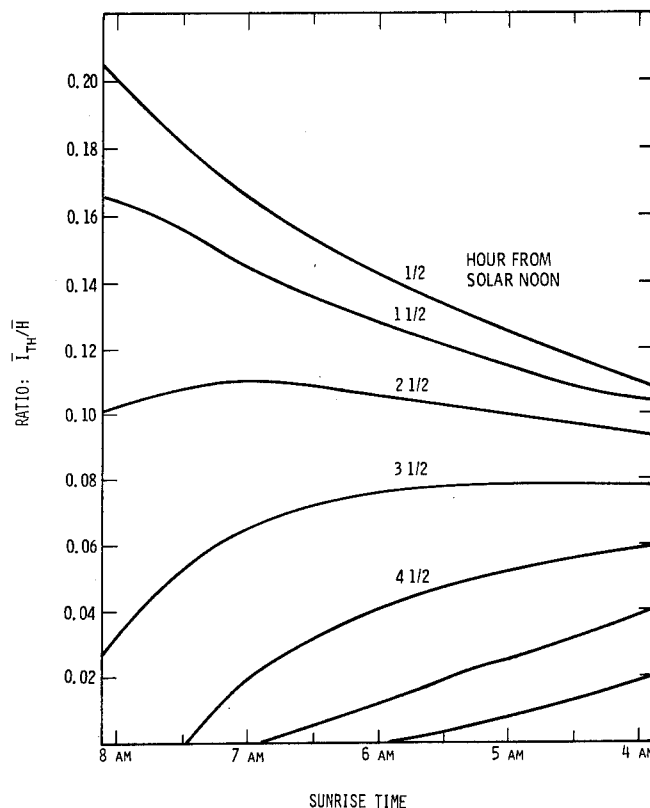


Figure 3. Curves for decomposing mean daily values of total-horizontal radiation, \bar{H} into mean hourly values, \bar{I}_{th} .

The results of this calculation are hourly average values for direct radiation and for diffuse radiation available to the collector. These are used in hour-by-hour calculations of collector performance, and the results are then combined to give the collector's average daily performance for the month. These hourly average direct and diffuse values can also be summed to give the monthly average daily total radiation for the given collector orientation.

The solar data modeling procedure described above is typical of the types of modeling used for estimating average solar collector performance before 1970. In fact, the procedure is still rather widely used in rather simple design and analysis calculations.

Numerous other solar data modeling techniques were also developed in the past. For instance, there were a number of models for estimating solar radiation intensity and for calculating hourly and daily totals of solar radiation for clear days. It is interesting that some of these were developed, not for calculating solar energy available to a collector, but for estimating the thermal requirements of buildings, especially summer heating loads.

Another solar data modeling device deserving of mention is a rather simple method for converting \bar{H} , the mean monthly value of daily total-horizontal radiation, to \bar{H}_t , a mean monthly value for the daily total radiation on a tilted surface. The conversion technique consists of simply calculating these two values, \bar{H}_o and \bar{H}_{to} , outside the earth's atmosphere, and treating their ratio as a conversion factor:

$$\bar{H}_t = (\bar{H}_{to}/\bar{H}_o)\bar{H}$$

The implicit assumption is that this ratio is not significantly affected by the earth's atmosphere.

A serious difficulty of these solar data modeling techniques is that they were based upon somewhat limited data samples, and that they were not thoroughly checked with other data samples. Unfortunately, to a limited extent, this is also a problem for some of the newer data modeling techniques described in the next section.

This discussion of solar data modeling techniques prior to 1970 is by no means comprehensive. Even the description given above of the data conversion technique developed by Jordan and Liu only describes a limited portion of their work. Their original paper [1] includes several other solar data modeling results including relationships between the atmospheric transmissions of direct-normal radiation, total-horizontal radiation, and diffuse radiation under clear sky conditions. This relationship is compared with three similar models in the next section.

3. RECENT SOLAR DATA MODELING

During the past several years there has been a rapid increase in the development and use of computer models for simulating and analyzing solar energy systems. These solar system analysis models typically perform hour-by-hour calculations of system energy flows based upon system loads and solar inputs. These models usually require

hourly solar, temperature, and wind data as inputs to the calculations. Consequently, quite a lot of effort has gone into developing solar data tapes - computer tapes containing hourly values for solar radiation, temperatures, wind information, and other meteorological parameters.

The largest computer data base available for developing solar data tapes consisted of the hourly solar tapes and the hourly weather tapes of NOAA. The hourly solar tapes existed for about 20 years for about 30 U. S. locations, and the weather tape data base was considerably larger. These tapes were processed and archived by the National Climatic Center; the data was recorded by the National Weather Service.

These hourly NOAA solar and weather data tapes were not suitable for using directly in the various solar system models for several reasons. First of all, the hourly solar tapes contained frequent data gaps and cases of data not in chronological order. Secondly, they only contained data records for daylight hours, so the number of hourly records per day varied. Thirdly, there were significant reservations regarding the accuracy of the solar radiation measurements on the tapes. These reservations were traceable to questions about instrument calibration procedures, instrument and recording equipment maintenance, radiation scale differences, etc.

Another limitation of the NOAA hourly solar tapes for use in solar system models was that they only contained values of total radiation measured on a horizontal surface. The solar system computer analysis models required a calculation of the amount of solar radiation available to the particular type of collector array under consideration, and this required splitting the recorded hourly total-horizontal value into its direct and diffuse components, followed by a conversion of these components to the collector's orientation. The best way to make the separation wasn't known however. Of course, this separation was also essential for any analyses involving concentrating collectors since these can only use the direct component.

Several efforts were begun with the objective of producing solar data tapes for use in solar system studies. Four of these efforts will be summarized here. The first was the production of hourly solar data tapes for the years 1962 and 1963 for approximately 30 U. S. sites by the Aerospace Corporation. These tapes were developed from the hourly NOAA solar and weather tapes described above. All missing total-horizontal data was estimated using models based principally upon the hourly opaque and total sky cover records. The tapes also contained hourly estimates of direct-normal radiation. These direct-normal values were generated with a simple regression formula.

The values are now believed to be generally too high, as the comparison which is presented later in this section indicates. Another problem of these tapes is that no attempt was made to correct the readings of total-horizontal radiation which were taken from the NOAA hourly solar radiation tapes described above. Nonetheless, the tapes proved to be very useful for many solar system studies over the past several years.

The second solar data tape development effort was conducted at Sandia. There, the emphasis was on developing quite accurate solar data tapes, especially relative to direct-normal radiation, for a few representative sites around the U. S. Sandia's work began with an extensive effort directed toward more accurately separating hourly values of total-horizontal radiation into its direct and diffuse components. The result was several different formulas, including one designed to reproduce the statistical distribution of the direct-normal values for given readings of total-horizontal radiation; see [5]. These models were applied to NOAA's hourly solar tapes for eight U. S. locations for the years 1962 and 1963. On these solar data tapes an attempt was made to use station histories and instrument calibration records to correct the recorded total-horizontal readings. However, some of the data gaps on the tapes were not filled, and the tapes were never widely distributed.

At this stage the three major solar data tape actors, NOAA, Aerospace, and Sandia, joined forces on a project to develop the Augmented SOLMET solar data tapes. The project included:

- Correcting all total-horizontal readings on NOAA's hourly solar tapes according to a clear solar noon radiation model.

- Developing a model for hourly total-horizontal radiation based upon sunshine and cloud cover, and using it to fill all data gaps.

- Developing a new model for separating the hourly total-horizontal values into direct and diffuse components, and using it to add hourly direct-normal values to the tapes.

The first of these three tasks was performed by agencies within NOAA. A "standard year" model for the intensity of total radiation on a horizontal surface for clear skies at solar noon was developed by D. Hoyt at the Atmospheric Research Laboratory (ARL) of NOAA; the model varied with date and location. At the National Climatic Center (NCC) of NOAA, actual readings of total-horizontal radiation for clear solar noons on the tapes were identified and adjusted to fit the model values. All other values of total-horizontal radiation on the tapes

were similarly adjusted by interpolation between these clear solar noon peg points.

The second task was also performed by NOAA; the sunshine and cloud cover model was developed by G. Cotton of ARL. Its general form is a product of a clear sky value reduced by a factor dependent upon minutes of sunshine or opaque cloud cover or both. The actual parameters in the model were derived separately for each site by regression on the existing data. This model was applied to the data gaps in the tapes by F. Quinlan at NCC.

The third task was performed by Aerospace under a contract with Sandia. The new model for separating the hourly values of total-horizontal radiation into direct and diffuse components was developed by C. Randall; see [6]. Its primary advantages are that it was derived from several recent, high quality sets of simultaneous total-horizontal and direct-normal data. Like one of the models described in [5], it reproduces the real statistical distributions of the direct-normal readings for given intervals of total-horizontal radiation. The model was then used at Aerospace to add hourly estimates of direct-normal radiation to the data tapes.

This is one of the most important solar data modeling projects of recent years. The end result is the set of augmented SOLMET solar data tapes, about 23 years of hourly direct and total solar radiation data and weather data for each of 26 U. S. locations. These tapes do have some residual problems. The two most noteworthy are that a great deal of the solar data was estimated, especially for certain locations, and that the standard year model technique forced all of the data from year-to-year at each site to fit a model which is certainly not appropriate for every year.

Nonetheless, these augmented SOLMET tapes are clearly the best, long-term solar data tapes with nationwide coverage which are currently available for solar system analyses. The tapes are available from the National Climatic Center of Ashville, NC, and are fully described in the SOLMET Manual which is available from that same agency.

The fourth major effort directed toward developing solar data tapes for use in computer models for solar system studies is the Typical Meteorological Year (TMY) project of Sandia Laboratories. The goal of this project is to produce for each of the SOLMET locations 1 year data bases which are typical of long-term solar radiation and weather conditions for the given locations. The basic procedure has been to choose Typical Meteorological Months (TMM's) independently for each site and connect these into a TMY. The basic criteria used in selecting the TMM's is

that their cumulative frequency distributions (CDF's) for certain key parameters, such as daily total-horizontal radiation, daily max temperature, and daily min temperature, fit the long-term distributions of these parameters for the given site and month. Thus, the TMM's are not selected solely on the basis of best fitting long term averages, since the cumulative distributions reflect parameter variability as well. The final TMM selection also considers the numbers and lengths of runs of certain combinations of extreme values of the parameters, such as consecutive cold days of low solar radiation, etc.

These TMY's are available from NCC with supporting documentation. At this time, they represent the best available "standard" solar data tapes. Their widespread use will allow better system designing and cross-comparisons between different systems' studies. A byproduct of this project is that some statistical information, such as CDF's and run sequences, is also available for the SOLMET sites.

Another solar data activity of recent years worthy of mention is the solar radiation availability project completed last year at Sandia. Under this project, the seasonal and geographic distributions of direct and of total solar radiation availabilities to various orientations and configurations of both fixed and tracking collectors were calculated. The major conclusions are:

Maps and tables of total-horizontal radiation seriously underestimate the amount of solar energy available to solar collectors.

There is approximately the same amount of direct radiation available to a tracking, concentrating collector as there is total radiation available to a fixed, tilted flat-plate collector.

A complete summary of this project, including extensive tables of solar energy availabilities to various fixed and tracking collectors across the U. S., can be found in [7].

The final topic of this section is a discussion of some of the more famous models for separating hourly readings of total-horizontal radiation into direct and diffuse components. The four formulas to be compared are of a similar type; they all have the form

$$k_B = f(k_T)$$

where

$k_T = I_{TH}/I_{HO}$ is the percent of possible total-horizontal radiation for the hour

$k_B = I_B/I_{SC}$ is the percent of possible direct-normal radiation for the hour.

In these formulas, I_{HO} is the calculated hourly extraterrestrial radiation on a horizontal surface, I_{TH} is the measured hourly total-horizontal radiation, I_{SC} is the calculated hourly extraterrestrial radiation on a surface normal to the sun's rays, and I_B is the desired hourly value of direct-normal radiation.

The four formulas of interest are plotted together in Figure 4. The curve labeled J & L is a formula presented by Jordan and Liu in their 1960 paper [1]. Since it was presented there as being empirically derived from clear sky data, it is not surprising that this curve does not predict direct-normal values well under all sky conditions.

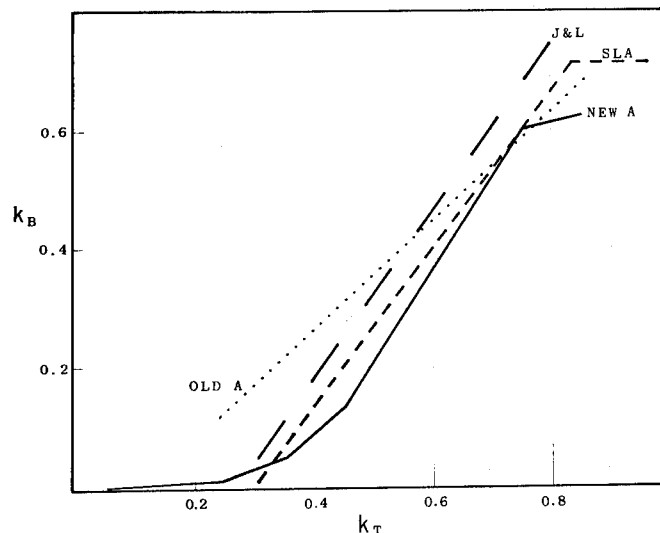


Figure 4. Four formulas for separating hourly total-horizontal radiation into direct and diffuse components.

The curve labeled "Old A" is the formula used by Aerospace in generating values of direct-normal radiation on their original 1962-1963 solar data tapes. This curve was derived by regression from a data base consisting of hourly total-horizontal values obtained from NOAA's hourly solar tapes combined with hourly values of direct-normal radiation interpolated from the direct-normal intensities which were published by NCC in their monthly publication "Climatological Data National Summary". It is now known that these direct-normal values were probably biased upward because low values of direct-normal radiation under cloudy conditions were often omitted. The reason seems to be that the principal purpose of these direct-normal measurements historically was for extrapolating information on the solar constant; thus, they were of little interest under cloudy conditions (or for estimating available energy).

The curve labeled SLA is the formula used by Sandia in their solar energy availability project [7]. This formula was derived by regression from data samples consisting of simultaneous readings of total-horizontal radiation and direct-normal radiation for three U. S. locations. The total and direct data were read from original strip chart records archived at NCC, and an attempt was made to trace and correct any data problems caused by calibration problems and instrument drift. It is now believed that, for percent of possible values in the range $0.3 < k_T < 0.5$, the direct-normal data may have been biased upward. Such values of k_T can occur under changing cloud conditions, and while it is difficult to read the corresponding value of k_B too low (since they are bounded by 0), it is possible to read it too high.

The final curve to be discussed is that labeled New A. This curve is based upon the total-horizontal separation algorithm developed and used by Aerospace in their addition of hourly direct-normal values to the Augmented SOLMET tapes described earlier. Basically, for each value of k_T , this curve specifies the mean of the distribution of values of k_B which that algorithm generates. This algorithm was derived from approximately one year of simultaneous direct-normal and total-horizontal data from each of four U. S. locations. Thus, the algorithm is based upon a total of four years of data, all quite recently and carefully recorded.

The formula labeled New A is considered to be the most reliable of these four. It is worth noting that these formulas are quantitatively very different, especially for intermediate values of k_T . For instance, for $k_T = 0.45$, the formula labeled SLA gives a value nearly 70 percent higher than the value given by New A; for both J & L and Old A the difference is even larger. As a consequence, for a relatively hazy or cloudy location where such intermediate values of k_T are frequent, these other three formulas can be expected to estimate unrealistically high mean daily totals for direct-normal radiation. (The solar radiation availability tabulations given in [7] are easily corrected using the addendum to that report.)

4. CURRENT SOLAR DATA MODELING EFFORTS

This section briefly mentions some of the solar data projects which are currently in progress.

ERSATZ Data Set. The sunshine and cloud cover based model for estimating hourly total-horizontal radiation which was developed by NOAA for filling gaps in the Augmented SOLMET tapes is being utilized to generate hourly total-horizontal data for an additional 220 U. S. sites for which no hourly radiation measurements exist.

Aerospace's algorithm for estimating direct-normal will also be applied to these data tapes, and it appears that the algorithm for selecting Typical Meteorological Years will also be applied for these locations. The result will be greatly expanded long-term hourly data bases and typical year data bases.

Representative Area Study. A study of how large a geographic area can be represented by a solar radiation measuring station is underway. For several sites around the country, this study will determine the regions surrounding each site for which solar energy availabilities are likely to be within 95, 90, and 75 percent of those measured at the site.

Microclimate Solar Radiation Studies. Three projects are underway which are directed toward characterizing the differences in solar radiation for specific types of microclimates. The three studies are specifically studying solar radiation differences in

- a mountain-valley region
- a metropolitan area
- a coastal-inland region

Tilted-Surface Algorithm Study. Several different algorithms for computing solar radiation incident upon tilted surfaces are being compared and checked with real data.

Circumsolar Data Project. A study is underway to characterize the distribution of solar radiation intensity from the center of the solar disc radially out to about 3 degrees. This is motivated by the fact that normal incidence pyrheliometers, the instruments most commonly used to measure direct-normal radiation, actually accept radiation from a disc of about 5.7 degrees diameter, while the solar disc is about 1/2 degree in diameter, and concentrating collectors have various, design-dependent acceptance apertures.

Research Data Sites. Eight universities have been funded to operate research solar radiation monitoring stations. Thus, high quality, specialized research solar data sets will be available in a few years.

Solar Energy Atlas. Plans are being formulated for the development and publication of an atlas containing statistical information on solar radiation and surface parameters of interest in solar energy. The atlas will include tables and maps of average solar radiation availabilities, information on heating and cooling loads, information on amounts of radiation above various threshold intensity levels, information on extremes and sequences of extreme values, etc.

New Data. The National Weather Service of NOAA has recently begun operating a new, 38 station solar radiation network. Both total-horizontal and direct-normal measurements are being made. This data will be made available by NCC on computer tapes and in a monthly solar radiation summary.

5. PRESENT STATUS AND RECOMMENDATIONS.

At the present time a number of hourly solar data tapes are available for use in computer analyses of solar systems:

 TMY Tapes, 26 U. S. Sites

 Augmented SOLMET Tapes, 26 Sites,
 23 years each

 ERSATZ Data Tapes, 220 U. S. Sites

 New Data from 38 Station Network

For hour-by-hour calculations for system design or performance analysis for typical solar and weather conditions, the TMY tapes are most appropriate. For locations between the 26 TMY sites, it is probably reasonable to perform the calculations for the 2 or 3 nearest TMY sites. For situations in which longer-term calculations are preferred, the

Augmented SOLMET tapes are appropriate.

For simulations in which real data is desired, even though it is probably not typical, the data from the new 38 station network is appropriate.

The ERSATZ data will be more fully developed and documented in the next few months. After that time, it will provide a data base for many more locations.

At present there are two major sources for statistical information on solar radiation availability. Information on average availabilities to various collector geometries should be obtained from [7], corrected as indicated in the addendum to that report. Information on frequency distributions of daily totals of solar radiation and daily max and min temperatures, etc., and on sequences of various combinations of these parameters are available with the TMY tapes from NCC. In the future, this statistical information will be available in the Solar Radiation Atlas.

It is generally recommended that the solar radiation information described above be used whenever reasonable. This information is believed to be reasonably accurate, and widespread adoption of these sources would permit more comparisons of systems' study results. As the comparison of the models for separating hourly total-horizontal values indicates, solar data models can have a significant impact on the amount of solar energy which is calculated to be available to a collector; consequently solar data models should be used very cautiously, and only when necessary.

References

1. B. Liu and R. Jordan, "The Inter-relationship and Characteristic Distribution of Direct, Diffuse and Total Solar Radiation." *Solar Energy*, 4(3), pp 1-19, July 1960.
2. B. Liu and R. Jordan, "A Rational Procedure for Predicting the Long-Term Average Performance of Flat-Plate Solar Energy Collectors." *Solar Energy*, 7 (2), pp 53-70, April 1963.
3. G. Lof et al, "World Distribution of Solar Radiation," Report No. 21, Solar Energy Laboratory, U. of Wisconsin, July 1966.
4. S. Klein, "Calculation of Monthly Average Insolation on Tilted Surfaces," *Solar Energy* 19 (4), pp 325-329, 1977.
5. E. Boes, "Estimating the Direct Component of Solar Radiation," Sandia Laboratories Energy Report SAND75-0565, November 1975.

6. C. Randall et al, "Hourly Direct-Normal Solar Radiation Data Tapes for the United States." Proceedings of the Amer. Section of the International Solar Energy Society Meeting, Orlando, FL, June 1977.
7. E. Boes et al, "Availability of Direct, Total, and Diffuse Solar Radiation to Fixed and Tracking Collectors in the U. S. A." Sandia Laboratories Energy Report SAND77-0885, August 1977.

OTEC BIOFOULING AND CORROSION TESTING PROGRAM

By: Eugene H. Kinelski, U.S. Department of Energy, Division of Solar Technology, Washington, D.C. 20545

Author's Biography

Eugene H. Kinelski is a Program Manager in Ocean Thermal Energy Conversion, U. S. Department of Energy, Division of Solar Technology. He is responsible for the planning and management of research and development in Biofouling, Corrosion, and Materials.

Prior to joining DOE, Mr. Kinelski was with the Copper Development Association where he was engaged in market development of copper alloys in electric vehicles, solar heating and cooling, and shipbuilding. Previous assignments were as Director of Technical Activities of the Process Equipment Group of Combustion Engineering and in Product and Market Development of nickel alloys with the International Nickel Company, Inc. He holds degrees in Metallurgical Engineering from Purdue University and the University of Pittsburgh.

Mr. Kinelski is a Commander, USNR (Retired), with experience in anti-submarine warfare and guided missiles.

ABSTRACT

The success of an OTEC power system is heavily materials oriented. The unprecedented requirement for high heat transfer and massive size of the OTEC heat exchangers has stimulated a test program where emphasis is placed on studies of heat transfer, corrosion, biofouling and its countermeasures, and materials selection. The OTEC hardware development program ranges from testing heat transfer by single tubes, to small multi-tube heat exchangers, and in large 1 MWt and 1 MWe "core" test units. The OTEC Seacoast Test Facility planned for start-up in the summer of 1979 offers an opportunity to consolidate all component development and testing.

Introduction

The concept of Ocean Thermal Energy Conversion — capturing the sun's warmth in the surface seawater and utilizing the temperature difference between the warm surface water and the cold, deep seawater to generate electricity — has intrigued a number of proponents for fifty years or more. Five years ago, the Federal government initiated an OTEC development program. The budget for OTEC is \$35.5 million during FY 1978.

As background information, it may be advantageous to consider some of the general details of an OTEC plant before we describe the testing program that is underway. Figure 1 is a schematic diagram of an OTEC closed cycle system. Figures 2 and 3 illustrate two conceptual designs produced by TRW and Lockheed. Figure 4 illustrates the grazing plant ship concept of the Applied Physics Laboratory of Johns Hopkins University. The grazing plant ship will operate in equatorial waters where the thermal resource is at its maximum and will use the generated electricity to manufacture an energy intensive product, such as ammonia for fertilizer or aluminum.

In the OTEC power system development program, the heat exchangers were considered to be the critical technology that needed to be developed. Because of the inherent low efficiency of an OTEC cycle based on annual average temperature differences of only 35-40°F, the heat exchanger thermal performance and size represent key problem areas.

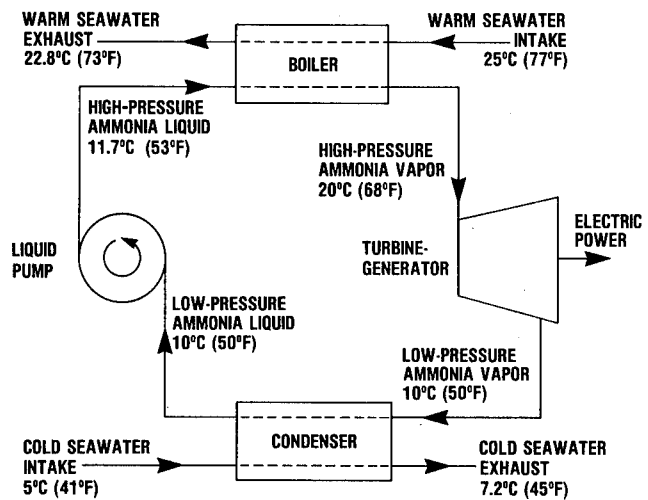


Figure 1

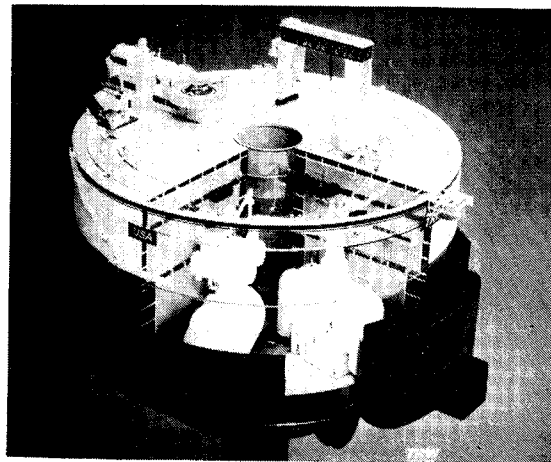


Figure 2

From an economic standpoint, a critical factor is the heat exchangers. Material selection, manufactureability, corrosion, and biofouling, also influence the cost of the ultimate commercial plant.

The principal components in which materials play a key role are:

- Heat exchangers-evaporator and condenser
- Turbine
- Inlet Screens
- Cold/Warm Seawater Intake Pipes
- Power Cable
- Demisters
- Pumps, valves and piping

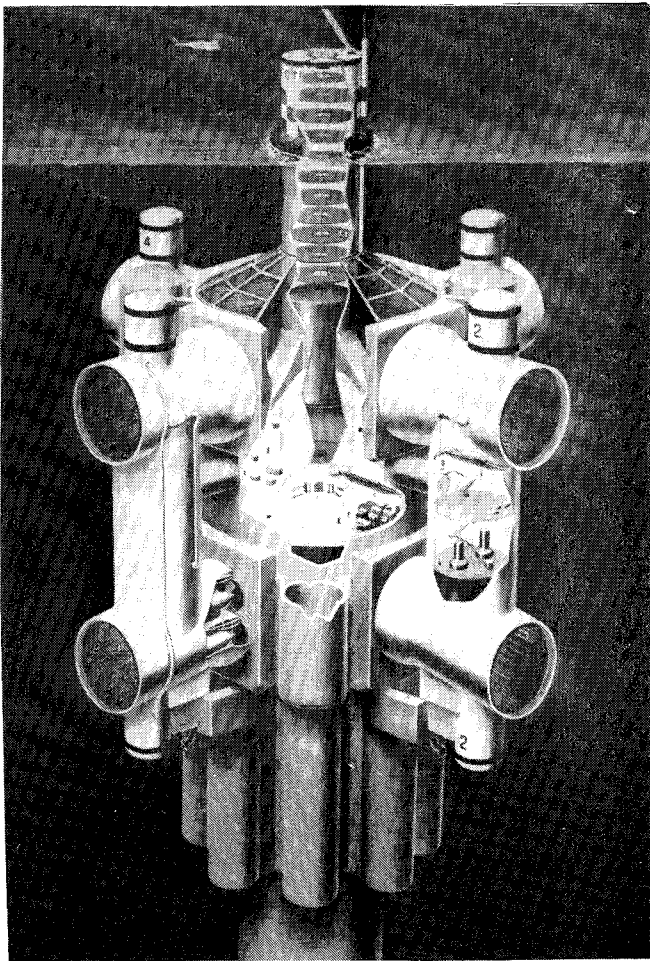


Figure 3

Hull

Mooring system

OTEC Test Philosophy

An OTEC power plant introduces some unique problems that will require special developmental tasks. As in any engineering development program, it is necessary to strike a balance between the degree of simulation of design conditions and size of the hardware required. OTEC experimental efforts commenced with small-scale studies in university and industrial laboratories. Subsequent projects involved single-tube tests, for example, at selected ocean sites. Small heat exchangers are being evaluated with a 1 MWt "core" test unit representing a bench scale model. Ocean tests of 1 MWe (40 MWt) heat exchangers are planned for a component testing facility aboard a platform to be known as OTEC-1.

Modular system experiments are being planned at the 10 MWe level. Commercialization should proceed if the competitive costs are attractive. This is expected to be achieved in U. S. island markets at an early date. Figure 5 illustrates our milestone chart for achieving these goals.

OTEC Heat Exchanger Tests

A number of concepts have been developed by universities and industry to provide the needed heat transfer capability for OTEC power plants. They are:

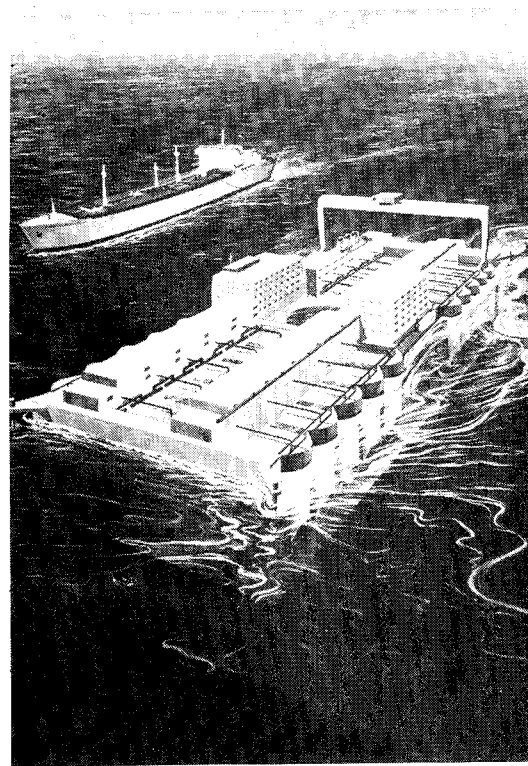


Figure 4

Spray film evaporators

Pool boiling evaporators

Falling film evaporators and condensers

Trombone evaporators and condensers (seawater on the outside of the tubes)

In these shell-and-tube heat exchangers (the trombone type is really a shell-less type), various types of tube enhancements were used. These involve flutes on the inside and outside of the tubes, metallic coatings on the outside of the tubes, and corrugated tubes. After evaluating these concepts with single tube heat transfer tests, 1 MWt units were manufactured and are being tested at the Argonne National Laboratory (ANL). These units use ammonia as the working fluid and demineralized water as the medium for supplying heating and cooling. After the ANL tests are complete, it is planned to install these units at the OTEC Seacoast Test Facility.

Biofouling Evaluations

In order to maintain design heat transfer coefficients in OTEC heat exchangers, the tube-side seawater biofouling must be closely controlled. If allowed to build up, thin microfouling films, of the order of a few microns, could have a significant impact on the thermal performance of OTEC heat exchangers.

A fouling thermal resistance, R_f , of $.0005 \text{ hr. ft.}^2 \text{ }^\circ\text{F/BTU}$ could be tolerated in an OTEC plant. However, an R_f of $.0001$ would be a marked improvement, while still being an attainable goal.

Carnegie-Mellon University has developed a device to measure the influence of biofouling on the heat transfer measured using a single tube. The apparatus is illustrated in Figure 6. Such CMU

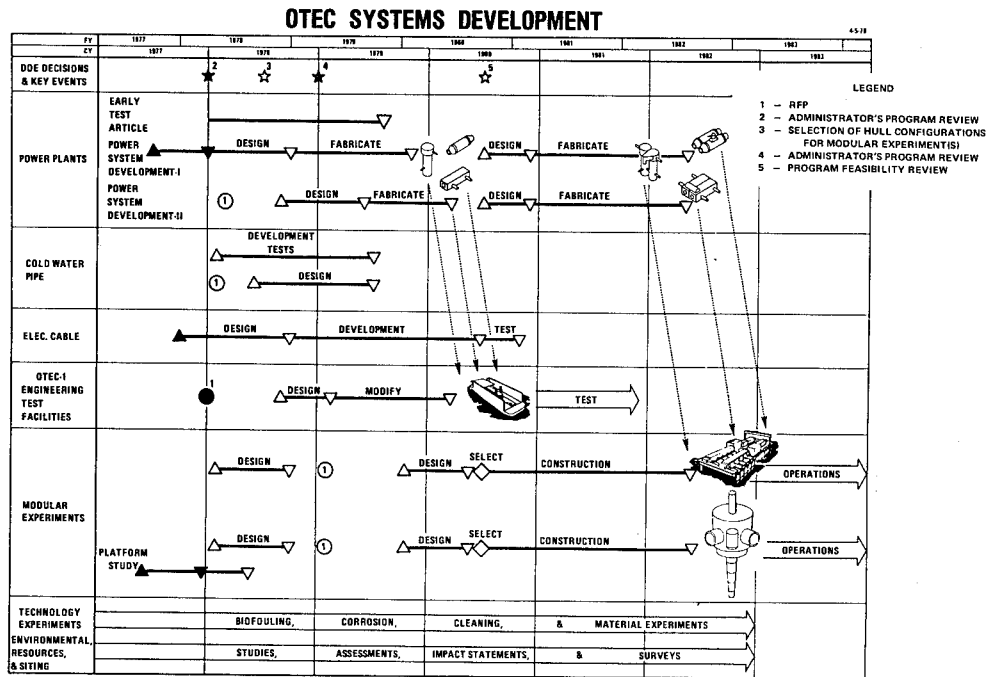


Figure 5

devices have been used to evaluate Rf versus biofouling build-up at the following ocean sites:

Ke-ahole Point, Hawaii

- on a research vessel, Noi'i
- on a submerged buoy (Figure 7)

St. Croix, U. S. Virgin Islands

- on a U. S. Navy barge

Gulf of Mexico

- on a tugboat
- on a NOAA 40' discus buoy 180 miles west of Tampa (Figure 8)

Typical data are given in Figure 9.

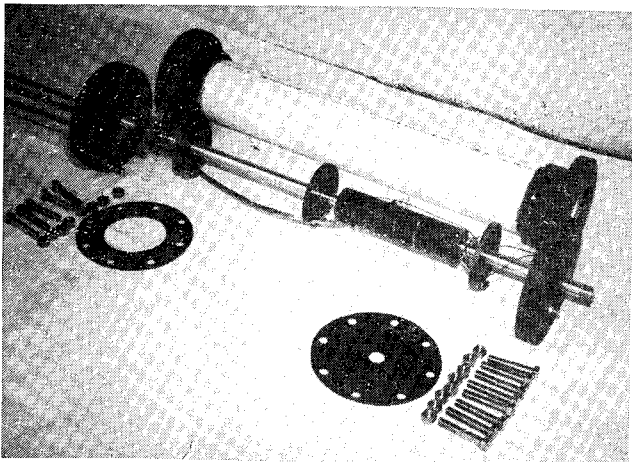


Figure 6

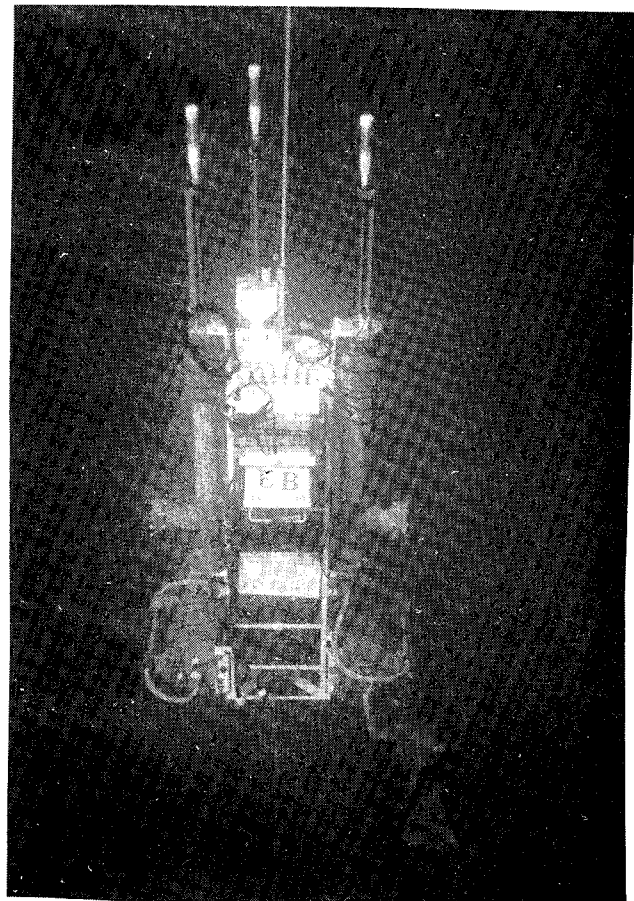


Figure 7

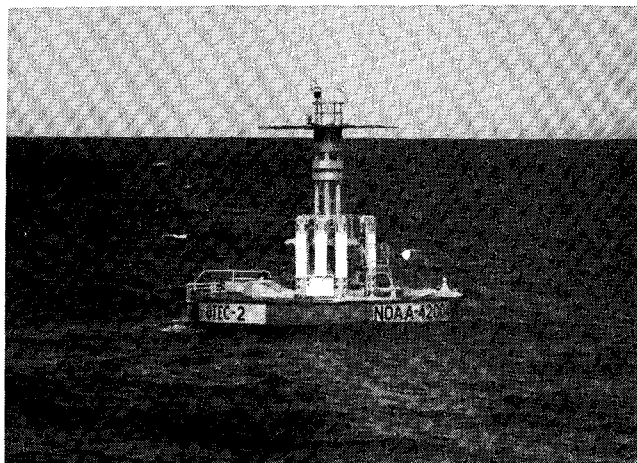


Figure 8

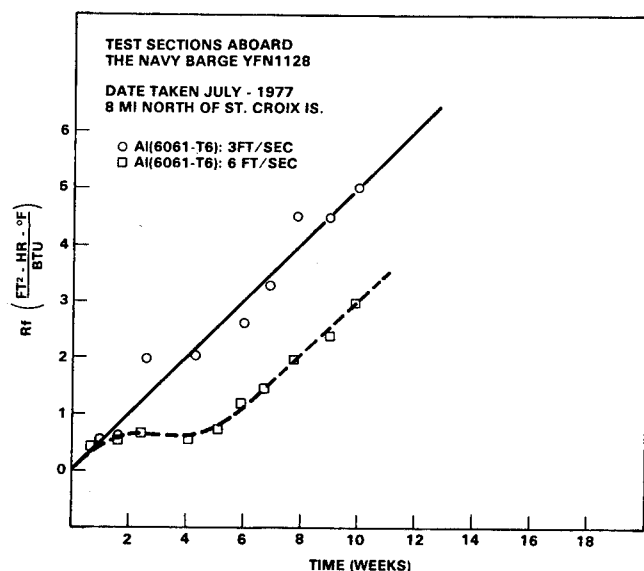


Figure 9

Countermeasures for Microbiofouling

Based on the data collected for the effect of biofouling on the degradation of heat transfer, it appears that a cleaning procedure involving one cleaning per week or less could keep the Rf below .0001. Cleaning experiments, as countermeasures to microbiofouling, have been designed and are under test at Panama City, Florida. They include:

- M.A.N. brushes
- Amertap balls
- Chlorination
- Slurry
- Water Jet

Very preliminary data on the M.A.N. brush system indicate that when one brush is propelled by a reversal of the water flow every 8 hours, microbiofouling can be kept below an Rf of .0001. Verification of this test and data from the other systems are required.

Corrosion Evaluations

The selection of materials for OTEC heat exchangers is a key item in the success of commercial OTEC power plants. Titanium is the likely candidate for the first generation of heat exchanger tests, for example, on the OTEC-1 test platform. The 1 MWe heat exchangers will use titanium tubes and titanium clad steel tube sheets. Although more expensive than aluminum in initial cost, their life cycle costs may be comparable, depending on their relative longevities against corrosion.

A great deal of test effort has gone into qualifying aluminum heat exchangers because of the potential capital cost reductions compared to other materials and the possibility of using extruded, enhanced fluted surfaces. In addition, tests are proceeding on the evaluations of AL-6X stainless steel and Copper Alloy 706 - 90% copper - 10% nickel. Stainless steel is a good candidate, ranking close to titanium. The copper-nickel alloy's resistance to corrosion in ammonia working fluids needs to be determined. Its resistance to seawater corrosion is excellent. Also, its anti-fouling characteristics might aid in keeping the seawater surfaces free of fouling.

Corrosion tests are being conducted at each ocean site. The tubes removed from the CMU devices are evaluated for corrosion damage in addition to analyzing biofouling deposits. At each site, additional tubes are evaluated without measuring heat transfer.

In addition to the ocean site tests, studies of the corrosion resistance of the various alloys and the effect of calcareous deposits are conducted at the Dow Chemical plant in Freeport, TX using Gulf of Mexico water. The problem of leakage of ammonia working fluid into seawater and the leakage of seawater into ammonia are of great concern. Tests in recirculating loops at Dow indicated a very heavy calcareous scale deposit on flat strips of metal exposed to small amounts of ammonia (8 to 800 ppm) in seawater. The resultant reduction of heat transfer has mandated a policy decision to monitor for ammonia leaks, locate any leaking tubes and plug them.

The tests of seawater leakage into ammonia are not yet conclusive. However, it seems that deposits of calcareous scale may not be a problem. Corrosion resistance of metal specimens is also being evaluated.

Future Test Plans

An OTEC Seacoast Test Facility is scheduled for start-up during the summer of 1979. It is specifically intended as a "center of excellence" in OTEC, and marine engineering, in general. The facility will serve to conduct heat transfer, biofouling, corrosion, cleaning, and material studies on heat exchangers ranging from single tubes to small complete heat exchangers to 1 MWt "core" test units. The studies will include testing of auxiliary components such as pumps, piping, screens, valves, and cables. A cold seawater intake pipe will provide seawater with deep, open ocean water quality. A warm seawater intake pipe will provide clean seawater characteristic of open ocean water. Plans have been initiated to eventually conduct marine corrosion, biofouling, and materials courses for interested individuals, such as utility personnel.

With the program underway that has been reported to you this afternoon, and the new activity planned for the new Seacoast Test Facility, the OTEC program should be ready for commercialization in the mid 1980's.

TESTING THE OTEC COLD WATER PIPE USING THE "DEEP OIL X-1" PLATFORM
Edward E. Horton¹, J. Randolph Paulling, Jr.² and Leonardo Pérez y Pérez¹

ABSTRACT

This paper describes the at-sea testing of an OTEC Cold Water Pipe model to be conducted from the "Deep Oil X-1", a test platform, previously used as a tension leg platform. The tests, to be conducted in the Fall of this year, have two objectives: 1) to compare the experimental responses to analytical predictions and 2) to evaluate the performance of the Cold Water Pipe in the open sea.

INTRODUCTION

In 1975, Deep Oil Technology, Inc. (DOT) conducted an at-sea test program of a Tension Leg Platform. This platform, the "Deep Oil X-1", is owned and operated by DOT and is presently moored in the Long Beach Harbor. In the Fall of this year, DOT will conduct at-sea Cold Water Pipe tests for the Department of Energy OTEC program under the direction of the Applied Physics Laboratory of The Johns Hopkins University from the "Deep Oil X-1".

The Cold Water Pipe tests will consist of supporting an instrumented steel pipe five feet in diameter and up to 1000 feet long from the "Deep Oil X-1". The dynamic behavior of the pipe will be measured for various sea conditions, platform motions, pipe lengths, and pipe supporting means. These measurements will be compared with computed values based on existing frequency and time domain computer programs. The results of the comparison will provide a basis for determining the capability of the computer programs to predict the response of the Cold Water Pipe. These tests will be carried out with the "Deep Oil X-1" operating in a catenary moored configuration (like a semi-submersible) in water depths up to 1000 feet.

In addition to the above, the tests will also provide a direct means of evaluating the overall workability of the system and thus provide insight into future OTEC design parameters. This is particularly important in defining the means by which the Cold Water Pipe is to be supported or coupled to the vessel. At the present time, this critical area is strongly influencing the selection of the vessel, i.e., whether the vessel should be a ship, semi-submersible, tuned sphere, etc. as well as the design of the pipe itself.

At the completion of the verification tests, it may be desirable to carry out further testing of a specific Cold Water Pipe design. The test methods and equipment will be suitable for this purpose. It may be possible to modify the five foot diameter steel pipe to simulate the new design by altering its overall stiffness.

In summary, the results of the Cold Water Pipe tests will provide a basis developed from actual operational experience for designing both the OTEC test plants and the large scale commercial plants.

BACKGROUND

In the various OTEC test and commercial systems which are currently in design or planning stages, the design of the Cold Water Pipe is emerging as a particularly difficult problem. This pipe is suspended beneath the floating OTEC platform and extends to a depth of approximately 3,000 feet. The diameter ranges from six feet in the OTEC 1 test project to upwards of 100 feet in the proposed large commercial plants. Suggested pipe materials include steel, aluminum, fiberglass and reinforced concrete. Essentially, the pipe behaves as an elastic body suspended from a floating platform. The pipe is set into motion by the action of waves upon it and by the motion of the platform to which it is attached. This results in a dynamic stress system within the pipe and possibly large lateral motions along the length, especially at the lower end.

ANALYSIS OF PIPE RESPONSE

In analyzing the motion and stresses in the Cold Water Pipe, two types of analysis have been followed:

- Linear frequency domain techniques
- Non-linear time domain techniques

Linear frequency domain techniques have been used by J. R. Paulling and Roderick Barr of Hydronautics Inc. to solve for the motion of the elastic pipe and floating platform. Although there are slight differences in the basic techniques used by these two investigators, both are capable of predicting the response to a random seaway by linearly superimposing solutions.

Non-linear time domain solutions of the OTEC pipe have been carried out by other investigators, using programs originally developed for investigating oil drilling riser pipe dynamics, such as MRDAP, a computer program developed by DOT. In most of these solutions the dynamic coupling to the floating platform is not modeled completely, but only represented by the time history of the motion of the top of the pipe. Complete dynamic system effects resulting from interaction between pipe and platform motions is therefore not thoroughly represented.

The principal advantage of the time domain approach is its ability to handle non-linear fluid effects such as interaction between waves and steady current and non-linear elastic effects which are encountered in some of the proposed cold water pipe materials. Most such analyses have been made for only regular wave trains since random simulation requires the expenditure of considerable computer time.

¹ Deep Oil Technology, Inc.

² Dept. of Naval Architecture, University of California at Berkeley

In both methods of analysis, certain critical assumptions are made regarding the hydrodynamic forces acting on the cold-water pipe. Typically, the forces are separated into components due to wave pressure, drag, and added mass, and somewhat simplified hydrodynamic procedures are used in computing each component. The drag forces may be equal in importance to the other components. The drag coefficient is Reynolds number dependent. It is clear therefore that any experiment designed to test the computed performance of the cold water pipe will have to be carried out in such a way as to represent the Reynolds number of the full scale Cold Water Pipe. Normally, this can be accomplished by utilizing a large scale model. To date, the only experiments on complete systems of elastic pipes which have any relationship to the present problem have been conducted on instrumented oil drilling risers. The proprietary position of the oil companies involved in such experiments have generally kept the results of the experiments out of the public domain.

PROPOSED EXPERIMENTAL PROGRAM

It is considered very desirable at the present time to conduct some large scale experiments with a model representing one or more of the OTEC Cold Water Pipe configurations. The "Deep Oil X-1" platform is of sufficient size and capability to serve as a floating test platform for a Cold Water Pipe of cross-section approximately equal to that proposed for the OTEC 1 program. The results of the proposed experiments will be especially valuable for two reasons:

- They will provide data near enough to full scale to be accurate. These can be used for testing and judging available and future Cold Water Pipe analysis techniques.
- They will provide essential basic hydrodynamic data on the nature of the fluid forces acting on the Cold Water Pipe.

In this experimental program the following parameters will be measured:

- Pipe motion in the two lateral directions at approximately 20 stations equally spaced along the length. Accelerometers will be used to measure these motions.
- Motions in six degrees of freedom of the floating platform.
- Wave input to the platform Cold Water Pipe system, preferably in the form of directional sea spectra.

The stiffness of the attachment of the Cold Water Pipe to the platform will be varied from zero (pin connected) to very stiff (built-in) by the relatively simple mechanical means shown in Figure 2 and described later. Provisions will also be made for optionally installing at least one in-line universal joint in the pipe itself.

The stations which are instrumented for motion sensing will be spaced closely enough to define the mode shape of the pipe response. Preliminary calculations have been performed that indicate that the Cold Water Pipe model will have mode shapes with three to six nodes. An example of these calculations is shown in Figure 3. It is important that the lower end of the pipe be instrumented since this location may experience large motions under certain conditions.

TEST EQUIPMENT AND PROCEDURES

The "Deep Oil X-1" platform will be used to suspend the Cold Water Pipe for the tests. Figure 1 shows the platform and pipe as they would appear on station. The platform motion characteristics are shown in Figure 4, without the Cold Water Pipe.

In order to accomplish the Cold Water Pipe tests the following test and operational equipment will be used:

- Instrumentation assembly
- Pipe support equipment
- Pipe handling equipment
- Mooring system

The instrumentation package is very similar to that used in the tension leg platform tests. All of the sensors for the environmental parameters and platform motions will remain the same. The only major modification will be the addition of accelerometer measurements along the Cold Water Pipe length. These accelerometers will be wire-line mounted and supported in four internal guiding tubes.

The pipe support equipment will consist of a gimbal at the platform deck and a lower ring centralizer as shown in Figure 2. The lower ring is restrained horizontally by the wire ropes and deck-level tensioners. By varying the resistance provided by the tensioners, the degree of fixity of the pipe support can be varied from near zero with almost no restraint at the lower ring to nearly built-in with the tensioners locked and thus a very stiff restraint at the ring.

The pipe handling equipment will be as simple as possible consistent with practical procedures. Plans are to use a skid system to transport the pipe joints to an A-frame that will position the joint for make-up. The pipe string will be lowered and lifted by wire ropes passing over the A-frame as shown in Figure 5 and landed in the gimballed spider as shown in Figure 6.

The catenary mooring system will consist of several anchors and mooring lines placed by an anchor handling boat and tied off to spring buoys. These are in turn connected to existing lines and winches on the platform that afford control.

FINAL RESULTS AND APPLICATIONS OF EXPERIMENTS

The results of these experiments will be compared with computed results for the measured wave input

using the Paulling frequency domain procedure and the DOT time domain procedure as well as other computer programs which might be appropriate and are made available to DOT by the Department of Energy. Factors to be examined and computed include:

- The basic nature of the pipe response including the distribution of motion amplitudes along the length (mode shape) and the frequency of the response.
- The agreement between measured and computed response and a comparison of the two different computed methods.
- Drag and other coefficients used in the computations, the sensitivity of response to these parameters, and choices of specific values for computation.
- A comparison of the relative accuracy and other features of the two analysis techniques.

COMPARISON WITH ANALYTICAL PREDICTIONS

Analytical predictions of the behavior of the Cold Water Pipe can be broadly classified as to their method of analysis into frequency-domain and time-domain. An example of frequency-domain solutions is J. R. Paulling's ATEC computer program, an example of time-domain solutions is DOT's MRDAP computer program.

The method of comparing experimental Cold Water Pipe behavior with analytical predictions is somewhat different if the predictions are made with frequency-domain methods than if they are made with time-domain method. Figures 7 and 8 show the basic approach in making the comparisons.

Comparisons with frequency domain predictions must be based on the response spectra: as calculated by the analytical program and as determined from the experimental records. Direct comparison of ranked maximum responses can only be achieved if further assumptions are made with respect to the statistical properties of the responses, such as broadness of their spectra.

Comparisons with time-domain predictions can be based on the response spectra: by treating the analytical time series similarly to the experimental time series and comparing their spectra. They can also be based on the ranked maximum responses without having to make any further assumptions.

ADDITIONAL TESTING

The testing set forth above is primarily directed toward evaluating the analytical methods currently available for predicting the behavior of the Cold Water Pipe. It may be desirable to carry out additional large scale model tests of specific Cold Water Pipe designs.

The equipment and procedures set forth herein are suitable for this purpose and a pipe model can be constructed which could approximate the hydroelastic properties of a full scale Cold Water Pipe.

The initial effort of the test program is directed toward verifying the analytical tools, but once this is accomplished, consideration should be given toward evaluating the performance of a specific design.

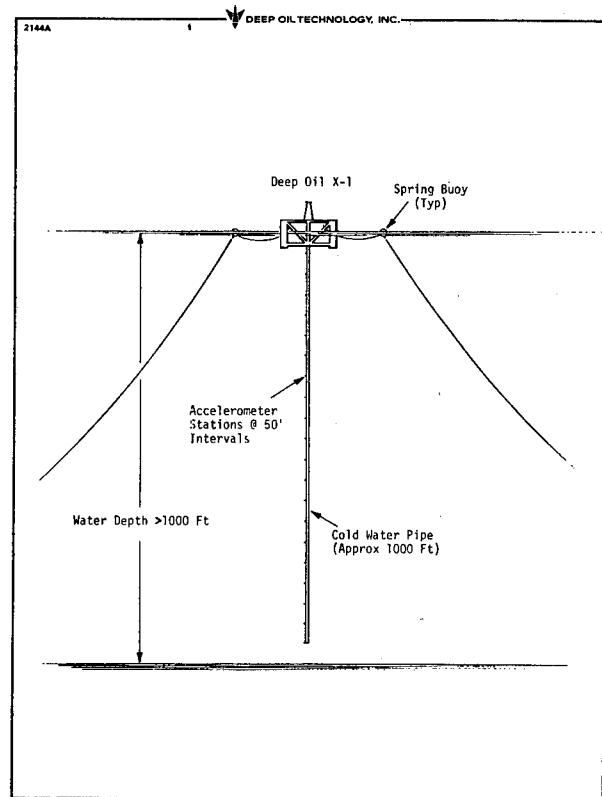


Figure 1. Cold Water Pipe Test with "Deep Oil X-1"

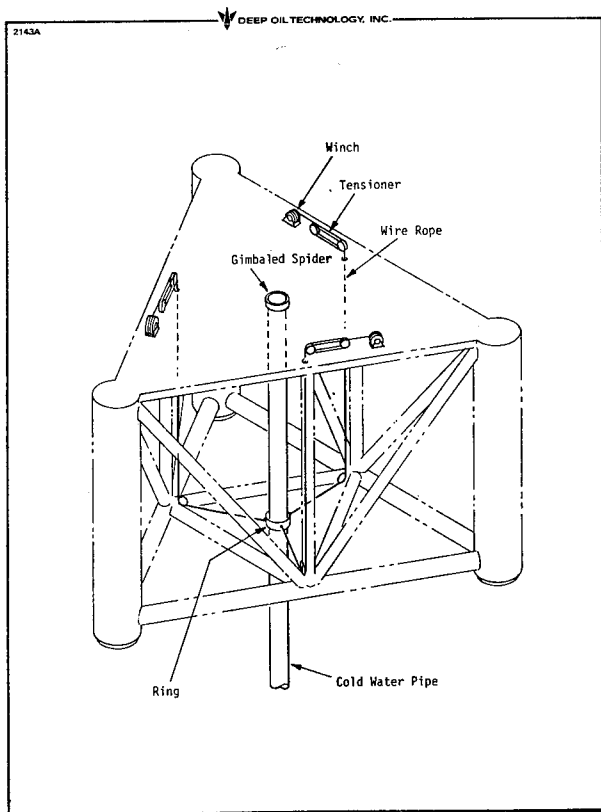


Figure 2. Cold Water Pipe Support System

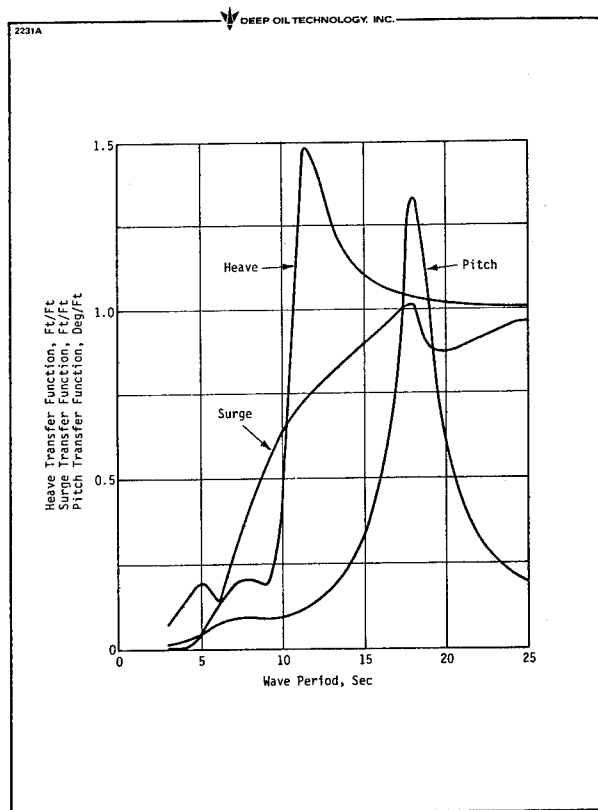


Figure 4. "Deep Oil X-1" Free-Floating Transfer Functions

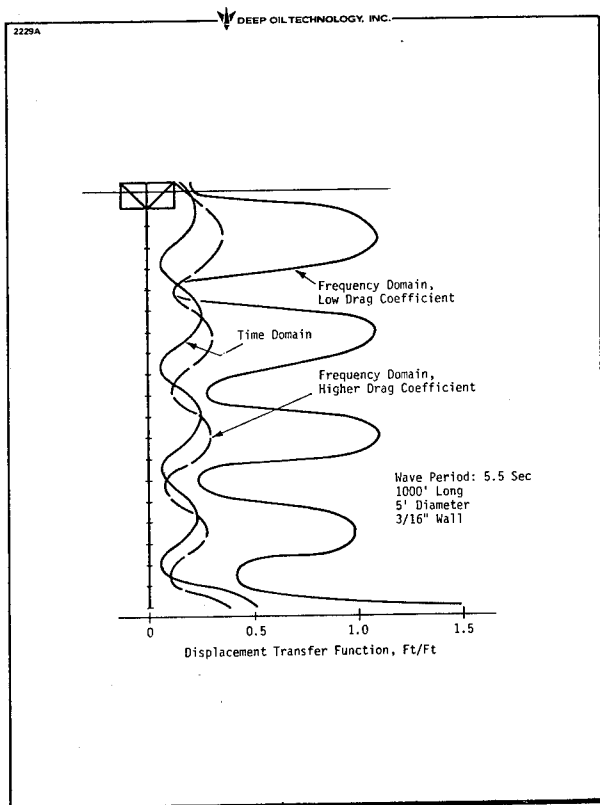


Figure 3. Typical Motion Transfer Function Prediction Comparisons

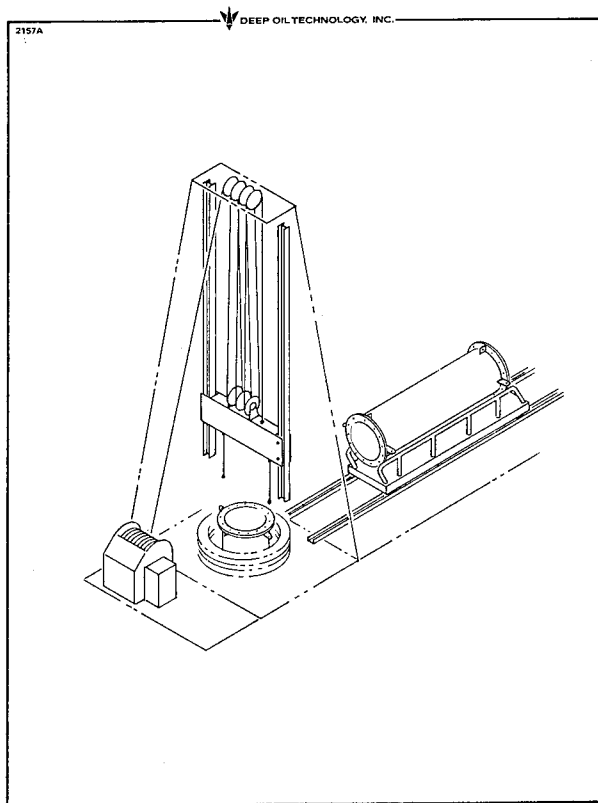


Figure 5. Hoist System

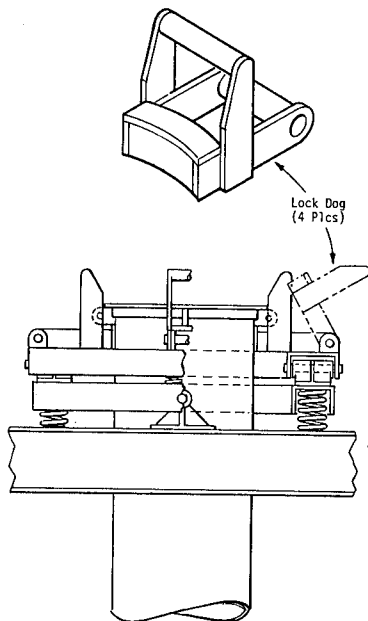


Figure 6. Gimbal Spider

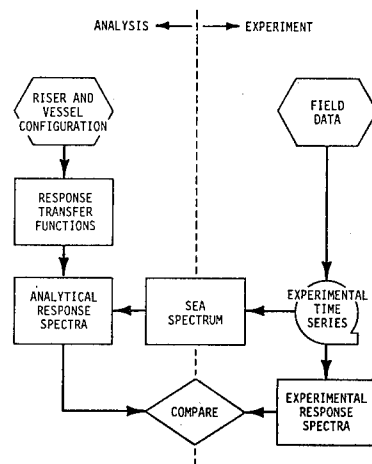


Figure 8. Experimental Data Comparison with Frequency Domain Programs

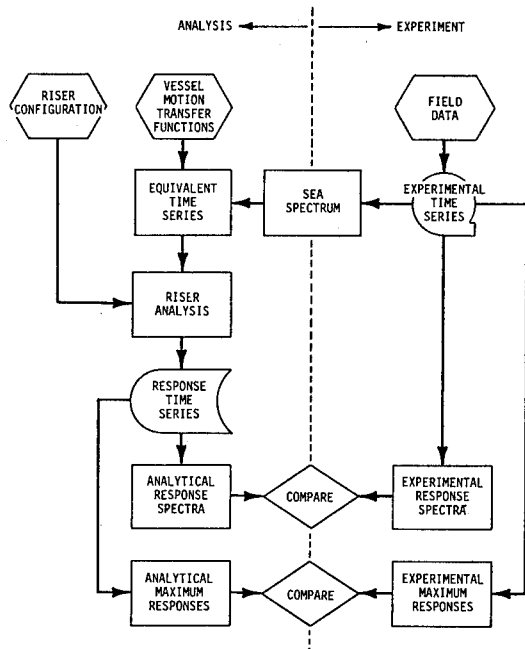


Figure 7. Experimental Data Comparison with Time Domain Programs

OCEAN THERMAL ENERGY CONVERSION (OTEC) POWER PLANT
INSTRUMENTATION AND MEASUREMENT

By: Lloyd G. Lewis, Argonne National Laboratory, Argonne, IL.

AUTHOR'S BIOGRAPHY

Present Position - Senior Physicist, Energy & Environmental Systems Division

Education - BS, Physics, University of Chicago, 1939; PhD, Physics, University of Chicago, 1946.

Member of the American Physical Society; Senior Member of the Instrument Society of America.

ABSTRACT

The objectives of the Ocean Thermal Energy Conversion (OTEC) program were analyzed in order to determine the types of measurements that will be needed on the power cycle, and the accuracies that will be required. The results indicate that precise measurements will be required to provide meaningful results on parts of the program. It is probable that conventional instrumentation of the type used in chemical manufacturing or petroleum refining will be inadequate. Some of the instrumentation used at the OTEC heat exchanger test facility at Argonne may be suitable for use in an OTEC plant, while other instrumentation may not be suitable even though the accuracies are high. This is the result of the large size of the equipment in an OTEC plant compared to the sizes of the laboratory exchangers.

INTRODUCTION

The primary goal of the OTEC program is to promote the use of the ocean thermal energy resource. This program includes research and development to enable the design of new, more cost effective equipment and to conduct tests to measure performance in an OTEC environment.

The heat exchangers needed for an OTEC plant are unusually large so that high performance designs offer economic rewards. High efficiency pumps and turbines also increase the attractiveness of the OTEC plant.

The research and design of high performance heat exchangers have been carried out under contracts sponsored by DOE. These use various heat transfer enhancement techniques. Data obtained from measurements on single tubes have been used to design exchangers of a one megawatt thermal size. Exchangers built to these designs by DOE contractors are now under test at the Argonne National Laboratory test facility. It is expected that the results of these tests will guide the development of the 40 megawatt thermal (one megawatt electric) exchangers that are needed for the next step in the program. These 40 megawatt thermal exchangers are to be tested on the OTEC-1 floating platform at a site in the warm ocean.

Measurements aboard the OTEC-1 will include evaluating the performance of the components employed in the power cycle. These measurements will evaluate the effects of corrosion on performance, evaluate the effects of biofouling of the heat exchanger surfaces on performance and evaluate the

effectiveness of various cleaning methods for restoring the performance of the fouled exchangers to that of new or clean exchangers.

The purpose of this paper is to describe the measurements that are required in the power cycle and to determine the accuracies needed to properly evaluate the effects of corrosion, fouling and cleaning.

The OTEC Power Cycle

A number of detailed design calculations have been made for the OTEC power cycle, to try to optimize the investment and operating costs. Some of these design calculations were done as parts of studies aimed at identifying and designing several test facilities that would be useful for the OTEC program (1), (2).

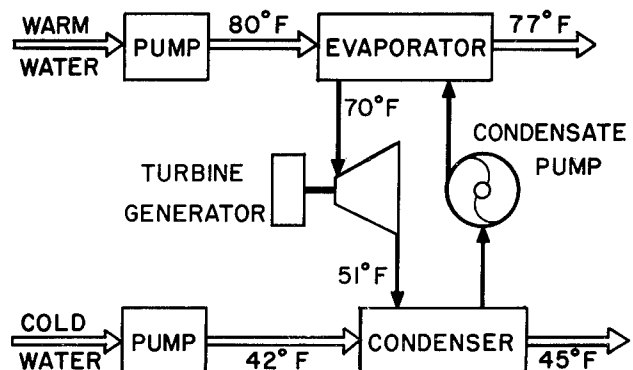


Fig. 1 A Typical OTEC Cycle

A typical OTEC cycle that uses ammonia as the working fluid is shown in Fig. 1. Warm water from the ocean surface is pumped through the evaporator to produce ammonia vapor under pressure to power the turbine and generator. The exhaust vapor from the turbine is condensed in the condenser by thermal contact with cold water pumped up from the deep ocean. The condensed ammonia is returned to the evaporator by the condensate pump. No demister has been shown in Fig. 1 because measurements to date at Argonne National Laboratory on enhanced heat exchangers have failed to show any measurable droplet carry over from the evaporator.

In an actual plant, auxiliary power must be available to operate the pumps until the turbine and generator can be started. During normal operation, power for the pumps is supplied by the turbine and generator.

The output of the turbine-generator is the GROSS power output. The Net power output is the

gross power less the power required to operate the pumps and to operate the auxiliary systems at the OTEC station. These include such things as cranes, station keeping equipment, air conditioning, potable water supply systems, ammonia cleanup systems, etc. We are concerned here with *NET* power because the effects of corrosion, biofouling and cleaning are larger for *NET* power. This has the effect of increasing the accuracies required for the several measurements.

The temperatures given for the various streams on Fig. 1 are typical or nominal, and have been given to the nearest °F. The difference between the warm water inlet and outlet temperatures varies for different designs as does the difference for the cold water. The difference between the warm and cold water temperatures is a function of the site selected and of the length of the cold water pipe but is usually about 38°F.

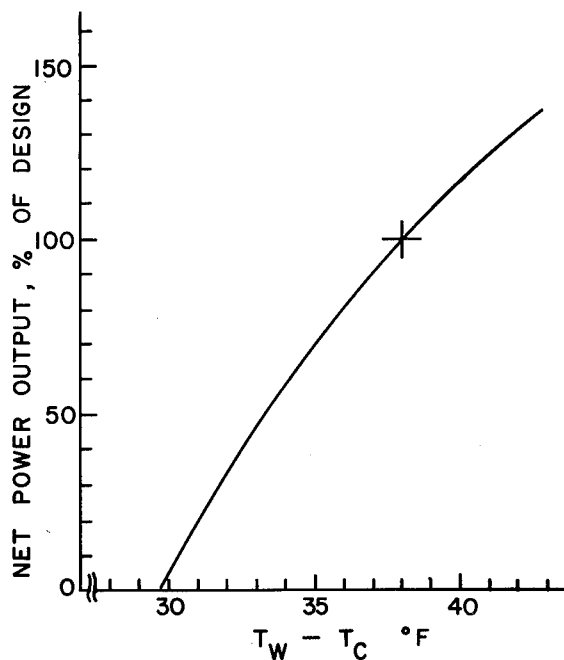


Fig. 2 *NET* Power as a Function of Water Temperature Difference

NET power output of a particular OTEC plant varies with the temperature difference between the warm and cold water but the functional relationship varies with the method of operating the plant. For example, if the water temperature difference decreases, the cold and warm water flows could be reduced to cut pump power. This would reduce the heat transfer coefficients in both the evaporator and condenser so that *NET* power would still drop faster than in direct proportion to temperature difference.

The results given in Fig. 2 are for a plant designed for 38°F water temperature difference and under the conditions that warm and cold water flow rates are held constant. Data for this figure were taken from the Lockheed report (2) and are for unenhanced titanium exchangers. These data are typ-

ical also for enhanced exchangers since the increased performance is expected to be used primarily to reduce the size and cost of the exchangers, rather than to increase the temperature difference across the turbine.

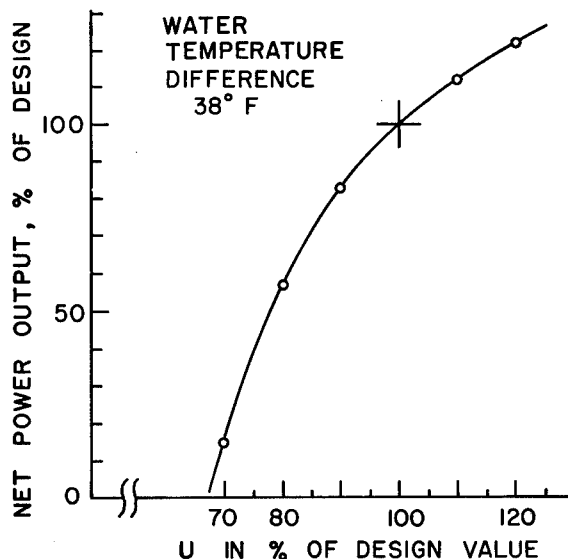


Fig. 3 *NET* Power as a Function of the Overall Heat Transfer Coefficient (*U*) for Evaporator and Condenser

The data given in Fig. 2 may be used with typical log-mean temperature differences from Fig. 1 to calculate *NET* Power as a function of the overall heat transfer coefficient. The results are given in Fig. 3 for a water temperature difference of 38°F.

The most striking feature of this graph is the steep slope. A decrease in *U* to 67% of the design value reduces the *NET* power to zero. In the range of 90% to 100% of the design value of *U*, the *NET* power varies by 17%. We note that a given change in *U* causes about twice as much change in *NET* power.

The allowable decrease in *NET* power and the corresponding decrease in *U* is governed by the electrical utility system economics and by judgement. From a utility load management point of view a 10% decrease in power is probably significant. From a return on investment point of view, a 10% reduction in power is also significant. On the other hand, present DOE thinking is that a fouling factor of 0.0001 is permissible before cleaning is needed. For the enhanced exchangers tested at Argonne and for a plant with the characteristics of Fig. 3, this fouling factor corresponds to a *NET* power reduction of from 13% to 18%.

From these several points of view we may conclude that we must be able to measure a change in *U* of from 5% to 8%. This requires that the *total* error in the measurement of *U* must be of the order of 1% or at most 2%. The allowable error in the individual measurements of temperature, flowrates, pressure, etc. must be very small so that the total error can be in the required range.

Measurements at Argonne (3) of heat fluxes through the evaporator indicate that two different

methods give heat balances that agree to about 2% on the average for 14 sets of data. Error studies made since that time indicate that the method that requires exactly steady state operation, contains more error than the direct method. We expect that 1% total error in U can be achieved in the laboratory and should be set as a goal for measurement on OTEC-1.

The balance of this paper describes the computations and the instruments that are needed to achieve this goal of 1%.

Computer Based Data System

The Argonne Test Facility has a computer based data system that can, on command, read the several sources of data, apply calibration factors and correction factors to these data, compute heat balances, compute overall heat transfer coefficients, and produce a hard copy and magnetic tape records of the raw and reduce data. As such, it is extremely convenient and should be included for OTEC-1.

It must be understood that a computer based data system cannot improve the accuracy of the data from the sensors. It can only prevent the errors from becoming worse by eliminating the chance of error in reading a meter and by applying the calibration and correction factors correctly.

If a flow meter contains a 10% error, or is not repeatable from one reading to the next, no computer data system can supply the correct data. This emphasizes that the real problem in obtaining accurate data can be resolved only by the correct choice of primary sensor instruments and by insisting that the OTEC power loop physical layout provide for the correct installation of each instrument.

Recent requests for proposals have produced responses that describe in great detail the computer hardware, the software, and the console displays. These same responses have been, with few exceptions, totally without statements concerning types of instruments, accuracies, methods of installation or even measurement objectives.

Calculations of U

The overall heat transfer coefficient for the evaporator and for the condenser may be calculated from the conventional definition:

$$U = \frac{Q}{A_o \Delta T_{LM}}$$

The heat transfer rate (Q) can be calculated in two independent ways: (1) from measurements of water flow rate, water inlet temperature and water outlet temperature, and (2) from measurement of the liquid ammonia flow rate under steady state conditions, from liquid ammonia temperature and from ammonia vapor temperature or pressure in the evaporator. This second method is not as accurate as the first but serves as a useful check. The log-mean temperature difference (ΔT_{LM}) is calculated from the measured inlet and outlet water temperatures and from the temperature of the ammonia vapor in the heat exchanger.

The calculation assumes negligible heat loss through the shell of the exchanger. If the loss

is not negligible, a correction to (Q) is required. A gain of heat by the condenser is probable, due to condensing moisture from the warm tropical air by the condenser shell.

Accurate measurements are required for two *bulk mean* water temperatures, one ammonia vapor temperature, one water flow rate, one ammonia liquid flow rate and one ammonia liquid temperature. Separate measurements are required for the evaporator and for the condenser.

Gross Power Measurements

Electrical wattmeters of high precision are available in both analog and digital types. It is therefore a simple job to precisely measure gross power from the turbine-generator. The turbine-generator may then be thought of as a very sensitive meter for indicating a change in plant performance. It is therefore strongly recommended that a turbine-generator be installed as a part of the OTEC-1 test equipment.

The inclusion of a turbine-generator in OTEC-1 does not eliminate the need for accurate temperature and flow data to calculate U. This follows since a change in gross power output may result from a change in U or from a change in the ocean water temperatures.

The gross power measurements before and after cleaning of the exchangers will be a powerful tool to study the effectiveness of cleaning. The gross power record over a period of time will provide a check on the performance of the exchangers independent of the calculation of overall heat transfer coefficients.

Temperature Measurements

Temperature measurements at the Argonne Test Facility are made in two ways. One is with a quartz thermometer and the other is with thermocouples.

A quartz thermometer is an instrument that uses the very linear relationship between the frequency of oscillation of a piezoelectric crystal made from quartz and the temperature of the crystal. The crystal is cut in a direction with respect to the crystal axes so that a very stable variation in oscillator frequency of one kilocycle per second per degree celcius is achieved. The difference frequency, obtained from a second quartz crystal housed in an oven, is counted in a digital counter for a precise one second time interval. The result is a number that reads directly in units of 0.001°C.

The same instrument will count the difference frequency for a precise 10 seconds to give a number that reads directly in units of 0.0001°C.

Each thermometer electronics is provided with two temperature sensing probes so that measurements of T_1 or T_2 or $(T_1 - T_2)$ may be made directly.

The latest model of this instrument incorporates a programmable read-only digital memory for storing the 40 point calibration table for each probe. A microprocessor automatically applies the proper correction factor to the raw temperature reading before displaying the temperature or

transmitting the temperature to the computer data system.

When the relatively simple calibration procedure is followed, the calibration is traceable to the Bureau of Standards.

The higher resolution scale provided by this instrument (0.0001°C) is not useable in our Test Facility because the water temperature is not steady enough from one measuring period to the next. We find that the 0.001°C resolution is adequate.

The thermocouples are used with a data logger system that is operated by the computer. Each thermocouple is calibrated in place at normal operating temperature with a quartz thermometer. This permits the resolution of 0.1°F to be significant.

Quartz thermometers are used for all critical measurements at the Argonne Test Facility and are recommended for the OTEC-1 tests.

Bulk Mean Temperature

A thermometer or thermocouple measures the temperature at a point or over a small volume. What is needed is the mean temperature measured over the mass of water flowing in the warm or in the cold water piping. The thermometer reading and the bulk mean temperature will be different if appreciable temperature gradients exist in the vicinity of the thermometer.

The test facility at Argonne has shown that the water pump and the normal turbulent flow in the long 14" piping between the pump and the exchanger provide excellent mixing, so that a single quartz thermometer in a well is adequate for measuring water inlet temperature.

The outlet water temperature is measured by a quartz thermometer in a well located after an elbow and after about 10 pipe diameters. A second quartz thermometer located after a Kinex static mixer shows no significant temperature difference. We concluded that the mixing in the exchanger plenum and in the elbow and pipe are sufficient to provide adequate temperature uniformity.

In the OTEC-1 facility, the pipe layouts and quartz thermometer locations must be carefully designed to provide bulk mean temperature readings. More than one quartz thermometer may be needed in the discharge piping. A moveable quartz thermometer to scan across the pipe may be needed and should be planned for.

Water Flow Measurements

Errors in water flow measurements contribute directly to errors in the calculated U values. For overall accuracies of 1% in U, an error of only a fraction of a percent of actual flow is required.

Measurement of the warm and cold water flow rates in the Argonne Test Facility are made with turbine type meters designed for custody transfer service in pipelines. They are rated for an accuracy of 0.15% of actual flow over a 10:1 range and have a repeatability of 0.02%. The water

systems composed of pump, flow control valve and meter give readings that repeat to one part in 2000 from hour to hour and day to day, even though the system is shut down at night.

Turbine meters in the size required for OTEC-1 would require some development work but would offer distinct advantages over other types.

An alternate flowmeter that has been suggested is a sonic device. Multiple paths are required to give a suitable average velocity across the pipe area. A computer is needed to correct for water temperature changes and for changes in salinity. Even so, the corrected value will have an error of about 1%.

It is recommended that the effort required to develop a suitable turbine flowmeter for OTEC-1 be evaluated in order to reach a decision on the best course of action to follow.

Flowmeter Installations

All flowmeters are sensitive to some extent to variations in velocity profiles across the pipe. In the case of turbine flowmeters, 10 diameters of straight upstream pipe and an upstream flow straightener as well as 5 diameters of straight pipe downstream of the meter are required to achieve the rated accuracy.

In the case of flow orifices or pitot tubes, 20 diameters of straight pipe upstream plus 10 diameters downstream are required to achieve accuracies of a few percent.

Magnetic flowmeters have been suggested as a type that requires a shorter run of straight pipe. The only large meter known to the writer that is calibrated to 1/4% is still relatively small compared to the OTEC-1 requirements and is mounted in a long straight run of pipe. It is recalibrated frequently.

It is apparent that the physical layout of the piping for OTEC-1 must take into account the requirements for long metering runs.

Ammonia Liquid Flowmeters

Precise turbine flowmeters suitable for use in liquid ammonia are in regular manufacture. No problem exists in this area for OTEC-1.

Ammonia Vapor Pressure

Precise measurements of the pressure of the ammonia vapor in the evaporator and the condenser are made at the Argonne Test Facility with quartz pressure transducers.

These instruments are based on a piezoelectric crystal made from quartz. In this case the crystal is cut in a direction with respect to the crystal axes to produce an oscillator crystal whose frequency is independent of temperature.

The piezoelectric crystal is mounted so that one side is in contact with a vacuum while the opposite side is in contact with the pressure to be measured. The pressure difference across the

crystal, mechanically bends the crystal and changes the frequency of oscillation. The cycles of the oscillator are counted for a precise time interval to obtain a digital number that is a function of the pressure applied to the crystal.

The functional relationship between pressure and frequency is very non-linear. The digital number from the counter is fed to a pre-programmed microprocessor included in the instrument. This microprocessor solves an equation in order to convert the number obtained by counting the oscillator, to pressure units. The display of pressure is to six decimal digits.

These instruments are filled with a silicone oil in order to prevent the ammonia from contacting the quartz crystal electrodes. As a result, the sensor must be carefully mounted to prevent hydrostatic offsets. Mountings must also provide vibration isolation, since the mass of the quartz crystal and the oil produce a sensitivity to accelerations. This isolation is in addition to that provided inside the crystal housing.

Water Pressure Measurements

Measurements of water pressure, measurements of pressure drop across exchangers, and measurements of liquid levels are made with strain gauge transducers at a variety of places in the Argonne Test Facility. These transducers are available from several sources in 0.1%, 0.25%, or 0.5% accuracies as required for OTEC-1.

Calibration Facilities

OTEC-1 should be provided with the necessary equipment to periodically recalibrate all the instruments with the possible exception of the large

water flowmeters. This is required to keep the instruments in condition to permit comparison of data taken at widely separated times during the two years that OTEC-1 is expected to be in operation at sea.

Conclusions

The instruments discussed above can provide data for evaluating the performance of OTEC-1 heat exchangers when subjected to corrosion, biofouling, and cleaning. The accuracies obtainable for calculated U and for gross power developed, are adequate for the projected needs of the OTEC-1 program. The data obtained on OTEC-1 will be adequate for predicting the long term performance of an OTEC power generating plant.

References

1. *Ocean Thermal Energy-Test Facilities Study*, prepared for USERDA by TRW Systems and Energy Division under contract No. E(04-3)-1158, TRW No. 28616-6002-TU-00 (Sept. 1976).
2. *Ocean Thermal Energy-Test Facilities Study*, prepared for USERDA by Ocean Systems Division of Lockheed Missiles and Space Co., Inc. under contract No. E(04-3)-1156, Lockheed No. LMSC-D506781 (Jan. 1977).
3. Sather, N. F., L. G. Lewis, J. J. Lorenz, and D. Yung, PERFORMANCE TESTS OF 1 MWT OTEC HEAT EXCHANGERS, presented at the Fifth Ocean Thermal Energy Conversion Conference, Miami, Beach, FL, Feb. 20-22, 1978 (to be published in the Proceedings).

OTEC-1 TEST CONDUCTOR PROGRAM

BY: P. Archbold, J. O. Bates

J. O. Bates

Mr. Bates is currently Program Manager, Energy Programs, reporting to the Vice President of ETEC (formerly LMEC). His assignments are to selectively broaden the scope of ETEC involvement in DOE-sponsored activities, and to manage the resultant ETEC programs. Previously, he was manager of the Test Engineering Group, responsible for conducting tests and evaluations of LMFBR components and instrumentation.

Mr. Bates was at Rocketdyne from 1955 to 1972, where he advanced in engineering from engine systems development to third-level management positions in program management, development, and technical marketing. He holds two patents, and has authored both publications and papers.

Graduated from the University of Virginia in 1955 with a B.S. in Aeronautical Engineering, Mr. Bates has taken post-graduate courses in management and engineering.

P. Archbold

Mr. Archbold holds a Mechanical Engineering degree from Newcastle, England. His marine engineering experience with the British Ministry of Transport led to registration as a First Class Marine Engineer (unlimited horsepower). He has over thirty years experience in heat exchange equipment design and development for the petrochemical, cryogenics and electronics industries. Recent assignments have been in technical management of heat transport component test programs. Mr. Archbold is a Registered Professional Engineer in the state of California.

INTRODUCTION

DOE has recently assigned to the Energy Technology Engineering Center (ETEC) the role of OTEC-1 Test Conductor. This job includes the development of the test requirements plan, or Test Request, prior to the onset of testing, and of the procedures to be used subsequently by the operators to conduct the experiments. During the test phase of the program, the Test Conductor directs the operation of all test systems. Actually, Test Director is a more appropriate descriptor, so the initials TDC, for Test Director Contractor, will be used herein.

ETEC is the new name for the organization formerly known as the Liquid Metal Engineering Center (LMEC), which was established by the AEC in 1966 as a government owned-contractor (Atomics International) operated facility to assist the government in the development of components for the LMFBR program. These components included large heat exchangers, valves, pumps, mechanisms and a variety of instrumentation. The LMEC roles were to manage the design and construction of the required test facilities and to plan and manage the formalized

component test programs conducted within these facilities.

In April, 1977, the LMEC charter was expanded to provide support to all DOE energy programs and we are now involved in such diverse energy tasks as both central and distributed solar energy, MHD, and laser fusion. We are also involved in testing for NRC. To better reflect our expanded charter, the LMEC name was changed to the Energy Technology Engineering Center earlier this May.

The purpose of this paper is to outline, in rather broad strokes, how we see the involvement of the TDC in the OTEC-1 test program, considering the preparation for and testing of the initial test heat exchangers and auxiliary equipment.

BACKGROUND

The principals involved in the OTEC-1 test program are sketched in Figure 1. As of this writing, the Systems Integration Contractor (SIC) has not been selected, the Test Article Contractor (TAC) for the initial heat exchanger set is TRW, and ETEC is the TDC. Under "Other Contractors" in Figure 1, we would flag-out Argonne National Laboratories (ANL) as having a very significant role. We feel there will be yet other contractors or consultants reporting directly to DOE, but cannot positively identify them at this juncture.

The key phasing of the program, from the TDC's standpoint, is illustrated in Figure 2. This chart indicates a great deal of preliminary work to be completed by the TDC before the SIC is selected. The timing dictates that the TDC provide inputs on test requirements to the SIC as soon as possible after selection; this means that in many cases the TDC will have to anticipate the early data needs of the selected SIC. To do this with any degree of effectiveness will require early development of interfaces between program participants and a free flow of information.

INTERFACES

A primary TDC function will be to help define the interfaces between the involved parties shown in Figure 1 and to effectively utilize them. Having obtained the necessary information to develop definitive test requirements for the SIC, the TDC will then prepare a comprehensive Test Request for the OTEC-1 program. The Test Request will define the conditions required for demonstrating the individual and combined performance of the various OTEC-1 components.

Figure 3 presents a concept of the OTEC-1 platform showing the various elements that must be considered in the development of OTEC-1 test requirements. Table 1 uses a subsystem breakdown (developed in an April, 1978 report by Gilbert/Commonwealth) to provide an index of current responsibilities, to the best of our knowledge. Because of the SIC's involvement in all subsystems, it is obvious that

a significant amount of coordination and interchange with the SIC will be necessary once this contractor is selected.

TRW's inputs on the types of tests and instrumentation requirements to adequately demonstrate the viability of the heat exchanger designs must be obtained in the early phase. ANL has been actively engaged in heat exchanger testing with NH₃ and with instrumentation for NH₃ subsystems, and is also being involved in biofouling effects in heat exchangers; obviously a significant amount of interchange will be required with ANL. Another obvious interface for the TDC is with the OTEC organization of DOE.

The SIC is required to establish a Test Planning and Instrumentation Working Group and a System Interface Control Working Group. As a member of both of these groups, the TDC will be active in the definition of the mission and selection of instrumentation so that the Test Request reflects a common understanding of the test goals.

TDC/SIC TEST RELATIONSHIP

After platform conversion, sea trials, and deployment of the platform have been accomplished by the SIC, the primary objective of the initial OTEC-1 test program will be to experimentally evaluate the evaporator and condenser hardware provided by the TAC. Other components and phenomena will be simultaneously evaluated: cold water pipe loads, biofouling, corrosion, etc. Still other subsystems will be evaluated as they provide support to the heat exchanger hardware testing, e.g., the ammonia system. As we see it, the job of the TDC will be to assure that all these evaluations are carried out in an organized and documented manner.

To perform the testing portion per se of the described task will require a good measure of TDC control over the functions of the platform which is manned and operated by the SIC. Some words on how we expect this relationship to function may be in order.

An analogous situation has existed in test programs performed at ETEC: A Test Article is provided to ETEC as Government-Furnished Equipment (GFE) by a contractor (this contractor generally writes the Test Request for ETEC acceptance, also). ETEC installs the GFE hardware into a facility and prepares from the Test Request the test documents (procedures) that direct the facility operators. As Figure 4 indicates, the ETEC organization includes two groups whose day-to-day activities involve testing: the Test Engineering Group, which is test-program oriented, and the Operations Group, which is dedicated to operating, maintaining (and preserving) the test facilities. The Test Engineering Group confers the requirements for testing the Test Article to Operations via Test Procedures; the facility itself is operated in accordance with Operating Procedures prepared by the Operations Group. Very rarely is there any conflict.

The analogy to the OTEC-1 test operation should be obvious from Figure 5. Note that each organization has closely-corresponding functions, but with different orientation: For example, the test facility has its own instrumentation, not required for describing Test Article performance, but necessary to define test facility performance in real time, and thereby permit the operators to keep track of the facility condition.

For OTEC-1, the "facility" provided by the SIC consists of the platform and the Test Bed for the OTEC Power Plant. The Test Bed consists of the NH₃ system, warm water and cold water pumping systems, expansion valve and desuperheater, foundations, and piping. The evaporator and condenser which complete the OTEC plant correspond of course to the Test Article(s). Continuing the analogy, the cold water pipe (CWP) is seen as a "facility" component which is to be evaluated in parallel with the Test Article test program. In this particular case we would anticipate that the instrumentation and data acquisition requirements would be worked-out between the TDC and SIC, with the TDC providing consultation, data acquisition, and data processing services to the SIC. The Test Bed would probably be treated in a similar manner. We are speculating at this point, however; CWP and Test Bed management areas are subjects for resolution by the SIC, TDC, and DOE.

The ETEC facilities are instrumented and controlled so that an automatic "SCRAM" is generated if conditions develop which jeopardize either the Test Article or the facility itself. We assume that, similarly, the overall OTEC-1 system will be designed and instrumented so that a similar philosophy of automatic protection and control can be implemented. Table 2 gives a preliminary indication of those parameters which may be control elements, as determined by Gilbert/Commonwealth.

Generalizing, we see the role of the TDC relative to the SIC during the test phase of OTEC-1 as that of an air group detachment aboard an aircraft carrier at sea: During air operations, the operation of the carrier serves the requirements of the air group commander. However, when any condition arises to potentially jeopardize the safety of the carrier and its crew, the captain of the carrier (SIC) has full authority to interrupt the operations of the air group commander (TDC) to whatever extent is required.

TEST REQUEST

ETEC will prepare the Test Request for OTEC-1 based on the format illustrated in Figure 6. The Test Request defines the objectives of the test program and the roles of the principals involved; it is a time-tested document evolved over the last dozen years by ETEC-DOE programs to define 1) test objectives; 2) instrumentation types, quantities, and accuracies; 3) data recording methods and rates.

TEST PROCEDURES

When a Test Request has been mutually accepted by the principals, the TDC will generate the Test

Specifications and Test Procedures which will be used by SIC personnel to implement the tests. We plan to use another proven format for Test Procedures, illustrated in Figure 7. The Test Procedure is a two-part document: Part I is the Test Specification which defines the purpose of the test, the test requirements and other pertinent data which fully describe the test. The Part I Specification forms the basis for writing a detailed procedure, and is approved by the principals involved before any testing takes place. Part II is the step-by-step Test Procedure used to perform the test. Each step of the procedure must be signed-off by the SIC individual performing the test before proceeding to the next step. This method minimizes the possibility of procedural error under the most exacting conditions. Approval of this part of the document is planned to be limited to the TDC, the SIC, and a Quality Assurance representative, if one is assigned. Figure 8 represents the flow of data required to prepare the documents we have discussed.

The Test Procedure lends itself to testing of complete systems, subsystems, or components. For example, if a test is to be run to evaluate the OTEC plant, the operational requirements for the rest of the platform and subsystems will be defined as prerequisites which must be signed-off before proceeding with the test. Changes in these subsystems will be monitored and either alarmed or set to shut down the test if necessary. The same logic can be applied if the test is geared to one or both heat exchangers. In this case all subsystem requirements including the OTEC Test Bed will be set up as prerequisites and monitored during the test. The TDC will define operating parameters, prerequisites and data acquisition requirements in the Test Procedures.

Should the need arise for special tests to resolve anomalies or problems that are discovered during the course of a planned test, Special Test Procedures will be used. The STP's are similar in content to the standard Test Procedure but approval to use them is limited to the Test Director and site representatives of principals involved. This approach allows for a quick response to the situation without sacrificing the control or post-test documentation. Requests for additional tests, approved by DOE, will also be accommodated in this manner.

The use of Test Specifications and Test Procedures as outlined above may sound overly complex, or inflexible, or both. In practice, however, we have found that the described system compels planning, coordination, and discipline in operation and recording. Our experience leads us to believe it is the safest and least-costly approach to a major test program.

DATA HANDLING

Data Acquisition Software for all test programs involving the OTEC plant, Heat Exchangers and/or Cold Water Pipe will be provided by the TDC. Data processing programs for the Data Reduction Facility will also be provided by the TDC. Mathematical models required for predicted performance will be requested from the SIC, TAC, and ANL.

These models will be used by the TDC in interpreting the data. On-line data presentations and printouts will be evaluated by the TDC during test and he will make the decisions regarding changes to the procedure if results indicate the need. Raw data will be transferred to the data reduction facility for processing and analysis. The results of this data processing will be transmitted to the OTEC-1 principals for evaluation and guidance in future testing. If the data indicates test procedure changes are required, the STP provides the facility to implement changes in a short time without relinquishing control over the test program.

BIOFOULING LABORATORY

A Government-Furnished Biofouling Laboratory will be on board the platform. This lab will be responsible for monitoring the nature and extent of biofouling and corrosion experienced. Changes in the heat transfer capability of the heat exchangers will provide an indication of biofouling film buildup. Requirements for treatment of the water and mechanical cleaning to maintain capability between prescribed limits will be assessed. Visual observations and measurements will be made and recorded for corrosion effects and for macrofouling of the platform and Cold Water Pipe.

TABLE 1.
OTEC-1 AREAS OF RESPONSIBILITY

SUBSYSTEM	FEATURE	RESPONSIBILITY
ENVIRONMENT	WAVE HEIGHT, PERIOD, etc. CURRENT WIND BIOFOULING	SIC SIC SIC ANL
PLATFORM	HEADING MOTIONS DEFLECTIONS BIOFOULING	SIC SIC SIC ANL
COLD WATER PIPE (CWP)	PLATFORM INTERFACE MOTIONS POSITION BIOFOULING	SIC SIC SIC ANL
POSITIONING	BEACONS TRANSPONDERS THRUSTERS	SIC SIC SIC
ELECTRIC POWER SYSTEM (PLATFORM)	UNITS AVAILABLE POWER QUALITY AND LEVELS AVAILABLE	SIC SIC
AUXILIARIES	PRIME MOVER FUEL SYSTEM PUMP STATUS NAVIGATION, etc.	SIC SIC SIC SIC
OTEC PLANT	NH ₃ SYSTEM WARM WATER (WW) COLD WATER (CW) TEST ARTICLES BIOFOULING	SIC & ANL SIC & ANL SIC & ANL TRW ANL

TABLE 2.
OTEC PARAMETER FUNCTIONS

SUBSYSTEM AREA	PARAMETER	FUNCTION	
		STATUS	CONTROL
ENVIRONMENT	AMBIENT CONDITIONS	X	
	WIND	X	
	WAVES	X	
	CURRENT	X	
	SEA WATER	X	
	BIOTA, etc	X	
PLATFORM	SPEED	X	X
	HEADING	X	X
	MOTIONS	X	X
	PLATFORM DEFLECTIONS	X	X
	DRAFT	X	X
	FOULING & CORROSION	X	
COLD WATER PIPE	HANDLING	X	X
	PLATFORM INTERFACE	X	X
	STRESS	X	
	MOTIONS	X	
	INLET POSITION	X	X
	INLET SCREEN CONDITION	X	X
	FLOW TEMPERATURE GRADIENT AND PRESSURE DROP	X	
	FOULING & CORROSION	X	
POSITIONING	ACOUSTIC BEACON	X	
	TRANSDUCER	X	X
	CWP INLET DEFLECTION	X	
	THRUSTER POSITION	X	X
	THRUSTER RPM & PITCH	X	X
	MOORING LINE TENSION	X	X

SUBSYSTEM AREA	PARAMETER	FUNCTION	
		STATUS	CONTROL
AUXILIARIES	PRIME MOVER STATUS	X	X
	FUEL STATUS	X	X
	HVAC STATUS	X	X
	FRESH & SEA WATER		
	SUBSYSTEM STATUS	X	X
	COMPRESSED AIR	X	X
	PUMPS	X	X
	VALVES	X	X
	NAV. COMMUNICATION, etc	X	X
OTEC PLANT	NH ₃ LOOP	X	X
	WARM WATER	X	X
	COLD WATER	X	X
	NH ₃ FEED PUMP	X	X
	NH ₃ THROTTLE VALVE	X	X
	DESUPERHEATER VALVE	X	X
	WW PUMP	X	X
	CW PUMP	X	X
	CW VALVES	X	X
	VENT	X	X
	NH ₃ STORAGE	X	X
	N ₂ PURGE	X	X
	CW & WW CONDITION	X	
	BIOFOULING & CORROSION	X	
POWER GENERATION AND DISTRIBUTION	UNITS ON-LINE	X	X
	LOAD DEMANDS	X	X
	LOAD DISTRIBUTION	X	X
	OPERATING PARAMETERS	X	X
	CURRENT QUALITY	X	X
	VOLT & AMP. LEVELS	X	X
	SWITCHBOARD STATUS	X	X

FIGURE 1.
OTEC-1 PRINCIPALS

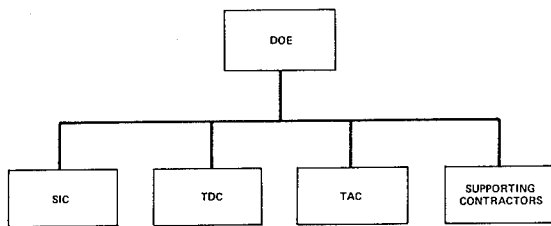


FIGURE 2.
OTEC-1 PHASING: TEST DIRECTOR ACTIVITIES

OTEC-1 PROGRAM		FY 1978	FY 1979	FY 1980	FY 1981
PHASE	TASK	CY 1978	CY 1979	CY 1980	CY 1981
MAJOR MILESTONES		▽	▽	▽	▽
PHASE - 1	PLANNING; OUTLINE TEST REQUEST	█			
PHASE - 2	PREPARE TEST REQUEST AND TEST PROCEDURES		█		
PHASE - 3	TEST DIRECTION; DATA ACQUISITION AND EVALUATION			█	
MAJOR MILESTONES:		▽	▽	▽	▽
		▽	▽	▽	▽
		▽	▽	▽	▽

START CONSULTING ACTIVITIES
 START TDC ACTIVITIES
 SIC CONTRACT AWARD
 COMPLETE PLATFORM CONVERSION PROGRAM
 COMPLETE TEST PROGRAM

FIGURE 3.
OTEC-1 CONCEPT

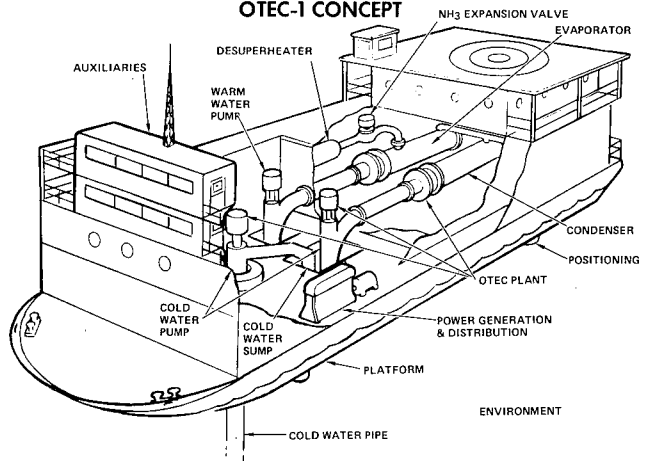


FIGURE 4.
ETEC TEST ORGANIZATIONS

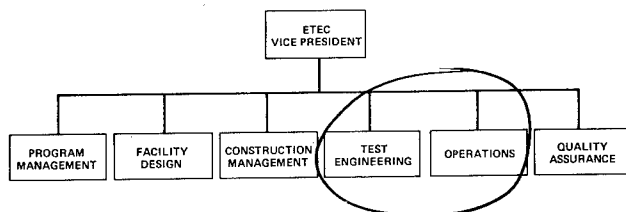


FIGURE 5.
ETEC/OTEC OPERATIONAL ANALOGY

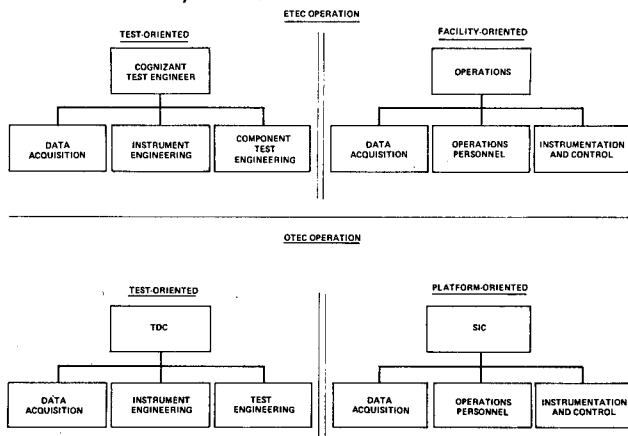
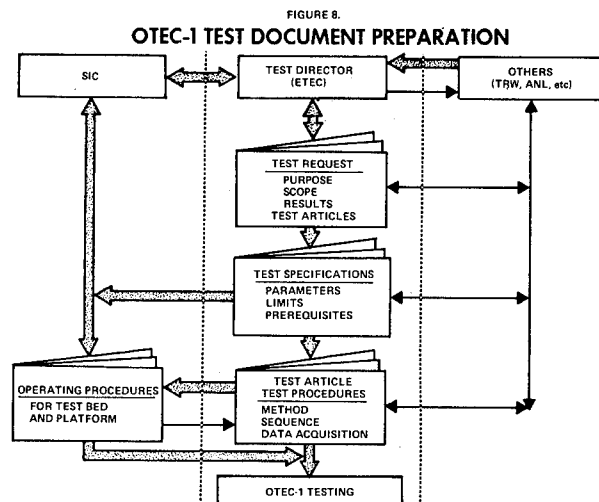


FIGURE 7.
ETEC TEST PROCEDURE FORMAT

- **APPROVAL SIGNATURE SHEETS** INDICATES CONCURRENCE BY ALL INTERESTED PARTIES
- **TEST SPECIFICATION** LISTS TEST OBJECTIVES AND TEST REQUIREMENTS. IDENTIFIES PLANT CONDITIONS REQUIRED. PROVIDES ACCEPTANCE CRITERIA AND DATA REQUIREMENTS NEEDED INCLUDING TYPE, RANGE SAMPLING RATE, etc. TEST PREDICTIONS ARE LISTED IF APPLICABLE
- **TEST PROCEDURE** REFERENCES ALL DRAWINGS, PROCEDURES, MANUALS, etc. NEEDED TO CONDUCT TEST. INDICATES TEST LIMITS INVOKED AND ANY SPECIAL PRECAUTIONS NEEDED. LISTS SPECIAL TEST EQUIPMENT NEEDED AND ALL CONDITIONS TO BE MET AS PREREQUISITE TO THE TEST. PROVIDES STEP-BY-STEP INSTRUCTIONS FOR PERFORMING TEST WITH SIGN-OFF REQUIREMENT FOR EACH STEP.

FIGURE 8.
ETEC TEST REQUEST FORMAT

- **OBJECTIVES** DEFINES PURPOSE OF PROGRAM
- **SCHEDULE**
- **TEST METHODS** DESCRIBES HOW REQUIREMENTS WILL BE MET
- **TEST RESULTS** SETS GUIDELINES FOR ATTAINMENT OF TEST OBJECTIVES OR FAILURE
- **DESCRIPTION OF TESTS** DEFINES T/A INTERFACE WITH FACILITY, SEQUENCE OF TESTING, DISCUSSES BASIC TESTS WITH "HOLD POINTS" AND LIMITS DEFINED. DEFINES MEASURED PARAMETERS, INSTRUMENTATION AND ACCURACIES
- **DATA** DEFINES DATA HANDLING, REDUCTION AND ANALYSIS, IDENTIFICATION, STORAGE, AND REPORTING REQUIREMENTS
- **SYSTEM SAFETY** PROVIDES EMERGENCY PROCEDURES FOR TEST ARTICLE AND FACILITY
- **QUALITY ASSURANCE** DEFINES TEST REQUESTER ORGANIZATIONS INVOLVED AND THEIR RESPONSIBILITIES. DEFINES QA DOCUMENTS APPLICABLE TO PROGRAM AND LISTS REFERENCED DOCUMENTS



THE EFFICIENCY OF SOLAR ASSISTED HOT WATER SYSTEMS

By: John Herlihy, P.E., Dayton T. Brown, Inc.

The author is a registered Professional Engineer in the State of New York. Since graduation from Manhattan College of Engineering, his career has involved the application of the principles of thermodynamics and heat transfer. He is currently doing graduate study in engineering at the State University of New York at Stony Brook.

Through his efforts, Dayton T. Brown, Inc. was selected as a Solar Heating Demonstration Project for the Department of Energy. At the Engineering and Test Division of Dayton T. Brown, Inc. he is presently responsible for development of new marketing areas in the energy field.

At the present time, Solar assisted domestic hot water systems show promise of wide application throughout the United States. In comparison to other applications of active Solar systems, the return on investment can be attained within a relatively short time after installation. Unlike Solar Heating systems which require professional involvement in the design and installation, the Solar assisted hot water application can be sold for specific requirements. For residential installations, these requirements are usually defined by the number of members in the family unit.

The definition and methods to determine the efficiency of Solar Collectors has been well defined by ASHRAE Standard 93-77, however the Solar Collector is merely one component of the Solar assisted hot water system. In view of its widespread consumer potential, the Solar assisted hot water installation must have a defineable "System Efficiency". On the basis of the system efficiency and cost, and intelligent rationale for selection between alternate systems can be developed for the consumer.

The typical Solar assisted hot water system consists of three independent piping loops. The collection loop usually contains an anti-freeze solution which circulates between Solar Collectors on the roof and a heat exchanger encircling the Solar storage tank. The transfer loop connects the Solar storage tank with the conventional water heater. The third loop delivers the hot water from the water heater to the load. Figure 1 is a schematic of the typical Solar assisted hot water system. Obviously, the equipment on the right side of the schematic distinguish the Solar assisted hot water system from the standard conventional system. If an energy balance is done on the auxiliary tank (Figure 2), the following terms can be defined:

Q_{Solar} = The actual input energy due to the Solar System. Although not directly stated, this input is the resultant of the difference between the Solar radiation incident upon the collector and the net energy losses between the collector and heat exchanger and the heat losses due to conduction, convection and radiation from the piping and storage tank.

Q_{Lost} = The amount of energy lost from the auxiliary tank due to convection, conduction and radiation heat transfer.

Q_{aux} = The actual input energy due to the auxiliary system. This would include any conversion inefficiencies since it is an actual input energy.

Q_{out} = The actual output energy of the total system.

These quantities are defineable for any Solar assisted system, regardless of the form of auxiliary energy input or the configuration of the Solar portion of the system.

If an experimental determination of the efficiency of the Solar assisted hot water system were attempted, it is conceivable that the following approach would be taken.

Step 1 - Operate the hot water system with the Solar input.

Step 2 - Operate the system without the Solar input.

In each step, the integrated values of the energy input and output would be recorded. The following energy balance could be written for the system operation corresponding to each step:

$$\text{Step 1) } Q_{\text{out}_1} = Q_s + Q_{\text{aux}_1} - Q_{L_1}$$

$$\text{Step 2) } Q_{\text{out}_2} = Q_{\text{aux}_2} - Q_{L_2}$$

If the two steps were performed such that the output energy were equal for both cases, the following equation could be written:

$$Q_{\text{aux}_2} - Q_{\text{aux}_1} = Q_s + (Q_{L_2} - Q_{L_1})$$

In all likelihood, the heat losses from the water heater would not be directly monitored during each test. There are several problems in attempting to do so. In addition to the variation of temperatures with time and location due respectively to the operational range of the heater on-off cycles and stratification, the accurate calculation and/or determination of the total "U" factor for the surface of the heater would be quite involved.

If it were assumed that the amount of heat lost from the tank was the same for each step, the Solar portion would be equal to the difference in auxiliary inputs for each operation or:

$$Q_{aux_2} - Q_{aux_1} = Q_s$$

At this point, it is necessary to determine the relative value of the Solar input energy.

Considering the energy balance, there are two basic ways in which the value of the Solar assist could be stated:

- A) Q_s/Q_{out} = The percentage of total energy output which is contributed by Solar.
- B) Q_s/Q_{aux} = The ratio of Solar input to auxiliary input.

If method A were chosen, the Solar input energy would be compared with the output energy. As can be seen by review of the energy balance equations, the output energy decreases as the amount of the heat lost from the water heater tank increases. Therefore an inefficient tank would indicate a high percentage of Solar contribution.

In method B, the Solar input is compared to the auxiliary input. Since the Solar input is now defined as the difference in the auxiliary inputs of Step 1 and 2, this method can be viewed as yielding the percent reduction in auxiliary input due to the Solar assist.

This value gives the best indication of the potential savings for a specific system when comparing operation with and without a Solar assist. Since the value of a Solar installation to a consumer can only be defined economically, this is the method which should be used in the evaluation of Solar assisted hot water systems.

Figure 1 - SYSTEM SCHEMATIC

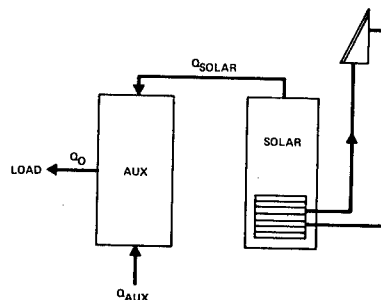
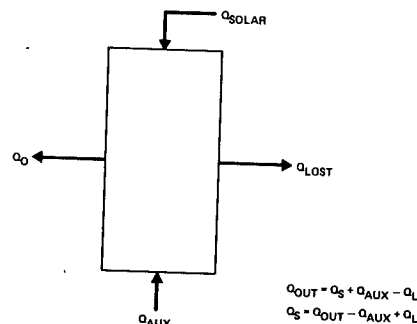


Figure 2 - ENERGY BALANCE



AIR COLLECTOR TESTING UTILIZING ASHRAE 93-77
By: Richard D. Whitaker and William T. Dokos
Desert Sunshine Exposure Tests, Inc.

WHITAKER, RICHARD D.

Mr. Richard D. Whitaker graduated from the University of Arizona with a B.S. degree in Aerospace Engineering in 1969 and a M.S. degree in Mechanical Engineering in 1970. Prior to his departure from the University, Mr. Whitaker was employed by the University of Arizona Engineering Experimental Station in the Physical and Biological Measurements Laboratory under Prof. M. R. Bottacini. There he gained experience in instrumentation and performed graduate research in desalinization of water by reverse osmosis. Mr. Whitaker then served with the United States Air Force, first as a satellite system computer programmer, and finally as a Space Systems Acquisition and Development Engineer. In 1977 Mr. Whitaker separated from the military and joined Desert Sunshine Exposure Tests, Inc. as a Test Engineer. Mr. Whitaker is now Assistant Manager of Solar Operations. In addition to his overall responsibilities within the Solar Division of DSET, Mr. Whitaker has direct operational management responsibility for the DSET Air Collector Test Facility and Computer Operations Section.

DOKOS, WILLIAM T.

Prior to obtaining a 1972 degree from Northern Arizona University (B.S. in Chemistry), Mr. Dokos worked for Interstate Electronics Corporation and California Computer Products, Inc., both in Anaheim. At CCPI, Mr. Dokos was Group Leader responsible for production of digital plotting systems and computer peripheral equipment, and for technical assistance for European operations. Mr. Dokos joined DSET in 1972 and is Manager of Solar Operations, responsible for performance testing of all types of solar collector devices.

ABSTRACT

A facility and procedures have been developed for the testing of collectors that utilize air as the heat transfer medium. The facility is specifically designed for testing in accordance with the requirements of ASHRAE Standard 93-77 and capitalizes on the inherent advantages of a sun-tracking altazimuth mount and the open loop principle.

A technique has been developed within DSET which expands upon the basic instantaneous efficiency measurement requirements of ASHRAE Standard 93-77 by accounting for the effect of water vapor upon the specific heat and density of ambient air. This technique is based on the use of an enthalpy balance across the air collector's inlet and outlet and on precise air flow measurements obtained using laminar flow elements configured to measure both flow into and flow out of the collector. The effects of air leakage upon instantaneous efficiency test results are discussed.

INTRODUCTION

As a result of numerous requests and our analysis of the Nation's testing requirements, DSET initiated design and construction of an air collector test facility in late 1976. Development of the computational model and test procedures occurred during the summer of 1977. Although construction was completed in August 1977, final calibration and facility checkout were not completed until October 1977 when the facility became fully operational. Now, after testing more than 30 air collectors, DSET has further improved upon use of the open loop principle.

DESIGN BASIS

Based upon DSET's experience in testing more than 400 water-type collectors, an air test facility was designed to utilize the two most important features of the hydronic test facilities in routine use: (1) the sun-tracking altazimuth mount, and (2) the open loop principle.

Sun-Tracking Mount

Exactly-normal-incident (ENI) mounts that follow the sun from morning to night are normally employed in all thermal performance testing that pertains to the use of ASHRAE 93-77 and the determination of Hottel-Whillier governing equations of the collector. An ENI mount is pictured in Figure 1. It is also known as an automatic-tracking altazimuth mount. The mount's operational limits are from 90° east to 270° west and 75° to 0° from the horizontal. The ENI mounts are bi-directionally controlled by two pairs of shaded, matched solar cells, one pair of which controls the azimuth angle (east-west) and the other the solar elevation. The altazimuth (ENI) mount maintains collectors always normal to the sun (from sunup to sundown, if technically feasible), and at the same time the collector surface is always plumb to the tangential earth-plane. The major reason for employing a normal incident mount is that the insolation rate can be held very near constant for a large portion of the day. The stable insolation minimizes one of the most critical variables in the performance of the test and thereby contributes to minimizing scatter in the test data.

Open Loop

The open loop principle is the least expensive and most basic testing approach for minimizing scatter and effecting exact results. As can be seen from Figure 2, excellent repeatability is possible in a water collector test utilizing the open loop principle. Such tightly grouped data are only possible with the constancy of flow rate and inlet temperature such as application of the open loop principle can afford (providing an altazimuth test mount is employed under cloud-free conditions).

CURRENT FACILITY

A schematic of the original air test facility is presented in Figure 3. As can be seen, the open loop principle is applied utilizing a positive pressure blower. The DSET air collector test facility is shown in Figure 1 with the altazimuth mount.

The principal elements of the air collector test facility are the Meriam laminar flow element and the temperature control scheme for the transfer fluid.

Meriam Laminar Flow Element

The Meriam laminar flow element functions on a metering principle. The element provides a calibrated constriction (screen) across the entire air duct. The resulting pressure drop across the capillary tube matrix (screen) is directly related to the actual gas flow through the device. Since the flow constriction functions on the capillary principle, the relationship between indicated pressure drop across the matrix and actual flow is nominally linear instead of second order, as in conventional metering flow measurement devices. The Meriam laminar flow element has an accuracy of $\pm 0.5\%$.

Differential pressure measurements across the flow element are obtained (as are all differential and gauge pressure measurements) with Meriam precision inclined manometers. The inclined manometers not only provide a highly accurate measurement technique but also afford a means for continuously monitoring the air flow rate, which may be affected by ambient wind conditions, electrical power surges, etc. The most sensitive inclined manometers can be read to a pressure accuracy of 0.005 inches of water column.

Indicated flow rates, which are determined from manometer-read pressure drop measurements, are then corrected to values for actual cubic feet per minute (ACFM) and standard cubic feet per minute (SCFM) by application of classical gas law compensations for temperature and pressure. A temperature measurement is made at the inlet to the flow element which is used to correct the indicated flow measurement for viscosity and to determine F_{Tot} , the ACFM flow rate. The temperature and pressure measurement are used to correct the indicated flow rate to what would be a corresponding flow rate of air at a temperature of 70°F and a pressure of 29.92 inches of mercury (Hg). This corrected flow rate (F_s), measured in SCFM, corresponds to dry air at a density of $0.075 \text{ lb}_m/\text{ft}^3$.

Temperature Control and Stabilization

The major element in the facility's temperature control scheme is the use of ambient air as the source test fluid. Though ambient air temperature will change over the course of a day, this change will be quite gradual (compared to the period of a test) and predictable.

The water-to-air heat exchanger inlet water is also highly temperature-stabilized by the use of a high circulation rate of water through the heat exchange system. This high circulation rate causes the water to reach a heat loss equilibrium quickly and then maintain a constant temperature based on the air flow through the heat exchanger.

The circulating water temperature is controlled and varied employing the 10-kw rheostat-operated in-line heater. Since the rheostat setting remains unchanged during testing, the inlet temperature is dependent solely on the rate at which energy is imparted to the air flowing through the heat exchanger and in any powerline surges to the rheostat. The water lines are sufficiently insulated that ambient temperature changes and wind have no effect by themselves. (They will affect collector performance "at the collector surface," however.) Depending on ambient air temperature and flow rates through the system, water temperatures from ambient to 210°F are possible (with the latter temperature achieved with the systems under controlled pressures). The water system is designed such that inlet water temperatures greater than 210°F can be achieved. Water temperatures near 210°F correspond to inlet air temperatures, again depending upon water and air flow rates through the exchanger, of in excess of 150°F.

For those cases in which it is desirable to cool source air (due to friction heating in the blower and conduction heating from sun-heated ducting) cold water is circulated through the heat exchanger from a large water storage tank. The constant temperature of the large water mass in the tank forms the basis for temperature stability in the cooling process.

Facility Performance

Figure 4 shows a representative air collector test result obtained with the DSET air test facility.

LESSONS LEARNED

Experience gained in utilizing this facility in over thirty (30) collector tests has elucidated two very important aspects of air collector testing.

Air Leakage

For the upstream flow measurement case, a leak on the inlet side of the collector will tend to erroneously inflate the measured instantaneous efficiency. The test results will be higher than appropriate for two reasons: First, because of the leak, the flow rate recorded by the upstream measurement device will indicate a flow higher than the actual fluid flow through the collector. This will cause m in the basic efficiency equation

$$\eta = \frac{\dot{m} C \Delta T}{I_{Tot} A_g}$$

to be higher than appropriate. Simple employment of heat transfer theory tells us that the actual ΔT measured across the collector will also be too high for the corresponding measured flow rate. Thus, two terms in the numerator will be high, resulting in an incorrect indication of the collector's efficiency.

A leak at the collector outlet will have very little effect upon the measured efficiency. In this case, the upstream-measured flow rate is assumed to describe accurately the actual flow through the collector. Since the fluid travels all the way through the collector passages before the leak occurs, it is probable that T_o will be very little changed by the

leak. We see that for an outlet-side leak the effect upon efficiency is most probably very small or none at all.

The third leak situation is the perplexing usual case -- leaks are more or less equally distributed throughout the collector. In this situation, it appears that two opposing mechanisms are at work. For simplicity, let us examine the case of a single leak placed exactly midway between collector inlet and collector outlet. The loss of fluid tends to cause the upstream flow measurement to be higher than that which actually passes through the entire collector. Thus, the effects of the inlet leak would tend to be present; however, with the loss of fluid at this mid-collector leak, there also is a loss of energy which tends to depress T_o and therefore ΔT (if T_i is held constant). Thus, the tendency exists for ΔT and m to be too high for the collector, but at the same time ΔT may also be driven downward by the energy loss. Therefore, the extent to which one or the other is the strongest will be collector-dependent. The important conclusion is that the location of a leak and the collector design, have as much to do with its effect upon the measurement as does the actual leak rate itself.

Investigation of "scenarios" involving downstream-from-the-collector flow measurements also show that the leak's effect upon the efficiency measurement is highly dependent upon the location of the leak. However, from a practical standpoint, a flow measurement on the collector's downstream side will at least always accurately describe the energy flow available for use, i.e., the outlet temperature in combination with the outlet flow rate describe the relative energy output from the collector via the common expression, $mC_p T_o$.

Duct Temperature Distribution

An accurate measurement of the bulk air flow temperature is, of course, critical to an accurate measurement of instantaneous efficiency. Experience at DSET has shown that the temperature distribution, particularly on the outlet duct, is collector, as well as temperature, and air flow rate-dependent. It is clear that no single flow mixer would insure even temperature distribution across the duct. Additionally, mixers cause pressure drop in the flow and limit test system capacity.

The DSET facility utilizes individually-sampled thermocouples, each of whose measurement is recorded on a scan-by-scan basis during the duration of the test. Calibrated Type "T" thermocouples in arrays of three-each sample air temperatures at the flow element (for density and viscosity corrections) and at both collector inlet and outlet. These arrays verify the uniformity of the temperature distribution in the duct work. The arithmetic average of the three thermocouple measurements in each array is used at the appropriate points in the thermodynamic calculations.

As a result of our experience in the wide variance of temperature distributions within test section ducting, the individually-sampled scheme of thermocouple readings will be maintained at DSET. This scheme is the only way to verify and insure temperature uniformity in the ducting.

NEW FACILITY

As a result of DSET's experience with the open loop positive-pressure-only system, a new facility has been designed and is being constructed at this writing. As will be noted from Figure 5, two variable-speed blowers are used to provide controlled and stable source air flow through the collector. Laminar flow elements are used to accurately measure that flow. A blower/flow element pair is positioned at both the inlet/outlet ports of the collector.

Dual Blower Configuration

The new air test facility utilizes two blowers in order to maximize the flow rate range and the versatility of the open loop principle. One blower pushes air through the collector inlet while the other blower draws air from the collector outlet. Two blowers in tandem are required to overcome aerodynamic drag losses within the test facility and the collector. The facility's flow rate range is continuous from 0 through approximately 1000 SCFM for the "nominal" collector pressure drop (i.e., less than 0.5 in H_2O).

The two-blower approach also offers the additional advantage of complete control over the collector's internal pressure. By adjusting the relative speeds of the two blowers, tests can be accomplished for both collectors which are designed to operate under positive pressure (air is pushed through the collector), and for those designed to operate under negative pressure (air is drawn through the collector).

Dual Flow Elements

DSET's new air test facility incorporates a laminar flow element measurement at both collector inlet and outlet positions. The major advantage of such a measurement scheme is that not only will the test accurately measure the energy output of the collector despite possible air leakages, but a real-time analysis of air leaks during the test can be performed also.

Improved Test Section

Temperatures are again monitored with calibrated copper-constantan (Type T) thermocouples. However, thermocouples have been added for redundant resolution of the bulk temperature measurement. Thermocouples are now mounted in arrays of six-each at appropriate locations in the air flow ducting. The array consists of a five-pointed star suspended in the flow with a thermocouple mounted at each point of the star and at the center of the duct and star. Such an array is mounted at the inlet to the laminar flow element and at both the collector inlet and outlet.

All thermocouples in the arrays are sampled during each data collection scan. Thus, consistency of duct temperature distribution is verified on a scan-by-scan basis. Each thermocouple is individually read, though the arithmetic mean of each array's six readings is used in the thermodynamic calculations. Mixers are only used when absolutely necessary.

THERMODYNAMICS OF AIR COLLECTOR TESTING

The following development presents the means used at DSET to account for the effect of water vapor upon ambient air's specific heat and density and shows how, by this method, air collectors can be tested accurately in any humidity region of the world.

The following equation provides the generalized expression for experimentally determining instantaneous efficiency data values:

$$\eta = \frac{\dot{m} C_p \Delta T}{I_{\text{Tot}} A_g} \quad (1)$$

where ΔT is $(T_o - T_i)$, T_o is the fluid outlet temperature, T_i is the fluid inlet temperature, \dot{m} is the mass flow rate. This general equation is valid for whatever fluid is used as the heat transfer medium through the collector. However, a special form of this equation is appropriate and convenient when ambient air is the source heat transfer medium.

In terms of air conditioning (and the testing of air-type solar collectors designed for normal space heating), ambient air can be thought to be a mixture of two gases, dry air (actually a mixture in itself of 10 gases) and water vapor. The relative proportions of these two gases has a real effect upon the density and specific heat of ambient air. Through the use of (1) enthalpy (energy per unit mass of air), and (2) specific humidity (the mass ratio of water vapor and dry air), the efficiency of an air collector can accurately be measured despite varying conditions of humidity.

Reference 1 explains that, for a perfect gas, as ambient air can be viewed for these purposes, C_p , the specific heat, is a function of temperature only and the following relationship holds:

$$h_{\text{out}} - h_{\text{in}} = \Delta h = \int_{T_{\text{in}}}^{T_{\text{out}}} C_p dT \quad (2)$$

where Δh is the specific (per unit mass) enthalpy change in a gas, C_p is the specific heat, and T_{in} and T_{out} are the end temperatures of the thermodynamic states at the collector inlet and outlet, respectively.

Since ambient air is a mixture of two perfect gases, dry air and water vapor, the above equation can be expanded to

$$\Delta h_{\text{Tot}} = \int_{T_{\text{in}}}^{T_{\text{out}}} C_{p_D} dT + \int_{T_{\text{in}}}^{T_{\text{out}}} C_{p_V} dT \quad (3)$$

where Δh_{Tot} is the total specific enthalpy of the dry air/water vapor mixture, C_{p_D} is the specific heat of the dry air, and C_{p_V} is the specific heat of water vapor. Air consists of two gases, both of

which have a non-constant specific heat; therefore, for the case of air, Equation (1) can logically be expressed as:

$$\eta = \frac{\dot{m} \int_{T_{\text{in}}}^{T_{\text{out}}} C_{p_D} dT + \int_{T_{\text{in}}}^{T_{\text{out}}} C_{p_V} dT}{I_{\text{Tot}} A_g} \quad (4)$$

and, on substitution of Equation (3) into Equation (4), we obtain:

$$\eta = \frac{\dot{m} \Delta h_{\text{Tot}}}{I_{\text{Tot}} A_g} \quad (5)$$

where Δh_{Tot} is determined for the mixture. To simplify future calculations, the specific enthalpy of the mixture, h_{Tot} , is determined and expressed in terms of dry air mass only by multiplying the enthalpy of the water vapor, h_V , by the specific humidity, W_V (mass ratio of water vapor to dry air), which results in the following equation:

$$h_{\text{Tot}} = h_D + W_V h_V \quad (6)$$

where h_{Tot} is the specific enthalpy of the mixture, h_D is the specific enthalpy of the dry air component, h_V is the specific enthalpy of the water vapor, and W_V is the specific humidity of the air (found knowing the atmospheric conditions of pressure, temperature, and relative humidity).

The appropriate values for h_D and h_V are found in commonly available enthalpy tables knowing the dry bulb temperature of the air. Equation (6) is then solved twice in order to determine the total enthalpy difference, Δh_{Tot} , in terms of dry air mass. The first calculation of h_{Tot} is made on the basis of inlet temperature. The second calculation is made on the basis of outlet temperature.

Since Equation (6) relates the specific enthalpy to the mass of only the dry air component of the air/water vapor mixture, Equation (5) can now be written as follows:

$$\eta = \frac{\dot{m}_D \Delta h_{\text{Tot}}}{I_{\text{Tot}} A_g} \quad (7)$$

where \dot{m}_D is the mass flow rate of the dry air component.

By the law of conservation of mass \dot{m}_D must be constant throughout the test facility/collector airstream. The term \dot{m}_D breaks down into two terms measurable in the air test facility: (1) F_{Tot} , total volume rate of flow (ACFM) of ambient source air measured at the Meriam laminar flow element, and (2) ρ_D , the dry air density of the air at the point where the flow rate is measured. The flow element measures the flow rate of whatever "perfect" gasses pass through it, be it water vapor, dry air, or a combination. Consequently, a simple viscosity correction applied to the Meriam element's indicated

flow rate yields F_{Tot} . The dry air density, ρ_D , is found by using a straightforward application of Dalton's law of partial pressures and the perfect gas law. This dry air density is found, knowing atmospheric conditions of pressure, temperature, and relative humidity, plus temperature and absolute pressure of the air at the laminar flow element.

The basic expression for air collector instantaneous efficiency is then

$$\eta = \frac{F_{Tot} \rho_D \Delta h_{Tot}}{I_{Tot} A_g} \quad (8)$$

which is a convenient expression to be used when observing water vapor's effect upon the specific heat and density of any dry air/water vapor mixture.

Finally, the correct expression used in practice is as follows:

$$\eta = \int_{t_1}^{t_2} \frac{F_{Tot} \rho_D \Delta h_{Tot}}{I_{Tot} A_g} dt \quad (9)$$

where t_1 and t_2 are the time and points of the integration data sampling period.

Note that all the numerator terms of the final equation, on which this method is based, are either directly determined or easily derived from measurements made in the air collector test facility. The value of F_{Tot} is found directly from the laminar flow element; ρ_D is found from duct and ambient air temperature, pressure, and relative humidity measurements. The value of Δh_{Tot} is found from humidity and temperature measurements (recall W_v) and collector inlet and outlet duct temperature measurements.

REFERENCES

1. Dillio, Charles C. and Nye, Edwin P., Thermal Engineering, International Textbook Company, ed., January 1969.

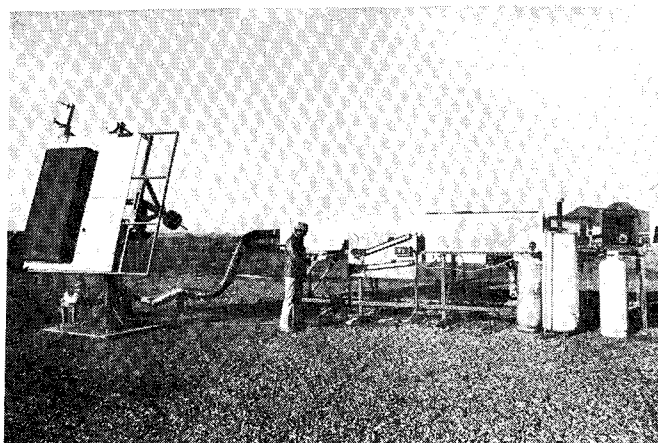


Figure 1. Altazimuth (ENI) Test Mount (And Air Tunnel).

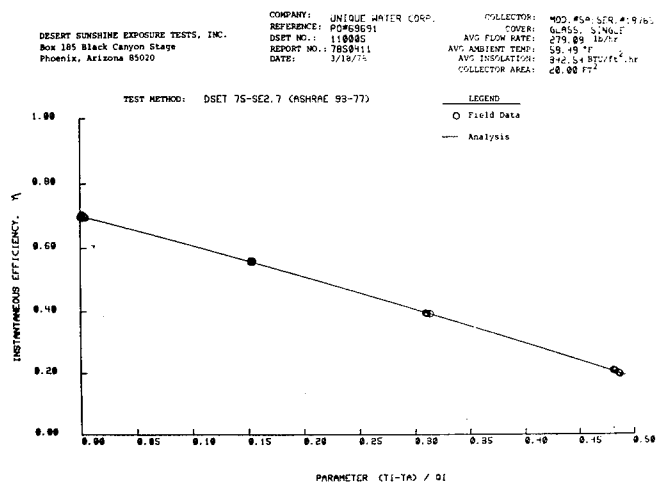


Figure 2. Representative Hydronic Collector Performance Curve Obtained at DSET.

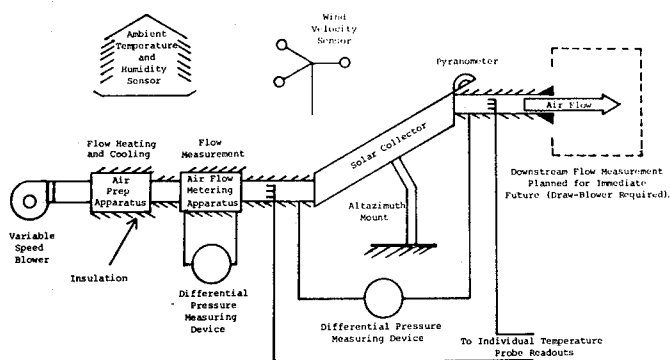


Figure 3. Schematic of DSET's Original Air Collector Test Facility.

DESERT SUNSHINE EXPOSURE TESTS, INC.
Box 185 Black Canyon Stage
Phoenix, Arizona 85032

COMPANY: UNIQUE AIR CORP.
REFERENCE: 1917
DSET NO.: 112233
REPORT NO.: 112233
DATE: 03/19/78

COLLECTOR: EXPERIMENTAL
COVER: PLASTIC, DOUBLE
AVG FLOW RATE: 88.65 SCFM
AVG AMBIENT TEMP: 82.84 °F
AVG INSOLATION: 385.51 BTU/ft².hr
COLLECTOR AREA: 45.12 FT²

TEST METHOD: DSET 75-SE2.7 (ASHRAE 93-77)

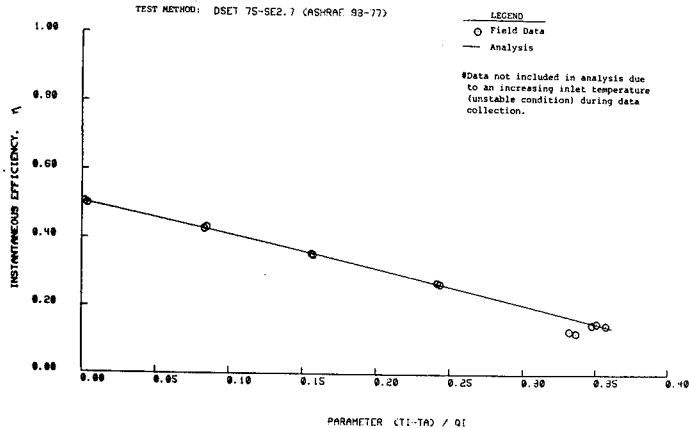


Figure 4. Representative Air Collector Performance Curve Obtained at DSET.

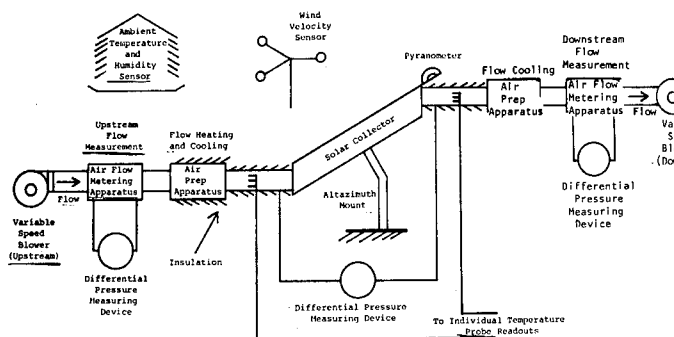


Figure 5. Schematic of DSET's New Push/Pull Air Collector Test Facility.

COST EFFECTIVE SOLAR COLLECTOR PERFORMANCE TESTING UNDER COMBINED INDOOR AND OUTDOOR CONDITIONS

By: L. Harold Usher, Wyle Laboratories

Author's Biography

Harold Usher, of Wyle Laboratories Solar Energy Systems Division, directs tests, evaluations and analyses of solar heating/cooling subsystems and systems at the Marshall Space Flight Center (MSFC) Solar Heating and Cooling Test Facility. As part of the subsystem testing capability, solar simulator test equipment has been utilized in performance of solar collector thermal performance evaluations. Previous to entering the solar energy program, Mr. Usher performed/directed engineering analyses and testing activities primarily related to space and military applications. His engineering analysis specialties are in heat transfer, fluid mechanics and thermodynamics. Mr. Usher is a BME graduate of Georgia Institute of Technology.

I. INTRODUCTION

Descriptive information is provided on solar facilities and equipment currently being operated by Wyle Laboratories to conduct thermal performance evaluation of solar energy industry products. This facility is located at the Marshall Space Flight Center, Alabama, and was designed to test residential, business and commercial solar heating and cooling systems and subsystems. The scope of testing which is discussed in this paper is limited to thermal performance evaluations of solar collectors using methods as advised in ASHRAE 93-77. The purpose of this paper is to detail the latest procedures which utilize combined indoor/outdoor facilities to improve the effectiveness of available equipment and manpower.

Discussions are made to show how the method of solar collector testing has evolved over a period from mid-1976 to the present time to improve the cost effectiveness in terms of manpower and facilities. Comparisons are made to show that by combining indoor and outdoor test facilities better equipment utilization has resulted. Other benefits which were evident are improved testing productivity in terms of solar simulator accumulative operational time per test unit and more efficient manpower utilization.

II. SOLAR TEST FACILITY DESCRIPTION

The NASA Solar Heating and Cooling Test Facility was constructed for evaluation testing in support of the Department of Energy solar development program. The Facility contains four different test beds to provide the capability to test either air or liquid media solar heating and cooling systems, subsystems and/or system

components. Solar collector testing is performed at the Test Bed site or at the indoor Solar Simulator Facility site, which is located at a nearby high bay building. The Facility Data Acquisition System provides means by which data may be monitored and recorded concurrently from all test sites and independent systems tests. A site plan of the Facility is presented in Figure 1. Wyle Laboratories initiated operation of these facilities in mid-1976.

III. SOLAR COLLECTOR TEST EQUIPMENT

Portable fluid conditioning test loops are used for indoor collector testing on the simulator or on outdoor tests at natural environmental conditions. Presented in Figures 2 and 3 are flow schematics which depict the major components and capabilities of the fluid conditioning test loops. Generally, water or ethylene glycol water solutions are used as heat transfer media in the liquid conditioning test loop.

The solar simulator utilizes 405 300-watt tungsten-halogen lamps and is capable of providing insolation rates of up to 430 BTU/Hr·Ft² over a 4 ft. x 8 ft. test area. Photograph 1 shows the MSFC simulator under operation with the tilting collector support stand. Photograph 2 shows a typical outdoor thermal performance test under operation at the Test Bed Facility. Remote teletype units at both test sites provide the test conductor with real time data in engineering units for data recording purposes.

IV. COLLECTOR TEST SEQUENCE

The sequence of testing activities for collector thermal performance evaluation was modified in the first part of this year. Specific test activities and corresponding test facilities which are utilized are indicated below.

<u>Collector Test Activity</u>	<u>Test Facility</u>
1. 3-Day Preconditioning	Test Bed #4
2. Thermal Time Constant	Solar Simulator
3. Thermal Efficiency	Solar Simulator
4. Incident Angle Modifier	Solar Simulator

This testing sequence has eliminated the collector exposure time previously required for collector preconditioning on the solar simulator. As the weather conditions permit, the preconditioning tests are performed on several collector units which are subsequently stored at the Simulator Facility

for scheduled tests.

Collectors which are oversized in terms of the 4 ft. x 8 ft. Simulator Facility test area and other collectors which have solar tracking capability are evaluated under outdoor conditions at the Test Bed Facility. Portable fluid conditioning test loops for air and liquid heat transfer media are interchangeable between the indoor/outdoor test facilities.

V. COMBINED INDOOR/OUTDOOR OPERATION

Testing activities required in the combined indoor/outdoor testing sequence and corresponding solar simulator exposure hours and labor manhours are compared in Chart 1 with the labor manhours associated with outdoor tests.

A major cost element to be considered when operating the simulator is the replacement of lamps. Our operational experience shows that the average life of the G.E. Model ELH lamps is approximately 60 hours. Replacement of lamps and necessary remaps of the intensity at the test plane requires significant labor, which is reflected in estimates as presented in Chart 2. The total maintenance cost of the simulator divided by the operational life expectancy of the lamps provides an hourly cost factor for simulator operation of \$56/hour. Utilizing the simulator hourly cost factor and the associated labor for tests, the following comparison was made for individual collectors:

Total outdoor test cost	-	\$780
Total combined outdoor/ indoor test cost	-	\$920

The outdoor test cost is lower than that for indoor test; however, the ability to perform collector test scheduling independent of weather conditions is an advantage for the Solar Simulator Facility. Simulator maintenance costs per operational hour will be significantly reduced in the near future when G.E. Model ENH replacement lamps are installed. These lamps are rated at 175 hour life expectancy but cost approximately \$3 more per unit. Total combined outdoor/indoor test cost per collector will be reduced to below \$400 when the Model ENH lamps are installed.

The costing estimates presented in this comparison reflect the direct operational test costs which have been experienced for individual collector testing under optimum weather conditions. Additional costs are involved in collector testing, including costs of instrumentation calibration, data acquisition and evaluation of data. These costs are not shown in the comparisons since they are generally equal for outdoor or indoor testing at our facilities. Also, the capital expenditure necessary to design

and construct the simulator has been assumed to be amortized over a sufficient period to negate these costs.

VI. CONCLUSIONS

Several conclusions are made based upon the cost comparisons which were made of combined outdoor/indoor testing versus outdoor testing.

- Combined indoor/outdoor tests of individual collector thermal performance have increased the facility productivity and lowered overall costs.
- Current combined indoor/outdoor collector thermal performance test costs approach outdoor test costs. Future plans to reduce solar simulator maintenance costs will result in a combined indoor/outdoor testing cost advantage over outdoor testing.

Test Activity	Solar Simulator Exposure Period	Combined Outdoor/ Indoor Test Manhours	Outdoor Test Manhours
3-Day Preconditioning	0*	2	2
Simulator Setup	0	3	3
Thermal Time Constant	0.5	1	1
Thermal Efficiency	8.0	9	30
Incident Angle Modifier	1.5	3	3
TOTALS	10.0 Hrs.	18	39

* It is noted that an improvement of approximately 15 hours exposure time on the simulator was realized by performing the 3-day preconditioning tests at outdoor conditions.

CHART 1

Operation	Replacement Lamp Cost	Manhours	Labor Cost, \$ @ \$20/Hr.
Change Lamps	\$3200	4	80
Remap Intensity	0	3	60
TOTALS	\$3200	7	\$140

CHART 2

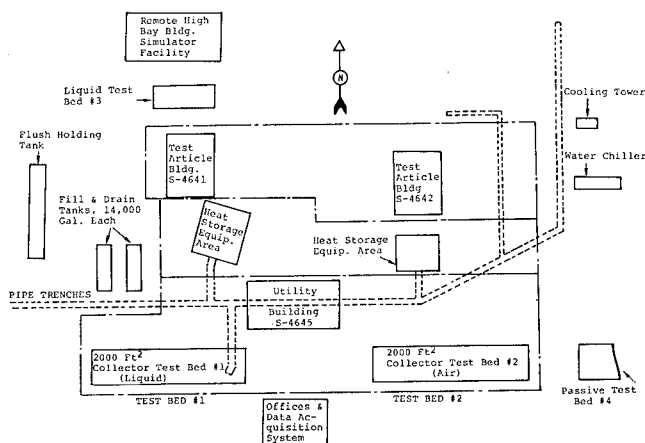


Figure 1. SOLAR FACILITY SITE PLAN

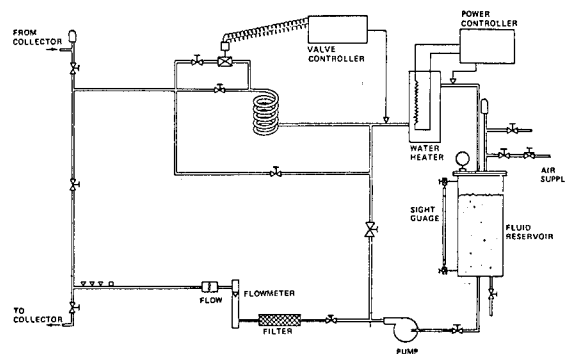


Figure 2. LIQUID LOOP CONDITIONING SCHEMATIC

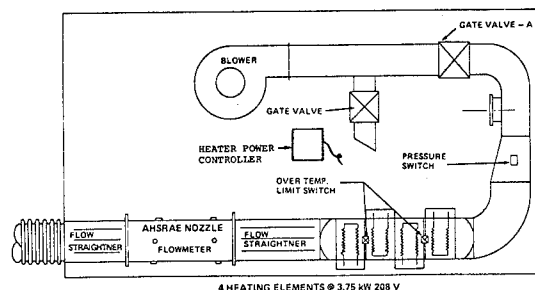
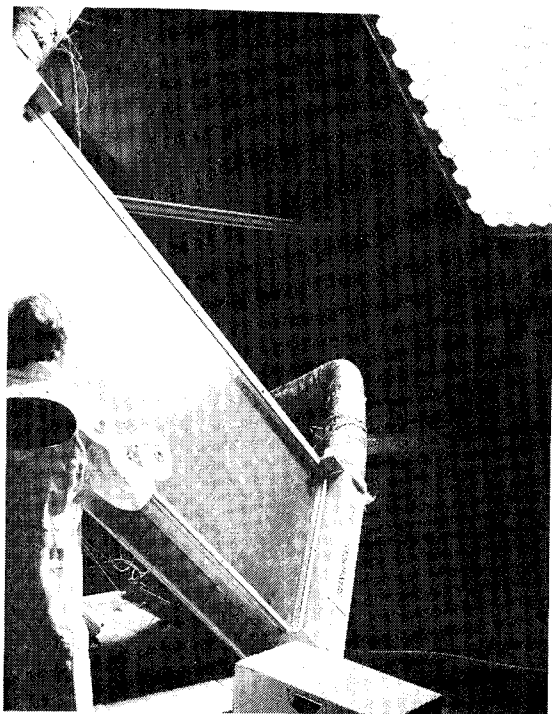
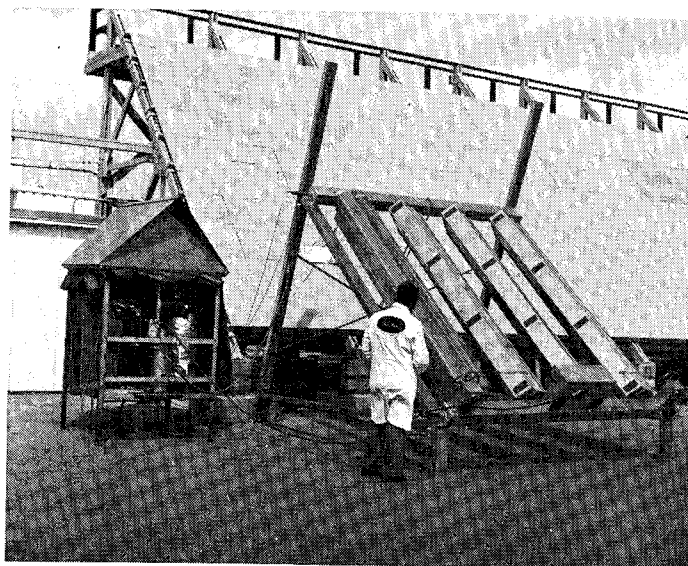


Figure 3. AIR LOOP THERMAL CONDITIONING SCHEMATIC



Photograph 1. Solar Simulator
Operation for Collector Incident
Angle Modifier Evaluation



Photograph 2. Typical Outdoor
Thermal Performance Test

PROBLEMS IN COLLECTOR TESTING

BY G. R. MATHER

AND D. C. BEEKLEY

SUNPAK™ COLLECTOR PROGRAM

OWENS-ILLINOIS, INC.

Introduction

This paper discusses problems associated with the thermal performance testing of collectors. One of the main purposes of testing is to provide data so that a rating or label statement can be made that contains pertinent information for consumers. Several groups, including the Solar Energy Research and Education Foundation and the Solar Energy Industry Association, are engaged in the development of these rating or labeling procedures. A second purpose of collector testing is to convey performance information to a design engineer or system designer so that system components can be sized properly to meet the design load.

Most current thermal test procedures rely on the Hottel-Whillier-Bliss[1] equation as a description of the performance characteristics of a collector. Certainly this equation has wide applicability and utility in collector testing; however, the instantaneous and steady state basis of the equation makes extensions to the world of transient and dynamic collector operation difficult. Further, while virtually any collector's performance can be cast in the form of the Hottel-Whillier-Bliss equation, some of the newer design collectors on the market defy interpretation by it. That is to say, the performance of some collectors cannot be described in a meaningful or useful way by this equation alone.

ASHRAE 93-77 appears to be the collector test procedure which is the closest to being accepted on a consensus basis. The test procedures prescribed in this document do extend, through the Incident Angle Modifier (IAM) and time constant measurements, the data base beyond that of the Hottel-Whillier-Bliss equation. Through these measurements, it is possible to interpret collector performance as a dynamic basis. Some specific areas of performance testing, however, are left out of the scope of the prescribed tests or only treated in a tangential way.

Collector Performance Under Diffuse Insolation

Most collector test procedures, including the ASHRAE tests, prescribe a minimum level of insolation during the test in order for the data to be considered valid. This minimum insolation is usually high enough that the test period can qualitatively be described as "sunny" or "bright"; at least "not cloudy." Even those test specifications that are not restrictive as to insolation level make no distinction between the treatment of beam

and diffuse insolation. Table I below indicates the long term percentages of diffuse to total insolation available in the tilt plane of the collector for several selector times and locations.

	Dec.	Jan.	July	Aug.
Boston	.31	.32	.44	.42
New York	.31	.33	.47	.43
Wash., DC	.20	.22	.44	.39
Cleveland	.31	.32	.38	.34
Chicago	.40	.51	.47	.43
Boulder	.17	.18	.43	.40

Diffuse/Total Insolation
Tilt = Latitude

Table I

Note that even in those locations normally considered "sunny" (mostly beam insolation) at certain times of the year a substantial portion of the available energy is diffuse in nature. Further, even in those locations having low percentages of diffuse to total insolation, the absolute energy available is quite high so the diffuse component can make a contribution to the energy output of the collector in an absolute sense.

Various studies have been made to define the character of diffuse insolation. Two of the more common viewpoints are that 1) diffuse insolation has its origin in some angular region of the solar disk, and 2) the diffuse insolation is distributed isotropically over the sky dome. We at Owens-Illinois, Inc. have been forced by the features of the SUNPAK™ collector geometry to treat the diffuse insolation component separately from the beam or total insolation. Our assumption is that the total insolation can be manipulated as a sum of beam and isotropic components. Regardless of the complete accuracy of this assumption under certain sky conditions, from an engineering viewpoint the mathematics for treating beam and isotropic insolation components separately are well understood and in sum cannot give results that are far from true. We have had very good results in a predicted performance sense in using this assumption.

One of the reasons, we feel, that the diffuse insolation component has not received more rigorous attention is that high percentages of diffuse to total insolation are often associated with low total energy levels. Many collectors cannot operate

effectively at low insolation levels because of their heat loss characteristics. This effectively masks any treatment of diffuse energy collector performance; that is not to say, however, that there is no separate effect of diffuse insolation on the operation of the collector.

We recommend that separate measurements of diffuse and total insolation be made during collector performance testing, that the diffuse components be treated as isotropically distributed and that a diffuse modifier term analogous to the Incident Angle Modifier be defined as a measured test parameter.

In detail, the product of the insolation and Incident Angle Modifier would be written in the form of equation [1].

$$I_p[(\alpha Z)_B(KZ_\alpha)_B(1-R) + (\alpha Z)_D(KZ_\alpha)_D R] \quad [1]$$

where

I_p - Total insolation in the collector plane.

$(\alpha Z)_B(KZ_\alpha)_B$ - Product of collector absorptivity, transmissivity and Incident Angle Modifier for beam insolation.

$(\alpha Z)_D(KZ_\alpha)_D$ - Product of collector absorptivity, transmissivity and modifier for diffuse insolation.

R - Ratio of diffuse to total radiation.

Under the assumption of isotropic diffuse insolation, the term $(\alpha Z)_D(KZ_\alpha)_D$, the diffuse modifier, is constant irrespective of the sun position in the sky. It might be possible to make a short and simple measurement of this term by covering the collector with a diffusing screen and measuring the collector output.

This procedure described above would be likely to produce two distinct "performance lines", one for beam and one for diffuse insolation. Since there are already generally accepted techniques for estimating the long term ratios of diffuse to total insolation, system designers would have more precise collector performance estimates, through interpolation between the two performance lines, for sizing collectors and components in any location.

In conclusion on this point, there is a need to treat diffuse insolation in a rigorous and consistent way. Large potential marketing areas of the country have weather conditions in which diffuse solar energy constitutes a large percentage of the available energy.

Incident Angle Modifier

The definition of the Incident Angle Modifier (IAM) in the ASHRAE 93-77 test procedure is a positive step forward in the description of collector performance, since the inclusion of this term recognizes that most of the day is not solar noon. There are some interpretation problems associated with the IAM, however.

For collectors whose cover surfaces are flat, the IAM is principally a measure of the Fresnel optical losses of these surfaces. For collectors similar to the SUNPAK™ collector or collectors using focusing devices such as compound parabolic concentrators, the IAM measurement is a combination of both optical losses and collector geometry effects. Despite the provision in the ASHRAE 93-77 test document for inclusion of a focusing term, in practice, there is no clear cut division between what are focusing and what are IAM effects. For some concentrator designs whose focus is a function of incident angle, it is impossible to measure the effects separately from one another. One attractive way around this problem is to define the focus as being constant and equal to the aperture to absorber area ratio. Unfortunately, for some collectors this definition of focus and IAM forms a mutually exclusive set under the current definition of terms in ASHRAE 93-77.

Further, many of the collectors that cannot be categorized as flat-plate collectors are competing for the same end uses as the flat-plate collectors. For the time being, the flat-plate collectors and the other collectors I have mentioned could be lumped generically into a general category of roof top devices. If this general collector category definition (or one similar to it) would be accepted, then the IAM and focusing terms could be lumped into one measurement term that describes the off-solar noon behavior of the collector. This step would require the measurement of collector performance at more points off solar noon than is presently required since a general mathematical form could not be derived that encompasses all geometries and focusing phenomena.

As a corollary to the discussion above, many of the non-flat plate collectors do not have incident angle effects that are polar symmetrical. That is, the incident angle effects in the East-West plane are different than those in the North-South plane. Since all fixed tilt angle collectors will have skew incident angles at some time of the year, the effects of the combination of the bi-axial nature of the incident angle must be included in some way to make accurate performance predictions. It seems economically prohibitive to measure the IAM at a large number of skew angles, so some reliable interpolation scheme must be devised to make representative calculations on a minimum data set.

Interpretation of Test Results

The most common method of presenting collector performance data is a graphical representation of the Hottel-Whillier-Bliss equation. Figure 1 is

a plot of the SUNPAKTM collector performance data in this form.^[2] Notice the several performance lines for various incident angles.

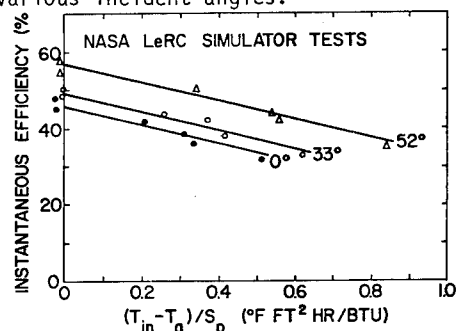


Figure 1

It is also common practice when making collector performance comparisons to plot each collectors' performance data on the same plot. If this were done in this case, which of the SUNPAKTM collector performance lines is to be taken as the norm? In order to make meaningful comparisons, it is necessary to evaluate each collectors' performance in some small time increment, with IAM effects, and then run the results over the design day chosen. This procedure is arduous at worst and time consuming at best in order to produce what is essentially a daily performance plot. What we argue here is that collector performance data be presented on a daily basis from the outset. Data in this form would remove any ambiguities in interpreting the instantaneous data and IAM and would surely reduce the amount of work required to produce viable collector performance comparisons. A daily presentation could involve the use of an average daily intercept derived from test results

Zerlaut and Dokos^[3] have already demonstrated the validity of interpreting ASHRAE 93-77 test data in a daily plot for "sunny" operating conditions and selected flat plate collectors. More work of this nature is required in order to generalize the technique, but there is every reason to think that good correlations will be found for a wide variety of test conditions and collector types.

In conclusion, three problems are apparent in the solar collector testing field:

- 1) Diffuse insolation needs to be treated as a separate entity in test procedures.
- 2) The definition of the Incident Angle Modifier needs to be generalized to encompass the focusing, geometric and optical phenomena accruing in collectors.
- 3) Performance data should be presented in a time frame of no less than a day.

References

1. A. Whillier, *Low Temperature Engineering Application of Solar Energy*, ASHRAE, New York (1967). "Design Factors Influencing Collector Performance."
2. F. F. Simon, "Solar Collector Performance Evaluation with the NASA-Lewis Solar Simulator - Results for an All-Glass-Evacuated-Tubular Selectively Coated Collector with a Diffuse Reflector," NASA TMX-71695 (1975).
3. Zerlaut, G. A.; Dokos, W. T., "The Use of Standard ASHRAE 93-77 in Predicting All-Day Performance of Flat-Plate Collectors", Proceedings: 1977 Flat-Plate Solar Collector Conference; D. B. Ward, ed.

CORRELATION OF INSTANTANEOUS AND ALL-DAY THERMAL PERFORMANCE OF FLAT-PLATE SOLAR COLLECTORS

By: D. M. Deffenbaugh, Southwest Research Institute

INTRODUCTION

Up until recently, the only solar radiation measurements available for most weather stations were in the form of daily totals. In order to do an accurate system simulation, hourly radiation had to be estimated from the daily totals so that a performance correlation for instantaneous operation could be used. This process has two major drawbacks. The first is the inaccuracy associated with the estimate of hourly solar radiation. The second is the large number of computations required. In order to eliminate these two shortcomings, an experimental program was undertaken to develop a performance correlation for all-day operation so that the actual daily radiation measurements could be used. This would reduce the number of computations required (1 instead of 96; i.e., every 15 minutes).

During the period when the collector is actually providing a net positive collection (collection period), the efficiency can be correlated using the same intercept and slope as is determined by the instantaneous performance test, if an appropriate operating parameter is defined. To extend the correlation to the period from sunrise to sunset (all day), all that is required is the ratio of solar radiation available during the collection period to the solar radiation available from sunrise to sunset, and the ratio of the length of the collection period to the length of the solar day. For the cases in this study, these two ratios were found to be constant. If this is the case in general, or if these ratios can be determined independently, then the information obtained from instantaneous testing can be used to calculate all-day performance.

TECHNICAL DISCUSSION

A. Collector Performance

The useful energy collected by a flat-plate solar collector is simply the difference between the incident solar radiation that is absorbed by the collector and the thermal energy lost from the collector due to a temperature difference between the collector and the surroundings. In mathematical terms,

$$Q_u = Q_a - Q_l \quad (1)$$

where Q_u = useful energy collected;
 Q_a = energy absorbed;
 Q_l = energy lost.

The incident solar radiation absorbed by the collector is

$$Q_a = \int [F'(\tau\alpha)_e IA] dt \quad (2)$$

and the thermal energy lost by the collector is

$$Q_l = \int [F'U_l A \Delta T] dt \quad (3)$$

where

F = $\frac{\text{actual useful energy collected}}{\text{useful energy collected if the collector surface was at the average fluid temperature;}}$
 $(\tau\alpha)_e$ = effective transmittance-absorptance product;
 I = instantaneous solar radiation intensity;
 A = collector area;
 U_l = collector loss coefficient;
 ΔT = temperature difference between the average fluid temperature in the collector and the ambient temperature;
 dt = time period.

Combining Eqs. (1), (2), and (3), and integrating over the collection period,

$$Q_u = \int_{cp} [F'(\tau\alpha)_e IA] dt - \int_{cp} [F'U_l A \Delta T] dt \quad (4)$$

The only terms in this equation that are functions of time are $(\tau\alpha)_e$, ΔT , and I , so that

$$Q_u = F'A \int_{cp} [(\tau\alpha)_e I] dt - F'AU_l \int_{cp} [\Delta T] dt \quad (5)$$

or

$$Q_u/A = F' \left[\int_{cp} [(\tau\alpha)_e I] dt - U_l \int_{cp} [\Delta T] dt \right] \quad (6)$$

The term $(\tau\alpha)_e$ is a function of angle as shown in Figure 1. If the collection period occurs such that the incident angle is less than about 45° , then $(\tau\alpha)_e$ can be taken to be essentially constant.

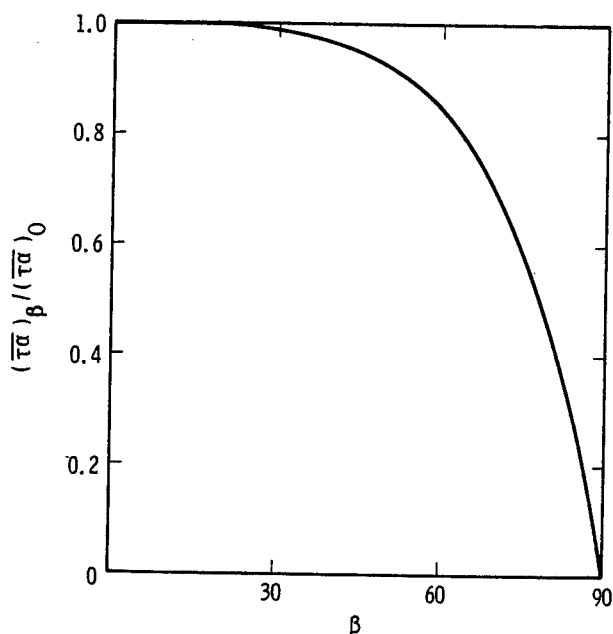


Figure 1. Transmittance-Absorption Product as a Function of Incident Angle

For a clear day, 61% of the energy is collected when the incidence angle is less than 30° and $(\tau\alpha)_e$ is 99% of the normal incidence value; 86% of the energy is collected at $(\tau\alpha)_e$ of 96% of the normal incidence value; and 97% of the energy is collected at $(\tau\alpha)_e$ of 90% of the normal incidence value. Therefore, Eq. (6) becomes

$$Q_u/A = F'[(\tau\alpha)_e \int_{cp} [I] dt - U_L \int_{cp} [\Delta T] dt] \quad (7)$$

Since the first integral is just the total solar radiation available during the collection period per unit area, and the second integral is the average temperature difference times the length of the collection period, then

$$\int_{cp} [I] dt = I_{cp} \quad (8)$$

and

$$\int_{cp} [\Delta T] dt = T_{avg} t_{cp} \quad (9)$$

Substituting Eqs. (8) and (9) into (7) yields

$$Q_u/A = F'[(\tau\alpha)_e I_{cp} - U_L \Delta T_{avg} t_{cp}] \quad (10)$$

We can define the collection period efficiency, η_{cp} , as the total energy collected during the collection period per unit area, Q_u/A , divided by the energy available per unit area, I_{cp} , so that

$$\eta_{cp} = Q_u/A I_{cp} \quad (11)$$

Combining Eqs. (10) and (11),

$$\eta_{cp} = F'(\tau\alpha)_e - F'U_L \frac{\Delta T_{avg}}{I_{cp}/t_{cp}} \quad (12)$$

Since the total solar radiation during the collection period divided by the length of the collection period is the average solar intensity over the collection period, $(I_{cp})_{avg}$, and if we then define the term

$$\zeta_{cp} = \frac{\Delta T_{avg}}{(I_{cp})_{avg}} \quad (13)$$

then

$$\eta_{cp} = F'(\tau\alpha)_e - F'U_L \zeta_{cp} \quad (14)$$

In addition to this efficiency, an all-day efficiency, η_{ad} , can be defined as

$$\eta_{ad} = Q_u/A \int_{ad} I dt \quad (15)$$

which reduces to

$$\eta_{ad} = Q_u/A I_{ad} \quad (16)$$

where I_{ad} = total solar radiation available during the day per unit area.

By combining Eqs. (11) and (16),

$$\eta_{ad} I_{ad} = \eta_{cp} I_{cp} \quad (17)$$

Therefore,

$$\eta_{ad} = \frac{I_{cp}}{I_{ad}} \eta_{cp} \quad (18)$$

If we define R_I as the ratio of solar radiation available during the collection period, I_{cp} , divided by the total daily solar radiation, I_{ad} , then

$$R_I = \frac{I_{cp}}{I_{ad}} \quad (19)$$

and

$$\eta_{ad} = R_I \eta_{cp} \quad (20)$$

Combining Eqs. (14) and (20) yields

$$\eta_{ad} = R_I F'(\tau\alpha)_e - R_I F'U_L \zeta_{cp} \quad (21)$$

where

$$R_I \zeta_{cp} = \frac{I_{cp}}{I_{ad}} \times \frac{\Delta T_{avg}}{I_{cp}/t_{cp}} \quad (22)$$

or

$$R_I \zeta_{cp} = \frac{\Delta T_{avg}}{I_{ad}/t_{ad}} \times \frac{t_{cp}}{t_{ad}} \quad (23)$$

where the ratio t_{cp} over t_{ad} is the ratio of the length of the collection period divided by the length of the solar day. This ratio will be defined as R_T or

$$R_T = \frac{t_{cp}}{t_{ad}} \quad (24)$$

and a new daily operating parameter is defined as

$$\zeta_{ad} = \frac{\Delta T_{avg}}{I_{ad}/t_{ad}} \quad (25)$$

or

$$\zeta_{ad} = \frac{\Delta T_{avg}}{(I_{ad})_{avg}} \quad (26)$$

Substituting Eqs. (24) and (25) into Eq. (23) yields

$$R_I \zeta_{cp} = R_T \zeta_{ad} \quad (27)$$

which, when combined with Eq. (21) gives

$$\eta_{ad} = R_I F'(\tau\alpha)_e - R_T F'U_L \zeta_{ad} \quad (28)$$

If the inlet fluid temperature is used in ΔT_{avg} instead of the average fluid temperature, then

$$\eta_{ad} = R_I F_R(\tau\alpha)_e - R_T F_R U_L \zeta_{ad} \quad (29)$$

where

$$F_R = \frac{\text{actual useful energy collected}}{\text{useful energy collected if the collection surface was at the inlet fluid temperature.}}$$

A solar collector test facility was constructed, and an experimental test program was performed to verify this correlation and to determine the variation, if any, in R_I and R_T . A description of the facility and experimental program follows.

B. Solar Collector Test Facility

A research facility was designed and constructed for testing solar thermal collectors. This facility was designed in accordance with NBSIR 74-635. A description of this facility is presented below.

Solar Collector Test Stand and Flow Circuit.

The collector test stand is made to accommodate four liquid-cooled solar collectors simultaneously. This stand faces due south, but features the capability for adjustments in the azimuth angle as well as the angle of collector tilt from the horizontal. The stand will accommodate collectors up to 0.9m x 3m (3 ft x 10 ft) in size. A photograph of the test stand is shown in Figure 2.

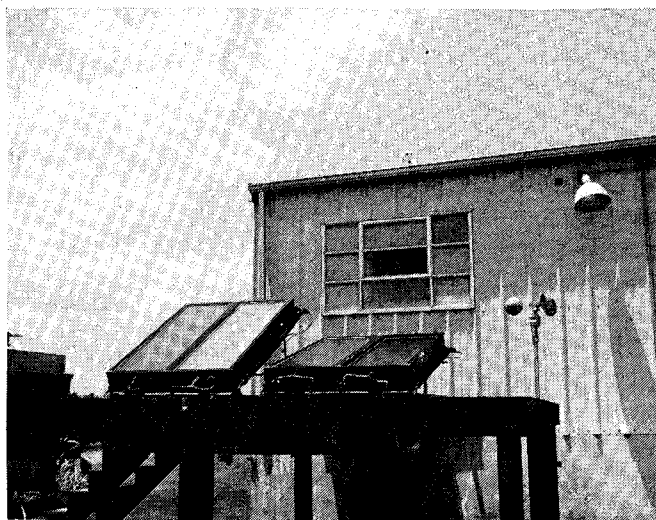


Figure 2. Solar Collector Test Stand

The flow circuit is a closed-loop system filled with a solution of 75 percent distilled water and 25 percent ethylene glycol. A 30-gal water heater equipped with a precision temperature controller is used to control the fluid inlet temperature to the collectors. With this heater and controls, the fluid inlet temperature to the collectors can be controlled at any constant value from near ambient to approximately 212°F. A centrifugal pump draws the fluid from the water heater and feeds a single header. The circulating fluid is then fed to each of the collectors by a separate supply line, and each line is instrumented with a precision rotameter for flow rate measurement. All lines from the header to the collectors are of equal length to promote a uniform fluid inlet temperature to the collectors. After passing through the collectors, the fluid enters another header and is returned through a single line to the water heater.

Instrumentation. Solar insolation is measured and recorded continuously at the facility with an Eppley precision pyranometer and a strip-chart recorder. Fluid inlet temperature to each collector is measured and recorded using type T thermocouples and a multichannel recorder. The temperature difference across each collector is measured with specially constructed six-junction, type T thermopiles, accurate to within $\pm 0.1^\circ\text{F}$. The output from the thermopiles is recorded on a dual channel

strip-chart recorder. Wind speed at the facility is measured and recorded with a Casella anemometer with a digital output. Accuracies of all instruments meet the recommendations given in NBSIR 74-635.

The instrument panel containing the recorders, rotameters, temperature controller, and flow system controls is located in the building immediately behind the collector test stand.

C. Experimental Program

An experimental program was undertaken to correlate all-day thermal performance of a flat-plate solar collector. Two test collectors were fabricated at the author's laboratory. Both employed tube-in-sheet absorber plates made of aluminum with a black chrome selective coating. One collector had a single white-water crystal glass cover, while the other had a single fiberglass-reinforced plastic cover. A summary of the collector characteristics for these two units is shown in Table I.

Table I. Test Collectors

	Unit No. 1	Unit No. 2
Gross Dimensions	19 in. x 51 in.	19 in. x 51 in.
Gross Area	6.7 ft ²	6.7 ft ²
Area of Absorbing Surface	5.9 ft ²	5.9 ft ²
Cover Plate		
Dimensions	18 in. x 50-1/8 in.	18 in. x 50-1/8 in.
Materials	white-water crystal glass	fiberglass-reinforced plastic
τ	.92	.83
Absorber Plate		
Dimensions	17 in. x 50 in.	17 in. x 50 in.
Material	1100 Al	1100 Al
Configuration of Flow Path	tube-in-sheet, parallel flow	tube-in-sheet, parallel flow
α	.868	.868
ϵ	.088	.088
Coating	Black Chrome	Black Chrome
Air Space	1/2 in.	1/2 in.
Insulation		
Material	Fiberglass	Fiberglass
Thickness	6 in.	6 in.
k	.32 Btu/hr ft ² F in.	.32 Btu/hr ft ² F in.
Performance		
$(\tau\alpha)_e$.799	.720
U_L	1.077	1.003
F_R	.917	.917

These all-day tests were conducted on various days during the period from March to June 1976. Test conditions included clear, as well as partly cloudy, skies; an average fluid temperature range of $140^\circ\text{F} \leq T_{f,i} \leq 190^\circ\text{F}$; an ambient temperature range of $65^\circ\text{F} \leq T_a \leq 90^\circ\text{F}$; and a daily total solar radiation range of $1000 \text{ Btu/day-ft}^2 \leq I_{ad} \leq 2600 \text{ Btu/day-ft}^2$.

The test procedures were a modification of those outlined in NBSIR 74-635. The all-day efficiency is determined by allowing the collector to operate all day no matter what the weather conditions may be. The system is brought up to the selected inlet temperature before sunrise, and a constant flow rate is set. As the solar intensity increases, and the fluid temperature across the collector goes from negative to positive, the test begins and continues until the fluid temperature across the

collector reverses. The solar radiation is integrated over the day, as well as the output from the thermopile that measures the fluid temperature difference across the collector. These two measurements are used to calculate the energy input to the collector and the energy output from the collector to determine its thermal efficiency.

RESULTS

The first step in the experimental program was to perform a complete instantaneous thermal performance test for both collectors. The results are shown in Figure 3. In this figure the efficiency, η_i ,

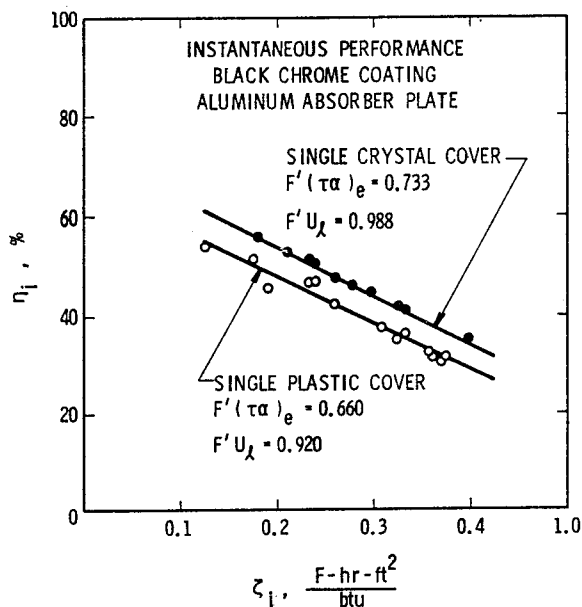


Figure 3. Instantaneous Thermal Efficiency as a Function of Operating Conditions

η_i is plotted versus the operating parameter, ζ_i . The solid points are for the crystal cover collector, and the open points are for the plastic cover collector. The intercept, $F'(\tau\alpha)_e$, and the slope, $F'U_\lambda$, for each collector are

$$F'(\tau\alpha)_e = 0.733$$

and $F'U_\lambda = 0.988$

for the crystal cover collector, and

$$F'(\tau\alpha)_e = 0.660$$

and $F'U_\lambda = 0.920$

for the plastic cover collector.

The next step in the experimental program was to perform the all-day efficiency tests. A summary of the conditions and results for these tests is shown in Table II. Variations in R_I and R_T are shown, where the average values are

$$R_I = 0.823$$

and $R_T = 0.534$.

The length of the collection period and the length of the solar day are both rounded to 15-minute

periods because that was the length of the integration period. An example of clear day operation is shown in Figure 4, while a partly cloudy day is shown in Figure 5. These results are plotted in Figure 6 as the collection period efficiency, η_{cp} , versus the collection period operating parameter, ζ_{cp} . The curves included in this plot have the same slope and intercept as those for the instantaneous test results. It can be seen that these curves provide an excellent fit to the data, even though a fair amount of scatter is present in the experimental data due to variations in different weather

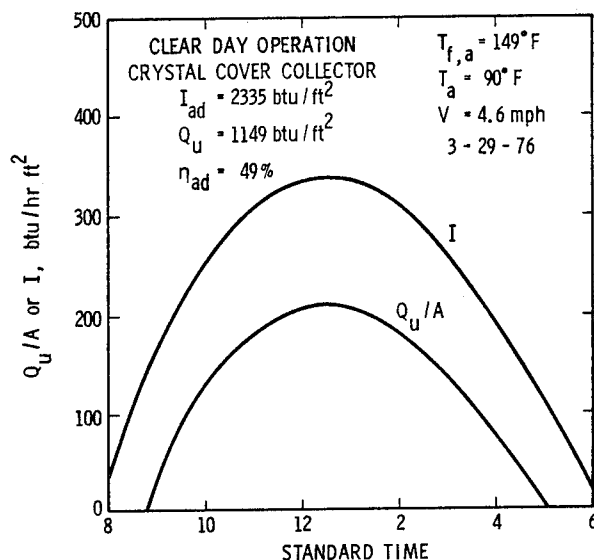


Figure 4. Clear Day Collector Operation

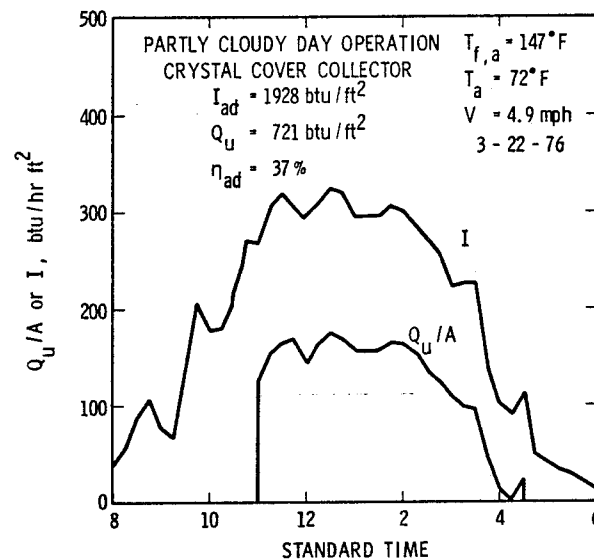


Figure 5. Partly Cloudy Day Operation

Table II. Test Conditions and Results

Date	T _{f,a} (°F)	T _a (°F)	I _{cp} (Btu/ft ²)	I _{ad} (Btu/ft ²)	T _{cp} (hrs)	T _{ad} (hrs)	R _I	R _T	Crystal Cover Q _u /A (Btu/ft ²)	Plastic Cover Q _u /A (Btu/ft ²)
3-17-76	145	67	2183	2443	8.00	11.75	.894	.681	957	874
3-19-76	150	85	887	1254	4.50	11.75	.707	.383	403	345
3-22-76	147	72	1462	1928	5.75	11.75	.759	.489	711	649
3-24-76	140	78	1137	1281	6.25	11.75	.888	.532	439	362
3-25-76	143	82	549	1020	3.25	11.75	.538	.277	190	160
3-26-76	147	86	918	1287	4.00	11.75	.713	.340	458	387
3-29-76	149	90	2166	2335	8.25	11.75	.928	.702	1149	1002
5-12-76	142	82	1309	1488	6.50	13.25	.880	.491	582	471
5-13-76	144	78	1300	1475	6.75	13.25	.881	.509	559	404
5-14-76	145	79	2167	2334	9.00	13.25	.928	.679	1006	816
5-17-76	142	82	1192	1684	5.75	13.25	.728	.434	559	506
5-18-76	144	77	2075	2287	8.75	13.25	.907	.660	966	876
5-27-76	186	82	2271	2615	8.25	13.50	.869	.611	707	586
5-28-76	185	82	2162	2494	8.25	13.50	.867	.611	705	601
5-29-76	184	84	2090	2443	8.00	13.50	.855	.593	650	542
5-31-76	185	89	1126	1533	5.00	13.50	.735	.370	339	263
6-2-76	187	85	1721	1995	8.25	13.50	.863	.611	460	402
6-3-76	188	88	1959	2234	8.50	13.50	.877	.630	613	507
Avg.							.823	.534		

conditions. Figure 7 shows a plot of the all-day efficiency, η_{ad} , versus the all-day operating parameter, ζ_{ad} . The intercept of the curves is equal to the intercept of the collection period perfor-

od. Since this was the case, then both R_I and R_T would be expected to be constant, and they are.

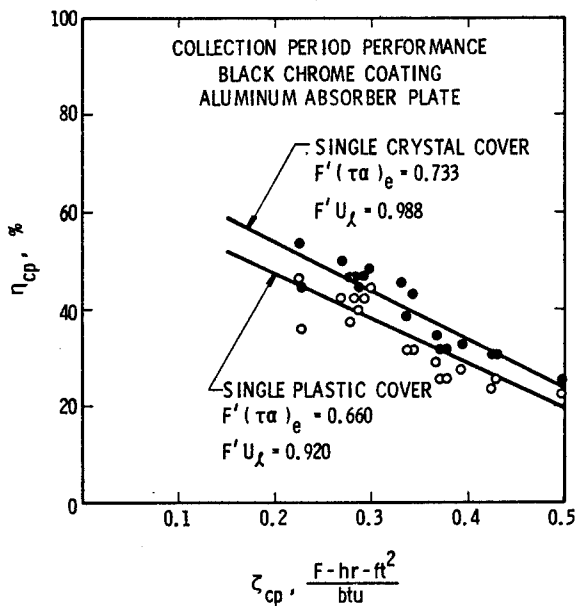


Figure 6. Collection Period Efficiency as a Function of Operating Conditions

mance curve, $F'(\tau\alpha)_e$, times the ratio of solar radiation available during the collection period to the daily total solar radiation, R_I , as determined from the experimental values listed in Table II. The slope of the curves is equal to the slope of the collection period performance curve, $F'U_L$, times the ratio of the length of the collection period to the length of the solar day, R_T , as determined from the experimental values listed in Table II.

It appears from these experimental results that collectors of similar construction and thermal capacitance begin positive collection as well as end positive collection within the same 15-minute peri-

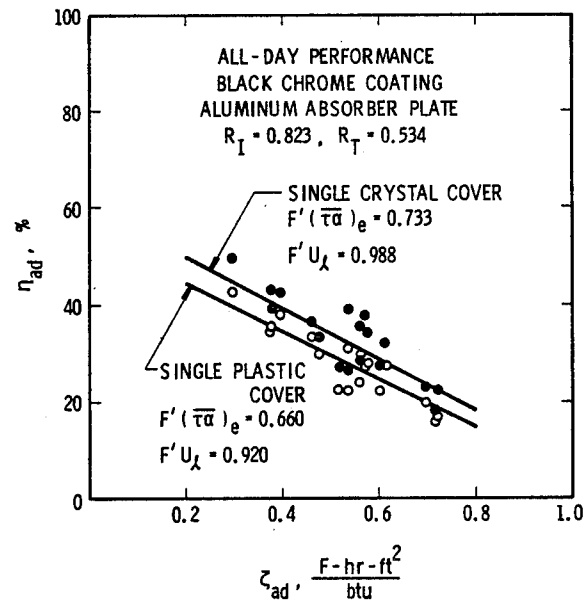


Figure 7. All-Day Efficiency as a Function of Operating Conditions

CONCLUSIONS

The major conclusion of this study is that there is a definite correlation between instantaneous thermal performance, as determined by either a standard NBSIR 74-635 test or an ASHRAE 93-77 test, and all-day thermal performance. This correlation was derived for two similar collector units, but needs to be tested for the general class of flat-plate solar collectors. While the parameters R_I and R_T were found to be constant for this study, it is anticipated that for a collector of significantly different construction, the collection period may be longer or shorter than what was determined here.

Once it is possible to independently determine R_I and R_T , then the only performance testing required will be the present instantaneous methods, as outlined in either NBSIR 74-635 or ASHRAE 93-77.

SPECULAR REFLECTANCE LOSS OF SOLAR MIRRORS DUE TO DUST ACCUMULATION*

By: R. B. Pettit, J. M. Freese, D. E. Arvizu
Sandia Laboratories, Albuquerque, New Mexico 87185

ABSTRACT

The specular reflectance properties of silvered glass mirrors have been studied after the mirrors experienced five weeks of outdoor exposure in Albuquerque, NM. The reflected beam profile from angular apertures of 3 to 15 mrad was determined from 400 to 900 nm using a bi-directional reflectometer. It was found that the main effect of the accumulated dust particles is to decrease the intensity of the specular beam while maintaining the same beam profile. At 500 nm, measured specular reflectance losses ranged from 6.5 to 24%. The diffuse reflectance outside an approximate 170 mrad cone around the specular direction was also measured from 320 to 2500 nm using an integrating sphere reflectometer. As expected, the reflectance losses determined from the two measurements were not in agreement. However, when properly normalized, the wavelength dependences of the reflectance loss determined by both measurements were identical for all areas measured. Thus it is possible to calculate the solar-averaged specular reflectance loss from a single measurement at 500 nm. For the silvered glass mirrors studied, the solar-averaged specular reflectance loss is equal to 0.78 ± 0.04 times the specular reflectance loss measured at 500 nm.

INTRODUCTION

Dust accumulation on solar mirror materials during outdoor exposure can reduce the specular reflectance values by up to ~25% in relatively short exposures.^{1,2} Therefore an understanding of the effect of accumulated dust on the optical properties of reflectors is important. Since the size of available dust particles is comparable to the wavelength of solar radiation,^{1,3} the specular reflectance properties after outdoor exposure would be expected to be wavelength-dependent. In this paper, the specular reflectance properties of silvered glass mirrors were determined as a function of wavelength after the mirrors experienced five weeks of outdoor exposure in Albuquerque, NM.

There are several reasons for studying the wavelength behavior of the specular reflectance properties with dust accumulation. First, the present bi-directional reflectometer, which is used to measure the reflected beam profile, is limited to a wavelength range from 400 to 900 nm, which covers only 63% of the solar spectrum.⁴ A substantial wavelength dependence in the reflectance properties could result in a large error in estimating the solar-averaged specular reflectance properties. Therefore the bi-directional results were compared to the diffuse reflectance properties measured

from 320 to 2500 nm (over 98.5% of the solar spectrum) using an integrating sphere reflectometer. Secondly, it would be very advantageous if the wavelength dependence in the reflectance properties was independent of the amount of dust accumulation on the mirror surface. Then a specular reflectance value at one wavelength would be sufficient to predict the values at all other wavelengths. This would substantially reduce the number of measurements required to characterize the specular reflectance properties of these mirrors after outdoor exposure. Finally, there is considerable interest in developing a portable bi-directional reflectometer for specular reflectance measurements on large mirror surfaces in the field. A universal wavelength dependence for the specular reflectance properties with dust accumulation allows this instrument to be limited to the measurement of the specular reflectance at a single wavelength.

EXPERIMENTAL TECHNIQUE

The mirror samples used in this study are second-surface, silvered, float glass which is 3 mm thick. The silvered glass panel has been laminated to a matching 3 mm thick float glass panel.⁵ These mirrors are currently being used in the 5 MW Solar Thermal Test Facility located in Albuquerque, NM.⁵ Test samples were mounted outdoors next to the heliostats at the Test Facility between July 21, 1977, and August 29, 1977. The results presented here are not necessarily indicative of the average reflectance properties expected after five weeks outdoor exposure. Instead, areas were selected for measurement that were relatively clean and very dirty in order to cover as wide a range of dust accumulation as possible. More detailed experiments in progress are designed to determine dust accumulation rates and the effect of weather conditions, sample orientation and cleaning technique on the specular reflectance properties.

The specular reflectance properties at wavelengths of 400, 500, 600, 700, 800 and 900 nm were measured for angular apertures from 3-15 mrad using a bi-directional reflectometer. The operation and data analysis procedure developed for these measurements have been previously described.⁶ The measurement beam diameter was 13 mm and the incident angle was 20° from normal.

It was very difficult to obtain consistent reflectance data as a function of wavelength since the sample must be removed from the mounting platform in order to recalibrate the reflectometer. Because the dust accumulation is nonuniform, slight changes in

* Supported by U.S. Department of Energy.

sample position can either increase or decrease the specular reflectance by several percent. Therefore great care was taken in mounting the mirrors for this study. In addition, it was found that even when clean, there were slight ($\sim 1\%$) variations in the reflectance properties of the areas measured. This was probably due to variations in the silvering process and/or the glass itself. Therefore it was essential, for the most accurate results, to compare the reflectance values measured before and after exposure for the same area.

The absolute accuracy of the specular reflectance values at each angular aperture is $\pm 1\%$. However, the primary interest in this study is the reflectance change after outdoor exposure. The error in the specular reflectance loss data, due to sample mounting problems and the reproducibility of the reflectometer, should be better than ± 0.006 reflectance units. Thus for small reflectance loss values, the percent error can be quite large.

The hemispherical reflectance properties from 320 to 2500 nm were measured with an integrating sphere reflectometer.⁷ The reflectance values were referenced to a specular reflectance standard calibrated by the National Bureau of Standards to $\pm 0.5\%$.

In addition, the diffuse reflectance of each sample was measured using the same integrating sphere reflectometer with the measurement geometry shown in Figure 1. The incident radiation is normal to the sample so that the specular component is reflected back out the entrance aperture in the sphere wall. The angular size of this aperture, as seen by the sample, is approximately 170 mrad. Thus the diffuse reflectance in this case is defined as all radiation reflected outside an approximate 170 mrad cone centered around the specular direction. For a perfect mirror, and for the clean mirrors assessed in this study, the diffuse reflectance is zero. The incident beam size was approximately 10 x 13 mm.

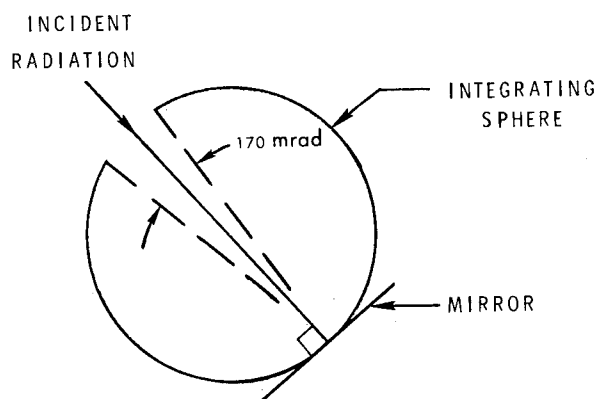


Fig. 1. Measurement geometry for determining diffuse reflectance using integrating sphere reflectometer.

It should be noted that measurements over the complete solar spectrum involve changing detectors so that the sample must be remounted once. This can lead to the same sample positioning problems as with the bi-directional reflectometer. However, since the wavelength range of the detectors overlap, the data were adjusted to coincide in the overlap region. Otherwise, the identical sample location was measured at all wavelengths.

RESULTS

The hemispherical reflectance properties of the silvered glass mirror from 320 to 2500 nm are shown in Figure 2. The large dip in reflectance at ~ 1000 nm results from absorption in the glass by iron impurities in the Fe^{+2} oxidization state.⁸ Because of this absorption, the solar-averaged reflectance is only 82%, which is much less than the value of 96% which can be obtained in very thin glass or glass with no absorption.⁸

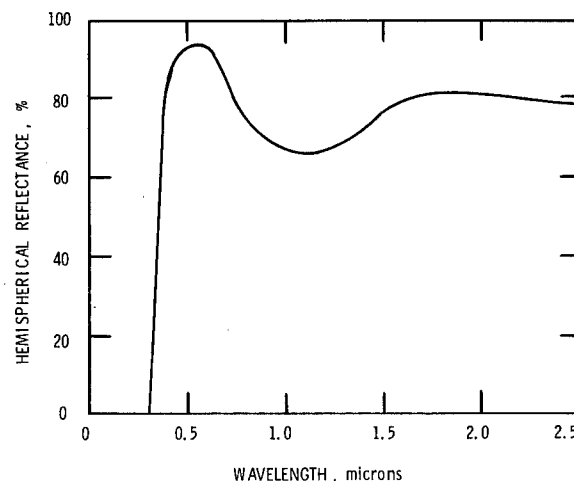


Fig. 2. Hemispherical reflectance as a function of wavelength for the silvered glass mirrors used in this study.

The specular reflectance properties at 500 nm as a function of angular aperture are shown in Figure 3 for a variety of locations on several mirrors. The data below ~ 3 mrad can vary slightly due to non-parallel surfaces in the glass mirror or alignment and focusing adjustments in the bi-directional reflectometer. Therefore data below 3 mrad have been omitted. The upper curve in the figure corresponds to a clean mirror. The difference between the specular reflectance at 15 mrad and 3 mrad is less than 0.2%. The lower curves correspond to areas with various amounts of dust accumulation. A difference is seen between the specular reflectance at 15 mrad and 3 mrad that increases slowly as the specular reflectance decreases. Thus when the specular reflectance at 15 mrad has decreased by $14\frac{1}{2}\%$ over that of the clean mirror, the difference between the specular reflectance at 15 mrad and 3 mrad is 1.8%.

At 900 nm, the difference for the same curve is only 0.8%. Thus the main effect of the dust is to reduce the intensity of the specular beam while maintaining approximately the same beam profile. This has also been observed for other mirror materials.¹ The slight slope in the specular reflectance properties for losses greater than ~10% is being studied and correlated with the dust accumulation. As noted above, the slope is less at longer wavelengths.

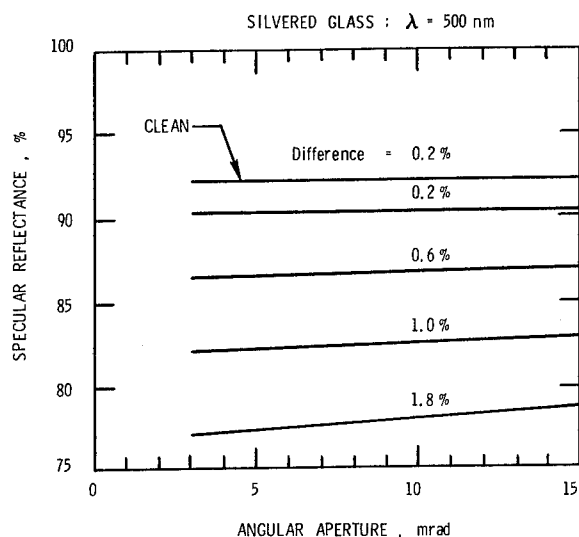


Fig. 3. Specular reflectance at 500 nm as a function of angular aperture for a clean mirror (upper curve) and after dust accumulation (lower curves). Values listed are the difference between the specular reflectance at 15 mrad and 3 mrad.

After cleaning the samples, the specular reflectance values were equal to the values before exposure. Therefore all changes in the specular reflectance can be directly related to the accumulated dust particles on the exposed upper glass surface.

The specular reflectance values at 15 mrad are shown in Figure 4 as a function of wavelength for several sample locations. At 500 nm, the specular reflectance loss varied from 6.5 to 24%. The loss decreased with increasing wavelength, so that at 900 nm the values ranged from 3.8 to 14%. The hemispherical reflectance values (which include both the specular and diffuse components) from the same areas were essentially identical to the hemispherical reflectance values before exposure. Therefore the effect of the dust on reflectance properties is to scatter some of the reflected radiation out to large angles, thereby decreasing the intensity of the specular beam.

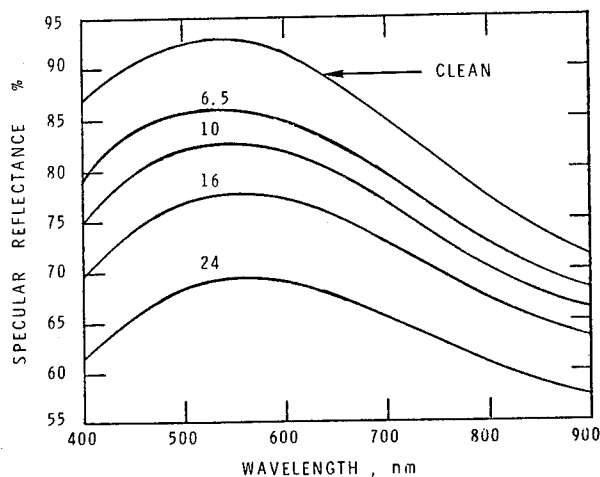


Fig. 4. Specular reflectance at 15 mrad as a function of wavelength for a clean mirror (upper curve) and after dust accumulation (lower curves) for several sample locations. Values listed are the reflectance loss at 500 nm due to dust accumulation

The diffuse reflectance values from the same areas used in Figure 4 are shown in Figure 5 as a function of wavelength from 320 to 2500 nm. As expected, the diffuse reflectance and the specular reflectance loss measured with the bi-directional reflectometer were not in agreement because of the differing incident beam sizes, collection apertures and area locations. However, if the specular reflectance loss values and the diffuse reflectance are normalized by their values at 500 nm, then the wavelength dependence of the reflectance loss determined from each measurement was identical within experimental error. Thus the integrating sphere reflectometer can be used to accurately and easily determine the relative wavelength dependence of the reflectance loss due to dust accumulation over the complete solar spectrum while the reflectance loss at 500 nm measured with the bi-directional reflectometer is used to quantify those data.

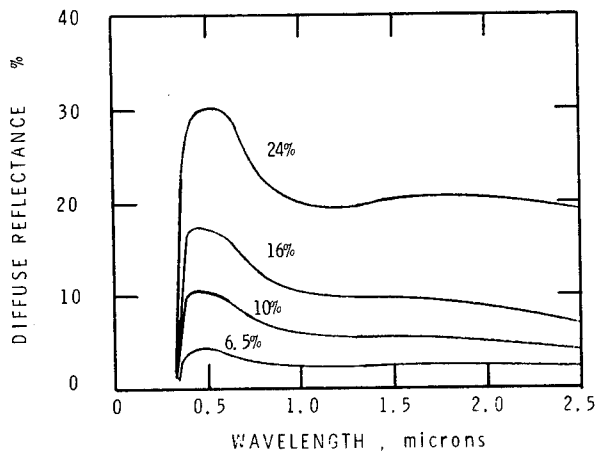


Fig. 5. Diffuse reflectance as a function of wavelength for the same areas shown in Fig. 4. Numbers identify the same curves.

When the normalized data from all areas were compared, it was found that the reflectance loss values had the same wavelength dependence within experimental errors. The results are shown in Figure 6. The HIGH and LOW curves in Figure 6 represent the maximum and minimum normalized loss values respectively from all areas measured. Generally areas with low reflectance loss values at 500 nm (~ 6 -10%) were closer to the HIGH curve in Figure 6, while areas with a large reflectance loss at 500 nm ($\sim 20\%$) were closer to the LOW curve. However, these variations are within the accuracy of the data. Note that in some cases the reflectance loss at wavelengths below 500 nm is greater than the loss at 500 nm. Thus the loss at 500 nm is not necessarily a maximum.

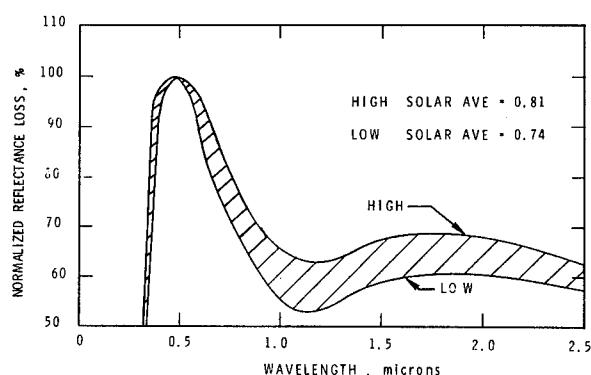


Fig. 6. Specular reflectance loss normalized by the reflectance loss at 500 nm as a function of wavelength for all areas measured. HIGH and LOW curves are described in text.

Because of the similar wavelength dependence for the reflectance loss, it is possible to easily calculate the solar-averaged reflectance loss from a single measurement at 500 nm. The solar-averaged normalized reflectance loss for the range of curves in Figure 6 is equal to 0.78 ± 0.04 . Therefore, for the silvered glass mirrors used in this study, the solar-averaged reflectance loss due to dust accumulation is equal to 0.78 ± 0.04 times the specular reflectance loss measured at 500 nm. For reflectance loss values at 500 nm less than 25%, the maximum range in the solar-averaged reflectance loss resulting from the range of curves shown in Figure 6 is less than $\pm 1\%$. Since specular reflectance losses greater than 25% represent a substantial reduction in focused sunlight in most concentrating collectors, a precision in the reflectance loss of $\pm 1\%$ should be sufficient for most applications.

CONCLUSIONS

The main effect of dust accumulation on the specular reflectance properties of silvered glass mirrors is to decrease the intensity of the specular beam while maintaining the same beam profile. The specular reflectance loss at 15 mrad determined with the bi-directional reflectometer decreases with increasing wavelength. If these results are compared with the diffuse reflectance which is measured with an integrating sphere reflectometer, when normalized by the reflectance loss at 500 nm, the wavelength dependence determined from both measurements was identical. Thus the integrating sphere reflectometer can be used to determine the relative wavelength dependence of the reflectance loss, while the reflectance loss measured at one wavelength with the bi-directional reflectometer can be used to quantify the loss.

In addition, the normalized reflectance loss values from all areas measured had the same wavelength dependence. Thus it is possible to calculate the solar-averaged reflectance loss from a single measurement at 500 nm. For the silvered glass mirrors used in this study, the solar-averaged reflectance loss is equal to the reflectance loss measured at 500 nm multiplied by 0.78 ± 0.04 . These results mean that a portable bi-directional reflectometer that is intended to measure the specular reflectance loss due to dust accumulation on solar mirrors can be limited to a single wavelength.

REFERENCES

1. R. B. Pettit and B. L. Butler, "Mirror Materials and Selective Coatings," Sandia Laboratories Report SAND77-0111 (February 1977), available from National Technical Information Services (NTIS), Springfield, VA 22151.
2. "Preliminary Draft, Central Receiver Solar Thermal Power System Phase I CDRL Item #2, Pilot Plant Preliminary Design Report, Volume 3, Book 2. Collector Subsystem" (May 1977), McDonnell Douglas Report MDC G 6776, Section 6.
3. R. S. Berg, "Heliostat Dust Buildup and Cleaning Studies," Sandia Laboratories Report SAND78-0510 (March 1978), available NTIS, Springfield, VA 22151.
4. M. T. Thekaekara, "Survey of Quantitative Data on Solar Energy and Its Spectral Distribution," Proceedings of Conference COMPILES (Cooperation Mediterranienne Sur l'Energie Solaire) Dahrhan, Saudi Arabia (November 1975).
5. "Solar Thermal Test Facility Experiment Manual," Sandia Laboratories Report Sand77-1173 (October 1977), Chapter 3,

Available from NTIS, Springfield, VA
22151.

6. R. B. Pettit, "Characterization of the Reflected Beam Profile of Solar Mirror Materials," Solar Energy 19, 733 (1977).
7. D. K. Edwards, et al., "Integrating Sphere for Imperfectly Diffuse Samples," J. Opt. Soc. Amer. 51, 1279 (1961), and Beckman Instructions 1220-B (1962).
8. See H. Taketani and W. M. Arden, "Mirrors for Solar Energy Applications," Proceedings of the 1977 Annual Meeting American Section of ISES (June 6-19, 1977), Orlando, FL, Volume ONE, pp. 5-15 to 5-19, and J. Vitko, "Optical Studies of Second Surface Mirrors Proposed for Use in Solar Heliostats," Sandia Laboratories Report SAND78-8228 (April 1978).

HELIOSTAT REFLECTIVITY VARIATIONS DUE TO DUST BUILDUP UNDER DESERT CONDITIONS
By: J. B. Blackmon, Ph.D. and M. Curcija, McDonnell Douglas Astronautics Company

Dr. Blackmon is a Senior Engineer Scientist in the Solar Central Receiver Energy Program. M. Curcija is an Associate Engineer Scientist in the Vehicle, Energy, and Biotechnology Department.

ABSTRACT

A series of tests were conducted of heliostat and mirror reflectance variations in a desert environment. Factors investigated included weather, site location, mirror type, and stowage position. Reflectivity variation data are presented for full-scale heliostats and sixty mirror specimens. Reflectance monitoring was conducted on heliostats and mirror specimens located at the Naval Weapons Center, China Lake, California, and on mirror specimens located at Sandia Laboratories, Albuquerque, New Mexico. Heliostats were monitored with two types of reflective surface: second surface silvered laminated glass and first surface silvered glass with an experimental acrylic protective coating. Specimens of different mirror types were mounted on racks providing five stowage positions: continuous face-up, continuous face-down, face-up in daytime and face-down at night, face-up in daytime and near-vertical at night, and face-up in daytime to face-down at night or during heavy cloud cover (controlled by a sun sensor). A method of obtaining reflectivity data on heliostats and specimens under field conditions is presented. Reflectivity degradation rates are determined for different stowage positions and compared with weather conditions. Time-averaged reflectivity values are determined. Natural cleaning effectiveness of rain, snow, or frost is presented. Heliostat operational procedures which appear to decrease reflectivity losses due to dust buildup are described.

INTRODUCTION

Major operations and maintenance considerations for solar energy collector systems are the reflectivity and transmissivity losses due to dust buildup, the associated cleaning frequency, and effects of various weather conditions on the dust buildup rates. For the central receiver solar thermal power system with its field of heliostats, these problems are of additional concern because of the implications of design criteria on the heliostat stowage position as well as the operational aspects for stowage at night or during inclement weather. Design requirements on heliostat stowage position depend in part on the possible decrease of reflectivity degradation rates by having a nightly inverted stow (reflector face-down) position or a near-vertical stow position, compared to the face-up position. Considerations of concern to future plant operators are the preferred stowage positions as a function of the weather conditions, the effectiveness of natural cleaning (rain, condensation, snow, frost, and ice), and the maintenance cleaning frequency.

The objectives of this test program were to: (1) obtain preliminary data on reflectivity variations at two desert locations with such variables as weather, mirror type, and stowage position, (2) evaluate the effectiveness of natural cleaning, and

(3) develop a practical field technique for obtaining site specific data on reflectivity variations. One aspect of particular interest was the possible existence of maximum or "equilibrium" dust buildup reflectivity loss.

The approach taken was to install one exposure fixture at the Sandia Laboratories, Albuquerque, New Mexico and one at the Naval Weapons Center, China Lake, California. Each exposure fixture had five racks with different stowage positions and different types of reflectors. Data on reflectivity were taken as frequently as practical, considering the scope of the program and weather conditions. The specimens at the NWC site were near an array of six heliostats so that direct comparisons could be made with actual, full size heliostats.

Results obtained to date support the conclusions that: (1) heliostat dust buildup rates are strongly dependent on stowage position, (2) variations in these rates are high, (3) natural cleaning can be highly effective, (4) losses of the order of 20 to 40 percent are seen if there is no cleaning, and (5) specimen buildup rates are comparable to full scale heliostat buildup rates. Data obtained suggest a number of ways of minimizing the dust buildup rates and hence washing frequency. It should be noted that the detailed surface chemistry and dust composition are not considered in this discussion, and that the overall soiling effect of particles, films, salts, etc., is loosely referred to as a "dust buildup."

SITE SELECTION

Site selection was dictated primarily by two factors: frequency of occurrence of certain meteorological conditions, and test support capability. Meteorological conditions expected to have bearing on the dust buildup rate were compared to select two sites representative of the extremes of interest. Table I summarizes these data for locations having the requisite test support capability. The Naval Weapons Center, China Lake, California has the least amount of thunderstorms, rain/drizzle, snow/sleet/freezing rain, and fog, and has low blowing dust/sand. Albuquerque has the highest frequency of occurrence of these conditions, and the same degree of blowing dust/sand. In view of the practical aspects of test site security, surveillance, monthly weather data and test support obtainable at both NWC and Sandia, it was fortuitous that these sites exhibited the extremes in averaged meteorological phenomena. The NWC site was used for heliostat array tests, and therefore, the location of one of the racks at this site allowed direct comparisons between specimens and heliostats to be made. Similar comparisons could be made with the Sandia heliostats and collectors.

The heliostat array at NWC is shown in Figure 1. Four octagonal noninverting heliostats and one inverting heliostat are positioned in a manner that simulates a portion of an actual central receiver field north of its tower mounted receiver. Three of the octagonal heliostats have acrylic first surface mirrors and are the noninverting, eight-petal design, normally stowed horizontally, face-up. A fourth

Table 1
METEOROLOGICAL SUMMARY

Station	Location	Elevation	Mean Percentage of Days Per Month For Occurrence of Various Meteorological Phenomena, From Daily Observations					Years of Observation
			Thunder-Storms	Rain/Drizzle	Snow/Sleet/Freezing Rain	Fog	Dust/Sand	
Naval Weapons Center	Indian Wells Valley, CA	760M	0.9	9.6	0.5	0.7	1.2	20
Edwards Air Force Base	Western Mojave Desert Near Mojave	770M	1.2	9.6	0.9	1.9	1.6	19
George Air Force Base	Western Mojave Desert Near Victorville	960M	1.7	10.1	1.4	2.3	1.0	18
Kirtland Air Force Base	Albuquerque, NM	1780M	10.2	22.9	6.9	2.7	1.2	26

NOTE:

Data compiled from Aerospace tapes.

Blowing dust/sand reported only when visibility is less than 1 km.

Heliostat Array Test Site located at Randsburg Wash, elevation 650M

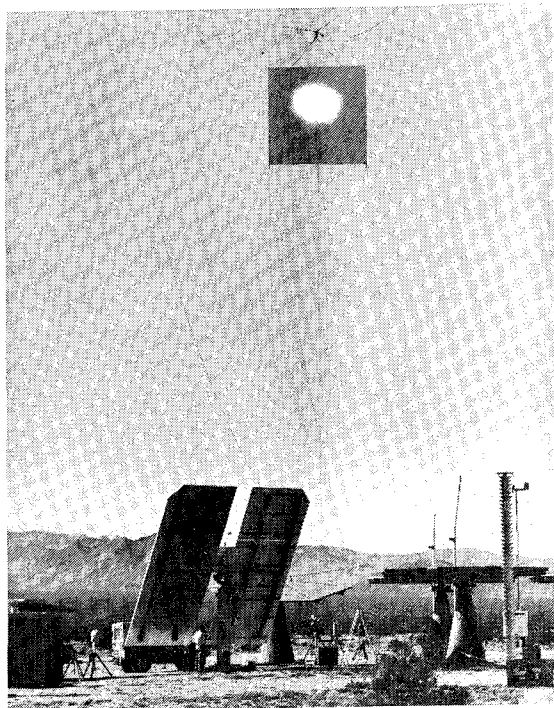


Figure 1. Heliostat Array Test Site, Randsburg Washington Naval Weapons Center.

noninverting emplaced heliostat has a laminate glass second surface mirror. The fifth is the inverted stow laminate glass heliostat. These heliostats are designated H1, H2, H3, and H4, and IH-1, respectively. A fifth noninverting laminate heliostat, mounted on a trailer 1,100 feet northeast of the target was exposed, but not washed for six months to determine maximum reflectance loss. The reflective area of each heliostat is approximately 400 square feet.

TEST EQUIPMENT

Figures 2 and 3 illustrate the dust buildup fixture. The test apparatus consists of the fixture containing five racks for mounting samples. The racks are supported about 12 feet above the ground by a truss structure.

Five exposure orientations are provided by racks: (1) continuous face-up, (2) continuous face-down, (3) face-up in daytime to face-down at night on an astronomical timer, (4) face-up in daytime to vertical at night on an astronomical timer, and (5) face-up in daytime to face-down at night on a sun presence photo cell. Up to twelve samples of mirrors under each stowage condition are tested at each location.

Primary samples include Sheldahl first surface silver, acrylic protective coating mirrors, ASG laminate glass mirrors and second surface, low iron content glass mirrors. Two 5" x 5" samples of each mirror type in each orientation are provided, where feasible, to simultaneously gather data on effects of cleaning frequency and equilibrium dust buildup.

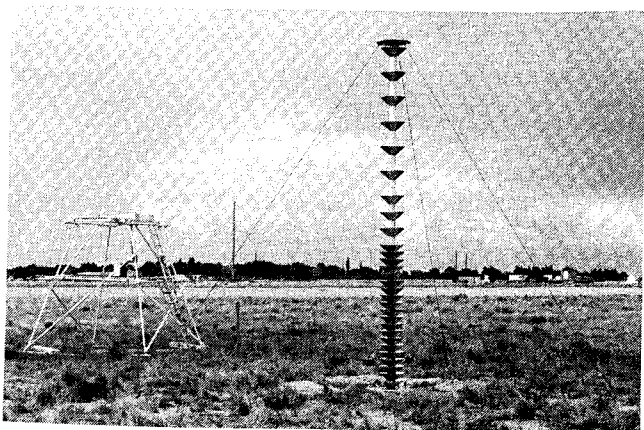


Figure 2. Exposure Fixture - Sandia Laboratories, Albuquerque, N.M.

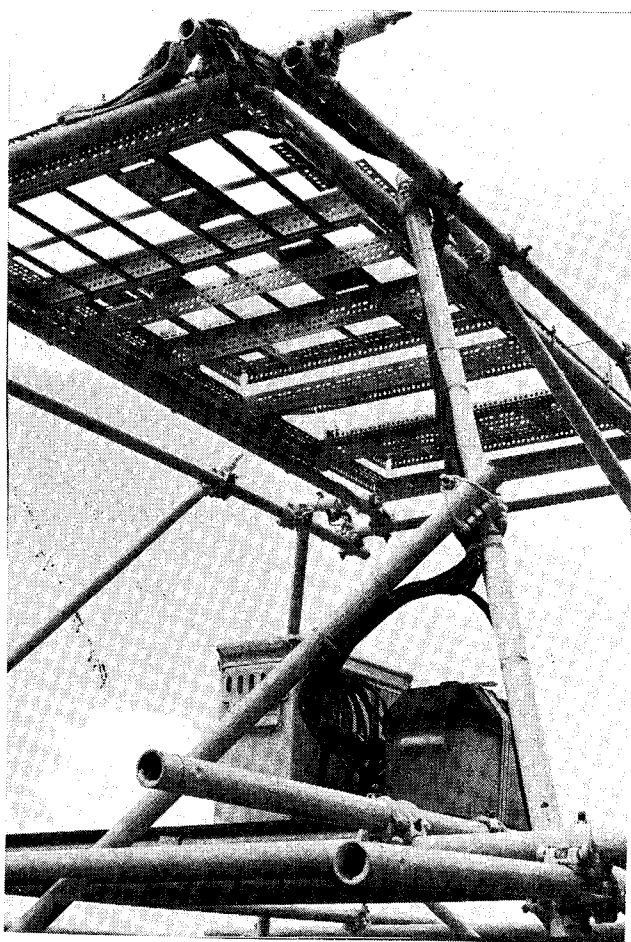


Figure 3. Exposure Rack.

The three movable racks are controlled by DC motors, and limit switches. The two racks operating off of the astronomical timer are connected by a chain and sprocket such that one rack is either face-up or face-down, while the other is face-up or near-vertical ($\sim 20^\circ$). The third movable rack is controlled by a sun sensor, adjusted such that the rack turns face-up at dawn and face-down at sundown on a clear day, and turns or remains face-down under overcast conditions which accompany heavy rains.

REFLECTIVITY MEASUREMENT TECHNIQUE

Since there is currently no suitable portable reflectivity instrument, a relatively practical technique for obtaining data in the field was devised using Eppley pyrheliometers. Eppley normal incidence pyrheliometers (N.I.P.) have a 5.8° (100 mr) included cone angle aperture. Since light reflected from a heliostat at a cone angle greater than approximately 1° would miss the receiver, data were taken with the Eppleys modified by an extender tube which provided a 1° aperture. Two techniques were used to obtain field reflectivity data. The first technique used one modified Eppley N.I.P. which was aligned to view the sun, a reading taken, then turned to view the reflected image of the sun in the mirror of heliostat, and the second reading taken. The ratio gave the net reflectivity. The second method used two modified Eppleys and one 5.8° N.I.P. One modified Eppley tracking the sun would be used for continuous readings while the other two would be used for readings of the reflected image. In both cases, the movement of the reflected beam is sufficiently slow that multiple measurements can be taken with a standard data logger. Variations of this technique were used, such as placing the mirror specimen on a tracking heliostat, and measuring the tracking heliostat directly. Heliostat tracking was maintained to within 0.25 to 0.5 milliradian. Calibration coefficients were verified by pointing all three at the sun simultaneously, recording the readings and comparing. Normally, these readings agreed to within 0.3 percent on bright, clear days. A variation in reflectivity for a single reading observed by either of these techniques can be due to the variable degree of dust buildup on the surface or the surface waviness. Therefore, measurements were made to evaluate these effects.

Multiple measurements were made at a convenient spot on the heliostats, care being taken to avoid bird droppings and other nontypical, heavily soiled areas such as the edges. Measurements were also made at several additional spots (approximately 1-3 feet apart) to determine the variation in reflectivity over the surface. Measurements made at six different locations on the bottom segment of each of the three acrylic surface heliostats showed a standard deviation of reflectivity of ± 2.5 percent; the glass mirror normally had approximately ± 1 percent standard deviation, but greater variations have been observed. Measurements could not be made with the available equipment on the upper portions of the heliostat, and therefore, greater reflectivity variations may be present, but not measured. For example, heliostat H2 has three visually noticeable swaths of what appears to be a permanent "staining" that is darker than the lower part of the heliostat, where measurements were made with the pyrheliometers. These variations suggest that total power received relative to the reflectivity value at one point may differ by several percent, for both the glass and acrylic heliostats, and a means of measuring the total power from a soiled heliostat is necessary. However, the visual uniformity of dust for the majority of the heliostat area, coupled with the relatively low deviation in the reflectivity as a function of position suggests that isolated measurements are adequate to meet the objectives of this program.

Nonuniformity of the reflected beam from certain types of reflectors has produced a much higher variation in the measured reflectivity than dust thickness variations. The surface waviness effects observed include striations, as sometimes occurs with float glass, concave/convex surface deformations, deformations due to glass bonding to various substrates, and nonuniform protective film layers. In some cases, these nonuniformities were so severe that the specimens could not be used to obtain consistent reflectivity measurements. In one case, full size heliostat panels reflected the light in such a nonuniform pattern that the reflectivity varied from 67 to 116 percent for the Eppley 1-3 feet from the panel, with measurement locations on one of the panels only a few inches apart. In other cases, the specimens gave unrealistically high values for reflectivity, as with a few of the ASG laminate glass specimens, due to a slight focussing effect, but were sufficiently constant when clean to be used to obtain relative degradation rates.

In order to obtain a representative reflectivity value for a soiled reflector, an area of the order of 1-6 inches in diameter must be measured, as a minimum, or multiple measurements made with small beams. This requirement results from the degree of nonuniformity observed visually for typical soiled surfaces. Often, the variations are due to droplet condensation, rivulets of water running off of the surface, etc., which make a "spotty" appearance of the order of 0.25 inch diameter or alternating heavily and lightly soiled regions of the order of .5 to 1 inch variation. Therefore, we normally positioned the Eppley approximately four feet from the heliostats and 2-3 feet from the specimens.

With specimens exhibiting a moderate focussing or defocussing effect (± 5 -10 percent) it was practical to measure these in the same manner each time. Confidence in this technique was gained by comparing measurements for the clean specimens, which showed

variations of two percent maximum in nearly all cases; since the ability to clean is probably of the order of two percent for most techniques used to simulate actual field washing, and since this variation is smaller than the usually observed degradation of approximately 10 percent, the nonuniformity due to specimen curvature was accepted in some cases. For large panels of glass, the degree of nonuniformity has been observed to be severe in some cases, and therefore, a technique was verified which allows these curvature induced reflectivity variations to be accommodated. Figure 4 shows a pattern from an unbonded low iron float glass mirror at a distance of approximately 30 feet. The alternating light/dark patterns illustrate that single reflectivity measurements made with an Eppley are subject to significant error. However, by making a series of measurements over a given region, it is possible to obtain a mean

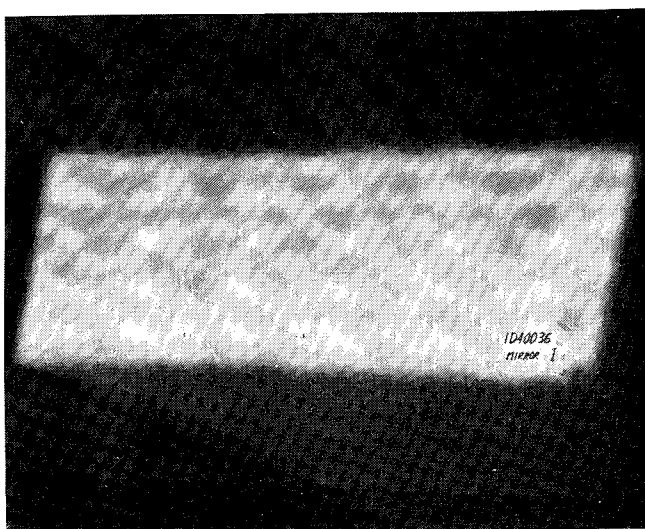


Figure 4. Reflected Image from Glass Mirror Panel

Table 2

REFLECTOR PANEL PERFORMANCE DATA

Specimen	Reflectivity Measurements			Reflectivity Measurements (%) with 17.5 mr Eppley Pyrheliometer (Mean + Standard Deviation of 100 Measurements)			
	Solar Spectrum, π R, Beckman %	Solar Spectrum, Specular Spectro- photometer, %					
		<u>4 mr</u>	<u>8 mr</u>	<u>16 mr</u>	<u>9 feet</u>	<u>18 feet</u>	<u>27 feet</u>
Low Iron Float S/N 30					87.8 ± 3.1	87.54 ± 6.7	86.7 ± 8.5
Low Iron Float S/N 31	92	82	88.7	89.7	88.1 ± 3.5	87.7 ± 4.7	86.9 ± 6
Laminate #1 (PPG Low Iron)					88.0 ± 2.5	90.7 ± 3.0	87.7 ± 2.9
Reflectivity = 87.9 ± 1.15 for all measurements							

value for the reflectivity which compares well with laboratory measurements. Table 2 shows a comparison of a series of measurements made on glass panels. An area of approximately 1' x 2' is measured with 10 measurements made vertically for 10 columns, or 100 measurements altogether, for a given distance from the mirror. The distance is then varied, and another set of 100 measurements taken. The mean and standard deviation of the reflectivities are then compared. From Table 2 it is seen that mean reflectivities are in agreement with laboratory measurements to within two percent, and that the standard deviation illustrates the degree of nonuniformity of the reflectance. We have found that these measurements can be made at a rate of better than one per 3-5 seconds by two technicians.

WASHING TECHNIQUE

The procedure for cleaning the heliostat by washing and rinsing the reflective surface was as follows:

1. A reflectance measurement of the reflective surface was taken immediately prior to washing.
2. Each reflector was positioned near vertical, approximately 70°, in a manner which avoided excessive irradiation of the surroundings.
3. The reflector was rotated so that it faced the direction of Northeast for early morning washing, North for mid-day washing, and Northeast for afternoon washing. This orientation minimized spotting of the surface due to drying of the wash solution and minimized glare.
4. The entire reflective surface was sprayed with a washing solution (see Figure 5).



Figure 5. Application of Wash Solution

5. At the end of the specified soak time for the washing solution (approximately one minute), the reflective surface was rinsed thoroughly with deionized water (see Figure 6).
6. A reflective measurement of the reflective surface was taken when the surface dried.

Heliostats H3, H4 and IH-1 were washed on 9 December 1976, with reflectivity increased by 9.1, 13.8, and 3.4 percent, respectively. McGean Chemical Co. A69M was used for H3 and CB 120 for H4 and IH-1.

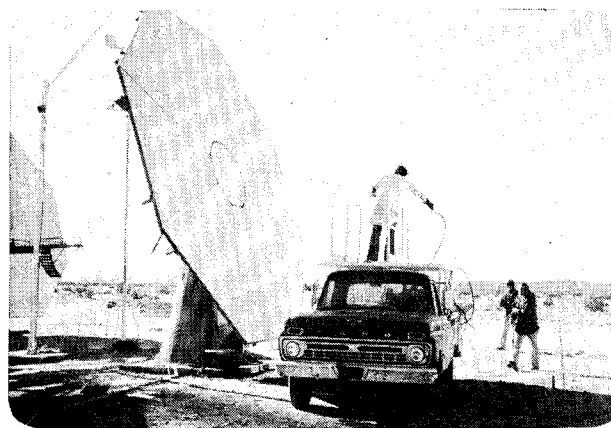


Figure 6. Deionize Water Rinse

Heliostats H1 and H2 (acrylics) were washed on 18 December 1976 with reflectivity increased by 13.5 percent and 5.3 percent, respectively. These heliostats arrived at the site in a soiled condition, and both had been used for tests at Huntington Beach. Both heliostats were washed with McGean Chemical A69M, a chemical cleaning agent shown to be compatible with acrylics.

For the initial wash, relatively large amounts of wash and rinse solution were used to obtain as high an initial reflectivity as considered practically achievable. Results are presented in Table 3. However, these results are not directly applicable to commercial plants, since the amounts used, wash time, etc., are probably not compatible with plant economics.

The five heliostats were washed on 15 March 1977 and reflectivity measurements made before and after. Results are summarized in Table 4. An effort was made to use minimum amounts of wash/rinse solution and to apply the solutions rapidly. For H4, wash solution was applied in one minute, followed by a one-minute dwell time to loosen the accumulated dust, and then deionized water rinse was applied for two minutes.

Based on our experience to date, it is likely that with automated equipment, wash solution can be applied in less than one minute (i.e., 30-45 seconds), followed by a 30-second to one-minute dwell time, and a 30-second to two-minute rinse. It also appears that one gallon of wash solution and five to six gallons of deionized water are minimal quantities. Both washing solutions (A69M and CB 120) are effective, with CB 120 more so. However, the CB 120 contains slight amounts of hydrofluoric acid which may eventually degrade the glass surface. Therefore, CB 120 has been reformulated without the hydrofluoric acid, but has not been found to be as effective. Efforts are still underway to obtain additional suitable cleaning agents and techniques.

RESULTS OF REFLECTIVITY VARIATION MONITORING

Preliminary results are presented below for the effects observed over the last one and one-half years on both heliostats and specimens.

Long Term Exposure

Specimens and heliostats have been exposed for periods ranging from several months to over a year without

Table 3

WASHING EFFECTIVITY RESULTS, 12/9/76 AND 12/17/76

Helio- stat No.	Prewash Reflect- ance	Postwash Reflect- ance	Reflect- ance Increase	Application Time		Solution Quantity		Solution Type		Nozzle Type		Waiting Period
	R1	R2	ΔR	Wash	Rinse	Wash	Rinse	Wash	Rinse	Wash	Rinse	--
	%	%	%	Min	Min	Gal	Gal	--	Water	GPM	GPM	Min
H1	67.78	81.29	13.51	4.07	3.80	5.25	12.50	A69M	D.I.	1	5	1.0
H2	64.89	70.20	5.31	5.98	5.75	6.40	15.00	A69M	D.I.	1	5	6.0
H3	77.25	86.34	9.09	5.50	3.43	9.25	10.50	A69M	D.I.	1	5	15.0
H4	72.07	85.89	13.82	3.92	2.45	6.63	10.25	CB120	D.I.	1	5	5.0
IH1	78.25	81.64	3.39	5.47	3.27	5.25	10.50	CB120	D.I.	1	5	2.0

H3, H4, IH1 washed on 9 December 1976

H1, H2 washed on 17 December 1976

A69-M dilution 1:10

CB 120 dilution 1:20

Table 4

WASHING EFFECTIVITY RESULTS, 3/15/77

Helio- stat No.	Prewash Reflectance	Postwash Reflectance	Reflectance Increase	Application Time		Solution Quantity		Solution Type		Nozzle Type	
	R1	R1	ΔR	Wash	Rinse	Wash	Rinse	Wash	Rinse	Wash	Rinse
	%	%	%	Min	Min	Gal	Gal	--	Water	GPM	GPM
H1	65.88	78.24	12.36	1.0	5.0	1.50	14.00	A69M	D.I.	1	5
H2	56.08	76.50	20.42	1.0	3.7	1.25	8.75	A69M	D.I.	1	5
H3	69.23	87.46	18.23	1.0	3.0	0.75	8.0	A69M	D.I.	1	5
H4	73.31	87.65	10.69	1.0	2.0	1.25	5.75	CB120	D.I.	1	5
IH1	76.80	86.5	8.30	1.4	2.8	1.60	7.75	CB120	D.I.	1	5
IH1'	72.16*	86.60	14.44								

Waiting period between wash and rinse = 1 minute

IH1' = 3/32 in. float glass (foam core)

IH1 = 1/4 in. float glass (laminated)

H4 = Laminated glass

H1, H2, H3 - Acrylic coating

*Reflectivity of IH1' as received from
plant following fabrication

washing to observe the reflectivity degradation. During this period, the surfaces have been exposed to a variety of weather conditions including rain, snow, frost, and high winds, sand/dust storms, as well as the common relatively benign conditions typical of the Southwest desert. For example, heliostat H5 was exposed face-up at NWC from December 1976 to June 1977. On June 22, H5 was found to have a reflectivity of 62.2 percent, for a drop of approximately 25 percent. Specimens exposed without washing from July 1976 to November 1977 were measured. Results are shown in Table 5. Each rack has two ASG laminate glass mirrors. The reflectance loss values were determined for each specimen and the mean and standard deviation values determined for each rack for the combined specimens.

Table 5

AVERAGED REFLECTANCE LOSS DATA FOR
SPECIMENS EXPOSED FROM JULY 1976 TO NOVEMBER
1977 AT ALBUQUERQUE, N.M.

Specimen Rack	Mean \pm Standard Deviation Loss for Six Specimens Per Rack (0/0%)
Permanent Face-up	27.0 \pm 12.8
Astronomical Timer Face-up/Face-down	14.5 \pm 3.7
Astronomical Timer Near Vertical Stow	13.6 \pm 2.3
Sensor Face-up/ Face-down	13.2 \pm 3.2
Permanent Face-down	5.3 \pm 4.8

The acrylic tends to show a greater degree of soiling than the glass, but the differences are not significant for this set of data. The long term results show that permanent face-up has a much higher loss than any of the three stowage positions, and the permanent face-down losses are surprisingly low. These results also illustrate the importance of stowing the heliostats at night in some position other than face up. Heliostats H1 and H4 were monitored from June 1977 until December 1977 without washing, and found to have dropped to 45 percent and 62.5 percent respectively, for losses of approximately 35 percent and 25 percent, respectively, compared to their clean values. During this period, there were three trace rains with a severe rain (1.7 inches on August 16, 17 and 18). These data indicate that equilibrium values of reflectivity, if they exist, are too low to be considered as a means of eliminating all mirror washing for the desert conditions observed.

It is possible that certain sites have rain, snow, frost, and ice in sufficient amounts and with sufficient frequency to essentially eliminate the need for mirror washing, but this has not been observed.

Weather Effects on Reflectivity

Key weather conditions which induce a form of natural cleaning are described below. In some cases, rain and frost have cleaned the mirrors, while in others they have tended to cause reflectance loss. However, by properly positioning the heliostats, these effects

can be used to advantage. Specific cases are described below.

Frost

During the week of 10 January to 17 January 1977, a heavy frost was deposited on the mirrors. Frost is an additional reflectance degradation effect and can deposit airborne dust during the condensation phase, but it can be a very effective method of cleaning the mirrors. We have noted that the heliostat radiates to the night sky, and reaches a temperature of the order of 2.5°F less than the ambient temperature, as seen in Figure 7. Since the heliostat thermocouple is located underneath the steel channel, the glass surface should have a temperature somewhat lower than that measured. Therefore, the top surface of the glass may be approximately 3°F less than the ambient temperature. Determination of the number of heavy frosts to be encountered for a particular site should account for this type of temperature difference, rather than using ambient temperature data alone.

The frost formed on the mirrors is shown in Figures 8 and 9. Approximately 30 minutes after bringing the heliostats onto track, the laminated mirrors (both the inverted and baseline designs) were cleared of frost. As the frost melted, the water and ice mixture flowed off the mirror, carrying off dirt and dust and cleaning the mirrors more effectively than the initial wash for heliostats H2, H4, and IH-1; H3 was cleaned as effectively as the initial wash, and H1 was cleaned somewhat less effectively. The glass mirrors, heliostats H4 and IH-1, were cleaned more effectively than the acrylics because the water/ice mixture could flow easily off the surface.

On the acrylic mirrors, the time required to cause substantial melting was approximately one hour. The water tended to bead up and remain in place, which decreased the washing effect. The difference in time required to melt the frost is primarily due to the nonwetting effect of water on the acrylic, but the additional absorption of radiation in the glass of the second surface laminate may be more than a negligible effect. Noticeable scattering of the reflected light due to the water beads was evident after 2.5 hours (10:30 AM).

These times correspond to the North field heliostats on track. For heliostats in the eastern and southern portion of the field, the mirrors would be approximately horizontal and the frost melting rate and cleaning effectiveness would be reduced. If frost is shown to occur frequently for a site, the loss in energy may have to be considered and adjustments made in the operating procedure for startup.

It has also been noted on almost all occasions in which frost and dew form on the mirror surfaces that the region directly above the structural supports does not tend to accumulate frost or dew as readily as the mirror surface outside of this region (see Figure 10). The effect is evident whether the structure is bonded to the glass or directly beneath it. Also, the areas immediately outside the structural member area accumulate a noticeable dust film, apparently due to the condensation depositing airborne dust particles and capturing wind-blown dust.

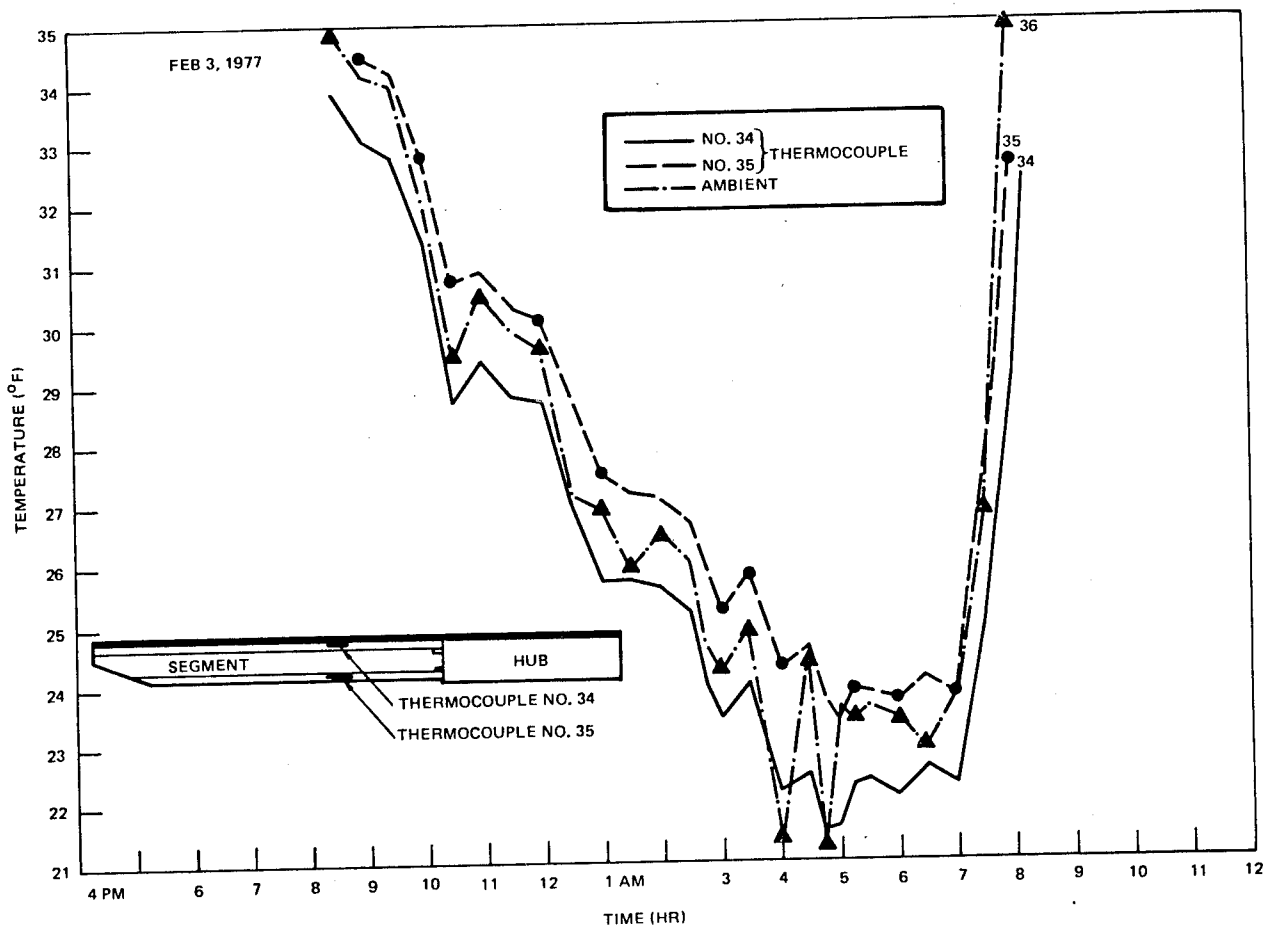


Figure 7. Nocturnal Temperature Variation

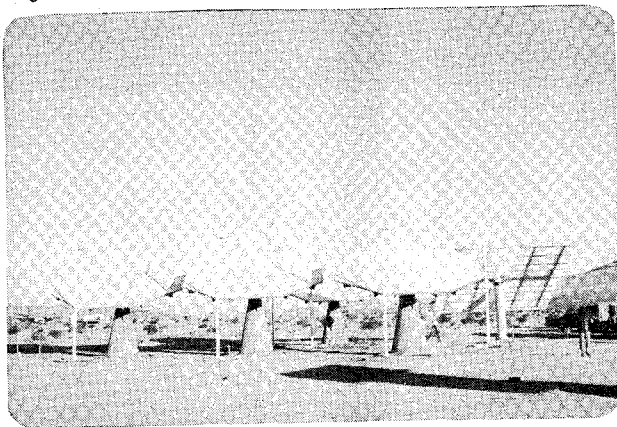


Figure 8. Frost Formed on Mirrors
(8 am, January, 1977)

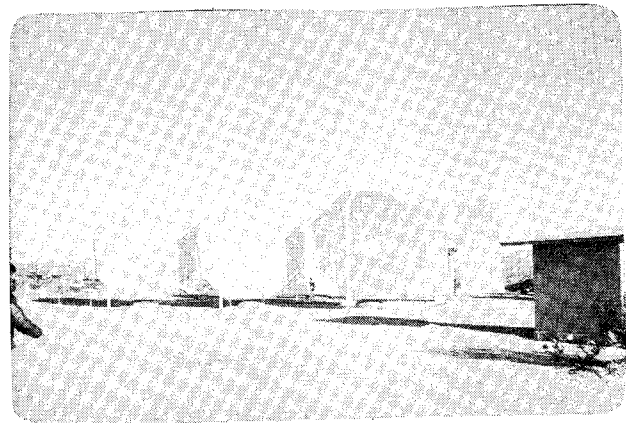


Figure 9. Frost Partially Melted on Mirrors
(8:40 am)

Rain/Snow

Rain has been observed to both improve and exacerbate the dust buildup problem. There was a relatively heavy rain on 5 and 6 January 1977. The total quantity measured was 1.26 inch. Since the baseline heliostats were stowed horizontally, the dirt/dust could not be washed off as effectively as in a near-vertical storage position. It was our visual observation that the rain had not cleaned the mirrors, and had left them with a "spotty" appearance. The improvement in reflectivity noted following the rain

is in fact due more to the following frost, which effectively cleaned the mirrors. The inverted heliostat had been stowed face-down during this period. It was observed that accumulated dirt from the mirror support structure was washed onto the mirror surface, causing substantial smearing of the surface within one to two feet of the outer edge of the mirror panels. It is apparent that both the baseline and inverted heliostats should be stowed near-vertically during substantial rain storms to obtain maximum rinsing of the reflective surface.

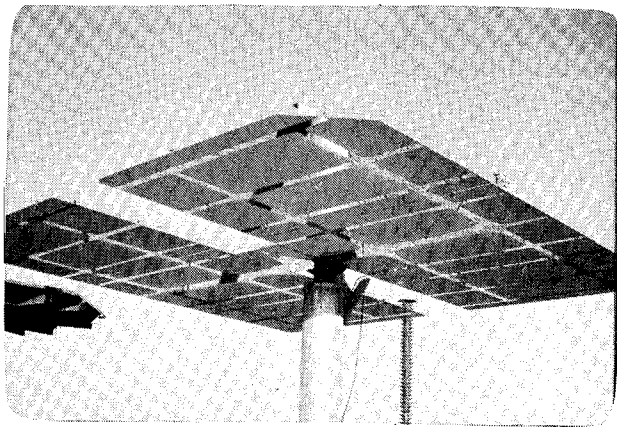


Figure 10. Dew Formation on Inverted Stow Heliostat

Approximately 1.5 inches of rain fell on December 27, 1977 and 0.5 inch on January 3. On January 10, 11, 15, and 16, the rainfall was 0.05, 0.08, 0.62, and 0.46 inch. On January 25 reflectivity measurements were taken of H1 and H4, giving 62 percent and 83.5 percent, respectively. H4, the laminated glass heliostat was within roughly three to four percent of its nominally clean value, indicating that it had been effectively washed. H1 data are not as encouraging, since H1 has a clean reflectivity of approximately 83 percent. The relatively ineffectual washing is probably due to: (1) water not being able to wet the acrylic surface as well as glass, (2) a possible greater degree of dust adherence to the acrylic, and (3) staining. Further understanding of these effects is not now available.

Approximately two inches of snow fell on 25 March 1977. The baseline heliostats were placed in a near-vertical position to determine if the snow would clean the surface. It was observed that snow slid off of the glass surface of H4, resulting in a very clean surface; although measurements could not be made, it was visually obvious that snow was a highly effective cleaning agent for glass. The snow did not readily slide off of the acrylic surface, and in fact caused part of heliostat H3 to delaminate.

Sand/Dust Storm

A rather severe sand/dust storm was encountered on 9 March 1977, the only one of its kind during the test period. Reflectance data were obtained on 2 March and on 14 March; therefore, the loss due to the sand/dust storm can only be approximated. It was visually observed that a fine dust was deposited on the surface by the storm, but measurements could not be taken until five days later.

The reflectance loss for H2 and H3 after the dust storm was observed to be 10.95 and 7.17 percent, respectively. These measurements were taken in a relatively small area (6 in. x 6 in.) of the bottom panel of each heliostat.

The reflectivity of the laminate glass baseline heliostat (H4) remained essentially unchanged (0.5 percent loss, which is within standard deviation for reflectivity loss), which indicated that the glass tended to stay substantially cleaner than the acrylic for dust storm conditions, perhaps because dust did not adhere to the glass as strongly as to the acrylic.

Effects of Soiling on Reflectivity

Two major effects of dust layers on reflectivity have been investigated: (1) effects of dust on the scattering of the reflected light, and (2) the effects of dust induced reflectance loss as a function of the incident light angle.

Preliminary results on the effect of dust scattering are shown in Table 6. Data were taken with the 5.8° and 1° N.I.P.'s and reflectivity in both cases is defined as the ratio of the reflected beam flux density (watts/m²) measured by the N.I.P.'s to the incident solar insolation measured with a 1° N.I.P. Thus, the difference in reflectivity between the higher value associated with the 5.8° N.I.P. and the lower value for the 1° N.I.P. is the amount of light scattered outside of the 1° cone and within the 5.8° cone. The variation observed is surprisingly large, and unexplained, but the impact on the reflectivity is significant in most cases. These data indicate that for certain types of solar collectors (flat plate, trough, etc.), the dust buildup effect is less significant than with heliostats required to reflect light within 1° cone angle.

REFLECTIVITY DEPENDENCE ON INCIDENT ANGLE

One test was performed in the field on heliostat H4 to determine the effect of incident angle on the reflectivity loss due to dust. The near-normal reflectivity loss was approximately five percent. The Eppler N.I.P. was set up to view reflected light from a heliostat oriented to give known angles; with the sun angles known, the incident and reflected light angles with respect to the heliostat were determined. Results are shown in Figure 11.

These data indicate that there may be an additional reflectance loss, but it is not large. In practice, most heliostats are not oriented to give small incidence angles, and therefore, the additional loss of ~ 5 percent at small angles is probably a negligible effect for plant operation. Further, these results show that errors due to off-normal incidence angles of as much as 30-45° have a negligible effect on the reflectance data obtained during our monitoring.

Reflectivity Degradation

Reflectivity degradation data have been obtained and time-correlated with the weather conditions for an overall period of one and one-half years. Representative data have been selected and are presented in the following for both the heliostats and the specimens. In general, dust buildup induced degradation rates are calculated by subtracting initial and final reflectivities, and dividing by the period between measurements, to obtain a value in percent reflectivity loss per day. However, if during this period significant rain, snow, etc., falls, the rate is not calculated, since the natural cleaning usually causes an abrupt increase in reflectivity. All data on degradation rates are therefore obtained for periods not including these natural cleaning phenomena.

In addition, the time averaged reflectivity for the heliostats over a period of approximately seven months has been calculated including the natural cleaning and manual washing.

Table 6
DUST BUILDUP EFFECTS ON ANGULAR DISPERSION

Specimen	Rack	1° Reflect. (%)	5.8° Reflect. (%)	1° Clean (%)	1° Loss (%)	5.8° Loss (%)	Δ Loss (%)
63-14 (SI)	Photocell face-up/ face-down	71.94	73.90	82.60	10.66	8.70	1.96
63-15 (SI)		68.42	70.0	88.32	19.90	18.32	1.58
63-22 (SI)		72.57	75.85	88.86	16.29	13.01	3.28
63-24 (SI)		71.16	77.00	88.27	17.11	11.27	5.84
64-2 (SS)		53.48	59.3	70.48	17.00	11.18	5.82
64-3 (SS)	Astronomical Timer Near Vertical Stow	59.06	62.60	70.66	11.60	8.06	3.54
65-17 (ASGL)							
65-18 (ASGL)							
63-16 (SI)		57.80	73.30	86.36	28.56	13.06	15.50
63-17 (SI)		60.33	72.49	85.44	25.11	12.95	12.16
63-18 (SI)	Astronomical Timer Face-up/ Face-down	65.83	71.64	88.22	22.39	16.58	5.81
64-4 (SS)		54.94	59.52	69.03	14.09	9.51	4.58
64-5 (SS)		55.59	60.90	69.46	13.87	8.56	5.31
65-12 (ASGL)		75.92	79.22	90.33	14.41	11.11	3.30
65-13 (ASGL)		75.87	81.03	91.02	15.15	9.99	5.16
63-19 (SI)	Permanent Face-up	69.73	75.91	87.18	17.45	11.27	6.18
63-20 (SI)		73.16	77.34	87.67	14.51	10.33	4.18
63-21 (SI)		73.13	75.40	89.78	16.65	14.38	2.27
64-6 (SS)		61.94	63.10	67.99	6.05	4.89	1.16
64-7 (SS)		59.60	61.97	69.44	9.84	7.47	2.37
65-14 (ASGL)		74.16	77.90	89.35	15.19	11.45	3.74
65-16 (ASGL)		80.67	86.05	93.01	12.34	6.96	5.38
63-12 (SI)		60.80	69.60	85.84	25.04	16.24	8.80
63-13 (SI)		60.20	63.80	88.17	27.97	24.37	3.60
63-28 (SI)		59.52	63.10	88.17	28.65	25.07	3.58
64-8 (SS)		48.2	55.0	69.98	21.78	14.98	6.80
64-9 (SS)		47.2	49.9	69.63	22.43	19.73	2.70
65-15 (ASGL)		61.12	72.5	89.80	28.68	17.30	11.38
65-19 (ASGL)		61.30	66.2	81.34	20.04	15.14	4.90

SUMMARY

Position	Glass Reflectivity Difference (%)	Acrylic Reflectivity Difference (%)
Photocell Face-up/Face-down	4.68 ± 1.6	3.16 ± 1.9
Astronomical Timer Near Vertical Stow	4.6 ± .9	11.2 ± 4.9
Astronomical Timer Face-up/Face-down	3.16 ± 1.8	4.21 ± 1.9
Permanent Face-up	6.4 ± 3.7	5.33 ± 3.0
Total	4.7 ± 1.3	5.97 ± 3.6

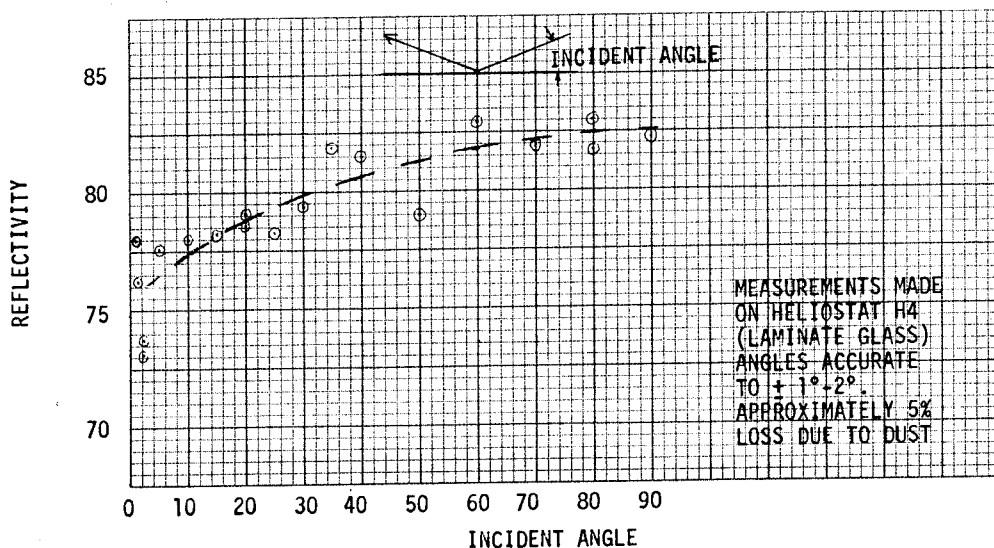


Figure 11. Reflectivity Dependence on Incident Angle

The rate of decrease in heliostat reflectivity under actual desert field conditions has been monitored from December 1976 to May 1977. Results are summarized in Table 7. Results for December and January indicate that reflectivity of both the acrylic and glass mirrors can be degraded by six to eight percent in two to three weeks and can remain essentially constant for approximately the same period. We have also noted a surprising difference during this period between heliostats H2 and H3, which are side by side and would be expected to show more closely similar reflectivity curves. H2 decreased from 70 to 64

percent between 17 December 1976 and 3 January 1977, whereas H3 decreased slightly, from 83.6 to 82.8 percent.

It is also interesting to note that IH-1 and H4 show a similar rate of reflectivity degradation, even though IH-1 was kept in the face-down stowage position for approximately three-fourths of this time, both day and night, to establish what was expected to be a baseline minimum degradation rate for near-continuous inverted stow relative to continuous face-up stow.

Table 7
SUMMARY OF HELIOSTAT REFLECTIVITY VARIATIONS

Heliostat No.	Reflectivity (%) (Degradation Rate, % Per Day)							
	12/9/76	12/9/76	12/17/76	12/17/76	1/3/77	1/14/77	1/28/77	2/4/77
H1	N/A	N/A	67.78	81.29	N/A	77.49±0.3	N/A	76.61±0.5 (0.42)
H2	N/A	N/A	64.89 (.35)	70.20	64.28±21 (.55)	74.13±1.5	66.45±0.8 (≈ 0)	65.15±0.7 (.17)
H3	77.25	86.34	83.63 (.34)	N/A	82.80±2.3 (.21)	85.53±0.19	81.85±2.2 (.26)	79.71±0.5 (.3)
H4	72.07	85.89	78.18 (.96)	N/A	83.62±1.6 (.13)	87.65±0.76	83.51±0.2 (.29)	80.37±0.6 (.45)
IH1	78.25	81.64	83.92	N/A	81.92±1.1 ~	86.49±0.19	85.05±0.2 (0.1)	85.78±0.1 (≈ 0)
Comment	Dirty	Washed	Dirty	Washed	Rain	Frost during week of 1/10 cleaned surfaces		

Heliostat No.	Reflectivity (%) (Degradation Rate, % Per Day)							
	2/15/77	3/2/77	3/14/77	3/15/77	3/25/77	4/1/77	4/7/77	4/8/77
H1	75.37±1.0 (.11)	67.33±0.5 (.45)	65.88±0.1 (.12)	78.24±0.5	82.0	77.95±0.9 (.58)	71.28±0.5 (1.1)	83.22
H2	70.15±0.5 (≈ 0)	67.03±1.0 (.17)	56.08±0.7 (.9)	76.50±0.4	75.0	71.90±0.5 (.59)	66.89 (0.835)	68.18
H3	78.11±1.0 (.14)	76.40±0.4 (.1)	69.23±0.2 (.6)	87.46±1.5		N/A	N/A	N/A
H4	81.79±1.1 (≈ 0)	73.79±0.4 (.44)	73.31±1.6 (.04)	84.00±1.3	87.0	81.56±1.8 (.77)	80.4 (.19)	85.43
IH1	85.58±0.2 (≈ 0)	N/A	76.80±0.8 (.29)	85.10±0.01		81.25±1.5 (.24)	82.09 (≈ 0)	80.04
Comment			Dust storm	Washed		Snow on 3/25/77 cleaned surfaces		Washed

Heliostat No.	Exposure Time (Days)	Time Averaged Reflectivity (%)	Time Averaged Degradation (%)	Degradation Rate (% Per Day) Mean ± Standard Deviation
H1 (Acrylic)	113	$\bar{\zeta}$ = 75.46	7.76	0.4±0.4
H2 (Acrylic)	113	$\bar{\zeta}$ = 68.37	8.13	0.45±0.32
H3 (Acrylic)	97	$\bar{\zeta}$ = 80.47	6.99	0.28±0.18
H4 (Laminate Glass)	121	$\bar{\zeta}$ = 81.10	6.55	0.36±0.32
IH1 (Laminate Glass)	121	$\bar{\zeta}$ = 83.30	3.19*	0.1±0.13

*NOTE: IH-1 was stowed in the face-down position for most of the test period (≈2/3 of exposure time).

From 3 January to 14 January 1977, H2 showed a ten percent increase (due to rain and frost) whereas H3, being initially cleaner, showed a 2.5 percent increase.

Comparing the 14 March 1977 prewash reflectivity measurements of Table 7 with the 2 March 1977 data shows that H1 lost 1.5 percent and H4 was essentially unchanged, whereas H2 lost 11 percent and H3 lost 7.2 percent. These variations in degradation rate for neighboring heliostats has not been explained. Better agreement is found on comparing data from 15 February and 14 March 1977. In this period, heliostat IH-1 can not be included; IH-1 had been disassembled on 1 March and reassembled on 4 March and was, therefore, not available for reflectivity measurements on 2 March. For the period 15 February to 14 March, heliostats H1, H2, H3, H4, and IH-1 had degradation rates of 9, 14, 9, 8, and 9 percent, respectively, for an average degradation of approximately 10 percent (.37 percent per day). February and March had higher wind conditions than December and January, and there was a dust storm on 9 March; such conditions would be expected to cause an increase in the reflectivity degradation rate.

Snow fell on 25 March and heliostats H1, H2, H3, and H4 were positioned near-vertical to observe the cleaning effect. Visually, H4 was cleaned as well as any washing case. However, weather conditions prevented measuring the reflectivity. Therefore, it is assumed that the reflectivity of H4 following the snowfall was near its maximum value of 88 percent. Between 25 March and 1 April, H4 thus lost approximately five percent reflectivity in seven days, but during the next week the reflectivity remained essentially constant.

The data available from December to April were time-averaged to estimate the effective heliostat reflectivity. Results summarized in Table 7 show that the three noninverting acrylics (H1, H2, and H3) lost approximately 7 to 8 percent and the noninverting laminate lost 6.5 percent. The average period between either washing or natural cleaning by frost, rain, and snow was roughly one month for the test period.

Calculating the degradation rates from Table 7 and determining the mean and standard deviation, it is seen that the rates for the four face-up heliostats are of the order of 0.36 to .45 percent per day. Comparable results were obtained for the specimens.

Tables 8 and 9 show reflectance degradation rates for the different rack positions and types of mirrors for two periods. A comparison of the permanent face-up specimen degradation rates shows these rates to be comparable to those of the heliostats. The rate variability is also comparable, exhibiting the same puzzling effects of essentially no loss in some cases, and relatively high losses in others. For both periods, the relative degree of degradation rate is highest for the permanent face-down, and roughly the same for the sensor and astronomical timer, and somewhat higher for the near vertical stow.

One uncertainty in applying the near vertical stow data to actual heliostats is that if heliostats were stowed near vertical, a significant fraction of their area would lie within the first 3-6 feet above the

ground. This region is expected to have higher dust levels than the region 12 feet above the ground where the specimens were located. Furthermore, actual heliostats cannot be stowed near vertical in high winds, and thus in operating plants, a near vertical stow cannot be used every night.

Table 10 compares the degradation rates for glass and acrylic for each stow position. The degradation rates as a function of specimen type lie within the uncertainty. Therefore, these data do not show a distinction due to acrylic or glass surface differences. The reflectivity degradation rate for the face-down data has been used to normalize the data for the other stow positions in Table 11. It is found that the face-up position has a degradation rate fifteen times higher, and the face-up/down and near vertical positions have rates of the order of six to ten times higher than the permanent face-down mean degradation rate. These data show again that a face-up nightly stow will increase the dust buildup rate and therefore benefits are to be gained by storing heliostats near-vertical or face-down.

CONCLUSIONS

A number of preliminary conclusions have resulted from this study, including:

- Specimen racks can simulate heliostat dust buildup
- Washing of heliostats by spray application is feasible
- Rain, snow and frost can be used to effectively clean heliostats by proper positioning
- Nightly stowage positions have a significant impact on the degradation rate
- Acrylic surfaces are harder to clean than glass by natural or spray application techniques and dust buildup rates are somewhat more rapid.
- The degradation rates are very strongly dependent on weather conditions, and exhibit large, puzzling variations occasionally.
- Dry climates will cause significant losses to occur, and therefore maintenance cleaning will be required. Losses can exceed 25 percent.

Additional exposure data and analyses are required to obtain a final resolution of the issues of dust buildup rates vs site and weather. There is a clear need for a convenient, portable reflectometer.

Plant operator algorithms to position heliostats at night and during inclement weather are suggested which deserve tests with full scale heliostats. For example, heliostats could be positioned approximately 20° to 45° from vertical during rain, snow, and frost conditions to maximize the cleaning effect. Vertical stow could be used during periods of low wind. Inverted stow would be used during periods of high wind. Lack of an inverted stow capability during periods of high wind would require a face-up stow position, which may result in loss of significant reflectivity due to soiling.

Table 8

NWC SPECIMEN REFLECTIVITY AND DEGRADATION RATE SUMMARY

JUNE 22 TO AUGUST 8, 1977

	ASG Laminate				Second Surface				Sheldahl			
	ID	Clean	Dirty	Degradation Rate (% Per Day)	ID	Clean	Dirty	Degradation Rate (% Per Day)	ID	Clean	Dirty	Degradation Rate (% Per Day)
Sensor Face up/ Face down	-	Data not available			64-2	69.61	53.48	.34	63-14	84.2	71.94	.26
					64-3	70.13	59.06	.24	63-15	87.8	68.42	.41
									63-22	90.35	72.57	.38
									63-24	90.98	71.16	.42
Astronomical Timer/Near Vertical Stow	65-12	90.67	75.92	.31	64-4	70.76	54.94	.34	63-16	87.48	57.8	.63
	65-13	96.39*	75.87	.44	64-5	68.97	55.59	.28	63-17	86.16	60.33	.55
									63-18	91.38	65-83	.54
Astronomical Timer Face up/ Face down	65-14	89.02	74.16	.32	64-6	67.66	61.94	.12	63-19	82.21	69.73	.24
	65-16	93.88	80.67	.28	64-7	69.86	59.61	.22	63-20	89.21	73.16	.34
									63-21	88.12	73.13	.32
Permanent Face up	65-14	91.44	61.12	.64	64-8	69.39	48.2	.45	63-13	91.33	60.2	.66
	65-19	82.73	61.3	.46	64-9	70.03	47.2	.48	63-28	89.81	59.52	.64
Permanent Face down	65-20	82.26	78.1	.09	64-10	69.11	65-8	.07	63-11	84.94	83.5	.03
	65-21	81.70	81.3	.01					63-25	89.22	87.9	.03
									63-26	87.83	86.4	.03

Table 9

NWC SPECIMEN REFLECTIVITY AND DEGRADATION RATE SUMMARY

NOVEMBER 11 TO DECEMBER 1, 1977

	ASG Laminate				Second Surface				Sheldahl			
	ID	Initial	Final	Degradation Rate (% Per Day)	ID	Initial	Final	Degradation Rate (% Per Day)	ID	Initial	Final	Degradation Rate (% Per Day)
Sensor Face up/ Face down	65-17*	78.43	78.18*	.01	64-2	60.1	59.65	0.02 ⁽²⁾	63-14*	88.0	87.5	0.02
	65-18	71.0	73.47	~ ⁽²⁾	64-3*	70.6	68.42	0.11	63-15	75.9	71.67	0.21
Astronomical Timer/Near Vertical Stow	65-12	89.4 ⁽¹⁾	75.36	0.41	64-4	72.3	63.97	0.42	63-22	79.6	78.68	0.05
	65-13*	91.0	87.69	0.16	64-5	69.4	66.15	0.16	63-24	78.6	76.27	0.12
Astronomical Timer Face up/ Face down	65-14*	89.2	89.23	~ 0	64-6*	68.9	65.22	.184	63-16	80.0	76.92	0.15
	65-16	92.6	83.58	0.45	64-7	61.4	61.43	~ 0 ⁽²⁾	63-17	75.3	76.92	~ 0
Permanent Face up	65-15	70.4	57.57	0.64	64-8	56.4	55.38	0.05 ⁽²⁾	63-18*	88.2	86.76	0.07
					64-9*	69.6	61.29	0.41	63-19	80.8	79.1	0.085
Permanent Face down									63-21*	89.8	81.82	0.40
									63-12*	85.8	80.77	.25
									63-13	72.6	69.70	.14
									63-28	69.5	63.63	.29

No data available due to weather

*NOTE: Certain specimens washed on November 11, 1977.

(1) Previous measurement for 65-12 made on 9/28, for 34 days duration

(2) Illustrates tendency for degradation rate to decrease as specimens are soiled

Table 10
SUMMARY OF DEGRADATION RATE
DATA FOR SUMMER AND WINTER

Ranking (In Order of Increasing Rate)	<u>Degradation Rate (% Per Day)</u>	
	<u>Glass (ASG Laminate and 2nd Surface)</u>	<u>Sheldahl Acrylic</u>
1. Permanent face-down	0.06 ± 0.04	0.03
2. Sensor face-up/face-down	0.12 ± 0.14	0.23 ± 0.16
3. Astronomical timer face-up/face-down	0.20 ± 0.16	0.283 ± 0.12
4. Astronomical timer/near vertical stow	0.315 ± 0.11	0.32 ± 0.28
5. Permanent face-up	0.45 ± 0.20	0.40 ± 0.24

Table 11
COMBINED RANKING OF
DEGRADATION RATES VS. STOW POSITION

<u>Combined Ranking for Both Glass and Acrylic</u>	<u>Rate (% Per Day)</u>	<u>Normalized Rate W.R.T. 0.03% Per Day</u>	<u>Average Rate</u>
1. Permanent face-down	0.03 to 0.06	1-2	1.5
2. Sensor face-up/face-down	0.12 to 0.23	4-7.7	5.8
3. Astronomical timer face-up/face-down	0.20 to 0.283	6.67-9.4	8.0
4. Astronomical timer/near vertical stow	0.315 to 0.32	10.5-10.67	10.6
5. Permanent face-up	0.40 to 0.45	13.3-15	14.15

EXPOSURE TEST RESULTS FOR REFLECTIVE MATERIALS

R. A. Rausch, Honeywell Inc.

B. P. Gupta, Solar Energy Research Institute

AUTHORS BIOGRAPHY

Mr. Rausch is a Senior Development Engineer in the Solar Power Systems group of the Honeywell Inc. Energy Resources Center and is engaged in the design and evaluation of concentrating solar collectors.

Mr. Gupta is now a Senior Research Scientist with SERI. He is engaged in research and development of systems and components related to the conversion of solar energy to high temperature thermal energy. He was formerly with the Energy Resources Center of Honeywell Inc.

ABSTRACT

Exposure tests have been conducted on a variety of candidate reflective materials for applications requiring concentration of solar energy. Materials tested include aluminized fiberglass, aluminized acrylic, aluminized and silvered Teflon®, aluminized and silvered glass, aluminized acrylic plexiglass, and anodized aluminum. Both first and second surface reflectors were included in the test samples. Three different, simultaneous exposure tests were conducted on the materials. Up to two and one-half years of real time exposure has been accumulated on most materials with reflectivity measurements at periodic intervals. With accelerated exposure tests, the samples have undergone an equivalent of 20 years solar exposure. The change in reflectivity with exposure time is presented for each of the materials and test conditions. These data assist the user in establishing the most economical time period before replacement of the reflective surface is required in a particular application. The activities reported herein were supported by the National Science Foundation and Energy Research and Development Association through a grant to the University of Minnesota and Honeywell Inc.

INTRODUCTION

Honeywell Inc. has, for the past several years been conducting research on components for use in high-temperature (300°C) solar thermal power systems. This work, sponsored by the National Science Foundation and the Energy Research and Development Administration through the University of Minnesota, has been conducted under two contracts (Phases 1 and 2). Phase 1 activities were conducted under NSF Grant No. GI-34781¹. Phase 2 activities were conducted under ERDA Contract No. EY-76-S-02-2993 and were concluded in December 1977.

The research activities of these two programs have included the exposure and evaluation of candidate reflective materials for application in solar collectors. Up to 2 ½ years of one-sun exposure and an equivalent of 20 years of accelerated exposure have been accumulated to date on most of the material test samples during exposure at an Arizona test site. This paper describes the test conditions, the test procedures, and presents reflectivity exposure time histories for the materials tested.

MATERIALS

The materials tested include aluminized fiberglass, aluminized acrylic, aluminized and silvered Teflon®, aluminized and silvered glass, aluminized acrylic plexiglass, and anodized aluminum. Both first or second surface reflectors were included in the test samples.

Samples of candidate reflector surfaces were originally obtained from a number of manufacturers and suppliers. Additional samples were added to the baseline sample set during the most recent program. Table 1 lists the manufacturer/source, general characteristics and identifier code for each of the samples tested to date. The sample code keys the source as well as the age for identical reflector materials. Thus HPP/2 material is an updated, near production version of HPP/1. The reflectivity data indicated in Table 1 and the following tables are the average values for the identical samples subjected to the same exposure test condition.

Table 1. Description of Reflector Sample

CODE	SOURCE/ MANUFACTURER	ORIGINAL AVERAGE REFLECTIVITY	MATERIAL*
GD/1	General Dynamics	0.85	Aluminized fiberglass with protective coating (1).
GD/3	General Dynamics	0.83	Aluminized fiberglass with protective coating (1).
GD/4	General Dynamics	0.92	Aluminized fiberglass without protective coating (1).
3M/1	3M Company	0.86	Aluminized acrylic (2).
H/1	Honeywell	0.76	Aluminized glass (2).
S/3	G.T. Sheldahl	0.77	Aluminized Teflon® (2).
S/1	G.T. Sheldahl	0.79	Aluminized Teflon® (2).
S/2	G.T. Sheldahl	0.86	Silvered Teflon® (2).
R/1	Ram Products	0.80	Aluminized acrylic plexiglass (2).
AK/1	Alcoa	0.82	Alzak anodized aluminum reflector sheeting (1).
HPP/1	Honeywell	0.86	Silvered glass (2).
HPP/2	Honeywell	0.87	Silvered glass (2).
A/1	Alcoa	0.82	Anodized aluminum (1).

* First and Second surface mirror types are indicated by (1) and (2) respectively.

TEST PROCEDURE

Reflective materials were fabricated into 5-cm x 5-cm (2-inch x 2-inch) samples. Spectral reflectivity data were obtained in the laboratory for each sample with a Cary 14 spectrophotometer, and a computer program was used to calculate the total solar reflectivity. In this computer program, the solar spectrum is divided into 12 energy bands and the fraction of total solar flux in each band is determined. This fraction is then multiplied by the value of the sample reflectivity corresponding to

the wavelength of each band's center. These values are then summed to obtain the total solar reflectivity. Reflectivity measurements during the current program were taken before and after the exposure period, which occurred between February and October, 1977.

Exposure tests were conducted at the test site of Desert Sunshine Exposure Tests Inc. near Phoenix, Arizona. Three exposure tests were conducted, one for each subsample set. One-sun exposure is provided on EEK test racks. These test racks are equatorially mounted and track the sun by means of a 24-hour synchronous motor. No attempt is made to shield the EEK samples from the elements during nighttime or overcast period.

Two accelerated exposure tests were also conducted. EMMA test racks are equatorially mounted and use mirrors for accelerating exposure at eight times the normal intensity of the solar radiation. Air is continually blown across the sample surfaces to prevent them from overheating. EMMA test samples are protected from the elements when the sun is not shining. The EMMAQUA test is identical to the EMMA test except distilled water is sprayed onto the samples for eight minutes of each sunny hour.

TEST RESULTS

Reflectivity exposure time histories are shown in Tables 2, 3, and 4 for samples exposed to the EEK, EMMA, and EMMAQUA test conditions, respectively. The tables indicate the original reflectivity values, the exposure periods, and reflectivity values at the end of each exposure period. The EEK data of Table 2 includes reflectivity values obtained before and after cleaning the samples at the completion of the exposure period. The cleaning method included the use of deionized water, a cotton swab and blow drying. The samples subjected to the accelerated exposure tests were not measured prior to cleaning. The tables also show the percent reflectivity loss (gain) during the accumulated exposure period. This loss is defined as the difference between the original and the current clean values divided by the original value.

Table 3. Reflectivity Histories for EMMA Test Exposure

Material	ρ_o	t_{weeks}	ρ_{clean}	Percent Loss (Gain)
GD/1	0.87	46	0.84	3
		62	0.84	3
		107	0.80	8
		139	0.76	13
GD/4	0.88	46	0.84	4
		62	0.84	4
		107	0.77	12
		139	0.70	21
3M/1	0.88	46	0.85	3
		62	0.86	2
		107	0.84	4
		139	0.83	6
S/1	0.78	34	0.81	(4)
		52	0.81	(4)
		97	0.81	(4)
		129	0.80	(2)
S/2	0.85	34	0.88	(4)
		52	0.85	0
		97	0.82	4
		129	0.79	7
S/3	0.79	34	0.79	0
		52	0.80	(1)
		97	0.72	9
		129	0.75	5
R/1	0.80	34	0.76	5
		52	0.72	10
		97	0.72	10
		129	0.72	10
H/1	0.76	46	0.76	0
		62	0.76	0
		107	0.75	1
		140	0.75	1
AK/1	0.82	34	0.76	7
		52	0.79	4
		97	0.78	5
		129	0.80	3
HPP/1	0.85	32	0.86	0
HPP/2	0.88	21	0.86	2

Table 2. Reflectivity Histories for EEK Test Exposure

Material	ρ_o	t_{weeks}	ρ_{clean}	ρ_{dirty}	Percent Loss (Gain)
3M/1	0.86	23	0.86	0.81	0
		50	0.85	0.83	1
		66	0.86	0.79	0
		111	0.86	0.83	0
		139	0.86	0.82	0
S/1	0.78	9	0.78	0.71	0
		39	0.82	0.79	(5)
		58	0.82	0.74	(5)
		103	0.82	0.77	(5)
		135	0.80	0.76	(2)
S/2	0.86	9	0.88	0.79	(2)
		39	0.87	0.83	(1)
		58	0.88	0.72	(2)
		103	0.86	0.82	0
		135	0.87	0.80	(1)
S/3	0.78	9	0.80	0.69	(3)
		39	0.78	0.74	0
		58	0.78	0.61	0
		103	0.77	0.72	1
		135	0.76	0.70	3
R/1	0.80	9	0.75	0.66	6
		39	0.78	0.71	3
		58	0.72	0.69	10
		103	0.73	0.70	9
		135	0.72	0.70	10
H/1	0.76	9	0.76	0.75	0
		44	0.76	0.76	0
		63	0.76	0.69	0
		108	0.75	0.70	1
		140	0.75	0.70	2
A/1	0.82	43	0.84		(2)
		75	0.83	0.78	(1)
HPP/1	0.86	32	0.86	0.80	0
HPP/2	0.87	21	0.86	0.83	1
GD/3	0.83	23	0.74	0.68	11
		50	Failed	Failed	100
GD/1	0.88	23	0.85	0.81	3
		50	0.76	0.79	14
		69	0.69	0.70	22
		114	Failed	Failed	100
GD/4	0.92	23	0.87		5
		55	0.82		11
		74	0.76		17
		119	Failed	Failed	100

Table 4. Reflectivity Histories for EMMAQUA Test Exposure

Material	ρ_o	t_{weeks}	ρ_{clean}	Percent Loss (Gain)
GD/1	0.87	52	0.75	14
		97	0.69	21
		129	0.52	40
3M/1	0.85	52	0.81	5
		97	0.73	14
		129	0.69	19
S/1	0.79	52	0.81	(3)
		97	0.80	(1)
		129	0.80	(1)
S/2	0.87	52	0.90	(3)
		97	0.80	8
		129	0.78	10
S/3	0.80	52	0.80	0
		97	0.77	3
		129	0.74	7
R/1	0.80	52	0.64	20
		97	0.65	19
		129	0.59	27
H/1	0.76	52	0.76	0
		97	0.70	8
		129	0.69	9
AK/1	0.82	52	0.77	6
		97	0.79	4
		129	0.74	10
HPP/1	0.86	32	0.84	3
HPP/2	0.87	32	0.85	3

The following is a summary of the test results for each reflective material:

GD/1, GD/3, GD/4--All of these aluminized fiberglass samples failed the EEK test and showed significant loss of reflectivity under the accelerated tests. Generally, the surface becomes pitted and small gold/green spots appear. These spots expand to cover the entire surface, causing failure.

3M/1--This aluminized acrylic has shown no degradation under EEK test conditions. Accelerated exposure has increased the reflectivity loss to six and 19 percent, respectively, for EMMA and EMMAQUA tests. Small scratches exist on one sample, but have not seriously degraded reflectivity.

S/1, S/2, S/3--The S/1 (aluminized Teflon®) samples show no loss of reflectivity under either normal or accelerated exposure conditions. Test results suggest that reflectivity actually increased as much as five percent during the EEK exposure tests. The S/3 (aluminized Teflon®) samples performed slightly poorer under each test. The S/2 (silvered Teflon®) material did not degrade under the EEK test, but under the accelerated test degraded at a faster rate than the aluminized Teflon. Green/gold spots have appeared on the S/2 accelerated test samples and small scratches exist on half of the sample lot.

R/1--The R/1 (aluminized acrylic plexiglass) samples generally have a better appearance than the 3M samples, however, the degradation is faster under each of the three tests, including a ten percent reflectivity loss under the EEK test. There is some evidence that the reflectivity loss diminishes after one year of EEK exposure. At least one sample has had a 30 percent area film/substrate separation.

H/1, HPP/1, HPP/2--Little if any degradation has occurred on the aluminized glass (H/1) and the silvered glass (HPP/1 and HPP/2) samples except under the EMMAQUA test. All samples still have a good appearance.

A/1, AK/1--The anodized aluminum samples show little loss of reflectivity after 1-1/2 years of EEK exposure and up to ten percent loss under the accelerated tests. Samples are generally in good visual condition except that white spots exist on the EMMAQUA samples. These spots may be caused by the water spray as they exist on several other material samples subjected to the EMMAQUA test.

CONCLUSION

An attempt was made to compare the samples within each of the three test groups. A linear average reflectivity was calculated for each of the test period increments indicated in Tables 2, 3, and 4. The final average ρ_n value was determined using

$$\left(\sum_{i=1}^n \bar{\rho}_i \Delta t_i \right) / \left(\sum_{i=1}^n \Delta t_i \right).$$

Table 2-5 indicates the four best materials in each test group and the corresponding average reflectivity values. Only the samples subjected to the full exposure period are included.

Table 5. List of Superior Reflective Materials

Test Condition	Material	Exposure Period (Weeks)	Average Reflectivity (ρ)
EEK	S/2	135	0.87
	3M/1	139	0.86
	S/1	135	0.81
	S/3	135	0.78
EMMA	3M/1	139	0.85
	S/2	129	0.84
	S/1	129	0.80
	AK/1	140	0.79
EMMAQUA	S/2	129	0.85
	S/1	129	0.80
	3M/1	129	0.78
	AK/1	129	0.78

Based upon this performance parameter, the aluminized acrylic (3M/1) and the silvered Teflon® (S/2) are the superior reflective materials. Materials with somewhat poorer performance include aluminized Teflon® and anodized aluminum. The newest silvered glass samples show potential but have not been sufficiently exposed to be compared on a long-term basis.

It is noted that the use of alternative cleaning techniques could have a significant impact on the above results. Rugged materials such as anodized aluminum and silvered/aluminized glass would probably show up as better candidates. Cleaning techniques other than that mentioned above were not investigated during this program.

ACKNOWLEDGEMENT

The authors wish to thank Mr. G. Kaplan and Mr. D. Spencer, Phase 1 ERDA and NSF program managers; Mr. J. Fortenberry and Mr. D. J. Boatman, Phase 2 project monitors at the Jet Propulsion Laboratory; and Dr. E. M. Sparrow and Dr. J. W. Ramsey of the University of Minnesota for their support during the above referenced programs. In addition, we thank Desert Sunshine Exposure Tests Inc. for their cooperation and assistance during the exposure tests.

REFERENCE

1. Research Applied to Solar Thermal Power Systems, Report No. 6 (1 January 1975 - 31 August 1975). NSF/RANN/SE/GI - 34871/PR/75/2.

SPECULARITY MEASUREMENTS BY FOURIER TRANSFORM EXAMINATION*

H. L. Hampton, J. S. Hartman, M. A. Lind

The authors are associated with the Engineering Physics Department at Battelle Pacific Northwest Laboratories. Mr. Hampton received his M.S. from Washington State University for his work on solid state solar conversion devices. Dr. Hartman and Dr. Lind received their doctorates from Iowa State University in Solid State Physics. The authors have strong backgrounds in physics, optics and electronics.

INTRODUCTION

Solar reflectors are frequently used in concentrating collectors to increase the operating temperature and enhance the overall system efficiency. A high value of solar reflectivity is usually desired. However, the requirements on reflector specularity depend directly upon the end use. The degree of specularity required is usually determined by the angular aperture of the receiver as viewed from the reflector.

In heliostat applications the effective aperture could be as small as 10 mrad, the angular divergence of the sun. Only materials of high specularity can be used for such applications. In other systems which incorporate larger receivers or shorter reflector to receiver distances, less specular materials may be adequate.

It is the intent of this paper to describe how the Fourier transform technique can be used to examine the scattering properties or specularity of solar reflector materials and to discuss some instrumentation which is being developed to measure the effect.

MATHEMATICAL PRELIMINARIES

One of the methods that can be used to characterize reflector specularity makes use of the complex two-dimensional Fourier transforming properties of lenses. A typical system such as outlined in Fig. 1 consists of a light source, an aperture, collimation optics, a scattering sample, collection optics, and collection optics.

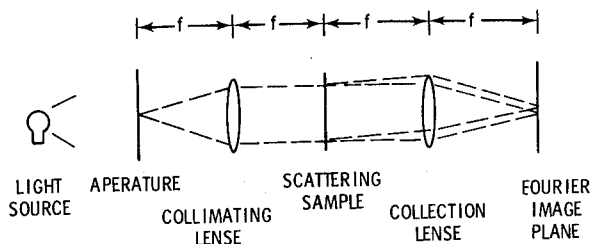


FIGURE 1. Typical Optical System for Examining Specularity Using the Fourier Transformation Properties of a Simple Lens.

This optical system can be represented in block form as shown in Fig. 2. Here $\psi(x, y; s_1)$ is the input wave function, $f(x, y)$ is the aperture function in the plane P_1 , $g(c, d)$ is the transmission or reflection function of the scattering material, P_2 and P_4 are the lens planes, and $h(m, n)$ is the resulting image function in the plane P_5 .

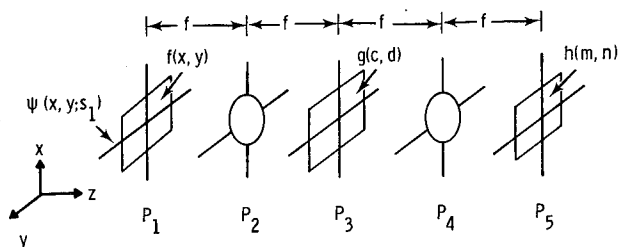


FIGURE 2. Block Diagram of the Spatial Domain of the Simple System Represented in Fig. 1.

The mathematical analysis of this system can be simplified by using the operational notation developed by A. Vander Lugt.¹ One can represent the action of lenses and propagation as elements in a system. In this notation a lens is denoted by the symbol \otimes which is equivalent to the physical space multiplier

$$L(x, y) = e^{-j\frac{k}{2f}(x^2 + y^2)} \quad (1)$$

The operational representation for propagation is a box \square , which is equivalent to a physical space convolution. One can apply this notation by defining a canonical function and its conjugate.

$$\psi(x, y; s) \equiv \exp \left[j\frac{ks}{2}(x^2 + y^2) \right] = \bar{\psi}(x, y; -s) \quad (2)$$

where s is a reciprocal distance given as either

$$s = 1/z \quad (3)$$

in the case of spatial propagation, or

$$s = 1/f = \hat{f} \quad (4)$$

in the case of interaction with a lens of focal length f .

Using this notation one can write a corresponding mathematical representation for each element of the block diagram in Fig. 2. The resulting expression is shown in Fig. 3.

¹A. Vander Lugt, "Operational Notation for the Analysis and Synthesis of Optical Data-Processing Systems", *Proc. IEEE* 54, 1055 (1966)

*Prepared for the U.S. Department of Energy under Contract EY-76-C-06-1830

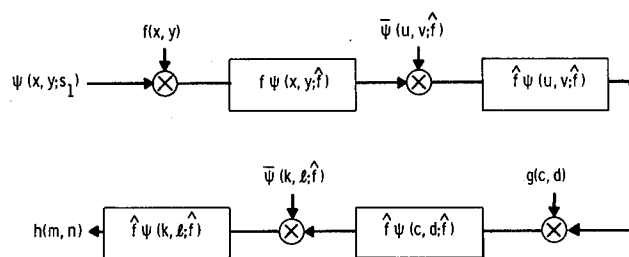


FIGURE 3. The Mathematical Representation of the Schematic Diagram Shown in Fig. 2.

The multiplication blocks are just the product of all the elements using a common set of variables. The convolution blocks are an integral of the product of an input function times a modified ψ function, where the term is written as the difference of two sets of variables, input minus output integrated over the input variables.

$$h(m, n) = \int_{P_1}^{\hat{f}^4} \int_{P_2} \int_{P_3} \int_{P_4} \psi(x, y; s_1) f(x, y) \psi(x-u, y-v; \hat{f}) \times \bar{\psi}(u, v; \hat{f}) \psi(u-c, v-d; \hat{f}) g(c, d) \psi(c-k, d-l; \hat{f}) \times \bar{\psi}(k, l; \hat{f}) \psi(k-m, l-n; \hat{f}) \delta x \delta y \delta u \delta v \delta c \delta d \delta k \delta l \quad (5)$$

The equation can be simplified by substituting the functional forms of ψ into the equation, integrating and utilizing the basic symmetry and algebraic properties of the canonical function².

$$h(m, n) = -\lambda^2 \hat{f}^2 \int_{P_1} \int_{P_3} \psi(x, y; s_1) f(x, y) \exp[-jk\hat{f}(xc+yd)] \times g(c, d) \exp[-jk\hat{f}(cm+dn)] \delta x \delta y \delta c \delta d \quad (6)$$

In the limiting case where $\psi(x, y; s_1)$ is a monochromatic plane wave and the aperture function, $f(x, y)$, has a small enough spatial extent to be approximated by a delta function, the equation simplifies further.

$$h(m, n) = \kappa \int_{P_3} g(c, d) \exp[-ik\hat{f}(cm+dn)] \delta c \delta d \quad (7)$$

Here κ is a constant which is a function of the wavelength of the incident radiation and the focal length of the lenses. Note that the assumptions that we have made are equivalent to illuminating the sample with a true collimated monochromatic plane wave.

Equation (7) shows that the intensity distribution at P_5 is the exact Fourier transform of the transmission or reflection function $g(c, d)$.

In practice it may not be desirable to employ apertures in the P_1 plane which are small enough to be treated as delta functions. For example, in the work performed by Pettit,³ a bilateral slit was used as the limiting input aperture, $f(x, y)$. The finite size of this aperture results in an

intensity distribution at P_5 that is no longer an exact Fourier transform of the scattering function but is rather a convolution of the normalized slit intensity profile with the Fourier transform of the transmission/reflection function of the sample. The deconvolution of the intensity distribution to derive the scattering function of the sample may be mathematically complex.

PRACTICAL IMPLEMENTATION

A system of the type shown in Figure 1 was assembled to demonstrate the usefulness of Fourier examination. The system contained the following components:

- Helium-Neon laser source ($\lambda=6328\text{\AA}$, 50 mw),
- Keplerian beam expander with spatial filtering (15 μm pinhole, 5/8" Beam diameter),
- Sample,
- Fourier transform lens ($f=8"$, dia=2"), and
- Image detector.

The sample to lens and lens to detector distances were both set equal to the focal length of the collection lens. The properties of Fourier transform images are shown for several test samples with two dimensional periodic structure in Figure 4. The intensity pattern observed in the Fourier image plane photographs demonstrates the spatial behavior predicted mathematically for the Fourier transforms of the sample patterns. Note that the Fourier transform exhibits the same symmetry as the test sample and that periodic structure in the sample results in periodic structure in the Fourier transform plane which is inversely proportional to the periodic spacing in the sample.

Figure 5 shows examples of the Fourier transform plane images of several reflector materials. The patterns observed in the photographs are directly related to the characteristics of materials under examination. Some materials do have anisotropies due to the fabrication procedures (roll marks, etc.) but they do not demonstrate a strong periodic structure that would be associated with the uniform spacing of these anisotropies. The material angular anisotropies result in the angular asymmetry of the observed Fourier transforms.

If the sample were perfectly planar and homogeneous it would not alter the nature of the beam incident on the collection lens. The Fourier transform due to the finite diameter of the sampling beam is the well known Bessel function solution of the diffraction limited spot for a round beam. But the sample alters the beam to some extent and the resulting beam contains components of both the unaltered and

²See for example, F. Paul Carlson, "Introduction to Applied Optics for Engineers", Academic Press, New York (1977) p 58

³R. B. Pettit, "Characterization of the Reflected Beam Profile of Solar Mirror Materials," Solar Energy 19, 733 (1977)

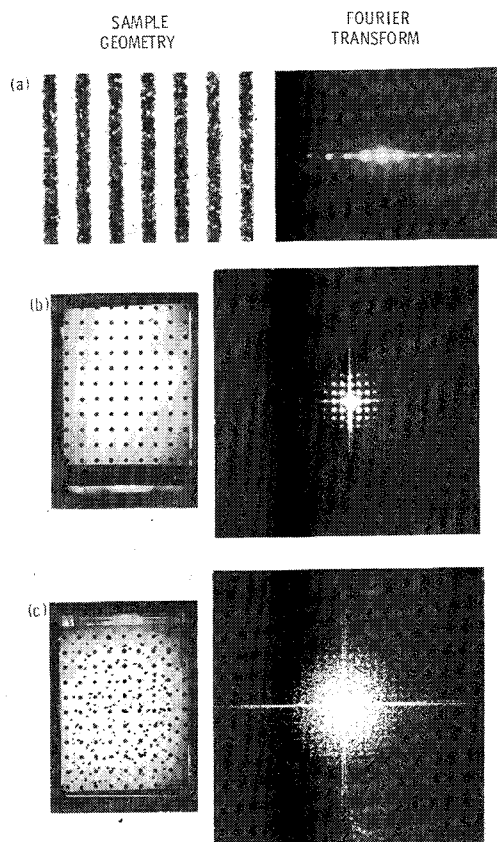


FIGURE 4. Sample Plane Transmittance Function and Resultant Fourier Plane Distribution.

the scattered light. The unaltered beam image is not related to the material inhomogeneities and is not of interest to this study. Samples causing more scatter are indicated by increased intensity in the Fourier image outside the diffraction pattern of the unaltered beam.

Light striking an image point in the Fourier plane is displaced from the optical axis by an amount proportional to the tangent of the angle through which it is scattered times the focal length of the lens. Simple geometrical considerations show that

$$r = f \tan \phi_{sc} \quad (8)$$

where ϕ_{sc} is the scattering angle at the material and r is the radial distance from the optic axis in the Fourier plane.

For the practical system in this study, equation 8 can be used to calculate the value of ϕ_{sc} for the light received at each radial position. Therefore, concentric circles can be drawn in the Fourier plane such that each circle of increasing radius corresponds to light scattered through a larger angle. This means that if a threshold

scattering angle can be determined between acceptable and unacceptable scattering, then the unacceptable scattering can be immediately determined. One could reject entirely the portion of the signal inside this circle and examine only the light scattered at angles greater than the predetermined threshold.

Although Figure 5 did not reveal a strong periodic structure in the materials examined, it is very possible that such structures exist but are not seen due to relatively small diameter of the beam passing through the sample and the finite dimensions of the system optics. The spatial frequency (lines/mm) of a periodic structure in the sample plane is directly proportional to the radial displacement of an image point in the Fourier plane. The finite diameter of the sampling beam can limit the spatial frequency (longest surface period) that can be determined from the Fourier transform. For the system used in this study, the low spatial frequency limit is (1 line/0.625 inch) = 0.06 lines/mm.

The optical system provides data on the non-specular transmitted light at very small scatter angles (1/2 to 1/3 milliradian). It is, therefore, important to evaluate the divergence of the input beam to determine its significance compared to the small scatter angles under examination. The input laser beam is expanded using a Keplerian beam expander with spatial filtering. The divergence calculation based on the specific experimental geometry of the beam expander used in our system indicates that the divergence varies from 0.17 to 0.19 milliradians depending on the size of the output beam that is used.

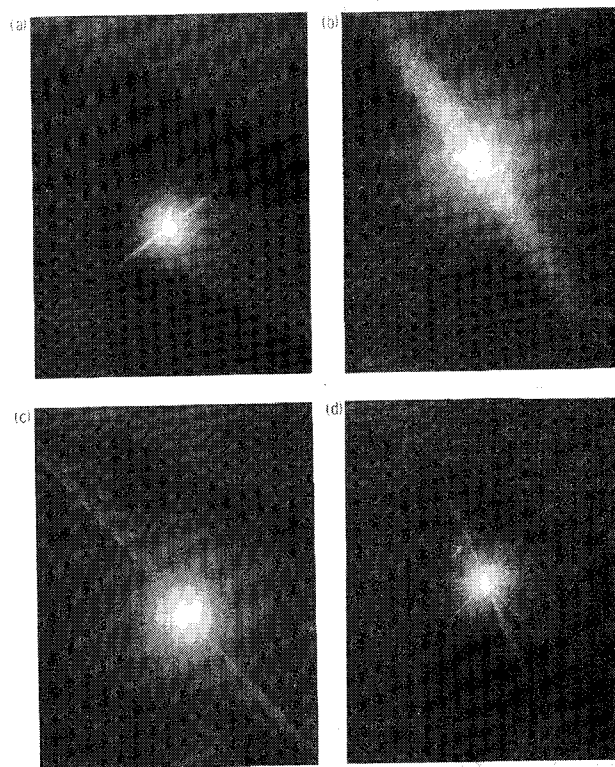


FIGURE 5. Fourier Plane Distribution Observed For Several Common Materials.

METHODS OF IMAGE EVALUATION

A number of methods exist for sampling Fourier intensity distributions. These techniques may be divided into four categories: 1) one dimensional sampling, 2) two dimensional sampling, 3) integrated sampling and 4) hybrid techniques.

Sampling in one dimension measures the intensity distribution along a single line in the Fourier plane. This may be performed by either translating a single small aperture detector along the line of observation or by using a linear array of detectors. The resolution of such a technique is then limited by the finite dimensions of the detector or aperture. Although providing useful intensity profile information, this technique assumes the scattered distribution is symmetric about the optical axis. Information in the Fourier plane regarding the angular anisotropy of the sample can be lost. However, one dimensional techniques lend themselves easily to reduction of data to useful engineering quantities, and are generally more easily interpreted than the more complex two dimensional sampling technique. Fig. 6a illustrates a one dimensional sampling experiment used to observe the convolution of a slit function intensity distribution with the Fourier transform of the sample transmission function. Figure 6c illustrates the real time intensity output of the array detector displayed on an oscilloscope. A broadband source was used in this experiment to reduce the interference effects observed when using a laser source.

With two dimensional sampling techniques, it is possible to display and measure the spatial variation of intensity in the entire Fourier transform plane. This method can produce detailed information regarding the sample scattering properties although interpretation of the data may be non-trivial. Two dimensional sampling is highly desirable for the observation of the anisotropy in the materials. The use of two dimensional sampling also reduces the requirements placed on critical alignment of the system.

An integrated sampling technique may utilize a single, relatively large area, detector to sample the energy flux incident on a fixed aperture in the Fourier plane. The proper selection of an aperture for this method can produce a very sensitive analytical screening tool. All information regarding the spatial distribution of the scattered energy is integrated by the detector and is consequently lost, thereby making detailed materials data extremely difficult to obtain.

Specularity measurements have been previously reported³ using an integrating detector with a variable aperture. Although this hybrid technique provides more detailed information than the integrating technique described above, the effects of an anisotropic scattering sample are not observable with a single measurement. Also, the requirements on the precise positioning of the aperture make the measurements difficult to perform outside the laboratory.

Several types of detectors were investigated for their suitability in measuring the specularity of various materials using the methods described above. The results of these studies, as well as

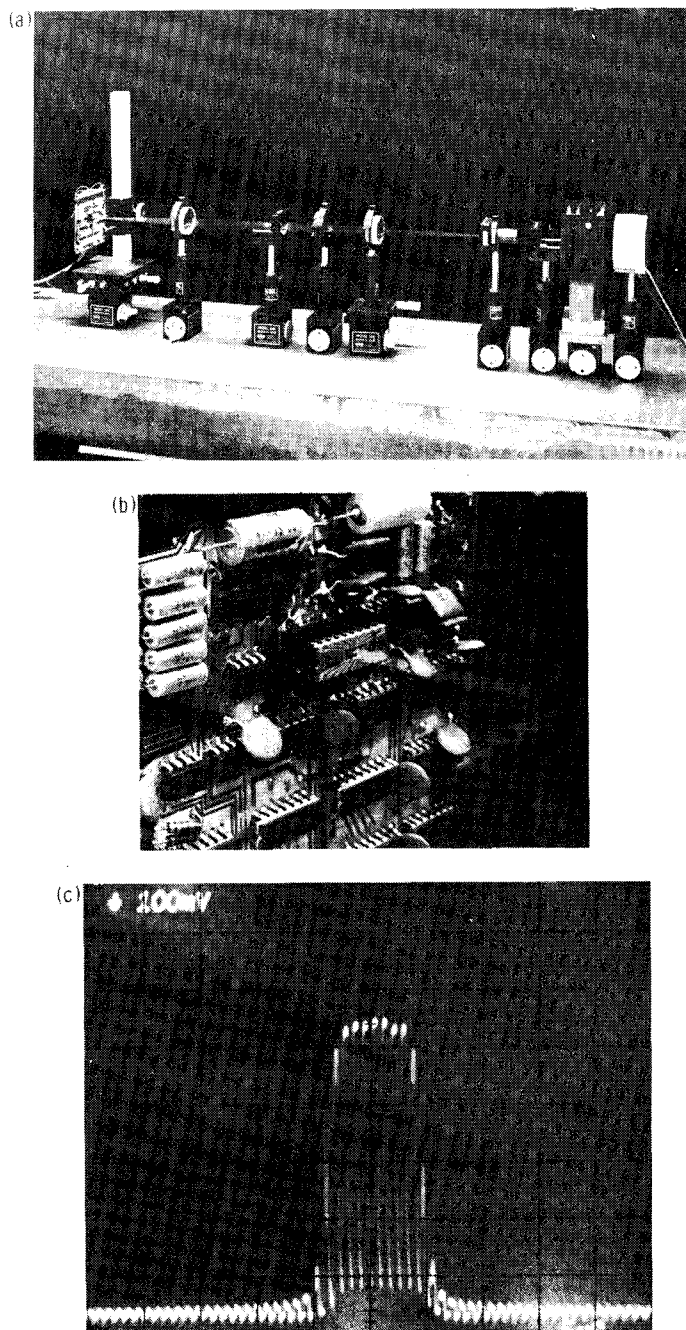


FIGURE 6. One Dimensional Sampling Technique, a) Optical Component Layout, b) CCD Linear Array Detector, c) Fourier Plane Intensity Profile Observed With Slit Function Illumination.

some of the advantages and disadvantages of each detector type, are discussed below.

LINEAR DIODE ARRAYS

The apparatus illustrated in Figure 6a employs a charge coupled device (CCD) linear array to detect light scattered from the sample. This detector shown in Figure 6b consists of a row of photo-sensitive elements on a single substrate that convert light to stored electrical charge. The charge stored in an individual element is propor-

tional to the total photon flux incident on the detector element. These stored charges are then serially shifted out of the array and detected to produce the intensity profile display in Fig. 6c. Relatively high resolution detection in the image plane is possible since the individual elements of the sensor are placed on $13\mu\text{m}$ centers. The use of this type of detector reduces the need for careful alignment of the sensing components and is easily interfaced to a rapid data acquisition system. The CCD arrays also have the desirable properties of being rugged and compact.

The principal disadvantage of this type of array is that the dynamic range of the device is limited by its intrinsic electronic properties to about 500:1. However, the rate at which the charge packets are shifted out of the array can be used to adjust the operating range of the device. Lower clock frequencies allow longer charge accumulation and are used for low illumination levels. At high photon fluxes, excess charge accumulation may occur and result in charge spillage into adjacent elements which affects the output linearity of the device as shown in Fig. 7b.

PHOTOGRAPHIC FILM

Another technique that can be implemented to record the spatial intensity distribution in the Fourier plane is photographic emulsion. This detector produces a high resolution image that can be used to determine the specular properties of materials. Quantitative information may be obtained by using a densitometer to determine actual spatial intensity levels. However, care must be taken to account for the non-linear behavior of the recording film.

Photographic techniques, although potentially easy and inexpensive to implement, have the drawback of limited dynamic range. They are usually also labor intensive. The dynamic range limitations may be overcome by successive exposures for varying times to observe information in both the center and the tails of the distribution, however, this serves to compound the problem of time consuming data reduction. A number of photographs of the scattering distribution caused by various materials are shown in Fig. 5. These pictures were obtained by placing a diffusing screen in the Fourier image plane of the instrument and photographing the observed distribution.

TWO DIMENSIONAL DIODE ARRAYS

Although valuable spatial information is obtained with photographic methods, real time data acquisition is not possible. However, this objection can be overcome by using a CID (charge injection device) array placed in the Fourier transform plane. The CID array operates in a fashion similar to the CCD array discussed previously. The CID array used in our experiment consists of a square matrix of 16,384 detector elements (pixels) as shown in Fig. 7a. Each element is roughly $46\mu\text{m}$ on a side. With proper electronic interfacing the intensity distribution on the array face may be viewed using a CRT monitor. Each pixel acts as an individual silicon detector and is displayed as such. Alignment of the two dimensional array is less critical than in the case of the linear array. With the

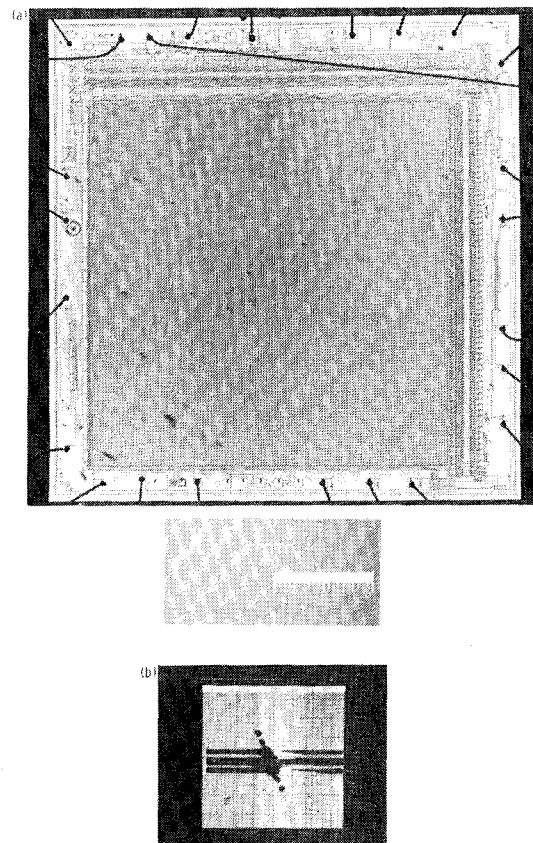


FIGURE 7. a) Two Dimensional CID Array Detector With 16,384 Element Resolution.
b) Charge Spillage Resulting From High Illumination Level.

proper selection of optical components much of the useable information in the Fourier plane can be viewed simultaneously on a real time basis. Because of the fixed geometry encountered when using a solid state array, constant scatter angle rings may be drawn on the viewing screen as mentioned earlier allowing the user to interpret directly the scattered intensity in terms of the scattering angle.

The output of our CID array may be displayed on a CRT in a threshold mode. The threshold mode displays each pixel location as either on or off, depending on the intensity of the illumination at the pixel location. This format is valuable in displaying the general spatial information but is not readily converted to quantitative results.

In addition, gray scale information is available that quantizes the pixel illumination into 256 discrete levels. With these electrical signals a microprocessor based system can be developed to display the scattering distribution in the Fourier plane in topographical or isometric formats. From this contour mapping, useful engineering informa-

tion regarding the scattering properties of the material may be derived.

A system employing one of these CID arrays would be relatively insensitive to alignment and environmental surroundings. The array appears to be well suited for a portable field instrument to monitor mirror specularity.

The CID array exhibits a limited dynamic range (500:1) and relatively low sensitivity making observation of the entire Fourier plane difficult. Overexposure of the array results in saturation of the pixel elements and subsequent charge spillage in the direction of scan, causing loss of information as shown in Fig. 7b. A method employed to prevent charge spillage in this type of instrument uses a spatial filter in the transform plane. This filter consists of an opaque block centered over the diffraction limited spot as discussed earlier. Since the array exhibits a relatively narrow dynamic range the beam block must be quite large. This makes the device unsuitable for use with highly specular materials such as most commercial glasses.

Fig. 8 shows the Fourier image plane intensity distribution exhibited by several materials as displayed using a CID array in the threshold mode. These results were obtained using the beam block discussed previously. These materials generally display anisotropic behavior. Note that one of the materials also exhibits the effects of a periodic scattering surface.

This instrument may also be used as a screening or ranking tool in the threshold mode by electronically counting the number of pixels illuminated by the scattered light. Ranking or screening of materials may then be accomplished by noting that the more light the material scatters, the higher will be the resultant pixel count.

SPATIAL RESPONSE LIMITATIONS

It should be mentioned that there are basic limitations on the Fourier transform examination imposed by the physical dimensions of the system and the detectors described above. If the samples exhibited periodic structure, a scattering angle could be related directly to the structure spacing

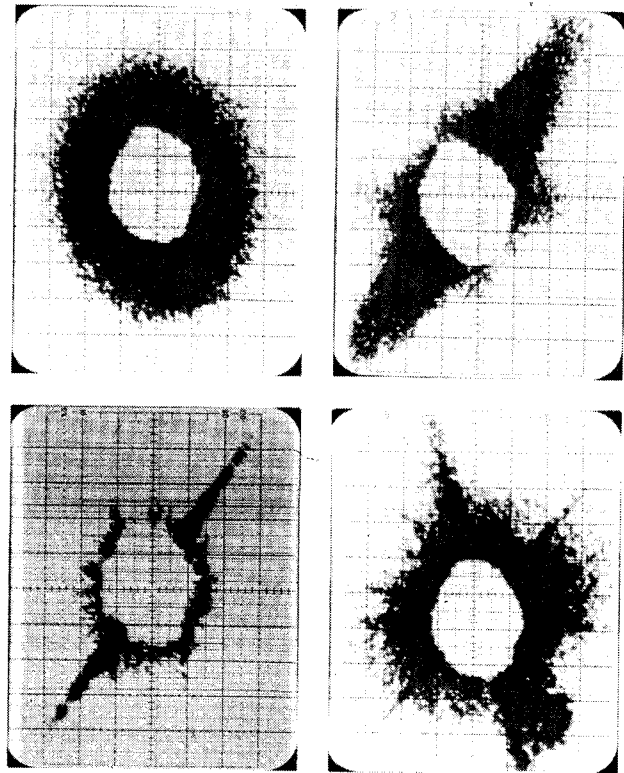


FIGURE 8. Fourier Plane Distribution Observed For Several Common Materials. Distribution Was Recorded by Placing CID Array in Fourier Plane and Photographing Corresponding Oscilloscope Display.

using diffraction theory. For a one dimensional grid, the first diffraction maximum occurs at an angle which satisfies

$$\sin \theta = \pm \lambda/h \quad (9)$$

where h is the characteristic spacing. This equation and the physical dimensions of the system elements can be used to predict the resolution limits of the system as shown in Table 1. The limiting factors at each end of the spatial frequency bandwidth are also shown.

TABLE 1: Experimental Optical System Constraints

	1-D Array (256 element)	2-D Array (128 x 128 element)	Photographic Film	
			Kodak 649-F	Kodak Plus-X
Angular Acceptance Range (mr)	0.064 - 8.19	0.22 - 14.4	0.0025 - 163	0.05 - 163
Limiting Factor (low angle)	Pixel Spacing	Pixel Spacing	Beam Size	Film Resolution
(high angle)	Array Dimension	Array Dimension	Lens Diameter	Lens Diameter
Spatial Frequency Bandwidth (lines/mm)	0.101 - 12.9	0.356 - 22.8	0.063 - 256	0.081 - 256
Sample Feature Dimensional range (mils.)	3.04 - 389	1.73 - 111	0.154 - 625	0.154 - 486

SUMMARY

Examination of the Fourier transform of the reflectance function of optical materials was shown to be a powerful technique for evaluating the specular characteristics of solar mirrors. Several methods for quantizing the intensity distribution of the light scattered into the Fourier plane were discussed. We have demonstrated that the information obtained by a two dimensional examination can be highly anisotropic. The use of a two dimensional image analysis device such as a solid state array has definite advantages over many other detection schemes. However, in their present state of development, the arrays are not suitable for performing measurements on highly specular materials, and other detection schemes must be implemented.

ACKNOWLEDGEMENTS

The authors would like to acknowledge B. P. Hildebrand and F. R. Reich for their helpful suggestions and contributions.

HIGH TEMPERATURE MATERIALS STUDY

Larryl Matthews received his masters in Mechanical Engineering from New Mexico State University in 1975. Since then he has worked with Sandia Laboratories in Albuquerque at the Solar Thermal Test Facility.

George P. Mulholland received his Ph.D. from Oklahoma State University in 1965. He worked at the Jet Propulsion Lab in Pasadena, California before becoming a professor of Mechanical Engineering at New Mexico State University. This study was conducted while Professor Mulholland was on sabbatical with Sandia Laboratories in 1977 and 1978.

ABSTRACT

This paper reports results from testing high temperature insulating materials in a highly concentrated solar furnace. These materials were subjected to as high as a 3750 kw/m^2 flux density.

The objective was to determine the flux density at which these materials would fail. The resulting information will be used for personnel and equipment protection at the Solar Thermal Test Facility in Albuquerque, New Mexico.

Many of the results were surprising and unexpected. Detail will be given on these results.

INTRODUCTION

With the coming of high concentrating solar facilities, the need for testing of high temperature materials became clear.

To help fill the void of information in this area several materials were tested. These materials were tested for failure versus flux density. Interesting and somewhat surprising results were found.

Testing was conducted at the White Sands Solar Furnace (WSSF) (1).

The information gained from these tests is being used to design thermal shielding for personnel, equipment, and experiments to be tested at the Solar Thermal Test Facility (STTF) in Albuquerque, New Mexico (2). This facility is operated for the Department of Energy (DOE) by Sandia Laboratories. Refer to Figure 1.

EXPERIMENTAL METHOD

Table 1 lists the materials tested and their corresponding melting temperatures.

The WSSF is capable of obtaining a flux density close to 4000 kw/m^2 . Figure 2 is a

diagram of the facility showing the major components. Control of flux density in the experiment plane is achieved by opening the attenuator to a position which gives the desired value as shown by a circular foil heat flux gage. The corresponding solar image size is 10.16cm in diameter.

The materials were tested using a 5.08cm diameter image. This reduced image was achieved with a water cooled stop. Refer to Figure 3.

Each material was subjected to low flux densities (approximately 500 kw/m^2) initially and then additional flux density was applied in steps of 250 kw/m^2 until failure. Measurement of each flux density level was obtained with a circular foil heat flux gage.

Whenever possible, thermocouples were used to determine when steady state was achieved. Sheathed Chromel-Alumel thermocouples were placed on the back of materials A2, A4, Z1, and Z2. An optical infrared thermometer was used to monitor surface temperatures.

RESULTS

Several interesting results were obtained from the testing.

These results are summarized in table 2. In general, the capability of these materials to withstand high concentrations of solar energy is not as strongly dependent on melting temperature as first believed.

Basically all the alumina-silica board materials melted at the same flux density levels. It was also noticed that extra thickness does not appreciably add to the time for melt through. A 1.91cm piece of material A2 melted through in 45 seconds whereas a 3.82cm piece melted through in 54 seconds. Once the mechanism for melting begins the time for melt through is short. The bricks are good materials for withstanding medium to high concentrations of solar energy. This appears to be due to the high density of the bricks. The best material tested is the zirconia board. The flux density handling capability of this board is considerably higher than any other material.

Before testing began manufacturers data was obtained for each material. None of this data was obtained using the solar spectrum. No data was given for failure versus flux density. The data contained information on melting temperature and thermal conductivity. It was soon realized that this information was of little use when using the solar spectrum.

The first clue came in the first tests using material Al. When the solar energy struck the material it was evident that some of the energy was passing through. This was first seen at low material temperatures ruling out the possibility of the visible energy being emission. It was then realized that sheathed thermocouples must be used for the experiments. To test the effects of sheathed versus non-sheathed thermocouples two holes were placed in the side of the material approximately 1.5cm from the front surface and terminating in the center of the material. One sheathed and one non-sheathed thermocouple were placed side by side in the holes. The material was then subjected to a 250 kw/m² flux density. At steady state the sheathed thermocouple read 121.1°C and the non-sheathed thermocouple read 171.1°C. This further confirmed the idea that energy was passing through the material. This has several implications. First, the thermal conductivity must be an effective thermal conductivity and dependent on the spectrum used. Second, the temperature of the material will be dependent not only on conductivity and surface radiation properties but also on internal radiation. Third, the interior interface boundary condition for a sandwich configuration of materials will be a function of radiation and conduction rather than just conduction properties. Therefore, it was deemed necessary to study the materials in more detail.

An analytical study was performed on these materials. The numbers that result cannot be taken as absolute. This is because thermophysical data is insufficient on these materials. The analysis helps explain the material failure mechanisms. In general, the results show that failure can occur before it is expected because the highest temperature is not an exterior node but an interior node.

STATEMENT OF EQUATIONS

$$\rho V C_p \frac{\partial T(x,t)}{\partial t} = k \frac{\partial^2 T(x,t)}{\partial x^2} - \frac{dI(x)}{dx}$$

assume

$$I(x) = I_1(o) (1 - \rho_r) e^{-\mu x} \quad (\text{Beer's Absorption})$$

where

T - temperature

t - time

k - thermal conductivity

ρ - density

x - distance

I(x) - beam strength @x

$I_1(o)$ - power/unit area striking surface

μ - absorption coefficient

ρ_r - reflectivity

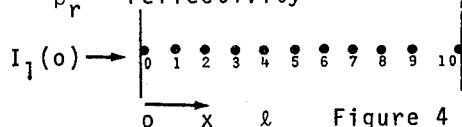


Figure 4
Nodal Representation

Boundary Conditions, T(x,t):

$$1. \quad \rho \frac{\Delta x}{2} C_p \frac{\partial T(o,t)}{\partial t} = (1 - \rho_r) \left[I_1(o) (1 - e^{-\mu \frac{\Delta x}{2}}) \right] + k \frac{\partial T(o,t)}{\partial x} - h(T(o,t) - T_a) - \sigma \epsilon (T^4(o,t) - T_a^4)$$

$$2. \quad \rho \frac{\Delta x}{2} C_p \frac{\partial T(l,t)}{\partial t} = (1 - \rho_r) I_1(o) \left[e^{-\mu \frac{19 \Delta x}{2}} - e^{-\mu \frac{20 \Delta x}{2}} \right] - k \frac{\partial T(l,t)}{\partial x} - h(T(l,t) - T_a) - \sigma \epsilon (T^4(l,t) - T_a^4)$$

Initial Condition, T(x,t):

$$1. \quad T(x,0) = T_o$$

These equations were written for an HP9825A.

STABILITY EXAMINATION

$$\frac{T(o,t+\Delta t) - T(o,t)}{\Delta t} = \frac{2}{\rho \Delta x C_p} \left\{ (1 - \rho_r) I_1(o) (1 - e^{-\mu \frac{\Delta x}{2}}) + k \frac{T(o+\Delta x,t) - T(o,t)}{\Delta x} - h(T(o,t) - T_a) - \sigma \epsilon (T^4(o,t) - T_a^4) \right\}$$

or

$$T(o,t+\Delta t) = T(o,t) + \left\{ \Gamma + \frac{k}{\Delta x} (T(o+\Delta x,t) - T(o,t)) - h(T(o,t) - T_a) - \sigma \epsilon (T^4(o,t) - T_a^4) \right\}$$

where

$$\theta = \frac{2 \Delta t}{\rho \Delta x C_p}, \quad \Gamma = (1 - \rho_r) I_1(o) \left[1 - e^{-\mu \frac{\Delta x}{2}} \right]$$

Rearranging

$$T(o,t+\Delta t) = \theta \left\{ \Gamma + \frac{k}{\Delta x} T(o+\Delta x,t) + h T_a + \sigma \epsilon (T(o,t) + T_w) (T^2(o,t) - T_a^2) T_a - \left[\frac{k}{\Delta x} - \frac{1}{\theta} + h + \sigma \epsilon (T(o,t) + T_a) (T^2(o,t) + T_a^2) \right] T(o,t) \right\}$$

and

$$\infty > \frac{k}{\Delta x} - \frac{1}{\theta} + h + \sigma \epsilon (T(o,t) + T_a) (T^2(o,t) + T_a^2) \geq 0$$

or

$$\infty > \frac{1}{\theta} \geq \frac{k}{\Delta x} + h + \sigma \epsilon (T(o,t) + T_a) (T^2(o,t) + T_a^2)$$

or

$$0 < \theta \leq \frac{1}{\frac{k}{\Delta x} + h + \sigma \epsilon (T(o,t) + T_a) (T^2(o,t) + T_a^2)}$$

or

$$0 < \Delta t \leq \frac{\rho \Delta x C_p}{2 \left(\frac{k}{\Delta x} + h + \sigma \epsilon (T(o,t) + T_a) (T^2(o,t) + T_a^2) \right)}$$

assume:

$$\rho = 5800 \frac{\text{kg}}{\text{m}^3}$$

$$\Delta x = .00127 \text{m}$$

$$C_p = .0023 \frac{\text{kw}}{\text{kg} \cdot ^\circ \text{K}}$$

$$k = .0017 \frac{\text{kw}}{\text{m} \cdot ^\circ \text{K}}$$

$$h = .057 \frac{\text{kw}}{\text{m}^2 \cdot ^\circ \text{K}}$$

$$T_a = 300 \text{K}$$

$$T(o,t) = 2000^\circ \text{K}$$

$$\sigma = 5.729 \times 10^{-11} \frac{\text{kw}}{\text{m}^2 \cdot ^\circ \text{K}^4}$$

$$\epsilon = .3$$

or

$$\Delta t \leq 0.0005 \text{hr}$$

Since the Δt given above is an approximation to the actual stability, a Δt of .0001 hr will be used.

NOTE: I checked this stability criteria on the HP 9825A and obtained excellent results.

$\Delta t = .0005$ hr; unstable, program bombs

$\Delta t = .0004$ hr; stable, program runs

These results are very encouraging.

THERMOPHYSICAL PROPERTIES

The largest unknowns in the equations are the thermophysical properties. It is difficult to find these properties as a function of temperature. The following is a list of references used.

Thermal Conductivity:

Thermal Conductivity, Nonmetallic Solids by U. S. Touloukian, et. al.

The Zirconium dioxide (Zirconia) and Yttrium oxide table on page 451 was used for a curve fit. This table gives good information vs. temperature.

Specific Heat:

Specific Heat, Nonmetallic Solids by Y. S. Touloukian, et. al.

The Zirconium dioxide (Zirconia) table on page 295 was used for a curve fit. This table does not have Yttria stabilized zirconia.

Reflectivity:

Thermal Radiative Properties, Non-metallic Solids by U. S. Touloukian, et. al.

The stabilized Zirconium dioxide (zirconia) table on page 541 was used. These tables are not given vs. temperature, therefore, reflectivity used in the program was only a rough approximation.

Emissivity:

Same source as above.

Only one value for hemispherical total emittance of Zirconium dioxide was given. At 2000°K the value is 0.31.

The film coefficient is also a common source of error in heat transfer calculations.

The Handbook of Heat Transfer edited by Rohsenow and Hartnett was used for the film coefficient.

Resorting to a crude rule of thumb, a turbulent boundary layer is assumed to occur for $Pr Gr > 10^9$. This is for free convection.

The handbook suggests using the following equation for air and laminar free convection:

$$Nu = .421 (Pr^{1/4} Gr^{1/4})^{1/4}$$

at 2000°K

$$Pr = .7$$

$$Gr = \frac{1.27 \times 10^8 (.00087)(1700)(.1016)^3}{(.66667)^2}$$

$PrGr < 10^9$

Therefore the above equation for a laminar free convection boundary layer should be used.

The results show that a somewhat surprising temperature profile exists in the material. Figure 5 is a listing of three runs in which the role of extinction was varied. In figure 5a no transmission was considered. All of the energy was either reflected or absorbed in the first node. As expected the first node was the hottest and the last node the coolest. Figure 5b includes transmission through the half inch material

but at a low level. This temperature distribution shows the effects of transmission. The highest temperature occurs in the fourth node and not on the first node. This occurs because of a trap effect. The interior nodes cannot lose heat by convection and therefore experience fewer losses than the exterior nodes. The temperature is also higher at the fourth node than at any position in figure 5a. This shows that failure can occur before it is expected if only the surface temperature is monitored. Figure 5c is an example of the same problem as in 5b but with more energy passing through the material (which means a correspondingly lower absorption coefficient). The same type of profile is observed as in 5b, however the peak temperature has shifted and the exterior nodal temperatures have changed somewhat. However, the same type of profile still exists.

Time	0.10000	Time	0.10000
T0	1778.29749	T0	1557.73335
T1	1711.07371	T1	1741.66883
T2	1644.40400	T2	1840.15731
T3	1578.42397	T3	1877.29858
T4	1513.24746	T4	1870.57758
T5	1448.96308	T5	1832.66438
T6	1385.63155	T6	1772.71888
T7	1323.28390	T7	1697.33719
T8	1261.92049	T8	1611.23896
T9	1201.51109	T9	1517.76760
T10	1141.99581	T10	1419.25541
Flux Density	2000.00000	Flux Density	2000.00000
Film Coef.	0.15799	Film Coef.	0.17298
Reflectivity	0.75000	Reflectivity	0.75000
Emissivity	0.31000	Emissivity	0.31000
Absorption Coef.	5800.00000	Absorption Coef.	253.45479
Density	5800.00000	Density	5800.00000
Thickness	0.01270	Thickness	0.01270
Figure 5a	No Transmission	Figure 5b	.25% Transmission
Time	0.10000	Flux Density	2000.00000
T0	1495.56568	Film Coef.	0.17620
T1	1674.20931	Reflectivity	0.75000
T2	1781.17361	Emissivity	0.31000
T3	1832.95111	Absorption Coef.	198.87627
T4	1842.35572	Density	5800.00000
T5	1819.32712	Thickness	0.01270
T6	1771.55610		
T7	1704.97132		
T8	1624.11887		
T9	1532.45916		
T10	1432.59975		

Figure 5c
.5% Transmission

CONCLUSIONS

Referring again to Table 2, these tests demonstrate the effects of the solar spectrum on high temperature materials. As shown the alumina-silica board materials all fail at approximately the same flux density regardless of manufacturer stated melting temperature. Therefore, in choosing such a material the workability and structural characteristics should be considered as well as cost. The zirconia board (Z2) is an excellent choice in high flux density regions. This material is expensive and not a good engineering material as far as structural strength is concerned, but its excellent properties in high flux densities out weigh the problems. The refractory bricks are very good materials in moderately high flux density regions. This appear to be true due to their density as well as their radiation properties.

The analytical study shows some very interesting results. The resulting temperature profile was not expected when the study began. This warrants further study, both analytical and experimental. This is planned as a future study.

In general the lesson learned is that materials to be used with solar energy must be tested in such an environment. Assuming that past results obtained in a different spectral environment hold in a solar environment can lead to erroneous results.

It is hoped that this study will aid in choosing materials for use with high concentrated solar energy and in making the engineer aware of some of the pitfalls solar energy environments have in store.

References:

- (1) Hays, R., White Sands Solar Facility (WSSF): Experimenter's Guide, 1977, Nuclear Weapon Effects Branch Applied Sciences Division, Army Materiel Test and Evaluation, White Sands Missile Range, New Mexico.
- (2) Otts, J. V., Holmes, J. T., Seamons, L. O., Kuehl, D. J., Davis, D. B., Matthews, L. K., Arvizu, D. E., Darsey, D. M., Brandvold, G. E.; The USA 5MW Solar Thermal Test Facility, ISES International Congress, January, 1978.

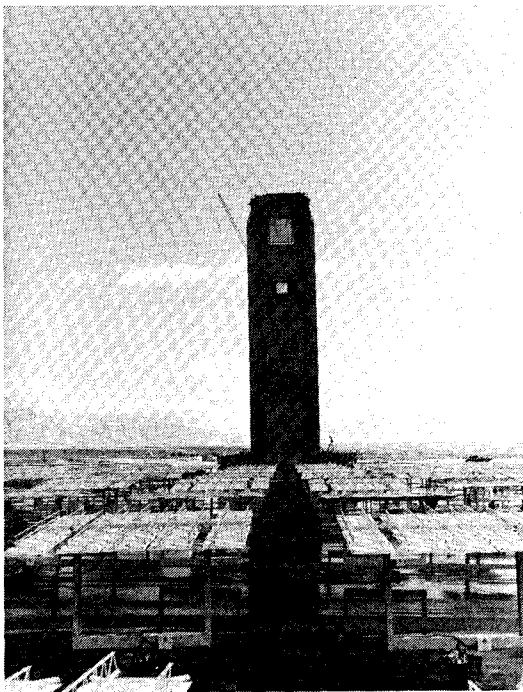


FIGURE 1.

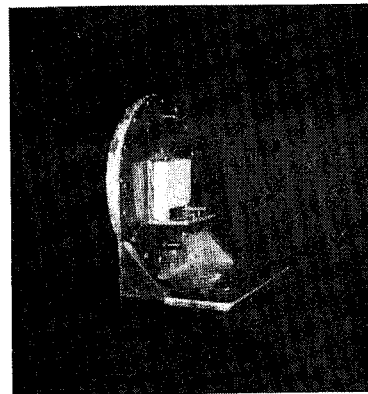


FIGURE 3. WATER COOLED STOP WITH TEST MATERIAL IN PLACE

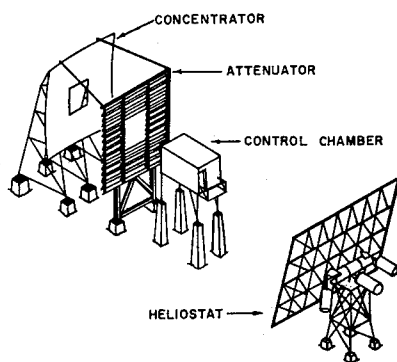


FIGURE 2. SCHEMATIC OF WSSF

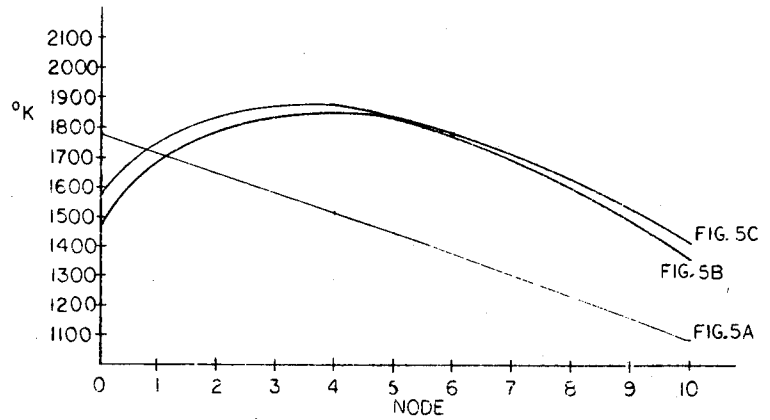


FIGURE 5D
TEMPERATURE GRAPH

TABLE 1		
Description of Material Tested		
Abbreviation	Melting Temperature (°C)	Description
A1		A common alumina-silica board with a recommended use limit of 1260°C
A2	1871	A 75% alumina-19% silica board with a recommended use limit 1650°C
A3	1871	An 85% alumina-15% silica board with a recommended use limit of 1500°C
A4	1871	A board with an alumina content in excess of 90%. The use limit is unknown
Z1	2204	A yttria stablized board consisting of 87% zirconia
Z2	2593	A yttria stablized board composed of 100% zirconia
B1	1843	An insulating firebrick composed of 76% alumina and 21% silica
B2	1916	A refractory firebrick composed of 90% alumina and 10% silica
B3	2016	A refractory firebrick composed of 99.7% alumina

TABLE 2
Results of Tests

Material	Comments
A1	This material survived 750 kw/m ² and failed at 1000 kw/m ²
A2	This material survived 750 kw/m ² and failed at 1000 kw/m ²
A3	This material survived 750 kw/m ² and failed at 1000 kw/m ²
A4	This material survived 750 kw/m ² and failed at 1000 kw/m ²
Z1	This material survived 1250 kw/m ² and failed at 1500 kw/m ²
Z2	This material could not be failed. 2 Flux densities as high as 3750 kw/m ² were used.
B1	This material failed under 5 minutes at 1000 kw/m ²
B2	This material after started to melt 3 minutes at 2000 kw/m ²
B3	This material started to melt after 4 minutes at 2500 kw/m ²

Michael Ray Jacobson, Research Associate and Director of the Measurement Laboratory at the Optical Sciences Center, received his A.B. in Physics from Harvard College in 1971. He then studied infrared astronomy at Cornell University, attaining an M.A. in 1975, and a Ph.D. in 1977 for his work on an 0.4-meter balloon-borne liquid helium-cooled telescope which discovered nine new galactic infrared sources in the summer of 1976. Dr. Jacobson is a member of the AAS, AMS, OSA and SPIE.

For a number of years, the Solar Energy Group at the University of Arizona's Optical Sciences Center has been developing and evaluating coatings for the photothermal conversion of sunlight. The Measurement Laboratory was organized to provide both diagnostic data at room temperature under normal atmosphere and durability and lifetime information under simulated operating conditions. A strong evaluation effort has been necessary, as our interest in producing a reliable and selective surface requires that we measure a number of optical and radiative properties.*

Let me place our program in perspective. The types of surfaces involved in solar energy conversion can be divided into five categories. Three are non-selective, in that their performance must be optimized only over the solar spectrum:

1. Solar absorber coatings, which must maintain a solar absorptance as close to unity, or that of a blackbody, as possible.
2. Solar transmitters, or cover plates, which must maintain the highest possible transmittance of available insolation.
3. Solar reflectors, or concentrating mirrors, which must maintain the highest possible reflectance of available insolation.

Since only one optical property is in question, the researcher is given considerable freedom to improve without tradeoffs. However, the properties of selective surfaces — heat mirrors and dark mirrors — must be optimized over both the solar spectrum and their own thermal spectrum. (See Figure 1). Heat

the solar irradiance remains.¹ Their inner layers are non-selective solar absorbers. Dark mirrors, our own research interest, have an outer layer designed to absorb as much insolation as possible, and to transmit well in the thermal infrared. The dark mirror's inner layer is a non-selective reflector. In both cases, the substrate's temperature rises until energy losses by reradiation, convection and conduction, and the removal of useful heat balances the incident flux.

Selectivity can be achieved by tailoring the intrinsic and/or structural properties of one or several materials. Of course, one would prefer a single material with the proper optical properties along with an inert, refractory character plus ease of fabrication and low cost. Some materials, such as transition-metal carbides and nitrides, come fairly close. Another approach, which provides greater selectivity, exploits the intrinsic optical properties of two materials; these tandem stacks are the subject of Figure 1. Structural properties are also important. Surface texture of the proper scale can repeatedly scatter sunlight until it is mostly absorbed while presenting a smooth, reflective surface to the longer infrared waves. Similarly, internal, or bulk, scattering of sunlight can result in selectivity. Interference effects make a critical contribution through antireflection coatings, which permit radiation to penetrate the coating. Once within, interference effects between interfaces can trap additional radiation, until it is absorbed. Actually, in many rather successful selective surfaces, many of these effects cooperate.

However, the complex structure of selective surfaces makes them vulnerable to a number of difficulties. Under operating conditions, intrinsic (molecular scale) and structural (micron scale) changes can cause an irreversible loss of selectivity. Layers can crystallize, oxidize, interreact or diffuse into each other, altering critical intrinsic properties. Among a number of possible structural changes are change of phase, exfoliation, whereby thermal mismatch or intrinsic changes cause layers to peel or flake off, and agglomeration, which refers to the formation of globs from thin films of some reflective metals. Less obvious reversible changes in just one of several layers can degrade selectivity as well.

ABSORBER-REFLECTOR TANDEM

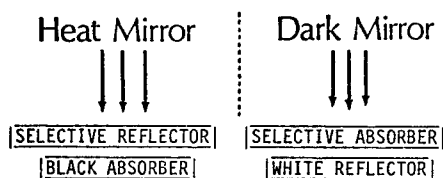


Figure 1.

mirrors have outer layers which must not only transmit the maximum amount of solar energy, but must reflect well in the thermal infrared, that is, wavelengths longward of about 3 microns, where $\approx 2\%$ of

Therefore, the value of a selective coating can be proven only through a number of measurements, which are guided by the conditions under which selectivity must be maintained. Non-normal, often hemispherical, optical properties are important because of concentrating optics and the structural properties of selective surfaces. Their measurement requires the use of an integrating sphere or equivalent arrangement in a spectrometer. The total radiative power loss from a surface requires knowledge of the hemispherical emittance, which can be measured either radiometrically or calorimetrically. The effects of high temperatures, both sustained and cycled, must be observed in order to identify irreversible changes and permanent degradation. Likewise, one must ask whether atmospheric conditions are important to the surface's lifetime. Lastly, high energy photons acting in concert with thermal excitation may contribute

to intrinsic changes in a film's optical properties. In most of these areas, the Measurement Laboratory has developed specialized instrumentation in order to support the group's work in realizing state-of-the-art dark mirror selective surfaces.

Currently, we are improving the capabilities of the Integrating Sphere Reflectometer and the High Temperature Spectrophotometer and developing a Cylindrical Vacuum Emissometer. The optical layout of the Integrating Sphere Reflectometer (ISR) is shown in Figure 2. It will operate in the indirect, or hemispherical-directional mode, with the sample mounted

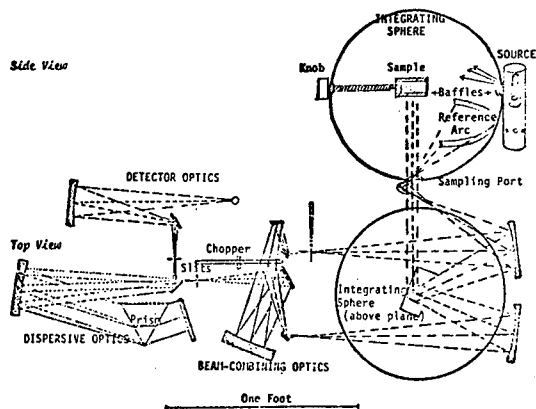


Figure 2: Schematic diagram of revised diffuse reflectometer showing integrating sphere mounted on modified Perkin-Elmer Model 21 spectrometer.

in the center of the twelve inch diameter sphere. The sample holder is mounted on an arm that extends through a side port; the assembly can be rotated to present various angles of exitence to the sampling port at the sphere's base. A suitable reference is substituted in the holder and measured before and after the sample measurement. From the port on the opposite side, a source irradiates the sphere, while a mask on the diffusing window and a baffle on that side of the sample holder prevent "first bounce" radiation from falling on the sample or reference arc on the sphere. Mirrors below the sampling port direct beams from the sample in the sphere center and from an arc on the sphere wall to the monochromator optics: a modified Perkin-Elmer dual-beam spectrophotometer used in reverse. The major changes in the spectrophotometer are a three-phase in place of a two-phase chopper and a two-color (silicon-photodiode — lead sulfide) detector at the original source position. Presently, the system is equipped for operation from 0.3 to 2.5 microns, with a tungsten-halogen source, a barium sulfate sphere coating, a silica prism, and the two-color detector.

Our data-taking system, which replaces a pair of lock-in amplifiers, is shown in Figure 3. The three-phase chopper provides a background level (Beam C) for both the sample (Beam A) and the reference (Beam B). Phase synchronization (chopper phase signals) are produced by LED/phototransistor pairs. One of the preamplified signals from the two-color detector is selected; the phase synchronization signals trigger gates and a crystal clock, which control, in turn, the three sample-and-hold lines, one for each chopper phase. The three analog signals are sequentially

digitized and sent on to a selectable display and a microcomputer. The microcomputer takes data at a

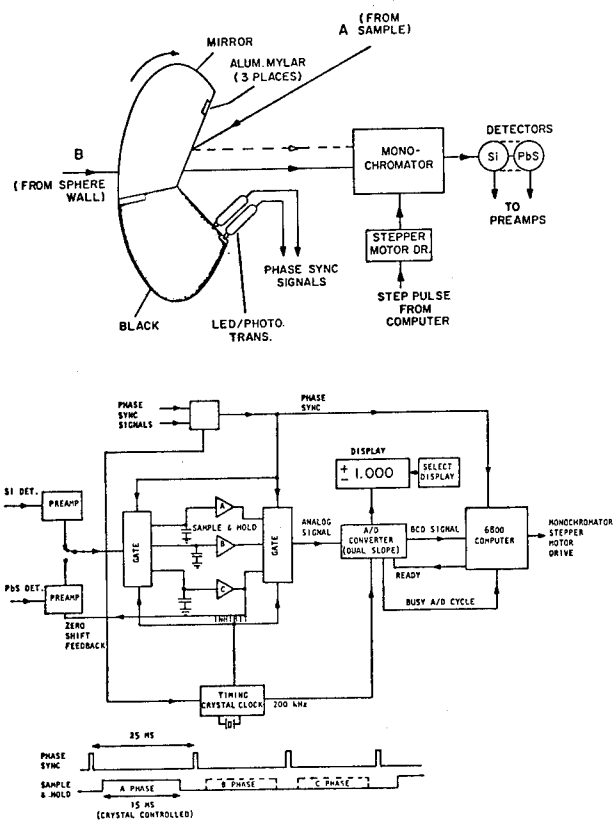


Figure 3: Integrating Sphere. Sample and Hold Electronics.

particular wavelength until the desired signal-to-noise level is reached and then advances the monochromator stepper motor. Data reduction on the complete spectrum can then proceed on this or a larger computer. Eventually, our other instruments will be interfaced with the microcomputer for both control and data reduction.

The layout of the High Temperature Spectrophotometer (HTS) appears in Figure 4. A simple double-beam arrangement begins with a pair of mirrors which image the source on a pair of choppers which rotate at different frequencies; the chopper frequencies go to the lock-in amplifiers which distinguish the beams. When measuring reflectance, the transmittance cell, currently under construction, is left empty, and the two beams are directed to the heated sample and to a room temperature reference, respectively. Further optics recombine the beams and pass them to a Leiss monochromator, equipped with NaCl prisms for IR operation. For transmittance measurements, substrates identical except for the thin film to be measured intercept the beams in the transmittance cell; the reflectance cell remains unheated and contains a reference mirror.

Since the monochromator operates from 0.38 to 15 microns, a tungsten-halogen lamp source and a silicon photodiode are not adequate for the whole range. We

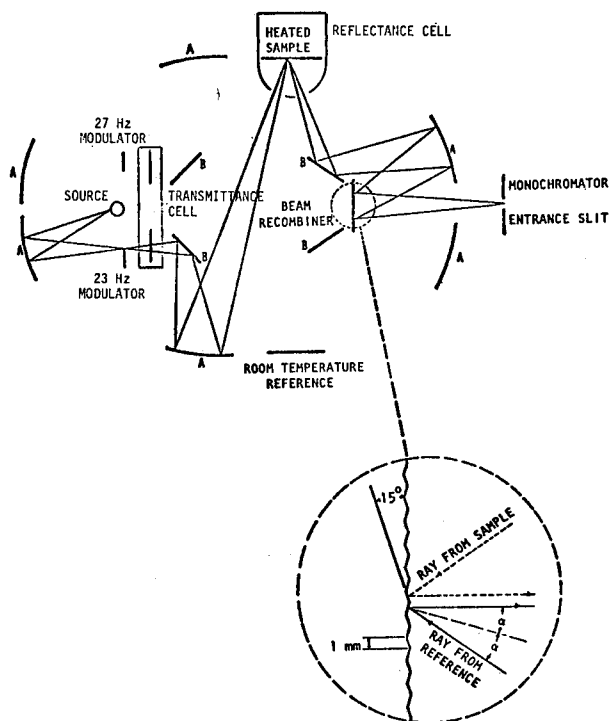


Figure 4: Schematic diagram of optical system for the high temperature reflectometer. Optical elements labeled A are concave mirrors, while those marked B are plane mirrors. Except for the inset which shows the detail of the beam combiner, the light path is drawn for only one channel.

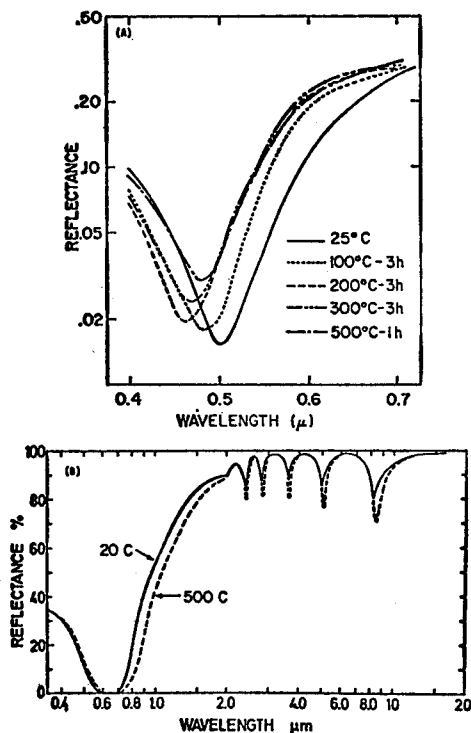


Figure 5: (A) Reflectance of red-colored stainless steel during a single heating sequence in the High Temperature Spectrophotometer. (B) Change in reflectance of a 1.75 μ thick amorphous silicon-on-silver selective surface due to heating from 20°C to 500°C in the HTS.

can move a Globar source and Golay cell detector into position for the infrared measurements. Data is presently acquired with the aid of two lock-in amplifiers, a ratiometer, and a strip chart recorder, but we intend to develop a microcomputer interface similar to that of the ISR.

Some recent measurements made with the HTS by Björn Karlsson are shown in Figure 5. Red-colored stainless steel, one of many colors made by immersing the metal in a hot aqueous solution of chromic and sulfuric acid and hardening by a cathodic treatment, is gradually heated. At first, the interference effects that give the material its red color and its selectivity move to shorter wavelengths as the film is dehydrated, causing its optical thickness to decrease. Then, oxidation thickens the film as heating continues, reversing the first trend. While the oxidation process is irreversible, and would be detectable after the sample cools to room temperature, the dehydration process may be reversible under humid conditions. If so, room temperature measurements after heating would not detect this change. Another example of a reversible effect is shown in Fig. 5(B). Here, a film of amorphous silicon deposited by chemical vapor deposition on a silver reflector is heated to 500°C in the HTS. The absorption edge shifts to longer wavelengths due to phonon assisted transitions, while the interference fringes deepen due to increased free carrier absorption. The first effect increases solar absorption, while the second strengthens thermal emission.

A third instrument, the Cylindrical Vacuum Emisometer (CVE), is under development along the lines of an apparatus at Dr. Richard Pettit's laboratory at Sandia.² Designed to measure the total hemispherical emittance calorimetrically, the sample will either be heated conductively by resistance coils or radiatively by sun-simulating lamps projected through a small window. This device, along with our life cycle furnaces, will allow us to closely simulate the operating conditions for selective surfaces. In addition, the calorimetric, hemispherical determination of emittance with the CVE will check the spectral values of emittance, derived from reflectance, gathered from the ISR and HTS.

Ultimately, a methodical standardized measurement procedure will be necessary to compare different selective surfaces, both for their optical properties and for their ability to maintain them under harsh conditions. Figure 6 shows a proposed measurement sequence for evaluating selective surfaces which employs the instrumentation I have described, along with commercially available visible and infrared spectrophotometers. The first part of the procedure is non-destructive and largely diagnostic. Baseline data are acquired from reflectance and transmittance measurements and microphotography. Important measurements of hemispherical-directional reflectance follow. Then, potentially destructive tests on at least four nominally identical samples are performed, beginning with high-temperature observations of optical properties with the HTS and physical degradation with a heated-stage microscope. The latter, which we are acquiring at present, can be taken as high as 1350°C to simulate stagnation temperatures. At the next stage, samples are subjected to simulated operating conditions in the emissometer and in the life cycle furnaces, where temperature cycles under controlled atmospheres or roughing pump vacuum are per-

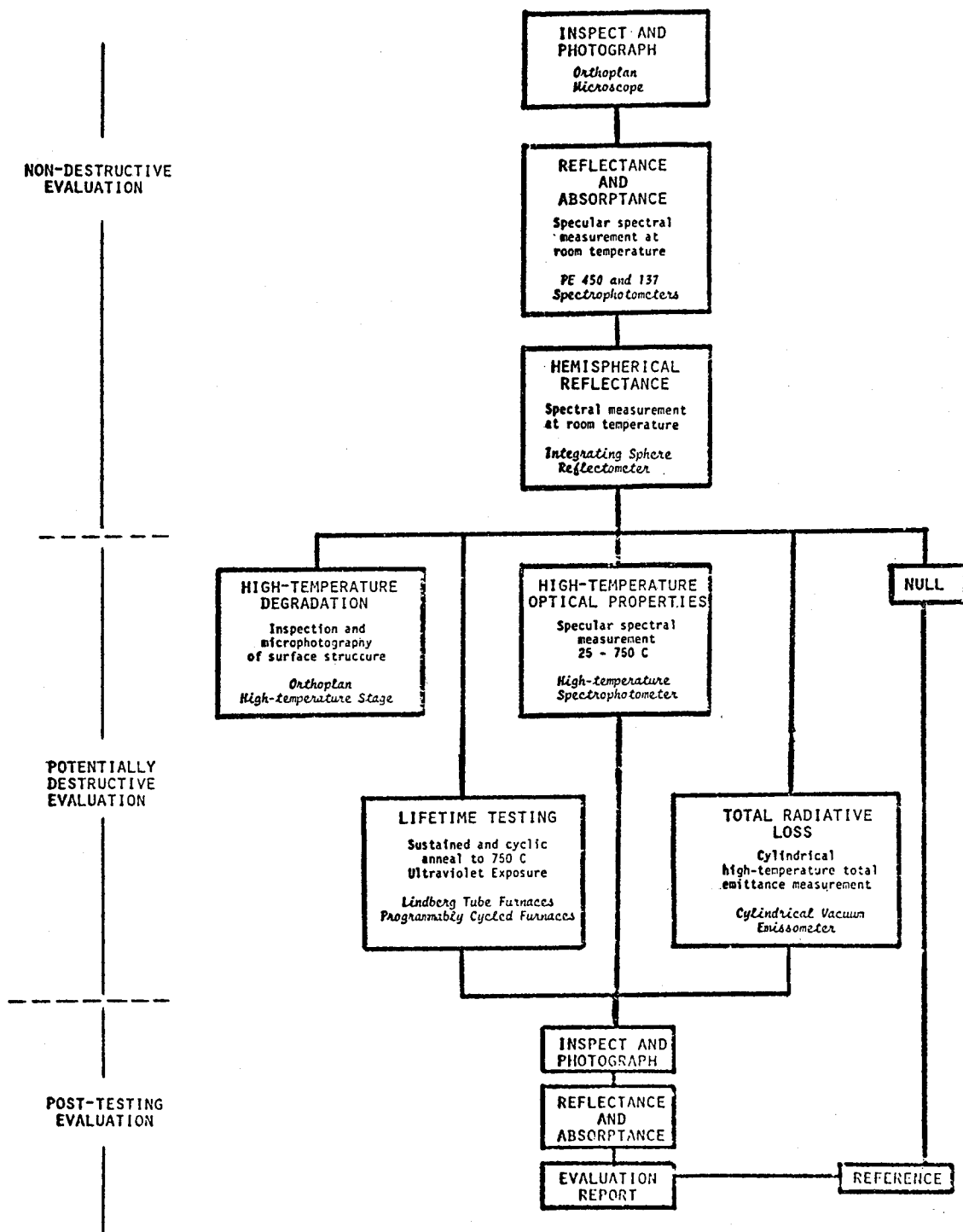


Figure 6: Plan for Selective Surface Evaluation.

formed. Eventually, we plan to include ultraviolet exposure at this point. At the last stage, we intercompare the four or more test samples with the null sample.

The optical and radiative properties of materials to be used under the operating conditions in solar energy converters are poorly known at present. Implicit in our measurement program is the intention to measure not only already developed surfaces, but to guide that development process through diagnostic measurements. We hope to make the Measurement Laboratory's facilities and personnel partially open to the solar materials community if sufficient resources can be found.

* This work has been supported by the following contracts:

"Chemical Vapor Deposition Research for Fabrication of Solar Energy Converters,"
NSF/RANN # AER72-03566 A02.

"High Temperature Stabilization of Thin Metal Films,"
NSF/Material Science Division # DMR/75-01267.

"Chemical Vapor Deposition of Refractory-Metal Reflectors for Spectrally Selective Solar Absorbers,"
DOE/Division of Solar Energy EY-76-S-04-3709.

"Chemical Vapor Deposition of Amorphous Silicon for Photothermal Solar Energy Converters,"
DOE/Division of Material Sciences EY-78-S-02-4399.

¹ ASTM, Solar Constant and Air Mass Zero Solar Spectral Irradiance, ASTM Designation E490-73a.

² R.B. Pettit, Total Hemispherical Emittance Measurement Apparatus for Solar Selective Coatings, Sandia Laboratories Energy Report SAND-75-0079, June 1975.

PARAMETERS, MEASUREMENT AND CRITERIA OF SOLAR MATERIALS TESTING

J.E. Gilligan, J.E. Brzuskiwicz and J.M. Madigan

IIT Research Institute, Chicago, Illinois

AUTHORS' BIOGRAPHY

Mr. Gilligan is a Senior Research Engineer and the Group Leader of the Energy Control Technology Group at IIT Research Institute (IITRI). He is a 1952 graduate of Gonzaga University with a B.S. degree in Chemical Engineering, and has taken graduate work at UCLA and IIT.

Before coming to IITRI in 1964, Mr. Gilligan was employed by the General Electric Co. at the Hanford Atomic Products operation, served two years as a Scientist in the U.S. Army Chemical Corps., and worked for Atomics International as a reactor engineer. In 1960 Mr. Gilligan worked in the Lockheed Research Labs, specializing in spacecraft thermal control materials R&D. He has continued his interest in this area at IITRI and has been involved in numerous space and defense materials programs. His activities over the last four years have centered on the characterization of materials for solar energy applications.

Mr. Brzuskiwicz is a Technical Assistant and is a 1977 graduate in Chemistry of the University of Illinois - Chicago Circle Campus. He has been involved in several materials R&D programs and is working on a current solar materials R&D program.

Mr. Madigan is an undergraduate student in Chemical Engineering at the University of Illinois - Chicago Circle Campus. He is an Assistant Experimentalist and is involved in the optical characterization of materials for solar energy and other applications.

INTRODUCTION

Of central importance in the testing of materials for solar energy applications are the associated optical property measurements. In this paper, we will address the key questions of which optical measurements are appropriate to a variety of applications, the parameters of these measurements, and some of the evaluation criteria. The solar community in general has suffered from a lack of knowledge of the various types of optical measurements and, more importantly, from not understanding their significance. Primarily, our discussions will relate to the geometries of optical measurements and to their relevance to Solar Utilization (SU) applications.

TECHNICAL DISCUSSIONS

Basic Optical Relationships

The relationship shown in Eq. 1 forms the foundation for optical measurements:

$$\alpha + \rho + \tau = 1.0 \text{ (or 100\%);} \quad (1)$$

it states that the sum of the fractions of incident radiation which are absorbed (α), reflected (ρ) and transmitted (τ) must equal unity. The relationship holds true, however, only when α , ρ , and τ are hemispherical values relating to identical wavelength regions. When the terms of Eq. 1 are unqualified*, they refer to measurements of spectral hemispherical properties. Because these terms can be used with many qualifications, they must be specified either by name or through mathematical notation. Their specifications (or parameters) include wavelength (λ), angles of incidence (θ_i) and of emergence (θ_r), divergence angle (ψ), polarization (P_{II} or P_I), and solid angles of incidence and emergence (Ω_i and Ω_r). Other specifications, such as Solar and Total, refer to integrations of spectral values over specific wavelength regions, while Normal and Hemispherical refer to two very common measurement geometries which are distinguished by the subscripts N and H, respectively.

Measurement Geometries

In SU applications the most common measurements are those made using integrating spheres in conjunction with conventional double-beam UV-Vis-NIR spectrophotometers. Four possible sample geometries are shown in Figure 1, along with the designation of the measured optical value. The diagram illustrates that in order to measure the Normal transmittance (τ_N), for example, the sample is remotely mounted such that only that component of the transmitted beam which lies within a total cone angle of approximately 5° will enter the integrating sphere; for hemispherical transmittance, it is mounted on the sphere wall such that all of the transmitted beam enters the sphere. In these cases, both τ_N and τ_H are absolute measurements, that is, they need not be referred to a measurement standard.

It is instructive to note that the τ_N geometry shown in Figure 1 is (or can be) exactly analogous and equivalent to the measurement configuration in a conventional spectrophotometer. The geometry in which the sample is center-mounted yields an absolute value of the hemispherical reflectance (ρ_H), or, in the event of a non-opaque sample, an absolute value of the quantity ($\rho_H + \tau_H$). On the other hand, wall-mounting a reflectance sample gives a relative hemispherical value of reflectance; the latter must be referred to a standard or other known reference material.

By far the most common SU-related measurements are those made to obtain $\tau_{N,S}$, $\tau_{H,S}$, ρ_S and α_S . The latter two result

*e.g., by subscripts or arguments

from convolutions of $\rho_H(\lambda)$ or $(1-\rho_H(\lambda))$, respectively, with the solar spectrum. Similarly, the normal and hemispherical transmittance spectra, $\tau_N(\lambda)$ and $\tau_H(\lambda)$ are convoluted with the solar spectrum to obtain total - in this case - solar values.

Optical measurements may also be made using Bidirectional (BD) optical equipment; the major differences between measurements made using integrating spheres and those made using BD equipment are that the possible measurement geometries are very limited (e.g., see Figure 1) in integrating spheres while they tend to be almost unlimited in BD equipment, and that a wide spectral range may be scanned continuously in integrating spheres, but not very readily in most BD equipment. In Figures 2 and 3, we present digrams of various BD measurement modes - their designations, geometries and the typical spectra obtained in each. The modes illustrated apply to BD reflectance measurements; similar modes exist for BD transmittance measurements.

In the N measurement mode (designated "N" mode), the angle of incidence is held fixed at normal incidence ($\theta_i = 0^\circ$) and the reflected (or transmitted) radiation is scanned from $\theta_r \approx 0^\circ$ to $\theta_r = 90^\circ$ (or θ_r from 90° to 180°). In the "B" mode, the angles of incidence and emergence are maintained equal and opposite ($\theta_r = -\theta_i$) to measure $\rho_B(\theta_r)$; this is the relative specular reflectance as a function of angle of incidence. The measurement of ρ_M requiring that $\theta_r \equiv \theta_i$ yields the retro-reflectance vs. angle of incidence. This measurement is made in the "M" mode.

The measurement of ρ_{GB} is exactly analogous to ρ_N , except that, although fixed, $\theta_i \neq 0^\circ$. The intensity profile of a reflected beam is obtained by scanning it in the "AB" mode; this is possible only when the detector aperture is considerably smaller than the reflected beam. Similarly the intensity of a retro-reflected beam can be determined by scanning through it in the "AM" mode - again with the same limitations on detector aperture width or diameter relative to the retroreflective beam size.

Optical Requirements vs. Applications

To avoid lengthy and unnecessary categorization of SU devices, we will simply define the two general geometry considerations which most affect the selection of appropriate measurements. These depend upon whether the collector remains in a fixed orientation relative to the earth (non-tracking), or relative to the sun (tracking); in the former case the dependence of optical properties as a function of the angle of incidence will be important. The appropriate measurements also depend upon whether the system focusses or concentrates incident radiation into a receiver subsystem, and thus upon the tolerance of this system for natural or

induced scattering.

The measurements to be performed consequently are those which measure gross optical properties, and less frequently their dependence upon angle of incidence; and still less frequently it is necessary to determine beam-spreading qualities and the dependence of the latter on angle of incidence. Generally, the requirements in all Solar Utilization applications are that the solar transmittance of transparent materials, the solar absorptance of absorber surfaces and the solar reflectance of reflective surfaces be initially high and remain high. A low thermal emittance, which characterizes selective absorbers, is very desirable in absorber surfaces, especially at high temperatures. The acceptance angle, $\Delta\theta_A$, of all these materials must be as great as possible. The important optical properties are then solar (hemispherical) transmittance (τ_{HS}), solar absorptance (α_s), solar (specular) reflectance (ρ_s), thermal emittance (ϵ_H), and acceptance angle ($\Delta\theta_A$). Taking into account the properties of available materials in these three classes, we can provide realistic acceptance criteria by quantifying the above:

$$\tau_s \geq 0.85 \quad (2a)$$

$$\alpha_s \geq 0.92 \quad (2b)$$

$$\rho_s \geq 0.80 \quad (2c)$$

$$\epsilon_H \leq 0.10 \quad (2d)$$

These criteria, except for Eq. 2c, apply exactly to tracking flat plate collectors. For all fixed orientation collectors, these requirements must be modified to indicate the angular range in which these properties must remain constant, viz.:

$$\tau_s(\theta_i) \geq 0.85 \text{ within } \Delta\theta_A \geq \pm 45^\circ; \quad (3a)$$

$$\alpha_s(\theta_i) \geq 0.92 \text{ within } \Delta\theta_A \geq \pm 60^\circ; \quad (3b)$$

$$\rho_s(\theta_i) \geq 0.80 \text{ within } \Delta\theta_A \geq \pm 60^\circ; \quad (3c)$$

for selective blacks:

$$\epsilon_H \leq 0.10 \text{ (no } \Delta\theta_A) \quad (3d)$$

Equations 3 reflect reasonable expectations of materials currently available. From these sets of equations we can establish the measurement methods which can be used to qualify candidate materials or validate their properties. All the solar (hemispherical) values, τ_s , α_s and ρ_s , can be determined directly from spectral properties obtained from the integrating sphere measurements - specifically, from normal hemispherical-transmittance spectra in the case of τ_s , and from normal-hemispherical reflectance spectra in the cases of α_s and of ρ_s . To determine whether the angular region in which normal-hemispherical measure-

ments are valid, BD measurements are needed. Though the minimum acceptable value of $\Delta\theta_A$ is somewhat arbitrary, it is important to determine the actual angular acceptance of each collector material. For this reason, BD measurements made in the Bistatic "B", mode are essential, but should be complemented by Normal, "N", mode measurements.

Much more sophisticated and complicated requirements come into play in the design of focussing and concentrating systems. In such systems the distances between reflective surfaces and absorber surfaces bear fixed and invariant relationships to their respective sizes, geometries and properties. To exemplify this point, consider parabolic line focus collector systems and central receiver (solar thermal power) systems. In the latter instance, the size of the absorber area relates directly to the area and imaging capability of the mirrors; in line focus (distributed) collector systems, the area of the receiver depends upon the desired concentration, which in turn depends upon the imaging capability of the mirror. In both cases, image quality is, quite clearly, a critical requirement; subsequently we will describe image quality in terms of beam spreading.

Line focus systems, and similar systems, not unlike flat plate absorbers, must utilize highly absorptive receiver materials, high quality reflective surfaces, and non-scattering transparent cover and protective envelope materials. As in flat plate applications, focussing systems may be used in fixed orientations or they may be sun-following. The azimuthal angle of fixed collectors, of course, must be periodically adjusted to maintain the collector normal to the solar vector. (Even for one-dimensional trackers, the non-tracking axis of the collector requires periodic adjustment). The basic parameters of optical materials for tracking collector systems remain the same as those for flat plate systems, except that the requirements become more stringent. BD properties, in particular, assume greater importance in focussing applications.

The line focussing concentrator illustrates the important parameters. The requirements we derive for these systems will apply in general to all focussing concentrators since only the line focussing systems do not necessarily require tracking. The solar radiation incident on the receiver assembly will have conferred upon it by the reflector surface(s) a specific directional character. The configuration of the receiver surface, however, is not critical unless angles of incidence upon it exceed 45° . (The solar absorptance of most surfaces - even selective - is generally not sensitive to angles of incidence up to at least 45° from normal). Translating this observation into a design guide means that the effective angular aperture of the

reflective surface should not result in angles of reflection exceeding 45° (or included angles of 90°).

Non-tracking collectors present the most difficult materials problems since the solar radiation will not be normally incident on the collector, except at solar noon. For these collectors BD properties will, therefore, be very important; for tracking systems, the optical properties determined from conventional integrating sphere (normal-hemispherical) measurements will suffice.

The receiver assemblies of focussing collectors operate at such high temperatures that positive means must be adopted to minimize thermal losses. To reduce radiative losses, the thermal emittance, ϵ_H , should be less than 0.1. The directional character of the emitted radiation is not important. Convective losses are reduced by operating the absorber tube in an high vacuum; the latter is maintained by enclosing the receiver tube within (an evacuated) transparent enclosure. It is essential that this protective enclosure be optically clear, that it not exhibit any significant (i.e., $> 1\%$) scattering of incident radiation.

Inevitably, focussing collector systems need protection against the effects of dirt accumulation, dust and sand erosion and other hostile atmospheric agencies. To minimize atmospheric interactions "dust covers" are frequently used. The optical requirement for dust covers closely follow those for the protective envelopes of the receiver tubes. They must be and remain clear - with no initial or induced scattering. This requirement stems from the fact that the collector can utilize only direct radiation; scattered radiation is for all intents and purposes lost to the system).

For distributed collector systems the minimum performance standards that we would establish are the following:

<u>Material Utilization</u>	<u>Tracking</u>	<u>Non-Tracking*</u>
Receiver Surface	0.9 (α_s)	$\pm 40^\circ$
Receiver Protective Enclosure	0.85 ($\tau_{N,S}$)	$\pm 45^\circ$
Collector Reflective Surface	0.85 (ρ_s)	$\pm 50^\circ$
System Transparent Cover	0.85 ($\tau_{N,S}$)	$\pm 60^\circ$

*Non-tracking applications demand that the properties pertinent to tracking applications are also available for fixed orientation applications; the value given in this column states the minimum acceptance angle for the property involved.

Central Receiver Applications

From a materials viewpoint, a central receiver (CR) power plant consists simply of a multiplicity of mirrors concentrating solar energy on a common receiver surface. The materials requirements for CR applications are not unlike those for distributed receiver applications. The major differences are that all central receiver systems employ sun-tracking mirrors, and that the receiver surfaces are unprotected and will operate at substantially higher temperatures (1000 - 1500°F). In the CR concept, solar radiation is intercepted by a large number of mirrors and re-directed to a relatively small absorber area. The net result is a very high concentration of solar radiation on the receiver surface even though each mirror has little, if any, focussing effect.

The important mirror parameters are solar reflectance, ρ_s , and specular purity (beam divergence), $\Delta\psi$. For the receiver surface they are solar absorptance, α_s , (technically, the important parameter is α_s^* , the absorptance for the solar radiation which is reflected by the heliostats), and retroreflectance. In a large CR facility, individual heliostats may be located at distances as great as 2000 feet from the receiver. Thus, in addition to wanting the solar reflectance to be as high as possible, we want all the reflected radiation to impinge on the receiver. The heliostats "see" the sun as a source which subtends about 0.5° (~8.7 mr) of arc: incident solar radiation at the earth's distance from the sun has a divergence of ~0.5°. A perfect mirror would reflect all of the incident radiation in such a manner that all of the incident radiation characteristics (polarization, divergence, etc.) are preserved in the reflected beam. In reality, heliostats will not reflect all of the incident radiation and will not maintain the polarization and directionality characteristics of the incident beam. Changes in the state of polarization are unimportant as long as the receiver surface(s) is (are) insensitive to polarization state. If the heliostat confers additional divergence upon the reflected beam, it thus creates the possibility of "spillage", that is, it redirects the incident solar radiation into a larger solid angle than can be intercepted by the receiver. Obviously, spillage is undesirable since it reduces the flux density at the receiver; if it cannot be overcome, the unproductive mirror area (and mirror cost) should be eliminated.

Heliostat quality, as noted above, has two important elements - solar reflectance and beam divergence. We can arbitrarily require and reasonably expect that ρ_s equal or exceed 0.80. The difficult specification is beam divergence. It is obvious that an heliostat which imposes, for example, a beam spreading of

$\Delta\psi = 20$ mr on reflected solar radiation will be useful only in those heliostats which are located closest to the CR. Clearly, we need heliostats which induce the least additional divergence.

The receiver system, of course, must have the highest effective absorptance attainable. Preferably, the absorber surfaces would have absorptance values well in excess of 0.9. Because of the uncertainty of obtaining materials with durable α_s^* values greater than 0.9 at temperatures in the range of 1200°-1500°F, cavity receivers may be employed. The advantage of a cavity receiver is that the surface absorptance value need not be very high, since the design of the cavity will enhance the effective absorption through multiple reflections. The major difficulty here lies in the validity of one of the assumptions commonly made in calculating the effective α_s value; viz., that all radiation reflected by the absorber surface is diffusely reflected. The assumption is generally valid for most absorber coatings. To assure its validity, however, the retroreflectance characteristics of potential surfaces should be examined. Retroreflectance is the reflection of radiation in the direction of the incident beam. A high retroreflectance would obviously invalidate the very basis on which a cavity receiver enhances its effective absorptance.

Summarizing the optical parameters for CR systems we have,

Heliostats

$$\rho_s \geq 0.80 \quad \Delta\theta_A \geq \pm 50^\circ$$

$$\Delta\psi < 12 \text{ mr}$$

Receiver Surface

$$\alpha_s^* \geq 0.95 \quad \Delta\theta_A \geq \pm 50^\circ; T = 1200^\circ - 1500^\circ\text{F}$$

$$\epsilon_H < 0.10 \quad T = 1200^\circ - 1500^\circ\text{F}$$

$$\rho_M < 0.05, \text{ if } \alpha_s^* < 0.95, T = 1200^\circ - 1500^\circ$$

The allowed beam divergence of 12 mr includes the natural solar divergence and thus provides for a maximum beam spreading of about 3 mr. The indication of $\rho_M(\theta_r)$ to be measured, if the surface α_s value (at temperature) lies below 0.95, refers to our earlier discussion of the effect of retroreflectance, which is measured in the monostatic mode, (hence the "M" subscript on $\rho(\theta_r)$).

Summary

In Table 1 we summarize all of the requirements we have discussed. The measurements which must be made to determine

*The value of α_s enhanced by multiple reflections within the cavity.

compliance with these requirements are give in Table 2. Tables 1 and 2 list the properties which should be measured to satisfy engineering requirements.

Table 1

Summary of Requirements

FLAT PLATE COLLECTORS

	<u>Tracking</u>	<u>Fixed</u>
$\tau_s(\theta_i)$	0.85	$\Delta\theta_A \geq \pm 45^\circ$
$\alpha_s(\theta_i)$	0.92	$\Delta\theta \geq \pm 60^\circ$
$\rho_s(\theta_i)$	0.80	$\Delta\theta \geq \pm 60^\circ$
ϵ_H	0.10	

FOCUSSING COLLECTORS

	<u>Tracking</u>	<u>Fixed</u>
Receiver Surface	$\alpha_s \geq 0.9$	$\Delta\theta \geq \pm 40^\circ$
Receiver Protective Enclosure	$\tau_{N,S} \geq 0.85$	$\Delta\theta_A \geq \pm 45^\circ$
Collector Reflective Surface	$\rho_s \geq 0.80$	$\Delta\theta_A \geq \pm 50^\circ$
System Transparent Cover	$\tau_{N,S} \geq 0.85$	$\Delta\theta_A \geq \pm 60^\circ$

CENTRAL RECEIVERS

Heliostats

$$\rho_s \geq 0.80 \quad \Delta\theta_A \geq \pm 50^\circ$$

$$\Delta\psi < 12 \text{ mr}$$

Receiver Surface

$$\alpha_s \geq 0.95 \quad \Delta\theta_A > \pm 50^\circ; T = 1200^\circ - 1500^\circ\text{F}$$

$$\epsilon_H < 0.10 \quad T = 1200 - 1500^\circ\text{F}$$

From an R&D viewpoint, however, we must make further measurements to appreciate mechanisms of degradation, to understand the effects of individual materials variables, and to assist the development of materials with improved functional properties and greater weather-durability. Some examples of R&D oriented measurement schedules are the following.

The normal, as well as the hemispherical, transmittance spectra of all transparent cover or protective materials should be measured, since normal transmittance is sensitive to scattering. Selective black surfaces should also be characterized in the thermal infrared region: spectral reflectance and BD measurements - at several wavelengths and

at temperatures ranging from ambient to, say, 700°F; the R&D measurement schedule for selective blacks would be essentially as Table 2 indicates but would include at least two additional wavelengths, one in the visible region and the other(s) in the thermal infrared region. Second surface mirrors should be characterized by BD measurement at a minimum of two different wavelengths. A normal transmittance spectrum should be attempted with all mirror materials to assure that the metallizing is not defective.

Conclusion

The appropriate measurements to make on any material depend strongly on the application. Generally, the requirements and the measurements to satisfy them are

Table 2

Measurements vs. Requirements

<u>Requirements</u>	<u>Appropriate Measurement</u>	
<u>Transmittance</u>		
$\tau_s > 0.85$	$\tau_H(\lambda)$	350 - 2600 nm
$\tau_{N,S}$	$\tau_N(\lambda)$	350 - 2600 nm
$\Delta\theta > \pm 45^\circ$	$\tau_N(\theta_i)$	$\lambda = 4800\text{\AA}$
	$\rho_B(\theta_i)$	$\lambda = 4880\text{\AA}$
<u>Absorptance</u>		
$\alpha_s > 0.95$	$\rho_H(\lambda)$	350 - 2600 nm
		T = R.T. - 1500°F
$\Delta\theta = \pm 60^\circ$	$\rho_N(\theta_i)$	$\lambda = 4880\text{\AA}$, T = R.T. - 1500°F
$\rho_M < 0.05$	$\rho_M(\theta_i)$	$\lambda = 4880^\circ$, T = R.T. - 1500°F
<u>Reflectance</u>		
$\rho_s > 0.80$	$\rho_H(\lambda)$	350 - 2600 nm
$\Delta\Psi > 12 \text{ mr}$		$\lambda = 4880\text{\AA}$
$\Delta\theta_A > 50^\circ$	$\rho_B(\theta_i)$	$\lambda = 4880\text{\AA}$

not as extensive or difficult in tracking applications as they are in those with fixed orientations. The use of bidirectional optical measurements addresses directly the problems presented by the facts that the solar vector changes continuously and that all materials exhibit directionally dependent optical properties. While other optical measurement schemes may be advisable or even necessary in certain specialized cases, the measurement schedule we have described here represents a reasonable and comprehensive approach to the engineering characterization of solar utilization materials. For R&D purposes, however, this schedule is not sufficient and must be supplemented by more extensive and more sophisticated measurements.

A majority of the work reported here was carried out for the U.S. Dept. of Energy under DOE Contract No. EY-76-C-02-0578-034. The work was sponsored by the Heating and Cooling Branch of the Division of Conservation and Solar Applications.

By acceptance of this article the publisher and/or recipient acknowledges the U.S. Government's right to retain a non-exclusive royalty-free license in and to any copyrights covering this paper.

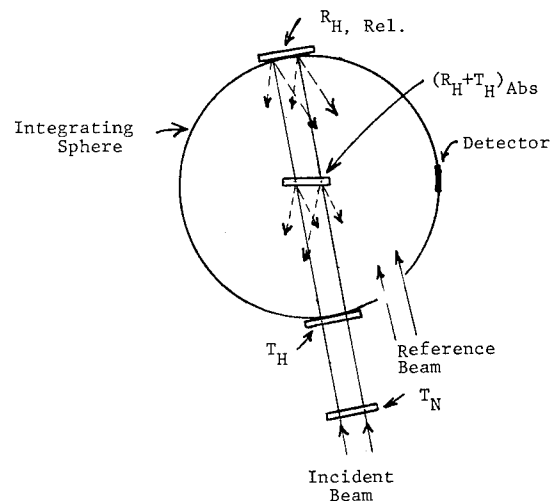


Figure 1

INTEGRATING SPHERE SAMPLE MEASUREMENT GEOMETRIE

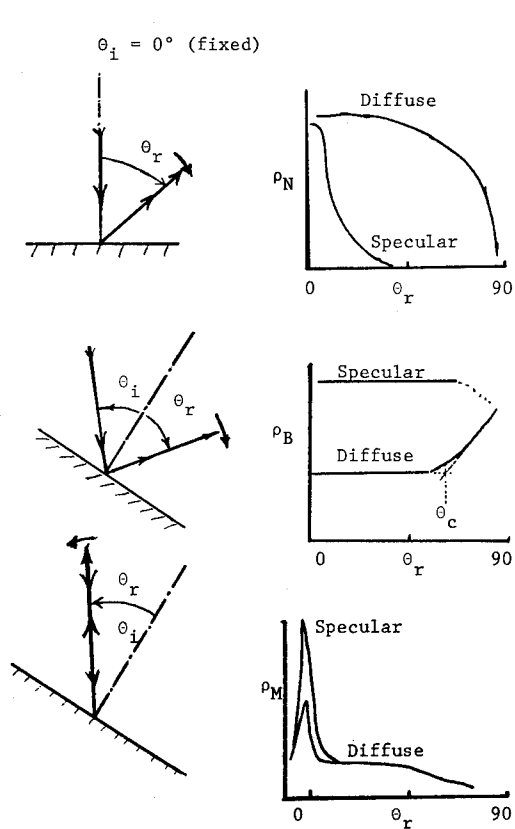


FIGURE 2. BIDIRECTIONAL MODES - NORMAL, BISTATIC AND MONOSTATIC

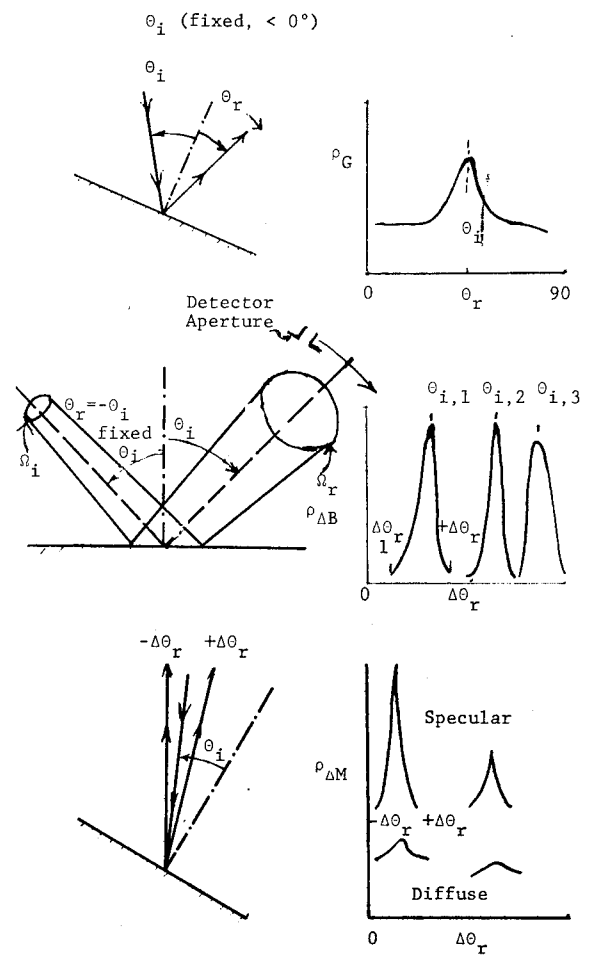


FIGURE 3. BIDIRECTIONAL MODES - GENERAL, DELTA BISTATIC AND DELTA MONOSTATIC

SOLAR ENERGY SYSTEMS - SURVEY OF MATERIALS PERFORMANCE

By: L. F. Skoda and L. W. Masters

Mr. Skoda is a Project Leader in the Building Materials Program of the National Bureau of Standards' Center for Building Technology. In addition to his materials project responsibilities, he has participated in the development of Interim Performance Criteria (IPC) and Intermediate Minimum Property Standards (MPS) for solar heating, cooling and domestic hot water systems. Mr. Masters is Chief of the Building Materials Program. He has participated in the development of the IPC and MPS documents and is heading a project to develop standards for solar absorptive coatings.

1. INTRODUCTION

1.1 Background

Standards for materials used in solar heating and cooling systems are urgently needed to fulfill the goal of the Department of Energy's (DOE) National Plan for Solar Heating and Cooling (ERDA-76-6) [1]^{1/}. The goal as stated in the Plan is to "stimulate the creation of a viable industrial and commercial capability to produce and distribute solar heating and cooling systems and thereby reduce the demand on present fuel supplies through widespread applications." The systems which are produced and installed must be capable of meeting the expected heating/cooling requirements for the buildings in which they are used and they must perform their functions for an acceptable period of time. Widespread acceptance of solar heating and cooling systems is unlikely to be achieved until adequate performance standards are established and compliance with these standards is demonstrated. The achievement of the goal therefore hinges upon the development of standards that ensure minimum acceptable levels of performance for solar heating and cooling systems. The performance standards must establish both measurements of initial properties and measurements of properties after in-service or simulated exposure and they must address materials performance as well as total system performance.

The study to be described in this paper was performed to define the needs for standards for materials used in solar heating, cooling and domestic hot water systems. A more detailed description of the findings is presented in NBSIR 77-1314 [2].

1.2 Objectives

The objectives of this study were 1) to obtain data on the performance of materials in operational solar energy systems, 2) to identify existing standards for evaluating materials and to assess the standards in terms of applicability to materials for use in solar systems, 3) to provide recommendations for the development of test method standards for materials and 4) to provide guidelines to aid the selection of materials for use in solar energy systems.

^{1/} Numbers in parentheses refer to references at the end of this paper.

The initial phase of the project included a survey of published literature, field inspections of 25 operational solar energy systems and the sending of questionnaires to manufacturers and installers of solar energy systems requesting information on materials usage and materials problems encountered.

2. MATERIALS PERFORMANCE IN OPERATIONAL SOLAR SYSTEMS

The field inspection phase of the project included visits to twenty-five operational solar system installations. The period of operation for the systems visited was from a few months to over three years. The inspections revealed that many materials problems had been encountered and that field expedient fixes had had to be made. In some cases, no adequate fixes were possible because of basic design deficiencies. In retrospect, it was obvious that design and materials performance can rarely be separated. In most cases, field expedient fixes for failures were accomplished with readily available materials which were not always the optimum solution to the problem. Unfortunately, some of the projects visited, which were sponsored by the National Science Foundation, were built this way originally, i.e. readily available materials were used which did not always perform satisfactorily.

Field inspections of working solar systems revealed materials problems in all major components of the various subsystems comprising solar systems. The four subsystems into which solar systems can be divided are the collector, transport, storage and control subsystems.

2.1 Collector Subsystems

The materials used within collectors for which problems were observed included cover plates (both glass and polymeric), absorber coatings, absorber plates, insulation, seals and gaskets and enclosures. The most frequently observed problems in collectors were 1) outgassing and other thermal decomposition of polymers under in-use or stagnation conditions, 2) moisture condensation on the undersides of cover plates, 3) gradual degradation of polymers (seals, coatings, covers, etc.) under in-use conditions and 4) incompatibility of joined materials. Other problems observed less frequently were glass cover plate breakage, corrosion, dirt accumulation on cover plates, insulation degradation and wood rot. Two systems utilizing evacuated tube collectors were visited. Of the problems encountered and those described by the owners, the primary cause of failures can most generally be attributed to overtemperature of materials or components during operation or during times of stagnation conditions. Problems encountered include leakage, gasket hardening, dimensional tolerances, tube breakage, tube coating discoloration, dirt accumulation in filter tubes, air entrapment, pump cavitation, manifold insulation discoloration, and system operational control problems.

2.2 Transport Subsystems

The greatest single problem encountered in regards to transport piping was with flexible hoses at inlet and outlet couplings of flat plate liquid collectors. At every site visited where flexible coupling hoses were used, leakage problems have occurred to a greater or lesser degree. Causes for leakage have been attributed to age hardening and loss of elasticity, plastic flow of hose materials through slotted holes of gear-type clamps resulting in reduced clamping forces, cumulative slippage of hoses due to thermal movements of collectors and ozone or ultraviolet attack of hoses exposed to weathering. Also, it was reported that it is sometimes difficult to replace collectors that are attached with rubber hoses because of the tightness of the hose/metal bond. Attempts to solve these problems ranged from application of sealants and adhesives to the exterior of leaking hoses to the complete replacement of polymeric hoses with metallic couplers.

Another potential problem in piping is the use of dissimilar metals within the system. The use of aluminum, copper and steel pipes in conjunction with galvanized connections, brass and steel valves, and steel or aluminum storage tanks was not unusual. Such conditions can lead to corrosion problems, especially in closed loop systems where metal ions are recirculated. Systems using dissimilar metals must be designed as carefully as possible taking into account the area ratio of one metal to another so that the proper inhibitor materials can be added and periodically adjusted to reduce corrosion to a minimum.

Pump problems were encountered at two of the sites visited. In one case, a substitution was made for the initially specified pump due to time constraints of the project and lack of availability of the proper pump. The substitute pump used a controlled leakage stuffing box system on the main shaft. Leakage occurred during periods when the pump was not running so that ingested air was present on start up. The air tended to damage the packing and increase the leakage rate resulting in an unusual amount of required maintenance. Replacement of the pump with a sealed shaft system solved the problem.

The other pump problem occurred on a sealed shaft unit. Leakage occurred that was traceable to deterioration of the impeller shaft packing material by the high concentration of chromate inhibitor used in the system. The solution to this problem was to fabricate a system that allowed the packing material to be washed with untreated water.

2.3 Storage Subsystems

Of the systems inspected, only three storage subsystem problems were encountered. The most serious problem occurred at a site that used two concrete transformer vaults for storage of liquid. In this particular case, project time and financial constraint resulted in the selection of transformer vaults to expedite completion of the project on schedule. Leakage from the two 4,000 gal (15 m³) capacity vaults occurred at varying rates of from 40 to 50 gals (.15-.19 m³) a day and appeared to

be related to the temperature of the stored liquid. Repairs to the tanks were initiated and the leakage rate was greatly reduced but not eliminated.

The other two storage problems had to do with the tank insulation. In one case, a liquid leak from a tank connection resulted in the deterioration of vermiculite plaster insulation used on the ends of the cylindrical roof mounted tank. In the other case, an insufficient amount of insulation was used on three buried tanks resulting in excessive heat losses. This was evidenced by the fact that the earth cover did not support the growth of vegetation. This heat loss was also substantiated by the rapid drying of the area above the buried tanks after a rainstorm when compared to adjacent areas.

2.4 Conclusions from Field Inspections

The observations made during the field inspections illustrate that numerous material-related problems have occurred in operational solar energy systems. Field problems were identified in each of the major subsystems, collector, transport and storage, of one or more of the solar energy systems surveyed. Also materials problems were identified for most components within the subsystems. For example, problems were identified in one or more collector subsystems with materials used for cover plates, absorptive coatings, absorber plates, insulation, seals, enclosures and structural supports.

Although some of the observed problems result from improper design considerations, most result from inadequate resistance of materials to the exposure conditions experienced in the solar systems.

3. TEST METHOD STANDARDS FOR MATERIALS

Numerous standard methods of test for materials have been developed by standards-setting organizations such as ASTM (American Society for Testing and Materials), ANSI (American National Standards Institute) and ISO (International Organization for Standardization). Also test methods are available in trade association specifications and guidelines and in Federal and military specifications and standards.

Existing standards for coatings, fluids, glass, insulation, metals, plastics and rubber materials were identified and assessed in terms of their applicability to materials for use in solar energy systems. Standards were identified for key attributes or properties of each material. For example, coatings standards were identified for abrasion resistance, adhesion, resistance to atmospheric pollutants, cleanability, color change, corrosion resistance, flammability, flexural strength, fungus resistance, gloss, impact resistance, resistance to moisture, optical properties, permeability, physical integrity, scratch resistance, surface uniformity, tensile strength, resistance to thermal aging, thickness and resistance to weathering.

It was obvious that many test method standards for materials are available, both for measuring properties and for exposing materials to accelerated aging environments. Although many of the property measurement tests are apparently

applicable to materials used in solar energy systems, most accelerated aging tests are not directly applicable because the in-use conditions in solar are very different than conditions for which the standards were developed. In some cases, modification of the exposure conditions may result in acceptable aging tests but laboratory verification is needed of the modified tests. Needs for new and modified standards are further described in reference [2].

4. CONCLUSIONS AND RECOMMENDATIONS

The observations made during inspections of operational solar energy systems, described in Chapter 2, illustrate that numerous material-related problems have occurred in operational systems and the results of the questionnaire [2] illustrate that many types of materials have been used in components and subsystems. Field problems were identified in each of the major subsystems, collector, transport and storage, of one or more of the solar energy systems surveyed. Also materials problems were identified for most components within the subsystems. For example, problems were identified in one or more collector subsystems with materials used for cover plates, absorptive coatings, absorber plates, insulation, seals, enclosures and structural supports.

It is imperative that premature failure of materials be minimized and that systems and subsystems be made as maintenance free as possible to ensure widespread consumer acceptance of solar as a viable energy alternative. The primary concern, then, is to identify a path of action to ensure improved materials performance in solar systems and subsystems.

There are at least two factors which contribute to the premature failure of materials in the field and must be addressed by the planned path of action: 1) improper design considerations and 2) inadequate resistance of materials to the conditions experienced in solar energy systems. Many of the field problems result from improper selection of materials for the particular design. At present, the process of selecting materials for specific applications is hindered by the lack of an adequate data base of materials performance under the conditions experienced in solar systems and subsystems. In particular, data are not available to characterize the long-term performance of various materials under expected in-service conditions. It is often impossible to adequately compare the expected long-term performance of various candidate materials and identify the best candidate. Clearly, the development of a data base of materials performance which identifies the attributes and limitations of materials under specific use conditions would significantly aid the process of selecting materials and hence reduce the extent of field problems.

The needed data base of materials performance can be obtained from experience based on actual installations and from laboratory studies (including tests performed in a laboratory and tests performed on materials and subsystems outdoors). The field experience with solar energy systems in recent years has provided a start toward obtaining an adequate data base. For example, changes

incorporated in recently marketed systems and subsystems by collector manufacturers and system designers to help alleviate problems observed with earlier designs reflect a growing data base of materials performance. One problem, however, is that information on the experience gained is often not widely disseminated within the solar industry. Another problem is that, even if data obtained from field experience were widely disseminated, the time required to obtain an adequate data base would be prohibitively long if trial and error in the field were the only source of data.

Laboratory studies of materials is another source of materials performance data. Initial properties of materials can often be determined using existing standard test methods, as shown in Chapter 3. Such property measurements are available for many materials used in components and subsystems, e.g. strength properties of glass, plastics and metals, hardness of rubber materials, thermal properties of insulation, etc. Aging tests which provide for exposure of materials to environments that may change their properties, can be useful in obtaining long-term performance data. The effect of the environment on materials properties during an aging test can be determined by measuring one or a group of properties before and after aging. Accelerated aging tests, which have been designed in an attempt to induce changes in materials properties in a short period of time, have been developed for many materials as mentioned in Chapter 3. One problem with testing by accelerated aging procedures is that it is difficult to relate the results of accelerated tests quantitatively with in-service performance [3, 4]. A systematic approach to predicting service life has been developed [5] which may aid in obtaining improved correlations between accelerated test results and in-service performance. The systematic approach has also been prepared as an ASTM standard practice by Committee E6 on Performance of Building Constructions. Another problem with existing accelerated tests for materials, is that the exposure environments are seldom adequate to simulate the exposure conditions of materials experienced in solar energy components and subsystems. Thus, in developing a data base of materials performance for solar energy applications, it will be necessary to first establish standard test procedures for obtaining the data. The test procedures needed are primarily accelerated aging tests in which the exposure environments simulate the service conditions experienced in solar. However, improved property measurement tests are also needed for some materials.

In order to expedite the development of urgently needed data base of materials performance for solar applications, the following is proposed:

1. Compile materials performance data from solar energy systems that are installed in the field.

Commentary. It was mentioned earlier in this chapter that experience gained from field installations is often not widely disseminated within the solar industry. One reason for this is that the materials used in many systems are proprietary. During the course of this study, it has been difficult to obtain from the private sector, the type of data needed. It is unlikely that a comprehensive compilation of

materials performance on operational systems can be obtained. It is suggested, therefore, that the data compilation be limited to Federally sponsored or owned installations. The data which could be obtained would serve two purposes: 1) it would provide an interim data base and 2) it would aid the interpretation of data from accelerated tests of materials and subsystems.

2. Perform laboratory studies of materials and subsystems to develop test method standards.

Commentary. Standard test methods are needed at the materials level, particularly for estimating the long-term performance of materials in solar applications. In order to develop test method standards, laboratory tests of available and currently used materials must be performed and the data obtained from the tests compared to actual field data from operational systems. Also accelerated tests of subsystems, particularly stagnation tests of collectors, must be performed to develop standard procedures and to obtain data for comparison with materials tests.

3. Develop a data base of materials performance for solar applications.

Commentary. The data base should be developed as rapidly as possible, utilizing input from the areas 1 and 2 above. The data base should be a compilation of materials test results, based on field and laboratory tests, which could be used by manufacturers and designers in selecting the best candidate material for each specific application. It is unlikely the data base could ever be complete. In particular, new materials will undoubtedly be utilized in solar applications in an attempt to lower the initial cost or improve the performance of systems. However, if there are standards by which the new materials can be evaluated quickly and reliably, and if data are available in the data base to minimize the selection of materials of poor or questionable performance, the benefits to the solar industry and to the consumer would be invaluable.

4.1 Recommended Priorities for the Development of Material Test Method Standards

The National Bureau of Standards has prepared a plan for the development and implementation of standards for solar heating and cooling applications [6]. Based upon that plan, upon the types of material-related problems which have occurred in operational systems and upon the availability of existing standards, the following components (listed in alphabetical order) are recommended for the development of material test method standards: absorptive coatings, coatings/liners for transport or storage subsystems, collector insulation, cover plates, dessicants, dielectric insulators, filters and getter columns, flexible couplings, heat transport liquids, metallic containment materials, non-metallic containment materials, transport and storage subsystem insulation, reflective surfaces, seals and thermal storage media. In addition,

standards are needed in two related areas: stagnation testing of collector subsystems and measurement of surface temperature of materials. Table 1 lists the areas for standard development according to recommended priority for actions. Priority ratings of high, medium and low are used in the table. The priority ratings reflect the need for standards to determine the functional and durability/reliability attributes of materials for use in solar systems. Criteria used in establishing the priorities were:

1. The importance of the material to the total system performance.
2. The extent of field problems observed within the material.
3. The availability of existing standards to measure functional and durability/reliability attributes.
4. The potential for developing useful consensus standards.

Reference [2] also provides specific recommendations for the types of studies needed for each of the areas in table 1.

Table 1. Recommended Priorities for the Development of Material-Related Standards

<u>Material Standards Area</u>	<u>Priority</u>
Absorptive coatings	High
Collector insulation	High
Cover plates	High
Heat transport liquids	High
Metallic containment	High
Nonmetallic containment and absorber substrates	High
Seals	High
Stagnation testing of collector subsystem	High
Surface temperature measurement	High
Flexible couplings	Medium
Reflective surfaces	Medium
Thermal storage media	Medium
Transport and storage insulation	Medium
Coatings/liners for transport or storage subsystems	Low
Dessicants	Low
Dielectric insulators	Low
Filters/getters	Low

5. GUIDELINES TO AID THE SELECTION OF MATERIALS FOR USE IN SOLAR ENERGY SYSTEMS

Factors which must be included in criteria for selecting materials to be used in solar energy systems include 1) ability of the material to perform the intended function, 2) durability/reliability, 3) safety, 4) maintainability, 5) cost and 6) compliance with local building codes. As

pointed out in Chapter 4, the process of selecting materials for specific applications is hindered by the lack of an adequate data base of materials performance under the conditions experienced in solar systems and subsystems. Because of the lack of an adequate data base, it is not possible to provide definitive recommendations for the use of materials. The purpose of this chapter is to present guidelines to aid the selection of materials for specific applications. The guidelines outline a general procedure for obtaining the data needed to make the selection. The guidelines should be useful in identifying the types of data that should be considered in selecting materials for use in solar energy systems.

The process of selecting a material for a specific application can be outlined into ten steps:

1. Define in-service performance requirements.
2. Identify key functional attributes (or properties).
3. Identify environmental conditions to which the material will be exposed in service.
4. Identify key durability/reliability attributes.
5. Identify key safety attributes.
6. Identify the types of test or field data needed to demonstrate compliance with requirements for function, durability/reliability and safety attributes.
7. Obtain test data.
8. Rank candidate materials in order of predicted short-term and long-term performance.
9. Consider factors related to maintainability, cost, and code compliance.
10. Select the "best" material.

Reference [2] includes further description of these guidelines and tables.

6. REFERENCES

1. National Program for Solar Heating and Cooling of Buildings, Report 76-6, Department of Energy (DOE), Washington, DC 20545, November 1976.
2. Skoda, L. F. and Masters, L. W., "Solar Energy Systems - Survey of Materials Performance," NBSIR 77-1314, October 1977.
3. Masters, Larry W., Wolfe, Winthrop C., Rossiter, Walter J., Jr., Shaver, James R., "State-of-The-Art on Durability Testing of Building Components and Materials," NBSIR 77-132, March 1973.
4. Masters, Larry W., Wolfe, Winthrop C., "The Use of Weather and Climatological Data in Evaluating the Durability of Building Components and Materials," NBS Technical Note 838, August 1974.
5. Masters, Larry W., "An Approach to the Development of Predictive Service Life Tests for Building Components and Materials," published in the Proceedings of the RILEM/ASTM/CIB Symposium on Evaluation of the Performance of External Vertical Surfaces of Buildings, September 1977.
6. Waksman, D., Pielert, J. H., Dikkers, R. D., Streed, E. R., "Plan for the Development and Implementation of Standards for Solar Heating and Cooling Applications," NBSIR 76-1143, August 1976.

DEGRADATION OF POLYMETHYLMETHACRYLATE BY RADIATION

By: Mohamed Abouelezz and Larry Masters, National Bureau of Standards
Paul Waters, American University

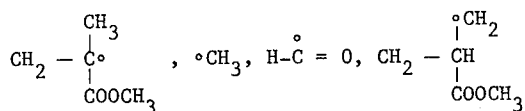
Mr. Abouelezz has an IPA Fellowship with the National Bureau of Standards. He received his BS in 1964 from Cairo University, Egypt. In 1975 he received his MS from Drexel University. He is now a Ph.D. candidate at American University. Mr. Abouelezz previously worked as a research chemist at the National Research Center in Cairo, Egypt and as a Chemist at Publicker Industrial, Inc., Philadelphia, PA. Mr. Masters is Chief of the Building Materials Program. He has participated in the development of the IPC and MPS documents and is heading a project to develop standards for solar absorptive coatings. Dr. Waters is a professor of chemistry at American University. His research includes light scattering, polymer fibrils, polymer electrets, desalination membranes, high voltage electrokinetics, sulfur dioxide removal, intermolecular interaction and liquid crystals.

INTRODUCTION

Poly(methyl methacrylate), PMMA, is used as a substitute for glass in windows, doors and cover plates in solar energy collectors. No information is available from controlled tests about the stability of the polymer to long-term exposure to sunlight.

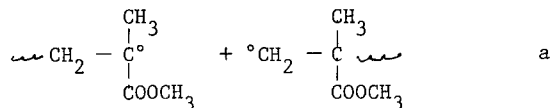
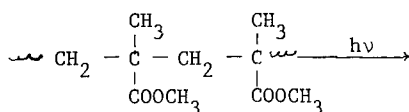
Studies of the degradation of PMMA on exposure to the 253.7 nm mercury line have been carried out [1-8]. Viscosity measurements showed that with this radiation there is a rapid decrease in molecular mass and very little volatile materials produced. Fox et al. [7], assuming a proportionality between the number of quanta absorbed and the number of backbone scissions, calculated 4×10^{-2} chain breaks per absorbed quantum on irradiation in 2.7 mPa (2×10^{-5} torr) of air. At atmospheric pressure the quantum yield was 1.7×10^{-2} . Both the UV and IR spectra change after irradiation. New bands appear at 240 nm and 285 nm. The former is associated with unsaturation; the latter with the carbonyl chromophore. New bands at $6.19\text{--}6.01 \mu\text{m}$ (1615 cm^{-1} and 1640 cm^{-1}) are attributed to unsaturation [7, 9, 10].

Free radicals resulting from 253.7 nm irradiation include [6, 11, 12]:

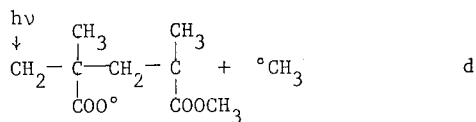
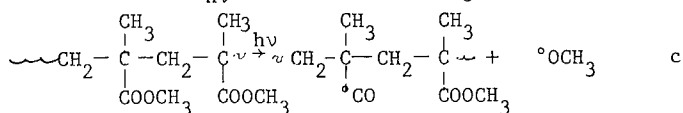
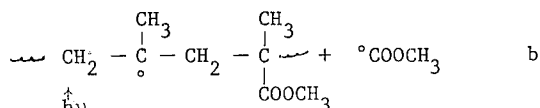


The photolysis of PMMA has been assumed to result in a random scission of the polymer backbone by radical process [1-3, 7, 13-20]. The major reactions thought to occur simultaneously are:

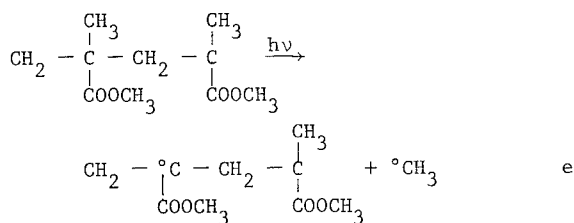
1. Random homolytic scission of the main chain carbon-carbon bonds:



2. Photolysis of the ester side group in three different ways:



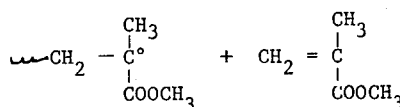
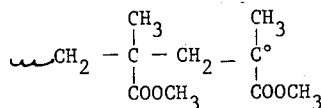
3. Photodissociation of the methyl side chain group:



The main volatile products of the photolysis of PMMA in vacuum are methyl formate, methanol and methyl methacrylate with quantum yields of 0.14, .48 and 0.20, respectively. In air, additional products include methane, hydrogen, carbon monoxide and carbon dioxide [7].

Monomer methyl methacrylate can originate in at least three ways during PMMA degradation:

1. End chain depolymerization (unzipping)



2. Trapped residual monomer from the initial polymerization.

3. Random thermal degradation.

The dominant product of thermal degradation of PMMA is monomer which is liberated in high yield at 250°C. The mechanism of monomer formation is assumed to be the reverse of free radical polymerization. After the initial chain homolytic scission generates radicals, the latter unzip to produce monomer [21].

When PMMA is exposed to sunlight for long periods of time it degrades. Since no 253.7 nm irradiation reaches the earth's surface, degradation studies above 300 nm were carried out in order to begin building a data base for understanding how the polymer degrades at higher wavelengths so that methods of stabilizing it might be developed.

The work had three objectives:

1. To investigate the effect of different lines of UV and visible light as well as combinations of these lines on the photodegradation of PMMA. The 253.7 nm, 313 nm, 365 nm, 436 nm and 546 nm lines of mercury were used.
2. To study the mechanism of the photodegradation caused by the individual line or combinations of the lines.
3. To investigate the effect of simulated natural weathering on the photodegradation of PMMA using a xenon-arc accelerated weathering machine.

EXPERIMENTAL

Material and Apparatus

Polymer

Test samples of PMMA were provided by the Research Laboratory Division of Rohm and Haas Co. The mass average molecular mass was 240,000. The polymer was reported to contain UV stabilizer and ca. 1% residual monomer and to have 75% syndiotactic character. It was purified by dissolving in boiling methylene chloride, cooling to about 10°C, and precipitating by adding to a cold methyl alcohol (also at about 10°C). The precipitated solid was filtered under suction. This process was repeated in order to insure the removal of most of the residual monomer and all the UV absorber originally present.

After purification, the polymer, dissolved in methylene chloride, was cast on polished black glass using a draw down blade. After evaporation of the solvent, the film was released by immersing the glass plate containing the film in water. The middle part of the film was used in the tests to insure a uniform thickness of 20 ± 5 microns. The film was heated to 100°C for 8-16 hours, then at 80°C under vacuum for 16 hours. This treatment removed the residual solvent and any stresses developed in the film during casting.

Light Sources

1. Mercury lamps

The photochemical reactor was a Rayonet Model RPR-100, obtained from the Southern New England Ultra-violet Company, Middletown, Connecticut. The apparatus consists of a sheet metal housing and a bank of 16 tubular UV lamps. Within the housing, the 285 mm length lamps were mounted vertically around a circle of 235 mm diameter. Surrounding the cylinder of lamps is a polished cylindrical reflector, 390 mm in height and 260 mm in diameter. A fan in the base of the reactor blows air through the irradiation space to cool the material being irradiated.

Three sets of lamps are available commercially, with spectral distribution peaking at 253.7 nm, 300 nm and 350 nm. The spectral distribution of the 253.7 nm lamp is shown in figure 1, while that of the 300 nm lamp is shown in figure 2.

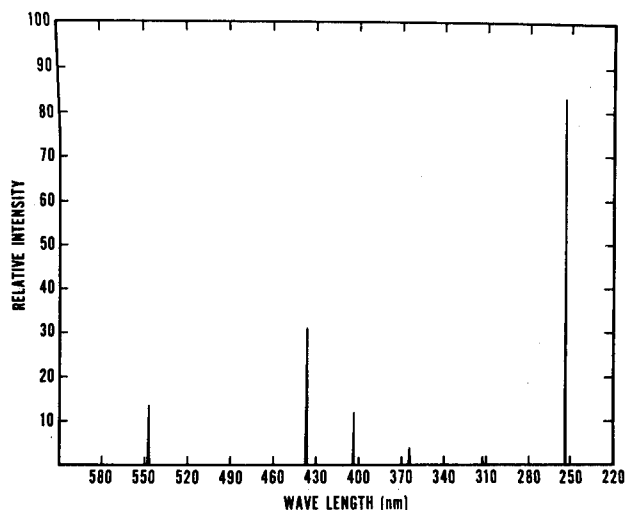


Figure 1. Spectral distribution of 253.7 nm lamp used in the reactor.

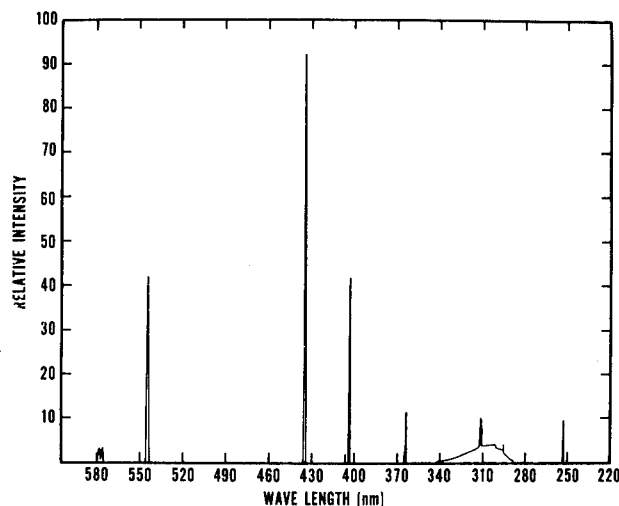


Figure 2. Spectral distribution of 300 nm lamp used in the reactor.

2. Xenon lamp

An Atlas Electric Model M-65WR xenon arc Weather-Ometer was used in irradiating the polymer. The xenon arc lamp was operated at 6500 watt and monitored at three different wavelengths (340, 420 and 580 nm) by the Atlas High Monitor and Control System.

The spectral distribution of the 6500 watt xenon lamp and that of sunlight at Chicago, Illinois are given in figure 3.

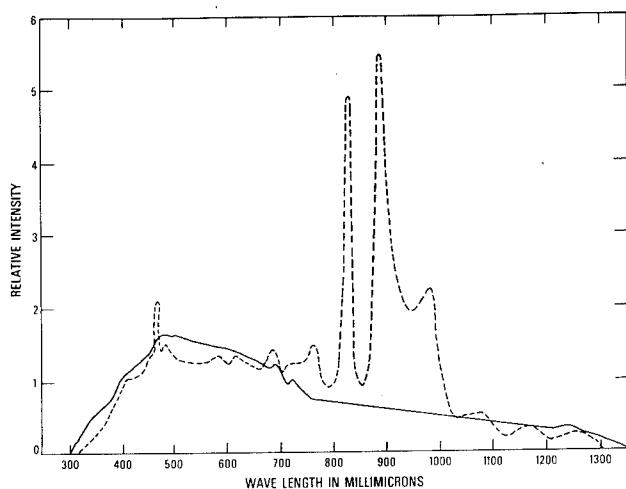


FIG 3 RELATIVE ENERGY DISTRIBUTION — NATURAL SUNLIGHT, NOON JUNE
--- 6500 WATT XENON WITH BORO SILICATE FILTER

Actinometry

Actinometry was performed during the exposure tests to measure the amount of radiation the samples received. These measurements were necessary in order to compare the irradiations from different lamps and to permit a determination of the quantum efficiency of the degradation. The procedure employed was that of McLaughlin et al. [22]. The colorless pararosaniline cyanide, used in the method, becomes deeply colored upon irradiation with ultraviolet radiation. Its sensitivity is 0.96 mol/photon up to 340 nm.

Molecular Mass

Molecular masses were measured by gel permeation chromatography (GPC) using a Waters Associates chromatogram. The columns used were packed with microstyrogel. Six columns were used - four of pore size 10^{-2} μ m and one each of .1 and 10 μ m. The diluent used, tetrahydrofuran was degassed daily during the measurements. The differential refractometer was a Waters Associates Model R401. The resulting chromatographic data were analyzed by computer to give both number and mass average molecular masses.

Glass Transition Temperature

The glass transition temperature for the original and the degraded polymers was measured using a thermal mechanical analyzer. Three

measurements were made on each sample and the data were averaged to the nearest degree.

UV and IR Spectra

UV spectra were recorded with a Beckman DK 1 spectrophotometer and IR spectra were measured with a Perkin Elmer Model 467 spectrophotometer.

Mass Loss

The mass loss, reported as volatile products, was measured to the nearest decamicrogram.

RESULTS AND DISCUSSION

The changes in mass average and number average molecular mass accompanying irradiation with the 253.7 nm in air and vacuum lamps are recorded in tables 1 and 2, respectively. The results from irradiation with the 300 nm lamps are given in tables 3 and 4.

Table 1. Molecular Mass Changes for PMMA During Irradiation with 253.7 nm Lamp in Air

Exposure Time in Hours	$\bar{M}_w \times 10^{-3}$	$\bar{M}_n \times 10^{-3}$	$\frac{\bar{M}_w}{\bar{M}_n}$
0.0	248	197	1.259
1.0	201	157	1.280
2.0	167	135	1.237
4.0	126	102	1.235
6.0	94	77	1.221
8.0	67	55	1.218

Table 2. Molecular Mass Changes for PMMA During Irradiation with 253.7 nm in Vacuum

Exposure Time in Hours	$\bar{M}_w \times 10^{-3}$	$\bar{M}_n \times 10^{-3}$	$\frac{\bar{M}_w}{\bar{M}_n}$
0.0	248	197	1.259
1.0	197	158	1.247
2.0	173	141	1.223
4.0	133	108	1.231
6.0	112	89	1.258
8.0	102	82	1.232

Table 3. Molecular Mass Changes for PMMA During Irradiation with 300 nm in Air

Exposure Time in Hours	$\bar{M}_w \times 10^{-3}$	$\bar{M}_n \times 10^{-3}$	$\frac{\bar{M}_w}{\bar{M}_n}$
0.0	248	197	1.259
2.0	232	183	1.258
8.0	192	150	1.280
16.0	166	131	1.267
32.0	141	110	1.280
64.0	101	79	1.270

Table 4. Molecular Mass Changes for PMMA I During Irradiation with 300 nm in Vacuum

Exposure Time in Hours	$\bar{M}_w \times 10^{-3}$	$\bar{M}_n \times 10^{-3}$	$\frac{\bar{M}_w}{\bar{M}_n}$
0.0	248	197	1.259
2.0	234	185	0.265
8.0	202	161	1.255
16.0	181	145	1.248
32.0	141	113	1.245
64.0	112	91	1.231

It is apparent from these results that irradiation with either of these lamps leads to a rapid decrease in the molecular mass of the polymer, with the 253.7 nm lamps being about four times as effective as the 300 nm lamps. The intensity of 253.7 nm radiation from the 300 nm lamps is only about 10 percent of that from the 253.7 nm lamps. Thus, higher wavelength irradiations (311 nm, 365 nm, 436 nm and 546 nm) cause PMMA to degrade. In each case, the initial rate of degradation is greater than the average rate and the rates in air are greater than those in vacuum.

Measurements on irradiation with 6500 watt xenon arcs, fitted with borosilicate filters, are entered in table 5. The rate of degradation is much less in this case than with either of the mercury lamps. Nevertheless, degradation does proceed and is considerable upon long-term exposure. The molecular mass measurements following irradiation of different samples with each of the sources are plotted in figure 4.

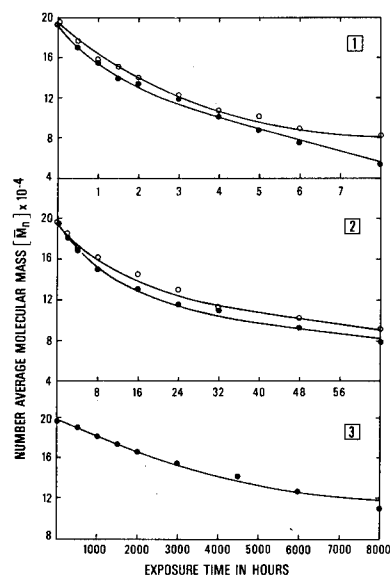


FIG. 4 CHANGES IN NUMBER AVERAGE MOLECULAR MASS VS. EXPOSURE TIME FOR PMMA IRRADIATED WITH (1) 253.7 nm LAMPS, (2) 300 nm LAMPS, (3) 6500 WATT XENON ARC LAMP (WEATHEROMETER) • IN AIR ○ UNDER VACUUM

Table 5. Molecular Mass Changes for PMMA Exposed to Xenon Arc Weather-Ometer (6000 Watt, Borosilicate Filter)

Exposure Time in Hours	$\bar{M}_w \times 10^{-3}$	$\bar{M}_n \times 10^{-3}$	$\frac{\bar{M}_w}{\bar{M}_n}$
0.0	248	197	1.260
500	242	191	1.270
1500	228	175	1.300
3000	206	156	1.320
6000	176	129	1.360
8000	155	113	1.370

The effect of irradiation on the glass transition temperature, T_g is shown in figure 5. The results are accurate to $\pm 2^\circ\text{C}$. As with the changes in molecular weight, the samples irradiated with 253.7 lamps show a greater decrease in the glass transition temperature than those irradiated with the 300 nm lamps. Also the rate of change of T_g is less in vacuum than in air. Another similarity between T_g and the molecular weight data is that the decrease of T_g with irradiation is faster at the beginning of irradiation. As expected, the rate of change of T_g induced by the xenon lamps is much less than that caused by the mercury lamps.

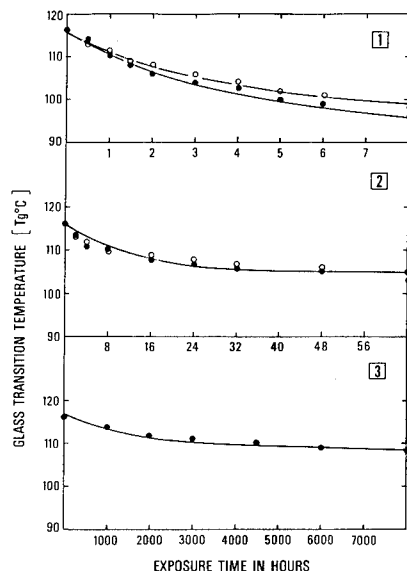


FIG. 5 CHANGES IN GLASS TRANSITION TEMPERATURE T_g vs. EXPOSURE TIME FOR PMMA IRRADIATED WITH [1] 253.7 nm LAMPS, [2] 300 nm LAMP [3] 6500 WATT XENON ARC WEATHEROMETER
• IN AIR ○ IN VACUUM

UV irradiation of PMMA causes an increase in the absorption of the thin film. A new band at 285 nm, previously observed by Shultz [4], Frolova [9, 10] and Fox et al. [7] was also observed in this work. This band is in the region usually associated with carbonyl chromophores and is believed to result from polymer chain absorption itself rather than from low molecular weight photolysis products.

The only changes in the infrared spectrum of PMMA during the irradiation were a broadening of the carbonyl band at $5.71 \mu\text{m}$ (1750 cm^{-1}) and the appearance of small new bands at $6.19\text{--}6.01 \mu\text{m}$ ($1610\text{--}1640 \text{ cm}^{-1}$). The latter bands are attributed to olefinic unsaturation produced during the photolytic chain scission.

As it has been seen in molecular mass and glass transition temperature changes, the spectral changes are much greater following irradiation with 253.7 nm lamps than with 300 nm lamps. Very slight changes were noted after irradiation with xenon lamps.

The percentage mass loss during the irradiation after 8 hours of exposure to 253.7 nm lamps were 1.39% and 1.55% in air and under vacuum, respectively. With 300 nm lamps, the mass losses after 64 hours of exposure were 3.68% in air and 4.3% under vacuum. With the xenon arc Weather-Ometer, the percentage mass loss was 2.37 after 8000 hours of irradiation. The greater mass loss in vacuum can be explained by the fact that in vacuum there is more diffusion of the volatile products out of the film than in air. Another observation is that the mass loss in PMMA irradiation with 253.7 nm lamps is much lower than that obtained with 300 nm lamps and with the xenon arc Weather-Ometer at equivalent levels of degradation.

CONCLUSIONS

The data reveal that UV irradiation degrades PMMA rapidly, with the production of relatively small amounts of volatile materials. The initial and average rates of degradation caused by the 253.7 nm lamps are greater than those induced by the 300 nm lamps. The intensity of the 253.7 nm line in the 300 nm lamps is only 10 percent of that in the 253.7 nm lamps whereas the quantum yield of the former is 25 percent of that of the latter. This implies that wavelengths greater than 253.7 nm also degrade PMMA.

Mass losses in air and in vacuum upon irradiation with the 253.7 nm lamps are less than those caused by the 300 nm lamps are comparable times. If we assume that the degradation due to the 253.7 nm lamps is primarily that of random scission [1-8], the degradation due to the 300 nm lamps is different, probably a combination of random scission and thermal degradation (unzipping).

Irradiation with xenon lamps produces much lower initial and average rates of degradation than either of the UV lamps. The mechanism(s) of degradation here are likely to be complex, due to the broad spectrum emitted by the source.

A better understanding of the mechanisms by which PMMA degrades at different wavelengths must await further studies which include:

1. the effect of filtering the 253.7 nm line from the 300 nm lamps
2. the effect of filtering all UV radiation from the 300 nm lamps
3. the effect of filtering all UV radiation from the xenon lamps
4. the effect of filtering all UV and IR radiation from the xenon lamps
5. the effect of filtering all UV and visible radiation from the xenon lamps.

Our purpose in presenting our work to this group at this stage of its development is to demonstrate that PMMA and, no doubt, other transparent polymers, are degraded not only by UV radiation but also by simulated sunlight. Moreover, when the degradation mechanisms are delineated methods of protecting the polymers can be devised so that these valuable materials can be preserved for long-term solar energy applications.

REFERENCES

1. P. R. E. J. Cowley and H. W. Melville; Proc. Roy. Soc. A 210, 461 (1952).
2. Ibid, A 211, 320 (1952).
3. Ibid., Nat. Bur. Std. Circ. No. 525, 59 (1953).
4. A. Shultz, J. Phys. Chem. 65, 967 (1961).
5. D. G. Gardner, J. Chem. Phys. 34 1653 (1961).

6. A. Charlesby and D. K. Thomas, Proc. Roy. Soc. A 269, 104 (1962).
7. R. B. Fox, L. G. Isaacs and S. Stokes, J. Polym. Sci., A 1, 1, 1979 (1963).
8. V. Ya. Shlyapintokh and V. I. Goldengerg, EUROP. Polym. J., 10, 679 (1974).
9. M. I. Frolova et al., Tr. Khim, i Khim. Tekhnol., 2, 1611 (1959).
10. M. K. Frolova et al., Tr. Khim, i Khim. Tekhnol., 7, 304 (1964).
11. R. E. Michel et al., J. Chem. Phys. 45, 4604 (1966).
12. V. K. Milinshuk and S. Ya Pshezhetskii, Vysokomol. Soedin., 6, 1605 (1964).
13. R. B. Fox et al., U. S. Naval Res. Lab. Report, No. 5720 (1961).
14. C. Forgacs and W. G. Hodgson, J. Polym. Sci., A 1, 2, 1275 (1964).
15. J. P. Allison, J. Polym. Sci., A 1, 4, 1209 (1966).
16. D. G. Gardner and G. A. Henry, J. Polym. Sci., B 5, 101 (1967).
17. J. R. MacCallum and C. K. Schoffs, Trans. Faraday Soc. 75, 2383 (1971).
18. K. Morimoto and S. Suzuki, J. Appl. Polym. Sci., 16, 2947 (1972).
19. J. R. Shelton, In Polymer Stabilization (Ed. W. L. Hawkin, Wiley-Interscience, New York, 1972).
20. E. Bystritskaya, et al., Visokomol Soeden A, 14, 1626 (1972).
21. N. Grassie, Polymer Science (Ed. A. D. Jenkins, American Elsevier, 1972).
22. W. L. McLaughlin, Intrn. J. of Appl. Rad. and Iso., 17, 85 (1965).

SERI SOLAR ENERGY STANDARDS ACTIVITIES

By: Helen Barker, Jim Castle, Gordon Gross
Solar Energy Research Institute

Ms. Barker holds the position of Staff Engineer in the Institutional & Environmental Assessment Branch at SERI. She has a broad program management background in technology performance evaluation and technology impact assessment.

Mr. Castle is responsible for concentrating collector thermal performance evaluation within the Thermal Conversion Branch. His work experiences have been concerned primarily with the fluid flow and heat transfer considerations pertinent in engineering systems.

Mr. Gross holds the position of Principal Scientist in the Materials Branch of SERI. His work experience spans 25 years of optical, thermal and mechanical research and he is now responsible for setting up the SERI Program on Reliability and Standards.

Introduction

The development of solar energy applications has had two significant problems. First, it has been characterized by fragmentation of effort and diversity of direction. Second, it has been fraught with uncertainty as to cost and performance. The first problem has been addressed by the Congress and the Department of Energy in the creation of the Solar Energy Research Institute; the second is to be addressed in part by SERI's Program on Reliability and Standards.

The Solar Energy Research Institute (SERI) was conceived in 1974 as the United States emerged from the worst fuel shortage in its peacetime history. Congress, concerned then as now about future energy supplies and over-dependence on foreign energy sources, passed the Solar Energy Research, Development, and Demonstration Act calling for the creation of SERI.

The Energy Research and Development Administration (ERDA) commissioned a study program to determine SERI's role, mission, and management methods. The studies recommended that SERI should be operated by a private entity under contract to the federal government. Accordingly, in March 1976, ERDA issued a request for proposals calling for a management plan, a management team, and an initial site with an option for a future site.

In March 1977, after extensive evaluation of 19 proposals, ERDA awarded Midwest Research Institute the contract to establish and operate SERI at a site in Colorado. The Solar Energy Research Institute formally opened in Golden, Colorado on July 5, 1977. The Department of Energy (DOE) undertook the supervision and funding of SERI in October 1977.

The Solar Energy Research Institute was mandated by Congress to provide significant support to the national DOE program of research, development, demonstration, and deployment of solar energy technologies. SERI is also directed to help create a solar energy industrial base that will foster the widespread commercial use of solar energy.

The overall objective of SERI is to accelerate the commercial development of all solar technologies. The process can be visualized as containing four distinct

phases: research (in which scientific feasibility is determined), development (in which engineering feasibility is established), demonstration (in which engineering feasibility is tested and design improvements are made), and deployment (in which the product reaches widespread production and consumer utilization).

To best accomplish these practical goals and best provide a focus for the DOE's national solar energy program, SERI has developed an organizational structure consisting of five main operating divisions (Figure 1):

RESEARCH explores new areas of solar technology and contributes to the development and evaluation of existing technology. The division also supports DOE in the technical management of selected research programs and the development of major solar energy experimental test facilities.

ANALYSIS AND ASSESSMENT performs the analytical investigations required to support the development of national solar energy program plans and strategies. The division makes economic feasibility analyses and studies the environmental, institutional, and social factors that influence commercialization.

INFORMATION, EDUCATION, & INTERNATIONAL PROGRAMS conducts substantial programs in solar energy information dissemination, education and training, and national conferences and workshops. SERI is establishing a comprehensive and accessible solar energy information data base and is helping foster U.S. participation in international solar energy programs.

TECHNOLOGY COMMERCIALIZATION maintains extensive communication links with all sectors of the solar community and assesses the market readiness of each solar technology. This division collects and distributes information on materials, markets, standards, regulatory requirements, business risks, market barriers and constraints, as well as consumer attitudes.

ADMINISTRATIVE AND TECHNICAL SERVICES provides support for the technical divisions. This division includes personnel and secretarial services and the branches dealing with accounting, contracts, and procurement.

The Solar Energy Research Institute is presently housed in rented office space in Golden, Colorado. Operations will continue in these facilities until permanent facilities are designed and constructed. Both the interim and future facilities accommodate administrative, laboratory, library, and conference operations, as well as outdoor field experiments. SERI has emphasized the recruitment of a highly qualified, multidisciplinary staff from industry, universities, government, and private laboratories throughout the nation. By April 1978, SERI had recruited 220 employees from 25 states--the largest group of professionals ever assembled for efforts devoted exclusively to the development of solar energy. According to current plans, the staff will grow to approximately 350 by October 1978; to 500-600 by October 1979; and will stabilize in the range of 600 to 800 by the time the permanent facilities are ready for occupancy in the early 1980s.

Solar Standards Activities in SERI

Three divisions in SERI currently have programs addressing the development and implementation of solar energy technology standards--the Technology Commercialization Division, the Analysis and Assessment Division, and the Research Division. The Technology Commercialization Division, with support from the Research Division, is responsible for the management of the Photovoltaic Standards Development Program. The FY78 objectives of this program are to establish preliminary performance criteria for private sector applications in the 25-500 KW_e range and preliminary system, subsystem, and component test standards and procedures. Gary Nuss, Branch Chief for the Technology Evaluation Branch, presented a detailed discussion of this program in Technical Session I: Problems in Solar Testing--Photovoltaics, "An Approach for Development of Performance Criteria and Test Standards in Photovoltaics." To avoid undue redundancy, the present paper will focus on the other solar standards program at SERI.

The Analysis and Assessment Division is assessing the status of standards and codes which may affect the

commercialization of the solar technologies. The objectives of this research are to:

- o Provide information on the relationship between the development of codes and standards and the diffusion of technology;
- o Provide a methodology for determining the point in the development of a new technology where standards and codes should be developed and implemented;
- o Provide information to the federal and state governments on certification and warranty programs;
- o Identify and examine issues relevant to the use of standards and codes for tax credits and other incentives;
- o Provide an overview of standard and code activity in the solar energy field.

The project will focus on several basic topics central to standard and code programs.

Solar Energy Research Institute

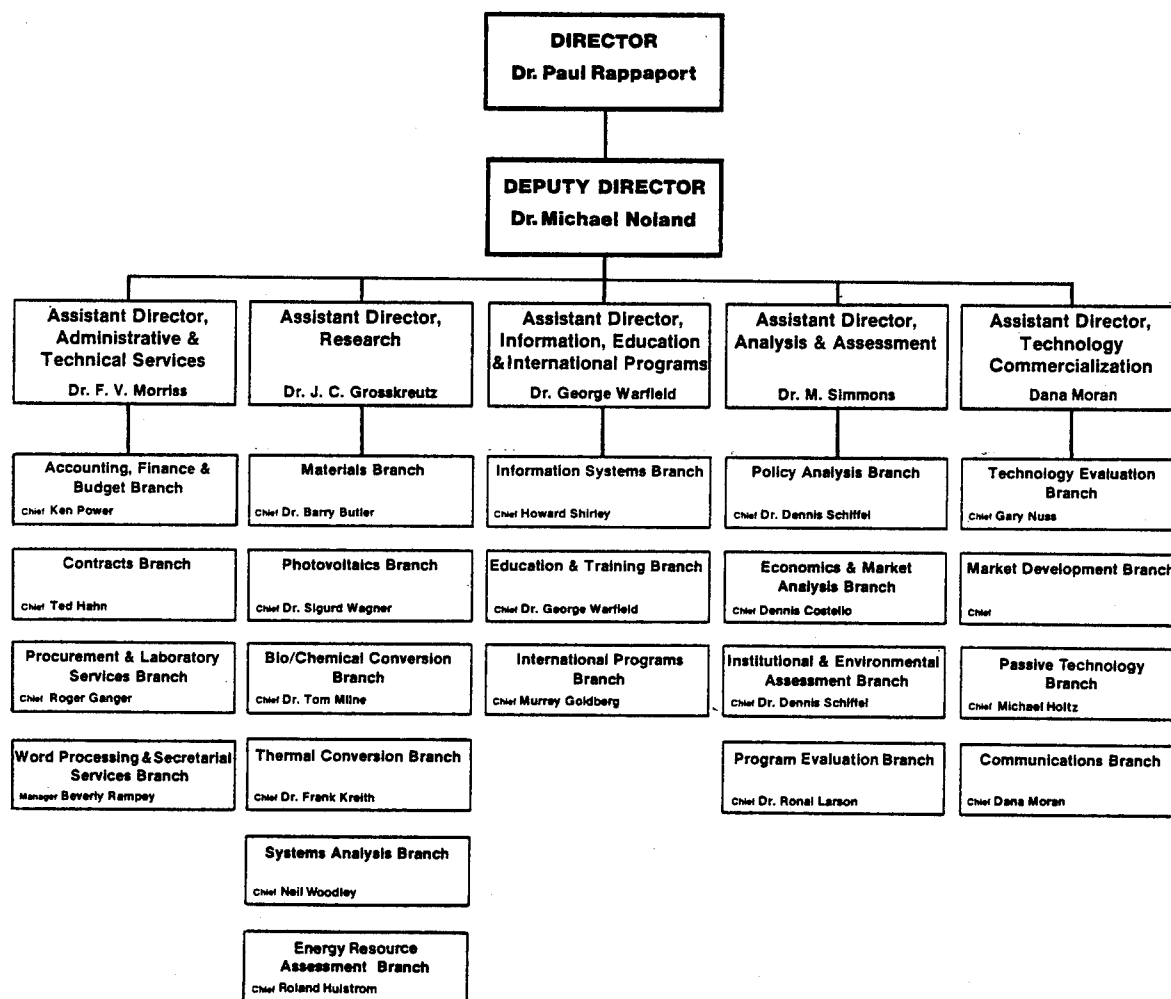


Figure 1. SERI Organization Chart

- o The formulation processes for standards and codes will be examined; e.g., Why are they developed? What are the institutions involved and their roles? Who and What do they affect and how? How have they responded to technology changes?
- o The implementation of standards and codes will be discussed. Who adopts them and why? How are they enforced?
- o The dynamics between technology development and standards and codes development will also be studied.

These discussions, combined with an assessment of the status of the solar energy technologies, will be used to examine the solar standards and codes environment.

This work will be based on an extensive literature search and discussions with principal actors in the standard and code and solar communities.

This effort will provide the baseline for further studies of institutional and social issues related to solar energy technology commercialization and the development and implementation of appropriate solar standards and codes.

Thermal Performance of Concentrating Collectors

A major task within the Thermal Conversion Branch of the SERI research division is the implementation of solar technologies in the mid-temperature range (100-300 C). The interest in this application range is a reflection of the large portion of the United States industrial process heat demand which occurs within this same temperature range. Figure 2 is a breakdown of industrial energy requirements as a function of the application temperature [1]. The figure indicates that approximately 30 percent of the total industrial energy demand is consumed at process end-use temperatures below 300C. A recent MITRE study

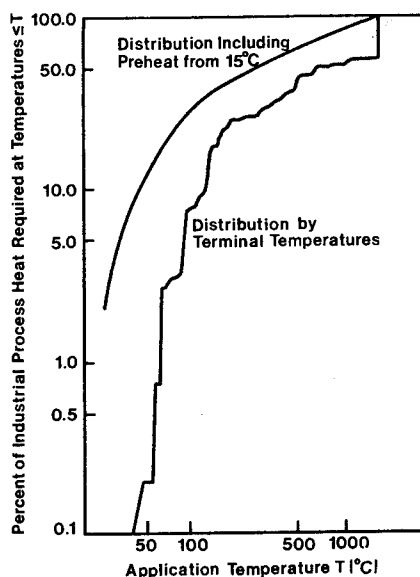


Figure 2. Distribution of industrial process energy requirements vs. application temperature.

[2] indicates that solar process heat systems are expected to be sufficiently cost effective to contribute 2 quads of energy by the year 2000 (23% of the potential market) and 13 Quads (54%) in the year 2020 within the United States.

Concentrating collectors are a generic type of solar device which can heat a working fluid most efficiently to 100-300 C. The more conventional flat plate technology is characterized by such low conversion efficiency in this temperature range that system costs become prohibitive, or temperatures unachievable.

Assessing the suitability of a specific concentrating collector in light of the end-use temperature demand is currently hampered by the absence of a widely accepted and practiced means for quantifying the thermal performance of such collectors. The consensus standard ASHRAE 93-77 (Methods of Testing to Determine the Thermal Performance of Solar Collectors) details a test and data presentation procedure which quantifies thermal performance for flat plate collectors. The national plan for the implementation of solar standards recognizes the need for a similar standard specifically directed at concentrating collectors [3]. One of the tasks of the Thermal Conversion Branch is to develop a procedure to fulfill this need. The subtasks involved in the implementation of this standard activity are:

- I.) Review flat plate and concentrating collector test procedures as conducted at universities, national and private laboratories, and industrial firms;
- II.) Generate a draft test procedure which produces, in a repeatable manner, all of the performance figures which would be required by users facing a variety of application needs;
- III.) Demonstrate the proposed test procedure in a field facility using several generic types of concentrators and revise the procedure as needed;
- IV.) Submit the refined standard to interested individuals knowledgeable with respect to the testing and use of concentrating collectors, revise as needed; and
- V.) Interact with the appropriate ANSI or ASTM committee in a nation-wide consensus standard process to promulgate the proposed thermal performance standard. Model standards will be used as a format guide.

It is expected that the thermal performance standard for concentrators will differ from ASHRAE 93-77 in several areas. Major unique items to be identified are:

- I.) The component or fraction of the incident radiation to which conversion efficiency will be referred. The specific field of view of the collector establishes this parameter,
- II.) The allowable range in circumsolar radiation permissible during testing,

III.) The definition of collector aperture,

- IV.) Allowance for the calorimetric ratio technique, or others, means in measuring performance as well as the $\dot{m} C_p \Delta T$ procedure,

\dot{m} = mass flow rate

C_p = specific heat of transfer fluid (at constant pressure)

ΔT = temperature rise of fluid through collector

- V.) The data presentation format for non-zero incident angles for collectors which are not fully tracking,

- VI.) The need for a time constant measurement, and

- VII.) Whether data can be presented in terms of the conventional $\Delta T/I$ -type parameter,

- VIII.) Where I is the insolation intensity and ΔT is a parameter indicating the increase in temperature of the fluid above ambient. Sometimes ΔT is given as:

$$\frac{T_{out} - T_{in}}{2} - T_{ambient}.$$

Parallel analytic studies are being conducted to help resolve issues which may be too expensive and time consuming to resolve by tests. Computer ray trace models can establish the sensitivity of concentrating collectors to the range in circumsolar conditions representative of various atmospheric conditions.

SERI will perform experimental studies of concentrating collectors in conjunction with its analytical efforts. These experimental studies will use facilities to build at 1650 m elevation near Golden, Colorado.

A test module is being designed which will permit a range of test conditions (fluid type, flow rate, and temperature) to be imposed on a variety of concentrating collectors. The field facility will include a rotating platform. Single axis collectors can then be operated in a dual axis mode so as to augment the portion of the day useful for testing. Laboratory support facilities will be available to consider such items as surface properties, absorber flow characters, surface contour errors, etc. It is anticipated that the field test capability will be implemented by the end of CY1978.

A concentrating collector thermal performance standard is needed if the potential mid-temperature solar user is to be able to reliably project the extent of his expected fuel savings over the useful life of the system. This will enable the user to compute the present worth of competing systems and, thereby, justify capital expenditures for solar systems in the appropriate circumstances. This current Thermal Conversion Branch task is structured to create a product that meets this need.

Materials Research

Successful commercialization of solar energy conversion technologies depends on their life-cycle costs in comparison with the benefits they provide. Those costs are, in turn, dependent on the costs of maintaining a given level of performance--maintenance costs--and on the value of lost benefits in case of failure. In addition to the simple economics of costs and benefits in solar technology, there is the problem of confidence in the system--i.e., system reliability. This matter is important in the decisions of users and, equally important, in the decisions of money lending organizations and investors. Therefore, in addition to the SERI efforts on analysis of institutional factors and performance of engineering experiments, there will be research efforts directed toward improved methods for prediction of system reliability from component and material performance information and toward improved methods for measuring and controlling such degrading factors as corrosion. These efforts are necessitated by the overall need for improvement in the technical and economic performance of solar energy conversion systems.

Reliability of systems is a complex statistical function of the reliabilities of their components and materials. The latter reliabilities must be determined by tests which simulate the degrading effects of usage and environment--effects which may be slowly cumulative. The tests must be, so far as practical, compressed into short time periods--accelerated--so that the reliability of system components and, hence of the systems, can be estimated before the system is built. Also, the results of tests can be combined with appropriate methodologies, usually statistical, to guide the design of a system to meet certain goals of reliability.

These tests and methodologies have reasonably clear meaning to the scientists and engineers who work with them. The users or investors, however, must have some system of codes and standards on which they can rely to assure them of a high probability that the system will perform in a suitable fashion--reliability--and that the effort required on their part to achieve that reliability is reasonable--maintainability.

The Materials Branch program will concentrate on development of methodologies for the assessment of the reliability of solar energy conversion systems, on development of lifetime and accelerated tests of the factors which affect reliability, and on studies of the degradation processes (corrosion, ultraviolet damage, etc.) which affect materials in solar energy conversion applications.

Present DOE programs--particularly the low-cost silicon array (LSA) and 10MW_e test programs--are developing reliability methods for specific problem areas. The SERI program would aim at generalization of these methods. The Materials Branch will address the following:

1. Identification and classification of reliability segments of present or planned DOE programs; a primary goal of this effort is the establishment of a "community of interest" and of open communication among all persons involved in reliability-related activities in solar energy conversion.

2. Collection and adaptation to solar systems of reliability engineering methods from other practices; e.g., automotive, electronic, aerospace. The initial goal of this effort is the development of a preliminary or "first draft" methodology for reliability analysis of a solar energy conversion system--probably photovoltaic or thermal electric.
3. Assessment of the status of lifetime and accelerated test projects in view of reliability program needs in order to identify limits of present reliability analyses and to direct attention to needs for further tests of material and component performance. One goal of this effort is a redirection or reemphasis on lifetesting and reliability prediction in materials research programs under DOE.

DOE demonstration programs are giving increasing attention to gathering of maintenance and reliability data. We will add to those efforts and begin the development of a centralized data bank of such information. We plan to include actual, instrumented data gathering on demonstrations not having their own measurement program and to collect processed data from those such as LSSA and the 10MW test, which will have complete reliability and maintenance programs. The program will include the following specific efforts for FY79:

--participation in the planning of solar demonstration programs to effect definite plans for measurements and records of reliability and related information;

--collection of reliability related data from DOE and private projects (e.g., Willard, N. Mex.; Mead, Nebr.; Clayton, N. Mex.); and

--initiation of a Reliability, Performance, Maintenance, and Failures data bank.

Conclusion

The SERI role in solar standards development is one of coordination aided by specific, in-house studies of some of the issues and phenomena involved in solar energy conversion technologies and their ultimate commercialization. The study of issues will identify the social, political, and economic factors which must be considered in creating standards and achieving their acceptance by industry and consumers. The technical studies of the phenomena involved in performance and reliability will provide information on which to base reasonable expectations of system performance and with which to design standardized performance tests. These technical studies will also yield methods for testing and improving the durability of materials used in the manufacture of components for solar energy conversion systems. The ultimate goal of these efforts is the availability of standards for comparison of performance and reliability of practical solar energy conversion hardware.

REFERENCES

- [1] Fraser, M.D., Analysis of the Economic Potential of Solar Thermal Energy to Provide Industrial Process Heat, Intertechnology Corporation, Report 00028-1, 1977.
- [2] Bennington, G.; Curts, P.; Miller, G.; Rebibo, K.; and Spervak, P., Solar Energy--A Comparative Analysis to the Year 2020, The MITRE Corporation, Report MTR-7579, March 1978, p.21.
- [3] Waksman, D.; Pieber, J. H.; Dikkers, R. D.; and Streed, E. R., Plan for the Development and Implementation of Standards for Solar Heating and Cooling Applications, Center for Building Technology, National Bureau of Standards, Report NBSIR 76-1143, August 1976.

CAST ACRYLIC FRESNEL LENSES FOR SOLAR ENERGY CONCENTRATION

Charles P. Lingle

Mr. Lingle is Engineering Manager at Swedlow, Inc. He graduated from Massachusetts Institute of Technology, Cambridge, Massachusetts, with an SB in Aeronautical Engineering, and from California State University, Long Beach, California, with an MBA.

In his position as Engineering Manager, Mr. Lingle is responsible for design of transparent and reinforced plastic articles; stress, thermal and optical analysis; and engineering research.

Prior to joining Swedlow, Inc., Mr. Lingle was employed by Rockwell International in several assignments over a 12-year period. His responsibilities there included development and delivery of three Saturn S-II Stages. Earlier responsibilities included development of mass spectrometers for Explorer XVII, production of a mobil dynamic checkout system for the Atlas pressurization system, structural analysis, experimental and analytical aerodynamics, analysis of nuclear weapons effects, and environmental testing.

ABSTRACT

Solar energy development clearly acknowledges that economic feasibility is a key to the viability of this alternate source of energy. Financial analyses have addressed both the initial capital investment and system life-cycle cost as critical concerns, and judicious selection of materials is recognized to be a key in both analyses. Acrylic is a low-cost, optically superior material suitable for use in lens concentrators. Discussion of material characteristics generally contained in solar energy technical literature tends to treat acrylics without regard to relevant fabrication-related differences. Acrylic (polymethyl methacrylate) can be fabricated by extrusion, compressive molding or casting. While each of the fabrication methods offers advantages, those peculiar to cast acrylic have been demonstrated to be ideally suited to prolonged outdoor exposure demanded of solar energy components.

This paper addresses the physical and mechanical characteristics of cast acrylic with emphasis on its use in fresnel lens concentrators. Experimental evidence is cited which confirms that cast acrylic is resistant to long-term degradation (optical and physical) when subjected to field weathering conditions. Various configurations of acrylic fresnel lenses that have been cast are discussed in the context of their most common system applications. Other applications of cast acrylic are cited which also entail prolonged outdoor exposure and in which degradation would have impaired the material acceptability. Mounting considerations relevant to acrylic lenses are discussed. The economic importance of weatherability is analyzed on a system life-cycle basis to demonstrate the significant advantages of cast acrylic over alternative materials.

INTRODUCTION

Evolution of solar energy technology has proceeded from laboratory novelty to interesting terrestrial opportunity to necessary spacecraft equipment, and is now widely recognized to be at least desirable — perhaps imperative — as a fundamental source of energy for numerous terrestrial applications. For many of those applications, concentration of the solar energy is economically and technically mandatory. The best technique for concentration is less clearly defined.

Requirements for a solar concentrator stem from technical, environmental and economic considerations. The degree of concentration that will enable optimum system performance is bounded on both the high and low side. Thermal and structural problems can ensue from excessive concentration. Low concentration, while more convenient to deal with, may result in sub-optimum receiver performance with the attendant economic penalties. Energy distribution on the receiver is also a key factor in optimizing system performance. Typically in a photothermal system, receiver size is a driving factor of system cost. Less commonly considered — electricity from photovoltaic cells is produced more efficiently toward the outer edge where conductors obscure a lesser proportion of the cell area than near the center. Concentration and distribution of incident solar energy must be matched to the receiver for optimum system performance.

A solar system must sustain long-term weathering. Degradation of system components may result from thermal cycling, UV radiation, moisture, and deposition of dust or other atmospheric pollutants. Life-cycle cost of a solar system will be increased by the need for periodic maintenance and replacement of concentrator, and system performance will be affected to some extent during the interim period. Resistance to weathering is certainly a significant attribute of a solar energy concentrator.

Currently, at least, concentrating systems must track the sun fairly accurately to maintain an acceptable level of effectiveness. Such factors as concentrator mass and wind loading on lateral areas increase the tracking problem (with additional cost penalties), and must be considered in the system design.

Judicious selection of a concentrator can minimize many problems, and can contribute other benefits. This paper addresses one option that is gaining increased acceptance — a fresnel lens cast directly of acrylic.

CHARACTERISTICS OF THE MATERIAL

Acrylic (polymethyl methacrylate) is a low-cost, optically superior material suitable for use in solar energy concentrators. It can be fabricated by extrusion, compression molding or casting. While each of the fabrication methods offers advantages, those peculiar to cast acrylic have been demonstrated to be best suited to prolonged outdoor exposure demanded of solar energy components.

Acrylic is transparent and extremely stable against discoloration. It offers good dimensional stability; desirable structural and thermal properties; good resistance to weather, breakage and chemicals; and resistance to loss of luminous transmittance due to UV irradiation.¹ The specific formulation (S-360) used by Swedlow in fresnel lenses is cast in the final lens geometry, highly cross-linked during polymerization and annealed to relieve residual stresses that may be present in the finished lens. General characteristics of S-360 acrylic are tabulated in Figure 1. Structural qualities, thermal behavior, optical performance and environmental resistance are parameters of specific concern in a solar energy collector, and a more detailed discussion of each follows.

Weight equates to cost in a tracking concentrator, therefore, the structural contribution of the acrylic lens can be used to reduce system weight. Structural characteristics of cast acrylic specifically of use to a system designer are contained in Figures 2 and 3.

SPECIFIC GRAVITY	1.19
WATER ABSORPTION	0.20 PERCENT
SPECIFIC WEIGHT	0.043 LB/IN. ³
ULTIMATE TENSILE STRENGTH	
PARALLEL TO FACETS	11,000 PSI
NORMAL TO FACETS	8,000 PSI
ELONGATION	4-10 PERCENT
ULTIMATE FLEXURAL STRENGTH	16,000 PSI
MODULUS OF ELASTICITY	450,000 PSI
BEARING STRENGTH	9,000 PSI
BARCOL HARDNESS	44
POISSON'S RATIO	0.35
THERMAL CONDUCTIVITY	1.2 BTU/HR/FT ² /°F/IN.
LINEAR THERMAL EXPANSION	4×10^{-6} IN./IN./°F
MAXIMUM SERVICE TEMPERATURE RECOMMENDED	200°F
HEAT DISTORTION TEMPERATURE	217°F
INDEX OF REFRACTION	1.50

Figure 1. Mechanical and Physical Characteristics of Cast Acrylic

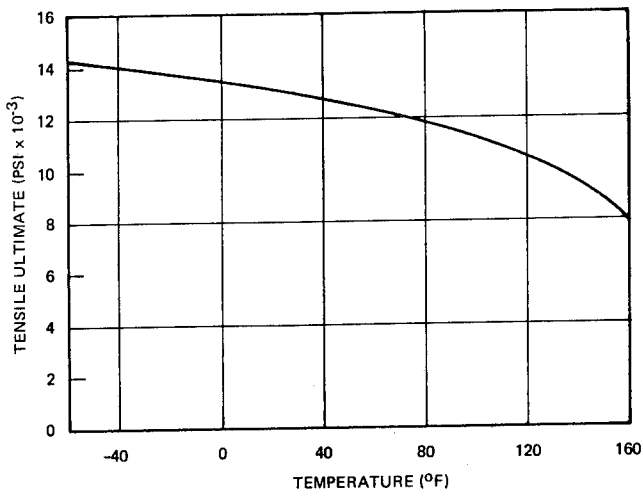


Figure 2. Cast Acrylic Tensile Strength

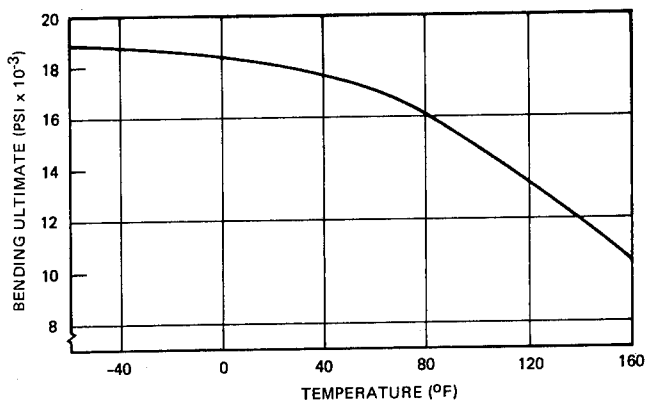


Figure 3. Cast Acrylic Flexural Strength

These data apply to Swedlow S-350 acrylic and differ to a degree from the more general information contained in MIL-HDBK-17A, a fairly common source for structural designers of plastic items, but correlate well with performance by the formulation used by Swedlow in lenses.

Hail damage may be of concern in many parts of the world. A nominal 3/16-inch thickness has been found to be sufficient to resist hail, and is the minimum recommended by Swedlow for lens concentrators.

Deflection of a lens can have a local effect similar to tracking error. Figure 4 shows deflection variation of a 3/16-inch-thick flat sheet under its own weight as a function of unsupported span. Deflection of a lens may be slightly greater depending on the facet configuration. Over the long term, creep may become a concern. Creep behavior of several acrylics are summarized in Figure 5. S-360 acrylic is too recent a development for equivalent data to exist, but its behavior may be inferred from the family characteristics. Creep of a lens in service will be much less, however, than the data would suggest due to variation of load direction as the collector tracks the sun during the day, and complete load reversal during the night when the collector may be stowed lens down.

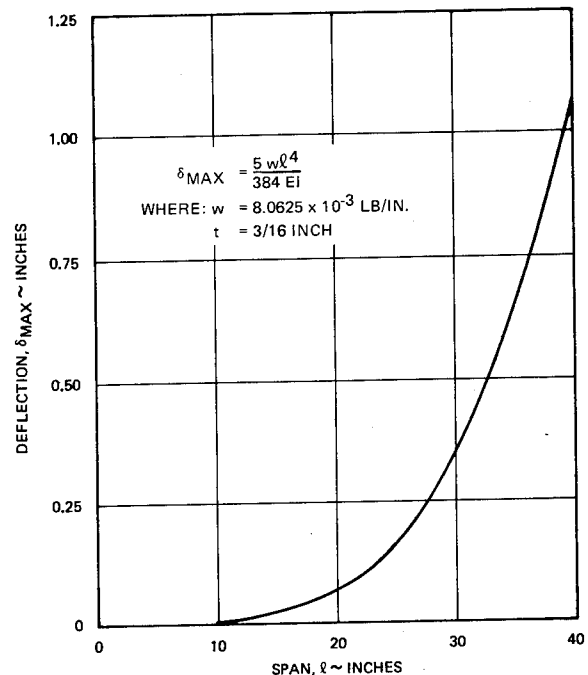


Figure 4. Deflection³ of Cast Acrylic Sheet Under Its Own Weight

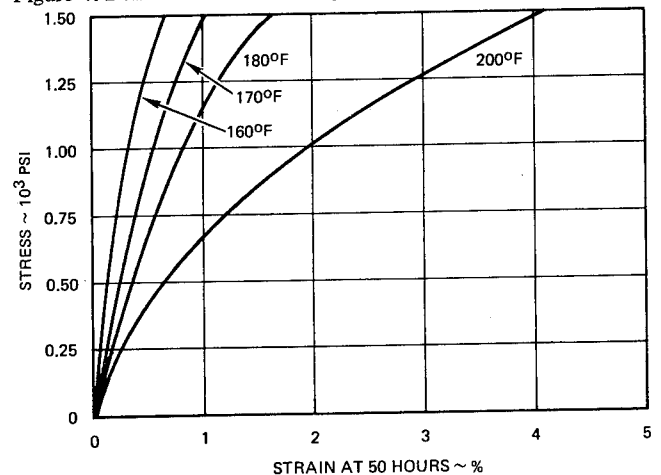


Figure 5. Creep Behavior of Cast Acrylic⁴

In addition to temperature related variations of structural characteristics, the thermoplastic nature of acrylic imposes another thermal consideration. The heat distortion temperature (contained in Figure 1) is that temperature at which the material becomes formable. Gross deformation of an unsupported lens may occur at this temperature. This characteristic has not proven significant in any solar collector to date; however, as higher concentration ratios are sought, convection from the receiver should be considered

to preclude heating the lens beyond the heat distortion temperature. Acrylic is a good insulator, so reradiation through the lens should be slight.

Optical distortion can be introduced into acrylic by residual stresses and density variation which may result from improper or incomplete polymerization. Care must be exercised to avoid banding or ripple. Luminous transmission as a function of wavelength is shown in Figure 6. As represented, the transmission data accounts for reflection losses as well as absorption by the acrylic, but excludes losses due to lens geometry. For solar energy applications, Air Mass 2 is a fairly average representation of the energy available during daylight hours. Integration of the spectral distribution of Air Mass 2 is shown in Figure 7. Thickness has a lower order effect on transmission. Although photothermal systems are concerned with the full range of spectral distribution, photovoltaic devices utilize only a limited wavelength range.

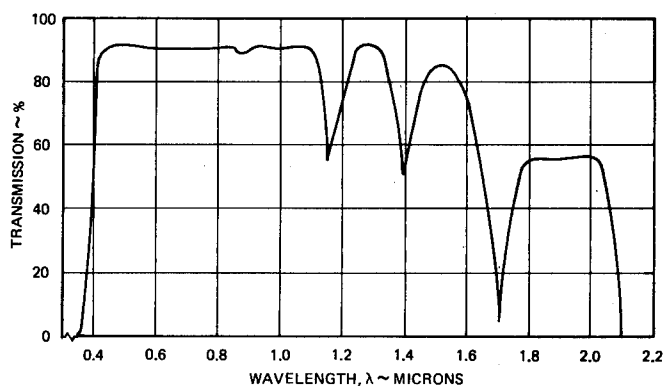


Figure 6. Luminous Transmission of 3/16-Inch Cast Acrylic (S-360)

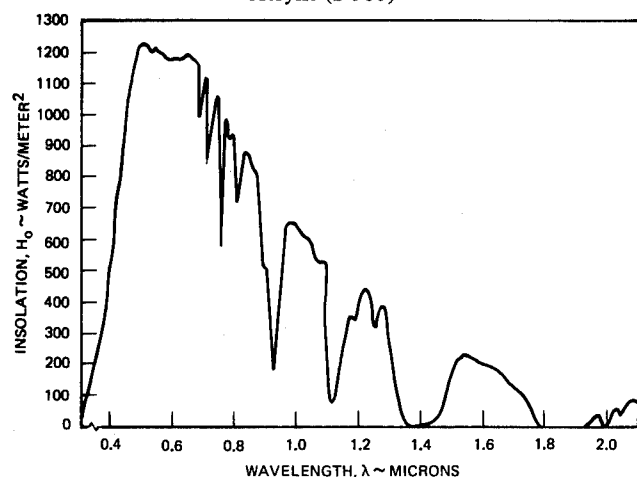


Figure 7. Air Mass 2 Spectral Distribution⁵

The lens of a solar energy collector also functions as the cover plate; hence, must provide good protection against environmental stresses. In general, acrylic is unaffected by most inorganic solutions, mineral and animal oils and alcohol in low concentrations. Lower esters, aromatic hydrocarbons, phenols, aryl halides, aliphatic acids and alkyl polyhalides usually have a solvent effect⁶. The longer term effects on acrylic of weathering were reported by Rainhart and Schimmel⁷. Cast acrylic sheet was found to be extraordinarily resistant to oxidative photodegradation during more than 17 years of exposure near Albuquerque. Behavior of aged specimens was compared with that of unaged control specimens with regard to optical transmission, chemical integrity, glass transition temperature and flexural properties. The transmission

data comparing unaged material, aged material as recovered, and aged material after polishing the exposed face are shown in Figure 8. No appreciable change of the chemical formula occurred⁸; however, reduction of the glass transition temperature from 114°C to 110°C indicates that chain length is reduced somewhat⁹. Flexural strength, tangent modulus and elongation compare as follows:

	Flexural Strength psi	Tangent Modulus psi	Elongation Percent
Aged	9,460	502,000	1.87
Unaged	18,200	467,000	5.43

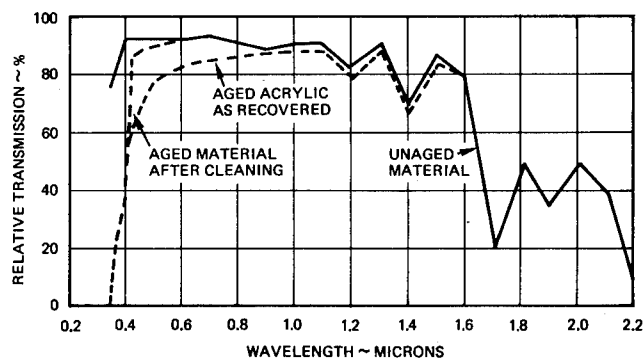


Figure 8. Effect of 17-Year Weathering on Cast Acrylic Sheet¹⁰

Existence of actual aging data is particularly fortunate. Recent experiments at Swedlow and the contrast between the Rainhart data and that of Anagnostou¹¹ seem to indicate that accelerated aging tests of acrylic (and possibly other plastic materials) can be grossly misleading.

CHARACTERISTICS OF THE LENS

Stated simplistically, a fresnel lens is developed by aligning surface increments of a conventional lens so that the bulk of nonbeneficial material customarily present in a lens is eliminated. Figure 9 illustrates this very simplified construction. If the individual facets are sufficiently narrow, the surface curvature can be approximated very closely by a flat surface.

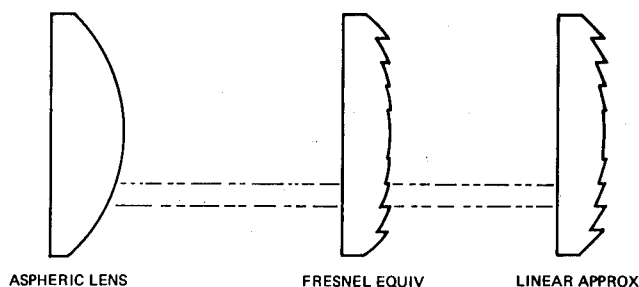


Figure 9. Development of the Lens Surface

Geometrical precision is critical, as might be expected, to control astigmatic and chromatic aberration, and a fresnel lens cut in optical glass is clearly uneconomical for any but experimental applications. The ability to replicate precisely in acrylic permits amortization of the costly machining over a large quantity of lenses. Figure 10 depicts Swedlow's current projection of fresnel lens cost as the quantity of lenses having a single design increases.

This relatively low cost makes refractive concentration viable for solar energy.

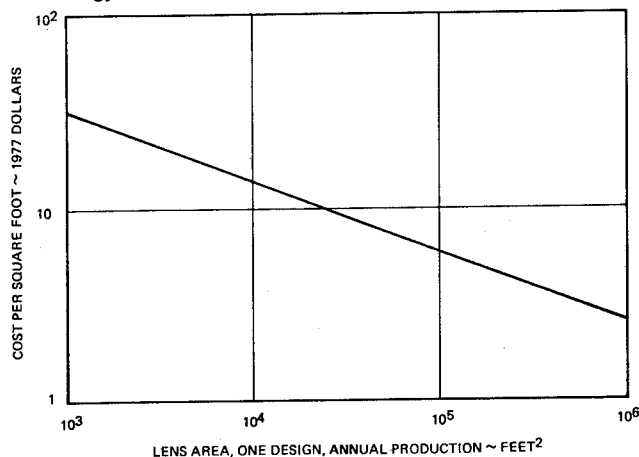


Figure 10. Projected Cost of Swedlow Fresnel Lens

Facets are cut individually to exacting dimensional tolerances. Typical tolerances of a casting die are summarized in Figure 11. The machining process is specific to each facet cut; hence, each facet

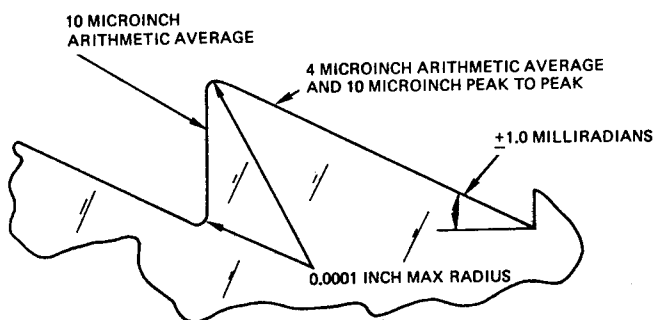


Figure 11. Lens Casting Tool Tolerances

can be designed to refract the energy to a specific area as shown in Figure 12. Using this capability, a fresnel lens can be designed to concentrate energy in a specific distribution across the receiver at a specific focal length and concentration ratio.

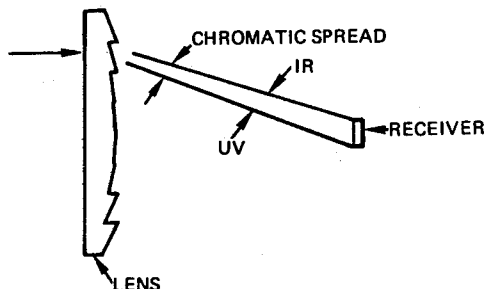


Figure 12. Fresnel Lens Concentration

Selection of lens focal length is influenced by the need to minimize loads on the tracking system caused by collector mass and wind loading; and by the need to concentrate energy on the receiver accurately and with the desired distribution. Longer focal length increases tracking system loads in two ways:

- Increased structural weight due to wider separation between lens and receiver.
- Greater wind loading due to the increased lateral area.

Shorter focal length increases system sensitivity to tracking error and increases reflection losses. Lens design involves optimization to fix the focal length for the best compromise among the competing objectives.

Concentration is also determined by the lens design. Considerable flexibility is available in selecting the concentration that will be employed, but, again, system penalties must be considered. The system design objectives that may be affected by concentration ratios are:

- Profile of the energy distribution across the receiver.
- Quantity of unused energy which must be disposed of as heat.
- Width of the receiver.
- Unit cost of the peak energy produced by the system.

Selection of the concentration ratio requires optimization among these parameters. With increased concentration, the rate at which the energy level falls off near the edges of the receiver tends to diminish. This characteristic is apparent in Figure 13 by the contrast between distributions A (lower concentration) and B (at the higher concentration) for a uniform distribution. The lower concentration permits a more uniform distribution. Allowable nonuniformity for efficient cell operation may require that a greater portion of the available energy in Case B be lost beyond the edge of the cell than in Case A to achieve higher concentration.

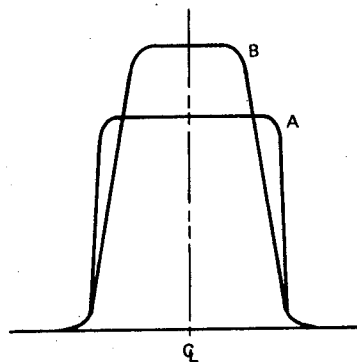


Figure 13. Effect on Energy Distribution on Concentration Ratio

Concentrations as high as 2000X are quite feasible with a circular lens using current technology. Linear focusing lenses with 80X concentrations are also within the state of the art.

Optimum energy distribution is very much a function of the receiver. The easiest for a system designer to specify is uniform, and a square wave the most commonly required of Swedlow. Other distributions may be superior.

Uniform distribution across a circular heat pipe results in reflection losses on the sides where the angle of incidence is high. Greater concentration toward the top of such a pipe would reduce this loss.

Uniform distribution across a photovoltaic cell places as much flux density near the center as near the edge of the cell. Typically, shadowing by conductors is far greater near the center of a cell.

Greater concentration toward the edges would increase system efficiency.

The inherent design flexibility of a fresnel lens permits optimization of the lens for its system application. Focal length, concentration ratio and energy distribution at the receiver can be tailored to assist in achieving the goal of reduced system cost of the energy produced.

OTHER SYSTEM CONSIDERATIONS

Use of a cast acrylic fresnel lens in a concentrating system presents some additional assets as well as limitations that must be considered. The structural qualities of cast acrylic can be utilized in designing the collector housing. With a sealed housing, the cover plate of the receiver can be eliminated, thereby reducing collector weight. By sealing the collector, intrusion into the concentrated beam by personnel or debris is prevented, thus making the installation inherently safer. Maintenance of the lens is reduced to periodic washing of the smooth exposed side, and conventional techniques can be used to refurbish the surface in the event of sandstorms or other abrasive damage without impairing optical performance.

Several lens installation options are available. Placed in tension, the lens can provide structural stabilization for the collector housing enabling further weight reduction. The tendency of plastics to creep argues against loading the lens with inplane compression, but conventional retainers can be used. The lens can be clamped or bolted into place.

As was implied earlier, a large lens may require support to preclude excessive deflection under its own weight or under wind loading. Deflection of the lens will introduce angular error which acts incrementally very much like tracking error, and should be avoided. Lenses can be assembled with integral acrylic beams, but thin metal supports can be used with minor shadowing. In each case, tensile loading of the lens can be designed in, and will reduce support requirements.

CONCLUSION

Cast acrylic fresnel lenses have been demonstrated to be effective, low-cost concentrators for solar energy systems. Ease of replication in acrylic offers a significant system cost reduction compared with alternative concentration techniques. Demonstrated superior resistance to long-term weathering and ease of maintenance further reduce the life-cycle cost of concentrating systems.

Opportunities for collector weight reduction imply that tracking systems' cost can also be reduced when an acrylic lens is used. Known mechanical and physical characteristics of cast acrylic enable the system designer to exploit the assets and provide for the limitations of the lens during system design. The nature of a fresnel lens and the methods used to produce it permit tailoring of energy distribution on the receiver, thereby enabling the system designer to better exploit performance potential of solar cells and thermal receivers. The goal of lower system cost of solar energy is benefited by understanding and use of cast acrylic fresnel lens concentrators.

REFERENCES

1. Modern Plastics Encyclopedia, Vol. 52, No. 10A, pp. 8-10, October 1975.
2. MIL-HDBK-17A, Part II, Plastics for Aerospace Vehicles: Transparent Glazing Materials, Richard S. Hassard, January 1973.
3. Timoshenko, S. and Gleason H. MacCullough, Elements of Strength of Materials, D. Van Nostrand Company, Inc., New York, p. 182, May 1952.
4. MIL-HDBK-17A, Part II, Plastics for Aerospace Vehicles, Part II Transparent Glazing Materials, AFML, Wright Patterson AFB, Ohio, p. 4-38, January 1973.
5. Handbook of Geophysics and Space Environment, AFCRL, p. 16-9, 1974.
6. Technical Data - Plastics Department, Rohm and Haas, p 2-5-32, 11/1/73.
7. Rainhart, L. G. and W. P. Schimmel, Jr., Effect of Outdoor Aging on Acrylic Sheet, SAND 74-0241, Sandia Laboratories, p. 5, September 1974.
8. *ibid.*, p. 9
9. *ibid.*, p. 10
10. *ibid.*, p. 18
11. Anagnostou, Evelyn and Americo F. Forestieri, Preliminary Results of Accelerated Exposure Testing of Solar Cell System Components, ERDA/NASA 1022/77/14, NASA TM X-73674, May 1977.

SIMULATION OF TERRESTRIAL SOLAR RADIATION

By: David Askin and Milton Resnick
ARRADCOM, Dover, NJ

Mr. David Askin (Supv General Engineer GS-14) is now Chief of the Instrument Engineering Branch, Fire Control Systems Division, ARRADCOM, Dover, NJ. From 1951-1977, Mr. Askin was Chief of the Environmental Laboratory at Frankford Arsenal, Phila. Penn. For two years prior to that he was Chief of the Environmental Test Laboratories of the Naval Air Development Center, Johnsville, Penn. For four years preceding this, he was Assistant Director, Research and Development Lab., Refrigeration Div., Philco Corp., Phila. Penn. During the Second World War he was Mechanical Engineer in the Small Arms Planning Div. of Frankford Arsenal, and from 1943 to 1945 was the Deputy Chief of the Fire Control Instrument Branch of the Gage Sub-Office, Office Chief of Ordnance, Philadelphia. Mr. Askin has a BA degree in Math & physics from Univ. of Penn. and a BS degree in Electronic Engineering from Lehigh Univ., and has a Vocational Teaching Certificate from the State of Penn. Mr. Askin has taught Refrigeration and Air Conditioning for three years prior to World War II and has been teaching in the evenings in various Pennsylvania Universities and Technical Schools since 1946. Mr. Askin has presented many papers and chaired many sessions at the Annual Meetings of the Institute of Environmental Sciences (IES). Mr. Askin is a Fellow in the IES and a former national Vice President of the IES, and holds a Professional Engineer License in the State of Penn.

Mr. Resnick received his BS in ChE from the City College of the City University of New York and his MS in Chemistry and Chemical Engineering from Stevens Institute of Technology. He joined ARRADCOM (formerly Picatinny Arsenal) in 1950 and has been involved in studying the effects of the natural environment on materials and munitions since 1957. He is presently assigned to the Technical Support Directorate as a project engineer. Mr. Resnick is a Senior Member of the Institute of Environmental Sciences and has served on many governmental committees relating to environmental testing.

Material exposed to direct solar radiation is markedly affected by the rays of sunlight. Depending on their composition and chemical structure and surface roughness and color, materials are heated, degraded, blistered, crazed, cracked and otherwise affected by solar radiation. Many studies have been made to determine the effects of exposure to solar radiation on a variety of materials, coatings, items and systems. But it often takes a long time to get the results of such field testing. Hence, the development of solar radiation chambers. These simulate natural solar radiation and thereby engage in accelerated and aggravated tests to reduce the time it takes for exposure to natural sunlight, and reduce costs of testing.

Solar radiation reaches the top of the earth's atmosphere at a constant rate. This rate, called the solar constant, has been given the best value of $1.95 \text{ cal/cm}^2/\text{min}$ ($434 \text{ Btu/ft}^2/\text{hr}$) by Drummond, et al. based on rocket and high altitude aircraft

and balloon flights (1) (2) (3). By the time the radiation reaches the earth's surface it has been attenuated by certain atmospheric gases (CO_2 , H_2O and O_3) and pollutants to a maximum value of $355 \text{ Btu/ft}^2/\text{hr}$ (103.8 W/ft^2 or $1.56 \text{ cal/cm}^2/\text{min}$).

The spectral distribution for solar irradiation is shown in Figure 1 (4). The upper solid curve shows the spectral distribution outside the atmosphere; the lower solid curve is the spectral distribution at sea level. It is this lower curve which we try to reproduce in chambers when simulating solar radiation to deal with ground based materials. Chambers and lamps designed to simulate space conditions are too sophisticated for simulating ground conditions. While the wavelengths leaving the sun range from 10nm to $100,000\text{nm}$ those reaching the earth's surface range from about 290nm to about 2500nm . The solar wavelengths reaching the earth can be split into three (3) bands: (a) ultraviolet from $290\text{--}380\text{nm}$, (b) visible light from $380\text{--}780\text{nm}$ and (c) infrared from $780\text{--}2500\text{nm}$. Radiation below 290nm and above 2500nm is mostly filtered out by the atmosphere. The atmosphere is transparent to radiation between 290nm and 2500nm , except for the 2 major absorption bands caused by H_2O and CO_2 . At sea level, 4.5 to 6% of the total radiation received at the earth's surface is ultraviolet, 50 to 53% is infrared and the balance is visible. The vast majority of the solar energy spectrum is produced in the wavelength region above 200nm . The shape of the continuous spectrum reaching the top of the earth's atmosphere, is that of a black body radiating at about 6000°K .

Total radiation from the sun also includes other types of wavelengths both below and above those normally considered solar radiation, i.e. X-rays, gamma rays and cosmic rays below, and radio waves and other electric waves above. The infrared waves of solar radiation are considerably filtered in regions of selective absorption by the water vapor and carbon dioxide in our atmosphere, which accounts for the lower percentages of infrared at sea level (see Figure 1). The ultraviolet is also considerably filtered by the time it reaches sea level, so that practically no ultraviolet lower than 290nm reaches the earth. Incidentally, the ultraviolet is also responsible, to a great extent, for the production of ozone in the atmosphere.

Only about 80% of the energy incident on top of the atmosphere reaches the earth's surface; most of the remainder being reflected, scattered or absorbed by the atmosphere. The total intensity reaching the earth's surface varies from 0 to over 104 W/ft^2 at different locations throughout the earth, being highest in hot desert areas and lowest, generally, in cold high humidity areas. The total intensity also varies considerably from season to season, but always has approximately the same spectral distribution at sea level (except for the absorption effects of H_2O and CO_2).

A characteristic curve for solar radiation vs time is given in Figure 2 which was recorded on a

cloudless day in Yuma, Arizona. The ordinate records intensity in $\text{cal/cm}^2/\text{min}$. The peak value, at solar noon, is $1.43 \text{ cal/cm}^2/\text{min}$ or $317 \text{ Btu/ft}^2/\text{hr}$. The bottom curve on the chart is an integrating curve from which we get a total value for the day of 712 Langleys ($712 \text{ cal/cm}^2/\text{day}$). The maximum air temperature on that same day, May 27, 1973, was 104°F which occurred 2-3 hours later than peak solar radiation intensity. Note that the peak value of solar radiation intensity remains at that point only for a short time, perhaps half an hour. This fact should always be considered when setting up a solar radiation chamber to simulate a solar day. Maintaining the peak value for a longer period results in accelerating or aggravating the test.

Solar radiation affects equipment in various ways. The ultraviolet portion has deleterious effects on most organic materials (Rubbers and plastics, etc. become brittle and crack and craze). The visible portion affects coloration and often causes fading of paints, leather and textiles. The infrared portion of the solar spectrum (along with the visible) provides the thermal absorption and penetration effects which cause heating. The human eye can perceive radiation in the very limited range of wavelengths between 400nm and 700nm only. Radiation between 700nm and 3000nm comprise the penetration type of thermal radiation. Radiation above 3000nm is non-penetrating infrared. Whereas ultraviolet and visible radiation can be destructive, infrared radiation is primarily not destructive.

In the past, solar radiation simulation consisted primarily in simulation of its heating effect only, by use of infrared lamps. The ultraviolet effect of solar radiation was provided separately by use of carbon arc and other ultraviolet producing lamps in devices such as weatherometers, etc. During and shortly after the second World War some attempts were made by various government laboratories and industry to combine the ultraviolet, visible and infrared of sunlight in one facility by combining ultraviolet producing lamps with infrared lamps. This combination actually did not closely simulate the actual spectral distribution of natural sunlight, but did provide the total intensity desired with a mixture of ultraviolet, visible and infrared.

Formerly, government specifications called for 8 to 12% ultraviolet (below 400nm) and 45 to 55% infrared (above 700nm) with the balance visible light, and with a total intensity of 360 Btu/hr/sq ft . ($105.5 \text{ watts/sq ft}$). Recently these specifications were corrected to more closely correspond to that which exists in nature at sea level. They now call for 4.5 to 6.0% ultraviolet (below 380nm), 50 to 60% infrared (above 760nm) and the rest visible, with a total intensity of 100 to 110 watts/sq ft . It should be noted that the percent infrared specified is somewhat higher than exists in nature, to allow for practical attainment by use of commercially available lamps.

The desire to simulate natural sunlight in the laboratory was hindered by the fact that commercially available lamps were designed for outdoor lighting (stadia, ballparks, etc.) and thus concentrated on providing visible light. With the advent of the space age, newer lamps have been developed to more closely simulate natural sunlight.

Frankford Arsenal has been in the forefront of solar radiation simulation since the 1950's. An investigation of all commercially available lamps was undertaken in 1955 to see which would be suitable for simulation of solar radiation. It was determined, at that time, that no single lamp or combination of commercially available lamps would provide a close approximation of the spectral distribution and proper percentages of relative intensity required. The specifications called for the simulation of the complete range of the solar spectrum and the capability to vary intensity between 0 to 130 watts/sq ft .

After a great deal of investigation, Frankford Arsenal narrowed its search to two high intensity mercury vapor lamps, the Westinghouse internal reflector 400 watt LH-1 and the GE 1200 watt UAll-B. Finally, 149 LH-1 lamps were installed on a ceiling rack in three electrical banks. The rack went into a 10 ft x 11 ft chamber to provide an illuminated area of 86 square feet. The rack could be lowered from 5 feet to within 30 inches of the specimen and the 149 lamps could provide up to 150 watts/ft^2 on the upper surface of the test specimen. The lamps could be raised up to five feet above the specimen and the three separate electrical circuits could be switched on or off to provide for variation in intensity.

The completed sun room was measured for uniformity of intensity by means of a quartz envelope pyrheliometer. It was found that the cross-sectional intensity was quite uniform in the central 64 sq ft area, varying from 0 watts/ft^2 to a maximum of 150 watts/ft^2 with the lamp rack located 30 inches above the pyrheliometer. The desired intensity levels and distribution had been achieved. But the spectral distribution was not truly representative of natural solar radiations. Whereas an NBS measurement of a single LH1 lamp gave percentages of ultraviolet, visible and infrared within the desired values, measurements of the bank of lamps in the sun room were far different. The lamp bank provided too much infrared and was deficient in the visible range. Hence the search for better lamps continued, although the sun room was used for test purposes with a realization of its limitations.

When the family of Multivapor Arc Lamps made their appearance in the early 1970's, Frankford Arsenal obtained samples of these lamps for evaluation. Mercury vapor arc lamps are deficient in the visible range and it was reported that the multivapor arc lamps were better in this respect. Multivapor lamps contain the iodides of Scandium and Sodium in addition to mercury vapor. This combination improves their visible output. However, these lamps were not available with built-in internal reflectors.

Frankford Arsenal ordered several coated and clear multivapor lamps and, at this time, decided to change from 400 watt lamps to the 1000 watt lamps. The larger size gave considerably increased intensity which was required since it was now necessary to use external reflectors to direct their energy downward on the test specimens. 1000 watt coated and clear mercury vapor lamps were also obtained for comparative purposes. The spectral distributions of the 1000 watt lamps, singly and in

combinations, were then determined by the Pitman-Dunn Laboratories. The results are shown in Figures 3, 4, 5 and 6. Figures 3 and 4 show the single lamp spectrum for the clear mercury vapor lamp and the coated multivapor lamp respectively. Figure 5 gives the spectral distribution for a two lamp mercury vapor/multivapor combination and Figure 6 gives the distribution for a three lamp combination of 2 mercury vapor/1 multivapor lamps. The best distribution occurred with the three lamp combination, Figure 6. Each of the curves was integrated with a planimeter and the percentage UV, visible and IR determined.

Table 1 gives the percentage of ultraviolet, visible and infrared for the curves in Figures 3, 4, 5 and 6 compared with the percentages found in natural sunlight.

Analysis of the spectral radiation curves and the data in Table 1 distinctly shows that the multivapor lamps produce much more visible light than the mercury vapor lamps. However, the multivapor lamps are low in ultraviolet. Accordingly, combinations of lamps were tried, Figures 5 and 6. The two lamp combination, Figure 5, was an improvement over the single lamp spectra. But the three lamp combination of 2 clear 1000 watt mercury vapor lamps and 1 coated 1000 watt multivapor lamp gave the best percentages of UV, visible and IR (See Table 1). The three lamp combination, however, was still too rich in the visible and deficient in the infrared.

Based on these studies of the spectral outputs of the lamps and combinations thereof, and the space available, an engineering decision was made to change the ratio from 2 to 1 mercury to multivapor to a 3 to 2 ratio. Accordingly, the lamp arrangement decided upon includes 25 GE, 1000 watt, H-36, Mercury Vapor Arc Lamps and 16 GE, 1000 watt, MV 1000, Multivapor Arc Lamps for a total of 41-1000 watt lamps. These lamps are housed in 17" diameter GE Luminaire reflectors made of a highly polished special aluminum designed to reflect all the wavelengths produced by the lamp. This works out to approximately a 3 to 2 ratio. The lamps were installed on the lamp rack so that the lamp would fill in the rectangular space with which we had to work. Spectral distribution measurements showed that the combination of lamps was still deficient in IR, so forty (40) 250 watt, internal reflector, infrared lamps were added to the lamp rack uniformly interspersed between the 41 mercury and multivapor lamps. The final arrangement of the 81 lamps is shown in Figure 7.

The spectral distribution of the lamps in the solar radiation simulation chamber first installed in Frankford Arsenal in 1957 was measured with a recording spectroradiometer built by Sunshine Scientific Co. in accordance with Frankford's specifications. This instrument was built around a prism type double monochromator which covered the spectral range of 220nm to 2500nm (7). After being used for more than 15 years it became uneconomical to repair. The new lamp arrangement could not be calibrated until new measuring equipment was obtained. Frankford Arsenal purchased a new recording spectroradiometer centered around a Schoeffel grating type single monochromator.

The apparatus includes: a Schoeffel GM250, grating type, single monochromator with three gratings which cover the wavelength range of 180nm to 2500nm to which a Centronix S-20 photomultiplier tube is directly attached in a Schoeffel D 500 T photomultiplier housing. A Schoeffel M460 Photomultiplier Photometer measures the output in picoamps and sends the signal to an H.P. X-Y plotter where intensity is plotted vs wavelength. Since this photomultiplier cuts off at about 800nm the system was originally designed with an adapter which would permit us to remove the photomultiplier assembly from the exit of the monochromator and affix in its place an Eppley 8 - junction bismuth - silver thermopile to measure the infrared output from the monochromator (wavelengths from 780nm to 2500nm). The output of the thermopile is fed to a Keithley Model 414 micro-microammeter which measures the output. The output then goes to the H.P. X-Y plotter.

The monochromator delivered so low an infrared light level to the thermopile that a lot of noise was developed preventing us from getting reliable infrared readings. We tried a 16 - junction thermopile but got no significant improvement. We had to abandon the thermopiles to determine the infrared intensity and decided to measure the total energy output with an Eppley Pyranometer (with a Schott glass envelop) and then get the IR by subtracting the UV & VIS from the total energy. Figure 8 is a block diagram of the light path through the spectroradiometer.

The spectroradiometer is calibrated with an NBS calibrated 1.0 KW quartz iodine lamp. The quartz - iodine lamp was set 25cm vertically above an MgO coated polished aluminum mirror set at a 45° angle. The entrance slit of the spectroradiometer was located horizontally 25cm from the center of the mirror so that the light path from the lamp to the entrance slit was exactly 50cm. The MgO coating provides a uniform source of diffuse light. The scanning speed was 100nm per minute and the grating range was 180-800nm.

The total irradiation of the lamp array was measured first to see how uniformly the radiation was being distributed. Measurements of total radiation were made at various points in the chamber with an Eppley pyranometer. A 9 ft x 9 ft square was laid out in the chamber and divided into 9 3 ft x 3 ft grid. The nine (9) sections in the grid were numbered as shown in Figure 9 and the sequence of measurement was one (1) through nine (9). Area nine (9) is the central section of the grid. The lamps were turned on gradually to full power and the lamps were allowed to become stabilized for 15 to 20 minutes before taking any measurements. The pyranometer was centered in each section when the light intensity of that section was measured. This procedure permitted us to determine how uniformly the radiation produced by the lamp array was being distributed throughout the 10 ft x 11 ft chamber over the area of interest. Radiation measurements were made with the bottom of the reflectors set at heights of three (3) feet, four (4) feet and five (5) feet above the pyranometer. Table 2 gives the results of these measurements. From these data it is possible to determine how uniformly the lamp array simulates natural sunlight.

Analysis of Table 2 shows that the radiation intensity varied inversely with the height, which is to be expected from the inverse square law. The best light distribution, or uniformity, occurred with the lamps set at the highest position. As expected, the four corner sections of the grid received the lowest amount of radiation since the lamp array was in the shape of a square. The highest value of radiation intensity was measured in the center section of the grid, section 9, at each height. It can be seen that the lamps provide adequate intensity to meet the value of 104.8 watts per sq ft (355 Btu/hr/sq ft) specified in MIL-STD-810C and as described in MIL-STD-210B for desert conditions. The height of the lamp array can be varied from within 30 inches of the floor to nine (9) feet above the floor by means of an electric winch. Various banks of lamps can be turned on or turned off, as desired. This capability of being able to raise or lower the lamp rack and/or turn on or off various banks of lamps enables the intensity to be varied from zero to 140 watts/ft² at will, and permits the simulation of a solar day.

The next step in the calibration of the chamber was to determine the spectral distribution of each section in the grid shown in Figure 9 with the calibrated spectroradiometer. The magnesium oxide coated aluminum mirror inclined at a 45° angle was added to the system to direct the light from the overhead bank of lamps to the entrance slit of the spectroradiometer because a horizontal light beam is required to enter the entrance slit. The inclined mirror was positioned at the center of each grid section. Grating No. 1, covering the spectral range of 280 - 780nm, was used in the spectroradiometer. The other conditions were the same as when the spectroradiometer was calibrated with the NBS-calibrated quartz - iodine lamp. A curve of relative intensity vs wavelength was drawn by the X-Y plotter. Measurements were started in Section 1 of the grid and proceeded in sequence to Section 9. Because the thermopile used with the spectroradiometer was unable to measure the infrared portion of the spectrum, only the range of 280 - 780nm was covered in the curve. The percent IR in the radiation produced by the lamps was obtained by taking pyranometer readings without a filter and then using a Schott RG-780 filter to screen out the ultraviolet and visible radiation. This gave us the percent infrared.

The curves of relative intensity vs wavelength were corrected to conform to the intensities obtained with the quartz - iodine lamp and then the corrected curves were integrated to give us the energy for the ultraviolet and visible in microwatts per square centimeter. From these data the percent UV and visible in the 280 - 780nm range could be calculated.

Table 3 shows the calculation of the percent IR and percent UV + Visible from the pyranometer readings with and without a filter when the lamp rack was 53 inches above the pyranometer.

Figure 10 is a curve for the raw data of relative intensity vs wavelength measured by the spectroradiometer with the corrected curve superimposed on it for Sector 9, the central sector of the grid. This curve was drawn for the condition

with the lamps five (5) feet above the spectroradiometer. The corrected curves were integrated to get the total energy for UV and Visible. Table 4 gives the relative values for UV and Visible obtained.

The contribution of the ultraviolet, visible and infrared, individually, to the total intensity recorded in each grid section can be determined from the data in Table 2 (pyranometer readings at 5 feet) and Tables 3 and 4. From these data the intensities of the UV, Visible and IR individually can be calculated as well as the percentages of each as a function of total intensity. Table 5 summarizes this information.

Table 5 shows that the distribution of the radiation is uniform throughout the chamber. The intensities and percentages of the UV, VIS and IR are very close from sector to sector. These data, however, show that the irradiation produced by the lamp bank is deficient in ultraviolet and visible which should be about 5% and 43% respectively and is too high in the infrared which should be about 52%.

These results are not discouraging since they indicated the direction in which changes must be made to produce the correct mix of radiation which will simulate the percentages of UV, VIS and IR in natural sunlight. Furthermore, it should be remembered that this system is relatively new and that the data presented in this paper are the first that were taken in calibration of the chamber (while still at Frankford Arsenal).

Meanwhile, it has been demonstrated that the lamp array can produce sufficient total radiation intensities to conform to all specifications for solar radiation testing at ground level. The system by which the rack of lamps can be raised or lowered and various lamp banks turned on or off permits us to simulate a solar day without any difficulty. Although the present system of lamps used produces too little UV and too much IR, it is expected that these relative percentages can be considerably improved by slight modifications to the lamps selected to be reinstalled at ARRADCOM.

The closing of Frankford Arsenal and the transfer of equipment to ARRADCOM prevented corrective action from being taken to improve the lamp array output. This equipment is scheduled for installation in the near future in ARRADCOM, Dover, NJ. The design of the new chamber calls for the lamp rack and electric winch to be installed in a partitioned-off 12 ft x 12 ft section of a larger chamber, capable of maintaining a constant air temperature of 120°F or being varied between 90°F and 120°F. Air flow will be maintained at 500 - 800 ft/min. When the new chamber is installed in ARRADCOM we intend to replace the 250W IR bulbs with 150W bulbs to reduce the percentage of IR and thereby increase the percentage of UV. This should bring the respective percentages within the desired limits. The new chamber, located in a much larger room, provides room for expansion. It is expected that the expanded capability will allow a range of items much larger than can presently be put in the chamber, perhaps the size of an armored vehicle or large weapon system, to be subjected to solar radiation testing.

BIBLIOGRAPHY

1. Drummond, A.J., Hinckley, T.R., and Scholes, "New Value for the Solar Constant" Nature, Vol 28 (20 April) pp 259-261, 1968.
2. Drummond, A.J. "A Review of Determinations of Solar Constant from Measurements Within and Above the Terrestrial Atmosphere", Proceedings of the Institute of Environmental Sciences, 26-30 April 1971.
3. Thekaekara, M.P. "Extraterrestrial Solar Spectrum", Proceedings of the Institute of Environmental Sciences, 26-30 April 1971.
4. Handbook of Geophysics and Space Environments, Valley, Shea L., Editor, pub by Air Force Cambridge Labs, 1965.
5. Military Standard MIL-STD-210B, "Climatic Extremes for Military Equipment", May, 1973.
6. Army Regulation AR 70-38, "Research, Development, Test & Evaluation of Materiel for Extreme Climatic Conditions", 5 May 1969.
7. Askin, D. and Wiland, J., "Laboratory Simulation of Solar Radiation" Proceedings of the Institute of Environmental Sciences, April, 1961.

TABLE 1

OUTPUT OF MERCURY VAPOR & MULTIVAPOR LAMP COMBINATIONS

	PERCENT RADIATION		
	UV	VIS	IR
SINGLE LAMP - 1000W MERCURY VAPOR - CLEAR	7.2	22.2	70.6
SINGLE LAMP - 1000W MULTIVAPOR - COATED	1.64	64.5	33.85
TWO LAMP - 1000W EA 1 CLEAR MERCURY/1MV COATED	2.52	65.73	31.75
THREE LAMP - 1000W EA 2 CLEAR MERCURY/1W COATED	5.9	62.6	31.4
NATURAL SUNLIGHT (AT GROUND LEVEL)	5.0	43	52

TABLE 2

AVERAGE TOTAL INTENSITY AT VARIOUS HEIGHTS FOR EACH GRID SECTION OF THE SOLAR RADIATION CHAMBER MEASURED WITH AN EPPLEY PYRANOMETER

SECTION	HEIGHT IN FEET		
No.	3	4	5
1	113 W/SQ FT	99 W/SQ FT	90 W/SQ FT
2	125 "	103 "	92 "
3	116 "	93 "	88 "
4	134 "	113 "	101 "
5	113 "	99 "	94 "
6	124 "	104 "	93 "
7	121 "	103 "	91 "
8	129 "	108 "	102 "
9	141 "	120 "	105 "

TABLE 3

PYRANOMETER READINGS WITH AND WITHOUT FILTER
FILTER USED: SCHOTT RG 780
TRANSMITTING IR AND CUTTING OFF ALL RADIATION BELOW 780NM
LAMP RACK HEIGHT - 53 INCHES

SECTOR	A	R	B/A	1 - B/A
No.	W/O FILTER	WITH FILTER	PERCENT	PERCENT
	MV	MV	IR	UV + VIS
1	8.0	4.63	0.59	0.41
2	3.9	5.22	0.59	0.41
3	7.6	4.50	0.59	0.41
4	3.9	5.31	0.60	0.40
5	8.3	5.04	0.61	0.39
6	7.3	4.50	0.58	0.42
7	8.0	4.95	0.62	0.38
8	8.2	4.68	0.57	0.43
9	9.4	5.49	0.58	0.42

TABLE 4

INTENSITY OF UV AND VISIBLE FROM SPECTRORADIOMETER
LAMP HEIGHT - 5 FEET

SECTOR	INTENSITY	(MICROWATTS/SQ CM)	TOTAL	PERCENT	PERCENT
No.	280-380NM	380-780NM	280-780NM	UV	VISIBLE
	UV	VISIBLE	UV + Vis		
1	86.4	1160	1246.4	7	93
2	86.0	1242	1328.0	6	94
3	86.4	1184	1270.4	7	93
4	90.8	1456	1546.8	6	94
5	82.4	1353	1435.4	6	94
6	71.1	1091	1162.1	6	94
7	64.6	1158	1222.6	6	94
8	69.9	1434	1503.9	5	95
9	100.8	1581	1681.8	6	94

TABLE 5

SUMMARY OF RADIATION INTENSITY IN EACH GRID SECTOR
LAMP HEIGHT - 5 FEET

SECTOR	TOTAL	INTENSITY			PERCENTAGE RADIATION		
		UV	VISIBLE	IR	UV	VISIBLE	IR
No.	W/SQ FT	W/SQ FT	W/SQ FT	W/SQ FT	%	%	%
1	90	2.58	34.32	53.10	3	38	59
2	92	2.26	35.46	54.28	2	39	59
3	88	1.80	34.28	51.92	2	39	59
4	101	2.42	37.98	60.60	2	38	60
5	94	2.20	34.36	57.34	2	37	61
6	93	2.34	36.72	53.94	3	39	58
7	91	2.07	32.51	56.42	2	36	62
8	102	1.75	42.11	58.14	2	41	57
9	105	2.65	41.45	60.90	3	39	58

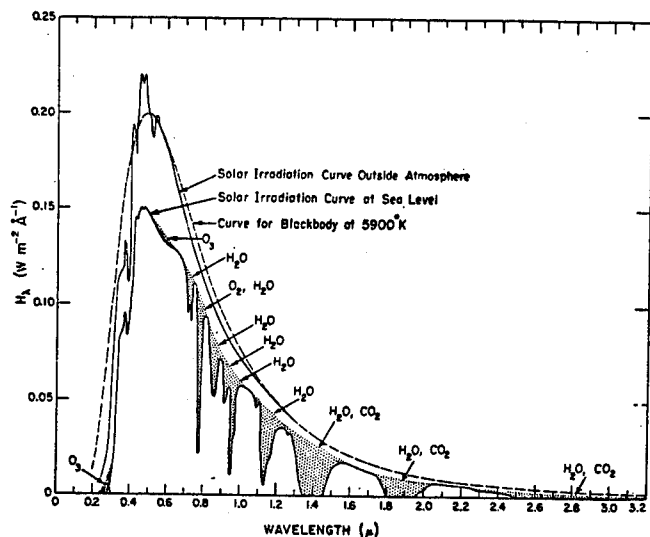


Figure 1. Spectral distribution curves related to the sun; shaded areas indicate absorption, at sea level, due to the atmospheric constituents shown.

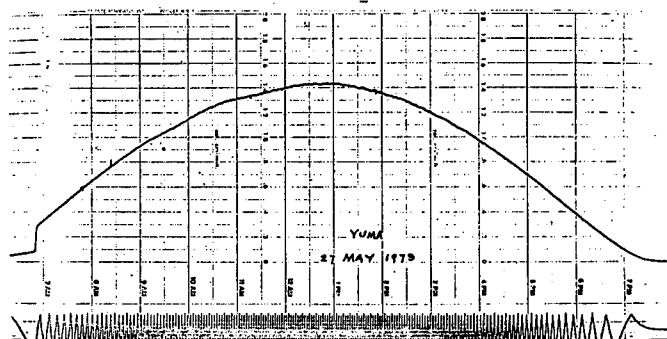


Figure 2. Curve for solar radiation taken at Yuma, Arizona.

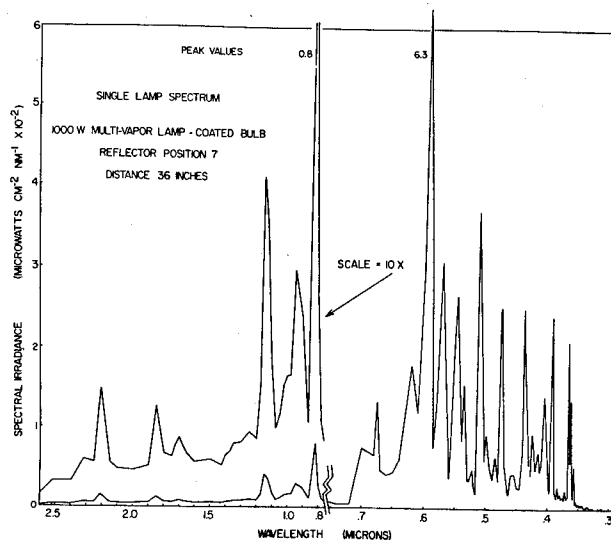


Figure 4. Single Lamp Spectrum Coated Multivapor Bulb.

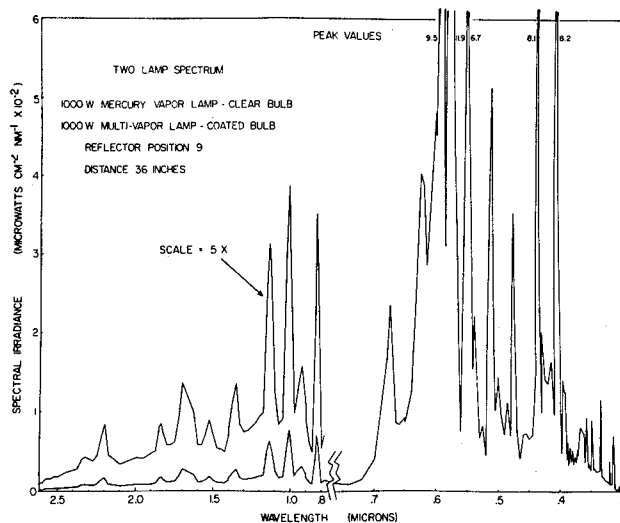


Figure 5. Two Lamp Spectrum. Clear Mercury Vapor + Coated Multivapor.

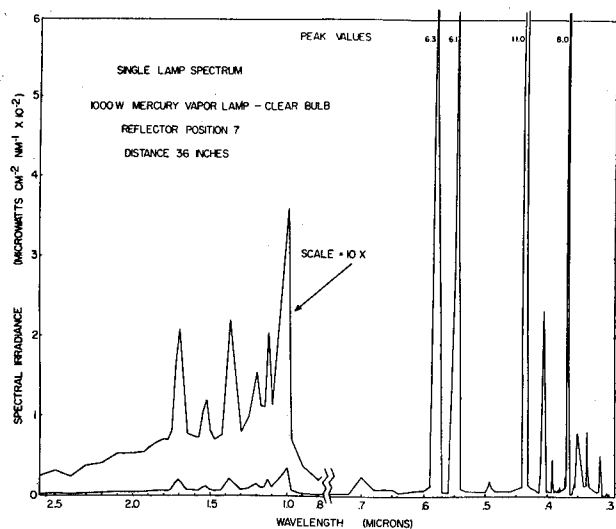


Figure 3. Single Lamp Spectrum Clear Mercury Vapor Bulb.

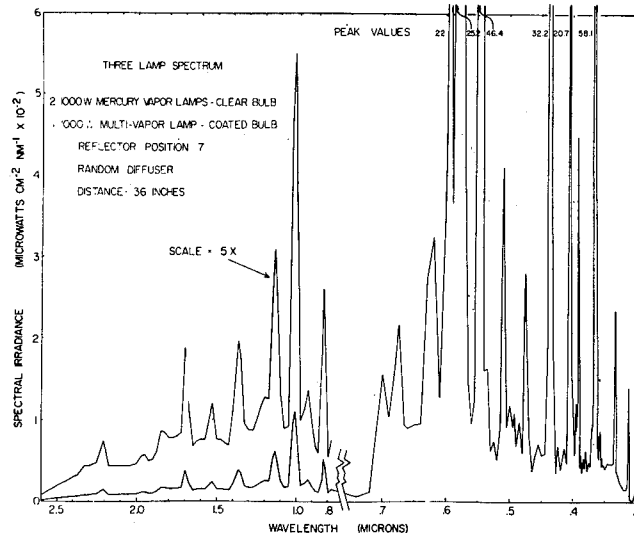


Figure 6. Three Lamp Spectrum. 2 Clear Mercury Vapor + 1 Coated Multivapor.

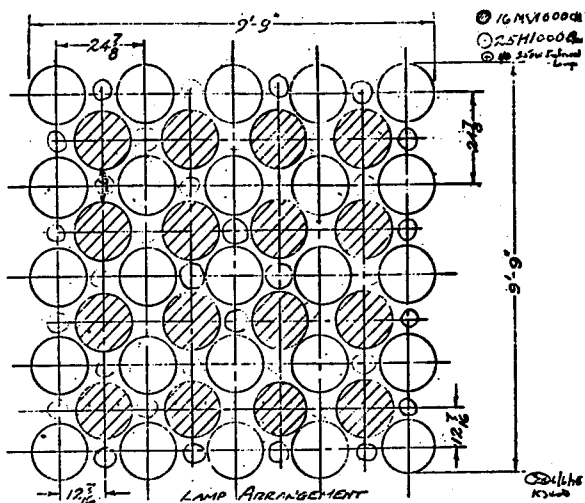


Figure 7.

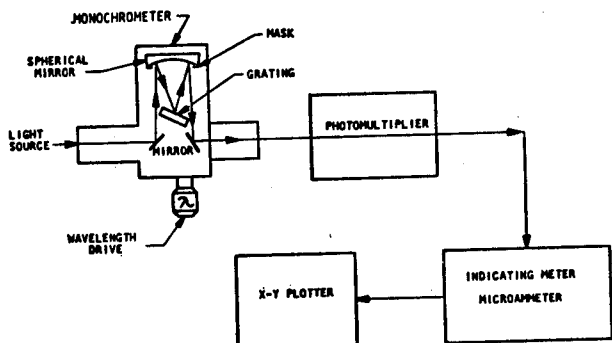


Figure 8. Diagram of equipment used for making radiometric measurements to determine spectral distribution. SPECTRORADIOMETER

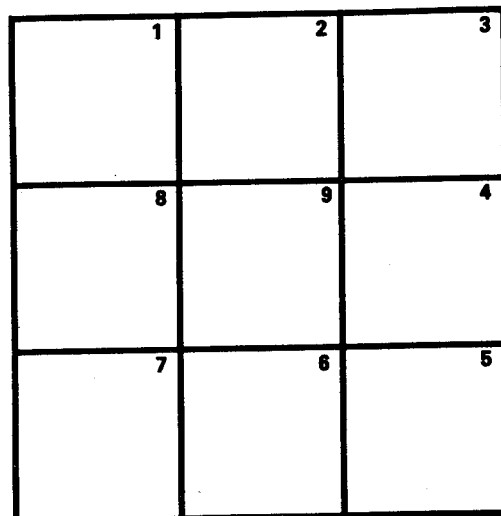


Figure 9. 9 ft x 9 ft Grid Subdivided into 3 ft x 3 ft Sectors

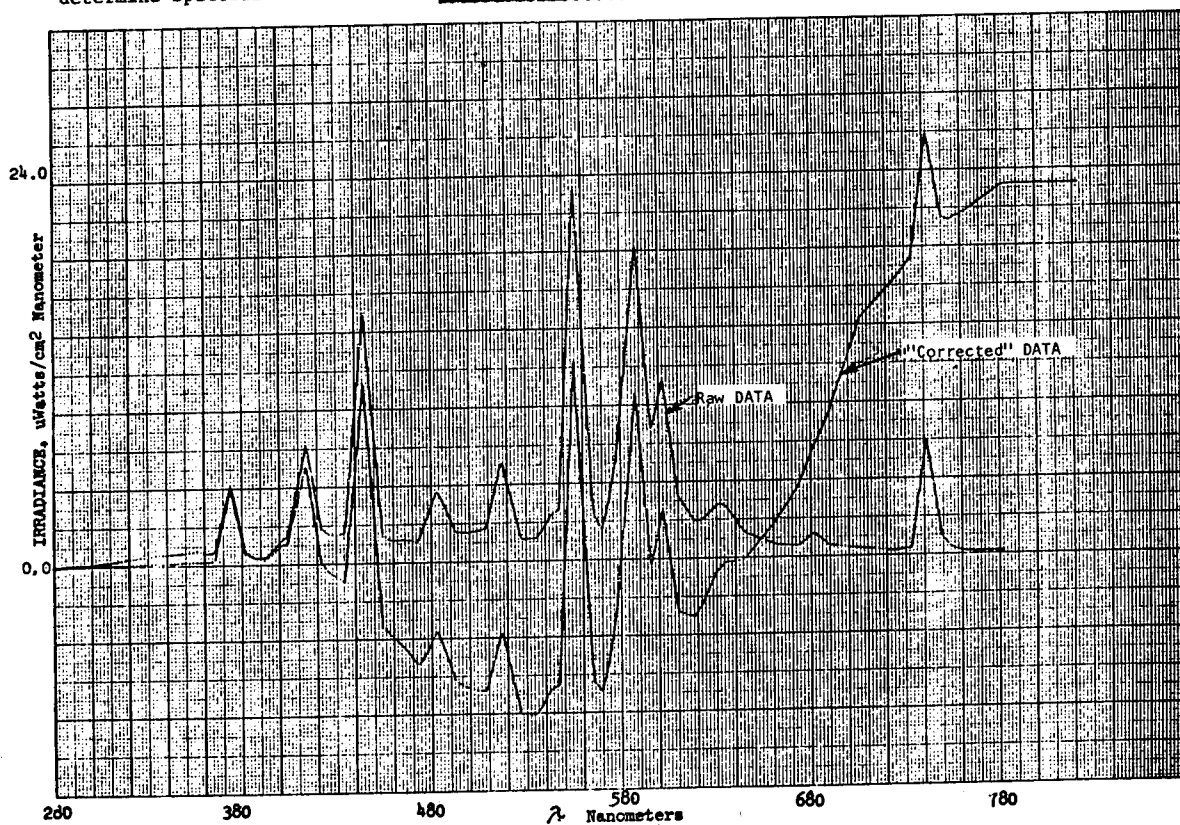


Figure 10. Curve of relative intensity vs wavelength for sector 9 lamp height: - 5 ft

DATA ACQUISITION AND SIGNAL PROCESSING FOR A VERTICAL AXIS WIND ENERGY CONVERSION SYSTEM*

By: B. Stiefeld and R. N. Tomlinson, Sandia Laboratories

Mr. Stiefeld is a member of the Sandia technical staff in Albuquerque, New Mexico. His present duties include instrumentation, data acquisition and data reduction from several solar and wind energy projects. He is the author of some thirty articles on test control operations.

Mr. Tomlinson is a Technical Staff Associate in the Facilities/Test Equipment Design and Development Division of Sandia Laboratories' Environmental Simulation Facility. This division is responsible for the application of mini/microcomputer systems to the acquisition and analysis of test data and for facility test control. Mr. Tomlinson has worked at Sandia for twenty years.

ABSTRACT

The development of large wind energy conversion systems (WECS) is being conducted as part of the solar contribution to the nation's energy needs. The need to evaluate WECS is an important aspect of this program. Sandia Laboratories has been involved in the development of a large scale vertical axis wind turbine. An important milestone in this program has been the installation of a 17-meter (54 foot) VAWT at Kirtland Air Force Base, Albuquerque, New Mexico. Analytical performance predictions in most instances are based upon steady state wind conditions. Verification of actual field performance of these predictions has resulted in the development of a WECS test facility.

This paper describes the data acquisition and analyses system developed to meet the needs of the 17-meter VAWT. The system employs a minicomputer-based data acquisition system with special peripheral equipment. Statistical methods will be described that are employed to evaluate the performance of the system from both a structural and performance viewpoint.

The data acquisition equipment includes a pulse code modulated (PCM) multiplexer/encoder and an analog to digital converter subsystem.

The airborne type PCM encoder is used primarily to obtain low-level structural data from the facility and is located on the turbine shaft near the measurement points. This location provides significant benefits in terms of data accuracy and equipment requirements. Once encoded, the digital signal stream may be transmitted via slip rings or an RF link to the remote control site where it is accessed by the computer.

The A/D converter is used to digitize data from the non-rotating portion of the facility.

Under computer control, the data from these devices may be analyzed for near real-time graphic display on the system CRT terminal/plotter. Concurrently, the data are also stored on the system's magnetic disc for subsequent analysis and for the combining of data acquired over extended periods of time. These combined values may then be plotted to characterize the turbine under variable conditions

of wind velocity and wind shear.

INTRODUCTION

Major factors considered in wind studies are determination of wind velocity history, gust related frequency parameters and terrain related wind shear factors (wind shear is evidenced by velocity difference with altitude in the area of 0 to 46 meters (0 to 150 feet) above the surface). This factor is critical in evaluating turbine efficiency as it is used in determining the wind power available to the VAWT. It should be noted that the power available in a moving fluid stream is proportional to the cube of the velocity, so an accurate determination of effective wind velocity is important.

The objective of this program is the development of an instrumented outdoor wind laboratory. This laboratory has the capability of evaluating various aspects of wind turbine performance as well as studies involved in detailed analysis of wind flow properties. While a number of turbines have been erected at the test site, this paper will concentrate on the instrumentation and analysis associated with the 17 meter (55 foot) vertical axis wind turbine (VAWT) and wind area studies.

In evaluating the performance of a large VAWT we consider two areas:

- 1) Structural aspects of turbine operation, primarily blade performance including vibratory response characteristics.
- 2) Performance characteristics of torque output vs wind velocity and related studies of system power losses and electrical output characteristics.

System Hardware

In addition to the system minicomputer, major system components consist of a magnetic disc for data and program storage; a CRT graphics terminal used as the system operator's console and graphics plotter; an airborne type pulse code modulated (PCM) encoder; a PCM bit synchronizer, docommutator, and custom computer interface; a medium speed analog to digital converter; and peripheral magnetic tape recorder and card reader units. Figure 1 is a block diagram of the system.

The use of the PCM encoder is patterned after a similar system designed for a large centrifuge test facility at this installation which was recently completed, demonstrating the application of aerospace techniques to the energy research field.

There was a need to measure the strain parameters associated with the rotating turbine blades. The conventional approach using slip ring contacts would restrict the number of data channels and from past experience would be unreliable due to poor contact between slip rings and contacts caused by dirt, wear and corrosion; particularly where low level signals are to be measured. The compact

*This work supported by the Department of Energy, DOE.

PCM encoder eliminates these problems. The data are digitized close to the source and the slip rings are used only for power and for the return of the encoded PCM signal to the decommutator. Only one quiet signal pair carrying a high level digital pulse stream is required. Any contact problems associated with the digital stream would be noticed immediately in a loss of PCM decommutator lock resulting in the interruption of data transfer to the computer. This is preferable to taking erroneous or degraded data which might not be discovered until after the test run.

The PCM encoder is capable of digitizing a mixture of 65 low and high level analog signals at the rate of 50 samples per second per channel with 10 bit resolution which results in a 33.5 KHz bit rate. The 50 Hz sampling rate is adequate to meet sampling criteria for the highest frequency mechanical vibration expected from the turbine blades. It is worth noting that the PCM unit not only acts as a data element, but physically contains 60 shunt regulated power supplies to provide separate excitation voltages for the strain gage units. Figure 2 diagrams the function of the encoder unit.

The composite PCM signal passes to a bit synchronizer and decommutator where the serial bit stream is reformed into parallel data words with strobe. A custom interface was designed and constructed to enable the transfer of only a software selected block of channels from the decommutator to the computer. Transfer is accomplished under computer Direct Memory Access (DMA) which allows the computer to perform other control or computation operations during the data acquisition time.

The analog to digital converter subsystem is used for all signals not coming from the rotating section of the turbine via the PCM unit. It is expandable and presently has the capability of digitizing up to 48 high and low level signal inputs. It contains a programmable pacer allowing data rates as high as 45 KHz. Inputs from the anemometers and wind direction transducers as well as electric power transducers are handled by this device. Several of the signals from the non-rotating elements are also fed back through the slip rings to the PCM for the data synchronizing purposes which simplifies the data plotting routines.

A key element in the system is the magnetic disc subsystem which serves as the mass storage device for test data and programs as well as supporting the software executive operating system for the minicomputer. The disc is a two platter device with one fixed and one removable platter providing 15 million bytes of on-line storage. The removable cartridge allows for an effective "infinite" storage capability with each unit capable of storing some 10 million bytes or 5 million 16-bit computer words. In our original planning, the 9 track magnetic tape was to serve as additional mass storage as well as a transfer medium to other computers. In practice, because of the flexibility and strength of the supporting software system, magnetic tape has been used only for occasional data transfers to Sandia's main computer complex.

The CRT operator console/graphics plotter is the only keyboard and printing unit in the system. An associated hard copy unit is used to make per-

manent duplicates of the CRT screen contents which may be a data plot or a data or program listing. The extensive use of report quality graphics has minimized the need for data listings.

The card reader has facilitated transfer of existing programs, written by individual staff members, from Sandia's CDC 6600 to the VAWT system.

System Software

Hewlett-Packard's Disc Operating System (DOS-III) was chosen as the software operating system for the facility. DOS supports an editor, assembler, FORTRAN IV compiler and a reasonable file manipulation scheme. Multi-user or task scheduling are not supported by DOS, however, the DOS executive system provides a large memory space (24 K words) for running application and plotting programs.

The DOS loader can link and load into a program module a combination of Fortran and assembly routines. We have taken advantage of this feature by providing a few key assembly level routines. These routines operate some of the data acquisition and control elements. As an example, the routine to use the A to D unit allows the user to make a Fortran call to the subroutine controlling that device, with parameters specifying sampling rate, the number of channels and the sequence of channels to be read. Using this approach all application programs are written in Fortran, calling the appropriate sub-routines to handle the control and acquisition requirements.

The point to be emphasized is that this approach means that any person with a reasonable command of Fortran can prepare his own application programs; an intimate knowledge of assembly language or minicomputers is not required. In the laboratory context in which this equipment is used, this advantage is important in providing flexibility and effective system utilization.

To facilitate the plotting of data, portions of Tektronix's PLOT-10* software have been modified and adapted to the HP DOS system and to the version of Fortran IV it supports. A good package of graphics sub-routines requiring a reasonable amount of computer memory is essential for condensing large amounts of data into a plot displaying data trends. The PLOT-10 package performs well in this function.

Application Software Examples

Turbine Performance

Basic turbine performance is related to torque developed vs wind velocity. The difficulty is that natural wind does not cooperate by taking a steady state value. In practice, a "steady wind" is quite gusty and variable. An instantaneous reading of wind velocity taken at a station other than the center of the VAWT may not represent the true wind acting on the VAWT. In addition, turbine torque varies with blade angle of attack during each rotation cycle of the turbine. ⁽¹⁾ Therefore, simple use of instantaneous readings of torque vs wind

*PLOT-10 is copyrighted by Tektronix, Inc.

velocity will not present a true picture of turbine performance.

The Method of Bins

The method of "Bins" was developed at Sandia in conjunction with testing of VAWT systems. (2) Versions of the Bins approach have also been used at the Rocky Flat Wind Systems Test Center and with the DOE/NASA MOD-0 turbine.

"Bins" provides a measurement of VAWT aerodynamic performance only. Two input parameters are sampled; a measure of turbine output and a reference anemometer. At our site the shaft torque just below the main lower bearing is used as a measure of output (near constant RPM is assumed), an anemometer mounted on the upper shaft extension is used as the wind velocity measurement. Its reading is corrected to give velocity at the turbine equator.

We have partitioned the range of wind speeds from 0 - 26.82 M/sec (0 - 60 MPH) into 120 bins .227 m/s (.5 MPH) wide. Simultaneous readings are taken of both torque and wind velocity, at a selected sampling rate. As each pair of readings are taken the proper bin is calculated, and the torque reading summed into the bin and a bin counter incremented. The use of the minicomputer system facilitates this process; allows thousands of readings to be conveniently taken and summed to the bins structure. As just 240 words are used (a pair for each of 120 bins) no matter how many readings are taken many hours of running time can be easily handled. This data can then be reduced to obtain curves of performance coefficient over the wind spectrum.

During any given operating run, even of several hours duration, one does not encounter a square wind distribution. To ease the problem of analyzing performance over the full wind range, a file system has been instituted. This filing system allows the data from each run to be stored on the disc; when desired under interactive control, any or all of these individual data files can be combined to provide an overall picture of turbine performance. There are several other fine points that are included; for example, after records are combined, the temporary record created can be adjusted for air density. This allows one to quickly evaluate turbine performance for any suggested location say on top of Mount Everest.

Structural Analysis Example

There are several programs on the system that are used for monitoring blade performance. The following illustrates only one of the methods used, but it does produce dramatic plots on a near real time basis. Figure 3 indicates the location of some of the strain gages of interest; for purposes of this example, gages 106, 107. These gages are located on the lower strut directly opposite each other and are arranged on the strut to be sensitive to strain along the long axis of the strut.

To evaluate blade reactions the appropriate application program is called up. This specific program interactively requires the operator to designate strain gages to be monitored, time period monitor-

ing is to be done and file name to be used for storage. Using the PCM unit a sequenced data buffer is filled with strain gage data; the buffer itself is pre-conditioned with a small header area. This data buffer can then be stored on the disc for later use or the data can be plotted immediately.

Plotting of the data is accomplished with a plotting sub-routine. It is desirable to plot the data in engineering units of microstrain; to accomplish this, the gage offsets and calibration factors must be provided. The gage offsets and calibration factors are stored on the disc on a small gage file that any program may access. The net result of all of this is the plot of Figure 4 indicating microstrain at gages 106, 107 and wind velocity. A review of Figure 4 indicates that the strut is undergoing nearly pure bending. Figure 5 is a frequency analysis of another strain gage run. The abscissa is a log scale of the ratio of frequency/rotational frequency. This normalizes the plot for comparisons of tests made at various rotation speeds. Points A, B and C indicate that the major energy is contained in frequencies at a 1 per revolution, 2 per revolution and 4 per revolution normalized value.

Wind Studies

The test site is equipped with a farm of some 10 anemometers arranged at heights from 3 to 30 meters (10 to 100 feet). This farm has been used for various wind studies; for example, determination of wind shear factor at our site and frequency content of wind gusts. Due to the variability of the wind, most of these wind studies are done on a statistical basis with great amounts of data being acquired. The combination of data acquisition and general software support is particularly useful for these type of studies.

CONCLUSIONS

Sandia has implemented a field laboratory capable of complex data acquisition procedures coupled with a versatile software system. A major strong point is the use of Fortran. This allows staff members unfamiliar with minicomputers to perform complex acquisition and analytic procedures. An extensive filing system enhances the flexibility and utility of the system allowing data acquired over extended time periods to be compared or combined as needed.

ACKNOWLEDGEMENTS

As in most complex installations, many organizations have contributed to the development of this system. The significant software contributions of Sandia staff members, Bob Akins, Bill Sullivan and Jim Banas, are noted. The hardware contribution of Florencio Aragon of Sandia's component environmental testing department is noted.

REFERENCES

- (1) Blackwell, B. F., The Vertical Axis Wind Turbine - How It Works, Sandia Laboratories, SLA-74-0160, April 1974.
- (2) Akins, R. E., Performance Evaluation of Wind Energy Conversion Systems Using the Method of BINS - Current Status, SAND77-1375, March, 1978.

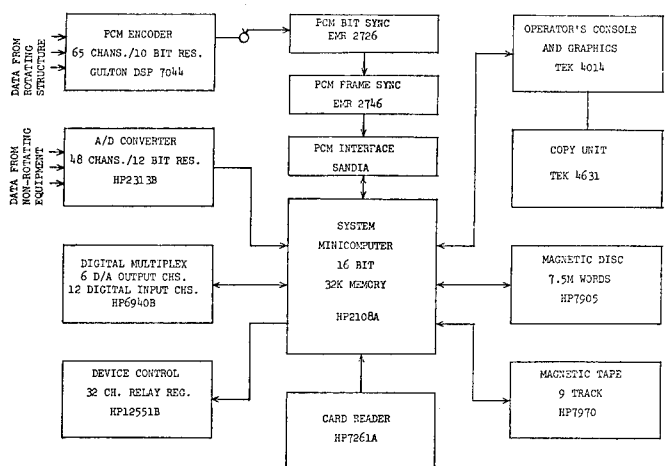


FIGURE 1. DATA ACQUISITION SYSTEM - VERTICAL AXIS WIND TURBINE FACILITY.

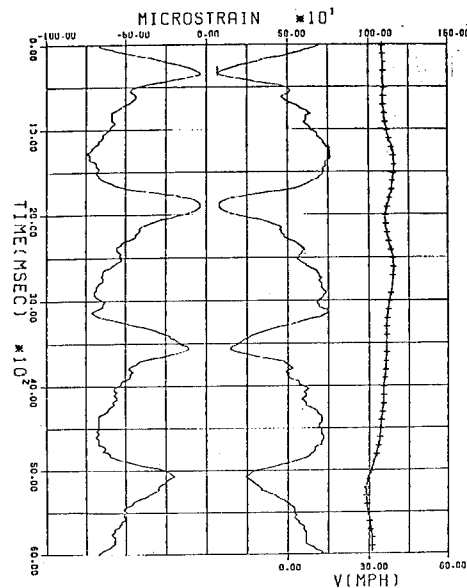


FIGURE 4. MICRO STRAIN PLOT.

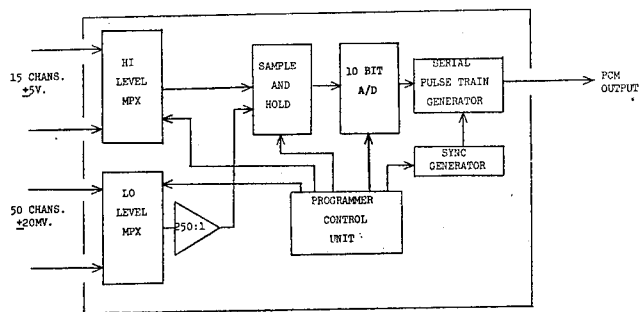


FIGURE 2. PCM ENCODER SYSTEM.

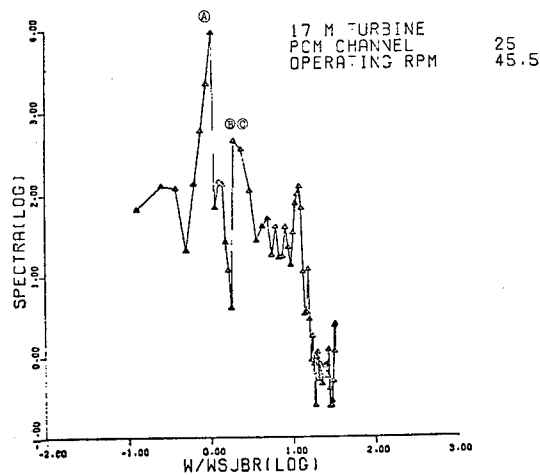


FIGURE 5. FREQUENCY ANALYSIS.

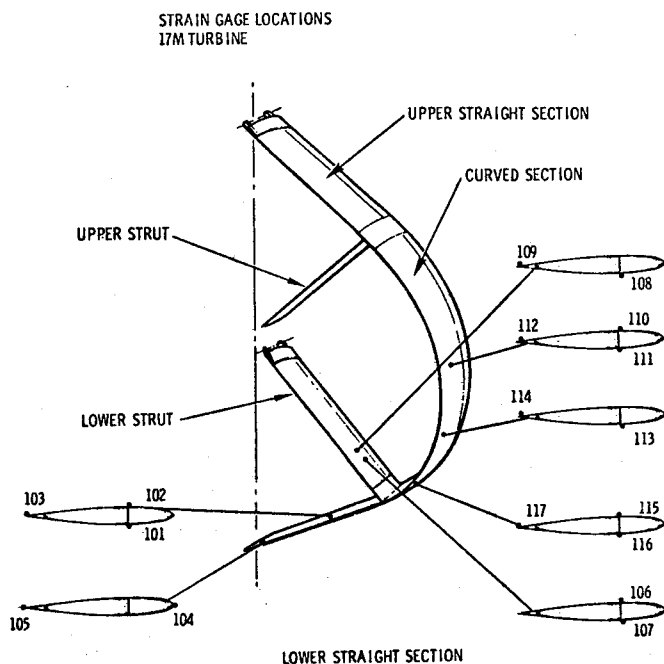


FIGURE 3. STRAIN GAGE LOCATIONS.

PHOTOTHERMAL CONVERSION SURFACE MEASUREMENTS USING
PHOTOTHERMAL AND PHOTOTHERMAL SPECTROSCOPIES

By: J. F. McClelland and R. N. Kniseley

John F. McClelland is an Ames Laboratory Postdoctoral Fellow currently working in the areas of solar energy and photoacoustic spectroscopy. His previous experience is in optical properties of solids and plasma spectroscopy. Richard N. Kniseley is a Senior Chemist at the Ames Laboratory conducting research programs in a number of areas of analytical spectrochemistry related to energy and environmental studies.

I. Introduction

The optical properties of solar absorber surfaces for photothermal conversion are of primary importance in understanding the performance of solar-thermal conversion systems. Measurements of these properties are required for purposes that may be grouped into the following categories:

1. research and development work on both materials and systems, and control of manufacturing processes
2. verification of specifications before installation and start-up
3. predicting and monitoring of performance on a long term basis under potentially degrading operating conditions.

Due to the variety of measurement conditions encountered in the above categories, and the extensive range of material types involved in active and passive solar thermal systems it is important to consider methods which complement conventional reflectance spectroscopy.

In this paper the photoacoustic¹⁻¹⁰ and photothermal¹¹⁻¹² spectroscopic techniques, which have recently been under development for other purposes, are discussed in the context of photothermal conversion measurements. These methods are of particular interest in solar applications because they have a more direct connection to the photothermalization process than reflectivity measurements due to the role of optical heating in the signal generation process. Figure 1 shows a schematic of the two classes of measurements.

In the next section the photoacoustic and photothermal effects are discussed and related to signal generation. The general signal expression introduced in this section is specialized for solar absorber studies in the following section. In the final section the experimental apparatus is described and several prospective

special applications are discussed.

II. The Photoacoustic and Photothermal Effects-Their Role in Signal Generation

The photoacoustic and photothermal effects have a common origin based on the intermittent heating of the sample by an intensity-modulated light beam. The light energy absorbed and thermalized in the sample causes a small temperature oscillation at the frequency of the intensity modulation. The temperature oscillation amplitude and phase as explained below, depend on the sample's optical and thermal properties.⁶ The thermal oscillations generate acoustical waves via thermal expansion in both the sample and adjacent media. The acoustical and thermal responses of the sample under photoexcitation comprise the photoacoustic and photothermal effects, respectively. Selection of acoustical or thermal detection in a given measurement is based on considerations of sample type and environment, and on the signal coupling efficiency between the sample and the transducer. The coupling may be done by direct or indirect means. Figure 2 shows a schematic of the various detection configurations.

To date, most measurements have used acoustic detection with direct coupling for gas phase samples (often termed optoacoustic spectroscopy)^{10,13} and indirect coupling for condensed phase samples via an adjacent gas medium⁵⁻¹⁰. Since condensed phase measurements are of interest in solar-thermal conversion, the relationship between the signal and the sample's optical properties will be considered in detail for this case.

In the measurement an acoustic signal is detected in the gas (commonly air) adjacent to the irradiated sample area by a sensitive microphone isolated from the surroundings in a constant volume cell which is either sealed to or contains the sample. Figure 3 shows a schematic of the incident light beam, cell body, microphone, and sample. Calculations of the pressure oscillation amplitude and phase have been done assuming one-dimensional thermal transport parallel to the incident light beam axis. Results from these calculations will be given below after a simplified physical description of the signal generation process has been presented. This description will be appropriate for most photothermal conversion studies where the absorption occurs in a thin surface layer due to a high absorption coefficient. For this sample type recent theoretical and experimental work¹⁴ has shown that the acoustic signal is generated by the oscillatory flow of

heat from the sample into the adjacent gas with acoustic signal generation within the sample itself being a negligible contribution. The signal generation sequence in high absorptivity samples involves essentially two steps: (1) the modulated flow of light energy through the gas into the sample followed by (2) an oscillatory flow of thermal energy back into the gas where pressure oscillations are generated by the intermittent heating. Considered in more detail, the incident light beam with a time dependent power given in complex notation by

$$P = P_0(1 + e^{i2\pi ft}) \quad (\text{II-1})$$

for a modulation frequency, f , is divided into reflected and transmitted components at the gas/sample interface. The component, P_t , entering the sample can be expressed as

$$P_t = P_0(1 - R)(1 + e^{i2\pi ft}), \quad (\text{II-2})$$

where R is the reflectivity of the interface. At a depth x in the sample the power, P_s , is given by

$$P_s = P_0(1 - R)(1 + e^{i2\pi ft})e^{-\beta x} \quad (\text{II-3})$$

where β is the sample absorption coefficient. The power thermalized in a sample layer at x with thickness dx is expressed as

$$dP_s = \alpha P_0(1 - R)(1 + e^{i2\pi ft})\beta e^{-\beta x} dx \quad (\text{II-4})$$

with α the fraction of absorbed power that is thermalized. This sequence is shown schematically in Figure 4. The presence of α in Equation II-4 is important because it ensures that absorptivity determinations by photoacoustic methods are insensitive to errors due to sample luminescence.

Each layer of the sample undergoing oscillatory heating acts as a source for thermal waves which propagate through the sample. The thermal waves have an initial amplitude at a given depth, x , scaled by the $e^{-\beta x}$ factor and a propagation decay constant, a_s , given by

$$a_s = \sqrt{\frac{\pi f}{\alpha_s}} \quad (\text{II-5})$$

where α_s is the sample's thermal diffusivity. Waves propagating to the thermal transfer surface contribute to the signal generation from a sample depth determined by a_s or β , whichever is larger. Equation II-5 shows that the thermal decay depth can be varied by adjusting the modulation frequency, f . Since the optical properties are of interest in this discussion, f is assumed set at a fixed value so that signal

generation can be considered as β increases from values smaller than a_s to larger values encompassing the range of typical solar absorber surfaces ($\beta \sim 10^3$ - 10^6 cm^{-1}). As β increases in the range below a_s the photoacoustic signal increases because the region where light absorption occurs moves (1) into the signal generation layer (which in this region is defined by a_s) and (2) closer to the thermal transfer surface. At $\beta = a_s$ all of the absorption occurs within the signal generation layer. For $\beta > a_s$ the signal continues to increase due to (2) until the signal generation layer (which for $\beta > a_s$ is defined by β) saturates against the thermal transfer surface. The signal dependence on β is shown by the experimental results plotted in Figure 5. After saturation the signal is not directly dependent on β and will vary only if R changes. A decrease in R causes an increase in the signal because of the rise in beam power entering the sample. This results in high relative signal levels for solar absorber materials which generally have high β and low R values in the solar spectral region. A calculation using the thermal transport equation and described in detail in Ref. 9 results in the expression for the photoacoustic signal, S , given by⁹

$$S = k g A. \quad (\text{II-6})$$

The symbol k is a transducer sensitivity constant while g and A are complex numbers depending, respectively, on the thermal properties and dimensions of the sample, gas, and cell body materials; and on the optical and thermal properties of the sample. g and A are also functions of f while k is essentially independent of f in the region of interest. Equation II-6 is derived neglecting acoustic signal generation in the sample and gas viscosity. These assumptions are reasonable due to the work¹⁴ mentioned earlier and to the ratio method discussed in the next section that will result in the cancellation of a scaling factor associated with gas viscosity. In the next section Equation II-6 will be developed into forms appropriate for solar absorber surface studies.

III. Photothermal Conversion Surface Measurements-Determination of the Thermalized Absorptivity, A_T

Measurement of the fraction of incident light that is absorbed and thermalized by surfaces is of interest both in absolute and relative terms. Absolute determinations are of particular importance in manufacturing process development and specification verification while relative or differential measurements are needed in process control and long term performance prediction and monitoring. In this section expressions will first be derived from Equation II-6 which serve as the foundation for absolute spectral measurements in the solar region. Broad spectral band (i.e. the solar spectrum) and IR emissivity measurements will

then be discussed. Finally, expressions and an associated experimental methodology are developed for differential measurements. The information contained in this section is intended to serve as a basis for future photoacoustic solar absorber measurements.

A. Absolute Measurements

The quantity of interest in the solar spectrum region is $A_T(\lambda)$, the fraction of incident light that is absorbed and thermalized by the surface. An expression for A_T can be derived from the conservation of energy expression

$$1 = R(\lambda) + A_T(\lambda) + A_{NT}(\lambda) + T(\lambda) \quad (\text{III-1})$$

where the symbols, in order of appearance on the right side of Equation III-1, denote the incident beam fractions reflected, absorbed and thermalized, absorbed but not thermalized (for instance a luminescence process), and transmitted. $A_T(\lambda)$ is also given by

$$A_T(\lambda) = \alpha(\lambda) [A_T(\lambda) + A_{NT}(\lambda)] \quad (\text{III-2})$$

where $\alpha(\lambda)$ is the fraction of absorbed energy that is thermalized. Since $T(\lambda)=0$ for the samples of interest $A_T(\lambda)$ can be written, using Equations III-1 and III-2 as

$$A_T(\lambda) = \alpha(\lambda) [1 - R(\lambda)] \quad (\text{III-3})$$

This expression appeared in Equation II-4 during the simplified description of the photoacoustic effect and is implicit in the A factor of Equation II-6. In a form appropriate for solar absorber materials A is given by⁹

$$A(\lambda) = [-\alpha(\lambda) [1 - R(\lambda)] P_O(\lambda) / k_s K_s] \left[\frac{1}{1 + k_s / \beta(\lambda)} \right] \quad (\text{III-4})$$

where $k_s = \sqrt{2i} a_s$, K_s is the sample's thermal conductivity, and the modulation term, $(1 + i2\pi f t)$, has been dropped. Equation III-4 was derived with the assumption that $a_s / \beta \ll 1$ which should be generally reasonable since for these measurements $a_s < 5 \cdot 10^2 \text{ cm}^{-1}$ and $\beta > 5 \cdot 10^3 \text{ cm}^{-1}$. With this assumption and expressing g/k_s as $re^{i\phi}$ Equation II-6 becomes, using Equations III-3 and III-4

$$S(\lambda) = \frac{-k A_T(\lambda) P_O(\lambda)}{K_s} re^{i[\phi + a_s / \beta(\lambda)]} [1 - a_s / \beta(\lambda)] \quad (\text{III-5})$$

In the measurement a lockin amplifier is used to process the signal providing the amplitude, $a(\lambda)$, and phase, $\theta(\lambda)$, of the real part of $S(\lambda)$ given by

$$a(\lambda) = [-k A_T(\lambda) P_O(\lambda) r / K_s] [1 - a_s / \beta(\lambda)] \quad (\text{III-6})$$

and

$$\theta(\lambda) = \phi + a_s / \beta(\lambda) \quad (\text{III-7})$$

A calibration measurement is done by depositing a thin layer of platinum^{9,15} or gold black¹⁶ on the sample. This layer will have, for properly controlled deposition conditions, $\beta > 10^3 \text{ cm}^{-1}$ and $R < 0.01$ across the solar spectrum with a thickness in the 1,000 Å range. Platinum black layers of this type have been shown experimentally to leave the sample's thermal properties essentially unchanged¹⁵ and this is supported by the small estimated decay of a thermal wave across such a layer. Under these conditions the calibration signal, $S_c(\lambda)$, is given by

$$S_c(\lambda) = -k P_O(\lambda) re^{i\phi} / K_s \quad (\text{III-8})$$

where it is assumed that $R=0$ and $\alpha(\lambda)=1$ for metal black surfaces.

The lockin detects

$$a_c(\lambda) = -k P_O(\lambda) r / K_s \quad (\text{III-9})$$

and

$$\theta_c = \phi \quad (\text{III-10})$$

Using Equations III-6, 7, 9, and 10 we obtain

$$A_T(\lambda) = [a(\lambda) / a_c(\lambda)] [1 + \theta(\lambda) - \theta_c] \quad (\text{III-11})$$

which is the basic expression for photoacoustic $A_T(\lambda)$ determinations. Since $a_s / \beta(\lambda) = \theta(\lambda) - \theta_c$ a check on the assumption $a_s / \beta(\lambda) \ll 1$ is obtained from the lockin phase measurements. Future work should include consideration of calibration surface corrections and comparison of photoacoustic and reflectivity results for various sample types.

B. Broad Spectral Band Measurements

Photoacoustic measurements can be made over broad spectral bands such as the solar spectrum for high absorptivity surfaces where $a_s / \beta(\lambda) \ll 1$. In this case the pressure oscillation contributions for each wavelength interval, $d\lambda$, are very nearly in phase and summed in the cell volume. The signal contribution from $d\lambda$ is given by

$$dS(\lambda) \approx -k A_T(\lambda) P_O'(\lambda) re^{i\phi} d\lambda / K_s \quad (\text{III-12})$$

where $P_O'(\lambda)$ is the incident power per unit wavelength interval. The signal summed over the wavelength band λ_B is

$$S(\lambda_B) \approx -k re^{i\phi} \int_{\lambda_B} A_T(\lambda) P_O'(\lambda) d\lambda / K_s \quad (\text{III-13})$$

The corresponding expression for the calibration signal is

$$S_c(\lambda_B) \approx -kre^{i\phi} \int_{\lambda_B} P'_O(\lambda) d\lambda / K_s \quad (\text{III-14})$$

The amplitudes of the real parts of equations III-13 and III-14 are measured by the lockin and given respectively by

$$a(\lambda_B) \approx -kr \int_{\lambda_B} A_T(\lambda) P'_O(\lambda) d\lambda / K_s \quad (\text{III-15})$$

and

$$a_c(\lambda_B) \approx -kr \int_{\lambda_B} P'_O(\lambda) d\lambda / K_s \quad (\text{III-16})$$

The broadband thermalized absorptivity is expressed as

$$A_T(\lambda_B) \approx \int_{\lambda_B} A_T(\lambda) P'_O(\lambda) d\lambda / \int_{\lambda_B} P'_O(\lambda) d\lambda = a(\lambda_B) / a_c(\lambda_B) \quad (\text{III-17})$$

C. Infrared Region Measurements

Emissivity measurements in the infrared are of interest for solar absorber materials to evaluate blackbody thermal losses. The emissivity of solar absorber materials can be expected to span a range from low values for selective surfaces in active systems to rather high values for some direct gain surfaces in passive systems. Photoacoustic measurements of emissivity via $A_T(\lambda)$ can be expected to encounter signal-to-noise problems with low excitation power from conventional global sources especially with low emissivity samples which reflect a large fraction of the incident light. Better signal-to-noise ratios will be possible with infrared laser sources at certain wavelengths but none of the beam irradiation methods readily provide the desired hemispherical emissivity data because the solid angle of the excitation is always too small and of uncertain distribution. Although conventional photoacoustic $A_T(\lambda)$ measurements do not look attractive, broadband hemispherical emissivity measurements using photoacoustic or photothermal detection appear practical. In this case, the sample is thermally coupled to a heat source at the expected operating temperature of the surface or a higher temperature if the emissivity can be considered independent of temperature. Instead of modulating an incident beam the infrared blackbody radiation from the sample is chopped by a highly reflective chopper which either reflects the emitted radiation back to the surface or allows the radiation to be absorbed by an infrared absorbing surface held at liquid nitrogen temperature. Such a system can easily modulate 10 mW for a surface emissivity of 0.1% which should provide a good signal-to-noise ratio. Development in the future of a detailed theory of operation and calibration method are required to establish this measurement. Joule heating^{9,15} may provide an accurate calibration method for materials which approximate surface emitters.

D. Relative or Differential Measurements

It is useful in solar absorber studies to be able to measure the differential quantity

$$dA_T(\lambda) = A_{T1}(\lambda) - A_{T2}(\lambda) \quad (\text{III-18})$$

for the relative comparison of two samples where $A_{T1}(\lambda)$ denotes the thermalized absorptivity for a reference surface and $A_{T2}(\lambda)$ the same quantity for a surface with a certain manufacturing process or duty exposure history. Plots of $dA_T(\lambda)$ versus λ contain information on thermalization efficiency via the dA_T axis while structure locations on the λ axis are diagnostic of photon interaction processes with the solar absorber material. In these terms high-sensitivity differential measurements are valuable in degradation studies for predicting long term performance and for understanding degradation mechanisms. A double beam system allows high sensitivity measurements with minimum error due to system drift. It also permits a low signal sensitivity to variations in the thermal properties of the reference and unknown sample as discussed below.

Experimental methodology and signal expressions will be developed which allow $dA(\lambda)$ to be determined for samples that undergo small changes of both optical and thermal properties. Inclusion of the latter is important since certain compositional and degradation studies will involve perturbations of thermal properties. Since the materials of interest are expected to have high absorptivities, the photoacoustic signal from each channel can be expected to be in the millivolt range for a 1000 W xenon lamp through an efficient monochromator having a 50 to 100Å bandpass. This gives a good possibility of 0.1 percent differential measurements or better using a lockin amplifier with 1 microvolt full scale sensitivity. This technique has the advantage over conventional reflectivity methods of increasing sensitivity as the sample reflectivity goes to zero and insensitivity to nonthermal deexcitation and scattered light effects.

In the measurement the difference between the reference and unknown sample signals is detected by a lockin amplifier with a differential input. The differential signal expression can be derived using expressions similar to Equation III-5 for each sample and to Equation III-8 for their respective calibration signals which are measured by irradiation of a small calibration area on each sample that has been coated with a metal black prior to measurements.

The experimental method for differential measurements involves an initial balancing of the double beam system with the reference and unknown calibration

surfaces being irradiated. This is done by adjusting the amplitude and phase of the unknown signal to equal that of the reference signal. After this procedure the factor $S_c(\lambda) = -kP_o(\lambda) \text{rel}\phi/K_s$ is identical for both the reference and unknown. Thus in balancing the $S_c(\lambda)$ factor we compensate for the effect of differences in each channel due to thermal properties, transducer sensitivity, and optical excitation power. The differential signal, $S_d(\lambda)$, can be written after the balance procedure as

$$S_d(\lambda) = S_{c1}(\lambda) \{ A_{T1}(\lambda) e^{ip_1(\lambda)} [1 - p_1(\lambda)] - A_{T2}(\lambda) e^{ip_2(\lambda)} [1 - p_2(\lambda)] \} \quad (\text{III-19})$$

where the subscripts 1 and 2 denote quantities associated with the reference and unknown samples, respectively, and $p(\lambda) = a_s/\beta(\lambda)$. As discussed above $p(\lambda) \ll 1$ which allows Equation III-19 to be written as

$$S_d(\lambda) = S_{c1}(\lambda) [dA_T(\lambda) + q(\lambda) - iq(\lambda)] \quad (\text{III-20})$$

where

$$dA_T(\lambda) = A_{T1}(\lambda) - A_{T2}(\lambda) \quad (\text{III-21})$$

and

$$q(\lambda) = A_{T2}(\lambda)p_2(\lambda) - A_{T1}(\lambda)p_1(\lambda) \quad (\text{III-22})$$

Using Equation III-8 and taking the real part of Equation III-20 results in

$$\text{Re}[S_d(\lambda)] = -k_1 P_{o1}(\lambda) r_1 \{ [dA_T(\lambda) + q(\lambda)] \cos \phi_1 + q(\lambda) \sin \phi_1 \} / K_{s1} \quad (\text{III-23})$$

If the in-phase and quadrature signals are detected the components are given respectively by

$$S_d(\lambda)_p = -k_1 P_o(\lambda) r_i [dA_T(\lambda) + q(\lambda)] / K_{s1} \quad (\text{III-24})$$

and

$$S_d(\lambda)_q = -k_1 P_o(\lambda) r_i q(\lambda) / K_{s1} \quad (\text{III-25})$$

$dA_T(\lambda)$ is then given by

$$dA_T(\lambda) = [-k_1 P_o(\lambda) r_1 / K_{s1}]^{-1} [S_d(\lambda)_p - S_d(\lambda)_q] \quad (\text{III-26})$$

where the factor in the first bracket is the lockin amplitude reading for the reference sample calibration surface. The differential measurement will, as in the case of absolute measurements, be sensitive to variations in the calibration surfaces from the assumptions of an ideal surface. Additional experimental and theoretical work will be required to determine the practical limitations of the measurements under different conditions.

Broad spectral band measurements should also be possible for differential measurements provided $p(\lambda) \ll 1$ and the balance conditions are satisfied over the wavelength band of interest.

IV. Experimental Apparatus and Applications

The instrumentation for photoacoustic and photothermal spectroscopy* consists of four main elements: a tunable variable band-width light source, a light modulation and optical system to focus the beam on the sample, a sample cell and transducer, and finally signal processing and data acquisition components. The system described below will be a general purpose single beam photoacoustic spectrometer with transducer coupling via the gas adjacent to the sample. This is the type of detection discussed above for solar absorber studies. Figure 6 shows a schematic of the apparatus.

The source most commonly used is a high intensity xenon lamp with a large aperture monochromator to provide a tunable incident beam in the high μW to mW range. Tunable lasers are also useful sources. The light beam is usually modulated with a rotating disc chopper of variable frequency. Optics to focus the beam on the sample should be of an efficient design to conserve beam power. The sample cell is designed to have a small volume but with a distance between the sample face and cell entrance window that exceeds the thermal diffusion length in the gas at the lowest expected chopping frequency. This prevents interference by the window in the signal generation process. The cell body and microphone position should be planned to minimize the background signal due to scattered light thermalizing on the cell walls or microphone diaphragm. Fabrication of the cell body from a transparent material and mounting the microphone so that it presents a small area to the scattered light has been shown to effectively control this problem.¹⁷ Electret microphone transducers are often used for the measurements although condenser types have also worked well. The signal is processed with a lockin amplifier referenced to the chopper. Usually the data are recorded on an XY-recorder with the monochromator scan motor driving the x-axis and the lockin output the y-axis. A pyroelectric or other spectrally flat power detector is often used to sample a small fraction of the incident beam thus allowing signal changes due to spectral variations in the incident beam power to be normalized. The spectrometer described can be used for $A_T(\lambda)$ measurements and in

*Photoacoustic spectrometers are manufactured by Gilford Instrument Laboratories Inc., Oberlin, Ohio 44074 and Princeton Applied Research Corporation, Princeton, New Jersey 08540.

a double beam version for $dA_T(\lambda)$ measurements.

The potential applications for the measurement technique include general solar absorber studies based on the discussion above and special applications involving both material and system investigations. An example of a possible special application to a current materials processing control problem might be in-situ optical monitoring of chrome black selective surface plating. In this process the thickness must be adequate for high solar absorptivity without excessive thickness which results in a high infrared emissivity and hence loss of selectivity. It may be possible to monitor the process with a photothermal measurement made in the spectral region where the plating solution is transparent (the red spectral region for solutions based on chromic acid). In the measurement a pyroelectric plate transducer would be used with a standard black surface on one side and a metal substrate surface on the other side which would be plated during the process. The light beam is switched back and forth between the two sides resulting in a signal amplitude proportional to $dA_T(\lambda)$. Hence in the limit $dA_T(\lambda)=0$ the two surfaces have identical absorptivities. A number of questions, of course, need to be answered to evaluate the practicality of this measurement including the adequacy of narrow band measurements to monitor the process, the signal-to-noise ratio, and the relationship between the coating properties of the pyroelectric substrate surface and those of the solar absorber plates.

A final application involves measuring the effective solar absorptivity of direct solar-gain window systems which are an important mode of passive solar-thermal conversion.¹⁸ Passive systems differ from the active systems approach, which have a pumped thermal transfer fluid, in that sunlight passes directly through large south-facing windows into the living space where it is thermalized and stored in the interior mass of the building. This approach has been gaining interest due to attractive economic and design potential. In order to realize this, measurements are required to characterize and optimize effective solar absorptivity as a function of insolation conditions and interior materials and configurations. Information on the latter are vital to give designers the flexibility to create attractive designs. Due to the complicated optical interactions in direct-gain rooms it is difficult to measure solar absorptivity by the methods used to characterize the surfaces in active systems. A detection technique is required that is directly proportional to absorptivity and which can sum absorptivity contributions over the interior surfaces. The photoacoustic method can, under properly controlled experimental conditions, meet these

requirements. In such a measurement small scale direct-gain model interiors comprise the photoacoustic cell which is excited by a solar simulator. The pressure oscillations from each surface point are summed in the cell volume and the measurement is calibrated by substituting calibration surfaces for those of the interior. The Ames Laboratory is currently planning to develop this application.

References:

1. A.G. Bell, Proc. Amer. Ass. Advan. Sci., 29, 115 (1880); Phil. Mag., 11, 510 (1881).
2. J. Tyndall, Proc. Roy. Soc., London, 31, 307 (1881).
3. L.B. Kreuzer and C.K.N. Patel, Science, 173, 45 (1971).
4. W.R. Harshbarger and M.B. Robin, Acc. Chem. Res., 6, 329 (1973).
5. A. Rosencwaig, Opt. Commun., 7, 305 (1973).
6. J.F. McClelland and R.N. Kniseley, Appl. Phys. Lett., 28, 467 (1976).
7. J.F. McClelland and R.N. Kniseley, Appl. Opt., 15, 2658 (1976).
8. M.J. Adams, A.A. King, and G.F. Kirkbright, The Analyst, 101, 73 (1976).
9. L.C. Aamodt, J.C. Murphy, and J.G. Parker, J. Appl. Phys., 18, 927 (1977).
10. Yoh-Han Pao, Editor, Optoacoustic Spectroscopy and Detection, (Academic Press, New York, 1977).
11. L-G. Rosengren, Infrared Phys., 13, 173 (1973).
12. G.H. Brilmyer, A. Fujishima, K.S.V. Santhanam, and A.J. Bard, Anal. Chem., 49, 2057 (1977).
13. See for example: M.E. Delany, Sci. Progr., 47, 459 (1959); R. Kaiser, Can. J. Phys., 37, 1499 (1959); L.B. Kreuzer, J. Appl. Phys., 42, 2934 (1971); L-G. Rosengren, Infrared Phys., 13, 109 (1973).
14. F.A. McDonald and G.C. Wetsel, Jr., Bull. Am. Phys. Soc., 23, 388 (1978) and J. Appl. Phys., 49, 2313 (1978); G.C. Wetsel, Jr. and F.A. McDonald, Bull. Am. Phys. Soc., 23, 388 (1978).
15. J.C. Murphy and L.C. Aamodt, Appl. Phys. Lett., 31, 728 (1977).
16. W.R. Blevin and W.J. Brown, Metrologia, 2, 139 (1966).
17. J.F. McClelland and R.N. Kniseley,

18. R.P. Stromberg and S.O. Woodall, Passive Solar Buildings: A Compilation of Data and Results, Sand 77-1204 (1977). Available from NTIS.

Acknowledgement

This work was supported by the U.S. Department of Energy, Office of Basic Energy Science, Chemical Sciences Division.

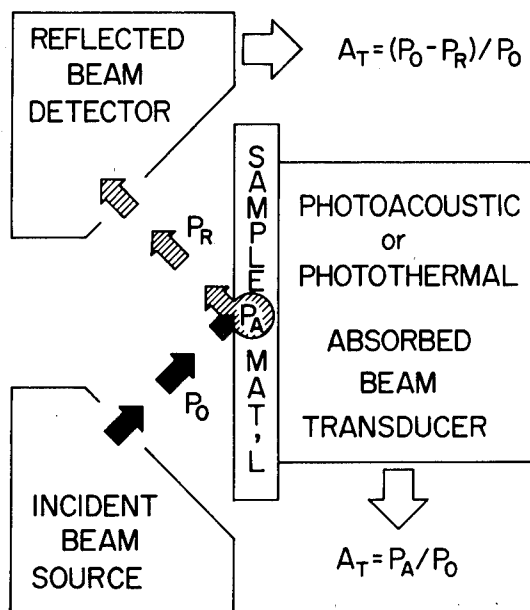


Figure 1. Schematic of reflectivity and photoacoustic or photothermal measurements to determine A_T , the fraction of the incident beam power thermalized by the sample. P_0 , P_A , and P_R are the incident, absorbed, and reflected beam powers, respectively. In the drawing it is assumed that no luminescence occurs.

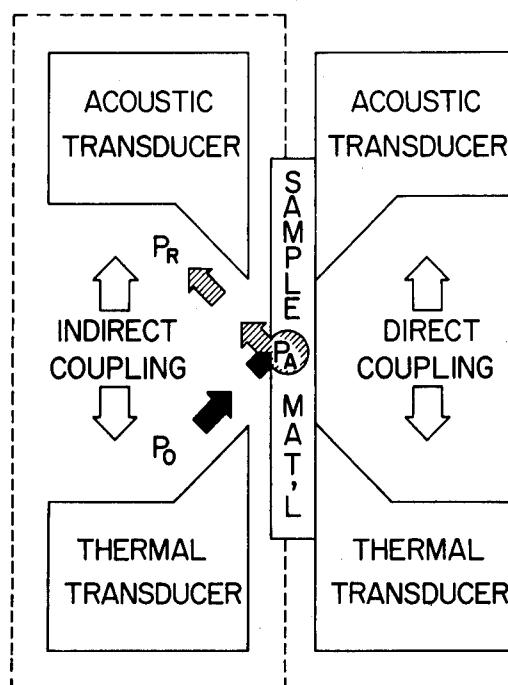


Figure 2. Configurations for indirect and direct coupling between the sample and photoacoustic or photothermal transducer.

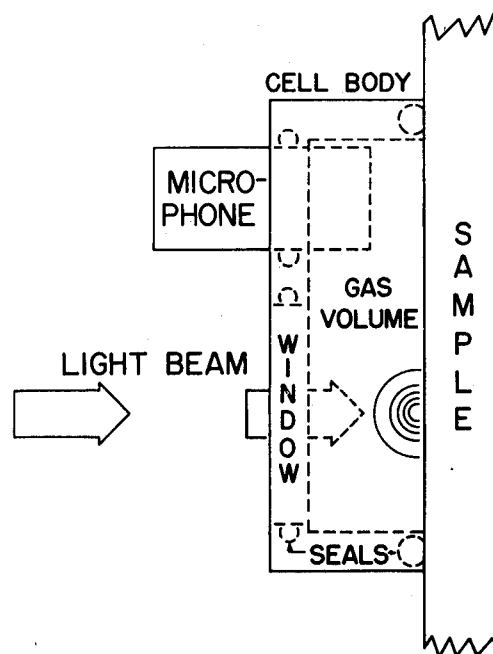


Figure 3. Schematic of a photoacoustic cell sealed to a sample.

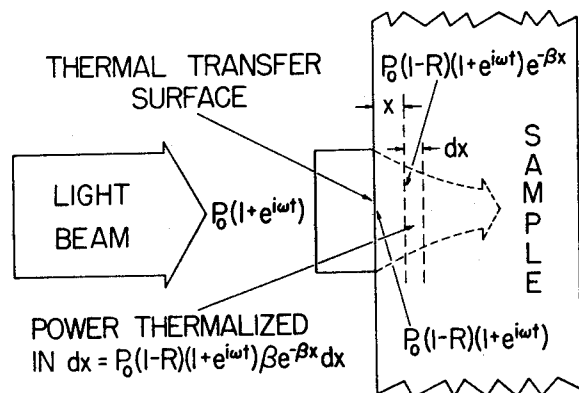


Figure 4. Illustration of the optical power deposition in a sample with incident power P_0 and sample reflectivity, R , and absorption coefficient, β .

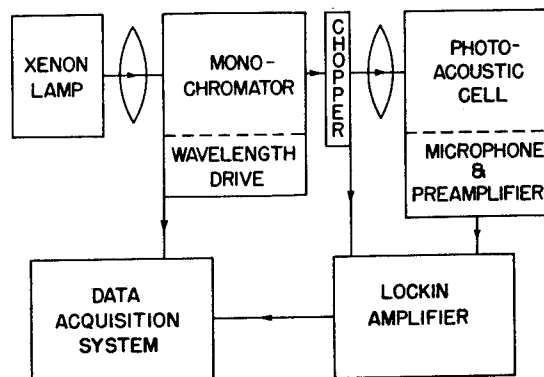


Figure 6. Block diagram of a single beam photoacoustic spectrometer.

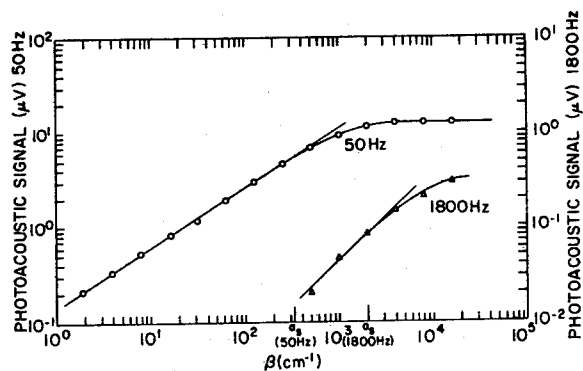


Figure 5. Experimental data showing the photoacoustic signal dependence on the sample absorption coefficient, β , for chopping frequencies of 50 and 1800 Hz. The onset of saturation can be seen at $\beta = \beta_s$ with full saturation at approximately $\beta = 10\beta_s$.

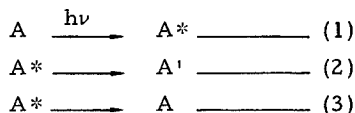
ACTINOMETRIC MEASUREMENT OF SOLAR ULTRAVIOLET AND DEVELOPMENT OF A WEIGHTED SOLAR UV INTEGRAL¹

By: Amitava Gupta and Clifford Coulbert, Jet Propulsion Laboratory

Dr. Amitava Gupta was appointed a Senior Scientist at JPL in 1975 after receiving his Ph. D. in organic photochemistry at the California Institute of Technology. His research interests include photochemistry of polymers, transient spectroscopy and polymer degradation mechanisms. He is currently developing a life prediction methodology for photovoltaic solar cell encapsulation materials, and studying mechanisms of photo-degradation in transparent polymers caused by solar ultraviolet.

Clifford Coulbert is manager of the Encapsulation Task of the Low-Cost Solar Array Project at the Jet Propulsion Laboratory. He holds an M. S. degree in mechanical engineering from UCLA. A major focus of his 30-year career has been the evaluation and prediction of the response of materials to hostile environments, including nuclear explosions, exotic fueled ramjet and rocket engines, fuel storage systems, human body implants, aircraft accident fires, and terrestrial solar arrays. He has published numerous papers and reports in the areas of heat transfer, refractory materials, rocket engine design, and combustion.

Actinometric measurement of radiation consists of determination of the rate of photochemical reaction whose rate constant or quantum efficiency is known with some precision. The principle may be stated in terms of Scheme I.



Scheme I

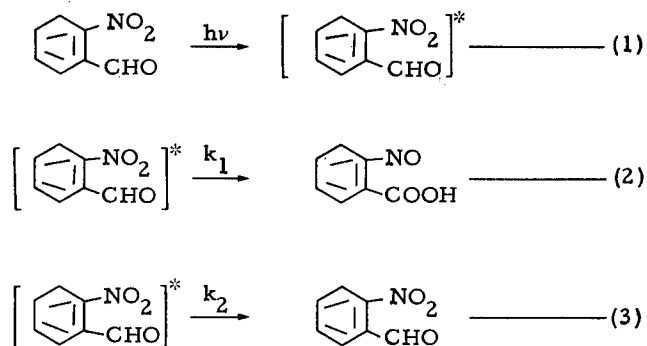
Here process (1) represents the excitation of molecules of material A that absorb the radiation. A* is the excited molecule that may undergo decay or relaxation to an excited state of different vibrational or electronic symmetry. The excited state then undergoes multiple decay processes represented by Eqs. (2) and (3), i. e., it decays partially to A', the photochemical product, and partially back to A. The quantum efficiency ϕ is defined as $k_2/(k_1 + k_2)$, so that the rate of formation of A' is $dA'/dt = \phi \times I$, assuming that ϕ is independent of wavelength. The rate dA'/dt is measured using the usual analytical techniques. This model assumes that intensity I is independent of t, but it can be extended to the case where the intensity is time dependent.

Desirable criteria for an actinometric system are:

- (1) Quantum efficiency should be independent of intensity of light for normal intensity levels.
- (2) The photochemical process should be temperature independent or have as low an activation energy as possible.
- (3) The materials, A, A', and substrate should be air stable, thermally stable, and stable to moisture.
- (4) The quantum efficiency should be independent of wavelength over the range of UV wavelengths of interest.

Relative radiant energy sensitivities of actinometric and radiometric techniques of measurement are difficult to estimate and are system dependent. A good estimate of radiometric sensitivity using analog measurement devices is about 10^{-8} watts/cm² of incident radiation prior to wavelength resolution, or 10^{-11} watts/cm² of radiation being incident on the photomultiplier. An optimum actinometric system can measure down to 4×10^{-7} joules. The main advantage of the actinometric systems is that they are stable and can integrate low light levels in time, while the main disadvantage is that they are far less sensitive than photomultipliers.

An actinometric system, initially developed by Pitts, et al.,² has been used to measure solar irradiance outdoors. This system is described in Scheme II, and involves photochemical rearrangement of O-nitrobenzaldehyde to form O-nitrosobenzoic acid.



Scheme II

¹ This paper presents the results of one phase of research carried out at the Jet Propulsion Laboratory, California Institute of Technology, for the U. S. Department of Energy, by agreement with the National Aeronautics and Space Administration.

² McCormick, R. N., Vernon, J. M., and Pitts, J. N., Jr., Pilot Study of Ultraviolet Radiation in Los Angeles, U.S. Department of HEW, Oct. 1965, p. 49.

Here the quantum yield of formation of the nitrosobenzoic acid is defined as $\phi = k_2/(k_2 + k_1)$. This has been measured in a variety of media to be 0.50 ± 0.03 . It has been found that the quantum yield is independent of wavelength in the range 253 to 380 nm, and the activation energy is less than 0.1 cal/mole in the range 20 to 52°C. The conversion may be followed variously, i.e., by following increase of absorption of the product at 450 nm, by following a decrease of pH, by ir spectroscopy following the decrease of the 1530 cm^{-1} band assigned to the asymmetric nitro stretch, or the increase of the 1598 cm^{-1} band assigned to the nitroso stretch.

To measure irradiance using this actinometer, we make up a stock solution of O-nitrobenzaldehyde (NBA) and polymethylmethacrylate, in the weight ratio of 1:10 in dichloromethane. This solution is slowly evaporated in a dry environment to cast thin films of the PMMA-NBA blend (~2 mil). The thickness and clarity of the film are critical and are routinely monitored by measuring absorption at 1498 cm^{-1} (carbonyl groups in PMMA) and scattering at the 450 to 650 nm range, which is affected by the clarity of the film. These films are mounted in slide holders and wrapped in light-tight paper until exposure to the irradiance to be measured. Absorption spectra of the films are measured to obtain the film's wavelength response, and also to determine a calibration factor that is the ratio of intensity of light incident on the film to the intensity absorbed. A calibration factor that is the ratio of intensity of light incident on the film to the intensity absorbed. A calibration plot is shown in Fig. 1.

Maximum linear conversion range has been experimentally determined for this actinometer. It depends on film thickness and the extinction coefficient of the product in the range of 290 to 450 nm. Usually a large batch of films is made up, and thickness can be controlled to $\pm 5\%$. The films are cut in 5 cm x 5 cm pieces, mounted in film holders and their ir spectra recorded. The ir spectra (peak height at 1480 cm^{-1}) can be used to measure the thickness of the films. After exposure of the film, one may record the conversion rate (either in moles per unit time or ein-

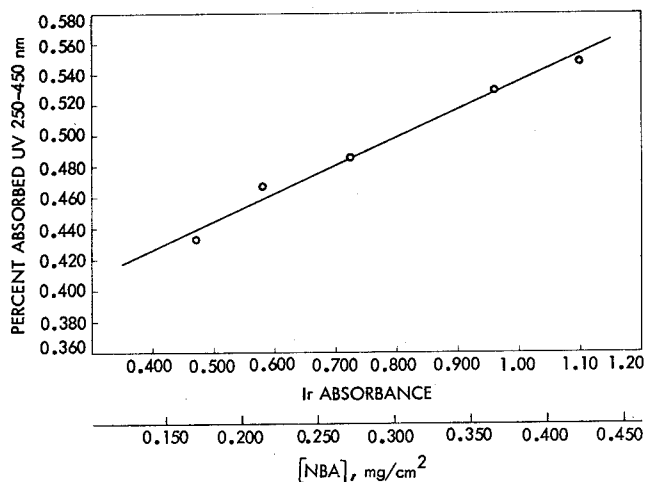


Fig. 1. Calibration plot for NBA actinometer

steins registered per unit time) and use it to correlate degradation processes. Strictly speaking, this correlation would be precise only when the wavelength responses of the actinometer and the material being studied are identical. However, the wavelength response of the NBA actinometer (Fig. 2) is similar to activation spectra of many polymers being studied for use in solar cell module encapsulation systems, and therefore the conversion of this actinometer measures accumulated UV dosage that correlates degradation of such polymers as polystyrene, polydimethyl siloxanes (silicones), and PMMA under exposure to different types of radiation sources. This conversion rate may be defined as a weighted ultra-violet wavelength integral, since it gives greater importance to short wavelength UV, which may be low in intensity in solar irradiance, but which causes most damage. Figures 3 and 4 demonstrate such correlation obtained for silicones and PMMA using two different radiation sources in each experiment. Moreover, the wavelength response of the actinometer can be varied by changing its thickness (see Fig. 1), so that one uses thin films to study PMMA while using thicker films to study polyurethanes, for example.

The actinometer may be used to obtain wavelength resolution of outdoor irradiance in the range of 295 to 400 nm. If the concentration of NBA in the film is c and the thickness of the film is d , then $\log I_0/I = \epsilon \lambda cd$ when the product cd can

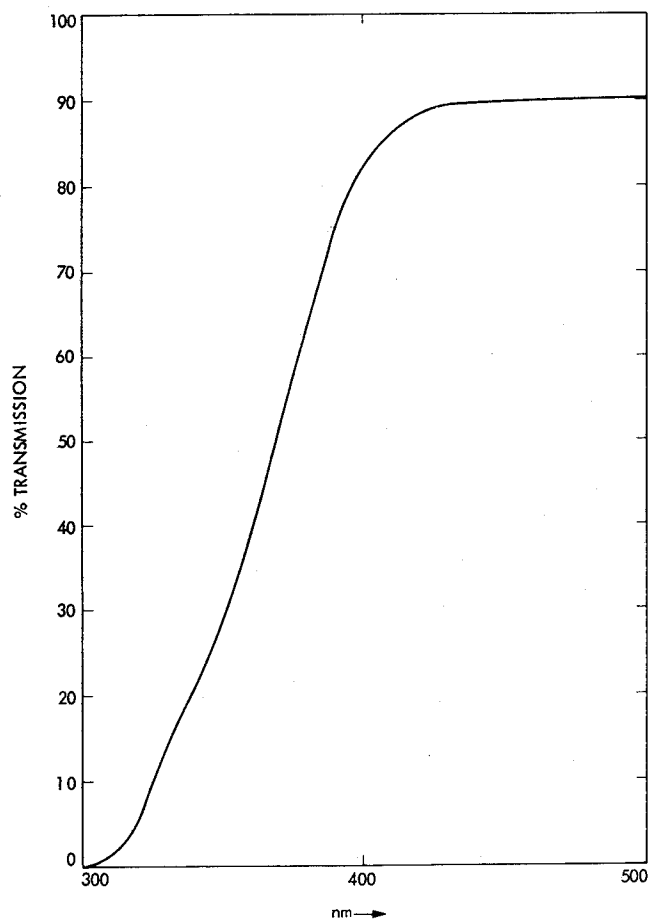


Fig. 2. Wavelength response of actinometer

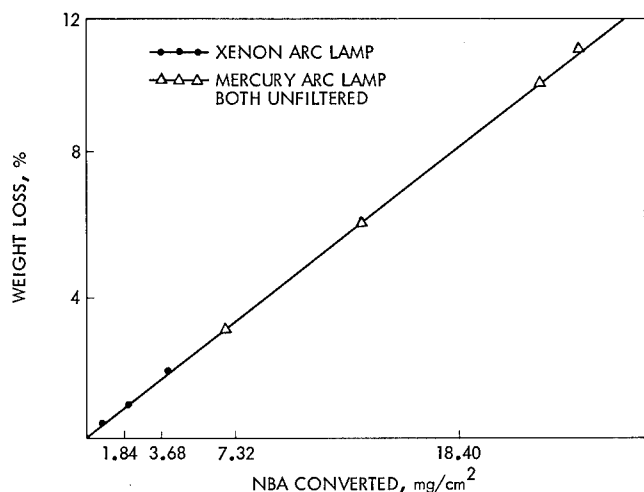


Fig. 3. Use of UV integral to correlate rate of photodegradation of PMMA

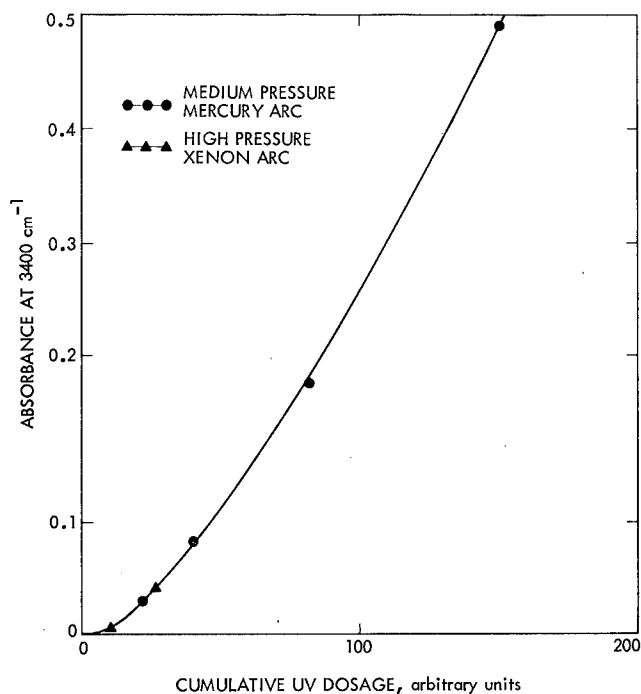


Fig. 4. Use of UV integral to correlate rate of photodegradation of RTV 615

be varied to obtain different transmittances at any wavelength λ , when ϵ_λ is the extinction coefficient of the film at wavelength λ , and when I_0 and I are incident and transmitted intensities of radiation,

respectively. A series of films of varying concentrations of NBA per unit area is made up.

If percent absorption at wavelength λ_x is a_{λ_x} , then total conversion per unit time for the j th film of the series is

$$c_j = \sum_{295}^{400} a_{\lambda_x} \times \Delta\lambda_x \times n_{\lambda_x} \times \phi_{\lambda_x} / N$$

in moles per unit time when a_{λ_x} is the average absorption in the range λ_x to $\lambda_x + \Delta\lambda_x$ for the j th film given a particular value of cd , n_{λ_x} is the number of photons incident on the film in the same wavelength range, ϕ_{λ_x} is the quantum yield (0.50 ± 0.03), and N is Avogadro's number. These equations can be solved if the number of wavelength intervals is equal to or less than the number of films of different NBA concentrations per unit area. In practice, the 105-nm region is broken up in unequal intervals (5 nm in the short wavelength side and 10 nm in the long wavelength side), and up to 15 different NBA concentrations per unit area may be used. This approach gives detailed information about the bandshape integrated in time.

In conclusion, measurement of irradiance (including solar irradiance) using the actinometer has the following advantages:

- (1) It becomes possible to obtain irradiance data over any given surface, including interfaces which are not otherwise accessible.
- (2) The irradiance data is real time integrated, so that fluctuations of power levels do not cause errors. With neutral density filters, it may be used to integrate solar irradiance continuously for periods up to one month.
- (3) The irradiance data is wavelength weighted, i.e., more importance is given to short wavelength photons, which may be fewer in number but can be absorbed more efficiently by polymeric encapsulation and cause more damage. This makes it possible to use the data to correlate degradation rates.
- (4) The response of the actinometer is almost independent of temperature, which makes it unnecessary to correct the data and makes the system suitable for remote site applications.
- (5) Using the techniques described above, one can obtain wavelength resolution (again, integrated in real time).

THE NBS SELF-STUDY MANUAL ON OPTICAL RADIATION MEASUREMENTS
By: Fred E. Nicodemus, National Bureau of Standards

Fred Nicodemus, born in Osaka, Japan, received an A.B. (physics) from Reed College, Portland, Oregon, in 1934. His work in radiometry started at Air Force Cambridge Research Laboratories, now at Bedford, Massachusetts, in 1946, and continued at Sylvania Electronic Defense Laboratories, Mountain View, California, and the Naval Weapons Center, China Lake, California, before he joined NBS as Editor of the *Self-Study Manual on Optical Radiation Measurements* in 1974. He has published papers on various aspects of radiometry and is a Fellow of the Optical Society of America and a member of the Society of Photo-Optical Instrumentation Engineers and of the U.S. National Committee of the C.I.E. (International Commission on Illumination).

Here at NBS we are preparing and publishing chapters for a *Self-Study Manual on Optical Radiation Measurements*. As the chapters are completed, they are issued in the form of NBS Technical Notes. At the end of this talk, I'll give you details on what's already available and how to obtain copies. First, however, I want to say a few words about the background and the reasons for undertaking this project. Then I'll briefly review the objectives and the general plan for the content and the level of presentation.

In recent years the need for radiometric measurements (including photometric measurements) and the degree of accuracy required have increased significantly in many areas, including the measurement of solar energy. Uncertainties of one to a few per cent would often be desirable but are seldom achieved. Measurements by different instruments or techniques commonly disagree by 10% to 50%, and resolving these discrepancies is time-consuming and costly.

The discrepancies are due both to the complexity of radiometric measurements and to the lack of adequately trained experts. Radiant power varies with the radiation parameters of position, direction, wavelength (frequency, etc.), time, and polarization. The response of most radiometers also varies with these radiation parameters and with a number of environmental and instrumental parameters, as well. Thus the accurate measurement of optical radiation is a difficult multi-parameter problem. But most of those who need to make these measurements haven't been trained to do so. Few schools have had programs in this area and tutorial and reference material that can be used for self-study is only partially available, is scattered throughout the literature, and is generally inadequate. In the *Self-Study Manual*, we are trying to make this material readily accessible in one place and in systematic, understandable form.

We've been working on the Manual since mid-1974 and our first issue, NBS Tech Note 910-1, with the first three chapters, came out in March 1976. Much time has been spent in thorough exploration of difficult questions about content and level of presentation. We want the Manual to be as simple

and easy to read as possible in order to reach directly as many users as we can. On the other hand, complexity and sophistication are unavoidable in trying to make one-per-cent measurements commonplace--which is an over-simplified statement of our goal. Furthermore, when we add to this complexity the fact that we are writing for workers in so many diverse fields (astronomy, mechanical heat-transfer engineering, illumination engineering, photometry, meteorology, photo-biology and photo-chemistry, optical pyrometry, remote sensing, military infrared applications, etc.) it becomes obvious that we can't possibly deal with each measurement in cookbook fashion, giving specific detailed procedures for each case; there are just too many possibilities. Accordingly, we must present general principles and help the reader to acquire sufficient understanding to work out his own procedures for his specific measurement problems. As a result, the material is not easy reading in spite of our best efforts in that direction. It requires a familiarity with science and mathematics at the level of a bachelor's degree in some branch of science or engineering, or the equivalent in other training and experience.

We're trying to make the Manual a comprehensive tutorial treatment of the subject that is complete enough for self instruction; hence the phrase "self-study" in the title. It does not contain explicitly programmed learning steps as that phrase sometimes denotes. In addition, through detailed, yet concise, chapter summaries, the Manual is designed to serve also as a convenient and authoritative reference source. Those already familiar with a topic may turn directly to a chapter summary for a quick review and to determine what, if any, of the body of the chapter they want to read for more details.

The basic approach and focal point of our treatment in the Manual is the measurement equation, an equation relating the radiometric quantity to be measured to the instrumental response data through a detailed characterization of the instruments used and the radiation field observed, in terms of all of the relevant parameters. The latter always include the radiation parameters, as well as environmental and instrumental parameters. It is our conviction that such a measurement-equation approach is the only way that the uncertainties in the measurement of optical radiation can generally be limited to one, or at most a few, per cent.

So far, we have dealt only with classical radiometry of incoherent, geometrical- or ray-optics, radiation. We realize that there is urgent need for similar treatment of coherent (including partially coherent) radiation, especially in connection with lasers, but the basic theory on which such a treatment must be based is just being developed at more sophisticated levels and it will be some time yet before we can incorporate it in the Manual.

The current plan for the Manual is to group the chapters into three parts: I. Concepts, II. Instrumentation, and III. Applications. To

date, six chapters of Part I have been completed and published:

- Chap. 1 Introduction
- Chap. 2 Distribution of Optical Radiation with Respect to Position and Direction--Radiance
- Chap. 3 Spectral Distribution of Optical Radiation
-- published as NBS TN 910-1, March 1976.
- Chap. 4 More on the Distribution of Optical Radiation with Respect to Position and Direction
- Chap. 5 An Introduction to the Measurement Equation
-- published as NBS TN 910-2, February 1978.
- Chap. 6 Distribution of Optical Radiation with Respect to Polarization
-- published as NBS TN 910-3, June 1977.

Currently in preparation and, we expect, to be published in this calendar year, are three more chapters, also still of Part I:

- Chap. 7 The Relative Spectral Responsivity and Slit Function of a Spectroradiometer
- Chap. 8 Deconvolution
- Chap. 9 Physically Defining Measurement-Beam Geometry by Using Opaque Barriers.

Topics planned for chapters to be written during the next three years include the following (Part I, II, or III is indicated by just the Roman numeral in parentheses): (III) Linearity Calibrations, (I) Physical Photometry, (III) Spectroradiometry of Continuous UV Spectra (incl. Appendix on Uncertainty), (I) Distribution of Optical Radiation with Respect to Time, (I) Spectrophotometry, (I) Coherence (if basic theory is adequately developed) or Diffraction Corrections to Throughput Calculations, (III) Spectroradiometry of Spectral Lines, (I or II) Detectors, (I) Blackbody Radiation and Temperature Scales, and (II) Radiometric and Photometric Source Standards. These plans, of course, are subject to change.

You can purchase copies of the NBS Technical Notes in the 910- series, containing chapters of the Self-Study Manual, from the Superintendent of Documents, U.S. Government Printing Office, Washington, D.C. 20402. The ordering information, including the stock numbers and prices, is listed on this page along with a cut-out coupon for requesting the Superintendent of Documents to send you the announcement lists for future publications by NBS. These are listings of all of the Bureau's new publications; this service is no longer provided for just a single series of reports or technical notes. Another way of learning about new issues is through our *Optical Radiation News*, a quarterly publication of the Radiometric Physics Division of NBS with articles about its current activities, including announcements of the publication of chapters of the Self-Study Manual. We will be glad to add your name to the distribution list for this newsletter upon request.

Currently available for purchase from:

Superintendent of Documents
U.S. Government Printing Office
Washington, D.C. 20402

SELF-STUDY MANUAL ON OPTICAL RADIATION MEASUREMENTS

Part I-Concepts

NBS Technical Note 910-1
Chapters 1 to 3
Issued March 1976
--order Stock No. 003-003-01590-3, Price \$2.10

NBS Technical Note 910-2
Chapters 4 and 5
Issued February 1978
--order Stock No. 003-003-01880-5, Price \$3.00

NBS Technical Note 910-3
Chapter 6
Issued June 1977
--order Stock No. 003-003-01785-0, Price \$2.10

(Add 25% additional to quoted prices for other than U.S. mailing)

If you wish to be automatically notified of the availability of future NBS publications, please complete and submit the form provided below:

----- cut here -----

ANNOUNCEMENT OF NEW PUBLICATIONS of the NATIONAL BUREAU OF STANDARDS

Superintendent of Documents
Government Printing Office
Washington, D.C. 20402

Dear Sir:

Please add my name to the announcement list of new publications as issued by the National Bureau of Standards.

Name _____

Company _____

Address _____

City _____ State _____

Zip Code _____

(Notification Key N519)

NBS CAPABILITIES FOR REFLECTANCE AND TRANSMITTANCE MEASUREMENTS

Jack J. Hsia and William H. Venable, Jr., National Bureau of Standards

HSIA, Jack J.; M.S. in Heat Transfer and Ph.D. in Thermophysics, Purdue University. Research Assistant -- Thermophysical Properties Research Center (now CINDAS), Purdue University. Physicist at NBS since 1969 doing work in reflectance.

VENABLE, WILLIAM H., JR.; B.S. and M.A. - Physics, University of Florida, Ph.D. - Physics, University of Alabama. Twelve years at NBS, the last seven of which have been as group leader of the NBS program in spectral reflectance and transmittance.

Establishing and improving the scales of spectral reflectance and transmittance are two main responsibilities of the spectrophotometry group of the Radiometric Physics Division (Center for Radiation Research, National Measurement Laboratory) of National Bureau of Standards. NBS has developed instrumentation and techniques for realizing the scales of spectral reflectance and transmittance[1-5]. Accuracy is ensured by thorough studies and error analyses and accuracy is maintained by stability checks, by intercomparing standards with other national and international laboratories, and by the exploration of alternative measurement techniques as a means of reducing possible systematic error. Commercial instruments are also available at NBS to transfer the scales by means of standards for measurements which require lesser accuracy.

Dissemination of scales is mainly through measurements by NBS of the master standards of instrument manufacturers and secondary laboratories. For individual users the dissemination is through Standard Reference Materials. In general, measurement services are not provided by NBS when they are widely available from commercial laboratories. However, suggestions will be offered of other sources of assistance on calibration or measurement problems when the Bureau's own equipment and personnel are unable to undertake the work.

Reflectance and transmittance are two of the key optical properties identified[6] for performance tests for materials commonly used in solar heating and cooling systems such as glass and plastics for cover plates, absorptive coatings, and reflective and anti-reflective coatings. For a mirror solar concentrator system, one of the key optical properties is specular reflectance.

The current applicable spectral ranges for the NBS-developed reference instruments are in the ultraviolet and visible regions. Plans have been made to extend the range of those instruments to 2500 nm during the coming year. The current and planned measurement capabilities for high accuracy reflectance, transmittance and related measurements are listed in Table 1 including geometry, wavelength range λ (nm), bandpass (nm) and estimated uncertainties in the measured data. This table also includes the commercial instruments which have higher uncertainties, but cover an extended wavelength range. Listed under geometry are regular transmittance $T(\theta/\theta)$, Hemispherical transmittance $T(\theta/h)$, specular reflectance $R(6/6)$ with angle of incidence 6° from normal, hemispherical reflectance factor $R(6/h)$, diffuse reflectance factor with angle of incidence 45° from

normal and viewing angle normal to the sample, gloss, haze and retrorreflectance. The geometries of the gloss and haze measurements are specified by standard test methods for assessing scattering due to reflection and transmission[7].

Calibrated standards provided by the spectrophotometry group of NBS are glass filters for transmittance standards[8], didymium and holmium glass filters for checking wavelength accuracy of instruments[9], and Vitrolite White Glass[9] for hemispherical reflectance factor standards. These standards are listed in Table 2 including wavelength range, bandpass, and estimated uncertainty.

Current and planned standard reference material managed by the Office of Standard Reference Material of NBS are listed in Table 3. SRM 2101 to 2105 are a set of five glass filters for checking the performance of colorimeters[10,11]. SRM 930d[12] is a set of glass filters with nominal transmittance of 10, 20, and 30%, for use in checking the accuracy of the photometric scale of spectrophotometers. The liquid filters, SRM 931b[13], are absorbance standards with nominal absorbance of 0.3, 0.6, and 0.9, for use in ultraviolet and visible spectrophotometry. The planned standard reference materials are didymium and holmium oxide glass wavelength standards for the visible and ultraviolet range with smaller uncertainties than those of the current calibrated standards listed in Table 2. Other planned standard reference materials of interest to solar energy work are aluminum and rhodium coated mirrors for specular reflectance standards. Both aluminum and rhodium mirrors have been coated since November, 1977 and are being aged in a laboratory environment to insure stability. These mirrors will be calibrated around the end of this year.

Suggestions about the coverage of the NBS spectrophotometric measurements are most welcome and will be helpful in determining future NBS programs.

REFERENCES:

1. Venable, W.H. Jr., Hsia, J.J. and Weidner, V.R., "Establishing a Scale of Directional-Hemispherical Reflectance Factor I: The Van den Akker Method", J. Res. NBS 82 (1), 29-55 (July-August 1977).
2. Venable, W.H. Jr., Hsia, J.J. and Weidner, V.R., "Optical Radiation Measurements: Development of an NBS Reference Spectrophotometer for Diffuse Transmittance and Reflectance", NBS Tech. Note 594-11 (October 1976).
3. Mielenz, K.D., Eckerle, K.L., Madden, R.P., and Reader, J., "New Reference Spectrophotometer", Appl. Opt. 12 (7), 1630-41 (July 1973).
4. Mielenz, K.D. and Eckerle, K.L., "Design, Construction, and Testing of a New High Accuracy Spectrophotometer", NBS Tech. Note 729 (June 1972).
5. Eckerle, K.L., "Modification of an NBS Reference Spectrophotometer", NBS Tech. Note 913 (July 1976).

6. Skoda, L.F. and Masters, L.W., "Solar Energy Systems - Survey of Materials Performance", NBS IR 77-1314 (October 1977).
7. Hsia, J.J., "Optical Radiation Measurements: The NBS 20-, 60-, and 85-Degree Specular Gloss Scales", NBS Tech. Note 594-10 (July 1975).
8. Keegan, H.J., Schleter, J.C. and Belknap, N.A., "Recalibration of the NBS Glass Standards of Spectral Transmittance", J. Opt. Soc. Am. 54 (1), 69-74 (January 1964).
9. Keegan, H.J. and Gibson, K.S., "On the Use of Working Standards of Didymium and Vitrolite Glasses for Spectrophotometric Measurements", J. Opt. Soc. Am., 34 (12), 770 (December 1944).
10. Keegan, H.J., Schleter, J.C., and Judd, D.B., "Glass Filters for Checking Performance of Spectrophotometer-Integrator Systems of Color Measurement", J. Res. NBS 66A (3), 203-221 (May-June 1962).
11. Eckerle, K.L. and Venable, W.H. Jr., "1976 Remeasurements of NBS Spectrophotometer - Integrator Filters", Color Research and Application 2 (3), 137-141 (Fall 1977).
12. Mavrodineanu, R. and Baldwin, J.R., "Standard Reference Materials: Glass Filters as a Standard Reference Material for Spectrophotometry - Selection, Preparation, Certification, Use SRM 930", NBS SP 260-51 (November 1975).
13. Burke, R.W., Deardorff, E.R., and Menis, O., "Liquid Absorbance Standards", NBS SP 378, Accuracy in Spectrophotometry and Luminescence Measurement, Proceedings of a Conference held at NBS, Gaithersburg, MD, March 22-24, 1972 (Issued May 1973).

Table 1
Measurement Capabilities for Reflectance and Transmittance

Geometry	λ (nm)	Bandpass (nm)	Uncertainty	Ref.
<u>REFERENCE INSTRUMENTS</u>				
T(θ/θ)				
.1-1	210-800(-2500*)	0.2-1.5	0.0002	[3,4,5]
.001	210-800(-2500*)	0.2-1.5	0.000002	[3,4,5]
R(6/h)	220-780(-2500*)	10	0.15%	[1,2]
R(45/0)	380-770	10	0.3%	
Gloss	Visible	--	0.5 unit	[7]
Haze	Visible	--	Under test	
Retroreflectance	Visible	--	3%	
<u>COMMERCIAL INSTRUMENTS</u>				
T(θ/θ)	400-1080	10	0.5%	
R(6/h)	400-1080	10	0.5%	
T(θ/θ)	200-2500	1-5	0.5%	
T(θ/h)	220-2500	1-5	0.5%	
R(6/h)	220-2500	1-5	0.5%	
R(6/6)	250-2500	1-5	0.5%	

*By Spring 1979

Table 2
Calibrated Standards

Material	Standard for	λ (nm)	Bandpass (nm)	Uncertainty	Ref.
Glass filters	T	390-750	1-5	0.5	[8]
Didymium glass	λ	400-750	10	1 nm	[9]
Didymium glass	λ	730-1080	20	2 nm	[9]
HoO ₂ glass	λ	240-650	<2	0.5 nm	
Vitrolite white glass	R(6°/h)*	400-1080	10	0.5%	[1,2]

*R \approx .9

Table 3
Standard Reference Materials

SRM No.	Material	Standard for	λ (nm)	Bandpass (nm)	Uncertainty	Ref.
<u>CURRENT</u>						
2101-5	Glass	Color	Visible		0.1-0.7%	[10,11]
930d [†]	Glass	T	440-635		0.5%	[12]
931b [†]	Liquid	Absorbance	302-678	1.0-6.5	1%	[13]
<u>PLANNED</u>						
	Didymium glass	λ	400-750	1.5-10.5	0.2-0.3 nm	
	HoO ₂ glass	λ	240-650	<2	<0.2 nm	
	Al,Rh mirrors	R(6/6,45/45)	220-770(2500)	5	0.2%	
	Beaded sheeting under glass	Retroreflectance	400-750	~15	2%	

[†]by Inorganic Analytical Research Division, NBS

AN INTEGRALLY POWERED SOLAR ENERGY RECORDER
By: D. D. Gibson, N. P. Bosted and W. R. Stephens, Sun Systems, Inc.

Duane Gibson—B. Sc., Electrical Engineering, University of Arizona, 1960. Joined National Reactor Test Site staff as instrumentation engineer in 1960; headed the Reactor Instrumentation Group, 1962-71. He was a founder of Sun Systems in 1971; currently executive vice president. Mr. Gibson is the principal designer of the ADASTOR solid state recorder.

N. P. Bosted—B. Sc. and M. Sc., Physics, Bucknell University. Senior Fellow, Carnegie-Mellon University, conducting research in solid-state electronics, 1954-58. Engineering/executive assignments with Westinghouse Electric and International Rectifier Corporations prior to joining Sun Systems in 1976, where he is currently president.

W. R. Stephens—Aeronautical Engineering, Cal-Aero Technical Institute; Electronics, University of Idaho. Instrumentation technician, 1960-73, NRTS. Joined Sun Systems in 1973, where he is currently senior instrumentation technician.

ABSTRACT: A completely solid-state, self-contained data recorder particularly adapted for capture, analysis and recording of insolation data is described and field operational experience presented. The CMOS based recorder operates from a commercially available solar panel, and is capable of indefinite operation at remote sites. Up to 64×10^{10} data points are stored in memory and may be read out as a histogram on field portable equipment or interfaced into an RS 232 or GPIB bus. The system is particularly useful for long term surveys at remote sites where reliability, small size and self-powered operation for extended periods are important.

I. INTRODUCTION

Heretofore, measurement of net total solar flux has required the use of various kinds of strip chart, circular chart or magnetic tape recorders. The drawbacks of these recording methods are many; their precision is limited, the mechanical or electrical drives require periodic attention and are subject to frequent failure, electro-mechanical systems are difficult to interface to solar detectors, analysis of the recorded data is frequently awkward and very time consuming, and generally such recorders cannot operate unattended for substantial periods of time.

Sun Systems' earlier experience with the U.S.F.S. and the Skylab programs' installations, using digital data acquisition systems to obtain and record climatological data, led to the development in 1976-77 of a new approach to the problem, designed to overcome field difficulties and make possible simple, reliable, long-term data acquisition and analysis. Operating criteria were:

- A. Long-term, unattended operation.
- B. Self-contained and powered.
- C. Rugged and weather-proof.
- D. Fast data access and analysis.

In order to realize these objectives, it was determined that the data recorder should be built around certain basic elements:

- A. Battery operation.
- B. All solid-state (no electro-mechanical assemblies)

- C. CMOS circuitry.
- D. Minimum case size compatible with ruggedness.
- E. Integral data formatting and reduction.
- F. Simple field-portable readout means.

The basic design criteria also included intrinsic capability to accept data from nearly any electrical analog transducer, and to provide internal references, amplification and signal conditioning for transducers. The present discussion is centered around the use of this recorder system for acquisition and analysis of solar data, using a pyranometer input, although other input devices such as anemometers, pressure sensors, rainfall gauges, flowmeters, accelerometers and strain gages can be used with equal ease.

The basic system design also permits the recorded data to be organized and formatted in several ways. For insolation measurement, the "time at load" format is most appropriate. Due to its very low power consumption (less than 100 milliwatts), it is quite easy and inexpensive to power the recorder from a solar panel. Figure 1 is a photograph of the recorder, the pyranometer and solar panel power source. The pyranometer is a Lambda Instruments Model 109, and the solar power panel is a modified unit made by Sensor Technology. The solar power panel delivers about 150 mA at ± 6 VDC in full sunlight, thus providing for maintenance of full battery charge even under prolonged sunless conditions.

II. RECORDER DESIGN AND ORGANIZATION

Figure 2 is a functional block diagram of the operational structure of the recorder.

The analog section provides an appropriate signal level for the A/D converter, with gain and offset panel controls where appropriate, as well as transducer excitation and internal calibration if needed.

The signal is digitized with an 8 bit analog-to-digital converter, under common control by the logic clock. In a time-at-level configuration, the full span analog voltage is divided into 64 increments (1.6% of full scale). The sampled signal is placed into one of the 64 discrete increments, converted into a BCD value which is stored in memory along with an on-going time count. Sample rates ranging from 1,000/sec. to 1/sec. are provided for. Storage of 10^{10} counts per memory address are provided, so that a count is stored in one of the memory addresses for each sample interval during which the signal amplitude remains at a given level. Since there are approximately 3×10^7 seconds in one year, it can be seen that even at a 1 msec sampling rate, more than 16 weeks would pass before the most active memory address was filled.

Optionally, the recorder can be set up to shut itself down during periods of nightfall, avoiding saturation at the lowest signal levels.

The memory consists of CMOS RAM chips and is provided with an independent Lithium Iodide cell powered data-save circuit having a life expectancy of three years or more in the event of main battery failure.

Basically, data is stored in the memory configuration as a typical histogram. Figure 3 is a typical histogram plot of time-at-solar flux. Note that an enormous amount of data compression is inherent in this presentation. At the same time, the nature of histogram recording ensures that even the least significant data are recorded and readily observable, providing, of course, that they are within the span range of the instrument calibration.

Several methods are available for reading out recorded data; the simplest is a visual readout which scans memory contents and displays amplitude and memory contents on an LED panel. This unit also provides a means of checking battery condition, calibration and allows reset of the memory. The unit is also battery operated and field portable. A portable hard copy printer may also be used in conjunction with the visual readout, and prints a hard copy data tape of memory contents in less than a minute. Figure 4 is a typical readout from the printer. This is a partial printout of the same data plotted in figure 3, and was taken with the accessory field portable printer.

At another level of sophistication, the ADASTOR can be readily interfaced to any ASCII or GPIB 488 device. A bench instrument provides for all of the visual numeric display functions, and additionally permits data to be graphically displayed, listed and manipulated.

III. DISCUSSION OF TYPICAL RECORDED DATA

Figures 3 and 5 are typical histogram plots of daily insolation values, plotted as time at power density on the logarithmic vertical axis, vs. power density expressed in Watts per square meter on the horizontal axis. Each bar along the X axis represents an incremental value of 31.25 Watts per square meter, and the vertical scale is in tenths of a second. Each bar then represents a section of a power spectrum, and the total measured energy for a period is equal to the summed values of the bars of the histogram. It should be noted that the power in each bar is a weighted value.

For example, in figure 3, the sixth bar shows a time count of 3.45×10^4 samples, equal to 0.96 hours, the time during which the mean solar flux level was equal to $\frac{156.25 + 187.50}{2}$ or 171.87 Watts/m². The power represented by bar six is therefore 182.38×0.96 or 165.0 Watt-hrs/m². The last bar in figure 3 shows a time value of only 1.6×10^3 counts, equivalent to 0.044 hours at a level of $\frac{531.25 + 562.50}{2}$ or 546.87 Watts/m² for a total of 24.1 Watt-hrs/m². The entire solar power available at the site on April 4 was 1.23 kW hrs/m². The day was heavily overcast and snow fell most of the day.

Contrast this with figure 5, which is a similar plot taken for April 12, during which the sun was completely unobscured. A total available energy of 6.5 kW hrs/m² was recorded. It should be noted that we have eliminated values which persisted for less than 100 seconds in the plots. There are two reasons for doing this; first, the net available power during such a transient period is insignificant and, second, many of the higher scale peaks are the result of transient phenomena (such as reflections

from vehicles) that are irrelevant to a study of available energy. In figure 5, the flux was in the 31.25 - 62.50 Watts/m² range for 70 seconds; a number of transient counts are always recorded on days of full sunlight at the highest end of the scale, usually as a result of reflections from windshields of passing motor vehicles.

Figure 6 is a summary record of measured energy available from March 15 through April 28. This six week period shows availability of 187 kW hrs/m². This figure is in good agreement with studies carried out by Wright and Jensen for the U.S.D.A.¹ at a site some ten miles south of ours during 1976-77, and observations reported by Wright and Jensen in 1975-76.²

The cited studies were done using conventional recording equipment which required a heated, insulated enclosure. This limited site location for studies to those where a source of electric power was available, and resulted in limitation due to shadows and other terrain feature problems. Both of these studies also reported difficulties due to equipment reliability.

IV. SUMMARY

A self-powered remote site data recorder, employing all solid-state circuit elements has been developed. It can operate unattended for long periods of time, and is basically unaffected by environmental conditions. Data on available solar energy is acquired in immediately useful format, and many months of data can be interpreted in less than one minute. As a self-contained instrument, it may be sited with total freedom from external sources or protection.

¹James L. Wright and Marvin E. Jensen, "Deer Creek Geothermal and Solar Radiation Demonstration Research Project Report", United States Department of Agriculture, Snake River Conservation Research Center, Kimberly, Idaho. February 1978.

²James L. Wright and Marvin E. Jensen, "1975 Evapotranspiration and Climatic Data, Blaine County, Idaho", State of Idaho, Department of Water Resources, Boise, Idaho. February 1976.

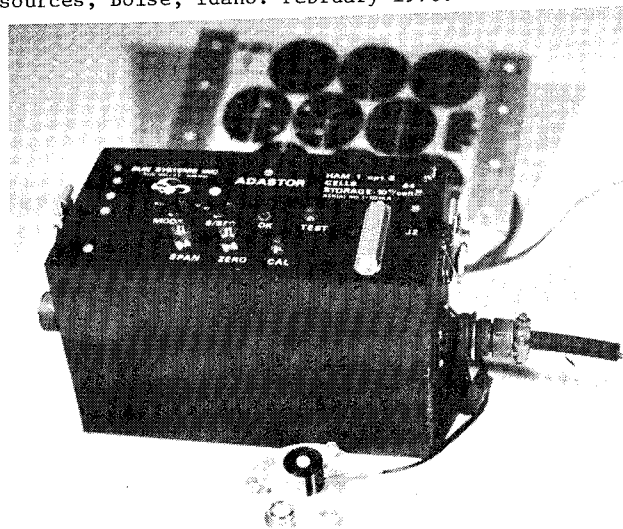


FIGURE 1.

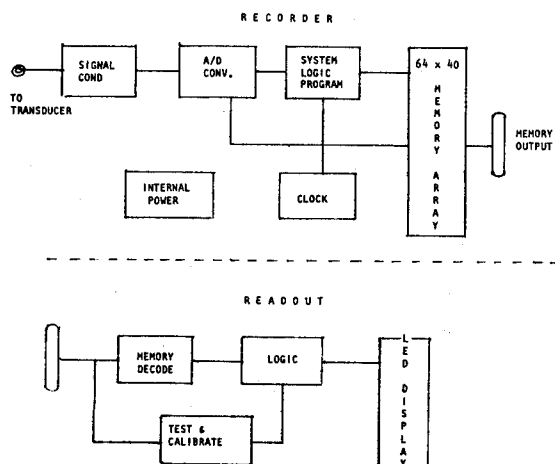


FIGURE 2.

4-4-78 1600
heavy ovcast with
with snow

CELL #
(EACH CELL
VALUE = 31.25
W/M²)

0000	9.399	6	# OF SAMPLES RECORDED, THIS LEVEL
0001	6.651	5	
0002	3.256	5	
0003	2.556	5	POWER OF TEN
0004	2.340	5	
0005	2.650	5	
0006	2.901	5	
0007	3.281	5	
0008	3.642	5	
0009	3.177	5	
0010	3.091	5	
0011	2.937	5	
0012	3.312	5	
0013	3.325	5	
0014	2.937	5	
0015	2.514	5	
0016	2.266	5	
0017	2.287	5	
0018	2.565	5	
0019	2.948	5	
0020	2.764	5	
0021	3.056	5	
0022	3.682	5	
0023	4.423	5	
0024	3.380	5	
0025	8.924	4	
0026	5.862	4	
0027	3.727	4	
0028	3.512	4	

FIGURE 4.

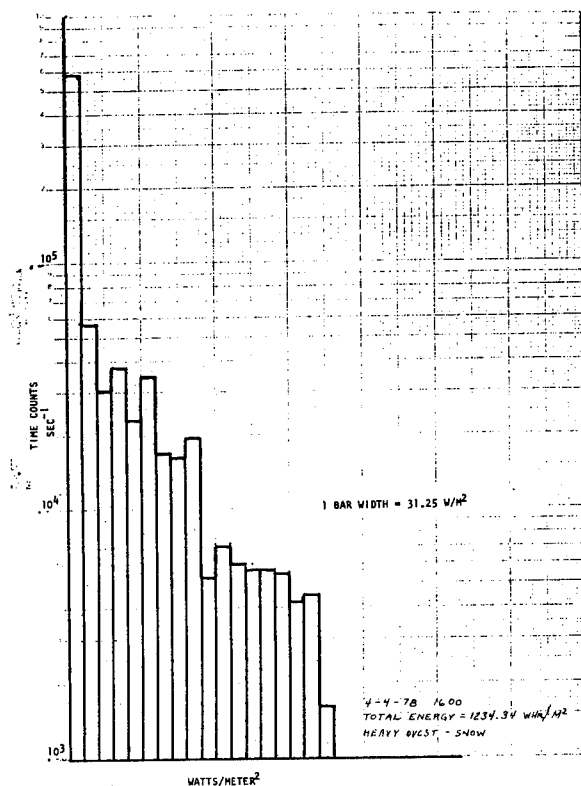


FIGURE 3.

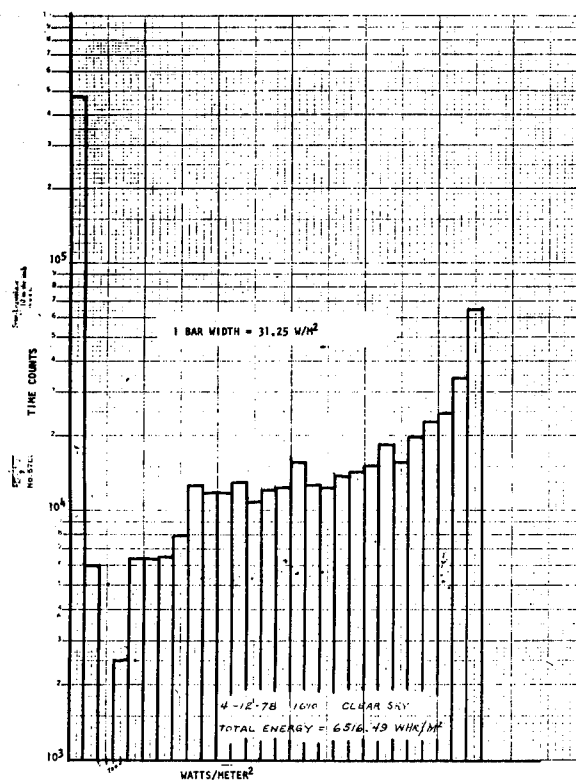


FIGURE 5.

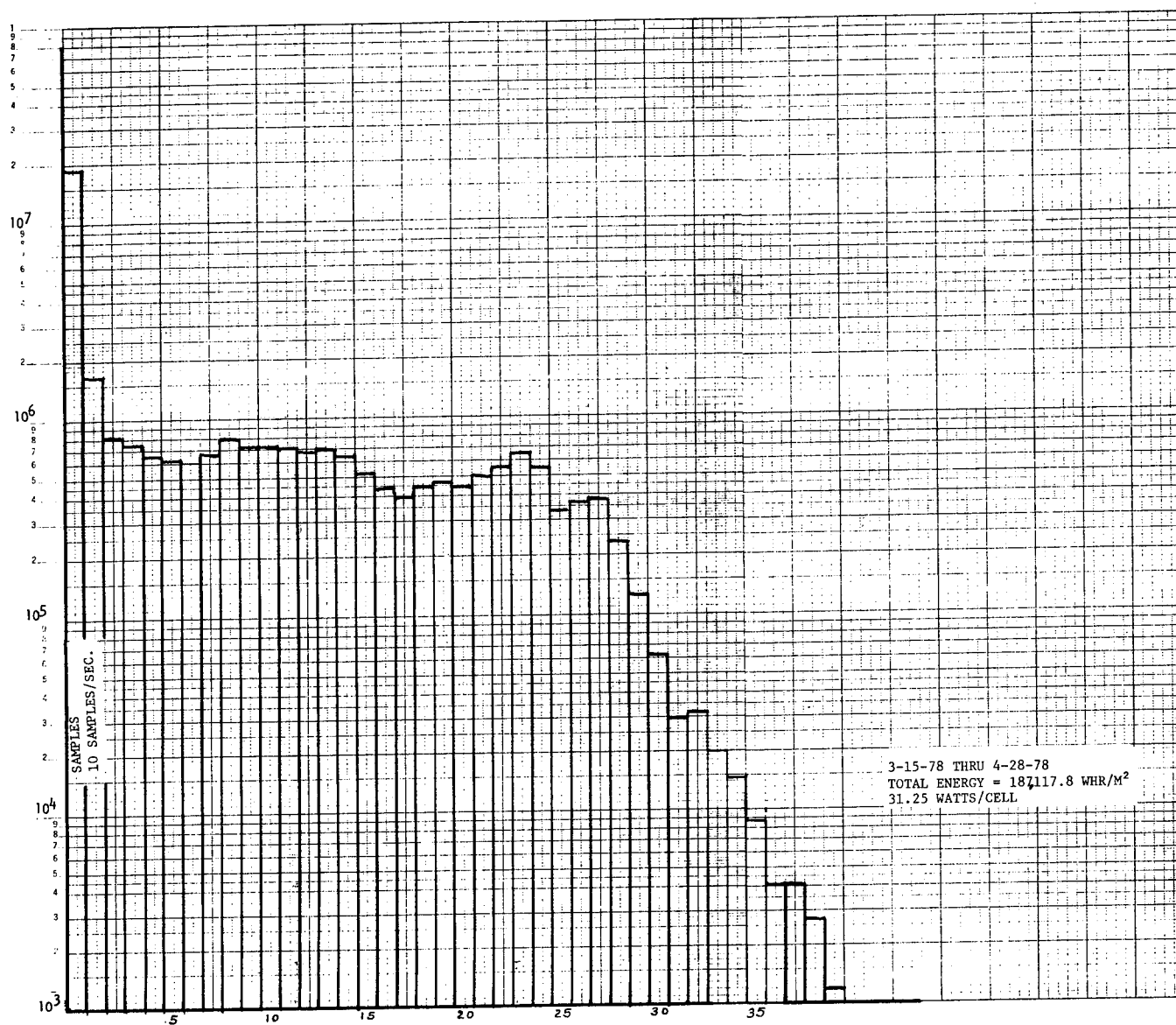


FIGURE 6.

SOLAR ENERGY SYSTEM TESTING: SOME EXPERIENCES WITH MINICOMPUTERS

W. W. Shurtleff, Sandia Laboratories

BSEE, 1965 from University of New Mexico; MSEE, 1967 from UNM. Completed all course work for Ph.D, 1977. Project leader in digital systems at Sandia Laboratories from 1967 to present. Specialist in application of minicomputers and microprocessors to real-time systems.

ABSTRACT

For the past few years, Sandia Laboratories has been involved with testing different components and systems associated with solar (and wind) energy studies. Sandia now has five minicomputer based controllers which aid in data acquisition and control of such projects as the Solar Total Energy Project, Photovoltaic Test Project, Solar Collector Project, Solar Thermal Test Facility (Power Tower), and the Vertical Axis Wind Turbine. The experiences associated with these projects have given some insight into developing a "philosophy of application" of minicomputers or microprocessors to this type of testing. In this paper, such ideas as versatility of hardware and software and "distributed" systems are explained with the purpose of outlining this philosophy.

INTRODUCTION

One of the recurring nightmares of many scientists and engineers interested in conducting experiments is that they will be handed a computer based system with which to do their work. Many people, after hearing the word computer, immediately envision a roomful of equipment, card readers, keypunching pools, and long delays in getting programs running. With the advent of the minicomputer, these concepts can be banished forever. The minicomputer, a smaller and less powerful version of its data processing big brother, can now be considered a research tool with programming capability. This paper discusses the application of four minicomputer based systems to solar and wind testing applications at Sandia Laboratories in Albuquerque, New Mexico. Also covered is the philosophy of applying minicomputers to general testing applications.

Background

Sandia Laboratories is heavily committed to supporting research in many areas of energy development. This paper will specifically address two of these areas, solar and wind energy systems, and describe the applications of minicomputer based controller-testers to them.

There are four solar research systems at Sandia, the Solar Total Energy System Test Facility (STESTF), the Photovoltaic Test Facility (PVTF), the Collector Module Test Facility (CMTF), and the Solar Thermal Test Facility (STTF). The first three systems are located relatively close together and comprise what can be called a solar computer network. These three systems are covered in this paper along with the Vertical Axis Wind Turbine Test Facility (VAWTF).

The STESTF is used to test the functional subsystems used in the solar total energy concept. This concept is that power, heating, cooling and hot water can be provided to a large building or a community with the principle energy input being solar energy and the "waste" energy from each stage being used to power the next stage. The functional subsystems being tested are various solar collectors, a turbine, heat storage and exchangers, and cooling.

The PVTF is used to test different types and arrays of photocells under various solar input and load conditions. This facility is being expanded to include long-term tests of photovoltaic components.

The CMTF tests various configurations of solar collectors on three fluid test loops. A fourth fluid loop is being considered.

The VAWTF is used to test various configurations of vertical axis wind turbines. The system can measure such factors as blade stress and rpm under applied loads.

To successfully apply minicomputer systems to experimental areas, certain guidelines should be followed. The guidelines developed at Sandia by the Facility and Digital System Design and Development Division have come from experience with developing over thirty minicomputer based systems. Before describing these guidelines a few definitions need to be made:

General Testing System - A system which will be used for general purpose testing of control and not production testing. Production testing implies testing of many items of the same type, whereas general testing implies testing many different items or subsystems.

Digital System - A digital system is one based on a minicomputer and controlled by an operator.

Distributed System - A network of computers, calculators, and microprocessors where the digital mainframes talk to each other.

Guidelines

The following guidelines can be used for building general testing systems:

*The system must be versatile.

The system versatility requirements is inherent in the nature of the type of testing. And this versatility is designed into a digital system by: 1) the fact the system is software programmable, 2) hardware can usually be added by inserting more input/output (I/O) cards, and 3) most types of instrumentation (counters, DVM, etc) are being designed to connect to standard digital busses (IEEE-488, RS232, etc), which can connect to standard computer I/O cards.

*The system must be easy to use.

The personnel who perform the experiments with the

system are usually not the same ones who designed the system. Furthermore, the users are normally not extremely familiar with the computer/controller and therefore the system designer must orient the system use around the final end users. This is done by providing applications programming capabilities in high-level languages such as BASIC and FORTRAN and by making all user contact with the instruments only at the analog end, i.e. all digital interfacing and assembly language "drivers" are provided. This allows the end user to look at the system as a "friendly black box" which he can program to perform certain functions.

*The system must support multiple tasks.

General testing systems are usually quite expensive, ranging from \$50K to \$150K just for the central processor and its supporting peripherals and instruments. Therefore it is usually impossible to justify buying a separate system to perform experiments on each subsystem. One solution is to have software inherent in the computer which allows multiple tasks. This is possible because the computer can normally perform much faster than the outside world, allowing each user or task to think that they alone have a system. A computer is not all powerful, however, and there are some cases such as fast analog-to-digital conversion where one user needs system control. In these cases, a user must have the capability to "lock-up" a multiple tasks system or use another monitor which only allows one user.

*The system must separate functions when this is indicated.

The more complicated a system is, the more chance there is that the system will break down. Digital systems, although they do have a good reputation for reliability, usually fail on one of the electromechanical components such as the magnetic tape or digital disc. Other causes of system failure can be software interaction between two users and instrument failure. Since digital systems are usually reliable, failure problems normally are not considered except in two cases, control applications and long-term tests. If a piece of equipment or process is being controlled and the results of a control failure would cause problems with other equipment, the utmost care should be taken that the digital controller be reliable. Therefore a separation of functions is needed where a separate digital controller with a minimum of peripherals can be used to handle the safety or time critical work and can communicate with the central controller for mass storage and supervision. This is the distributed systems concept.

*The system must have quick-look data presentation capability.

The end result of many experiments is that they are used as the basis for defining other experiments. This requirement suggests quick-look data presentation in a form which is most meaningful to the operator. This data could be in the form of tabular listings or plots which are generated using the capabilities of the computer.

*In the case of a public use end product, the system must be easily changeable to commercial pro-

duction.

The end goal of many energy testing programs is to provide data for building commercial systems. Therefore one of the general testing system capabilities should be that its results can be used for defining specific systems. For instance, most testing starts with a lot of parameters being monitored. From the results of these tests, certain critical parameters and efficient control algorithms can be determined. These can be used with a dedicated, simpler control system in the final commercial end product. The general testing system should be capable of monitoring one of the simpler control systems so generated.

*The system must get the data in digital form as soon as possible.

One of the problems with data acquisition in an industrial environment is noise inherently generated by motors, relays, etc. These especially affect the accuracy of low-level signals such as those from thermocouples. One of the techniques of overcoming the noise problem is to get the signals into digital form as soon as possible. Digital signals have more inherent noise immunity than most analog ones, especially when the signals are required to be sent over a long distance. Therefore it is best to digitize signals as close to the source as possible.

*The system must provide a range of software languages so that the user can choose the most efficient one for his task.

There is an inherent tradeoff between the various applications software languages, the tradeoff normally being ease-of-use versus speed-of-execution. For instance, BASIC, an interpreted language, is checked line-by-line as it is input for syntax errors. To correct a line, one only needs to enter it again. This language is very operator convenient because it is easily changed. However, at run time each line must be interpreted before it is run, thus making BASIC comparatively slow. FORTRAN, on the other hand, is a compiled language. This means that a whole set of program lines are input to the machine and changed to machine language at one time. During run time, no compilation takes place and the program runs much faster. However, the source text must be edited off-line to change the program. Thus, we trade-off changeability for speed.

Applications to Solar and Wind Systems

The above guidelines were applied in designing the three solar and one wind experimental systems. The minicomputer portions of the systems are outlined in the following paragraphs.

Solar Total Energy System Test Facility (Figure 1)

The STSTF minicomputer system was the first system designed and therefore the one with the most use. Since the requirements for this facility were so broad, it was designed with the widest variety of inputs including shaft encoders, pressure sensors, flow meters, temperature sensors and discrete contact closure sensors. Control outputs include analog signals (DAC) and contact closures. The

system operates under the Hewlett Packard (HP) RTE-II monitor which allows multiple tasks to run concurrently. The initial applications language of preference was BASIC.

The original task of the system was to monitor the various solar total energy subsystems such as the turbine, thermal storage units, and collectors. However, monitoring all of these subsystems simultaneously proved to be a task which stressed the capability of the minicomputer. To solve this problem, two steps have been taken. First, some applications programs have been converted to FORTRAN, a much faster language. This conversion is relatively simple since the program flow is almost the same for both languages. Second, some of the newer collectors are being interfaced to their own microcomputer system (Figure 2). These microcomputers will communicate with the central system for setpoint information and to return data. Thus the data will be digitized close to the source and the collector will be controlled by a reliable subfunctional unit (distributed system).

Photovoltaic Test Facility

The PVTF required less of a variety of data inputs, since the basic task (measure solar input, power output versus load) is more restricted. However, due to the increase in requirements for long-term tests, the PVTF system will be developing into a large distributed system (Figure 3). The long-term tests will be conducted by local microprocessors which will transmit data to the central computer. Programmable calculators will also talk to the central for fast setup tests, but will also be able to be operated independently.

Collector Module Test Facility (Figure 4)

The main requirements for the CMTF were that it could run multiple programs simultaneously. Since it monitors three (and possibly four) fluid test loops, each loop must be capable of being programmed separately while other loops are running. The HP RTE-III monitor allows this capability and can perform the required tasks because the input data rate for each loop is slow. FORTRAN will be used for applications programs to preserve system throughput.

Vertical Axis Wind Turbine Test Facility (Figure 5)

The simplest of the four systems is the VAWTTF. This facility monitors data from one of three vertical wind turbines, the data usually being blade stress, wind speed, shaft torques, and output power under load. Since only one task must be performed at a time, the system operates under the HP DOS monitor and FORTRAN applications programs. One unique feature of the system is the use of a PCM encoder to input data from the rotating portion of the system. This eliminates many requirements for the slip ring assembly.

Summary

This paper has outlined some guidelines for applying minicomputers in the solar and wind energy areas based on Sandia's experience with four such systems. If these guidelines are used with care, useful testing systems can result.

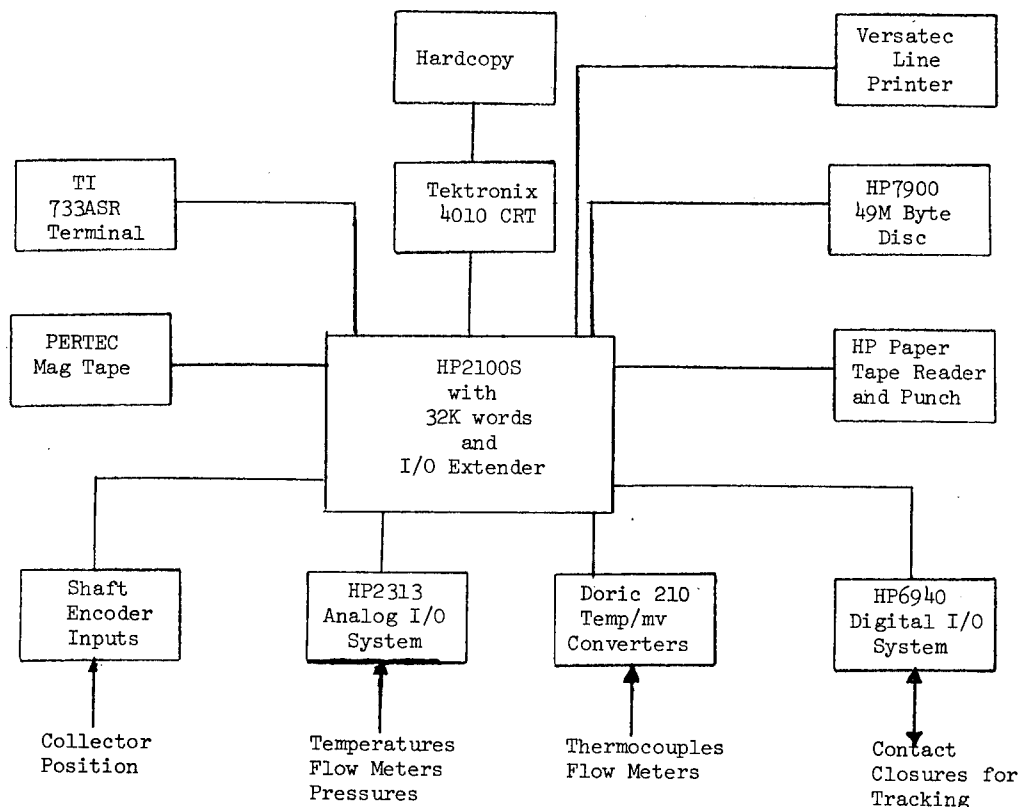


Figure 1. STESTF Block Diagram

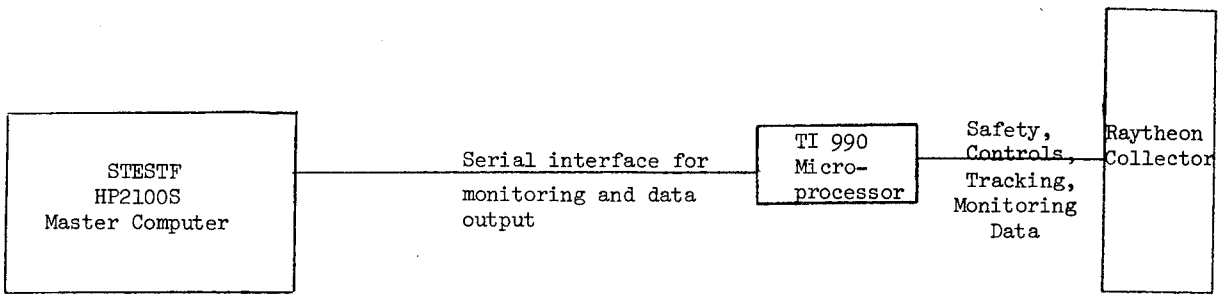


Figure 2. Microprocessor Slave System for Remote Collector

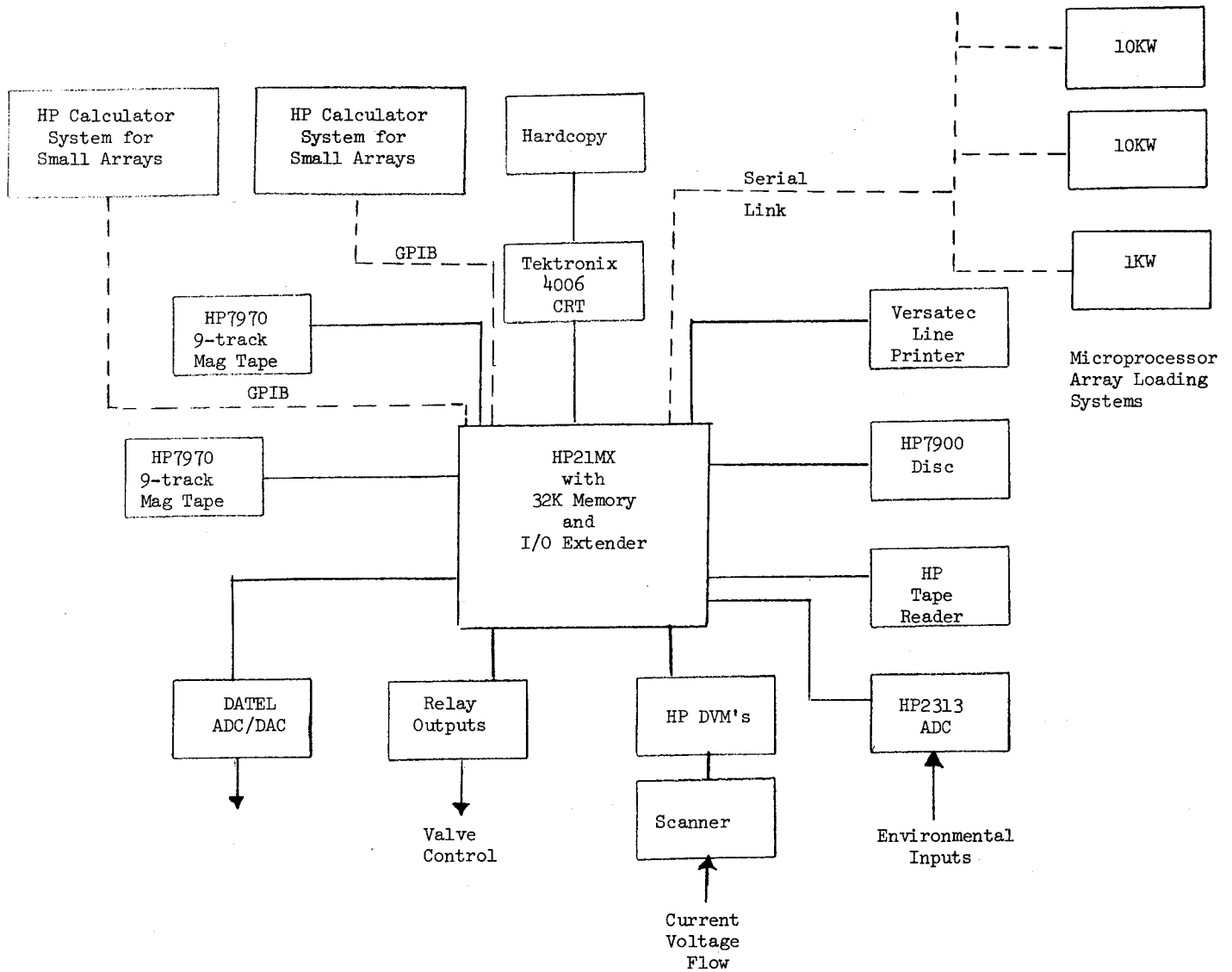


Figure 3. Photovoltaic Test Facility Block Diagram

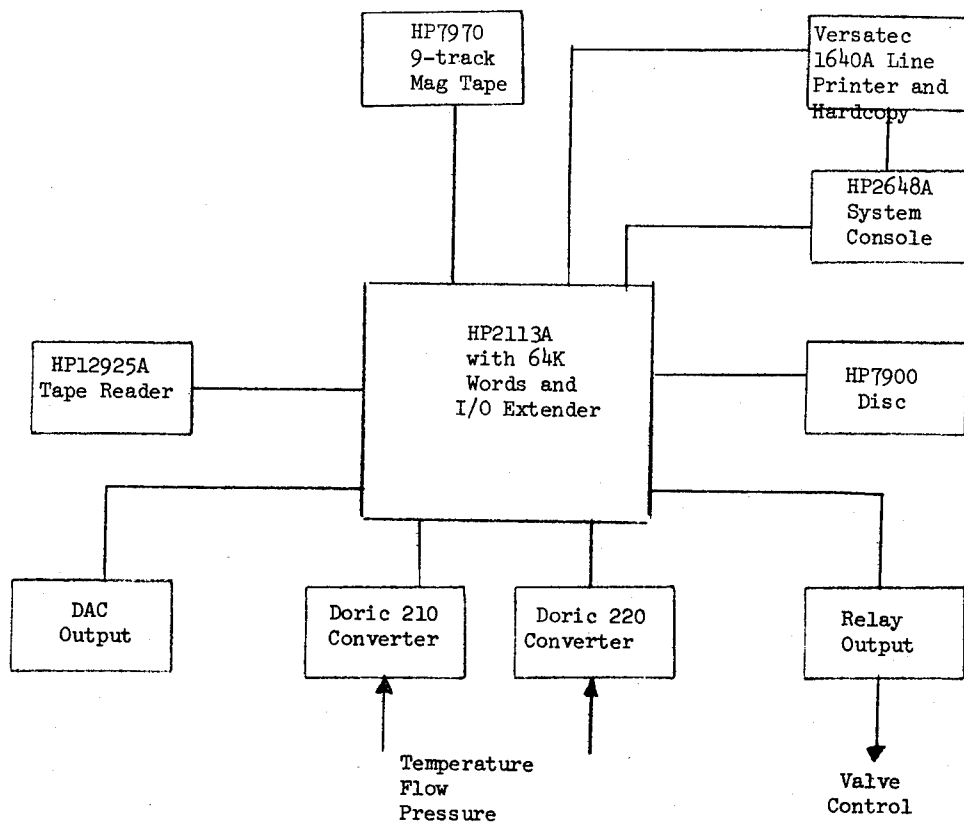


Figure 4. Collector Module Test Facility Block Diagram

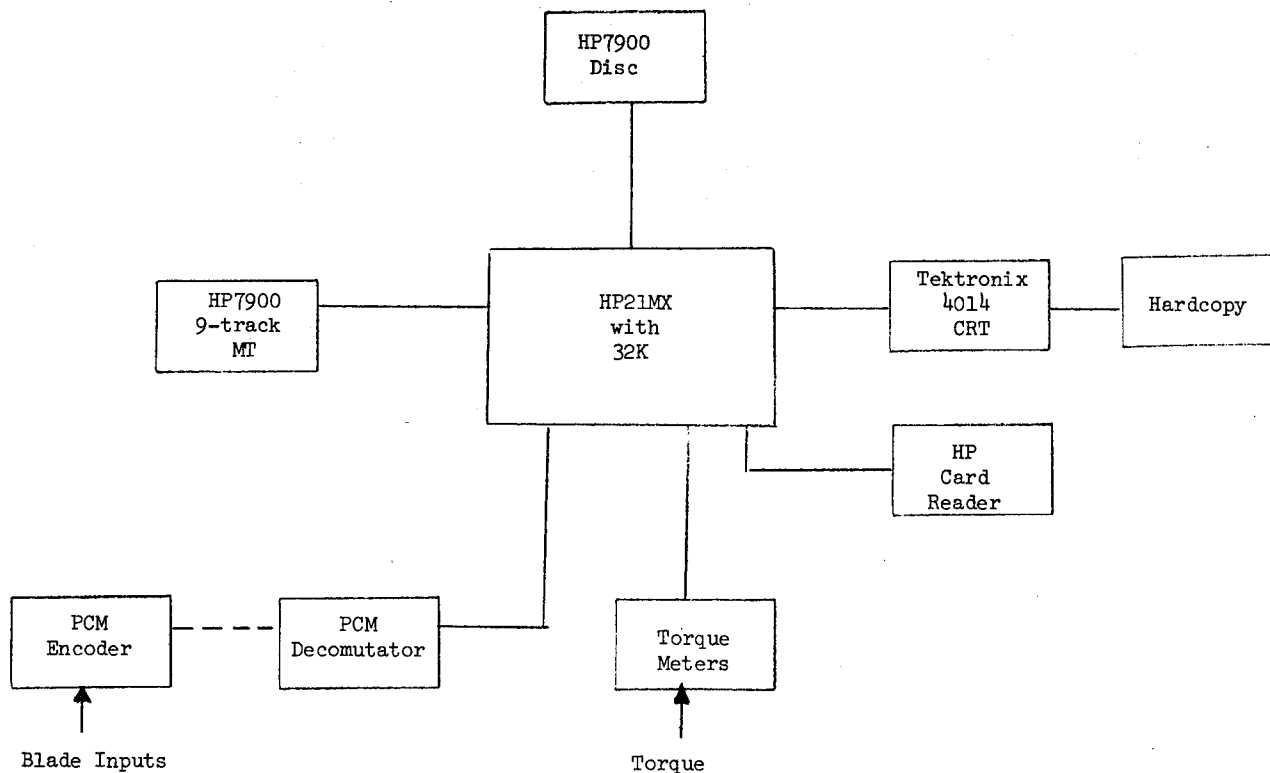


Figure 5. Vertical Axis Wind Turbine Test Facility Block Diagram